ASME
SETTING THE STANDARD

Transactions of the ASME, Journal of Fluids Engineering
(ISSN 0098-2202) is published monthly by
The American Society of Mechanical Engineers,
Three Park Avenue, New York, NY 10016.
Periodicals postage paid at New York, NY
and additional mailing offices.
POSTMASTER: Send address changes to Transactions of the
ASME, Journal of Fluids Engineering, c/o THE AMERICAN
SOCIETY OF MECHANICAL ENGINEERS,
22 Law Drive, Box 2300, Fairfield, NJ 07007-2300.
CHANGES OF ADDRESS must be received at Society
headquarters seven weeks before they are to be effective.
Please send old label and new address.

Journal of Fluids Engineering

Published Monthly by ASME

VOLUME 132 • NUMBER 5 • MAY 2010

RESEARCH PAPERS

Flows in Complex Systems

Fundamental Issues and Canonical Flows

(Contents continued on inside back cover)

This journal is printed on acid-free paper, which exceeds the ANSI Z39.48-1992 specification for permanence of paper and library materials. ♾™
♻ 85% recycled content, including 10% post-consumer fibers.

Multiphase Flows

Techniques and Procedures

TECHNICAL BRIEFS

The ASME Journal of Fluids Engineering is abstracted and indexed in the following:

Applied Science & Technology Index, Chemical Abstracts, Chemical Engineering and Biotechnology Abstracts (Electronic equivalent of Process and Chemical Engineering), Civil Engineering Abstracts, Computer & Information Systems Abstracts, Corrosion Abstracts, Current Contents, Ei EncompassLit, Electronics & Communications Abstracts, Engineered Materials Abstracts, Engineering Index, Environmental Engineering Abstracts, Environmental Science and Pollution Management, Excerpta Medica, Fluidex, Index to Scientific Reviews, INSPEC, International Building Services Abstracts, Mechanical & Transportation Engineering Abstracts, Mechanical Engineering Abstracts, METADEX (The electronic equivalent of Metals Abstracts and Alloys Index), Petroleum Abstracts, Process and Chemical Engineering, Referativnyi Zhurnal, Science Citation Index, SciSearch (The electronic equivalent of Science Citation Index), Shock and Vibration Digest, Solid State and Superconductivity Abstracts, Theoretical Chemical Engineering

A Method for Three-Dimensional Navier–Stokes Simulations of Large-Scale Regions of the Human Lung Airway

D. Keith Walters
e-mail: walters@me.msstate.edu

William H. Luke
e-mail: whl30@msstate.edu

Department of Mechanical Engineering,
Mississippi State University,
CAVS SimCenter,
P.O. Box ME,
Mississippi State, MS 39762

*A new methodology for CFD simulation of airflow in the human bronchopulmonary tree is presented. The new approach provides a means for detailed resolution of the flow features via three-dimensional Navier–Stokes CFD simulation without the need for full resolution of the entire flow geometry, which is well beyond the reach of available computing power now and in the foreseeable future. The method is based on a finite number of flow paths, each of which is fully resolved, to provide a detailed description of the entire complex small-scale flowfield. A stochastic coupling approach is used for the unresolved flow path boundary conditions, yielding a virtual flow geometry that allows accurate statistical resolution of the flow at all scales for any set of flow conditions. Results are presented for multigenerational lung models based on the Weibel morphology and the anatomical data of Hammersley and Olson (1992, "Physical Models of the Smaller Pulmonary Airways," J. Appl. Physiol., **72**(6), pp. 2402–2414). Validation simulations are performed for a portion of the bronchiole region (generations 4–12) using the flow path ensemble method, and compared with simulations that are geometrically fully resolved. Results are obtained for three inspiratory flowrates and compared in terms of pressure drop, flow distribution characteristics, and flow structure. Results show excellent agreement with the fully resolved geometry, while reducing the mesh size and computational cost by up to an order of magnitude.* [DOI: 10.1115/1.4001448]

1 Introduction

Relative to experimental studies, computational simulations are a noninvasive and inexpensive method for obtaining flow data in the human lung for research and clinical purposes. Three-dimensional Navier–Stokes computational fluid dynamics (CFD) simulations allow detailed information to be obtained regarding, for example, impedance, mass flow distribution, and local particle deposition patterns in the lung, and provide a means of examining the effects of abnormal, pathophysiological conditions.

The human lung airway is comprised of repeated dichotomous bifurcations, resulting in a multiscale branching network of significant complexity. Such large-scale, geometrically complex multibranched flow networks are common in nature due to their effectiveness at either distributing a centralized flow stream over a large area (e.g., the water/nutrient delivery system in plants), or coalescing multiple small flow streams into a single large stream (e.g., river systems). CFD has proven, in recent years, to be a viable tool for the predictive simulation of such systems, and has been used extensively to examine them in detail and provide insight into their mechanistic and/or physiologic function. One major challenge associated with CFD simulation is the sheer magnitude of such systems. For example, a common morphological description of the human lung includes over 16 million individual flow segments. The full CFD resolution of every segment requires an estimated mesh size of hundreds of billions of elements. Since fully resolved, deterministic flow simulation is therefore beyond the reach of current and even next-generation computing architectures, CFD simulations have been limited to relatively small subsections of the lung geometry, with flow in the lower (small-scale) airways either ignored completely or modeled using simple 1D or axisymmetric approximations. Similar limitations exist for CFD simulations of the human circulatory system.

One of the primary difficulties is the description of the geometry. The earliest morphological description of the bronchopulmonary tree was the symmetric model of Weibel [1]. An alternative morphology was proposed by Horsfield and Cumming [2], which specifies asymmetric geometrical attributes such as airway diameter and branching angle. Hammersley and Olson [3] presented asymmetric, cadaver-based bifurcation patterns for the human lung appropriate for generations 6–12. Hegedüs et al. [4] provided a detailed mathematical description of a morphologically realistic airway for the first five generations. Similar high-resolution models were presented by Sauret et al. [5], Schmidt et al. [6], and others. Algorithmic approaches for accurately describing the geometry of the lower airways were proposed by Kitaoka et al. [7] and Tawhai and Burrowes [8].

Bronchial flow simulations were reported in the literature for numerous idealized symmetric and asymmetric representations of subcomponents of the bronchial tree [9–14]. Several efforts reported in the literature have compared the differences between particle deposition patterns computed for idealized geometries and for realistic geometries generated by medical imaging techniques. Current studies using realistic morphologies for lung airways employ CT-scan and MRI techniques [15,16], which, while providing a more realistic geometry, cannot provide airway definitions beyond seven to nine generations. van Ertbruggen et al. [17] simulated the three-dimensional steady inspiratory flow for a model starting in the trachea and terminating at the seventh-generation airways. Their model can be characterized as a hybrid method that employs the data of Horsfield and Cumming [2] to define the generational characteristics and medical imaging techniques to provide local branch orientations.

A number of studies have demonstrated the inherent complexity of lung flow dynamics, as well as sensitivity to changes from the

Contributed by the Fluids Engineering Division of ASME for publication in the JOURNAL OF FLUIDS ENGINEERING. Manuscript received June 11, 2009; final manuscript received March 8, 2010; published online April 27, 2010. Assoc. Editor: Neelesh A. Patankar.

standard case of a simple symmetric branching morphology under steady state inspiration. Zhang and Kleinstreuer [18] performed CFD simulations in a four-generation symmetric branching model and found that flow structures arising during expiration were more complicated than those arising during inspiration. They also found that unsteady flow typical of normal breathing led to different flow features than in the steady state case, and that this difference was exacerbated during high frequency ventilation. Guan and Martonen [19] demonstrated quite clearly, using a simple curved tube model of branch segments defined by the Horsfield–Cumming [2] morphology, that the flow in the upper airways of the lung is not fully developed. The authors used dimensional analysis to conclude that it is unlikely that fully developed flow is achieved within any of the airways of the human lung, suggesting that a 1D or axisymmetric model is inappropriate, even for the smallest airways. A symmetric four-generation model was recently used by Luo et al. [20] to investigate the effect of COPD on particle deposition in the upper lung airways. Results showed significant influence on particle deposition efficiency within and downstream of obstructed airways. Furthermore, Yang et al. [21] previously examined three-generation airway models for both healthy and COPD cases, and found that the velocity profile entering individual flow segments has a substantial effect on flow patterns, deposition, and pressure drop, highlighting the importance of accurate coupling between the upstream and downstream flow regions.

Very few CFD studies have attempted to simulate the flow in either the entire conducting zone or the entire lung. Four notable attempts include the sequential simulations of Nowak et al. [22] and Zhang et al. [23], the hybrid CFD/1D model of Ma and Lutchen [24], and the partially resolved 17-generation model of Gemci et al. [25]. Nowak et al. [22] performed a series of simulations in progressively smaller 3.5 generation symmetric branching segments, for which the inlet condition applied to each section was obtained from the previous simulation of the next larger section (for inspiratory flow). In order to "close" the model, the unresolved outlet boundary conditions in each section needed to be prescribed a priori. The authors concluded that a constant pressure boundary condition was inappropriate, but that a constant mass flow rate condition (in which the mass flow was equally divided among all outlets) resulted in a relatively small error. While this conclusion may hold for the simple, symmetric, 90 deg oriented branching geometry used in their study, such an approach will produce physically unrealistic results in more geometrically accurate asymmetric models of airway structure [14].

Zhang et al. [23] recently documented a similar sequential methodology for prediction of nanoparticle deposition throughout 16 generations. In contrast to Nowak et al. [22], a constant pressure outlet boundary condition was used for each three-generation subsection. For both studies, the sequential solution method did not allow a full simultaneous coupling of the flow in the lung at all scales.

The hybrid model of Ma and Lutchen [24] combined fully resolved CFD simulation of the upper airways up to generation 6 with a 1D transmission line model of the impedance of the small-scale airways. Their results showed good prediction of overall lung impedance when compared with experimental data for healthy lungs with breathing frequencies up to 8 Hz. A detailed investigation of small-scale flow and particle deposition was not included in the study. Nevertheless, the effort represents a state-of-the-art attempt to simulate unsteady respiration using combined CFD and reduced order modeling.

Most relevant to this study, Gemci et al. [25] recently presented a simulation of 17 generations of the human lung based on the anatomical model of Schmidt et al. [6]. The geometry was only partially resolved, containing 1453 bronchi as opposed to approximately 2^{17} for a fully resolved model. In contrast to Ma and Lutchen [24], the authors applied an equal constant pressure condition at all flow outlets. The pressure drop across the entire geometry obtained from the simulations was 33% lower than the measured value reported by Hyatt and Wilcox [26]. It should be noted that the mesh contained only 6.7 million cells, which, according to the authors, did not allow mesh independent results to be obtained. However, the study represents a significant attempt to represent the flow in large sections of the bronchopulmonary tree using 3D CFD simulation of a reduced number of resolved flow paths. In that sense, the methodology presented in this paper bears much in common with the approach adopted in Ref. [25].

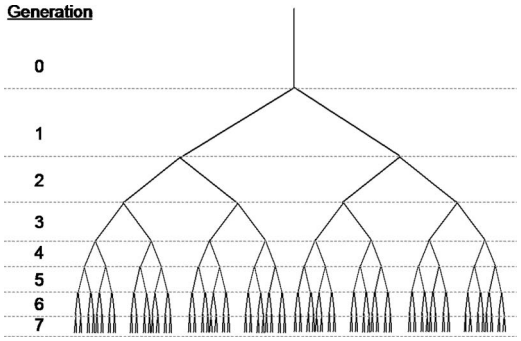

Fig. 1 Illustration of the generational description for a dichotomous branching network

Because the flow in the lung is highly complex, sensitive to the details of anatomical features and ventilation rates, and strongly coupled across all scales, it is desired to perform CFD simulations that provide true multiscale and simultaneous resolution of the entire flow network. Such an approach eliminates the need for reduced order or empirical modeling and has the potential to provide a truly predictive computational analysis methodology. One solution is to rely on computing systems to become large enough and fast enough to perform fully deterministic simulations of the entire airway geometry. Assuming that simulation of eight generations is representative of the current capability (most recent studies have used smaller geometries) and that Moore's law holds, then the computational power necessary to simulate the entire lung for practical research and clinical applications is still at least 30 years away. This paper presents an alternative methodology with the intent of leapfrogging that delay.

2 New Modeling Methodology

The new method presented here consists of three elements: a systematic, statistical description of the geometry and branching characteristics (morphology); selection of a set of distinct representative flow paths to be included in the simulation (flow path ensemble); and application of physically realistic boundary conditions to the unresolved flow inlets and/or outlets.

2.1 Morphology. The human airway tree consists of several million distinct flow segments, making a complete patient-specific anatomical representation intractable. An alternative approach adopts a morphological description based on available data obtained from prior experiments. For this effort, we adopt the generational description of the bronchopulmonary tree first proposed by Weibel [1]. As shown in Fig. 1, it is characterized by successive branch points with one parent and two daughter airways. The complete airway is typically represented by 23 generations, with generation 0 corresponding to the trachea, generations 1–3 to the upper bronchi, generations 4–16 to the bronchioles, and generations 17–23 to the pulmonary zone terminating in the alveolar sacs. The generational description is convenient and physiologically realistic, although an alternative method was presented by Horsfeld and Cumming [2], in which individual flow segments are numbered according to the number of branch points between them and the alveoli. It should be pointed out that the simulation

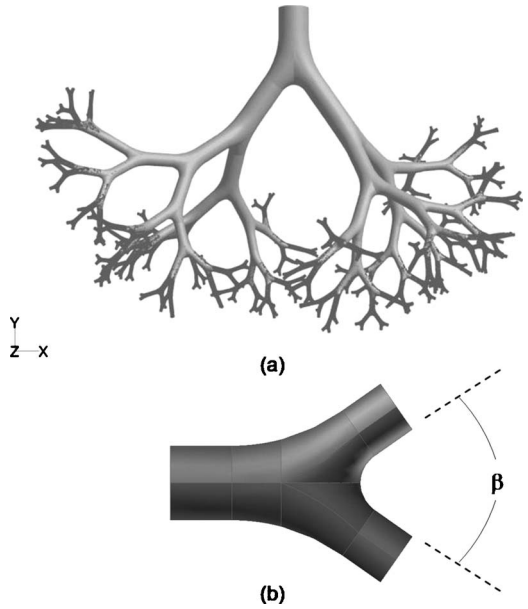

Fig. 2 Eight-generation model of the bronchial region based on the (*a*) Weibel [1] lung morphology, comprised of (*b*) successive parent-daughter branching units

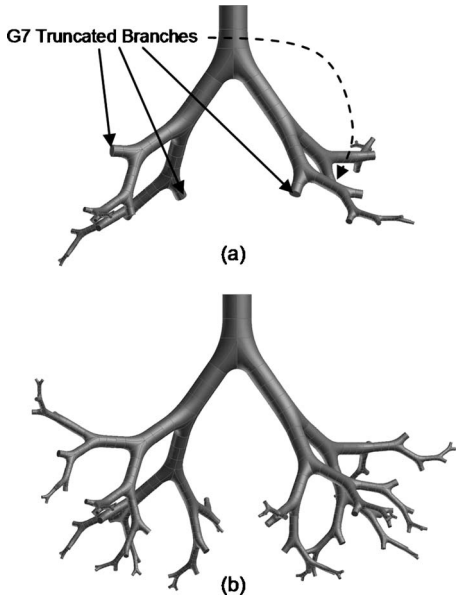

Fig. 3 Flow path ensemble models obtained by truncating the eight-generation airway tree shown in Fig. 2(*a*): (a) 4-path ensemble and (b) 16-path ensemble

method presented here can be applied to any network morphology, provided that a statistical representation of the geometry can be explicitly defined.

An example of an eight-generation airway tree is shown in Fig. 2(*a*). The tree is constructed of repeated symmetric parent-daughter bifurcations illustrated in Fig. 2(*b*), with a constant branching angle (β) of 70 deg. The bifurcation plane rotation angles following each branch location were randomly selected using an online random number generator with equally weighted probability between 0 deg and 180 deg. The geometry was constructed using a "top down" approach, in which the generations were constructed sequentially by addition of successive parent-daughter branching units. If, in the process of adding and rotating the next branching unit, it was found that there was interference or intersection between separate parts of the geometry, then a new random orientation angle was computed for that branching unit. The total number of included airway segments in the model is 511. The number of flow paths, defined as the number of possible distinct paths that may be taken by a fluid particle traveling through the branching network, is equal to the number of terminal flow outlets—256.

2.2 Flow Path Ensemble. A reduced geometry that approximates the airway tree in Fig. 2(*a*) may be constructed by truncating all but a relatively small number of the flow paths. Examples are shown in Fig. 3, in which 4 and 16 flow paths are retained from the original model in Fig. 2(*a*). We refer to these as four-path and 16-path ensembles, respectively. To construct the four-path ensemble model, for example, the following procedure is followed. First, noting that the inlet parent airway is generation 4 (G4), the full geometry representation is retained through G6. Beyond G6, one of the two daughter branches following any bifurcation is truncated (cut) halfway to the next bifurcation. The other daughter branch is retained. So, as shown in Fig. 3(*a*), there are four truncated branches for G7 (note that the rightmost truncation in the view shown is located behind one of the resolved branches). Following the retained G7 branches, a similar procedure is applied to the G8 branches after each bifurcation, with one G8 daughter branch being truncated and one retained. The process is continued down the length of the geometry, with one path truncated and one retained, following every bifurcation downstream of G6. The decision of which daughter branch to truncate and which to retain was made randomly, i.e., an online random number generator (based on a 50/50 probability) was used to arbitrarily determine which branch to cut. Once all of the truncations had been performed, the remaining geometry consisted of four distinct flow paths, defined as a set of successive branches that lead from the inlet airway to the terminal (G12) outlets. Likewise, for each generation between G6 and G12, there are four truncated daughter branch segments. The resulting flow path ensemble (FPE) model is similar to reduced geometry models used by previous investigators for large sections of the bronchial tree [22,23,25]. Following the majority of studies in the literature, the modeling approach adopted here assumes that the terminal outlet (G12) pressure is known. However, at each of the truncated branch outlets between G6 and G12, the pressure is unknown. These boundaries are therefore referred to as unresolved flow outlets.

Note that the procedure described above can be used to derive models containing any number of complete flowpaths that are a multiple of 2. For example, a 16-path ensemble is illustrated in Fig. 3(*b*). In that case, truncation of daughter branch segments begins downstream of G8. For all generations between G8 and G12, there are therefore 16 unresolved flow outlets.

As reported in previous studies, the primary difficulty associated with simulations of such reduced geometries is the application of physically realistic boundary conditions at the unresolved flow outlets, which arise due to the truncation of the geometry at generations higher than the terminal one, as indicated in Fig. 3. Two approaches previously adopted for inspiratory flow include application of an a priori pressure condition, and iterative manipulation of the pressure conditions to achieve an equal mass flow split within each daughter branch.

2.3 Stochastically Coupled Boundary Conditions. The alternative boundary condition method proposed here is stochastic coupling of the retained flow paths via the unresolved boundary conditions. For the case of inspiration, it is necessary to apply a static pressure condition at each unresolved boundary. The value of static pressure at each unresolved outlet is set equal to the plane-averaged value of static pressure at an equivalent location (i.e., in the same generation) within one of the resolved flow paths, as illustrated in Fig. 4. Since the truncations were made in the middle of the branch segment (between bifurcation locations),

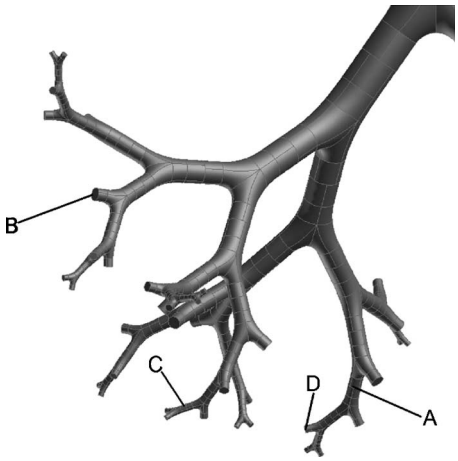

Fig. 4 Example of the stochastic coupling method for unresolved boundary conditions. The resolved pressure at location A is mapped to the unresolved outlet location B, C is mapped to D, etc.

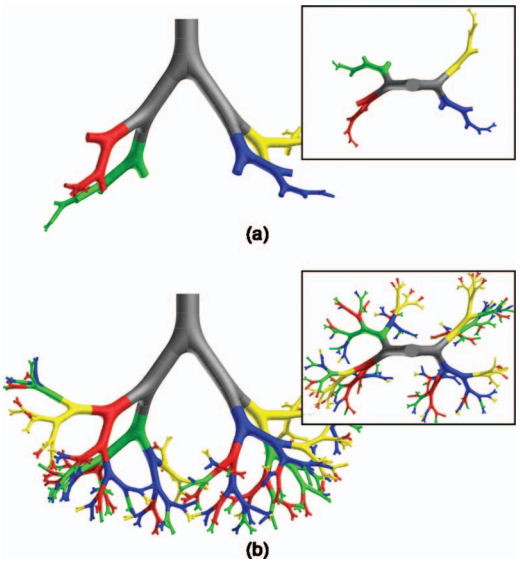

Fig. 5 Illustration of the virtual geometry created by stochastic coupling of unresolved boundary conditions. The real 4-path geometry is shown in (*a*), and the virtual geometry in (*b*).

the pressures are similarly mapped from the middle of the retained branch segments. Because the number of retained and truncated branches for any generation is equal, a one-to-one mapping is used, i.e., each unresolved outlet has a unique pressure mapped from one (unique) interior location. The pressure at the unresolved outlets is therefore variable, even among unresolved outlets in the same generation. Significantly, the unresolved boundary conditions are not applied a priori, but instead evolve along with the predicted flow within the resolved flow paths as the simulation proceeds. In theory, the method may therefore be applied to both steady and unsteady (breathing) cases.

The coupling between resolved and unresolved locations is chosen randomly as follows. First, the unresolved outlets and retained interior locations are numbered arbitrarily. For example, in the four-path ensemble, each generation contains unresolved outlets of 1–4 and resolved branches 1–4. To select the interior location to be mapped to unresolved outlet number 1, simply apply a random number generator (with 25% probability) to select between the interior locations. Proceeding to unresolved outlet number 2, apply a random number generator (now with 33% probability) to select between the remaining interior locations, and so on. This procedure is followed at each generation that contains unresolved flow outlets.

By applying analogous pressure conditions at each unresolved outlet, it is possible to create a "virtual geometry" in which all flow paths are coupled to one another in a probabilistic or stochastic sense. The virtual geometry concept is illustrated in Fig. 5. The four-path ensemble is shown in Fig. 5(*a*), with each flow path shown in a different color. The coupling between unresolved and resolved locations is conceptually illustrated in Fig. 5(*b*), in which the "virtual" downstream geometry at each unresolved outlet is indicated by the color of the resolved flow path from which the boundary condition is chosen. The exact nature of the virtual geometry is dependent on the choice of coupling, but the key point is that a realistic statistical approximation of the full geometry is possible even though only a (relatively) small number of flow paths are actually resolved in the simulation.

3 Validation Test Cases

In order to validate the proposed methodology, CFD simulations were performed using the eight-generation airway in Fig. 2(*a*), a model of generations 4–12 in the human bronchopulmonary tree. Results were obtained for four-, eight-, and 16-path ensemble models, and compared with results obtained with the full geometry. For the FPE models, two sets of simulations were run, in which the unresolved outlet boundary conditions in the geometrically reduced models were set with either an a priori applied pressure or with the stochastic coupling approach described in Sec. 2.

3.1 Rationale. CFD simulation of flow in the lung is nontrivial, and differences between computations and real patient-specific airflows can be attributed to many factors. These include differences in geometry, both the morphological parameters and the anatomical details such as carinal ridges and mucosal layers, as well as differences in boundary conditions, such as dilation versus pressure-driven flow and variable pressure conditions at the terminal alveoli in different sections of the lung. Likewise, the CFD simulations may contain errors due to insufficient mesh resolution, numerical methods, and turbulence modeling.

The effort presented here seeks to provide computational investigators with a means of performing fully coupled, three-dimensional Navier–Stokes simulations throughout large sections of the airway tree, using currently available and next-generation computing hardware. The objective is to develop a method that yields results with a computationally inexpensive reduced geometry CFD model that closely approximate the results that would be obtained with a complete, fully resolved CFD model. The relevant comparison required to validate the new approach is therefore between fully resolved models and reduced (FPE) models, rather than between CFD simulations and experimental data. It is expected that the method presented here will allow future large-scale simulations (up to the entire lung airway) that can be used to further investigate and refine the use of CFD for prediction of lung airway dynamics during respiration.

3.2 Simulation Details. The geometry for the test cases is depicted in Fig. 2(*a*). It is based on the Weibel [1] morphology, and assumes uniform branching angle (β=70 deg), length-to-diameter ratio (L/D=3), and parent-to-daughter diameter ratio (D_p/D_d=1.33) for all generations. These values were chosen based on the approximate averages of the intragenerational data of Hammersley and Olson [3], and represent a reasonable approximation of the upper bronchiole region. Bifurcation plane rotation angles were chosen randomly between 0 deg and 180 deg, as discussed above. During the top down construction of the model, if an initially chosen rotation angle resulted in interference

Table 1 Geometry and flow parameters

Generation	Segments	D (cm)	Q (cm^3/s)	V_{avg} (m/s)	Re_{avg}
4	1	0.570	20.83	0.82	319
5	2	0.427	10.42	0.73	213
6	4	0.320	5.21	0.65	142
7	8	0.240	2.60	0.57	94
8	16	0.180	1.30	0.51	63
9	32	0.135	0.65	0.45	42
10	64	0.101	0.33	0.40	28
11	128	0.076	0.16	0.36	19
12	256	0.057	0.08	0.32	12

between two separate airways, a new random angle was chosen, until all airways were completed.

Simulations were performed for steady inspiratory flow at three volumetric flow rates: 10.42 cm^3/s, 20.83 cm^3/s, and 31.25 cm^3/s, corresponding to inhalation rates of 167 cm^3/s, 333 cm^3/s, and 500 cm^3/s, respectively. The geometric and average flow parameters for each generation are shown in Table 1 for the middle flow rate (20.83 cm^3/s) case.

All simulations were performed with the commercial CFD code FLUENT®. Steady state solutions were obtained, assuming air as the working fluid with a constant density $\rho=1.225$ kg/m^3 and dynamic viscosity $\mu=1.7894\times10^{-5}$ kg/m s. The segregated solver was employed with the SIMPLE method [27] for pressure-velocity coupling, second order upwind discretization [28] for the velocities, and the PRESTO! discretization scheme [29] for the pressure. Because the simulations began at the fourth generation, and based on the Reynolds numbers shown in Table 1, laminar flow was assumed for all cases. Uniform inlet velocities were prescribed at the flow inlet, uniform (zero) pressure was applied at the terminal (G12) outlets, and the no-slip condition was applied at all walls. The stochastic coupling method for unresolved outlets was implemented using the user-defined function capability available in FLUENT ®.

In order to determine an appropriate level of mesh resolution, a grid refinement study was undertaken using a partial geometry made up of five parent-daughter bifurcations. Simulations were performed on three successively finer mesh levels consisting of approximately 356 K, 560 K, and 1.29M cells. The finest and coarsest meshes are illustrated in Fig. 6. Results were compared in terms of pressure drop, mass flow distribution, and magnitude of primary and secondary velocities at the outlets. All quantities were within 1% between the three grids, so the coarsest resolution level was chosen for the larger test models.

The meshes for the larger test cases were constructed using geometrically similar topology and sizing within each generation. As such, the number of mesh cells for each bifurcation section was approximately the same throughout the model. As shown in Fig. 6, a triangular prism mesh was used in the near-wall region to effectively resolve the boundary layer development, and tetrahedral cells were used in the core region. An illustration of the surface mesh near the terminal (G12) outlets is shown in Fig. 7.

The overall mesh size for the fully resolved geometry was 23M cells. Mesh sizes for the 4-, 8-, and 16-path FPE models were 1.4 M, 2.5M, and 4.3M cells, respectively. It was found that the required CPU time for convergence was proportional to mesh size, regardless of the approach used. Application of the stochastic coupling method resulted in a negligible increase in CPU time per iteration and no increase in the number of iterations required for convergence. The decrease in computational expense versus the fully resolved model therefore ranged from approximately 81% (16-path) to 94% (four-path) with the new methodology.

3.3 Results. Pressure contours on the airway walls for the middle flow rate ($Q_{in}=20.83$ cm^3/s) are shown in Fig. 8 for the fully resolved geometry, as well as for the 4- and 16-path FPE models with stochastic coupling. All three simulations show qualitatively similar distributions of pressure. Most significant is the pressure levels at the unresolved outlets in the FPE models with stochastic coupling. These values closely match the pressures at the same locations in the fully resolved model, highlighting the effect of the stochastic coupling methodology. In contrast, results obtained with uniform zero outlet pressures are shown in Fig. 9. The difference in pressure distribution between the full and the FPE geometries is apparent, as is the difference between the 4- and 16-path ensemble cases.

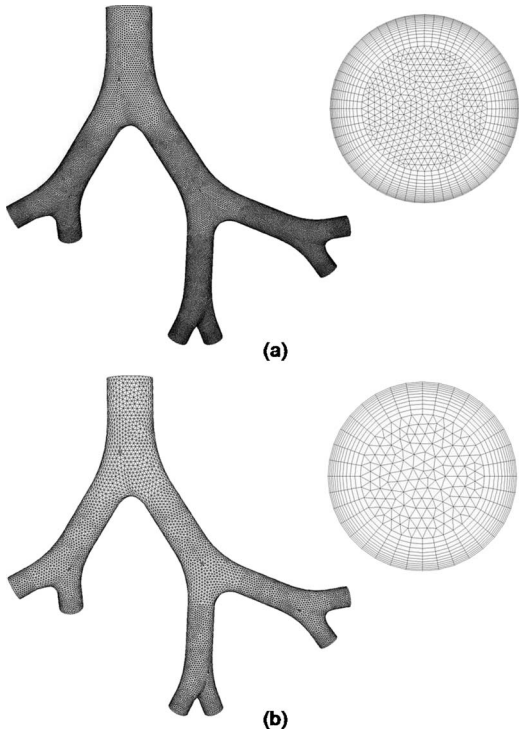

Fig. 6 (*a*) Fine mesh and (*b*) coarse mesh used in mesh resolution study. Validation test case results were obtained with the resolution level showed in (*b*).

Velocity contours and in-plane velocity vectors for the middle flow rate case are shown in Fig. 10 within two randomly selected flow segments, one in generation 9 and one in generation 11. Results shown are from the same locations in the fully resolved model and the FPE model with stochastically coupled boundary conditions. Two planes within the flow segment are shown in each case, one approximately 10% of the segment length downstream

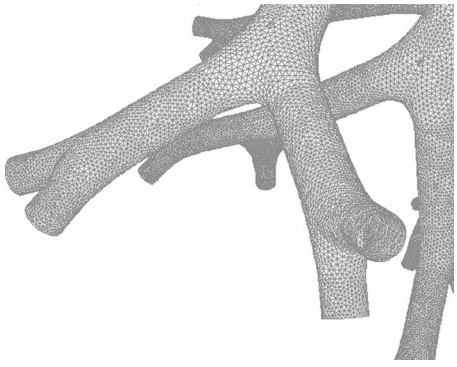

Fig. 7 Illustration of mesh resolution near terminal outlets for all validation cases

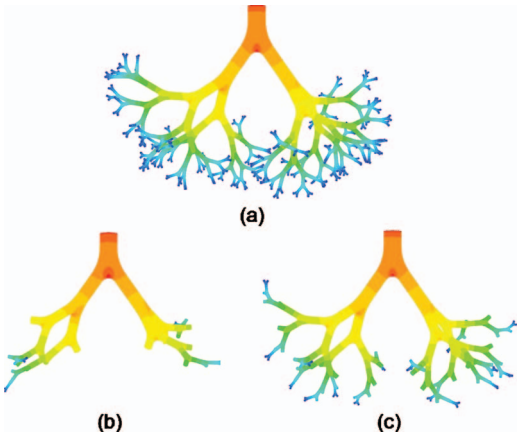

Fig. 8 Predicted pressure contours on airway walls using stochastically coupled boundary conditions: (*a*) full geometry; (*b*) 4-path ensemble; (*c*) 16-path ensemble

of the preceding bifurcation, and one 90% of the length through the segment. The asymmetry in the velocity field and the secondary flow features are apparent just downstream of the bifurcation, however, viscous effects quickly lead to a Poiseuille type flow by the end of the segment. A reduction in secondary flow and asymmetry as the generation number increases (and Re decreases) is also apparent. The qualitative agreement between the fully resolved geometry and the FPE models is again quite good.

Quantitative results for the middle flow rate case are given in Table 2, which lists the computed dimensionless pressure drop through the airway tree and the average flowrate at the terminal outlets for each of the seven models employed. Dimensionless pressure drop is here defined as

$$C_{\Delta P} = \frac{\Delta P \cdot D_{\text{in}}^3}{\mu \cdot Q_{\text{in}}} \tag{1}$$

$$\Delta P = P_{t,\text{in}} - P_{\text{out}} \tag{2}$$

where D_{in} is the diameter at the inlet section, Q_{in} is the inlet volumetric flowrate, $P_{t,\text{in}}$ is the computed total pressure at the inlet plane, and P_{out} is the static pressure applied at the terminal outlets. The table also shows the percent error for each method, relative to the case using a fully resolved geometry. Not surprisingly, the cases using a uniform outlet pressure show some improvement as the number of flow paths increases from 4 to 16, however, even

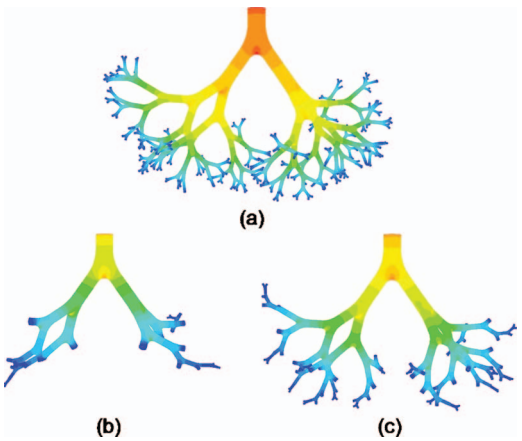

Fig. 9 Predicted pressure contours on airway walls using a priori pressure boundary conditions: (*a*) full geometry; (*b*) 4-path ensemble; (*c*) 16-path ensemble

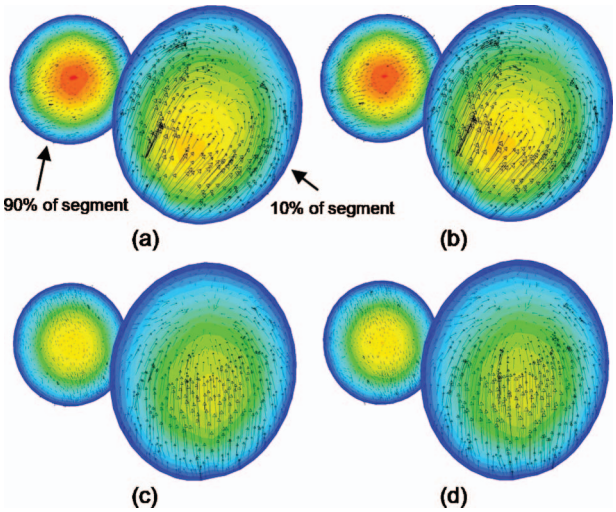

Fig. 10 Velocity magnitude contours and in-plane velocity vectors: (*a*) generation 9, full geometry; (*b*) generation 9, 16-path FPE model; (*c*) generation 11, full geometry; (*d*) generation 11, 16-path FPE model

the 16-path FPE shows an error in pressure drop of 38%, and an error in the average terminal outlet mass flow rate of 84%. In contrast, the stochastic coupling method yields very good agreement with the fully resolved model, even for the four-path FPE.

The variation in dimensionless pressure drop with inlet flow rate is plotted in Fig. 11, for both the 16-path FPE model with

Table 2 Comparison of results—validation case

Case	$C_{\Delta P} \times 10^{-3}$	(% error)	Q_{outlet} (cm^3/s)	(% error)
Full geometry	2.967	–	0.0810	–
		Coupled BCs		
4-path FPE	3.007	1.32	0.0826	2.00
8-path FPE	2.976	0.30	0.0814	0.49
16-path FPE	2.970	0.08	0.0811	0.14
		Constant BCs		
4-path FPE	1.228	58.6	0.0036	95.6
8-path FPE	1.519	48.8	0.0065	91.9
16-path FPE	1.846	37.8	0.0127	84.4

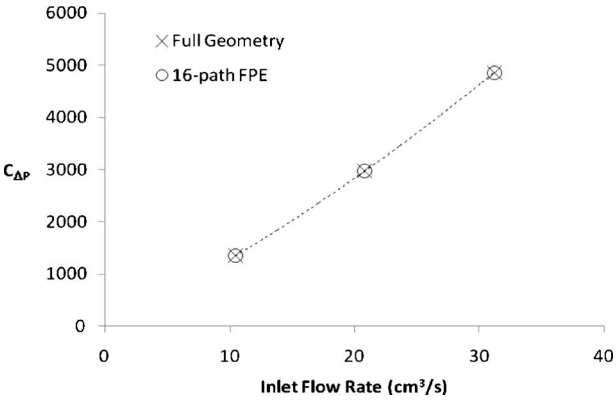

Fig. 11 Dimensionless pressure drop versus inlet mass flow rate for validation test cases

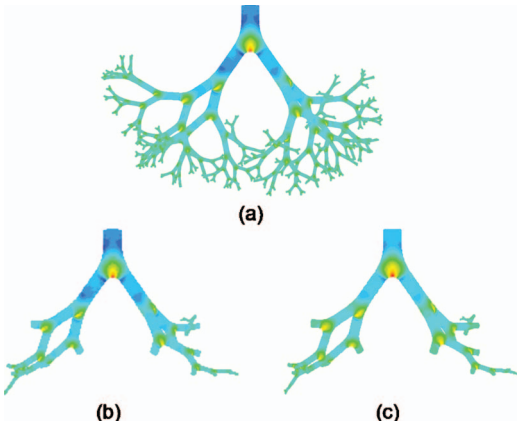

Fig. 12 Predicted pressure contours on airway walls for the high-Re case: (*a*) full geometry; (*b*) 4-path ensemble with stochastically coupled BCs; (*c*) 4-path ensemble with uniform pressure BCs

stochastically coupled boundary conditions and the fully resolved model. The results lie essentially on top of one another, and are well fit by a quadratic equation of the form

$$C_{\Delta P} = 0.0046 \cdot Q^2 + 115.29 \cdot Q \tag{3}$$

where Q is the inlet flow rate in cm^3/s. The fact that pressure drop varies nonlinearly with flow rate indicates a Reynolds number dependence and suggests that the formation of secondary flow and nonuniform velocity distributions due to branching is significant in the bronchial zone, consistent with previous observations [14,19,21].

4 Discussion

4.1 Reynolds Number Scaling. The results presented above suggest that the new modeling methodology provides an effective means of simulating large-scale branching networks using significantly reduced geometries, without the need for a priori specification of unresolved boundary conditions. One concern, however, is the fact that the flowfield in the model investigated is dominated by viscous effects, as evidenced by the rapid damping of secondary flow features shown in Fig. 10. Specifically, it was questioned whether the agreement highlighted in Table 2 would scale to larger Reynolds numbers, in which inertial effects, turbulence, and secondary flow formation play a more important role in the flow development.

To test this, an artificial case was constructed using an identical geometry as the cases above, but with a Reynolds number 1000 times the middle flow rate case above. While this is well beyond the range of realistic lung flow, it was chosen in order to evaluate the performance of the methodology at the opposite extreme from viscous-dominated flow. Since the Reynolds number ranged from approximately 320,000 at the (G4) inlet to 12,000 at the (G12) outlets, the flow was assumed to be turbulent. The simulations used the standard k-ω model available in FLUENT® [29], with turbulence inlet conditions corresponding to turbulence intensity (Tu) equal to 1%, and a turbulence length scale equal to 1/10th of the inlet diameter.

Pressure contours for the artificial high-Re case are shown in Fig. 12, comparing the fully resolved geometry with the four-path FPE case. Note the qualitative differences between this figure and Fig. 9, including the much higher stagnation pressures at the branch locations relative to the inlet pressure. In Table 3, the dimensionless pressure drop and average terminal outlet mass flow rate are compared between the FPE model and the case with fully resolved geometry. Significantly, the relative error in the FPE method with stochastic coupling remains very small, suggesting

Table 3 Comparison of results—high Re case

Case	$C_{\Delta P} \times 10^{-3}$	(% error)	Q_{outlet} (m^3/s)	(% error)
Full geometry	139.3	–	0.0810	–
		Coupled BCs		
4-path FPE	140.3	0.75	0.0807	0.35
		Constant BCs		
4-path FPE	157.2	12.8	0.0921	13.7

that the approach may be used over a wide range of Reynolds numbers. Note also that the results using an applied constant pressure condition for the unresolved outlets are significantly better for the high-Re cases than for the cases in Sec. 3. Interestingly, the results using constant pressure outlet conditions for the high-Re case tend to overpredict the pressure drop and average outlet mass flow rate, exactly the reverse of the trend shown in Table 2. However, the stochastically coupled boundary conditions still yield errors that are smaller by approximately an order of magnitude, despite the fact that the qualitative agreement illustrated in Fig. 12 appears to be similar for both types of boundary conditions.

4.2 Extension to Larger Networks. The eight-generation network used here was chosen in order to make possible multiple simulations with the fully resolved geometry, which could be used for comparison with and validation of the FPE method. The true potential of the method lies in its extension to much larger networks. For example, possible use of the FPE method for whole lung simulations is highlighted in Table 4. Based on the Weibel [1] morphology, a fully resolved simulation would require inclusion of 23 generations, with a resulting model size as shown. Analogous 16-, 64-, and 256-path ensemble models are also included in the table for comparison. The resulting number of branch points and estimated mesh size (based on the mesh resolution used in this study) for each model is shown in the table. It is clear that simulation of the full geometry is well beyond the capabilities of currently available computer systems. However, even the 256-path FPE model, with approximately 187M mesh cells, is achievable using modern high performance computing systems, and is likely to be within the capability of next-generation desktop architectures. Such a model would provide 256 different realizations of the flow in segments for each of generations 9–23, allowing statistical measures of flow characteristics such as impedance and particle deposition efficiency to be accurately obtained from the simulations.

It should be reiterated that the method proposed here does not require a generational description of the geometry as used by the Weibel [1] morphology. The only requirement is that a statistical description be used so that equivalent locations in the flowpath can be defined. For example, the method could be used with the morphology model of Horsfield and Cumming [2], in which equivalent locations for boundary condition coupling would be identified by their diameter and their number distance to the terminal alveoli. The method could also be adapted for use with newer, lung-filling morphology models, such as those developed by Kitaoka et al. [7] and Tawhai and Burrowes [8].

Table 4 Estimated cost of whole lung simulations

Model	Resolved branches	Mesh size (cells)
Full geometry	16,777,215	7.2×10^{11}
16-path FPE	335	14×10^6
64-path FPE	1215	52×10^6
256-path FPE	4351	187×10^6

5 Conclusions

The FPE method presented here is intended to provide a means of efficiently representing a large-scale flow network, by using a reduced geometry consisting of only a small fraction of the number of discrete flow paths in the overall network. For the case of airflow in the lung, the FPE method allows approximate representation of the smaller airways in a statistical sense, based on available morphological data. The stochastic coupling boundary condition method outlined here addresses one of the critical issues related to reduced geometry Navier–Stokes simulations, namely, the application of physically realistic boundary conditions for unresolved flow outlets arising from truncation of the geometry. Results obtained on a representative geometry based on the Weibel [1] morphology indicate that the FPE method with stochastically coupled boundary conditions can provide statistical results, including pressure drop and mass flow rate distribution, to within a few percent of similar simulations using the fully resolved geometry. However, the simulations based on the FPE method can reduce the computational cost by an order of magnitude or more.

It is anticipated that the approach outlined here can be used to improve the predictive capability CFD simulations of the lung airway for research and clinical purposes. For example, the flow path ensemble method could be used to model the lower airways, coupled with a realistic, fully resolved, patient-specific model of the orotracheal region and upper airways such as those in Refs. [15,16]. Such an approach would effectively take advantage of high-resolution anatomical reconstructions for the large scales, as well as the capability of the flow path ensemble method to accurately reproduce the details of the small-scale flowfield in a statistical sense.

Acknowledgment

The authors gratefully acknowledge the National Science Foundation for their support of this work under Grants No. EPS-0556308 and EPS-0903787.

References

[1] Weibel, E. R., 1963, *Morphometry of the Human Lung*, Academic, New York.
[2] Horsfield, K., and Cumming, G., 1968, "Morphology of the Bronchial Tree in Man," J. Appl. Physiol., **24**(3), pp. 373–383.
[3] Hammersley, J., and Olson, D., 1992, "Physical Models of the Smaller Pulmonary Airways," J. Appl. Physiol., **72**(6), pp. 2402–2414.
[4] Hegedüs, Cs. J., Balásházy, I., and Farkas, Á., 2004, "Detailed Mathematical Description of the Geometry of Airway Bifurcations," Respir. Physiol. Neurbiol., **141**(1), pp. 99–114.
[5] Sauret, V., Goatman, K. A., Fleming, J. S., and Bailey, A. G., 1999, "Semi-Automated Tabulation of the 3D Topology and Morphology of Branching Networks Using CT: Application to the Airway Tree," Phys. Med. Biol., **44**(7), pp. 1625–1638.
[6] Schmidt, A., Zidowitz, S., Kriete, A., Denhard, T., Krass, S., and Pietgen, H.-O., 2004, "A Digital Reference Model of the Human Bronchial Tree," Comput. Med. Imaging Graph., **28**(4), pp. 203–211.
[7] Kitaoka, H., Takaki, R., and Suki, B., 1999, "A Three Dimensional Model of the Human Airway Tree," J. Appl. Physiol., **87**(6), pp. 2207–2217.
[8] Tawhai, M. H., and Burrowes, K. S., 2003, "Developing Integrative Computational Models of Pulmonary Structure," Anat. Rec., **275B**(1), pp. 207–218.
[9] Zhang, Z., Kleinstreuer, C., and Kim, C., 2001, "Flow Structure and Particle Transport in a Triple Bifurcation Airway Model," ASME J. Fluids Eng., **123**(2), pp. 320–330.
[10] Zhang, Z., and Kleinstreuer, C., 2002, "Transient Airflow Structures and Particle Transport in a Sequentially Branching Lung Airway Model," Phys. Fluids, **14**(2), pp. 862–880.
[11] Zhang, Z., Kleinstreuer, C., Donohue, J., and Kim, C., 2005, "Comparison of Micro- and Nano-Size Particle Depositions in a Human Upper Airway Model," J. Aerosol Sci., **36**(2), pp. 211–233.
[12] Liu, Y., So, R. M. C., and Zhang, C. H., 2002, "Modeling the Bifurcating Flow in a Human Lung Airway," J. Biomech., **35**(4), pp. 465–473.
[13] Longest, P. W., and Vinchurkar, S., 2007, "Effects of Mesh Style and Grid Convergence on Particle Deposition in Bifurcating Airway Models With Comparisons to Experimental Data," Med. Eng. Phys., **29**(3), pp. 350–366.
[14] Soni, B., Lindley, C., and Thompson, D., 2009, "The Combined Effects of Non-Planarity and Asymmetry on Primary and Secondary Flows in the Small Bronchial Tubes," Int. J. Numer. Methods Fluids, **59**(2), pp. 117–146.
[15] Sera, T., Fujioka, H., Yokota, H., Makinouchi, A., Himeno, R., Schroter, R. C., and Tanishita, K., 2003, "Three-Dimensional Visualization and Morphometry of Small Airways From Microfocal X-Ray Computed Tomography," J. Biomech., **36**(11), pp. 1587–1594.
[16] Burton, R. T., Isaacs, K. K., Fleming, J. S., and Martonen, T. B., 2004, "Computer Reconstruction of a Human Lung Boundary Model From Magnetic Resonance Images," Respir. Care, **49**(2), pp. 180–185.
[17] van Ertbruggen, C., Hirsch, C., and Paiva, M., 2005, "Anatomically Based Three-Dimensional Model of Airways to Simulate Flow and Particle Transport Using Computational Fluid Dynamics," J. Appl. Physiol., **98**(3), pp. 970–980.
[18] Zhang, Z., and Kleinstreuer, C., 2004, "Airflow Structures and Nano-Particle Deposition in a Human Upper Airway Model," J. Comput. Phys., **198**(1), pp. 178–210.
[19] Guan, X., and Martonen, T. B., 2000, "Flow Transition in Bends and Applications to Airways," J. Aerosol Sci., **31**(7), pp. 833–847.
[20] Luo, H. Y., Liu, Y., and Yang, X. L., 2007, "Particle Deposition in Obstructed Airways," J. Biomech., **40**(14), pp. 3096–3104.
[21] Yang, X. L., Liu, Y., So, R. M. C., and Yang, J. M., 2006, "The Effect of Inlet Velocity Profile on the Bifurcation COPD Airway Flow," Comput. Biol. Med., **36**(2), pp. 181–194.
[22] Nowak, N., Kadake, P. P., and Annapragada, A. V., 2003, "Computational Fluid Dynamics Simulation of Airflow and Aerosol Deposition in Human Lungs," Ann. Biomed. Eng., **31**(4), pp. 374–390.
[23] Zhang, Z., Kleinstreuer, C., and Kim, C. S., 2008, "Airflow and Nanoparticle Deposition in a 16-Generation Tracheobronchial Airway Model," Ann. Biomed. Eng., **36**(12), pp. 2095–2110.
[24] Ma, B., and Lutchen, K. R., 2006, "An Anatomically Based Hybrid Computational Model of the Human Lung and Its Application to Low Frequency Oscillatory Mechanics," Ann. Biomed. Eng., **34**(11), pp. 1691–1704.
[25] Gemci, T., Ponyavin, V., Chen, Y., Chen, H., and Collins, R., 2008, "Computational Model of Airflow in Upper 17 Generations of Human Respiratory Tract," J. Biomech., **41**(9), pp. 2047–2054.
[26] Hyatt, R. E., and Wilcox, R. E., 1963, "The Pressure-Flow Relationship of the Intrathoracic Airways in Man," J. Clin. Invest., **42**, pp. 29–39.
[27] Patankar, S. V., 1980, *Numerical Heat Transfer and Fluid Flow*, Taylor & Francis, London.
[28] Barth, T.J., and Jespersen, D., 1989, "The Design and Application of Upwind Schemes on Unstructured Meshes," AIAA Paper No. AIAA-89-0366.
[29] 2006, *FLUENT® 6 User's Guide*, Fluent, Inc., Lebanon, NH.

Romeo Susan-Resiga
Professor
Department of Hydraulic Machinery,
"Politehnica" University of Timisoara,
Bvd. Mihai Viteazu 1,
RO-300222 Timisoara, Romania
e-mail: resiga@mh.mec.upt.ro

Sebastian Muntean
Senior Researcher
Center for Advanced Research in Engineering Science,
Romanian Academy–Timisoara Branch,
Bvd. Mihai Viteazu 24,
RO-300223 Timisoara, Romania
e-mail: seby@acad-tim.tm.edu.ro

Vlad Hasmatuchi
Doctoral Assistant
Laboratory for Hydraulic Machines,
École Polytechnique Fédérale de Lausanne,
Avenue de Cour 33Bis,
CH-1007 Lausanne, Switzerland
e-mail: vlad.hasmatuchi@epfl.ch

Ioan Anton
Professor
Department of Hydraulic Machinery,
"Politehnica" University of Timisoara,
Bvd. Mihai Viteazu 1,
RO-300222 Timisoara, Romania
e-mail: anton@acad-tim.tm.edu.ro

François Avellan
Professor
Laboratory for Hydraulic Machines,
École Polytechnique Fédérale de Lausanne,
Avenue de Cour 33Bis,
CH-1007 Lausanne, Switzerland
e-mail: francois.avellan@epfl.ch

Analysis and Prevention of Vortex Breakdown in the Simplified Discharge Cone of a Francis Turbine

We perform a numerical analysis of the decelerated swirling flow into the discharge cone of a model Francis turbine operated at variable discharge and constant head, using an axisymmetric turbulent swirling flow model and a corresponding simplified computational domain. Inlet boundary conditions correspond to velocity and turbulent kinetic energy profiles measured downstream the Francis runner. Our numerical results are validated against experimental data on a survey section further downstream in the cone, showing that the Reynolds stress turbulence model with a quadratic pressure-strain term correctly captures the flow field. It is shown that the diffuser performance quickly deteriorates as the turbine discharge decreases, due to the occurrence and development of vortex breakdown, with a central quasistagnant region. We investigate a novel flow control technique, which uses a water jet injected from the runner crown tip along the axis. It is shown that the jet discharge can be optimized for minimum overall losses, while the vortex breakdown is eliminated. This flow control method is useful for mitigating the Francis turbine flow instabilities when operating at partial discharge.
[DOI: 10.1115/1.4001486]

1 Introduction

The variable demand on the energy market, as well as the limited energy storage capabilities, requires a great flexibility in operating hydraulic turbines. As a result, turbines tend to be operated over an extended range of regimes quite far from the best efficiency point. In particular, Francis turbines operated at partial discharge have a high level of residual swirl at the draft tube inlet as a result of the mismatch between the swirl generated by the guide vanes and the angular momentum extracted by the turbine runner [1]. Further downstream, the decelerated swirling flow in the draft tube cone often results in vortex breakdown, which is recognized now as the main cause of severe flow instabilities and pressure fluctuations experienced by hydraulic turbines operated at part load [2]. More than 3 decades ago Palde [3] concluded that the draft tube surge is a hydrodynamic instability, known as vortex breakdown, occurring in the draft tube as a result of rotation remaining in the fluid as it leaves the turbine runner and enters the draft tube throat.

Contributed by the Fluids Engineering Division of ASME for publication in the JOURNAL OF FLUIDS ENGINEERING. Manuscript received January 14, 2007; final manuscript received March 15, 2010; published online April 27, 2010. Assoc. Editor: Rajat Mittal.

The main goal of a hydraulic turbine draft tube is to decelerate the flow exiting the runner, thereby converting the excess of kinetic head into static head. Modern hydraulic turbines have compact elbow draft tubes, with a rather short discharge cone. As a result, the draft tube hydrodynamics is very complex due to the combination of swirling flow deceleration with flow direction and cross-section shape/area changes. In practice, the hydraulic performance of a turbine draft tube is quantified with the wall pressure recovery coefficient

$$\chi \equiv \frac{\left(\frac{p_{\text{wall}}}{\rho}+gz\right)_{\text{outlet}}-\left(\frac{p_{\text{wall}}}{\rho}+gz\right)_{\text{inlet}}}{\frac{Q^2}{2A_{\text{inlet}}^2}\left[1-\left(\frac{A_{\text{inlet}}}{A_{\text{outlet}}}\right)^2\right]} \simeq \frac{(p_{\text{wall}}/\rho+gz)_{\text{outlet}}-(p_{\text{wall}}/\rho+gz)_{\text{inlet}}}{Q^2/(2A_{\text{inlet}}^2)} \quad (1)$$

Most of the pressure recovery occurs in the draft tube cone. For economical reasons, this conical diffuser is short and it has a rather large angle. To minimize hydraulic losses associated with kinetic-to-potential energy conversion in the draft tube cone, a certain level of residual swirl is provided at the runner outlet. This swirling flow at the cone inlet is tuned for optimal performance at

best efficiency operating point. However, for fixed pitch runners, the swirl ingested by the draft tube cone departs significantly from the best configuration as the turbine discharge varies.

It is known that a moderate level of residual swirl downstream the runner delays boundary layer separation at the cone wall and so aids the pressure recovery. Fox et al. [4] investigated the effect of inlet swirl flow on performance and outlet flow of conical diffusers. They found that the swirling inlet flow did not affect the performance of diffusers with only slightly separated flow. However, for diffusers that were moderately or badly separated for axial inlet flow, adding swirl at the inlet caused large performance increases. Similar results have been reported by Neve and Wirasinghe [5] and Senoo et al. [6]. Large swirl intensity, however, can degrade performance by forming recirculation regions within the core flow. Clausen et al. [7] found that generally there is a small range of swirl number, defined in their paper as the ratio of maximum circumferential to average axial velocity, that avoids both recirculation and separation. They measured the mean velocities and Reynolds stresses in a swirling diffuser flow that was close to separation at the wall and recirculation at the centerline in order to investigate the effects of various perturbations and to provide a test case for the development of turbulence models for complex flows. Their results highlight the interaction between the tendency toward boundary layer separation and the advent of recirculation in the core flow. The former is a viscous-dominated effect, whereas the latter is essentially inviscid and occurs only in swirling flow. Since both separation and recirculation phenomena must be avoided for good performance, the design of runner-diffuser tandem needs to account for these competing phenomena.

The obvious practical importance of predicting the complex flow downstream the turbine runner, in the draft tube, led to the FLINDT research project of flow investigation in draft tubes [8]. The main objective of this project was to investigate the flow in hydraulic turbine draft tubes, for a better understanding of the complex 3D swirling flow physics and to build up an extensive experimental database describing a wide range of operating points. Full 3D unsteady flow simulations, carefully validated with FLINDT experimental data, led Mauri et al. [9] to the conclusion that the peculiar sudden drop in the FLINDT draft tube pressure recovery coefficient near the best efficiency operating point could be associated with the Werlé–Legendre separation originating somewhere in the draft tube bend. The same phenomenon is associated with Susan-Resiga et al. [10] with the transition of the swirling flow ingested by the FLINDT draft tube from supercritical to subcritical as the discharge decreases, and this transition matches the turbine discharge where the sudden variation in the pressure recovery coefficient occurs. A similar approach was used by Zhang et al. [11] to explain the unsteady vortex rope formation, with associated severe pressure fluctuations, by the absolute instability of the swirling flow at the conical inlet of the turbine's draft tube.

The present paper continues our previous investigations [10] by addressing the decelerated swirling flow in the FLINDT draft tube cone for variable discharge. Using a turbulent axisymmetric swirling flow model we capture the vortex breakdown occurrence and development as discharge decreases. This vortex breakdown generates additional hydraulic losses with a corresponding depreciation of the kinetic-to-potential energy transformation efficiency. Therefore, to minimize these hydraulic losses, we introduce a novel flow control methodology for diffusers with swirl, which mitigates the vortex breakdown by injecting a liquid jet along the centerline at the runner crown tip. The control jet parameters are optimized to achieve overall best efficiency while removing the vortex breakdown and stabilizing the diffuser swirling flow. Section 2 presents the problem setup for numerical analysis, including the computational domain and boundary conditions. Section 3 briefly reviews the axisymmetric turbulent flow models and presents the numerical methodology further used in our study. Numerical results are validated against experimental data in Sec. 4, then analyzed with respect to kinetic-to-potential energy conversion, and the vortex breakdown occurrence and development is revealed. Section 5 is devoted to the description and analysis of the jet flow control technique, with an optimization method for control jet parameters. The paper conclusions are summarized in Sec. 6.

2 Computational Domain and Boundary Conditions

Figure 1(*a*) shows the draft tube of a Francis turbine investigated within the FLINDT project [8]. Within the draft tube cone, two survey sections, S_0 and S_1, have been used to measure the radial profiles for axial and circumferential velocity components, as well as for turbulent kinetic energy. The experimental data further used in this paper were obtained with a two-component probe laser Doppler anemometer, using backscattered light and transmission by an optical fiber, with a 5 W argon-ion laser. The geometrical location of each measurement point is controlled within a 0.05 mm accuracy, and the uncertainties in velocity measurement are estimated to be less than 2% of the measured value for the axial and tangential velocity components. The radial component measurements were found to be not accurate enough because of the low magnitude of this component.

The elbow draft tube from Fig. 1(*a*) combines both cross-section area and shape variation with the change in mean flow direction. However, for the present study, we want to discriminate the effect of cross-section increase on the additional flow complexity induced by bending the mean flow path. Moreover, we neglect the changes in cross-section shape and consider an axisymmetrical straight diffuser. In doing so, we practically focus on the decelerated swirling flow in the discharge cone, since most of the pressure recovery is achieved in this part of the draft tube. In order to build the simplified straight diffuser, we first compute the equivalent radius for cross sections, as plotted with circles in Fig. 1(*b*). Then, a least-squares procedure is used to build a cone-cylinder geometry. The resulting axisymmetric straight diffuser has an 8.5 deg half-angle cone, equal to the angle of the actual discharge cone of the Francis turbine, with inlet radius of 0.2 m, and cone length $2\times$ inlet diameter, followed by a long cylindrical discharge pipe. The actual computational domain starts at survey section S_0, since we use the measured velocity field as the inlet condition for our numerical investigations. As a result, the wall geometry for our axisymmetric computational domain is given by

$$\text{cone: } r[\text{m}] = 0.2126 + 0.15z[\text{m}] \quad \text{for} \quad 0 \le z \le 0.716 \text{ m}$$

$$\text{cylinder: } r = 0.32 \text{ m} \quad \text{for} \quad z > 0.716 \text{ m} \tag{2}$$

where the axial coordinate z is measured from S_0. The survey section S_1 is located 158 mm downstream S_0. A second survey section S_2, located at 1 m from S_0, just downstream the diffuser cone, Fig. 1(*b*), is further used in this paper to examine the cone energy balance and to evaluate the hydraulic losses for variable operating regimes. A 30×10^3 quadrilateral structured grid is used to discretize the computational domain in the meridian half-plane, with boundary layer refinement near both wall and symmetry axis. This grid has been further refined to 120×10^3 in order to perform a grid-convergence study. The boundary conditions used for the numerical simulations are summarized in Table 1 and further detailed in this section.

On the inlet section S_0 we prescribe the radial profiles for axial and circumferential velocity components in cylindrical coordinates, as well as for turbulence quantities. Measurements using a two-component probe laser Doppler anemometer provide data for axial and circumferential velocity components, as well as for the turbulent kinetic energy. In order to perform a parametric study with respect to the turbine discharge we have built suitable parametric analytical representations for these experimental data, as shown in the remainder of this section. Because of the relatively high uncertainty of the radial velocity measurements, we prefer as Mauri et al. [12] to use a simple linear variation of the radial

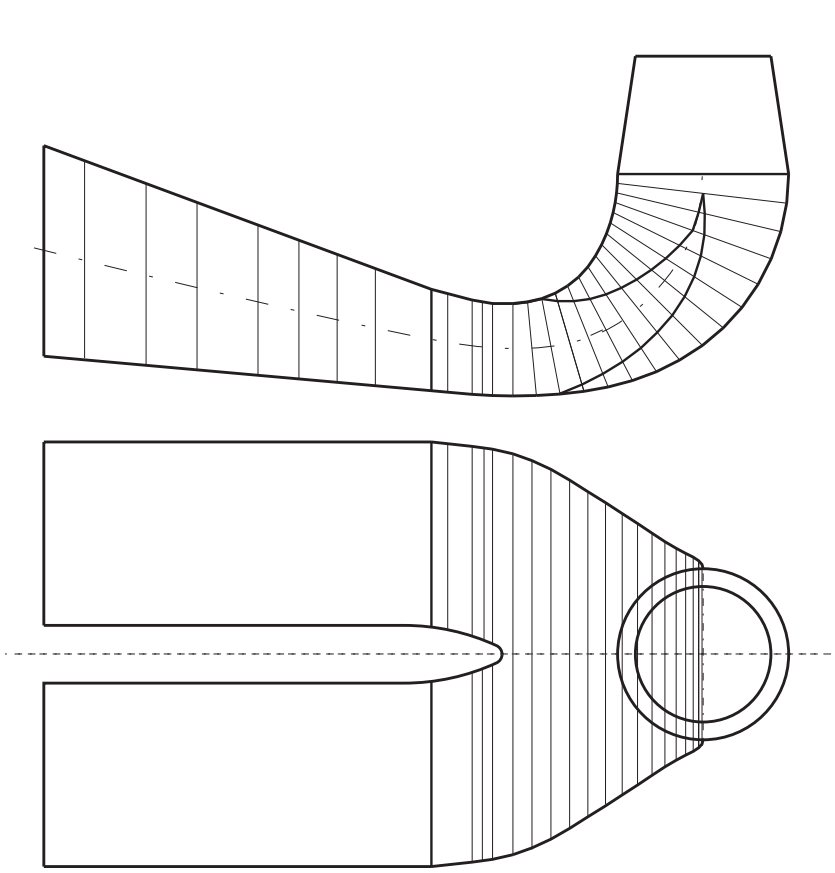

a) Side and top view, respectively, of the FLINDT draft tube

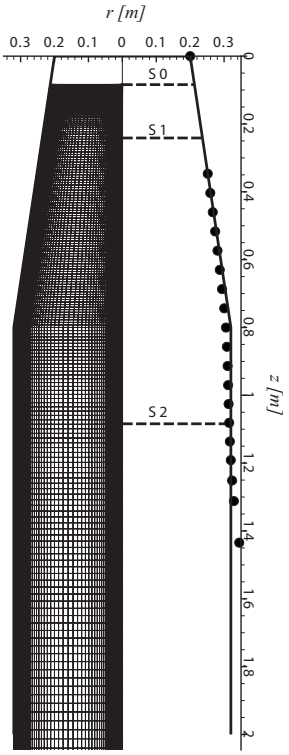

b) Simplified straight conical diffuser

Fig. 1 FLINDT draft tube and the simplified straight conical diffuser, with the computational domain in a meridian half-plane

velocity component with a value of $0.15 \times V_{z\ \mathrm{wall}}$ close to the wall for matching the cone wall angle. On the outlet section a pressure condition is used, with radial equilibrium for swirling flows $\partial p/\partial r = \rho V_\theta^2/r$. For flows without a swirl the above condition simplifies to constant pressure on the outlet. However, when a swirl is present, i.e., $V_\theta \neq 0$, the above condition correctly accounts for pressure rise in radial direction provided that the radial velocity is negligible. Moreover, we did not find any backflow for our numerical investigations, even when vortex breakdown occurs preventing us to apply this outlet boundary condition.

In Ref. [10] we have developed an analytical representation for the axial and circumferential velocity components measured on survey section S_0. We have found that the mean swirling flow downstream the Francis turbine runner can be accurately represented as a superposition of three distinct vortices

$$V_z(r) = U_0 + \underbrace{U_1 \exp\left(-\frac{r^2}{R_1^2}\right)}_{\text{coflowing}} + \underbrace{U_2 \exp\left(-\frac{r^2}{R_2^2}\right)}_{\text{counter-flowing}} \tag{3}$$

$$V_\theta(r) = \Omega_0 r + \underbrace{\Omega_1 \frac{R_1^2}{r}\left[1 - \exp\left(-\frac{r^2}{R_1^2}\right)\right]}_{\text{counter-rotating}} + \underbrace{\Omega_2 \frac{R_2^2}{r}\left[1 - \exp\left(-\frac{r^2}{R_2^2}\right)\right]}_{\text{corotating}} \tag{4}$$

According to the qualitative picture of this three vortex system, vortex 0 is a rigid body rotation with angular speed Ω_0 and we can associate with it a constant axial velocity U_0. Vortex 1, which has a vortex core extent about half the wall radius, is counter-rotating and coflowing with respect to vortex 0. The strength of this vor-

Table 1 Boundary conditions for axisymmetric flow computations

Boundary segment	Boundary condition
Inlet	Axial velocity (3) and circumferential velocity (4) components, linear profile for radial velocity, turbulent kinetic energy (5), and turbulence dissipation rate (10)
Outlet	Radial pressure equilibrium for swirling flow $\partial p/\partial r = \rho V_\theta^2/r$
Wall	No-slip boundary condition
Axis	Zero radial and circumferential velocity components, zero radial gradient of axial velocity, pressure, and turbulence quantities

tex, both in Ω_1 and U_1, grows as the turbine discharge increases. Vortex 2 has a core at least four times smaller than vortex 1, is corotating and counterflowing with respect to vortex 0, and its strength increases as the discharge decreases.

The eight parameters defining analytical representations (3) and (4) are then plotted versus the discharge coefficient φ, resulting in a quite simple picture of the swirling flow evolution with discharge in the parameter space, Fig. 2. The linear or at most parabolic (for Ω_2) variation of the swirling flow parameters with the discharge coefficient shows that at constant head the complex structure of the swirling flow downstream the Francis runner can be very well represented analytically only as function of φ [10]. The above swirl representation is in very good agreement with experimental data within $\pm 10\%$ the discharge at best efficiency point, as we will show in Sec. 4.

Experimental data are available for the turbulent kinetic energy k profile on the inlet section S_0, at six operating regimes with variable discharge coefficient $\varphi=0.34\cdots0.41$ and constant specific energy coefficient $\psi=1.18$. The turbulent kinetic energy has two local maxima: a large one at the axis, corresponding to the wake of the crown, and a smaller one close to the wall corresponding to the vorticity generation at the junction of the blades with the band. A four parameter analytical expression

$$k(r) = \underbrace{k_C \exp\left(-\frac{r^2}{R_C^2}\right)}_{\text{crown wake}} + \underbrace{k_B \frac{R_0 - R_B}{R_0 - r}\left[1 - \exp\left(-\frac{(R_0 - r)^2}{(R_0 - R_B)^2}\right)\right]}_{\text{band wake}} \tag{5}$$

is considered in this paper to represent the turbulent kinetic energy profiles for all operating points. The magnitude of k in the crown and band wakes is related to k_C and k_B, respectively, and the particular form of the two terms in Eq. (5) corresponds to a radially diffusive process. The radial extent of these wakes is related to R_C and R_B, respectively, both being smaller than the wall radius at S_0 section R_0. Equation (5) can represent very well the $k(r)$ profiles for all six operating points where experimental data are available, as further shown in Sec. 4. Least-squares fit of the turbulent kinetic energy profiles provides the four parameters in Eq. (5) versus discharge, as shown in Fig. 3. Once again, one can see that in a suitable parameter space the radial profile of the turbulent kinetic energy has a simple variation with the discharge coefficient φ.

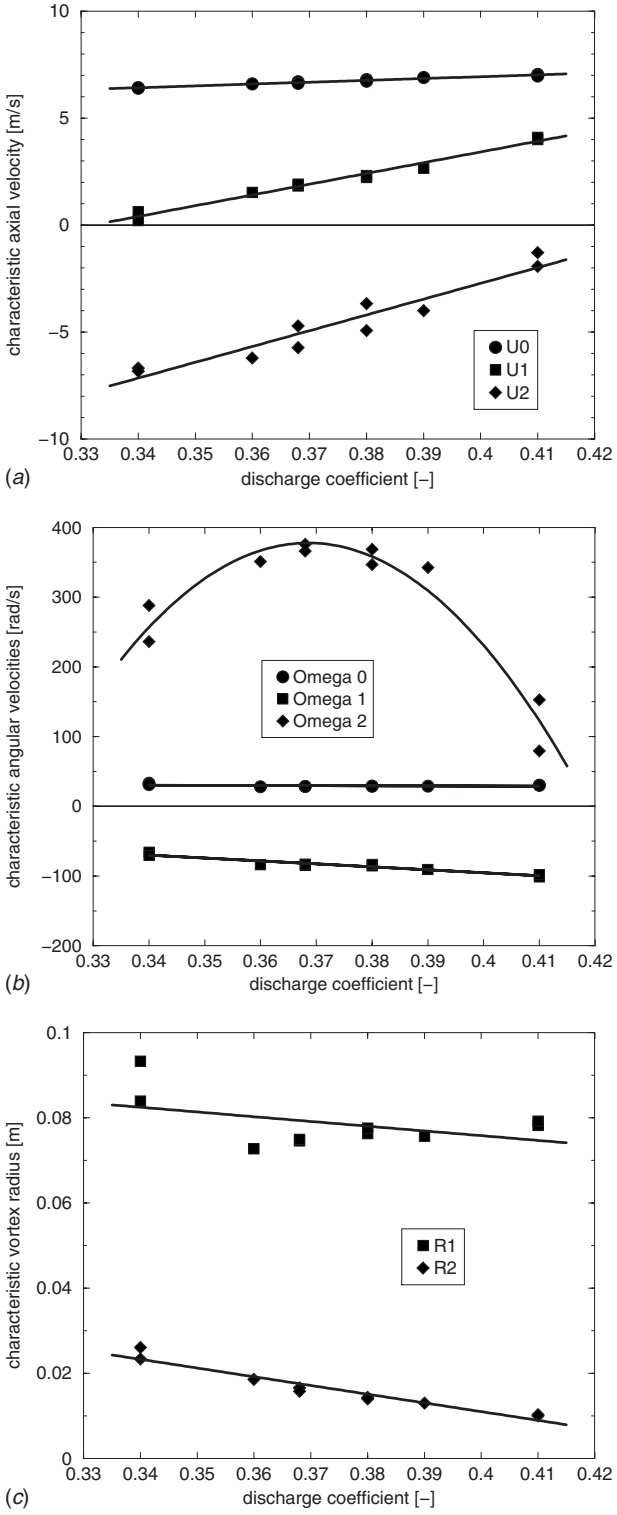

Fig. 2 Variation of the parameters in swirling flow analytical representation of Eqs. (3) and (4) versus the discharge coefficient on the survey section S_0

3 Numerical Simulation of Turbulent Axisymmetric Swirling Flow

Axisymmetric swirling flow models for incompressible Navier–Stokes equations have been successfully used in numerical simulation of vortex breakdown, with very good accuracy in comparison with experimental data [13]. However, for high-Reynolds number turbulent flows, the turbulence modeling introduces additional difficulties. The state of the art in modeling of turbulent swirling flow 2 decades ago is presented by Sloan et al. [14] in a comprehensive review focused on combustion systems. There are two main viewpoints: The first is focused on isotropic eddy viscosity and a modified Boussinesq hypothesis, while the second assumes that the eddy viscosity approach is inherently inadequate and a redistribution of stress magnitudes is necessary via high-order closure. Fletcher and co-workers [15–17] developed and evaluated both $k-\varepsilon$ and algebraic Reynolds stress models (RSMs) for swirling flows in conical diffusers, but validation was performed against the experiments of Clausen et al. [7] where no separation or vortex breakdown was present. Yaras and Grosvenor [18] tested several turbulence models to establish the prediction accuracy with respect to axisymmetric separating flows and flows with a high streamline curvature. They concluded that the prediction of strongly swirling confined flow was rather poor, with all models (Rodi's $k-\varepsilon$, Menter's two-equation shear-stress-transport (SST) model, and the one-equation model of Spalart and Allmaras) significantly overestimating the radial diffusive transport.

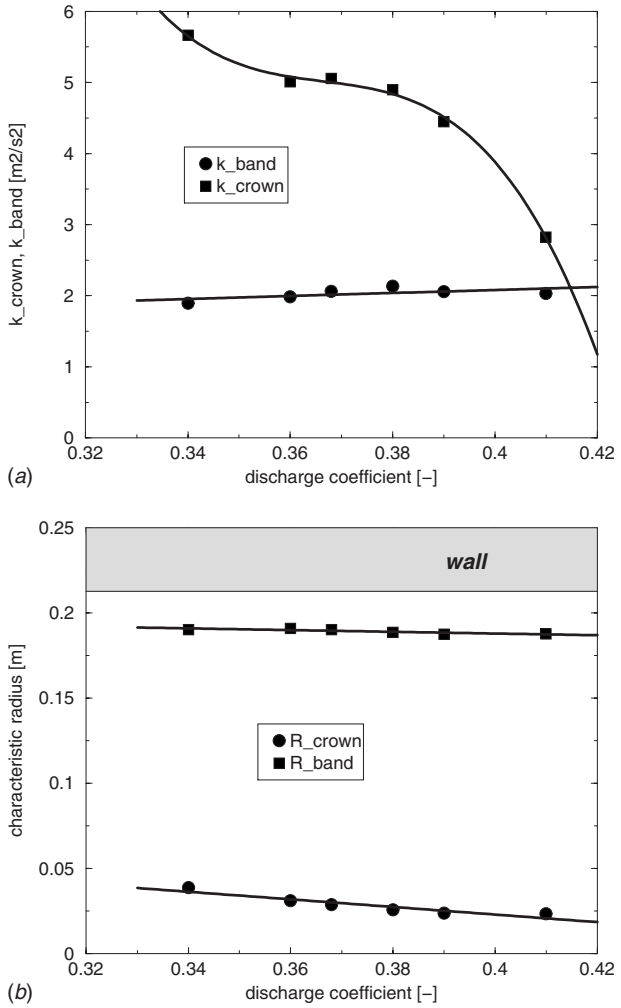

Fig. 3 Variation of the parameters in turbulent kinetic energy analytical representation of Eq. (5) versus the discharge coefficient on the survey section S_0

Among these models, the SST model yielded the worst prediction. The use of the streamline-curvature corrections in the turbulence transport equations has a little impact on the prediction accuracy. Xu et al. [19] compared various commonly used general $k-\varepsilon$ turbulence models with respect to their ability to predict the separation and reattachment of turbulent flows inside an axisymmetric diffuser with a curved surface center-body. They concluded that the high-Reynolds number $k-\varepsilon+$ one-equation model gives the best numerical prediction for separation and reattachment positions, with reasonable CPU time. Lu and Semião [20] proposed an improved anisotropic model for the dissipation rate ε of the turbulent kinetic energy k to be used together with a nonlinear pressure-strain correlation model. An important conclusion is that for the case of strongly swirling flows the results are very sensitive to the pressure-strain model, which has to be nonlinear in this case.

The realizable $k-\varepsilon$ (RKE) developed by Shih et al. [21] was aimed at providing superior performance for flows involving rotation, boundary layers under strong adverse pressure gradients, separation, and recirculation. The term "realizable" means that the model satisfies certain mathematical constraints on the Reynolds stresses, consistent with the physics of the flow. The RKE model has been successfully used by Susan-Resiga et al. [22] to compute the circumferentially averaged swirling flow in the discharge cone of a Francis turbine at low discharge where a strong precessing helical vortex is developed. Although the flow is three-dimensional and unsteady, the RKE axisymmetric swirling flow computation was found in good agreement with time-averaged laser Doppler velocimetry measurements for axial and circumferential velocity profiles.

For highly swirling flows the RSM is then strongly recommended [23]. The effects of strong turbulence anisotropy can be modeled rigorously only by the second-moment closure adopted in the RSM. The Reynolds stress model involves calculation of the individual Reynolds stresses using differential transport equations. The individual Reynolds stresses are then used to obtain closure of the Reynolds-averaged momentum equation. The exact equations for the transport of Reynolds stresses $\overline{\rho u_i' u_j'}$ are

$$\underbrace{\frac{\partial}{\partial t}(\overline{\rho u_i' u_j'})}_{\text{local time derivative}} + \underbrace{\frac{\partial}{\partial x_k}(\rho u_k \overline{u_i' u_j'})}_{\text{convection } C_{ij}} = \underbrace{-\frac{\partial}{\partial x_k}[\overline{\rho u_i' u_j' u_k'} + \overline{p(\delta_{kj} u_i' + \delta_{ik} u_j')}]}_{\text{turbulent diffusion } D_{T,ij}}$$

$$+ \underbrace{\frac{\partial}{\partial x_k}\left[\mu \frac{\partial}{\partial x_k}(\overline{u_i' u_j'})\right]}_{\text{molecular diffusion } D_{L,ij}} \underbrace{-\rho\left(\overline{u_i' u_k'}\frac{\partial u_j}{\partial x_k} + \overline{u_j' u_k'}\frac{\partial u_i}{\partial x_k}\right)}_{\text{stress production } P_{ij}}$$

$$+ \underbrace{\overline{p'\left(\frac{\partial u_i'}{\partial x_j} + \frac{\partial u_j'}{\partial x_i}\right)}}_{\text{pressure strain } \phi_{ij}} \underbrace{-2\mu\overline{\frac{\partial u_i'}{\partial x_k}\frac{\partial u_j'}{\partial x_k}}}_{\text{dissipation } \varepsilon_{ij}} \tag{6}$$

Some terms in the right-hand side of Eq. (6), such as convection, molecular diffusion, and stress production, do not require any modeling. However, the turbulent diffusion, pressure-strain, and dissipation terms need to be modeled to close the equations. The turbulent diffusion term is modeled as

$$D_{T,ij} = \frac{\partial}{\partial x_k}\left(\frac{\mu_t}{\sigma_k}\frac{\partial \overline{u_i' u_j'}}{\partial x_k}\right) \tag{7}$$

where $\sigma_k = 0.82$ and μ_t is the turbulent viscosity. For the pressure-strain term the quadratic model proposed by Speziale et al. [24]

has been demonstrated to give superior performance in a range of basic shear flows including axisymmetric expansion/contraction. This is the model successfully employed by Lu and Semião [20] as well, and it is available in the commercial code FLUENT within the axisymmetric swirling flow solver. The dissipation tensor ε_{ij} is modeled as

$$\varepsilon_{ij} = \tfrac{2}{3}\delta_{ij}\rho\varepsilon \quad \text{for incompressible flows} \tag{8}$$

The scalar dissipation rate ε is computed via a transport model equation similar to that used in the standard $k-\varepsilon$ model. Finally, the turbulent viscosity μ_t is computed similar to the $k-\varepsilon$ models

$$\mu_t = \rho C_\mu \frac{k^2}{\varepsilon} \quad \text{with} \quad C_\mu = 0.09 \tag{9}$$

The turbulent kinetic energy $k=\overline{u_i' u_i'}/2$ is obtained by taking the trace of the Reynolds stress tensor.

On the inlet section, one must specify the individual Reynolds stresses $\overline{u_i' u_j'}$ and the turbulence dissipation rate ε. However, because only the turbulent kinetic energy was available from measurements at the inlet, we assume turbulence isotropy thus setting $\overline{u_i'^2}=2k/3$, $i=1,2,3$, and $\overline{u_i' u_j'}=0$ on the inlet section. The inlet profile for the turbulence dissipation rate is computed from the turbulent kinetic energy profile as

$$\varepsilon = C_\mu^{3/4}\frac{k^{3/2}}{\ell} \quad \text{with} \quad C_\mu = 0.09 \tag{10}$$

where the turbulence length scale $\ell=0.02R_{\text{inlet}}$ has been chosen in best agreement with experimental data downstream in the conical diffuser. Analysis of the LDV measurements, as well as considerations on the order of magnitude for turbulent eddy size between runner blades, led Mauri et al. [12] to $\ell=0.01R_{\text{inlet}}$. Similar values for the turbulence length scale are provided by other authors, e.g., $\ell=0.02R_{\text{inlet}}$ [17] and $\ell=0.01R_{\text{inlet}}$ [25].

Both the RKE and RSM turbulence models are available in the commercial code FLUENT 6.2.16 [26], for axisymmetric swirling flow computations. The near-wall treatment employs the nonequilibrium wall function for both turbulence models, with the potential benefit of better accounting for the adverse pressure gradients in comparison to the standard wall functions. However, for the decelerated flows analyzed in this paper, there is no flow detachment from the wall; thanks to the swirl. Instead, we focus on the severe deceleration along the symmetry axis, leading to the recirculation bubble specific to vortex breakdown.

We use both RKE and RSM turbulent flow models for the present numerical simulations, with the axisymmetric computational domain, structured grids, and boundary conditions described in Sec. 2. All numerical solutions were converged down to residuals as low as 10^{-10}.

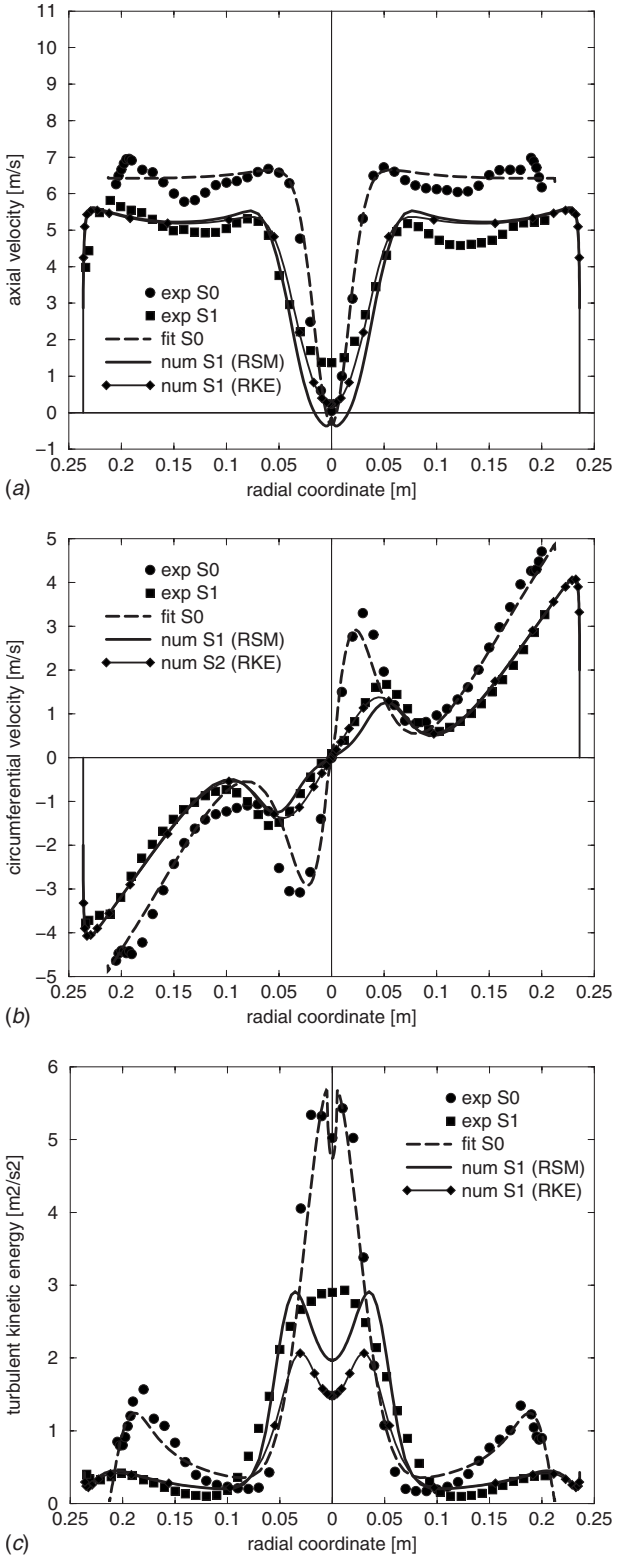

Fig. 4 Velocity components and turbulent kinetic energy for discharge $\varphi=0.340$

4 Numerical Results Validation and Analysis

Numerical simulations for turbulent swirling flow in the simplified discharge cone from Fig. 1(*b*) have been performed for 12 turbine operating points corresponding to discharge coefficient $\varphi=0.33\cdots0.42$. Experimental data for validation in survey section S_1 were available for four regimes, $\varphi=0.340$, 0.368, 0.380, and 0.410, with $\varphi=0.368$ the discharge coefficient value corresponding to the Francis turbine best efficiency operating point.

Figure 4 shows a first set of numerical results for discharge coefficient $\varphi=0.340$, corresponding to 91% the discharge at the turbine best efficiency operating point. The three plots correspond to the axial and circumferential velocity profiles, as well as to the turbulent kinetic energy profile. Experimental data correspond to both survey sections S_0 and S_1 shown in Fig. 1. The dashed lines

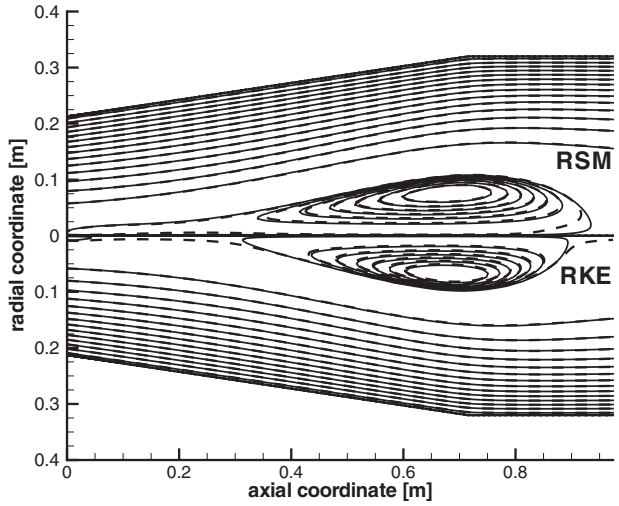

Fig. 5 Streamline pattern computed with RSM—upper half-plane, and with the realizable RKE—lower half-plane

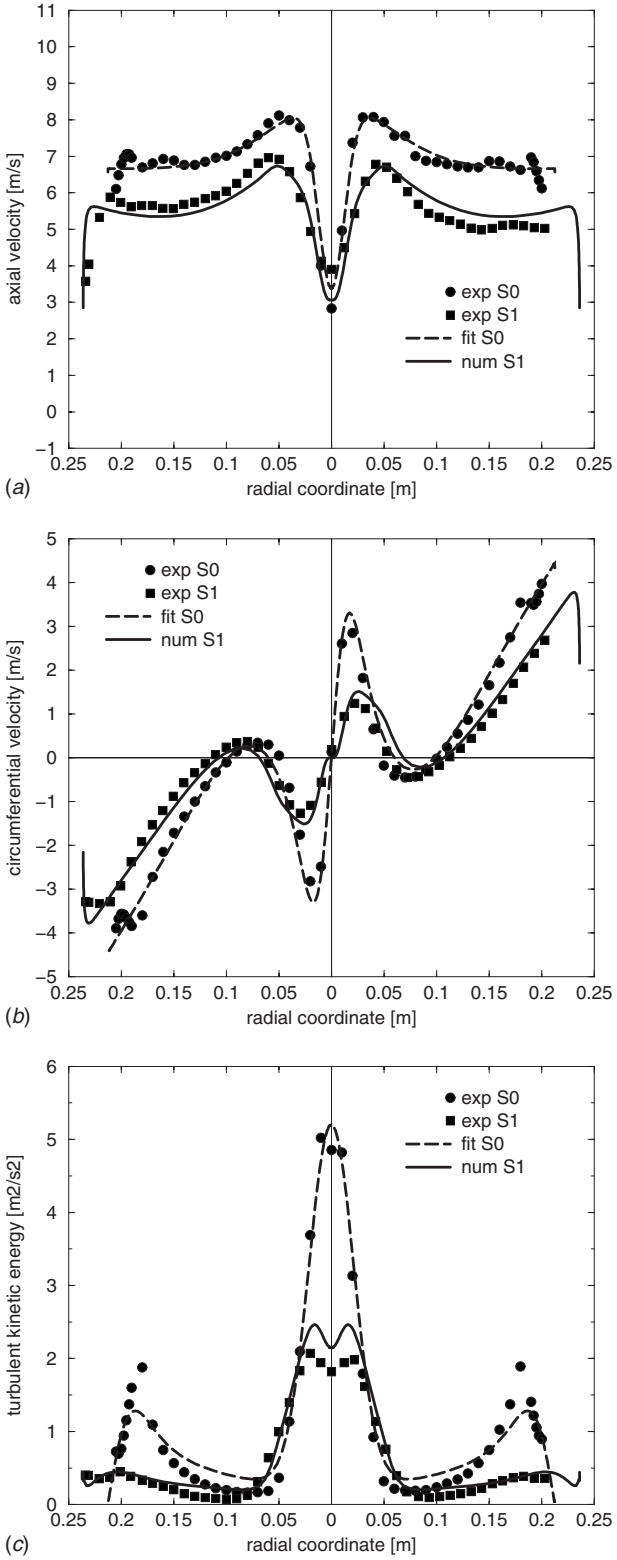

Fig. 6 Velocity components and turbulent kinetic energy for discharge φ=0.368

are fitted using Eqs. (3)–(5) and correspond to the inlet conditions for the computational domain. The solid lines show the computed results at survey section S_1, with both RSM and RKE turbulence models. We conclude that the axisymmetric turbulent swirling flow model correctly captures the flow deceleration and dissipation of the turbulent kinetic energy. The RKE model is more dissipative than the RSM, as clearly shown in the plot of the turbulent kinetic energy. Moreover, over the relatively short distance between the two survey sections, the RSM leads to a slightly stronger flow deceleration than the RKE model, especially near the axis. A global assessment of the two turbulence models is shown in Fig. 5, where the streamline pattern is shown for the meridian half-plane. It is shown that both RSM and RKE lead to similar shape and size of the recirculation bubble, which is developed as a result of the flow deceleration along the axis. However, due to the slightly larger dissipation of the RKE model, the recirculation region shown in the lower half-plane of Fig. 5 is slightly smaller than the corresponding region obtained with the RSM in the upper half-plane. A grid-convergence study has been performed, by using an initial grid of 30×10^3 cells (solid lines in Fig. 5) and 120×10^3 cells (dashed lines in Fig. 5). We conclude that the results obtained on the fine grid are practically identical to the ones on the initial grid; thus only the 30×10^3 cell grid is further used for our computations. Moreover, the results further presented in this paper are obtained using the RSM, although the RKE turbulence model could also be employed with similar accuracy.

Figures 6–8 show the axial and circumferential velocity profiles, as well as the turbulent kinetic energy profile, for increasing discharge coefficient. We conclude that the numerical model employed, using the axisymmetric swirling flow with RSM for turbulence modeling and a structured grid of 30×10^3 cells, accurately captures the main flow features.

Figure 9 shows the evolution of the axisymmetric flow streamlines in the discharge cone as the turbine discharge decreases. We can see the progressive development of the central recirculation bubble as a result of the vortex breakdown. This recirculation region grows both in the axial and radial directions, and its leading point moves upstream as the discharge decreases. The velocity on the axis, upper picture in Fig. 10, shows a unidirectional flow at Q_{BEP} (φ=0.368), while the reverse flow region can be clearly identified at a lower discharge (φ=0.340). At a lower turbine discharge, the vortex sheet bounding this so-called "dead-water" region is rolled up and results in the well-known precessing helical

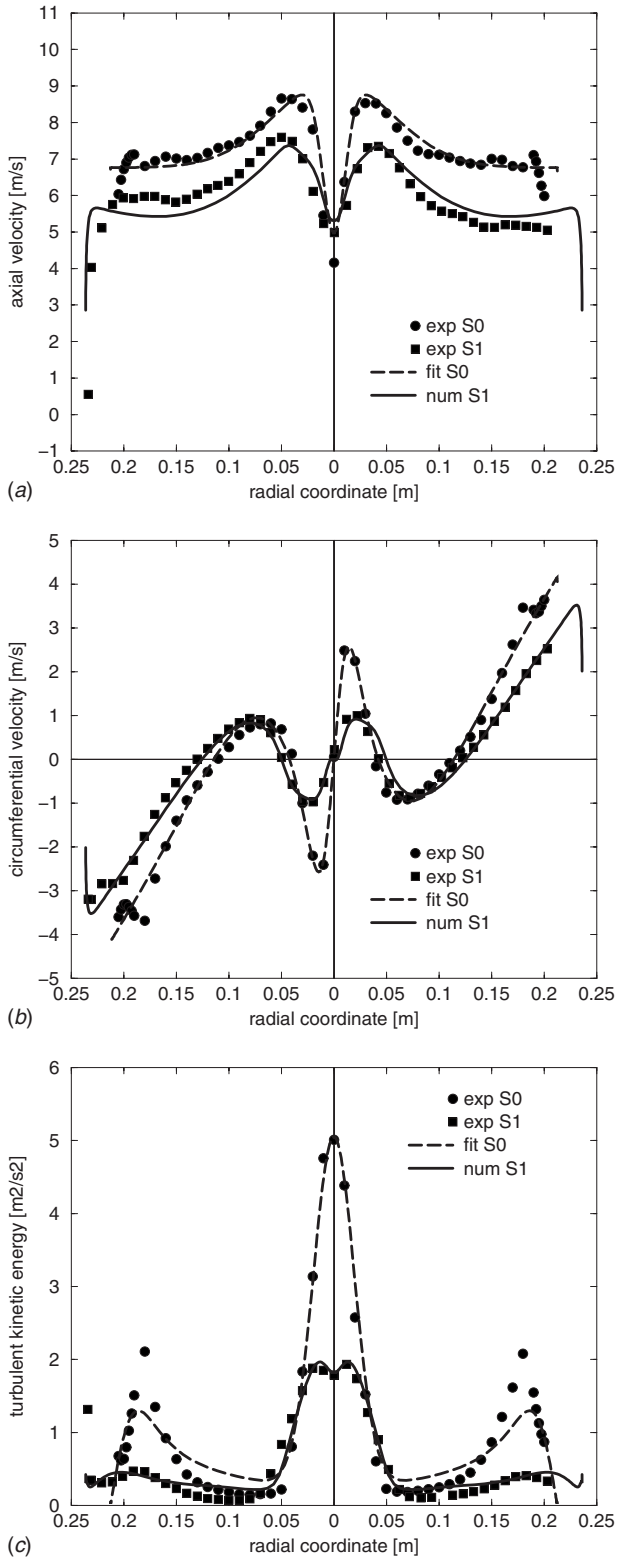

Fig. 7 Velocity components and turbulent kinetic energy for discharge φ=0.380

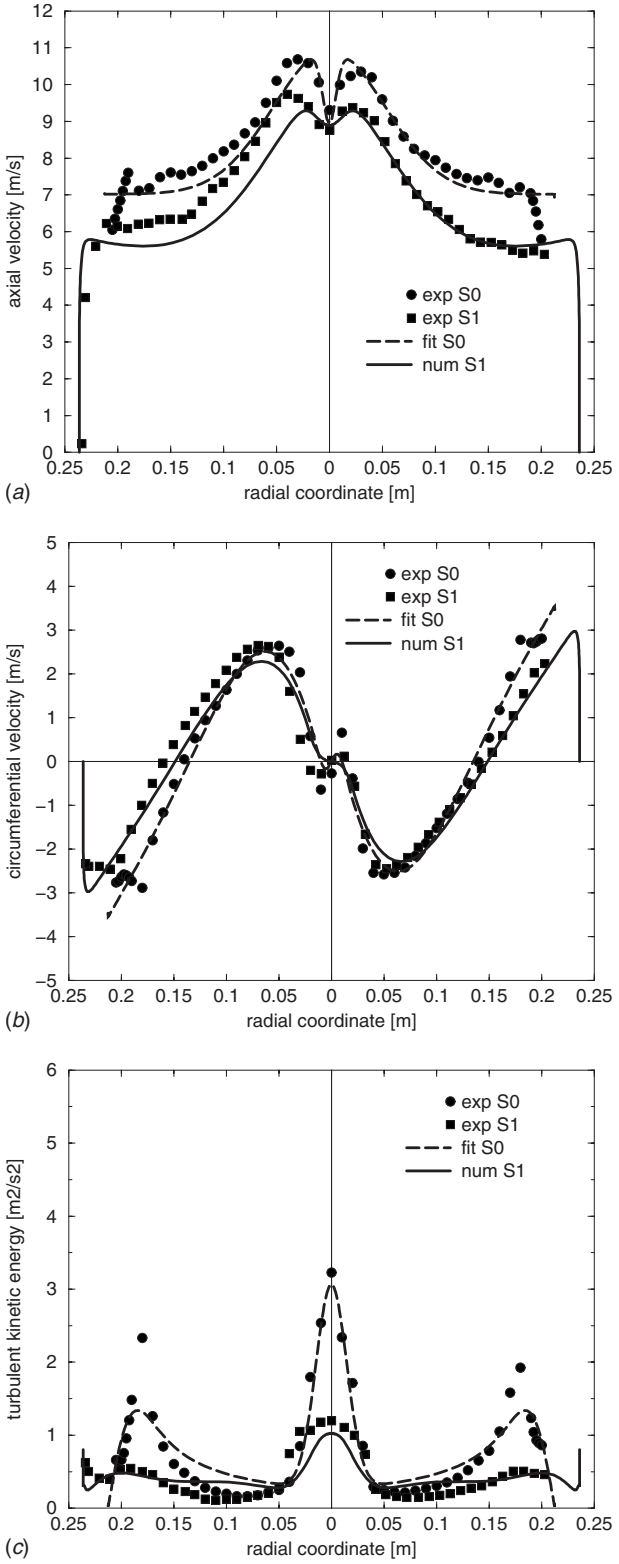

Fig. 8 Velocity components and turbulent kinetic energy for discharge φ=0.410

vortex. Although this is a three-dimensional unsteady phenomenon it can be inferred from the axisymmetric steady flow field. Gallaire et al. [27] showed that the spiral form of vortex breakdown can be interpreted as a nonlinear global mode originating at the convective/absolute instability transition point downstream of the axisymmetrical vortex breakdown bubble. Similar results have been obtained by Zhang et al. [11].

The swirl number

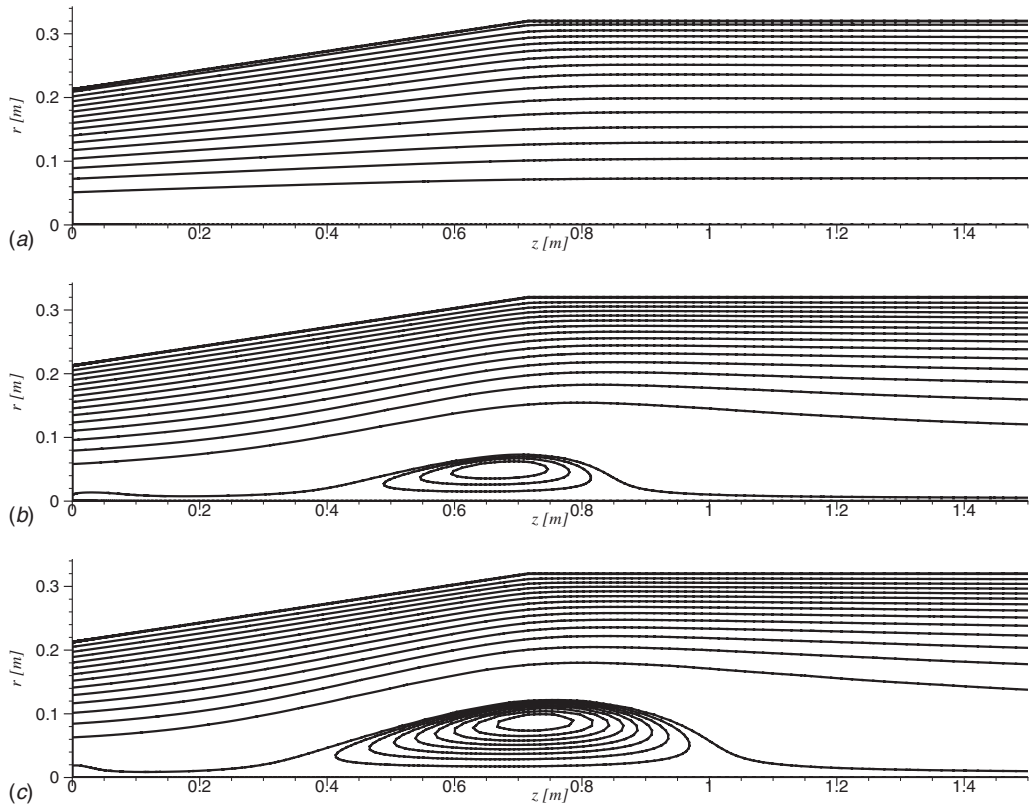

Fig. 9 Streamline pattern for axisymmetric flow in the draft tube cone, with development of vortex breakdown as discharge decreases

$$\mathrm{SW}(z) \equiv \frac{\int_0^{R(z)} [rV_\theta(z,r)]V_z(z,r)r\mathrm{d}r}{R(z)\int_0^{R(z)} V_z^2(z,r)r\mathrm{d}r} \tag{11}$$

increases linearly in the discharge cone for $\varphi=0.368$, then slowly decreases further downstream in the cylindrical section, dashed line in the lower picture of Fig. 10. For a lower discharge, $\varphi=0.340$, the swirl number is already larger in the inlet section, then it further increases in the cone up to a critical value where vortex breakdown occurs. This critical value is maintained over the axial extent of the recirculation bubble, and then the swirl number has a small increase in the cylindrical section reaching an asymptotic value. We conclude that vortex breakdown in conical diffusers is a mechanism for limiting the increase in the swirl number, and it occurs once the inlet flux of circumferential momentum is large enough with respect to the flux of axial momentum. This situation is always expected downstream the Francis turbine runner as the turbine discharge decreases.

The main purpose of the hydraulic turbine draft tube is to convert as much as possible the kinetic energy at the runner outlet into pressure potential energy with minimum hydraulic losses. In order to analyze the kinetic-to-potential energy transformation process, as well as its efficiency, we introduce the following integral quantities on a generic cross section $S(z)$ at the axial distance z from the inlet section:

$$\text{flux of potential energy } \Pi(z) \equiv \int_{S(z)} p(z,r)\mathbf{V}\cdot\mathbf{n}\mathrm{d}S \ [\mathrm{W}] \tag{12}$$

$$\text{flux of kinetic energy } K(z) \equiv \int_{S(z)} \frac{\rho V^2(z,r)}{2}\mathbf{V}\cdot\mathbf{n}\mathrm{d}S \ [\mathrm{W}] \tag{13}$$

$$\text{flux of mechanical energy } E(z) \equiv \Pi(z) + K(z) \tag{14}$$

For a loss-free flow the flux of total mechanical energy E is constant. However, when hydraulic losses are present, E decreases monotonically as the cross section $S(z)$ is moved downstream, i.e., for increasing z in our case. If we denote $\Pi_0=\Pi(z=0)$ and $K_0=K(z=0)$, where $z=0$ corresponds to the inlet section of our computational domain, the total hydraulic power dissipated up to a section $S(z)$ is $E_0-E(z)>0$, where obviously $E_0=\Pi_0+K_0$. A dimensionless *loss coefficient* ζ is usually defined as [28]

$$\zeta(z) \equiv \frac{E_0 - E(z)}{K_0} = \left(1 - \frac{K(z)}{K_0}\right) - \frac{\Pi(z) - \Pi_0}{K_0} \tag{15}$$

The first term in Eq. (15) corresponds to what we call *kinetic energy recovery coefficient*

$$C_{KR}(z) \equiv 1 - \frac{K(z)}{K_0} \tag{16}$$

while the second term in Eq. (15) corresponds to the so-called *potential energy recovery coefficient*

$$C_{PR}(z) \equiv \frac{\Pi(z) - \Pi_0}{K_0} \tag{17}$$

Since $\zeta>0$ for viscous flows, we always have $C_{KR}>C_{PR}$. Moreover, for diffusers, we have $K(z)<K_0$ because the flow is generally decelerated; therefore $C_{KR}<1$. In addition, because of the pressure rise in diffusers, we have $\Pi(z)>\Pi_0$; thus $C_{PR}>0$. As a

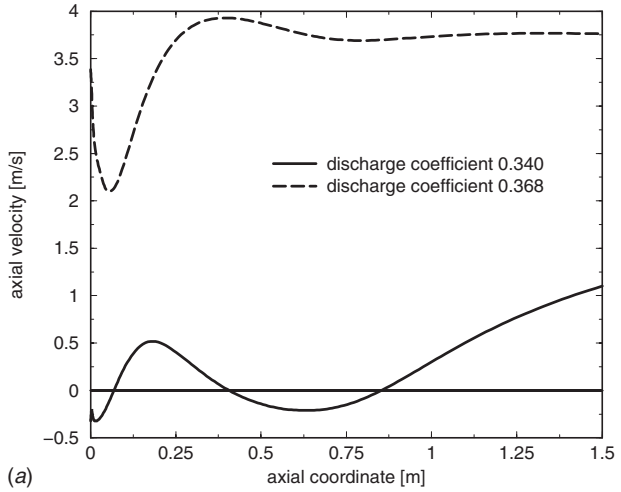

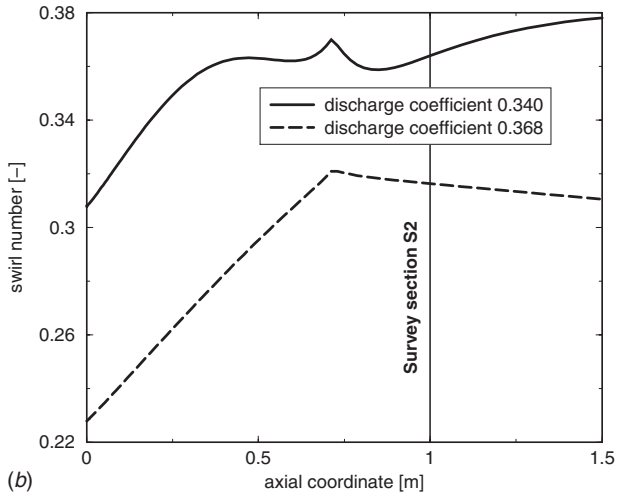

Fig. 10 Velocity on the axis and swirl number variation in the discharge cone

result, the kinetic and potential energy recovery coefficients satisfy the following inequalities for diffuser flow:

$$0 < C_{PR} < C_{KR} < 1 \tag{18}$$

The *kinetic-to-potential energy conversion ratio* can be quantified as

$$\chi(z) \equiv \frac{\Pi(z) - \Pi_0}{K_0 - K(z)} < 1 \tag{19}$$

Accurate evaluation of χ requires the evaluation of integrals from Eqs. (12) and (13). This is possible only if both velocity and pressure profiles are known. In practice, one often uses simplified expression (1), since wall pressure and overall discharge are readily available.

The above considerations show that the flow in the diffuser can be quantified with two dimensionless coefficients, either ζ and χ, or C_{PR} and C_{KR}. Once a pair of coefficients is evaluated, the other pair follows immediately as:

$$\zeta = C_{KR} - C_{PR}, \quad \chi = \frac{C_{PR}}{C_{KR}} \quad \text{and} \quad C_{PR} = \frac{\zeta\chi}{1-\chi}, \quad C_{KR} = \frac{\zeta}{1-\chi} \tag{20}$$

For diffusers with a large outlet/inlet area ratio it is common practice to neglect the outlet kinetic energy; thus $C_{KR} \simeq 1$. As a result, there is only one coefficient to be used in evaluating the diffuser

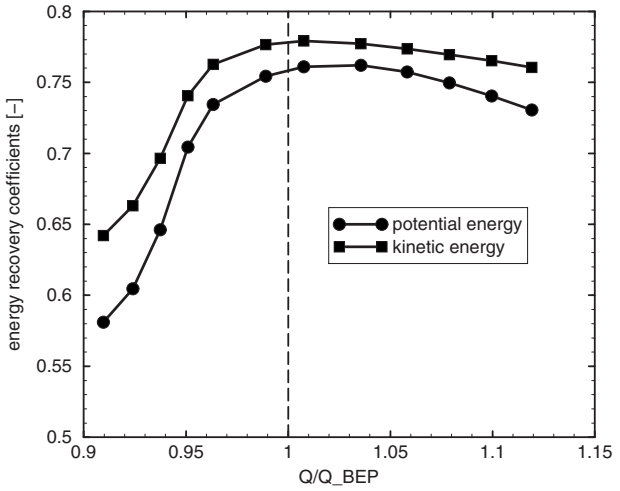

Fig. 11 Potential C_{PR} and kinetic C_{KR} energy recovery coefficients versus turbine discharge

performance, either the pressure recovery coefficient C_{PR} or the loss coefficient $\zeta = 1 - C_{PR}$.

In our case, we compute the dimensionless coefficients between the inlet section S_0 and the downstream survey section S_2, and we examine their variation with respect to the turbine discharge normalized with the discharge at best efficiency point. One can see from Fig. 11 that both C_{KR} and C_{PR} reach their maximum values close to the turbine best efficiency operating point. The hydraulic loss coefficient ζ, Fig. 12, and the kinetic-to-potential energy conversion ratio χ, Fig. 13, also reach their minimum and maximum values, respectively, quite close to the turbine best efficiency operating point.

The evolution of the loss coefficient $\zeta(z)$ in the discharge cone, Fig. 14 upper, emphasizes the rapid increase in the hydraulic losses at partial discharge (solid line) with respect to the turbine best efficiency operating point (dashed line). This is also associated with an overall performance deterioration of the discharge cone, as shown in the variation of the potential energy recovery coefficient $C_{PR}(z)$, Fig. 14 lower.

5 Jet Control of Decelerated Swirling Flow

The analysis of decelerated swirling flow in the turbine draft tube cone shows that the flow is abruptly decelerated near the centerline as the turbine discharge decreases, resulting in a central

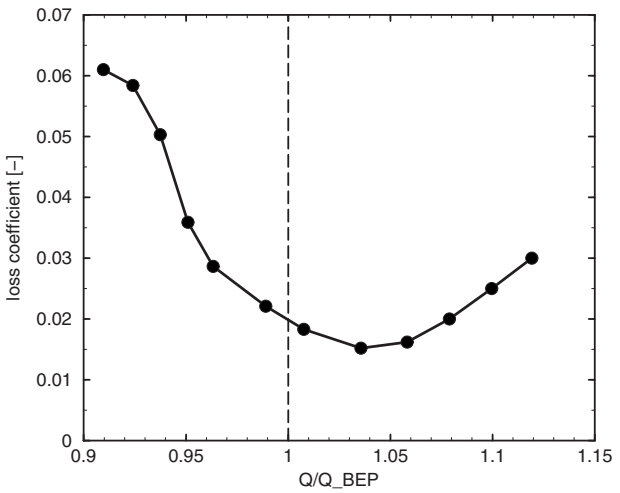

Fig. 12 Energy loss coefficient ζ versus turbine discharge

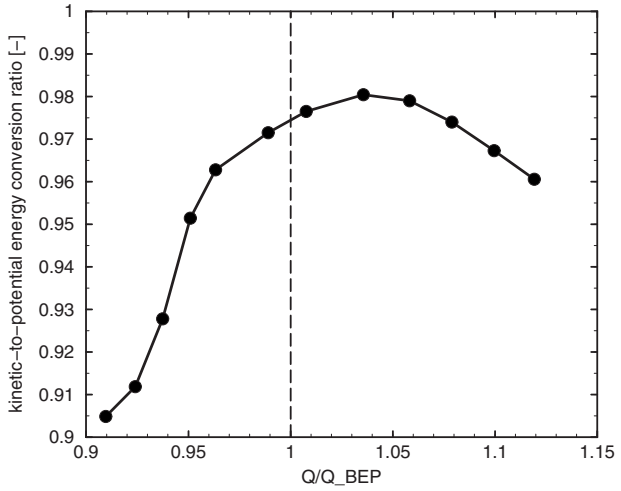

Fig. 13 Kinetic-to-potential energy conversion ratio χ in the draft tube cone versus turbine discharge

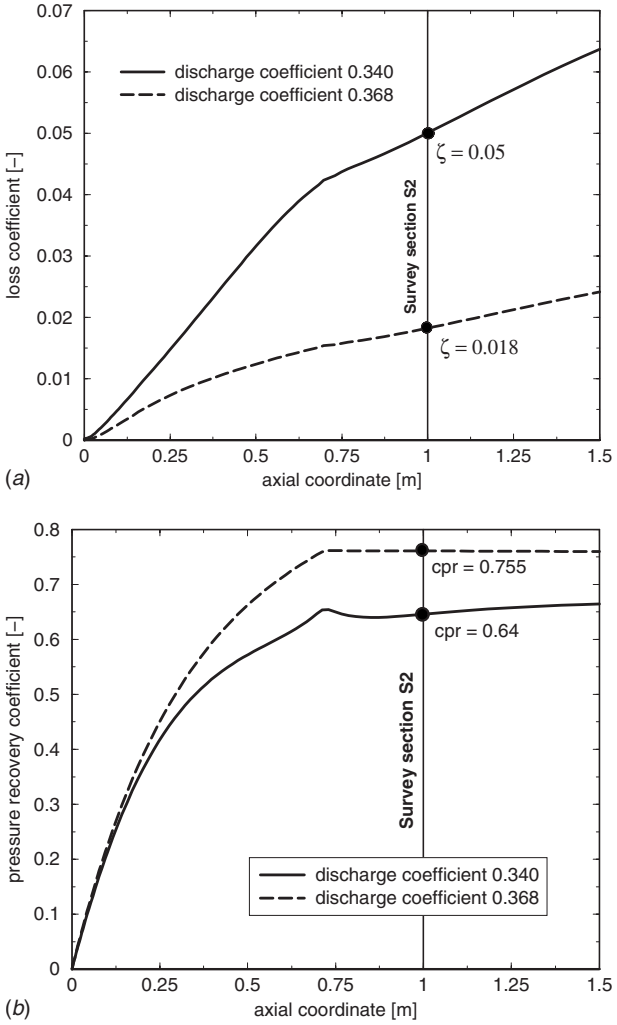

Fig. 14 Energy loss coefficient ζ and the potential energy recovery coefficient C_{PR}

quasistagnant region. The vortex breakdown phenomenon leads to an increase in hydraulic losses, and as the turbine discharge is further decreased an unsteady helical vortex breakdown develops. It is obvious that flow deceleration near the centerline is further enhanced by the presence of the runner crown wake. The radial extent of the velocity deficit region in the crown wake rapidly grows as discharge decreases as a result of the fixed pitch runner behavior at part load. All these observations suggest that preventing the vortex breakdown in the draft tube cone is the main approach for improving the Francis turbine operation at discharge significantly smaller than the one corresponding to the best efficiency operating point.

There are two main approaches for reducing or eliminating the vortex breakdown downstream the Francis turbine runners. First, one can reduce the swirl intensity in the cone. Thicke [29] reviewed the development and performances of stabilizer fins installed on the cone wall, and Nishi et al. [30] performed extensive experimental investigations on various configurations of fins. The idea is to hinder the circumferential flow mainly in the neighborhood of the cone wall. The fin shape, size, and location are mainly subject to trial-and-error approaches. The main drawback of this solution is that it introduces additional losses and it cannot be adjusted with the operating point. Recently, Kurokawa et al. [31] proposed and examined the so-called "*J*-groove" for controlling and suppressing the swirl component of the flow in the draft tube cone of Francis turbines. The *J*-groove is a very simple passive device composed of shallow grooves mounted on the diffuser wall, parallel to the pressure gradient. The reduction in swirl intensity obtained with such devices decreases the pressure fluctuations caused by the rotation of vortex core around the dead-water region near the diffuser inlet. Along the same lines, other technical solutions propose the introduction of various structures (e.g., splitter plates) in the draft tube cone, aimed at reducing the swirl intensity or destroying the coherent helical structures at part load. Kjelsen et al. [32] developed a technology for mitigation or reduction in pressure pulsations in Francis draft tube by injecting high speed water jets from distributed positions at the draft tube walls. The jets are injected tangentially and angled downstream with respect to the machine axis. This injection system would presumably have the following effects: (i) By injecting water in opposite direction of the swirl downstream the runner one can reduce the large scale swirls, and (ii) by filling the boundary layers with high impulse water jets separation at the wall can be delayed. Injecting multiple water jets at the wall has the drawback of large water consumption, thus significantly reducing the overall turbine efficiency. The second approach for mitigating the vortex breakdown in the cone is to act on the axial momentum of the flow instead of reducing the circumferential momentum. Runner cone extensions attached to the crown have been shown to play an important role in controlling the velocity distribution in the draft tube below the runner. Falvey [33] presented this solution starting from the idea that reducing the draft tube surges can be achieved by filling the stagnant of reverse flow region with a solid body of rotation. Obviously, such large runner cone extensions would be subject to large lateral forces in addition to a significant decrease in kinetic energy recovery within the cone. Practical solutions shown by Thicke [29] use rather small conical or cylindrical extensions of the runner crown. Vekve [34] investigated several configurations of runner cone-attached semitapered cones, and concludes that the necessary size required to avoid the vortex breakdown vary with the part-load operating point. He suggested that an ideal solution would be to attach an arrangement to the runner cone, which can vary the diameter and length according to the operating point. Unfortunately, this is not practical. Karashima [35] investigated numerically the interaction between a swirling flow and a coaxial jet in order to clarify the feasibility of vortex breakdown control by means of a small blowing. He found that applying the blowing to a broken vortex flow having a bubble induces an amount of downstream movement and bubble shrinking, and concluded that this technique can offer a significant improvement in breakdown characteristics of the swirling flow.

The above analysis of various solutions for mitigating the vor-

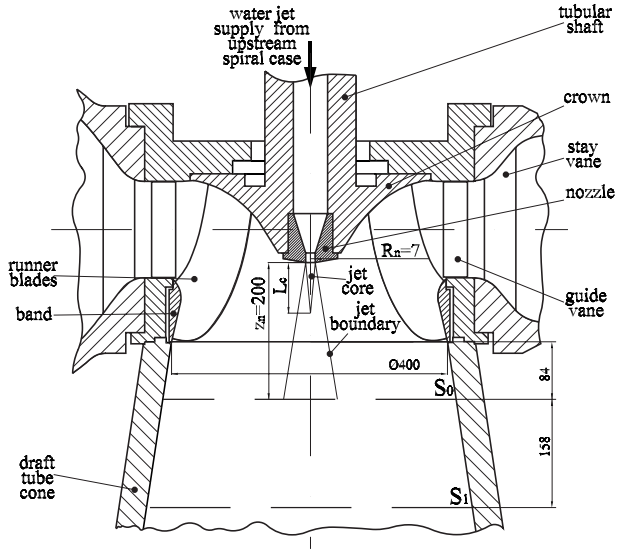

Fig. 15 Cross section through the Francis turbine model, with the control jet nozzle at the crown tip

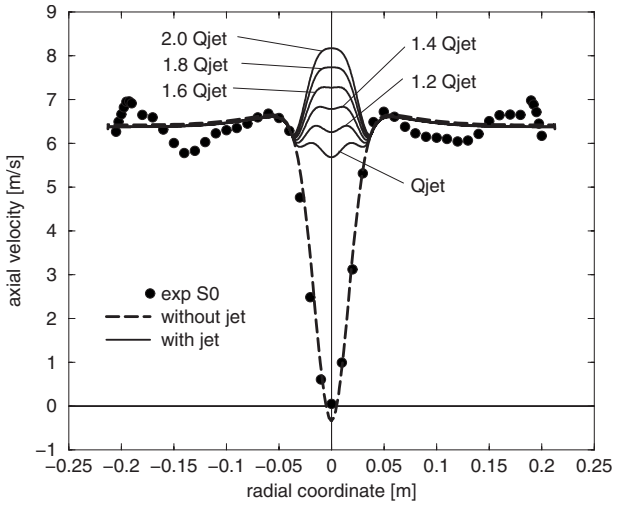

Fig. 16 Modified axial velocity profile on the survey section S_0 by injecting an axial control jet for turbine discharge φ=0.340

tex breakdown in conical diffusers with inlet swirling flow led us to the conclusion that a successful approach should address the axial momentum deficit near the axis rather than reducing the circumferential momentum near the wall [36]. As a result, we investigate the influence of an axial water jet injected from the runner crown tip downstream in the draft tube cone, Fig. 15. Since the computational domain we have considered starts from the survey section S_0 at the draft tube inlet, we need to estimate the velocity profile induced on this section by a jet issued from the nozzle located upstream.

Let us evaluate first the jet velocity V_{jet} and nozzle radius R_n. For a Francis turbine, the most straightforward choice for supplying the control jet is to bypass a fraction of the turbine discharge from upstream the spiral chamber, through the turbine shaft, to the nozzle attached to the runner crown. As a result, the jet velocity depends on the turbine head and can be evaluated as

$$V_{\text{jet}} = \sqrt{2gH} = \omega R_{\text{ref}} \sqrt{\psi} \tag{21}$$

Equation (21) obviously does not account for the hydraulic losses through the duct up to the nozzle, but since the jet discharge is very small we can neglect them for a first estimate. Note that the jet velocity at the nozzle does not depend on the turbine discharge. The jet discharge is

$$Q_{\text{jet}} = \pi R_{\text{jet}}^2 V_{\text{jet}} \tag{22}$$

with the corresponding hydraulic power

$$P_{\text{jet}} = \frac{\rho}{2} \pi R_{\text{jet}}^2 V_{\text{jet}}^3 \tag{23}$$

The fraction of turbine discharge and hydraulic power to be supplied to the control jet is

$$\frac{Q_{\text{jet}}}{Q} = \frac{P_{\text{jet}}}{P} = \frac{\sqrt{\psi}}{\varphi} \left(\frac{R_n}{R_{\text{ref}}} \right)^2 \tag{24}$$

The jet discharge should be practically associated with the turbine volumetric losses, since it bypasses the runner blades. Let us exemplify the order of magnitude for the jet with respect to the turbine main parameters. For the operating point ψ=1.18 and φ =0.34, a jet with 0.5% turbine discharge or power will be produced by a nozzle with a diameter of 4% runner throat diameter. This is the order of magnitude for the jet investigated in this paper for mitigating the vortex breakdown at partial discharge, but close to the best efficiency point.

An accurate description of the velocity field at the draft tube inlet should obviously include in the computational domain the turbine runner at least. However, this analysis is beyond the purpose of the present paper and this is why we further consider the jet evolution from the runner crown up to the inlet section of our computational domain; see the Appendix.

Since we assume that at the nozzle the jet velocity will be practically determined by the turbine head, the jet discharge could be adjusted by modifying the nozzle radius R_n. This can be done with a needle-controlled nozzle arrangement, similar to the ones used in injectors of Pelton hydraulic turbines. We consider five nozzle radius values in the range R_n/R_{ref}=0.025···0.035. Figure 16 shows the axial velocity profile on the inlet section S_0, modified by the control jet in the central region. It is remarkable to note that practically the axial velocity deficit in the crown wake is removed by the jet injection since the lowest jet discharge value.

However, for determining the optimum discharge jet, we need to consider the overall energy balance for the whole turbine, with both the dissipation in the draft tube cone and the hydraulic power used for the control jet considered as "losses" from a practical viewpoint. Figure 17 shows that as the jet discharge increases, the

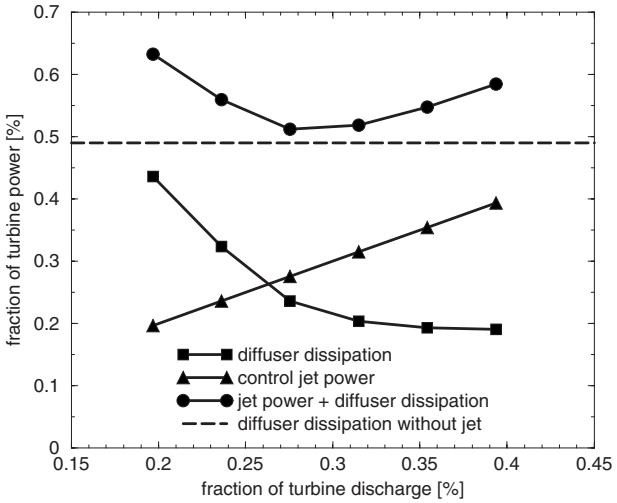

Fig. 17 Diffuser dissipation ΔE and jet power P_{jet} as fractions of the turbine hydraulic power $P=\rho gHQ$ versus jet discharge as fraction of the turbine discharge at φ=0.340

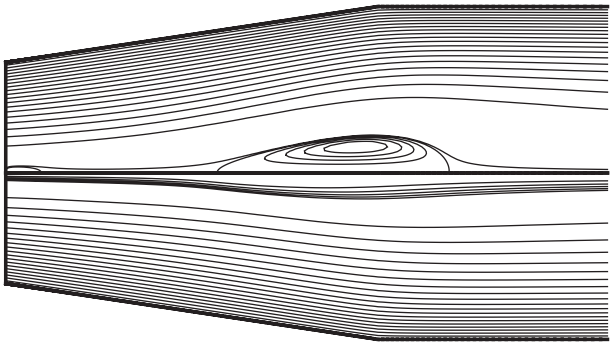

Fig. 18 Streamline pattern at turbine discharge $\varphi=0.340$, without control jet (upper half-plane) and with optimal control jet (lower half-plane)

hydraulic power associated with the jet increases linearly, while the power dissipated in the diffuser decreases. However, their sum reaches a minimum at a certain jet discharge, and this minimum corresponds to the optimum opening of the jet nozzle. The minimum hydraulic power is practically at the same level with the hydraulic power dissipated in the diffused without control jet. In conclusion, this flow control technique practically does not decrease the overall machine efficiency. One can see from Fig. 18 that the optimum jet removes the recirculation region in the cone thus avoiding the vortex breakdown phenomenon. It is expected that the same qualitative behavior and jet optimization procedure remains valid for other turbine operating points at partial discharge.

6 Conclusions

The paper investigates the swirling flow downstream the Francis turbine runner, in the draft tube cone, and introduces a novel flow control method for mitigating the vortex breakdown at partial discharge. Numerical simulations are performed using a turbulent axisymmetric flow model, with inlet data corresponding to measured velocity and turbulent kinetic energy radial profiles at the runner outlet. A simplified straight conical diffuser is considered, in order to focus on the decelerated axisymmetric swirling flow in the draft tube cone. It has been found that the Reynolds stress model with a quadratic pressure-strain term accurately reproduces the experimental data available in a survey section downstream in the cone, although the realizable $k-\varepsilon$ turbulence model leads to quite close and accurate results. We capture the vortex breakdown occurrence and development as the turbine discharge decreases. This phenomenon is clearly related to the decrease in the conical diffuser performances, quantified either with kinetic and potential energy recovery coefficients or with hydraulic loss and kinetic-to-potential energy conversion efficiency coefficients.

A water jet from the runner crown tip is injected along the machine axis, downstream into the cone, for removing the central quasistagnant flow region developed as a result of vortex breakdown. The jet is supplied with high pressure water from upstream the turbine spiral case, and since the jet discharge bypasses the runner blades it should be accounted for as a volumetric loss. It is shown that while the jet hydraulic power increases with the jet discharge, the hydraulic power dissipated in the cone decreases, and their sum reaches a minimum for an optimum control jet discharge. In conclusion, the jet control of the swirling flow effectively removes the vortex breakdown at partial load, practically without affecting the overall turbine efficiency.

Acknowledgment

The present research is supported from the Joint Research Project No. IB7320-110942/1 funded by the Swiss National Science Foundation within the "Scientific cooperation between Eastern Europe and Switzerland" (SCOPES program), as well as by the Romanian National University Research Council (CNCSIS) under Consortium Grant No. 33/2005 and Exploratory Research Project No. 799/2008, respectively. Moreover the authors wish to thank the partners of the FLINDT Project Eureka No. 1625, ANDRITZ Hydro, ALSTOM Hydro, Electricité de France, VOITH Hydro, PSEL Funds for Projects and Studies of the Swiss Electric Utilities, and the Commission for Technology and Innovation CTI of the Swiss Confederation, for their financial support.

Nomenclature

C_{KR}, C_{PR} = kinetic and potential energy recovery coefficients, respectively
H = turbine head (m)
L_c = jet core length (m)
P = turbine hydraulic power, $P=\rho gHQ$ (W)
P_{jet} = control jet hydraulic power, $P_{\text{jet}}=\rho gHQ_{\text{jet}}$ (W)
Q = turbine discharge without control jet (m^3/s)
$Q_{\text{jet}}=V_{\text{jet}}\pi R_n^2$ = jet discharge at the nozzle (m^3/s)
Q^+ = jet discharge at survey section S_0 (m^3/s)
R_1, R_2 = characteristic radii for velocity component profiles (m)
R_n = nozzle radius (m)
$R_{\text{jet}}, R_{\text{core}}$ = jet outer radius and jet core radius (m)
R_0 = radius of the survey section S_0, $R_0=0.2126$ m (m)
R_{ref} = runner throat radius, $R_{\text{ref}}=0.2$ m (m)
R_C, R_B = characteristic radii for turbulent kinetic energy profile (m)
S_0, S_1, S_2 = survey sections at the draft tube inlet, in the cone, and downstream the cone, respectively
U_0, U_1, U_2 = characteristic velocities for axial velocity profile (m/s)
V_z, V_r, V_θ, V = axial, radial, and circumferential velocity components, and velocity magnitude, respectively (m/s)
V_{jet}, V_m = jet velocity at the nozzle and maximum jet velocity downstream the nozzle, respectively (m/s)
$V_0=Q/(\pi R_0^2)$ = average discharge velocity at the inlet section (m/s)
V_z^+ = jet velocity profile at survey section S_0 (m/s)
k, k_C, k_B = turbulent kinetic energy and its amplitudes in the crown and band wakes, respectively (m^2/s^2)
p = static pressure (Pa)
z, r = axial and radial coordinates (m)
z_n = distance from the nozzle to the survey section S_0 (m)
Π, K, E = potential, kinetic, and total energy fluxes, respectively (W)
$\Omega_0, \Omega_1, \Omega_2$ = characteristic angular velocities for circumferential velocity profile (rad/s)
$\alpha=Q^+/Q_{\text{jet}}$ = jet entrainment coefficient
$\varphi=Q/(\omega R_{\text{ref}}\pi R_{\text{ref}}^2)$ = turbine discharge coefficient without control jet
$\psi=2gH/(\omega^2 R_{\text{ref}}^2)$ = turbine energy coefficient, $\psi=1.18$
ε = turbulence dissipation rate (m^2/s^3)
ρ = density (kg/m^3)
ω = runner angular velocity, $\omega=100\pi/3$ rad/s (rad/s)
ζ = energy loss coefficient
χ = kinetic-to-potential energy recovery ratio

Appendix

The behavior of a jet discharged in surrounding fluid is well understood and described quantitatively [37]. A large body of experimental data was available to validate either theoretical results or empirical formulas. We will use such a jet model to evaluate the jet velocity profile in the survey section S_0, representing the inlet section of our computational domain, when the nozzle is located at a distance z_n upstream. A suitable model corresponds to the so-called confined jets, i.e., jets that are expanding in ducts with a mean axial flow of velocity V_0. The maximum velocity in the jet V_m initially remains constant within the vortex core of length L_c, then decreases as

$$(V_m - V_0) = \begin{cases} (V_{\text{jet}} - V_0) & \text{for } z_n < L_c \\ (V_{\text{jet}} - V_0)\dfrac{L_c}{R_n}\dfrac{1}{z_n/R_n} & \text{for } z_n \geq L_c \end{cases} \tag{A1}$$

The core radius R_{core} decreases as

$$\frac{R_{\text{core}}}{R_n} = 0.95 - m_1\frac{z_n}{R_n} \tag{A2}$$

thus the jet core length corresponds to the vanishing core

$$\frac{L_c}{R_n} = \frac{0.95}{m_1} \tag{A3}$$

The jet extends radially up to the jet radius R_{jet}, which grows linearly downstream,

$$\frac{R_{\text{jet}}}{R_n} = 1.04 + m_2\frac{z_n}{R_n} \tag{A4}$$

The coefficients m_1 and m_2 depend on the V_0/V_{jet} ratio [37]. The radial velocity profile in a jet cross section is approximated within the jet core $z_n < L_c$ by

$$\frac{V_z^+(r) - V_0}{V_m - V_0} = \begin{cases} 1 & \text{for } r \leq R_{\text{core}} \\ \dfrac{1}{2}\left[1 - \cos\ \pi\left(\dfrac{R_{\text{jet}} - r}{R_{\text{jet}} - R_{\text{core}}}\right)\right] & \text{for } R_{\text{core}} < r < R_{\text{jet}} \\ 0 & \text{for } r \geq R_{\text{jet}} \end{cases} \tag{A5}$$

while outside the vortex core $z_n \geq L_c$ we have

$$\frac{V_z^+(r) - V_0}{V_m - V_0} = \begin{cases} \dfrac{1}{2}\left[1 + \cos\ \pi\dfrac{r}{R_{\text{jet}}}\right] & \text{for } r < R_{\text{jet}} \\ 0 & \text{for } r \geq R_{\text{jet}} \end{cases} \tag{A6}$$

The discharge surplus associated with the control jet in section S_0 is $Q^+ = \int_0^{R_{\text{jet}}}(V_z - V_0)2\pi r dr$, and it can be evaluated using Eqs. (A5) and (A6) as

$$Q^+ = (V_m - V_0)\pi R_{\text{jet}}^2\frac{1}{2}\left[1 + \frac{R_{\text{core}}^2}{R_{\text{jet}}^2} - \frac{4}{\pi^2}\left(1 - \frac{R_{\text{core}}}{R_{\text{jet}}}\right)^2\right] \quad \text{for} \quad z_n < L_c$$

$$Q^+ = (V_m - V_0)\pi R_{\text{jet}}^2\frac{1}{2}\left(1 - \frac{4}{\pi^2}\right) \quad \text{for} \quad z_n \geq L_c \tag{A7}$$

The above model seems to be suitable for a jet injected from a nozzle on the crown into the flow downstream the runner. However, when the turbine is operated at partial discharge, the jet is actually injected into the growing wake of the runner crown, i.e., into a quasistagnant and possibly recirculating region near machine axis. Therefore, since our jet is intended to control the flow in the draft tube cone at part load it is more appropriate to assume that the jet is issued into a stagnant fluid with $V_0 = 0$. In this case the jet will be decelerated faster than with coflow $V_0 > 0$. The discharge associated with the jet increases as we move downstream from the nozzle due to entrainment of surrounding fluid. We can define a jet entrainment coefficient α for $V_0 = 0$ as

$$\alpha \equiv \frac{Q^+}{Q_{\text{jet}}} = \begin{cases} \dfrac{V_m}{V_{\text{jet}}}\left(\dfrac{R_{\text{jet}}}{R_n}\right)^2\dfrac{1}{2}\left[1 + \dfrac{R_{\text{core}}^2}{R_{\text{jet}}^2} - \dfrac{4}{\pi^2}\left(1 - \dfrac{R_{\text{core}}}{R_{\text{jet}}}\right)^2\right] & \text{for } z_n < L_c \\ \dfrac{V_m}{V_{\text{jet}}}\left(\dfrac{R_{\text{jet}}}{R_n}\right)^2\dfrac{1}{2}\left(1 - \dfrac{4}{\pi^2}\right) & \text{for } z_n \geq L_c \end{cases} \tag{A8}$$

When adding the jet velocity profile corresponding to Eq. (A5) or Eq. (A6) to the main flow axial velocity we must take into account that the total discharge is $Q + Q_{\text{jet}}$. However, $Q + Q^+ > Q + Q_{\text{jet}}$ because of jet entrainment, which actually slows down the outer main flow. This effect is taken into account by the following expression for the modified axial velocity profile:

$$V_z(r) = \left[U_0 + U_1\ \exp\left(-\frac{r^2}{R_1^2}\right) + U_2\ \exp\left(-\frac{r^2}{R_2^2}\right)\right]\left[1 - (\alpha - 1)\frac{Q_{\text{jet}}}{Q}\right] + V_z^+(r) \tag{A9}$$

The total discharge for the modified axial velocity profile (Eq. (A9)) is $Q + Q_{\text{jet}}$, and remains constant independent of the nozzle location with respect to the section S_0.

References

[1] Escudier, M., 1987, "Confined Vortices in Flow Machinery," Annu. Rev. Fluid Mech., **19**, pp. 27–52.

[2] Arpe, J., Nicolet, C., and Avellan, F., 2009, "Experimental Evidence of Hydroacoustic Pressure Waves in a Francis Turbine Elbow Draft Tube for Low Discharge Conditions," ASME J. Fluids Eng., **131**, p. 081102.

[3] Palde, U. J., 1972, "Influence of the Draft Tube Shape on Surging Characteristics," American Society of Civil Engineers National Water Resources Engineering Meeting, Atlanta, GA.

[4] Fox, R. W., McDonald, A. T., and Van Dewoestine, R. V., 1971, "Effects of Swirling Inlet Flow on Pressure Recovery in Conical Diffusers," AIAA J., **9**(10), pp. 2014–2018.

[5] Neve, R. S., and Wirasinghe, N. E. A., 1978, "Changes in Conical Diffusers Performance by Swirl Addition," Aeronaut. Q., **29**, pp. 131–143.

[6] Senoo, Y., Kawaguchi, N., and Nagata, T., 1978, "Swirl Flow in Conical Diffusers," Bulletin of JSME, **21**(151), pp. 112–119.

[7] Clausen, P. D., Koh, S. G., and Wood, D. H., 1993, "Measurements of a Swirling Turbulent Boundary Layer Developing in a Conical Diffuser," Exp. Therm. Fluid Sci., **6**, pp. 39–48.

[8] Avellan, F., 2000, "Flow Investigation in a Francis Draft Tube: The FLINDT Project," *Proceedings of the 20th IAHR Symposium on Hydraulic Machinery and Systems*, Charlotte, NC, Paper No. DY-03.

[9] Mauri, S., Kueny, J.-L., and Avellan, F., 2004, "Werlé-Legendre Separation in a Hydraulic Machine Draft Tube," ASME J. Fluids Eng., **126**, pp. 976–980.

[10] Susan-Resiga, R., Ciocan, G. D., Anton, I., and Avellan, F., 2006, "Analysis of the Swirling Flow Downstream a Francis Turbine Runner," ASME J. Fluids Eng., **128**, pp. 177–189.

[11] Zhang, R.-K., Cai, Q.-D., Wu, J.-Z., Wu, Y.-L., Liu, S.-H., and Zhang, L., 2005, "The Physical Origin of Severe Low-Frequency Pressure Fluctuations in Giant Francis Turbines," Mod. Phys. Lett. B, **19**(28–29), pp. 99–102.

[12] Mauri, S., Kueny, J.-L., and Avellan, F., 2000, "Numerical Prediction of the Flow in a Turbine Draft Tube. Influence of the Boundary Conditions," *Proceedings of the ASME 2000 Fluids Engineering Division Summer Meeting*, Boston, MA, Paper No. FEDSM'00-11084.

[13] Darmofal, D. L., 1996, "Comparisons of Experimental and Numerical Results for Axisymmetric Vortex Breakdown in Pipes," Comput. Fluids, **25**(4), pp. 353–371.

[14] Sloan, D. G., Smith, P. J., and Smoot, L. D., 1986, "Modeling of Swirl in Turbulent Flow Systems," Prog. Energy Combust. Sci., **12**, pp. 163–250.

[15] Armfield, S. W., and Fletcher, C. A. J., 1986, "Numerical Simulation of Swirling Flow in Diffusers," Int. J. Numer. Methods Fluids, **6**, pp. 541–556.

[16] Armfield, S. W., and Fletcher, C. A. J., 1989, "Comparison of $k-\varepsilon$ and Algebraic Reynolds Stress Models for Swirling Diffuser Flow," Int. J. Numer. Methods Fluids, **9**, pp. 987–1009.

[17] Armfield, S. W., Cho, N.-H., Clive, A., and Fletcher, J., 1990, "Prediction of Turbulence Quantities for Swirling Flow in Conical Diffusers," AIAA J., **28**(3), pp. 453–460.

[18] Yaras, M. I., and Grosvernor, A. D., 2003, "Evaluation of One- and Two-Equation Low-Re Turbulence Models. Part I—Axisymmetric Separating and Swirling Flow," Int. J. Numer. Methods Fluids, **42**, pp. 1293–1319.

[19] Xu, D., Khoo, B. C., and Leschziner, M. A., 1998, "Numerical Simulation of Turbulent Flow in an Axisymmetric Diffuser With a Curved Surface Centre-Body," Int. J. Numer. Methods Heat Fluid Flow, **8**(2), pp. 245–255.

[20] Lu, P., and Semião, V., 2003, "A New Second-Moment Closure Approach for Turbulent Swirling Confined Flows," Int. J. Numer. Methods Fluids, **41**, pp. 133–150.
[21] Shih, T.-H., Liou, W. W., Shabbir, A., Yang, Z., and Zhu, J., 1995, "A New $k-\varepsilon$ Eddy Viscosity Model for High Reynolds Number Turbulent Flows—Model Development and Validation," Comput. Fluids, **24**(3), pp. 227–238.
[22] Susan-Resiga, R., Muntean, S., Stein, P., and Avellan, F., 2009, "Axisymmetric Swirling Flow Simulation of the Draft Tube Vortex in Francis Turbines at Partial Discharge," International Journal of Fluid Machinery and Systems, **2**(4), pp. 295–302.
[23] Jawarneh, A. M., and Vatistas, G. H., 2006, "Reynolds Stress Model in the Prediction of Confined Turbulent Swirling Flows," ASME J. Fluids Eng., **128**, pp. 1377–1382.
[24] Speziale, C. G., Sarkar, S., and Gatski, T. B., 1991, "Modelling the Pressure-Strain Correlation of Turbulence: An Invariant Dynamical System Approach," J. Fluid Mech., **227**, pp. 245–272.
[25] Benim, A. C., 1990, "Finite Element Analysis of Confined Turbulent Swirling Flows," Int. J. Numer. Methods Fluids, **11**, pp. 697–717.
[26] Fluent Inc., 2005, FLUENT 6.2 User's Guide.
[27] Gallaire, F., Ruith, M., Meiburg, E., Chomaz, J.-M., and Huerre, P., 2006, "Spiral Vortex Breakdown as a Global Mode," J. Fluid Mech., **549**, pp. 71–80.
[28] Gebart, B. R., Gustavsson, L. H., and Karlson, R. I., 2000, "Proceedings of the Turbine-99 Workshop on Draft Tube Flow," Luleå University of Technology, Report No. 2000:11.
[29] Thicke, R. H., 1981, "Practical Solutions for Draft Tube Instability," Int. Water Power and Dam Construction, **33**(2), pp. 31–37.
[30] Nishi, M., Wang, X. M., Yoshida, K., Takahashi, T., and Tsukamoto, T., 1996, "An Experimental Study on Fins, Their Role in Control of the Draft Tube Surging," *Hydraulic Machinery and Cavitation*, E. Cabrera, V. Espert, and F. Martinez, eds., Kluwer Academic Publishers, Dordrecht, The Netherlands, pp. 905–914.
[31] Kurokawa, J., Kajigaya, A., Matusi, J., and Imamura, H., 2000, "Suppression of Swirl in a Conical Diffuser by Use of J-Groove," *Proceedings of the 20th IAHR Symposium on Hydraulic Machinery and Systems*, Charlotte, NC, Paper No. DY-01.
[32] Kjeldsen, M., Olsen, K.-M., Nielsen, T., and Dahlhaug, O. G., 2006, "Water Injection for the Mitigation of Draft-Tube Pressure Pulsations," IAHR International Meeting of W.G. on Cavitation and Dynamic Problems in Hydraulic Machinery and Systems, Barcelona, Spain.
[33] Falvey, H. T., 1971, "Draft Tube Surges—A Review of Present Knowledge and an Annotated Bibliography," U.S. Bureau of Reclamation, Report No. REC-ERC-71-42.
[34] Vevke, T., 2004, "An Experimental Investigation of Draft Tube Flow," Ph.D. thesis, Norwegian University of Science and Technology, Norwegian University of Science and Technology, Trondheim, Norway
[35] Karashima, K., 1984, "Effect of a Small Blowing on Vortex-Breakdown of a Swirling Flow," *Computational Techniques and Applications CTAC-83*, North-Holland, Amsterdam, pp. 553–564.
[36] Susan-Resiga, R., Vu, T. C., Muntean, S., Ciocan, G. D., and Nennemann, B., 2006, "Jet Control of the Draft Tube Vortex Rope in Francis Turbine at Partial Discharge," *Proceedings of the 23rd IAHR Symposium on Hydraulic Machinery and Systems*, Yokohama, Japan, Paper No. F192.
[37] Rajaratnam, N., 1976, *Turbulent Jets*, Elsevier, Amsterdam, Chap. 6, pp. 115–129.

LES of the Slipstream of a Rotating Train

Hassan Hemida[1]
School of Civil Engineering,
University of Birmingham,
B15 2TT, UK
e-mail: h.hemida@bham.ac.uk

Nahia Gil
School of Electrical Engineering,
University of Birmingham,
B15 2TT, UK

Chris Baker
School of Civil Engineering,
University of Birmingham,
B15 2TT, UK

The slipstream of a high-speed train was investigated using large-eddy simulation (LES). The subgrid stresses were modeled using the standard Smagorinsky model. The train model consisted of a four-coach of a 1/25 scale of the ICE2 train. The model was attached to a 3.61 m diameter rotating rig. The LES was made at two Reynolds numbers of 77,000 and 94,000 based on the height of the train and its speed. Three different computational meshes were used in the simulations: course, medium and fine. The coarse, medium, and fine meshes consisted of 6×10^6, 10×10^6, and 15×10^6 nodes, respectively. The results of the fine mesh are in fairly agreement with the experimental data. Different flow regions were obtained using the LES: upstream region, nose region, boundary layer region, intercarriage gap region, tail region, and wake region. Localized velocity peak was obtained near the nose of the train. The maximum and minimum pressure values are also noticed near to the nose tip. Coherent structures were born at the nose and roof of the train. These structures were swept by the radial component of the velocity toward the outer side of the train. These structures extended for a long distance behind the train in the far wake flow. The intercarriage gaps and the underbody complexities, in the form of supporting cylinders, were shown to have large influences on the slipstream velocity. The results showed that the slipstream velocity is linearly proportional to the speed of the train in the range of our moderate Reynolds numbers.
[DOI: 10.1115/1.4001447]

1 Introduction

When a train moves in the atmosphere a significant air velocity can result at the side and the wake-train slipstream. This phenomenon poses a safety risk for passengers and trackside workers and can cause problems for pushchairs and luggage trolleys. Own to its impact on the external environment, the Rail Safety and Standards Board (RSSB) [1] has recently identified this topic as an active one where research work of different types is required. A recent study conducted by RSSB shows that in Britain the overall risk associated with train slipstreams is small in comparison to other risks; however, train slipstreams can have a significant effect on the safety of passengers on platforms and trackside workers if the risk from them is not managed effectively. Since 1972, 24 incidents have been reported in mainland Britain, which involve not only airflow induced forces mainly on wheeled items on station platforms (pushchairs, wheelchairs, trolleys) but also on passengers and their belongings [2,3]. The aerodynamic forces on an object on the platform or trackside, however, depend on the shape of the object and are proportional to the square of the slipstream velocity. The slipstream velocity itself is, in general terms, proportional to the speed of the train. Thus, since the new generation of trains is characterized by high-speed to reduce the time of the journey and to accommodate a maximum possible capacity of passengers on the rail network, the risk of slipstream has become larger and thorough understanding of the mechanism of the flow around high-speed trains is required.

There are two current approaches to the measurement of train slipstreams either at full scale or at model scale. These approaches are fully described in Refs. [4,5]. Baker et al. [5] used hot films positioned close to a 1/25 scale model consisted of four coaches in a moving model rig to measure the velocities around the train. In their work a small number of particle imaging velocimetry (PIV) experiments were also carried out. Sterling et al. conducted similar work on a full scale freight and passenger trains. However, since the train slipstream is a transient phenomena associated with a highly turbulent flow, a large number of realizations is needed to be carried out in order to obtain adequate results for the ensemble average and standard deviations of time histories. This makes the two experimental techniques demand intensive time and financial resources. For this reason, a rotating rig with a diameter of 3.61 m, at the Railway Research Centre in University of Birmingham, was used to measure the velocity in the slipstream. The new experimental technique makes it possible to measure the assemble average of the velocity at certain points along the length of the train. However, the complete picture of the flow field and the coherent structures of the slipstream as well as the pressure field are still missing and out of the range of experimental investigations [6].

Until recently, it was impractical to predict numerically the time-dependent flow around trains even at relatively low Reynolds number. In recent years, the increase in the computer capability has made these simulations (at moderate Reynolds numbers) possible. The application of computational fluid dynamics (CFD) becomes attractive when experimental investigations are expensive, not applicable or are difficult to perform. In general, experimental techniques demand intensive time and financial resources. Total alleviation of these drawbacks through the use of scale wind tunnels is not possible because of Reynolds number restrictions. Also for a nontrivial number of flow cases, reproduction of some specific boundary and/or operating conditions in wind tunnels is beyond realization. Moreover, open air testing is governed primarily by atmospheric conditions, which makes the replication of experiments extremely difficult.

With the speed-up of trains and production of the new generation of high-speed trains many aerodynamic problems, which have been reasonably neglected at low speeds, are being raised with regard to aerodynamic noise and vibrations, impulse forces occurring as a result of train passing, impulse wave at the exit of a tunnel, ear discomfort of passengers inside train, etc. These are the major limiting factors to the speed-up of train system [7]. Therefore, the aerodynamics of high-speed trains has received considerable attention from many researchers during the last 2 decades trying to improve their performance [8–12].

[1]Corresponding author.
Contributed by the Fluids Engineering Division of ASME for publication in the JOURNAL OF FLUIDS ENGINEERING. Manuscript received June 26, 2009; final manuscript received March 5, 2010; published online May 6, 2010. Assoc. Editor: Meng Wang.

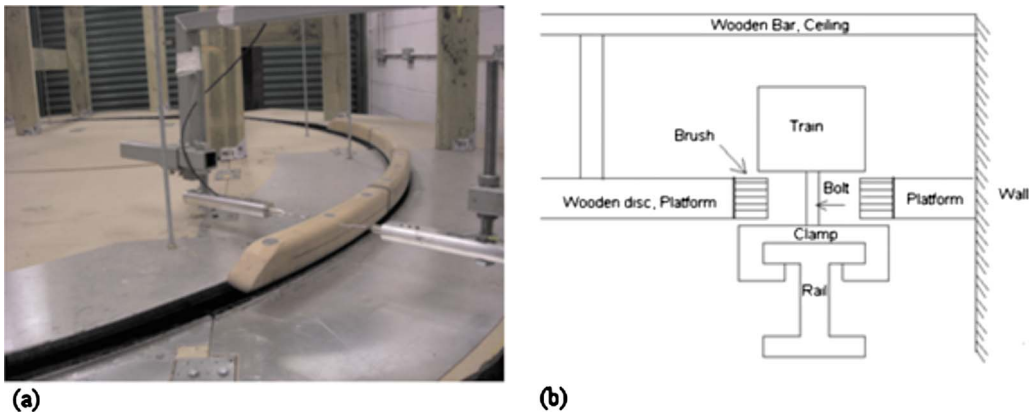

Fig. 1 Experimental set-up. (*a*) Train model and measuring probe. (*b*) Schematic diagram of the rail and train support.

Muld et al. [13] conducted CFD simulations of the flow around an aerodynamic train model (ATM) using detached-eddy simulation (DES) to analyze the flow in the wake of the train. They compared the CFD results against experimental data and the overall levels and trends are captured using DES. However, the peak value of the velocity magnitude in the wake and boundary layers is overestimated by the DES. Recently, large-eddy simulation (LES) with the standard Smagorinsky model has been successfully used to investigate the flow around trains subjected to side winds [14–16].

In the present paper, the transient behavior of the slipstream around a rotating model is investigated using LES with the standard Smagorinsky model. Two Reynolds numbers (Re) of 77,000 and 94,000 based on the height of the train and the train speed are used in this investigation. The computational package CFX5 [17] is utilized to simulate the rotation of the model using the sliding mesh technique.

2 Experimental Set-Up

The rotating rail rig consists of a 3.61 m diameter railway track on a frame that can be rotated at up to 118 rpm, which corresponds to a rail speed of 22 m/s, see Fig. 1. It was originally designed so that standard rail sections could be mounted on the frame to enable investigations into the removal of accreted organic matter using novel laser based techniques [5] and has since been used to investigate conductor shoe icing with a stationary conductor shoe held above the rotating rail while the temperature was lowered to below freezing conditions. In the current investigation, a 1/25 ICE2-like train model with height $H=70$ mm and wagon length $L=0.5$ m is mounted on the rotating rail via a clamp and a bolt (two sets in each carriage) so that they both move as a whole (see Fig. 1(*b*)). The wagons are connected by three intercarriage gaps. A typical intercarriage gap has an equal depth and width W, which is one-seventh of the train height. In order to reduce the turbulence arising from the rotation of the wheel, as well as to provide a ground plane over which the train moves, a wooden platform with a circular slot slightly bigger than the rail is positioned above the rig. The gap between the train and the ground plane is closed with brushes. The way the train is attached to the rail allows the carriages to be assembled and disassembled as required. Thus, measurements of the flow can be performed using any combination of the cars of the train. The most important aspect of this rig is of course that multiple train passes can be achieved very quickly (one per revolution of the rig) and thus, in principle, experiments can be carried out much more rapidly than with the current full scale and model scale techniques

3 Train Model

The train model consists of four curved couches. The problem that emerged from the straight coaches was that the length of the train wagons (about 50 cm) was relatively large in comparison to the radius of curvature of the rig $R=180.5$ cm and thus there were sharp discontinuities in train orientation at the end of each carriage. Moreover, the distance between the probe and the surface of the train was not constant so there was a significant variation in the probe measurement position from both the train top and sides. To tackle these problems, it was decided to construct a "curved" train so that measurements are provided along "curved lines" next to the vehicle (Fig. 1(*a*)). In addition, this new train has been designed as a simplified 1/25 scale ICE2 train so that results can be compared with those obtained at the TRAIR rig, where a 1/25 scale four-coach ICE2 train model was employed. Obviously, these results will be affected by the curvature of the train (the more carriages used in the test the higher the effect) with the boundary layer increasing more in the convex side of the train than in the concave side (see Refs. [18,19]). In the experiment, the slipstream and wake velocities are measured using stationary Cobra probes (turbulent flow instrumentation P/L), which are four-hole pressure probes that can measure three components of velocity at speeds of up to 100 m/s. More information about the probe can be found in Ref. [6].

4 Numerical Method

The flow around a moving train is very complicated and consists of large range of turbulent scales. It is believed that the large turbulent scales contribute most in the train aerodynamics. Moreover, the wake flow and boundary layer are dominated by large turbulent structures. Hence, a simulation method that resolves the large structures such as LES is preferable for simulations of the flow around trains. Although LES is computationally more expensive than the Reynolds Averaged Navier–Stokes (RANS), it can provide more accurate time-averaged results and also give information about the instantaneous flow that is out of reach of RANS. LES has already been proved to be a reliable technique in prediction of the flow around simplified trains and bluff bodies [14–16].

Generally, LES decomposes the structures of the flow into large and small scales. The large motions of the flow are directly simulated while the influence of the small scale on the large scale motions is modeled. Hence, LES is a kind of compromising between RANS and direct numerical simulation.

The filtered continuity and momentum equations for incompressible flow are

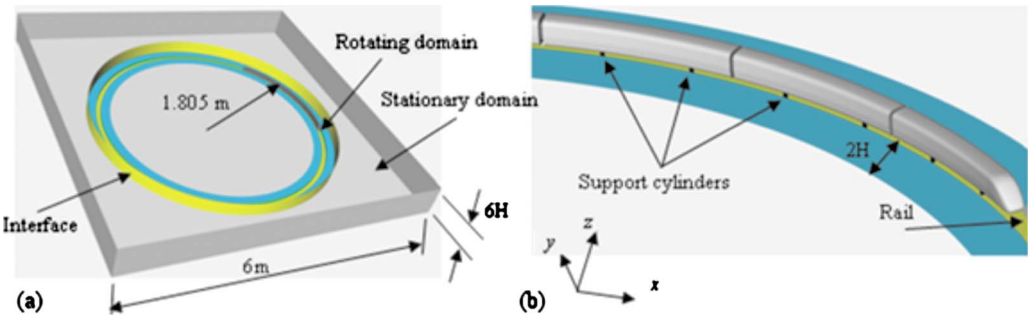

Fig. 2 Computational domain showing (*a*) dimensions of the rotating and stationary domains and (*b*) computational model and supporting cylinders

$$\frac{\partial \bar{U}_i}{\partial x_i} = 0 \tag{1}$$

and

$$\frac{\partial \bar{U}_i}{\partial t} + \bar{U}_j \frac{\partial \bar{U}_i}{\partial x_j} = -\frac{1}{\rho}\frac{\partial \bar{p}}{\partial x_i} + \frac{\partial}{\partial x_j}\left(\nu \frac{\partial \bar{U}_i}{\partial x_j}\right) + \tau_{ij}^R \tag{2}$$

where $\overline{U_j}$, $\bar{p}$, and τ_{ij}^R are the filtered velocity, filtered pressure, and residual stresses, respectively.

The residual stresses are unknown and they need to be modeled. The linear eddy viscosity model is used to relate the subgrid stresses to the resolved strain-rate tensor $\bar{S}_{ij}$ as

$$\tau_{ij}^R - \frac{1}{3}\tau_{kk}^R = -2 \cdot \nu_{\mathrm{SGS}} \cdot \bar{S}_{ij} = -\nu_{\mathrm{SGS}} \cdot \left(\frac{\partial \bar{U}_i}{\partial x_j} + \frac{\partial \bar{U}_j}{\partial x_i}\right) \tag{3}$$

where the coefficient of proportionality ν_{SGS} is the eddy viscosity of the subgrid motion.

The most common model of ν_{SGS} is the Smagorinsky model, which takes the form:

$$\nu_{\mathrm{SGS}} = (C_s f \Delta)^2 \sqrt{2\bar{S}_{ij}\bar{S}_{ij}} \tag{4}$$

Here, Δ is the filter width, C_s is the Smagorinsky coefficient, and f is the Van Driest damping function. The value of the SGS model coefficient C_s is 0.1 in the present work. Since the resolved strain-rate tensor does not vanish at the wall, the value of the model coefficient C_s should be adjusted to take partially into account the effect of the wall. Thus the Van Driest damping function f is used to damp the turbulence length scale next to the wall. This function takes the form

$$f = 1 - \exp\left(\frac{-y^+}{25}\right) \tag{5}$$

where y^+ is the normalized wall distance.

More information about LES on ANSYS-CFX can be found in Ref. [17].

5 Computational Domain and Boundary Conditions

The numerical set-up is made to match the experimental set-up as close as possible. The computational configuration consists of two domains: stationary and rotating, as shown in Fig. 2(*a*). The base of the stationary domain is a squarelike shape with an edge length of 6 m. The height of the stationary domain is 6*H*. A no-slip boundary condition is applied on the floor of the stationary domain while opening boundary condition is applied on the sides and roof of the domain. The rotating domain extends 2*H* in both sides of the surface of the train and its height is 4*H*, as shown in Fig. 2(*b*). The train model, rail, and supporting cylinders are based in the rotating domain. The rotating domain rotates clockwise with an angular velocity equal to that corresponding to the speed of the train. A no-slip boundary condition is applied at the bottom face of the rotating domain. In order to have similar boundary conditions to those of the experiment, the rail rotates at the same speed and direction of the train while the platform rotates in a reverse direction to that of the rotating frame. A transient general grid interface (GGI) is employed between the two domains where information are exchanged at each time step. A no-slip boundary condition is used on the model wall. Both the stationary and rotating domains are initialized by zero velocity at the start of the simulation. The Cartesian coordinate system is shown in Fig. 2(*b*). The origin is in the center of the domain on the platform level. The *z*-direction points up toward the normal direction of the platform while *x*-*y* plane coordinates are on the horizontal plane (platform level).

6 Results

This section reports the results from the LES at two Re of 77,000 and 94,000 based on the height of the train and the train speed. The speed of the train is used to normalize the velocity in the slipstream while the height of the train is used to normalize the boundary layer displacement thickness. Most of the analysis will be made for slipstream at the lower Re while the influence of Re in the slipstream structure is reported at the end of this section.

6.1 Assessment of the Numerical Accuracy. The LES equations were discretized using a three-dimensional finite volume method in a collocated grid arrangement. To investigate the influence of the mesh resolution on the results and to establish numerical accuracy, three computations on three different computational grids, coarse, medium and fine, were made. The ICEM-CFD commercial grid-generator package was used to create both the model geometry and meshes around it. The ICEM-CFD hexa package was employed to generate a hexahedral mesh around the model. An *O*-type mesh was made in the belt of thickness of 0.1*H* around the train. This allows the generation of a smooth mesh in all directions, see Fig. 3(*b*). Figure 3(*a*) shows the surface mesh on and close to the intercarriage gap while Fig. 3(*c*) shows the medium mesh around the front nose of the train. A hyperbolic stretching is used to make a finer mesh close to the train model and a coarser mesh in the regions away from the train. The total numbers of nodes are 6×10^6, 10×10^6, and 15×10^6 for the

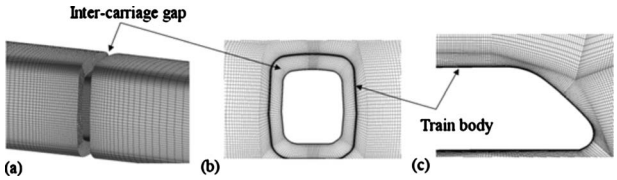

Fig. 3 Medium mesh. (*a*) Surface mesh on and close to the intercarriage gap. (*b*) Cross section showing the mesh shape on and around the intercarriage gap. (*c*) Mesh around the nose of the train.

Table 1 Maximum spatial resolutions for the coarse, medium, and fine meshes

Mesh	No. of nodes	$y^+=nu*/\nu$	$x^+=lu*/\nu$	$z^+=su*/\nu$
Fine	15×10^6	0.8	100	20
Medium	10×10^6	1	200	100
Coarse	6×10^6	5	900	300

coarse, medium, and fine meshes, respectively. The maximum resolutions and number of nodes of the different meshes are shown in Table 1, where u^* is the friction velocity, n is the distance between the first node and the train surface in the wall normal direction, s is the cell width in the streamwise direction, and l is the cell width in the spanwise direction.

The convective, viscous diffusion plus subgrid fluxes were approximated by the second-order-accurate central difference scheme. To reduce numerical dissipation, no upwind schemes were used in the simulations. Since the central difference scheme is more sensitive to the stretching ratio in the places where large flow variations are expected the mesh stretching ratio was kept below 1.1 in the rotating domain and around the train model. The time integration was done using the Crank–Nicolson second-order scheme using a coupled solver. A constant time step of 5×10^{-5} s is used through out the entire simulation. This gives a maximum Courant–Friedrichs–Lewy number of about 1 and its rms value of about 0.5.

The time-averaged flow is computed using five full laps. The positions at which the slipstream velocities are measured are shown in Fig. 4. Figure 5 illustrates the velocity magnitude V_m in the slipstream at half the height of the train and at a distance $0.084H$ from the outer surface of the train above the platform level $z/H=0.5$, plotted against the distance from the train nose normalized by the length of one carriage. The origin is being aligned with the peak of the nose pressure pulse. The distance is calculated by counting the time elapsed from the moment at which the nose of the train passed an imaginary fixed probe, similar to the technique used in the experiment, times the speed of the train divided by the length of the wagon. This convention is being used with all the plots that are described below unless otherwise stated. The results are obtained using the three different meshes; course, medium and fine. In general, the coarse, medium, and fine meshes give similar results.

The results of the LES fine mesh at Reynolds number 77,000 based on the height of the train and train speed are compared with the experimental data at the same Reynolds number. To investigate the reliability of using RANS model to predict the slipstream

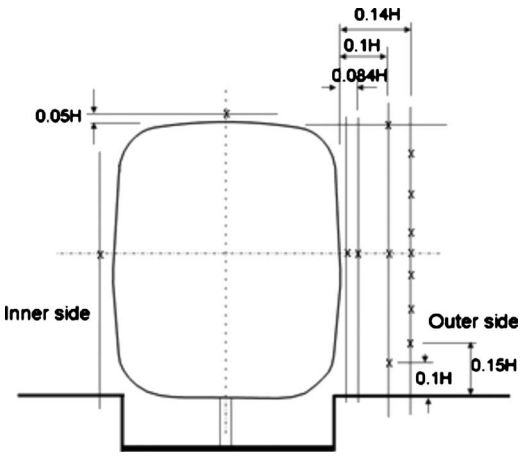

Fig. 4 Schematic representation of the positions at which the slipstream velocities are measured

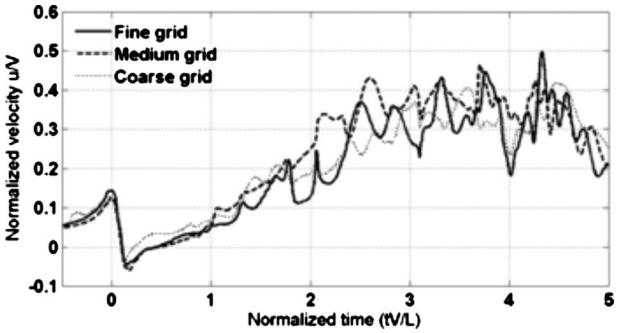

Fig. 5 Slipstream velocity (based on the velocity magnitude) at half train height and a distance $0.084H$ from the outer surface (Re=77,000)

velocity, a RANS simulation has been performed using the SST-KOmega model on the fine mesh at the same Reynolds number as the LES simulation. Figure 6 represents the LES tangential velocity distributions, the component of the velocity parallel to the surface of the train V_θ at a distance $0.084H$ from the outer and inner (concave) surface of the train at its half height. Here, the tangential velocity component is used because it is the one being measured in the experiment. The RANS and experimental tangential velocity are shown in Fig. 6, at the same position from the outer surface as the LES. The first observation is that, far from the nose, the velocity distribution in the inner part of the slipstream is completely different from that in the outer (convex) part. This difference is due to the rotation of the train as it is expected. Generally, the overall levels and trends, however, are captured by the LES. Some discrepancies are noticed close to the nose, where the LES and RANS underestimate the slipstream velocity. This can be related to the alignment of the experimental probe close to the train nose. The probe is designed to measure the component of the velocity in the direction of travel of the train and is sensitive to its alignment. Moreover, the flow around nose is highly three-dimensional, which makes it difficult to measure one velocity component using the Cobra probe. Close to the nose, the LES shows a separated flow, which produces a negative value of the velocity component. The RANS results also show a negative tangential velocity on this region. However, the region of negative velocity obtained from the RANS simulation is small compared with that of LES, which can be attributing to the failure of RANS models in predicting separation. Figure 6 shows that the separation extends to about half the length of the first wagon. Again, the experiment probe is not designed to measure the reversed flow. This is shown as a discrepancy between the LES and experiment close to the nose as shown in Fig. 6.

Our LES results, however, are in agreement with the measure-

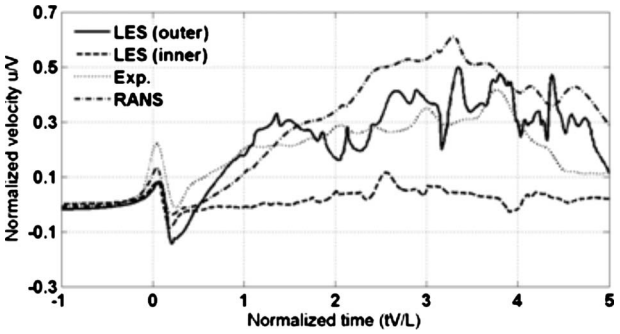

Fig. 6 Slipstream velocity (based on the tangential velocity V_θ) at half train height and a distance $0.084H$ from the inner and outer surfaces (Re=77,000)

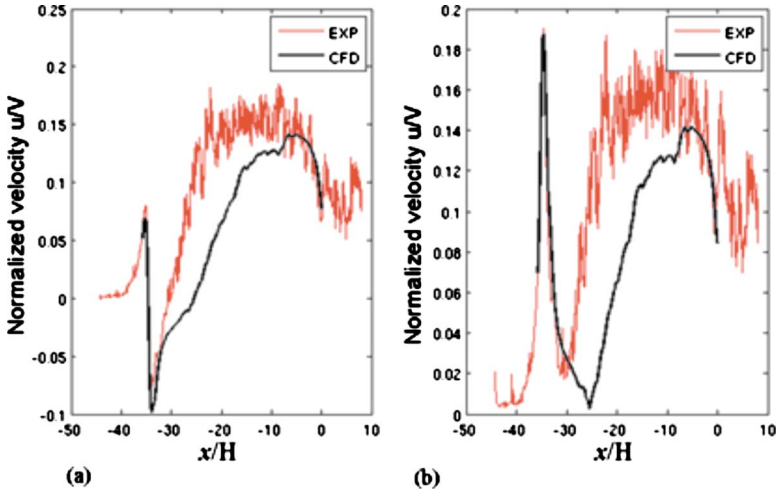

Fig. 7 Slipstream at height 0.4*H* from the platform and 0.25*H* from the surface of the train (Muld et al. [13]—used with permission): (*a*) based on the axial component of the velocity and (*b*) based on the velocity magnitude

ments of Muld et al. [13], where they used PIV to measure the slipstream on a straight ATM-model consisting of four cars. The results of Muld et al. [13] are shown in Fig. 7. Here, the origin of the x-axis is at the tail of the train. The separation is shown as a negative value of the axial component of the velocity close to the nose as shown in Fig. 7(*a*).

For more comparison with the experiment, the tangential velocity distribution, parallel to the surface of the train, at distance $0.05H$ above the train and at its centerline is shown in Fig. 8. The flow separates at two positions on the roof of the train; close to the front nose and close to the tail. This describes the discrepancies shown in Fig. 8. Although the LES underestimate the slipstream velocity above the third wagon, the trends and levels are well captured. The results from the RANS model are included in Fig. 8. The RANS model overestimates the nose peak and slipstream velocities.

6.2 Velocity Field. Figure 9 shows the time-averaged and a snapshot of the velocity magnitude normalized by the speed of the train at Re=77,000 together with the associated turbulent intensity. The results are at a distance of $0.14H$ from the outer surface of the train and at the half height of the body. The turbulent intensity is defined as

$$I = \frac{u'}{V_m} \tag{6}$$

where V_m is the time-averaged velocity magnitude and u' is the root-mean-square of the turbulent velocity fluctuations, defined as

$$u' = \sqrt{\frac{1}{3}(u_x'^2 + u_y'^2 + u_z'^2)} \tag{7}$$

Here, u_x', u_y', and u_z' are the velocity fluctuations in x-, y-, and z-directions, respectively. Figure 9 shows that the flow in the slipstream is highly transient and the time-averaged velocity is completely different compared with the transient one. The turbulent intensity is high close to the nose of the train. It drops along the length of the first wagon and the flow seems to be steadier than that close to the nose. After the first wagon and along the length of the train, the boundary layer starts to build up and higher turbulent intensity is noticed.

Figure 9 shows also that the flow in the slipstream can be divided into six regions: upstream, nose, boundary layer, intercarriage gap, wake, and far wake.

In the upstream region, the flow is essentially inviscid with low turbulent intensity level. Low upstream velocity values have been reported in Figs. 6 and 8. These velocities are from the history of

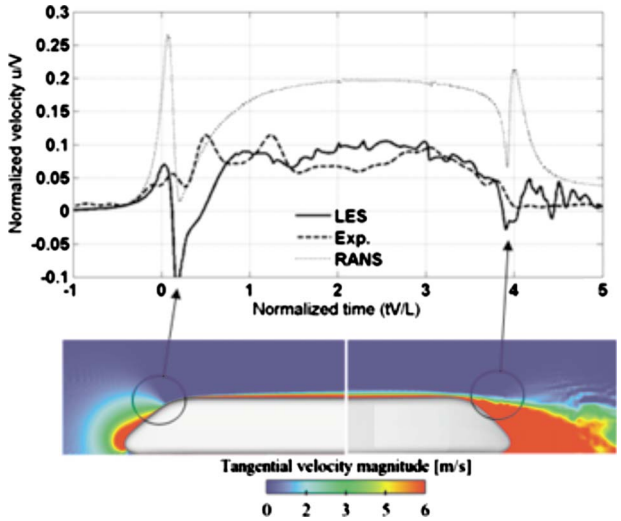

Fig. 8 Slipstream velocity (based on the tangential velocity V_θ) at 0.05*H* above the train at its centerline (Re=77,000)

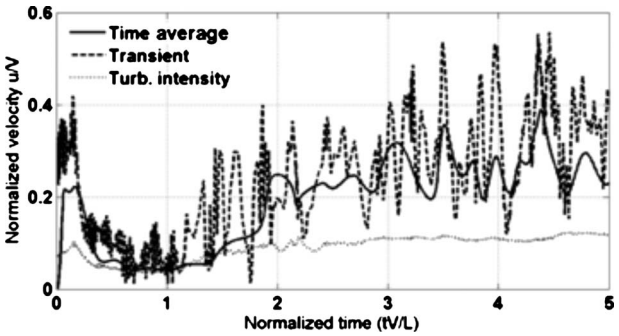

Fig. 9 Slipstream velocity (based on the velocity magnitude V_m) at half height of the body and a distance 0.14*H* from the outer surface (Re=77,000)

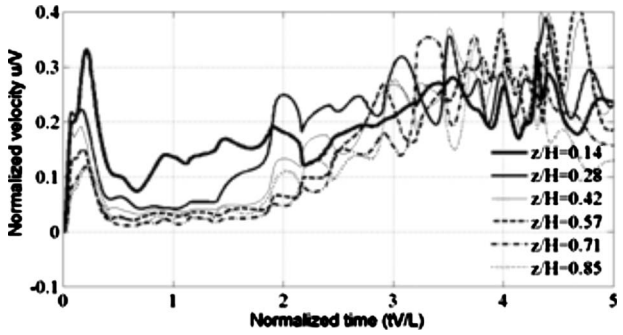

Fig. 10 Slipstream velocity (based on the velocity magnitude V_m) at a distance 0.14H from the outer surface (Re=77,000)

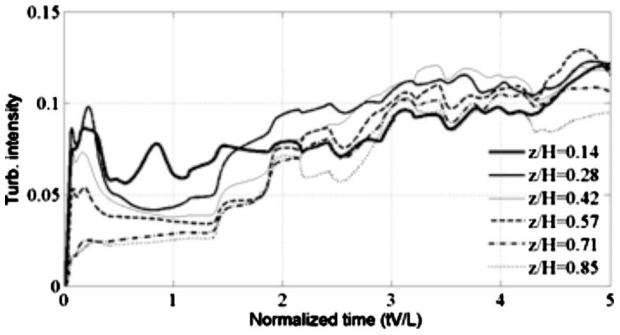

Fig. 11 Turbulent intensity at a distance 0.14H from the outer surface (Re=77,000)

the rotation of the train in the rig. Baker et al. [15] showed that for train moving in a still air, the effect of the moving train in the upstream velocity is negligible.

The slipstream velocity increases suddenly around the nose of the train. The train nose pushes the flow around it, resulting in a large increase in the flow velocity. The flow in this region is highly three-dimensional with high turbulent intensity level. This region can extend to half length of the leading car depending on the shape of the nose and velocity of the train. However, in our investigation on the ICE2 train the nose flow extends to about quarter of the length of the first car. Due to the sudden increase in the air velocity, the flow around the train separates to form a separation bubble. This separation reduces the slipstream velocity and the build up of the boundary layer starts. Figure 9 shows that the boundary layer starts to grow at the end of the first car and a high turbulent intensity level is noticed. Figure 9 also shows variations in the boundary layer time-averaged velocity. There are two possible reasons for these variations. The first one is flow disturbances caused by the intercarriage gaps. This is reflected as increase or decrease in the velocity magnitudes at the end of each car. The second reason is effect of the flow from the supporting cylinder fitting the model to the rail. The effect of the supporting cylinder is shown as an increase and decrease in the velocity magnitude at two places along the length of each car. These variations have been also noticed in the experimental data shown in Fig. 6. Similar behavior was reported in experimental works of Baker et al. [5] and Sterling et al. [4]. Although in their investigations they used straight trains moving on rails the existence of underbody complexities such as wheels and bogies and the intercarriage gaps resulted in wiggles in the transient and time-averaged flow. The variations appeared also in the experiment of Muld et al. [13] but not in their DES as shown in Fig. 7. However, the contribution of RANS in DES simulations damps out the fluctuations in the velocity field.

Figure 10 demonstrates the slipstream time-averaged velocity magnitude at a distance 0.14H from the outer surface of the train at different heights from the platform, $z/H=0.14$, 0.28, 0.42, 0.57, 0.71, and 0.85 while Fig. 11 illustrates the corresponding turbulent intensity levels. The nose peak and its associated turbulent intensity can be seen to be very significant close to the ground $z/H=0.14$. On the other hand, far away from the platform, a significant drop in both the nose peak and the associated turbulent intensity can be observed. The influence of the supporting cylinder (underbody complexities) and intercarriage gaps are more pronounced in the slipstream velocities close to the platform. As a consequence the slipstream velocity is more significant under the half height of the train along the first and second cars. In contrast, the build up of the boundary layer is more rapid above the half height of the train after the second car. In general, a similar order of magnitude of the time-averaged slipstream velocity is noticed at the wake and far wake flows. The highest turbulent intensity level is obtained close to the top of the train in the far wake flow. The interaction between the slipstream flow and the wake flow makes the flow in this region very complex and highly turbulent.

6.3 Boundary Layer Structures. In order to investigate the boundary layer development, the normalized displacement thickness δ^* is established for the roof and outer side boundary layers. The height of the train H is used to normalized the displacement thickness. The normalized displacement thickness δ^* is defined as

$$\delta^* = \int Udz/H \tag{8}$$

where U is the scaled velocity profile. Although this expression of the displacement thickness is based on a two-dimensional configuration it is still useful to use it here to get a feeling about the development of the boundary layer. Moreover, although the displacement thickness is different than the boundary layer thickness, which is more significant in our investigation, the trend is expected to be similar. Furthermore, it is hard to define a precise definition of the boundary layer thickness around a moving bluff body similar to our case in this investigation. A radial velocity component V_r is present in the flow due to the rotation of the model. Since the flow above and around the train is three-dimensional, it is not obvious which component of the velocity can be used in the definition of the displacement thickness.

We expect the contribution of the radial velocity in the velocity magnitude to be significant in the flow above the train. Hence, δ^* is calculated for the flow above the train using the velocity magnitude V_m and the two velocity components V_θ and V_r. The results are shown in Fig. 12. The nose peak can be seen to be of more significance for those measurements with the velocity magnitude. The peak is less significance based on V_θ or V_r. Figure 12 demonstrates that the radial component close to the nose has no role in the displacement thickness. The difference here is related to the vertical velocity component, which is large close to the nose of the train. At the middle of the second car, both the displacement

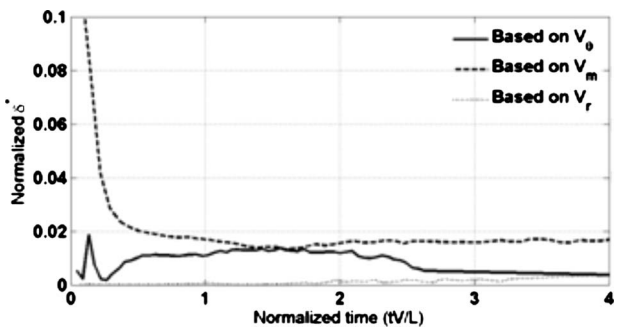

Fig. 12 Normalized displacement thickness above the train at its centerline (Re=77,000)

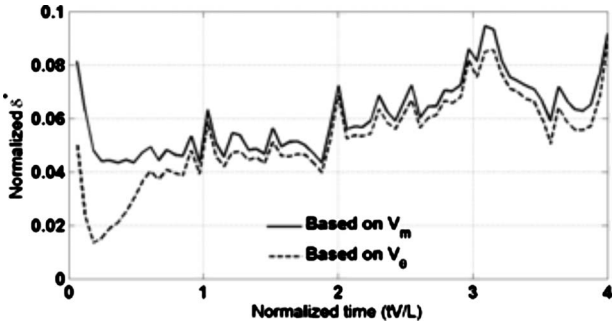

Fig. 13 Normalized displacement thickness at half height of the train on the outer side (Re=77,000)

thicknesses obtained using V_m and V_θ are collapsed in one curve. On the other hand, the displacement thickness based on the radial velocity component V_r starts to build up. In general, the displacement thicknesses based on the velocity magnitude and on the radial velocity component grow along the train length while the one based on the tangential velocity damps out at the middle of the second car.

In a similar way, the displacement thickness is calculated on the outer side flow using V_m and V_θ. Figure 13 displays the results at half the height of the train. Large differences can be noticed close to the nose of the train. These differences are related to the three-dimensional behavior of the flow in this region. After the first car in the direction of the train length, we noticed a slight difference between the two methods and can be retaining to the radial component of the velocity. A clear influence of the intercarriage gaps and support cylinders can be noticed on the displacement thickness in Fig. 13. The displacement thickness is reduced just before the intercarriage gap and is increased behind it. There is also a jump on the displacement thickness near the places where the support cylinders exist. The magnitude of the normalized displacement thicknesses in Fig. 13 is larger than those presented in Fig. 12. This indicates a more significance boundary layer thickness on the sides of the train more than that above the train.

It is however important to note that the displacement thickness shows the trend of the boundary layer but its value could be many times of magnitude smaller than the boundary layer thickness. If we defined the boundary layer thickness as the distance from the surface of the train to the place in the slipstream where the velocity of the flow drops to 95% of the speed of the train, we can roughly identify the boundary layer thickness. Because of the rotation of the model the air around the model is not still. This makes it hard to define a boundary layer based on 99% reduction in the velocity. Figure 14 shows a plane at the half height of the train colored by the relative tangential velocity. The dark line shows the boundary layer based on the last definition. It can be seen that the boundary layer grows along the train length with a thickness equal to about twice the height of the train near the tail of the train.

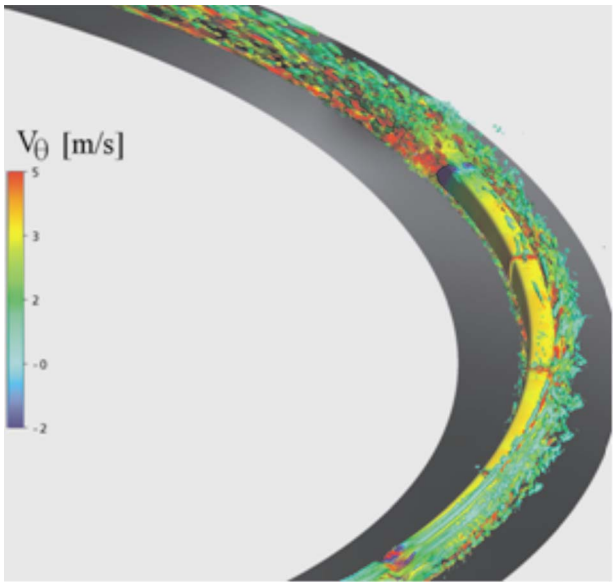

Fig. 15 Second invariant f the velocity gradient Q=2000 colored by the tangential velocity component V_θ (Re=77,000)

The coherent structure of the turbulent flow is shown in Fig. 15 using the isosurface of the positive second invariant of the velocity gradient Q defined as

$$Q = -\frac{1}{2}\frac{\partial u_i}{\partial u_j}\frac{\partial u_j}{\partial u_i} \tag{9}$$

More information about Q can be found in Ref. [20].

All the vortices that are born on the roof of the train are swept by the radial velocity component toward the outside slipstream. Figure 14 also shows that the outer part of the slipstream is dominated by large vortex structures, which grow in size along the train length. These vortices extend along distance in the far wake flow behind the train.

6.4 Surface Pressure. When trains move in the air they do not only change the air velocity around them but also the pressure distribution on their surface and around. Figure 16 represents a plane at the half height of the train colored by the time-averaged static pressure. The pressure is maximum at the nose front and minimum close to the nose and tail. It is however important to note that the pressure changes depend very strongly on the aero-

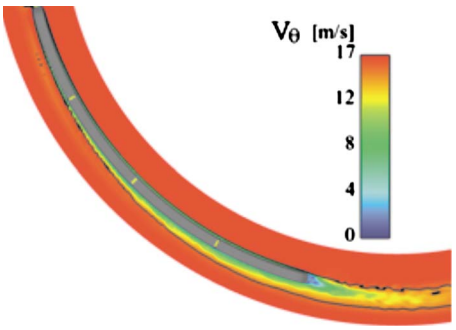

Fig. 14 Plane at the half height of the train colored by the relative tangential velocity, showing the boundary layer thickness (Re=77,000)

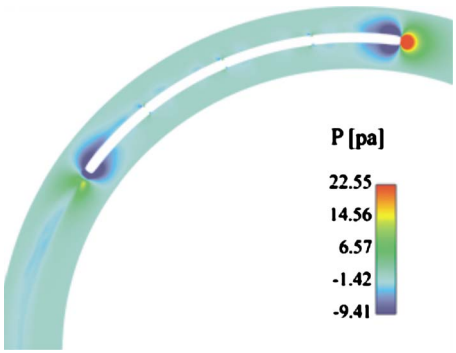

Fig. 16 Plane at the half height of the train colored by time-averaged static pressure (Re=77,000)

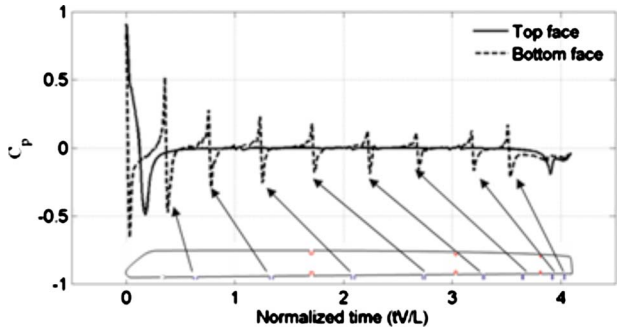

Fig. 17 Surface pressure coefficient on top and bottom faces of the train at its centerline (Re=77,000)

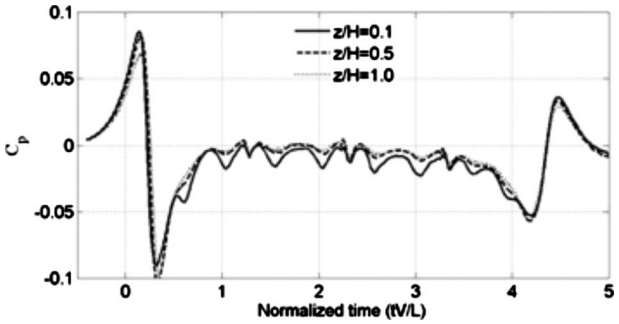

Fig. 19 Pressure coefficient at distance 0.1*H* from the outer surface of the train (Re=77,000)

dynamic shape of the train (for which we have a simple model).

The surface (top and bottom faces) pressure distribution is shown in Fig. 17 expressed in terms of the local pressure coefficient C_p at the centerline of the train. C_p is defined as

$$C_p = \frac{p - p_\infty}{\frac{1}{2}\rho U_T^2} \tag{10}$$

Here, p is the static pressure, p_∞ is the far-field static pressure, and U_T is the speed of the train. The maximum value of the C_p is reported on the tip of the nose while the minimum is reported on the bottom of the nose. Regions of high pressure and low pressure are reported upstream and downstream the supporting cylinders. The intercarriage gaps influence the surface pressure but not as much as the supporting cylinders. The disturbances in static pressure caused by the intercarriage gaps and supporting cylinders influence the entire velocity field.

Figure 18 shows the time-averaged and transient C_p along a line on the cross section of the train at a distance equal to the width of the intercarriage gap W before and after the third intercarriage gap. The C_p value is drawn against the coordinate θ as shown in Fig. 18. The origin here is at the half height of the train on the inner side. Before the intercarriage gap, the pressure is higher on the top and outer side faces than that on the bottom and inner side faces. In contrast, after the intercarriage gap the pressure is higher on the inner side and bottom of the train than that on the top and outer side faces.

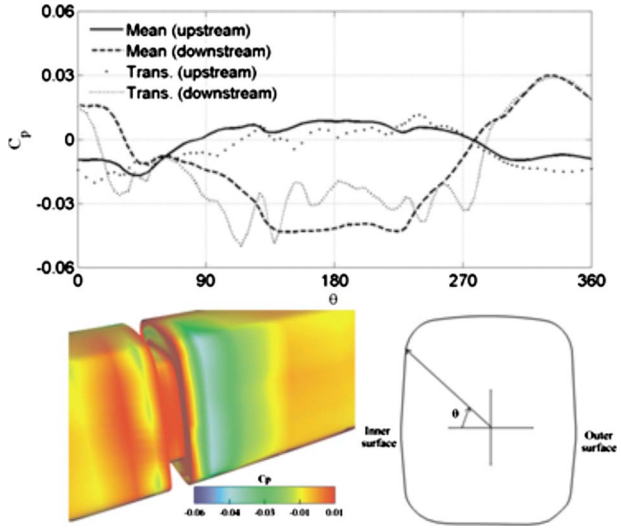

Fig. 18 Surface pressure coefficient at one intercarriage gap length upstream and downstream of the second intercarriage gap (Re=77,000)

Figure 19 represents the time-averaged values of C_p at distance $0.1H$ from the outer surface of the train. There is no significance change in the value of C_p along the train height. However, the influence of the intercarriage gaps and support cylinder on C_p is stronger close to the platform than that close to the roof of the train. The peak of the pressure is reported close to the tip of the nose followed by a large drop at about one quarter the length of the leading car. There is also a large drop in the pressure in the wake of the train close to the tail followed by a build up in the pressure after about half car length from the tail.

6.5 Effects of Re. To investigate the influence of the speed of the train on the slipstream structure and turbulent intensity, the LES of the flow around the rotating train is made at higher Re of 94,000 based on the height of the train and its speed.

Figure 20 shows the slipstream velocity at half the height of the train and at a distance $0.05H$ from the outer surface and Fig. 21 represents the corresponding turbulent intensities. It can be seen that the velocity profiles are similar and the effect of the model

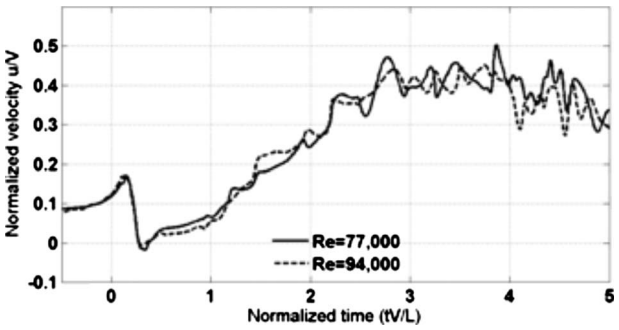

Fig. 20 Slipstream velocity (based on the velocity magnitude) at half train height and a distance 0.05*H* from the outer surface

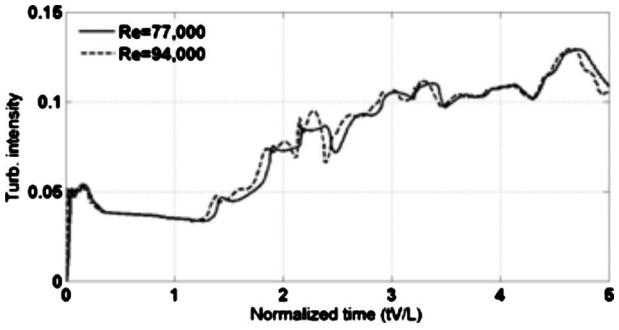

Fig. 21 Turbulent intensity at half the train height and a distance 0.05*H* from the outer surface

speed on the normalized velocity is small. However, the difference between the two Re numbers is not large and we would still expect some Reynolds number dependency for larger, more realistic values of Re.

7 Conclusions

The LES was successively employed to solve the flow around a rotating train model at two different Reynolds numbers. The LES results reasonably agree with the experimental data. On the other hand, the slipstream velocity was overestimated by the SST-KOmega RANS model using the same mesh and Reynolds number of the LES. The train model consisted of a four-coach of a 1/25 scale of the ICE2 train. The coaches were separated by intercarriage gaps and each was fixed to the rotating rail through two supporting cylinders. From the LES results, the following conclusions can be drawn.

1. In general, the slipstream can be divided into six regions: upstream, nose, intercarriage gaps, tail, wake and far wake regions. This is slightly different than those described in Refs. [4,5], where the intercarriage gap region was omitted.
2. A localized velocity peak was obtained close to the nose of the train with the maximum velocity magnitude in the slipstream. The maximum velocity was reported near the platform surface while its magnitude damps out in the direction of the roof of the train. The flow is shown to be highly turbulent and three-dimensional in the nose region.
3. The maximum and minimum values of the surface pressures are obtained on the nose region near the nose tip on the top and bottom faces of the nose, respectively.
4. On the roof of the train, the boundary layer appears to reach equilibrium after the first car. On the other hand, the turbulent boundary layer on the outer side of the train started to build up after about half the length of the leading car in the direction of the train body. The thick part of the boundary layer is obtained near the wake of the train on the outer slipstream with a thickness of almost twice the height of the train.
5. All the turbulent structures that were born on the roof of the train were swept by the radial component of the velocity towards the outer side of the train. The outer side of the train is dominated by large structures that are highly turbulent.
6. The underbody complexities and intercarriage gaps were shown to have a significance influence on the slipstream velocities and pressure.
7. The pressure field was found to have slightly uniform values across the height of the train. However, some strong influences from the intercarriage gaps and underbody complexities appeared on the pressure field near the platform surface.
8. The effect of the Reynolds number on the slipstream is small if the velocity is suitably normalized.

Acknowledgment

This work is sponsored by the Rail Research UK, Project No. RRUKA5. The authors would like to acknowledge the computer resources and software licenses provided by the Birmingham Environment for Academic Research, BlueBEAR.

References

[1] Pope, C., 2006, "Safety of Slipstreams Effects Produced by Trains," A Report Prepared by Mott Macdonald, Ltd., for RSSB.
[2] RSSB, 2006, "Slipstream Risks: Phase 1 (a) Commentary on Existing GB Position," http://www.rssb.co.uk/
[3] Figura-Hary, G. I., 2007, RSSB Slipstream Safety Analysis of Existing Experimental Data on Train Slipstreams Including the Effects on Pushchairs.
[4] Sterling, M., Baker, C. J., Jordan, S. C., and Johnson, T., 2008, "A Study of the Slipstreams of High-Speed Passenger Trains and Freight Trains," Proc. Inst. Mech. Eng., F J. Rail Rapid Transit, **222**, pp. 177–193.
[5] Baker, C. J., Dalley, S. J., Johnson, T., Quinn, A., and Wright, N. G., 2001, "The Slipstream and Wake of a High Speed Train," Proc. Inst. Mech. Eng., F J. Rail Rapid Transit, **215**, pp. 83–99.
[6] Gil, N., Baker, C. J., and Roberts, C., 2008, "The Measurement of Train Slipstream Characteristics Using a Rotating Rail Rig," BBAA VI International Colloquium on Bluff Bodies Aerodynamics and Applications, Milan, Italy.
[7] Raghunathan, R. S., Kim, H.-D., and Setoguchi, T., 2002, "Aerodynamics of High-Speed Railway Train," Prog. Aerosp. Sci., **38**, pp. 469–514.
[8] Andersson, E., Haggstrom, J., Sima, M., and Stichel, S., 2004, "Assessment of Train-Overturning Risk due to Strong Cross-Wind," Proc. Inst., Mech. Eng., F J. Rail Rapid Transit, **218**, pp. 213–223.
[9] Orellano, A., and Schober, M., 2006, "Aerodynamic Performance of a Typical High-Speed Train," WSEAS Transactions on Fluid Mechanics, Vol. 1.
[10] Holmes, S., Schroeder, M., and Toma, E., 2000, "High-Speed Passenger and Intercity Train Aerodynamic Computer Modelling," The 2000 International Mechanical Engineering Congress (ME2000).
[11] Robert, A., and Harvey, S. L., 2002, "Measurement of the Aerodynamic Pressures Produced by Passing Trains," Proceedings of the 2002 ASME/IEEE Joint Rail Conference.
[12] Bocciolone, M., Cheli, F., Corradi, R., Muggiasca, S., and Tomasini, G., 2008, "Crosswind Action on Rail Vehicles: Wind Tunnel Experimental Analyses," J. Wind Eng. Ind. Aerodyn., **96**, pp. 584–610.
[13] Muld, T., Efraimsson, G., Henningson, D., Herbst, A., and Orellano, A., 2009, "Detached Eddy Simulation and Validation on the Aerodynamic Train Model," EUROMECH Colloquium, Berlin, Germany, March 24–25.
[14] Hemida, H., and Krajnovic, S., 2009, "Exploring Flow Structures Around a Simplified ICE2 Train Subjected to a 30° Side Wind Using LES," Eng. Appl. of Comp. Fluid Mech., **3**(1), pp. 28–41.
[15] Hemida, H., and Krajnovic, S., 2008, "LES Study of the Influence of a Train Nose Shape on the Flow Structures Under Cross-Wind Conditions," ASME J. Fluids Eng., **130**(9), p. 091101.
[16] Hemida, H., and Krajnovic, S., 2010, "LES Study of the Influence of Yaw Angles and Nose Shape on Flow Structures Around Trains," J. Wind Eng. Ind. Aerodyn., **98**(1), pp. 34–46.
[17] ANSYS-CFX Documentations, http://www.ansys.com/products/fluid-dynamics/cfx/
[18] Bradshaw, P., 1973, "Effects of Streamline Curvature on Turbulent Flow," Agardograph 169.
[19] Kim, N., and Rhode, D. L., 2000, "Streamwise Curvature Effect on the Incompressible Turbulent Mean Velocity Over Curved Surfaces," ASME J. Fluids Eng., **122**, pp. 547–551.
[20] Jeong, J., and Hussain, F., 1995, "On the Identification of the Vortex," J. Fluid Mech., **285**, pp. 69–94.

Patrick Gilliéron
Department of Research,
"Fluid Dynamics and Aerodynamics" Team,
Renault SA Service 68260,
Code API: TCR AVA 058 1,
Avenue du Golf,
78288 Guyancourt Cedex, France
e-mail: patrick.gillieron@renault.com

Annie Leroy[1]
e-mail: annie.leroy@univ-orleans.fr

Sandrine Aubrun

Pierre Audier

Institut PRISME,
University of Orleans,
8 rue Leonard de Vinci,
F-45072 Orleans Cedex 2, France

Influence of the Slant Angle of 3D Bluff Bodies on Longitudinal Vortex Formation

This paper presents the experimental results and analytical arguments concerning simplified geometries of the rear window and windscreen of automotive vehicles in order to contribute to a better understanding of the swirling structure formation and vortex bursting processes. Static pressure distributions and skin friction line visualizations on both sides of the edge where the swirling structure is generated on the rear window of an Ahmed body are presented for different slant angles. Results show the influence of the slant angle on the swirling structure formation and further show that the vortex bursting process can be promoted by small rear window angles. These results are then extrapolated with the help of analytical demonstrations to the windscreen configuration to demonstrate that large windscreen slopes would have the same disintegration effect.
[DOI: 10.1115/1.4001450]

Keywords: slant angle of bluff bodies, vortex breakdown, longitudinal vortices, swirl number

1 Introduction

The study of longitudinal swirling separated structures is of great interest in reducing the advance resistance of ground and air vehicles. In automobile aerodynamics, these structures account for close to 15% of resistance [1] and their suppression could reduce carbon dioxide emissions by 6 g/km (according to the New European Driving Cycle [2]). From a geometrical point of view, these structures can be eliminated by increasing the local radius of curvature from the side edges of the windscreen and rear window. However, this solution would have a strong impact on the vehicles' capacity and design, which cannot be considered at the present time. Work is therefore in progress to analyze and control the development of these structures and limit their impact on aerodynamic drag without constraining the automobile geometries.

Blowing and aspiration solutions are being developed on simplified geometries to burst, reduce, or increase the radial development of the longitudinal swirling structures of the windscreen and rear window. For the rear window, a reduction of 6% [3,4] in aerodynamic drag is possible, thanks to blowing when the swirl number, here defined as the maximum value of the ratio of the azimuthal velocity V_θ (rotational motion) to the longitudinal velocity V_X (advection motion), in a system coordinate linked to the swirling structure, is close to 1.5 [5,6]. For the windscreen, aspiration of the swirling structures provides reductions close to 5% [7]. Other definitions of the swirl number have been introduced in the past. Each definition is associated with a distinct vortex breakdown criterion. Rusak et al. [8] proposed a definition of the swirl number in accordance with a theory on the axisymmetric vortex breakdown process, which is applied to vortices in pipes and above slender wings in order to exhibit a criterion for the appearance of breakdown [9]. In this paper, focusing on vortices around simplified automobile geometries, the above definition is retained for the swirl number allowing a direct comparison with some results on the features and breakdown of such vortices [3,4,6,7].

Analysis of the longitudinal velocity field of these structures clearly shows differences between the structures of the windscreen and those of the rear window [6,7]. When bursting or swirl destructuring are not forced, the transverse fields of the axial velocities are, respectively, wakelike [7] and jetlike [6]. Improving the energy efficiency of the control requires a better knowledge of the origin of these differences.

This paper proposes a contribution to the analysis of the physical mechanisms responsible for these structural differences by focusing on the influence of the slant angle of the windscreen and rear window. Analytical considerations and experimental results concerning pressure distributions and skin friction lines are used to study the influence of different geometrical factors on the formation and swirling processes.

2 Field of Analysis

The analysis of longitudinal swirling separated structures is carried out, thanks to the results obtained on simplified geometries of plane windscreens and rear windows, which make a slant angle of θ with regard to the upstream flow direction V_0 (Figs. 1 and 2). As in most previous studies for windscreen flow and rear window flow, a dihedral bluff body [7] and an Ahmed body [10], as described in Figs. 1 and 2, are, respectively, investigated.

Flow separations are observed on the left and right sides of the windscreen. They are responsible for the appearance of two main contrarotating longitudinal swirling structures [7] (Fig. 3). As regards the rear window, flow detachments are observed on the top and on the left and right sides to form and feed a detachment sheet D, two main contrarotating longitudinal swirling structures A, and two contrarotating swirling structures B centered on two separation foci [11] (Fig. 4). The source of the swirling structures on the top is the upstream flow and the left and right side flows which move up toward the end of the roof before the separation line [12]. It is well known that each principal longitudinal swirling structure creates a secondary longitudinal swirling structure, which can be clearly discerned on wall visualizations (Figs. 3 and 4). The topology of the flow on the rear window is similar to an Ahmed body [10–15] for slant angles of rear window ranging between 12 deg and 30 deg (Fig. 4).

The nature of these longitudinal swirling structures differs depending on the attachment line direction. When bursting or swirl

[1]Corresponding author.

Contributed by the Fluids Engineering Division of ASME for publication in the JOURNAL OF FLUIDS ENGINEERING. Manuscript received June 10, 2009; final manuscript received February 16, 2010; published online May 6, 2010. Assoc. Editor: Zvi Rusak.

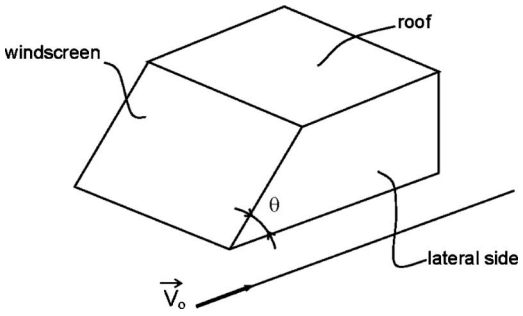

Fig. 1 Schematic representation of windscreen with a slant angle θ

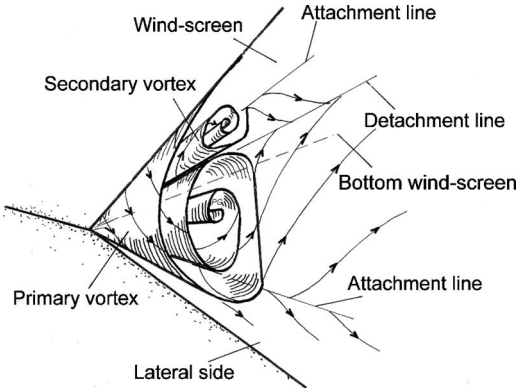

Fig. 3 Schematic representation of amount of the windscreen detachment, left back view; the secondary structure is linked to the existence of the principal longitudinal swirling structure

destructuring are not forced, the axial velocity profiles of a transverse velocity field are wakelike [7] and jetlike [6] for the windscreen and rear window, respectively.

On the rear window in a left rear view, the vortex emanates from the $y=0$ line and evolves in the $y>0$ plane (Fig. 5). As the attachment line is windward, the velocity vector **W**, resulting from the composition of the azimuthal velocity V_θ and the freestream velocity V_0, is convergent in direction toward the longitudinal vortex axis, continuously increasing the axial flow rate. Hence, the local axial velocity profile evolves to a jetlike velocity profile according to the continuity equation, as shown in Fig. 6.

On the lateral edge of the windscreen, the attachment line is leeward. The azimuthal velocity decreases as the distance from the vortex core top increases. Consequently, this resulting velocity vector **W** (Fig. 7) diverges in direction from the longitudinal vortex axis, decreasing the axial flow rate contrary to the rear window. Hence, the local axial velocity profile evolves to a wakelike velocity profile according to the continuity equation, as shown in Fig. 6.

Experiments focusing on these separated longitudinal swirling structures around simplified rear window or windscreen geometries [6,7] confirm this observation.

In Secs. 4–6, the results of experiments performed on an Ahmed body and analytical considerations are used to study the influence of different factors such as slant angle values and pressure gradient distributions on the formation processes and on the flow topology.

3 Experimental Setup

Tests were run in the Lucien Malavard wind tunnel at the PRISME Institute. It is a closed-circuit wind tunnel with a square 2×2 m^2 section 5 m in length. The maximum inflow velocity is 60 m s^{-1} with differences of less than 1% of the mean value in the effective test section and with a turbulence level of 0.4%. For the present experiments, the reference velocity was $V_0=30$ m s^{-1}, leading to a Reynolds number based on the length of the model L of 2×10^6.

The Ahmed body at a scale of 1:1 is made of PVC and its dimensions are $L=1.044$ m long, $l=0.389$ m wide, and $H=0.288$ m high, see Fig. 2. Several configurations of slant angle were designed and tested: $\theta=15$, 20, and 25 deg (the slanted edge length is uniform $l_w=0.222$ m). The model was fixed in the center of the test section, on a 3 m long plate, using four feet each 0.030 m in diameter and 0.1 m in height. The blockage ratio is about 3%.

The model was equipped with 43 pressure taps located on the slanted edge and on one side of it along the lines D_1, D_2, D_3, D_4, and D_L (Figs. 8 and 9). The lines D_1, D_2, D_3, and D_4 are located on the side of the rear window and meet the point P (coordinates $x=0$, $y=0$, and $z=0$). D_1 is vertical. The lines D_2 and D_3 are uniformly evenly spaced between D_1 and D_4. The line D_4 is parallel to the edge between the rear window and the rear window side and is located 0.005 m from it. The line D_L is parallel to the edge between the rear window and the rear window side and is located, on the rear window, 0.005 m from it (Fig. 9).

The pressure taps were connected by a 0.15 m long plastic tubing to 43 PSI pressure transducers (ESP-32HD and ESP-16HD). The precision of the pressure transducers is ±0.1% of the

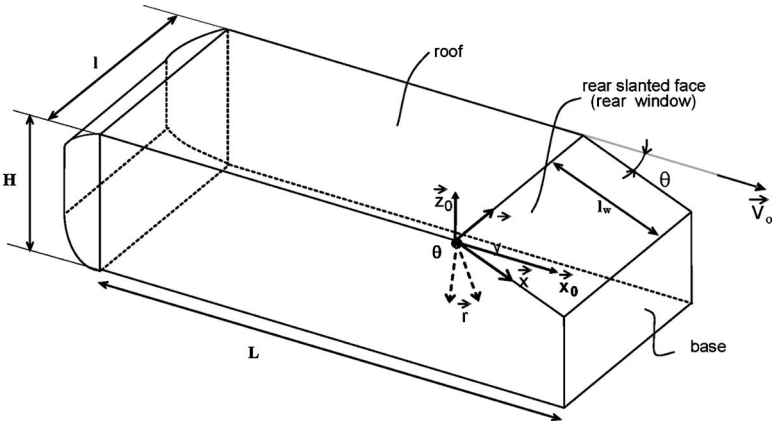

Fig. 2 Ahmed body geometry, from Ref. [7]. Slant angle θ of rear window (x_0, y_0, z_0) and (x, y, z): frames linked to the freestream velocity direction and to the left side line of the rear window, respectively

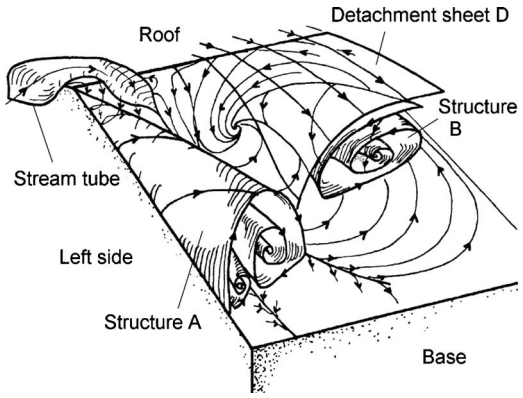

Fig. 4 Schematic representation of the left part of rear window detachment for slant angles θ ranging between 12 deg and 30 deg, according to Refs. [7,9], back view

full scale for the ESP-32HD and ±0.06% of the full scale for the ESP-16HD. Each of the pressure transducer inputs was scanned at 200 Hz during 10.25 s.

The pressure is given in the usual form of the pressure coefficient $Cp=(p-p_0)/0.5\rho V_0^2$, where p_0 and V_0 are the freestream static pressure and velocity, respectively, far upstream of the model. The static pressure distributions enable the influence of the slant angle on the wall signature of the longitudinal swirling structures to be quantified since it is well known that the more the slant angle increases, the stronger the longitudinal swirling structures will become.

Friction line visualizations on the slanted edge and on its side were performed using a viscous coating made of oleic acid, dodecane, silicon oil, and titanium dioxide [16]. The wall was coated with the mixture using a brush. The model was then exposed to a

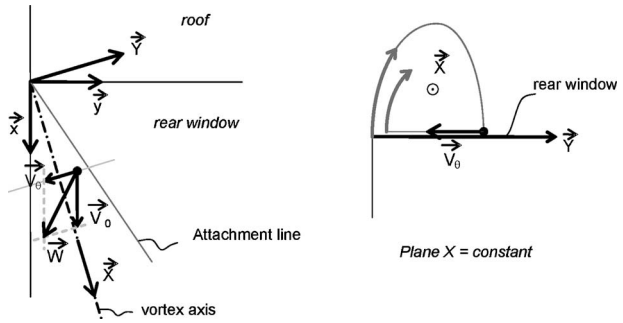

Fig. 5 Composition of azimuthal and freestream velocities V_θ and V_0 on the rear window, resulting velocity vector W; (X, Y, Z): coordinate system linked to the swirling structure axis

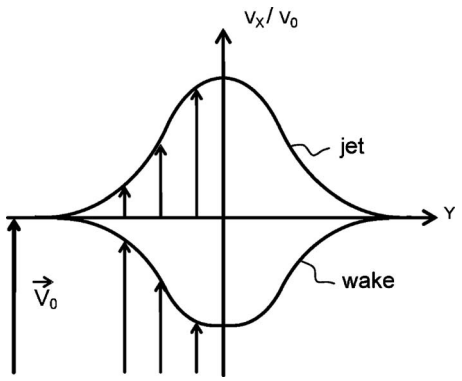

Fig. 6 Axial velocity profiles: jet and wake profiles

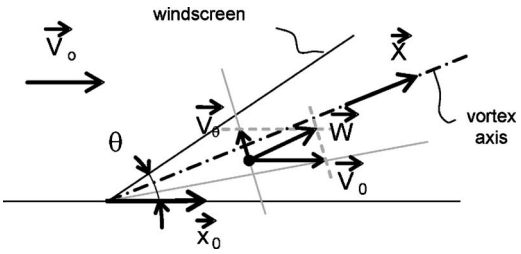

Fig. 7 Composition of azimuthal and freestream velocities V_θ and V_0 on the windscreen edge, resulting velocity vector W

constant wind until the friction lines became visible. These visualizations make it possible to study the influence of the slant angle on the friction line directions upstream of the geometrical discontinuities between the side of the main body and the rear window.

No similar experimental results on the windscreen configuration are available in the present paper.

4 Influence of Geometrical Discontinuities on Static Pressure Coefficient Distributions

Longitudinal swirling structures result from a complex interaction mechanism between adjacent and convergent flows around

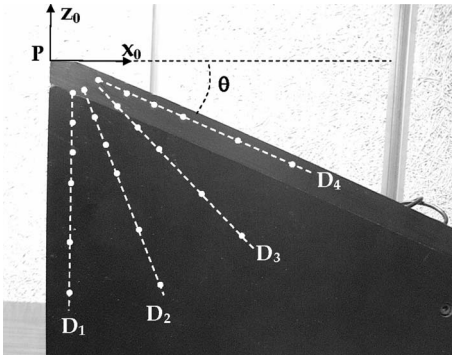

Fig. 8 Location of the static pressure tabs on the left side of the rear window. The four lines intersect at *P*

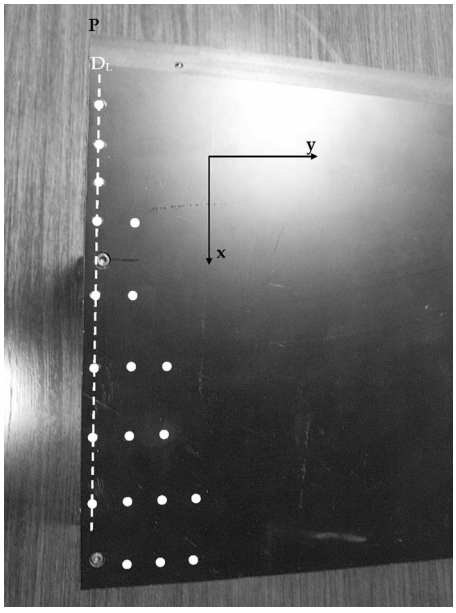

Fig. 9 Location of the static pressure tabs on the rear window

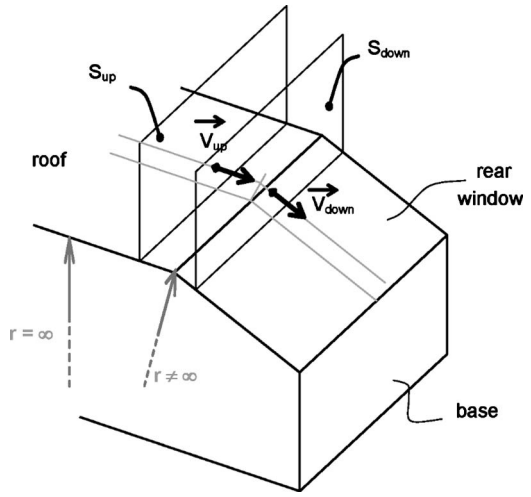

Fig. 10 Streamline representation along roof and rear window

geometrical discontinuities of convex surfaces. These discontinuities influence static pressure coefficient distributions and consequently vortex formation.

For the rear window, the longitudinal vortices result from convergence of the Ahmed body roof flow and the two lateral side flows. According to the Euler equations in the transverse flow direction, and because of the geometrical discontinuities that create a sharp spreading associated with a reduction in radius of curvature, the flow is accelerated and static pressure coefficient values are the lowest on the top and side of the rear window, as mentioned in Ref. [15] and shown in Fig. 11. It is well established that this zone of highest depression is observed just behind the top edge of the rear window. This feature can also be deduced from an analytical point of view. Following a friction line along the roof and the rear window, the static pressure diminishes because of the reduction in the radius of curvature according to the Euler equations. If S_{up} and S_{down} are parallel sections of the same streamtube perpendicular to the geometry surfaces and if V_{up} is the air flow velocity in the boundary layer upstream of the end of the roof, as shown in Fig. 10, the total pressure (or volume energy) loss ΔP_i associated with the sharp spreading is given by

$$\Delta P_i = \left(1 - \frac{S_{up}}{S_{down}}\right)^2 \frac{\rho}{2} V_{up}^2 \quad \text{with} \quad S_{down} = S_{up}(1+\varepsilon) \quad \text{and} \quad \varepsilon \to 0 \tag{1}$$

As ΔP_i tends to locally vanish, local velocities and static pressure coefficients are linked by the equation

$$C_P^{down} - C_P^{up} = 1 - \left(\frac{V_{down}}{V_{up}}\right)^2 \tag{2}$$

The flow can be considered as a flow along a flat plane a without longitudinal pressure gradient, and therefore

$$\left(\frac{V_{down}}{V_{up}}\right)^2 \approx 1 - C_P^{down} > 1 \tag{3}$$

and V_{down} is higher than V_{up}. The lowest value of the static pressure coefficient C_P^{down} is therefore observed in the upper part of the rear window.

Figure 11 shows the static pressure coefficient distributions on the lateral side of the rear window and on the rear window for different slant angles. It is noticeable that the static pressure gradients increase on the lateral side and at the edge of the rear window, close to P, as the slant angle increases. This engenders the formation of a vortex structure and amplification of swirling. Furthermore, the signature of the longitudinal swirling structures, characterized by an additional static pressure loss below them, is more and more visible on the rear window.

In the case of the windscreen, the longitudinal vortices result from convergence of the lateral and transverse flows on the windscreen. When the slant angle θ increases, two main phenomena contribute to make higher underpressure apparent [6]. First, it is well established that a positive Cp zone is observable in the central region of the base of the windscreen, and that its size increases with the slant angle. Second, the normal component of the upstream velocity (Fig. 12) increases as the angular deviation λ increases; hence the static pressure coefficient near the junction edge decreases. The consequence of these two phenomena is an increase in the pressure gradient in the direction of the friction lines, which causes an increase in local velocities near the top and lateral parts of the windscreen. Associated with this velocity increase is a reduction in the peripheral static pressure coefficients that enlarges proximal areas with a weak radius of curvature.

Beyond a deviation angle of 90 deg, the axial component of the shedding velocity near the lateral geometrical discontinuities vanishes and the three-dimensional nature of the detachment mechanism becomes a bidimensional problem (the case of the windscreen or completely vertical rear part perpendicular to the freestream velocity).

Finally, the lowest values of static pressure coefficient and the highest values of velocities are observed at downstream junction lines between the roof and the rear window, between the vertical lateral sides and the rear window, and between the windscreen and lateral windows. When the slant angle increases, higher underpressure can be observed. This engenders the vortex structure formation and amplification of swirling.

5 Influence of the Radial and Transverse Pressure Gradients

The static pressure coefficient distributions are shown in a different manner in Figs. 13 and 15. They can be used to assess, with the finite difference method, the static pressure gradients along the radial directions centered on P: $\partial Cp/\partial r|_{D_1}$, $\partial Cp/\partial r|_{D_2}$, $\partial Cp/\partial r|_{D_3}$, and $\partial Cp/\partial r|_{D_4}$ (Fig. 14), and the difference of static pressure coefficients across the edge between the side of the body and the rear window $\Delta Cp = Cp|_{D_4} - Cp|_{D_L}$ (Fig. 16).

The static pressure coefficient on the side of the rear window continuously increases along the four line D_i ($i=1-4$), when the radius increases and/or when the slant angle decreases (Fig. 13), except for the line D_4 at $\theta=20$ and 25 deg. An inversion of trend is visible close to the point P when the slant angle increases. A spot of higher pressure appears at $r/l=0.07$ on D_4 for $\theta=25$ deg. The $\theta=20$ deg case seems to be a transition case between the two trends since it presents some noninterpretable oscillations [3]. The most noticeable flow modification when the slant angle increases is the progressive formation of a streamwise swirling structure on both sides of the Ahmed body, with a centerline origin merged with the point P. It is then logical to try to link the appearance of this spot of relatively high pressure close to P when θ increases with the formation mechanism of the streamwise swirling structures.

The static pressure coefficients measured on the rear window along the line D_L are shown in Fig. 15. For the three slant angles, the static pressure coefficients increase with the reduced abscissa, except for the measurement location closest to P, in $x/l=0.07$. This local spot of relatively higher pressure close to P suggests the existence of attachment nodes on the upper corners of the rear window. The Refs. [11,12] showed that the influence of these nodes on the local topology increases with the slant angle.

The static pressure coefficients measured on the rear window are compared in Fig. 15 with the static pressure coefficients measured on the side of the body, along the line D_4. The difference between these coefficients $\Delta Cp = Cp|_{D_4} - Cp|_{D_L}$ when the distance

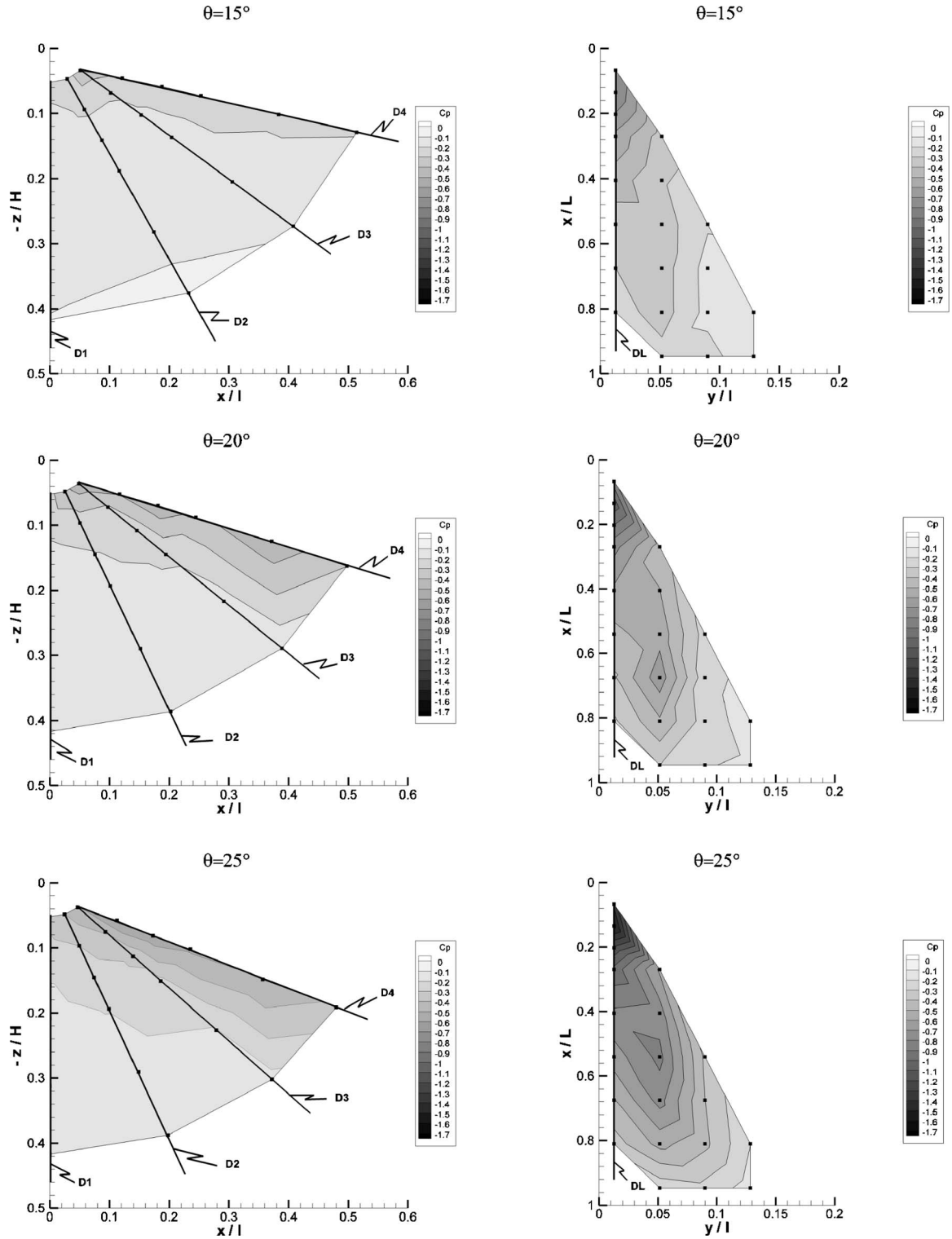

Fig. 11 Static pressure coefficient distribution on the side of the rear window (left) and on the rear window (right)

from *P* increases is plotted in Fig. 16. The difference is in all cases positive and increases with the slant angle, illustrating the local suction effect on the rear window responsible for the distortion of streamlines coming from the side part of the body and attracted to the rear window, thus leading to the swirling structure formation. The static pressure coefficient difference is particularly high for the locations closest to *P*. This tendency was also visible on the static pressure coefficient gradient calculated along the radii on the rear window side (Fig. 14). Smaller pressure coefficients are measured close to *P* on the lateral part but also on the rear window.

The present results show that the static pressure coefficients decrease and that the radial gradients of the static pressure and transverse differences of static pressure increase, as the distance from *P* decreases (except for the very local influence of the attachment nodes, which tend to locally raise the pressure close to

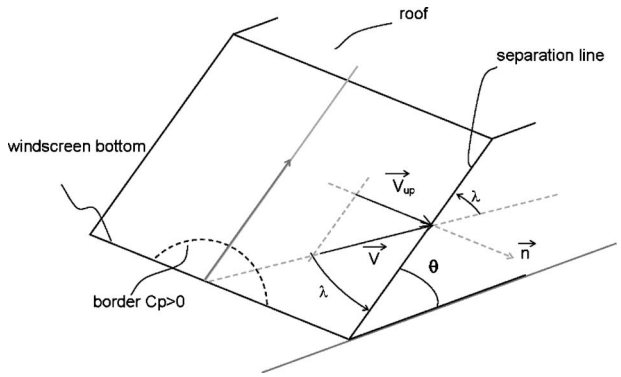

Fig. 12 Normal and tangential components of the flow velocity on the windscreen near the separation geometrical edge

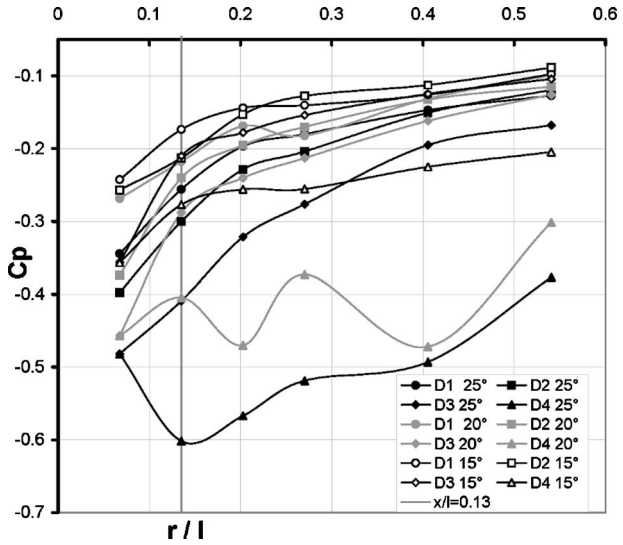

Fig. 13 Static pressure coefficients *Cp* along the lines D_1, D_2, D_3, and D_4 on the side of the rear window, $V_0=30$ m s^{-1}

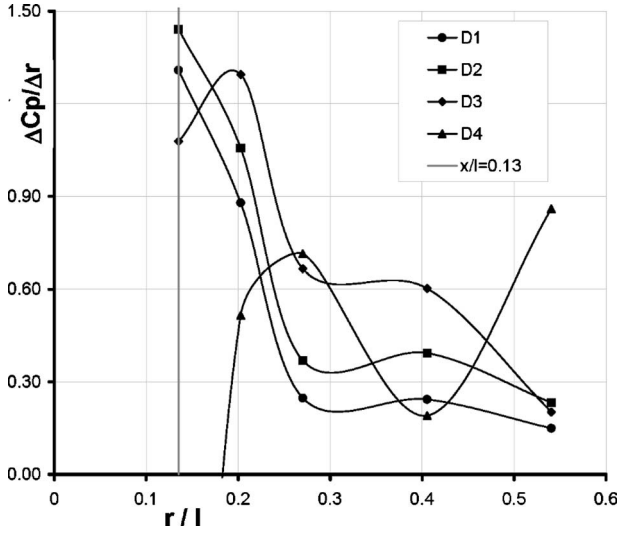

Fig. 14 Radial static pressure coefficient gradients along the lines D_1, D_2, D_3, and D_4; $\theta=25°$ and $V_0=30$ m s^{-1}

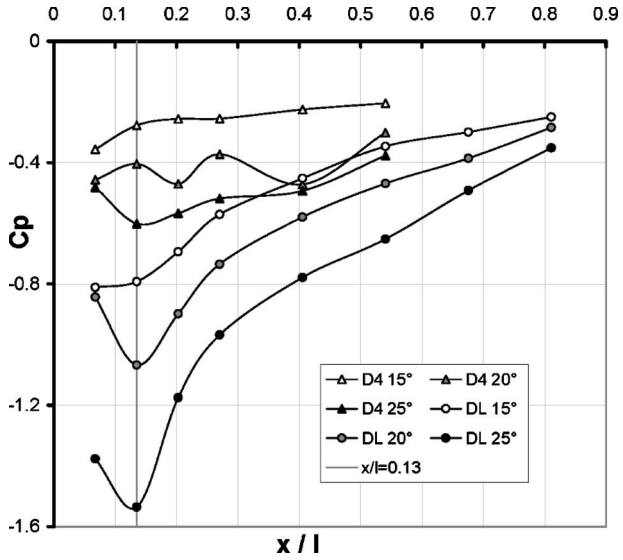

Fig. 15 Static pressure coefficients *Cp* along the lines D_L and D_4, $V_0=30$ m s^{-1}

P). The point *P*, the apex of the swirling cone, could then be considered as the curvature center of the local flow. In these conditions, the acceleration is centripetal, the motion is characterized by a central force, the kinetic momentum is constant, and the tangential velocity, along a circle centered on *P*, decreases as the distance from *P* increases.

The influence of radial acceleration on the lateral flow trajectory, which feeds the swirling structures, is studied. Figures 17 and 18 show the angular deviation λ and the ratio between the angular deviation and the slant angle λ/θ, respectively, versus the distance from *P* for $\theta=15$, 20, and 25 deg. The angular deviation λ is measured on the friction line visualizations made with viscous coating on the side of the rear window, for slant angles $\theta=15$, 20, and 25 deg (Fig. 19).

Globally, as the distance from *P* increases, the centripetal acceleration of the central force motion decreases, the flow trajectory moves away from the curvature center *P* and the angular deviation decreases, as shown in Fig. 17, where the linear regression curves clearly exhibit this evolution. In addition the plots

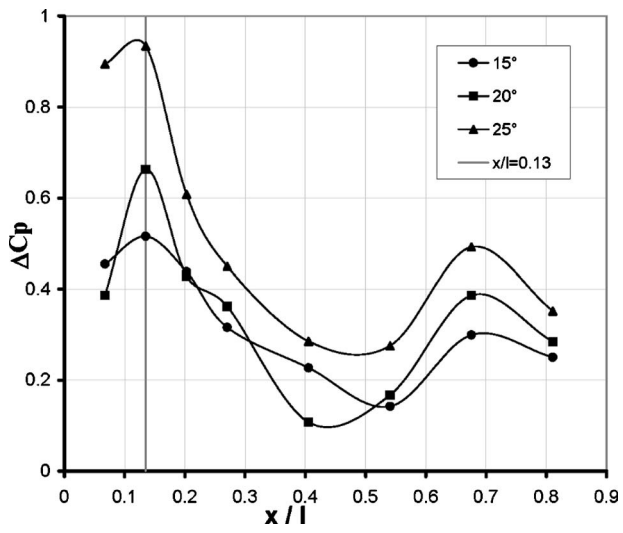

Fig. 16 Difference in static pressure coefficients along the lines D_4 and D_L: $\Delta Cp=Cp|_{D_4}-Cp|_{D_L}$ and $V_0=30$ m s^{-1}

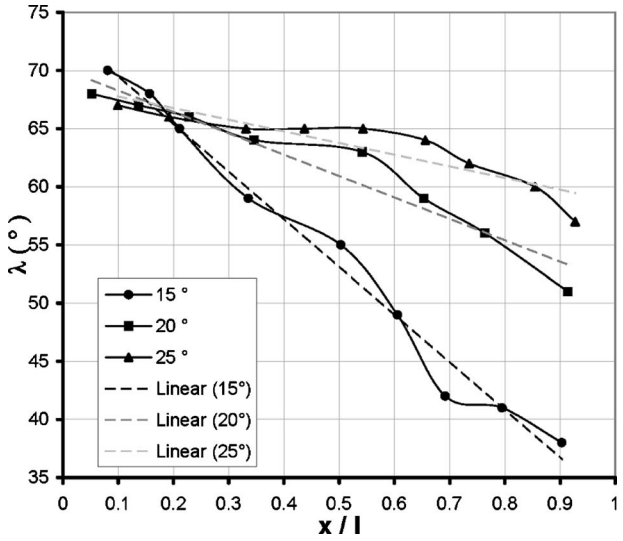

Fig. 17 Angular deviation λ versus the reduced distance from *P*, *x*/*l*, for slant angles θ=15, 20, and 25 deg; V_0=30 m s^{-1}

show that the angular deviation λ decreases continuously for the smallest slant angle whereas it remains nearly constant until x/l =0.6 for the largest slant angle. The middle configuration shows an intermediate tendency. This proves that the spatial domain along the lateral edge axis x, where the central acceleration acts, increases with the slant angle. However, the angular sector of the lateral side of the rear window (90 deg-θ), where the central acceleration acts, decreases as the slant angle increases. One would therefore expect the magnitude of the central acceleration to be lower and the angular deviation to be smaller for large slant angles. However, this feature is only visible very close to the point P, where λ is higher for smaller slant angles. Figure 18 shows that the angular deviation growth rate is globally higher for smaller slant angles and is maximum close to P. This result tends to confirm again that the central acceleration acts the most for smaller slant angles. To summarize, the magnitude of the central acceleration decreases but the area over which it acts increases as the slant angle increases. These results will be used in Sec. 6 to establish that the swirl number increases as the slant angle decreases.

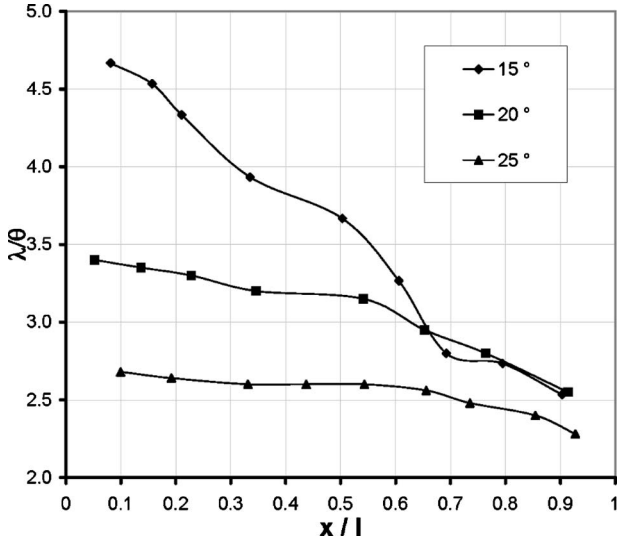

Fig. 18 Ratio between the angular deviation and the slant angle versus the reduced distance from *P*, *x*/*l*, for slant angles θ=15, 20, and 25 deg; V_0=30 m s^{-1}

6 Slant Angle Influence on the Swirl Number

A phenomenon of special importance to swirling flows is vortex breakdown [4,5]. It can be beneficial in automotive applications where drag reduction is a goal. It is established that the maximum of ratio of the swirling (azimuthal) velocity V_θ to the longitudinal velocity V_X is one of the most effective parameters to predict vortex breakdown. When the maximal value of this ratio, called the swirl number, goes beyond a critical value close to 1.5, then vortex breakdown will occur.

In this section, we analyze the influence of the slant angle on the swirl number defined here, in the (X,Y,Z) coordinate system linked to the swirling structure, as the maximum value of the ratio of the azimuthal velocity V_θ to the longitudinal velocity V_X of the flow velocity vector V_λ emanating from the separation edge of the rear window. This velocity vector is projected on the symmetrical axis and in a normal plane to the swirling structure axis (Fig. 20). By noting α and β, the precession and nutation angles, respectively, its azimuthal and longitudinal components can be calculated as

$$V_\theta = V_\lambda[[\sin\lambda\cos\alpha - \cos\lambda\sin\alpha\cos\beta]^2 + \cos^2\lambda\sin^2\beta]^{0.5} \tag{4}$$

$$V_X = V_\lambda[\sin\lambda\sin\alpha + \cos\lambda\cos\alpha\cos\beta] \tag{5}$$

The swirl number expression in relation with the deviation angle λ can be deduced from Eqs. (4) and (5) considering small values of α and β close to 8 deg and 7 deg [3,4], respectively:

$$S = \max\frac{V_\theta}{V_X} \approx \max(\tan\lambda) \tag{6}$$

Finally, the evolution of V_θ/V_X is shown in Fig. 21. This ratio increases as the deviation angle increases.

As shown in Fig. 17, higher values of the deviation angle λ, and consequently higher values of the swirl number, are observed around the top of the rear window edge for the smallest values of the slant angle. Hence, vortex breakdown may occur (a necessary but not a sufficient condition [4]) for low slant angles.

This result is then compared with numerical and experimental results from the literature. Vortex breakdown achieved for jet [3,4,17,18] and wake [7] swirling flows, confined or unconfined, occurs when the swirl number is close to 1.5. This value corresponds to a value of 64 deg for the deviation angle (Fig. 21).

According to the experimental results presented in Secs. 3–5, the λ value increases as the slant angle decreases, and the highest value is 70 deg for θ=15° (Fig. 17). This value is greater than the theoretical value of 64 deg (Fig. 21). This result here confirms the fact suggested by Billant et al. [5] that the condition is necessary but not sufficient. Moreover, it suggests that vortex breakdown or dramatic changes in vortex structures may occur for a slant angle lower than 15 deg. According to Lehugeur et al. [3], drag reduction is associated with this phenomenon. Drag measurements performed on an Ahmed body in Refs. [10,11] have shown that for a slant angle of 12 deg, when these lateral longitudinal structures appear and grow, a drag increase is observed.

In the case of windscreen separation, by analogy with the results obtained for the rear window, the deviation angle λ, the azimuthal velocity, and the swirl number are the highest when the slant angle of the windscreen is high and they diminish upwards from the bottom to the top of the windscreen edge. Hence, vortex breakdown may occur for high slant angles, as shown in Ref. [7], where numerical simulations of vortex breakdown were carried out for windscreen slant angles of 30 deg and 45 deg.

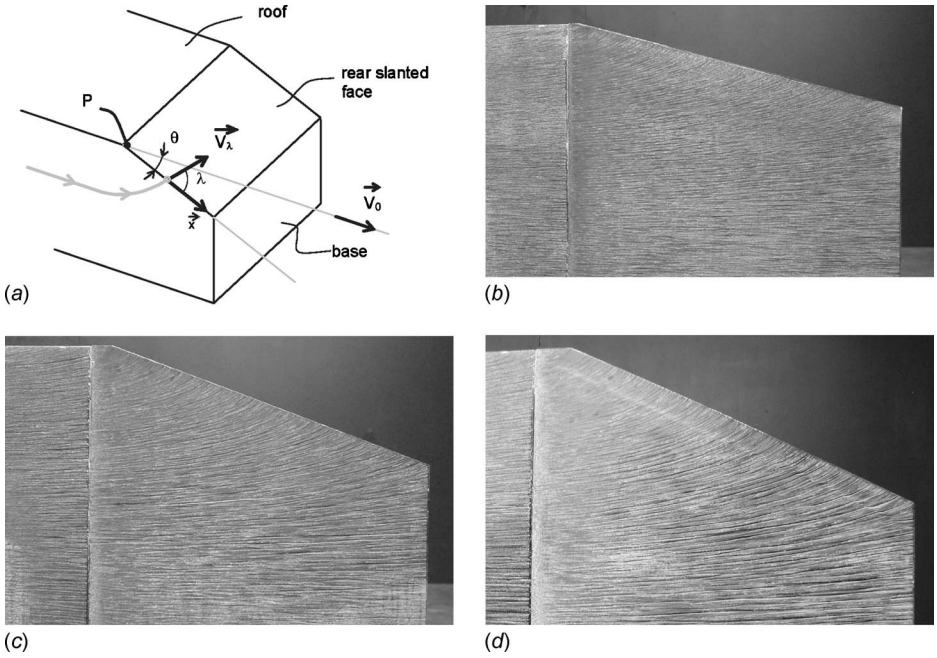

Fig. 19 (*a*) **Slant angle and angular deviation of the lateral friction line λ;** (*b*) **friction line visualizations on the side of the rear window,** $\theta=15$ **deg,** $V_0=30$ **m s**$^{-1}$**;** (*c*) **friction line visualizations on the side of the rear window,** $\theta=20$ **deg,** $V_0=30$ **m s**$^{-1}$**;** (*d*) **friction line visualizations on the side of the rear window,** $\theta=25$ **deg,** $V_0=30$ **m s**$^{-1}$

7 Conclusion

Analytical approaches and experimental results on simplified geometries have made possible the analysis of the flow topology near the longitudinal swirling structures of a rear window and windscreen. End roof and windscreen geometrical discontinuities increase velocity and decrease the static pressures, which amplify the formation and rolling up processes of the swirling structures. For the rear window, parietal visualizations and static pressure cartographies at the top of the swirling cones show that a centripetal acceleration locally curves the flow trajectories before separation. The local flow is then subjected to a central force motion and the friction lines tend toward the arcs of circle. Local velocities and angular deviations of the flow measured at the line of separation and projected onto the plane of the rear window or side plane decrease as one moves away from the center of curvature.

The influence of the slant angle compared with the direction of the incident flow on the swirl number value has been analyzed. The swirl number depends on the angular deviation of the incident flow compared with the separation line. Its value decreases and increases, respectively, when the slope of the rear window and windscreen increases. The bursting and swirl destructuring processes are promoted by small rear window angles and large windscreen slopes. The results obtained in experiments and/or numerically on simplified geometries of the rear window and windscreen confirm these results.

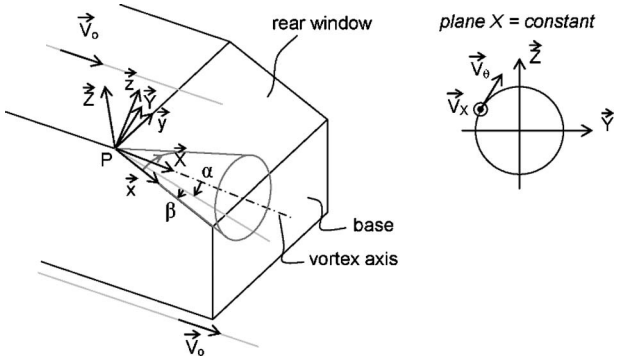

Fig. 20 Referential system linked to the swirling structure: precession and nutation angles. Azimuthal V_θ **and longitudinal** V_X **velocities in a** $X=Cte$ **plane.**

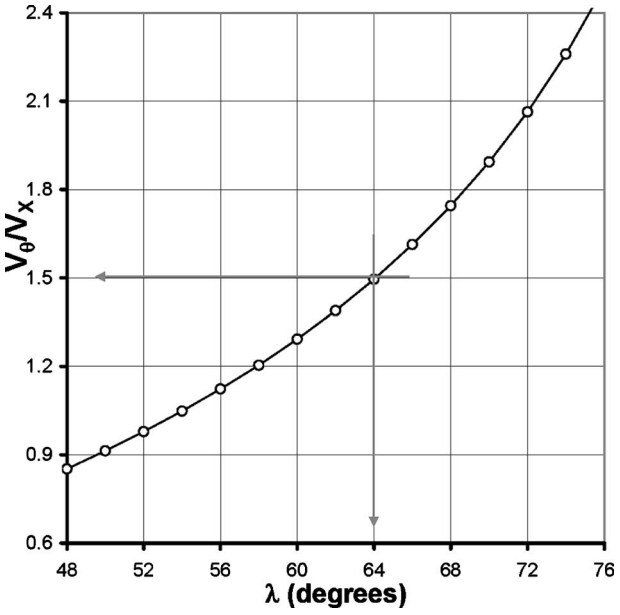

Fig. 21 Evolution of the ratio of azimuthal V_θ **and longitudinal** V_X **velocities as a function of the deviation angle λ**

Nomenclature

V_0 = freestream velocity
(x_0, y_0, z_0) = coordinate system linked to the freestream velocity
(x, y, z) = coordinate system linked to the left lateral edge (rear view)
(X, Y, Z) = coordinate system linked to the swirling structure axis from the rear window
P = intersection point between the left lateral edge (rear view) and the end of the roof
H = Ahmed body height
L = Ahmed body length
l = Ahmed body width
l_w = rear window length
r = radius of curvature
S = swirl number (the maximum value of the ratio of V_θ to V_X)
ΔP_i = volume energy loss
S_{up} = area normal to the freestream direction located upstream of the end of the roof
S_{down} = area normal to the freestream direction located downstream of the end of the roof
V_{up} = air flow velocity in the boundary layer upstream of the end of the roof
V_{down} = air flow velocity in the boundary layer downstream of the end of the roof
C_P^{up} = static pressure coefficient upstream of the end of the roof
C_P^{down} = static pressure coefficient downstream of the end of the roof
$\mathbf{n}$ = unit vector normal to the wall and directed toward the fluid domain
V_λ = air flow velocity in the boundary layer at the lateral edge of the rear window
V_X = longitudinal component of V_λ projected on x
V_θ = azimuthal component of V_λ

Greek Symbols

ρ = air density
θ = slant angle
λ = angle of the local velocity V_λ against the rear window
α = swirling structure axis angle against the rear window
β = swirling structure axis angle against the lateral side of the rear window

References

[1] Onorato, M., Costelli, A., and Garonne, A., 1984, "Drag Measurement Through Wake Analysis," International Congress and Exposition, Detroit, MI, SAE Paper No. SP-569, pp. 85–93.
[2] Tzirakis, E., Pitsas, K., Zannikos, F., and Stournas, S., 2006, "Vehicle Emissions and Driving Cycles: Comparison of the Athens Driving Cycle (ADC) With ECE-15 and European Driving Cycle (EDC)," Global NEST Journal (University of the Aegean, Greece), **8**(3), pp. 282–290.
[3] Lehugeur, B., Gilliéron, P., and Ivanic, T., 2006, "Contribution de l'Éclatement Tourbillonnaire à la Réduction de la Traînée des Véhicules Automobiles: Approche Numérique," Comptes Rendus Mecanique, **334**, pp. 368–372.
[4] Lehugeur, B., and Gilliéron, P., 2006, "Active Control of Vortex Breakdown Phenomenon in the Wake of a Simplified Car Geometry," ASME Paper No. FEDSM2006-98349a.
[5] Billant, P., Chomaz, J. M., and Huerre, P., 1998, "Experimental Study of Vortex Breakdown in Swirling Jets," J. Fluid Mech., **376**, pp. 183–219.
[6] Lehugeur, B., Gilliéron, P., and Ta Phuoc, L., 2005, "Characterization of Longitudinal Vortices in the Wake of a Simplified Car Model," AIAA Paper No. 2005-5383.
[7] Lehugeur, B., Gilliéron, P., and Ta-Phuoc, L., 2007, "Characterization and Control of Longitudinal Vortices Over a Dihedral Bluff Body: Numerical Approach," J. Mech. Eng., **58**(5), pp. 249–273.
[8] Rusak, Z., Wang, S., and Whiting, C. H., 1998, "The Evolution of a Perturbed Vortex in Pipe to Axisymmetric Vortex Breakdown," J. Fluid Mech., **366**, pp. 211–237.
[9] Rusak, Z., and Lamb, D., 1999, "Prediction of Vortex Breakdown in Leading-Edge Vortices Above Slender Delta Wings," J. Aircr., **36**, pp. 659–667.
[10] Ahmed, S., Ramm, R., and Falting, G., 1984, "Some Salient Features of the Time Averaged Ground Vehicle Wake," SAE Paper No. 840300.
[11] Gilliéron, P., and Chometon, F., 1999, "Modelling of Stationary Three-Dimensional Detached Airflows Around an Ahmed Reference Body," International Workshop on Vortex, ESAIM, Vol. 7, pp. 182–183.
[12] Spohn, A., and Gilliéron, P., 2002, "Flow Separations Generated by a Simplified Geometry of an Automotive Vehicle," IUTAM Symposium on Unsteady Separated Flows, France.
[13] Krajnovic, S., and Davidson, L., 2004, "Contribution to Large-Eddy Simulation of the Flow Around a Simplified Car Model," SAE International Congress and Exposition, SAE Paper No. 2004-01-0227.
[14] Rouméas, M., Gilliéron, P., and Kourta, A., 2008, "Separated Flow Around the Rear Window of a Simplified Car Geometry," ASME J. Fluids Eng., **130**, p. 021101.
[15] Vino, G., Watkins, S., Mousley, P., Watmuff, J., and Prasad, S., 2005, "Flow Structures in the Near Wake of the Ahmed Model," J. Fluids Struct., **20**, pp. 673–695.
[16] Anne-Archard, D., Du Colombier, D., Boisson, H., and Herbert, V., 2006, "Analyse des Enduits de Visualisation Pariétale Utilisés en Aérodynamique," 41ème Colloque National du Groupe Français de Rhéologie, France.
[17] Beran, P. S., and Culick, F. E. C., 1992, "The Role of Non Uniqueness in the Development of Vortex Breakdown in Tubes," J. Fluid Mech., **242**, pp. 491–527.
[18] Carvalho, I. S., and Heitor, M. V., 1996, "Visualization of Vortex Breakdown in Turbulent Unconfined Jet Flows," Optical Diagnostics in Engineering, **1**, pp. 22–30.

Particle Trajectory Study in Submerged Flows With Baffles Using $\overline{\nu^2}-f$ and $k-\varepsilon$ Turbulence Models

A. Mehdizadeh
Department of Mechanical and Aerospace Engineering,
University of Florida,
P.O. Box 116300,
Gainesville, FL 32611-6300
e-mail: ameh@ufl.edu

B. Firoozabadi
Associate Professor
Department of Mechanical Engineering,
Sharif University of Technology,
P.O. Box 11365-9567,
Tehran, Iran
e-mail: firoozabadi@sharif.edu

S. A. Sherif
Professor
Fellow ASME
Department of Mechanical and Aerospace Engineering,
University of Florida,
P.O. Box 116300,
Gainesville, FL 32611-6300
e-mail: sasherif@ufl.edu

In this paper, the structure of a wall jet deflected by a baffle along with the trajectory of particles has been studied. This baffle is used to produce a stable deflected surface jet, thereby deflecting the high-velocity supercritical stream away from the bed to the surface. An elliptic relaxation turbulence model ($\overline{\nu^2}-f$ model) has been used to simulate this submerged flow. In recent years, the $\overline{\nu^2}-f$ turbulence model has become increasingly popular due to its ability to account for near-wall damping without use of damping functions. In addition, it has been proven that the $\overline{\nu^2}-f$ model is superior to other Reynolds-averaged Navier-Stokes (RANS) methods in many flows where complex flow features are present. In this study, we compare the results of the $\overline{\nu^2}-f$ model with available experimental data. Since erosion and deposition are coupled, the study of this problem should consider both of these phenomena using a proper approach. In addition to erosion over the bed, the trajectory of the particles is examined using a Lagrangian–Eulerian approach, the distribution of deposited particles over the bed is predicted for a two-phase test case based on a series of numerical simulations. Results show that the maximum erosion happens in a place in which no particle can be deposited, which causes the bed to deform very rapidly in that region. This should help prevent or reduce erosion over the bed. On the other hand, the study will help predict the trajectory of particles and the deposition rates at any section of the channel, and should thus provide useful information to control the erosion and deposition on the channel bed.
[DOI: 10.1115/1.4001557]

1 Introduction

In practice, when a wall jet emanates from the outlet gate of a dam on a river, the water depth downstream of the dam is typically larger than that required for the formation of a hydraulic jump. This may cause erosion over the riverbed because the high-velocity jet or stream may continue moving without significant dissipation for relatively large distances. However, employing a small baffle on the bed can deflect the flow, thus making erosion of the riverbed downstream less likely to happen. On the other hand, the wall jet contains particles that are depositing in a manner commensurate with the applied forces in the flow field. Erosion and deposition are typically coupled with each other. Thus, a thorough study of the flow field should also be coupled to the study of particle transport.

As far as studying flow fields is concerned, we will focus on submerged jumps with baffles. Even though submerged jumps were well studied [1–5], very little work was done on a submerged jump with baffle walls. Based on a series of experiments, Wu and Rajaratnam [6] introduced a diagram that predicts the conditions under which a surface jet is produced. In the deflected surface jet regime, the flow from the gate is typically deflected at the baffle, all the way to the water surface; thus, creating a surface hump downstream of the baffle. The main flow in the downstream channel, on the other hand, exists near the water surface, below which a large eddy is typically formed. In the upstream region of the baffle, another eddy with significant circulation typically forms near the gate. This condition may be favorable for protecting the channel bed, but may also cause some erosion on the banks of the channel downstream. In a reattached wall jet (RWJ) regime, the main flow passes over the baffle and is reattached to the bed. Behind the baffle, a small eddy having a length of the same order of magnitude as the height of the baffle typically forms. This flow condition should be avoided in practice because the main flow, after reattachment, possesses high velocity and could cause severe erosion in the bed downstream of the baffle.

Particle transport, erosion, and deposition play a major role in filtration, combustion, air and water pollution, coal transport and cleaning, microcontamination control, xerography, nanotechnology applications, and many other industrial processes. The trajectory of particles or bubbles has been studied by several researchers. Previously published studies include those of Shams et al. [7], Zhang et al. [8], Sbrizzai et al. [9], and Chen et al. [10] who worked on two-phase flow modeling and published work pertaining to the deposition rate in specific flow regimes. Other published work includes that of Jayanti and Narayanan [11] who studied the effect of particle-eddy interactions in sedimentation tanks using the commercial computational fluid dynamic software FLUENT. Wang et al. [12] tracked nanoparticles and developed a numerical methodology capable of accurately characterizing the performance of aerodynamic lens systems.

In recent years, the $\overline{\nu^2}-f$ turbulence model, originally suggested by Durbin [13], has become increasingly popular due to its ability to correctly account for near-wall damping without the use of damping functions. The implementation of the $\overline{\nu^2}-f$ model has proven superior to other RANS methods in many complex fluid flows. For example, Parneix et al. [14] successfully computed a highly three-dimensional flow around a wall-mounted appendage. Using the $\overline{\nu^2}-f$ model, Hermanson et al. [15] observed some improvements in predicted heat transfer rates as compared with $k-\varepsilon$ computations for a stator vane flow. Another class of flows where the $\overline{\nu^2}-f$ model seems to work well is separated flows.

Manuscript received April 30, 2007; final manuscript received March 30, 2010; published online May 6, 2010. Assoc. Editor: Ian Eames.

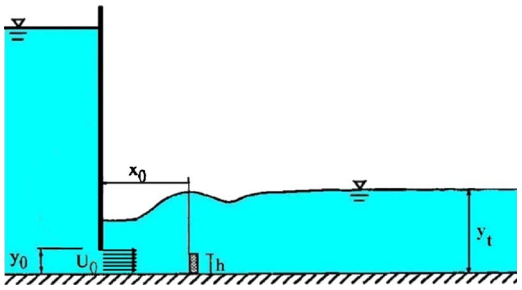

Fig. 1 Schematic of flow with baffle wall (not to scale)

Cokljat et al. [16] computed a set of recirculating flows and found that the $\overline{v^2}-f$ model outperforms two-equation models in most cases. The same trend was observed by Iaccarino [17], where the flow in an asymmetric diffuser was computed using the $\overline{v^2}-f$ model and the Launder–Sharma low-Reynolds number $k-\varepsilon$ model [18]. The separation bubble characteristic of this flow was fairly accurately predicted with the $\overline{v^2}-f$ model, whereas the $k-\varepsilon$ model predicted no recirculation at all. Due to the somewhat unstable formulation of the wall boundary condition of the relaxation parameter f in the original formulation of the $\overline{v^2}-f$ model, Lien and Kalitzin [19] redefined f in a slightly different way in order to have a numerically more attractive boundary condition. Due to the improved numerical properties of the redefined model, it has become more popular than the original, which, in most cases, requires a coupled solution procedure. In the more recent study of Sveningsson and Davidson [20], the behavior of two versions of the $\overline{v^2}-f$ model was compared in an attempt to investigate where the two models differ, in addition to improving the overall understanding of the performance of the models. Also Mehdizadeh and Firoozabadi [21] compared four different turbulence models and showed that the result of the modified $\overline{v^2}-f$ model is superior to the other models in calculating the characteristics of density currents. Comparison between $k-\varepsilon$ and $\overline{v^2}-f$ models have recently been studied in submerged flows with a baffle by Mehdizadeh et al. [22].

Figure 1 shows a schematic of a submerged jump with a baffle wall where y_0 and U_0 are the depth and mean velocity of the supercritical stream (leaving gate), respectively, h is the height of the baffle located at a distance x_0 from the gate, and y_t is the tail water depth.

In this study, the effects of the baffle on submerged flows is simulated with the $k-\varepsilon$ and $\overline{v^2}-f$ models to identify the possibility of using baffle walls for submerged flows for energy dissipation and the protection of the downstream riverbed from erosion. On the other hand, using a Lagrangian–Eulerian approach (one-way coupling two-phase flow equations), we have studied the movement, trajectory, and deposition of particles.

2 Mathematical Modeling

2.1 Governing Equations. Figure 1 shows that the surface boundary has a curvature, however, in many cases (which we have studied here), the maximum difference of this curvature with a flat surface is less than 2.5% [6]. Using this fact, we have applied no shear stress boundary condition at the free surface. In other words, a free surface may be thought of as a straight lid and could be modeled as a flat symmetrical boundary. Thus, the effects of wind and small ripples on the flow field could be neglected. The equations of this flow can therefore be expressed as follows:

$$\frac{\partial u}{\partial x}+\frac{\partial v}{\partial y}=0 \tag{1}$$

$$u\frac{\partial u}{\partial x}+v\frac{\partial u}{\partial y}=-\left(\frac{1}{\rho}\right)\frac{\partial P}{\partial x}+\frac{\partial}{\partial y}(\upsilon+\upsilon_t)\frac{\partial u}{\partial y} \tag{2}$$

$$u\frac{\partial v}{\partial x}+v\frac{\partial v}{\partial y}=-\left(\frac{1}{\rho}\right)\frac{\partial P}{\partial y}+\frac{\partial}{\partial y}(\upsilon+\upsilon_t)\frac{\partial v}{\partial y} \tag{3}$$

where the above equations are the continuity and the x- and y-momentum equations, respectively. The quantity ρ is the density and υ is the kinematic viscosity of the fluid. The pressure term is expressed as

$$\frac{P}{\rho_\omega}=\frac{P_0}{\rho_\omega}+\rho g(y_t-y)/\rho_\omega \tag{4}$$

P_o is the surface pressure and y_t is the water depth.

2.2 Turbulence Modeling. Most predictions in the industry involve the use of standard or modified versions of the $k-\varepsilon$ turbulence model, available in many existing CFD packages. These models have mostly been developed, calibrated, and validated for flows parallel to the wall. Historically, standard $k-\varepsilon$ models showed poor results in the near-wall region. Moreover, the $k-\varepsilon$ model, which has been standardized for a high Reynolds number and isotropic turbulent flow, could not simulate the anisotropy and nonhomogeneous behavior near the wall. In order to integrate $k-\varepsilon$ into the wall, it is a common practice to introduce low-Reynolds number damping functions. These are tuned to mimic certain near-wall behaviors [18]. However, all the $k-\varepsilon$ class of models use a single-point (IP) approach [13] that are incapable of representing the nonlocal effects of pressure-reflection that typically occur near solid boundaries. In many cases, the damping functions in question involve an ill-defined normal distance to the wall, which cannot be used in complex geometries. They are also highly nonlinear and sometimes introduce numerical stiffness in the solution.

An attractive alternative to the $k-\varepsilon$ model is the $\overline{v^2}-f$ turbulence model [13]. The reason why the above damping functions can be avoided is the availability of an additional turbulent velocity scale generic wall normal Reynolds stress component $\overline{v^2}$. By considering the exact transport equations for the Reynolds stresses in a fully developed channel flow, it can readily be shown that the production of $\overline{uv}$ (the only Reynolds stress component that affects the mean flow field) should be proportional to $\overline{v^2}$. In two-equation models, this velocity scale (squared) is not explicitly available, but is replaced by the turbulent kinetic energy k. As k has a different wall distance dependency of order $O(y^2)$ rather than $\overline{v^2}$, which is of order $O(y^4)$, this method is expected to be inaccurate as walls are approached. This deficiency in the method can be somewhat controlled by introducing a damping function that improves the wall distance dependency of the term $\overline{uv}$. Durbin [13] showed that by simply replacing k with $\overline{v^2}$ in the definition of the eddy viscosity, results could substantially be improved. Hence, an alternative interpretation, or definition of the damping function, say f_μ, is $\overline{v^2}=f_\mu k$. The main problem with a damping function is that it can only be tuned to a limited number of test cases. In $\overline{v^2}-f$ models, on the other hand, $\overline{v^2}$ is governed by a separate transport equation, and thus, has a potential of being applicable to a wider range of flow situations. In general, $\overline{v^2}$ should be regarded as a scale for the velocity component responsible for turbulent transport. It is proportional to k far from solid walls, while in the near-wall region, it becomes the velocity fluctuation normal to the solid surface, regardless of the orientation of the surface. The fourth and final transport equation (the f-equation) is an elliptic partial differential equation that accounts for nonhomogenous and anisotropic wall blocking effects in the v^2 transport equation. The quantity f is a parameter that operates more or less like a damping function. It is a parameter closely related to the pressure strain redistribution term. This parameter, if used in conjunction with the Navier–Stokes (NS) equations and appropriate turbulence models,

can help calculate the turbulence characteristics of the flow field from the near-wall region to areas away from the solid boundaries. One important feature of the $\overline{\nu^2}$ equation is its ability to account for nonlocal effects (e.g., kinematic blocking) by solving an elliptic relaxation equation for f. A modified Helmholtz operator introduces ellipticity, which is amenable to numerical computations. It introduces wall effects by a linear equation. This operator generates turbulence profiles that evolve from the near-wall behavior to form suitable areas far from the solid boundaries. Finally, a mathematical constraint has been added to prevent the nonrealizability of the eddy viscosity, especially in the stagnation-point region [23].

The $\overline{\nu^2}-f$ model could be thought of as a simplification of a full second moment closure (SMC) model [24]. For instance, the source terms in the f equation represent return to isotropy and isotropization models for energy redistribution. In this and other ways, important effects of near-wall anisotropy are represented. However, the $\overline{\nu^2}-f$ model has the advantage of solving the mean flow with an eddy viscosity, which avoids some computational stability problems encountered with the full SMC models. It is a general geometry turbulence model, valid right up to solid walls. It does not need wall functions whose universality is increasingly being called into question.

In the modified $\overline{\nu^2}-f$ turbulence model, the following transport equations must be solved in order to estimate the eddy viscosity

$$\frac{\partial k}{\partial t}+U_j\frac{\partial k}{\partial x_j}=\frac{\partial}{\partial x_j}\left(\left(\upsilon+\frac{\upsilon_t}{\sigma_k}\right)\frac{\partial k}{\partial x_j}\right)+p_k-\varepsilon \tag{5}$$

$$U_j\frac{\partial \varepsilon}{\partial x_j}=\frac{\partial}{\partial x_i}\left(\left(\upsilon+\frac{\upsilon_t}{\sigma_k}\right)\frac{\partial \varepsilon}{\partial x_j}\right)+\frac{C_{\varepsilon 1}p-C_{\varepsilon 2}\varepsilon}{t} \tag{6}$$

$$U\,.\,\nabla\overline{v^2}=\frac{1}{\rho}\nabla\,.\left[\left(\mu+\frac{\mu_t}{\sigma_k}\right)\nabla\overline{v^2}\right]+k\tilde{f}-6\frac{\varepsilon\overline{v^2}}{k} \tag{7}$$

Furthermore, the following elliptic equation must be solved (f equation):

$$\tilde{f}-L^2\nabla^2\tilde{f}=\frac{c_1}{T}\left[\frac{2}{3}-\frac{\overline{v^2}}{k}\right]+C_2\frac{P}{k}+5\frac{\overline{v^2}}{kT} \tag{8}$$

In these equations, the production term is $P_k=\upsilon_t((\partial U_i/\partial x_j)+(\partial U_j/\partial x_i))(\partial U_i/\partial x_j)$, and υ_t, which is the eddy viscosity, is defined as $\upsilon_t=c_\mu\overline{v^2}T$, in which $c_\mu=0.22$. The source term on the right side of the f-equation is analogous to the IP (single-point approach, as explained by Durbin [13]) from the closure model. The constants are $C_2=0.3$ and $C_1=0.4$.

The length and time scales in these equations are introduced as

$$L=C_L\max\left\{L',C_K\left(\frac{\upsilon^3}{\varepsilon}\right)^{1/4}\right\} \tag{9}$$

$$L'=\min\left\{\left(\frac{k^{3/2}}{\varepsilon}\right),\frac{1}{\sqrt{3}}\frac{k^{3/2}}{C_\mu\overline{\nu^2}\sqrt{2S^2}}\right\} \tag{10}$$

$$T=\max\left\{\frac{k}{\varepsilon},6\left(\frac{\upsilon}{\varepsilon}\right)^{1/2}\right\} \tag{11}$$

The constants are $C_L=0.2$ and $C_\eta=85$.

The $\overline{\nu^2}-f$ model requires that values of k and ε be known. They are determined by their equations, the only revision being to replace $C_{\varepsilon 1}$ either by $1.41[1+0.045\sqrt{k/\overline{\nu^2}}]$ or by $1.3+0.25/[1+(0.15d/L)^2]^4$, as suggested by Parneix et al. [14]. Either of these increases dissipation near the wall and improves the predictions of the turbulent kinetic energy k.

2.3 Equations of Particle Motion. There are mainly two ways to deal with the behavior of dispersed two-phase turbulent flows: the Eulerian–Eulerian approach and the Eulerian–Lagrangian approach. The former approach is often referred to as a two-fluid model approach because the particle phase is also treated as a continuum. In the latter approach, on the other hand, trajectories of individual particles are computed according to the particle equation of motion in the Lagrangian frame of reference.

In addition to examining the characteristics of the flow field in a channel, this study is also aimed at examining the motion of a particle within a channel. That latter part of the study is accomplished, employing a force balance that accounts for the pressure forces, the added mass, inertial effects, the buoyancy force, weight, and the steady drag action on the particle. The particle is small compared with the channel dimensions, and interactions between the particle and the walls are thus neglected. We will neglect changes to the liquid velocity caused by the presence of the particle (Eulerian–Lagrangian approach; one-way coupling equations). It seems that this is a logical assumption for a low concentration particle-water mixture. The aim of this part of the study is to predict trajectories of different types of individual particles in the channel, then using numerous runs and some logical assumptions, calculating the distribution of deposited particles on the bed. This study also helps predict the pattern of bed formation due to the deposition of particles or due to bed deformation caused by erosion at the initial stages.

We have solved the full Navier–Stokes equations using the $\overline{\nu^2}-f$ turbulence model and then, with considering the flow field and using a Lagrangian approach, the trajectory of particles was predicted. We consider a spherical particle of radius R_0, volume $V_p=(4/3)\pi {R_0}^3$, and density ρ_p in all tests equal to 2600 $\mathrm{kg/m^3}$ Kaolin particles moving with velocity $\boldsymbol{v}_p$ in a liquid, which (in the absence of the particle) moves with velocity $\boldsymbol{V}=(u,v)$.

The added mass force (acceleration reaction) is

$$F_{a1}=C_mV_p\rho\left(\frac{\partial \boldsymbol{V}}{\partial t}+\boldsymbol{V}\,.\,\nabla\boldsymbol{V}-\frac{d\boldsymbol{v}_p}{dt}\right) \tag{12}$$

The coefficient $C_m=0.5$ in unbounded flows, but it increases when the particle is inside a liquid-filled pipe. The particle radius is assumed small compared with the scale of the channel so the effect of the channel is negligible, thus, a value of $C_m=0.5$ could be justified.

When the fluid moves (relative to the axes) with a uniform, time-dependent velocity, the volume of fluid is accelerated and it experiences an inertial force (or buoyancy) $\boldsymbol{F}_I$ independent of the presence of the body. This force comprises two parts, $\boldsymbol{F}_{Iu}=\rho V_p d\boldsymbol{V}/dt$, which is due to the fluid acceleration, and $\boldsymbol{F}_{IS}=\rho V_p(\boldsymbol{V}.\nabla\boldsymbol{V})$, which is due to the fluid convection [25]. So with combining the added mass and the inertial force, we can define a modified (including inertial force) added mass force as

$$F_a=F_I+F_{a1}=V_p\rho\left(\frac{\partial \boldsymbol{V}}{\partial t}+\boldsymbol{V}\,.\,\nabla\boldsymbol{V}\right)+C_mV_p\rho\left(\frac{\partial \boldsymbol{V}}{\partial t}+\boldsymbol{V}\,.\,\nabla\boldsymbol{V}-\frac{d\boldsymbol{v}_p}{dt}\right) \tag{13}$$

The buoyancy force on a particle is

$$F_b=-(\rho_p-\rho)V_p\boldsymbol{g} \tag{14}$$

where the gravitational vector can be expressed in vector form as $\boldsymbol{g}=(0,9.81)$, where the zero implies no horizontal component, and where the quantity 9.81 is the magnitude of the acceleration of gravity.

The steady drag force is sometimes written in the form

$$F_D=\frac{1}{2}C_D\rho\pi R^2|\boldsymbol{V}-\boldsymbol{v}_p|(\boldsymbol{V}-\boldsymbol{v}_p) \tag{15}$$

where the drag coefficient C_D depends on the particle Reynolds number according to

Table 1 Details of Runs

Run No.	y_0 (mm)	Fr_0	y_t (mm)	x_0 (mm)	h (mm)	Flow state
1	10	5.48	442	300	11.6	DSL
2	10	5.48	442	350	11.6	DSL
3	10	5.48	442	350	11.6	RWJ
4	10	5.48	442	400	11.6	DSL
5	10	5.48	442	400	11.6	RWJ
6	10	5.48	442	450	11.6	DSL
7	10	5.48	442	450	11.6	RWJ
8	10	5.48	442	500	11.6	DSL

"DSL=deflected surface jet; RWJ=reattached wall jet"

$$\mathrm{Re}_p = \frac{2R_0\rho|\boldsymbol{V}-\boldsymbol{v}_p|}{\mu} \tag{16}$$

In all of the results presented here, to compute the drag coefficient C_D, we follow and use the formula, which was introduced for a wide range of Reynolds numbers for spherical particles as [7]

$$C_D = 24/\mathrm{Re} \quad \text{for} \quad \mathrm{Re} < 1$$

$$C_D = \frac{24[1+0.15\ \mathrm{Re}^{0.687}]}{\mathrm{Re}} \quad \text{for} \quad 1 < \mathrm{Re} < 1000$$

$$C_D = 0.4 \quad \text{for} \quad 1000 < \mathrm{Re} < 2.5\times 10^5$$

Finally, the equation of motion of a particle can be expressed as

$$\rho_p V_p \frac{d\boldsymbol{v}_p}{dt} = m\vec{g} + \boldsymbol{F}_b + \boldsymbol{F}_D + \boldsymbol{F}_{a1} + \boldsymbol{F}_I + \ldots \tag{17}$$

It is important to note that we have neglected the effects of particle interactions with each other along with wall effects. Also, the effect of the lift force is very small and not comparable to the other forces. With an-order-of-magnitude analysis, it can be shown that the lift force is negligible relative to the other forces. A good review of the forces acting on a particle or bubble motion can be found in Ref. [25].

2.4 Boundary Conditions. The boundary condition at the inlet is known, which is similar to the experimental models. Water with uniform velocity enters the channel under the still bodies of water passing through a sluice gate. At the outflow boundary, the streamwise gradients of all variables are set to zero. It is expected that modeling of the outlet only has a local effect on the flow field. At the free surface, no shear stress approximation is made. Then the symmetry condition that includes zero gradients and zero fluxes perpendicular to the boundary is applied.

At the rigid walls, due to the no-slip condition, the velocities are set to zero. Also, for the $\overline{\nu^2}-f$ equations, no-flux conditions are imposed at the free surface, i.e., $\partial k/\partial y = \partial\varepsilon/\partial y = \partial\overline{v^2}/\partial y = \partial f/\partial y = 0$, and at the inlet $k_{\mathrm{ent}} = (0.1u_{\mathrm{int}})^2$ and $\varepsilon_{\mathrm{ent}} = k_{\mathrm{ent}}^{3/2} C_\mu^{3/4}/KL$, in which K is the von Karman constant. No flux can go through the obstacle since it is assumed to be a rigid wall.

Eight runs to study the effect of the baffle position on erosion were performed. Details of these runs are given in Table 1. In the next stage, more than 80 runs to study the trajectory of the particles and their deposition were also performed. This will be subsequently explained.

2.5 Solution Procedure. The flow and turbulence equations have to be accurately resolved to obtain the velocity distributions. All computations were performed in Cartesian coordinates with a rectangular geometry. Cartesian grids were used with a high resolution near all solid boundaries. In all cases, for the $\overline{\nu^2}-f$ model, the first grid point was selected at $y^+ \approx 1$ or less, and the first grid point for the $k-\varepsilon$ model was selected at $y^+ \approx 35$. All runs were grid independent. There are 30,000 cells in the computational domain.

2.6 Solver. We have developed our own finite volume code by using the pressure correction scheme SIMPLEC and a collocated grid arrangement with a Rhie–Chow interpolation. The Loda scheme was used to discretize the momentum and turbulence equations. Those equations were solved with a coupled tridiagonal matrix solver (TDMA). All fluid properties were treated as being constant.

3 Results and Discussion

Experiments on submerged flows with baffle walls by Wu and Rajaratnam [6] showed that in any particular experiment, one might get a stable deflected jet that would finally form a surface jet or a stable reattached wall jet, after an initial separation at the baffle. These two flow cases are referred to as the "deflected surface jet" (DSJ) and the RWJ regimes, respectively. There is also a transition state in which some external distributions could change the flow from one regime to the other. At first, the flow field will be discussed to extract the skin friction coefficient in order to be able to investigate erosion. Then we will examine the trajectory of the particles in order to study the deposition characteristics. Figure 2 shows the streamlines of the two flow regimes that were obtained from numerical simulations performed in this study (Runs 4 and 5).

3.1 Flow Field and Erosion Study. Velocity vectors for the deflected surface jet regime (Run 4) of Wu and Rajaratnam's [6] experimental study and this numerical work are shown in Fig. 3. As can be seen, the circulation region upstream of the baffle is very strong and may cause erosion at that region. However, the region in question may not be as important as the downstream region, since the objective here is protection of the bed from erosion downstream of the baffle. Figures 4(*a*)–4(*d*) display a comparison of the results of the $\overline{\nu^2}-f$ and $k-\varepsilon$ turbulence models with the experimental data in the prediction of the decay of the maximum velocity $V_{\max}$ and the locus of maximum velocities for the DSJ and RWJ regimes. In Figs. 4(*a*) and 4(*b*), it can be seen that the maximum velocity and the locus of maximum velocities upstream of the baffle are almost the same for both turbulence models in the DSJ regime, but downstream of the baffle, the $k-\varepsilon$ model deflects the jet more rapidly than the $\overline{\nu^2}-f$ model. The reason for this is that the $k-\varepsilon$ model is incapable of providing good prediction of the turbulence length and time scales at the point of impingement on the baffle. Behnia et al. [26] showed that because of this weakness of the $k-\varepsilon$ model, it can overpredict by more than 100% the heat transfer at the stagnation point (impingement point), while the results of the $\overline{\nu^2}-f$ model were very good in that region because of the new definitions of the turbulence length and time scales (Eqs. (9)–(11)). In submerged flows with a baffle, the characteristics of the impinging point are not completely similar to those in the classical stagnation-point flows. In the former case, the flow stoppage occurs in a nonisentropic process because of the existence of the shear layer, but using the new definitions of length and time scales (Eqs. (9)–(11)), the predictions of the $\overline{\nu^2}-f$ model are a little better than those of the $k-\varepsilon$ model. The superior results of the $\overline{\nu^2}-f$ model are more noticeable downstream of the baffle than upstream (Fig. 4(*a*))

Figures 4(*c*) and 4(*d*) show that the $k-\varepsilon$ model produces slightly better results than the $\overline{\nu^2}-f$ model in the case of the RWJ regime. However, in general, the predictions of both models are not as accurate as those of the DSJ regime. It was expected that the spread of the jet predicted by the $k-\varepsilon$ model downstream of the baffle is faster than what is calculated by the $\overline{\nu^2}-f$ model (because of the larger turbulent energy production term of the $k-\varepsilon$ model). It is a bit hard to tell whether or not the rather inaccurate results predicted by both models for the RWJ regime are

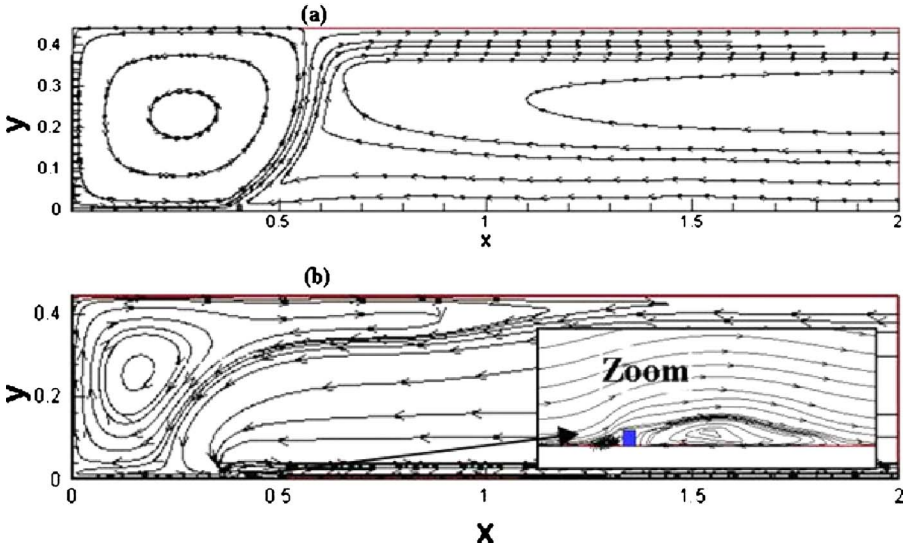

Fig. 2 Flow regimes (streamlines) of submerged flow with baffles: (*a*) deflected surface jet regime—Run 4; (*b*) reattached wall jet regime—Run 5

due to the weaknesses of the turbulence models or to the complicated instability characteristics of the Navier–Stokes equations. The discrepancy between the experimental and numerical results may be explained by one of the following arguments. The first is the possibility that Wu and Rajaratnum's [6] experiment did not cover all possible stable modes of the RWJ regime. The second argument may simply be that neither model could precisely predict the RWJ regime. Luckily, the DSJ regime, which was precisely predicted by the $\overline{\nu^2}-f$ turbulence model, is the only practical regime in typical submerged flows with a baffle.

It is important to note that the differences between the models' result in the case of submerged flows with a baffle, as reported in this paper, are less than those reported by Mehdizadeh et al. [27] for density current type flows. The latter type flow is a kind of wall jet at a low-Reynolds number (in the order of 1000). The height of the density current predicted by the $k-\varepsilon$ model in Ref. [27] was almost twice as great as the experimentally measured height. On the other hand, the height predicted by the $\overline{\nu^2}-f$ model matched the measured height. One possible explanation of the poorer results reported for the $k-\varepsilon$ model may have to do with the relative importance of the anisotropic effects and near-wall behavior in density current flows relative to submerged flows with a baffle.

Comparison of the skin friction coefficient over the bed for the DSJ and RWJ regimes is shown in Fig. 5. Since the flow topology is complicated and the velocity changes direction across the channel, one possible reference velocity to use in defining a nondimensional skin friction coefficient is the inlet jet velocity since its value is constant. So the skin friction factor can be defined as

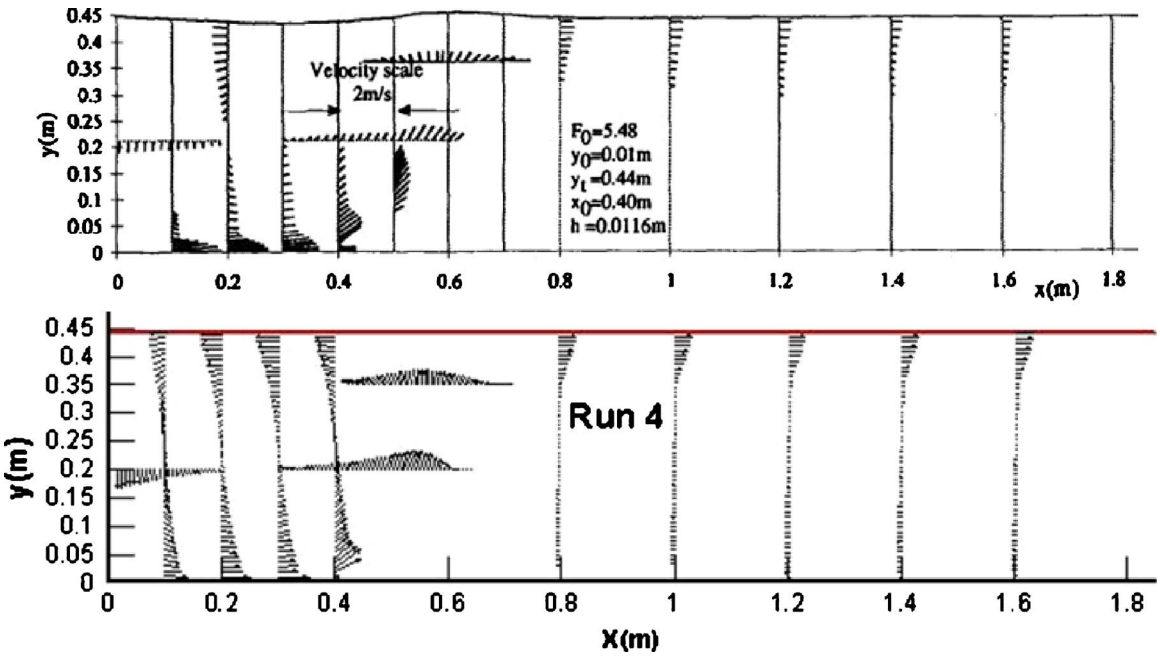

Fig. 3 Experimental velocity vectors (top), numerical prediction of the velocity vectors, $\overline{\nu^2}-f$ (bottom)

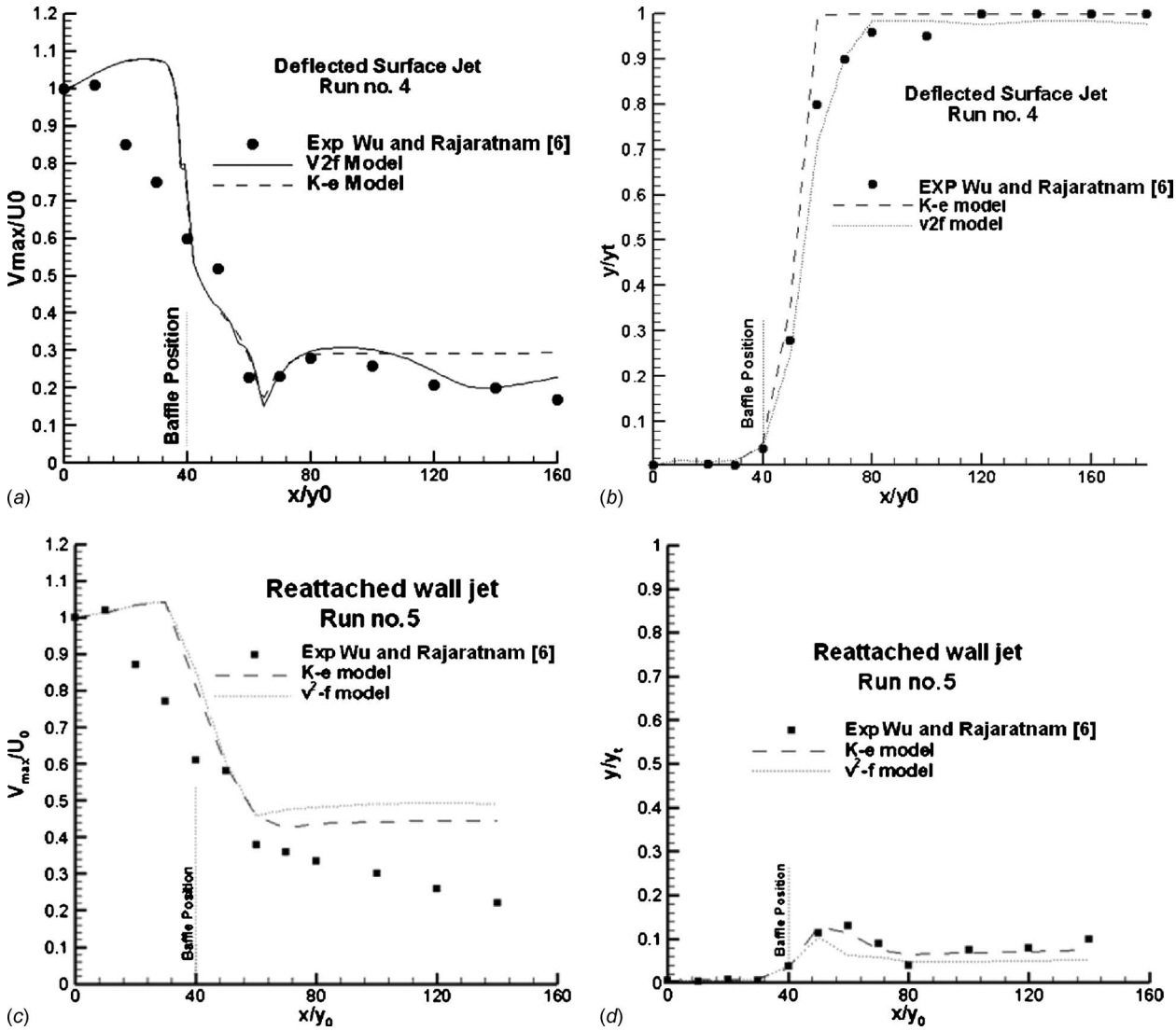

Fig. 4 Comparison of decay of the maximum velocities and locus of maximum velocities for the (*a* and *b*) DSJ and (*c* and *d*) RWJ regimes

$$C_f = \frac{\tau_w}{\frac{1}{2}\rho U_0^2} \tag{18}$$

where τ_w is the wall shear stress. Figure 5 shows that both regimes have a large skin friction coefficient in the upstream region because of the high velocity near the bed. In addition, in the DSJ regime, the maximum skin friction coefficient upstream of the baffle becomes larger than that of the reattached wall jet regime due to the existence of strong circulation upstream, which is enhancing the velocity magnitudes. However, the upstream region is not a very important region in submerged flows with a baffle. Moreover, Fig. 5 shows that the maximum of the skin friction coefficient, in the deflected surface jet regime downstream of the baffle, is almost 3.3 times smaller than that in the reattached wall jet regime. In the latter regime downstream of the baffle, there exist two maxima for the absolute value of the skin friction coefficient. These maxima exist shortly downstream of the baffle (5 and 20 times of the baffle's height, respectively). The first maximum is produced because in the corner of the baffle, reverse flow is generated close to the bed, so the skin friction coefficient C_f has a negative value. The negative sign is not important since the absolute value of C_f is the significant parameter so far as erosion

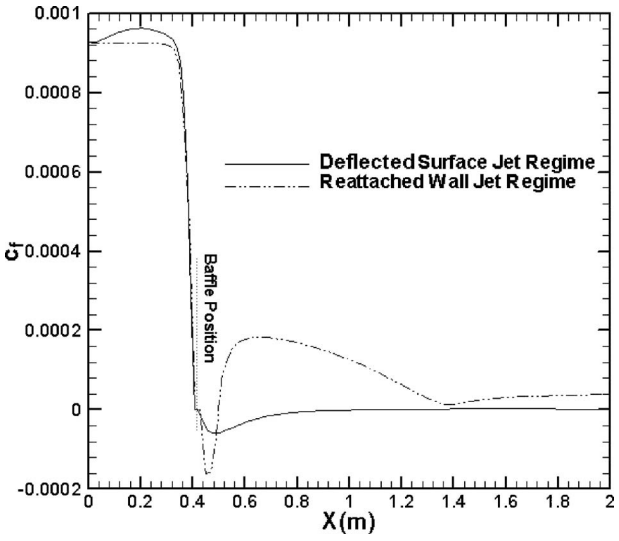

Fig. 5 Comparison of the skin friction coefficient over the bed for the two regimes (Runs 6 and 7)

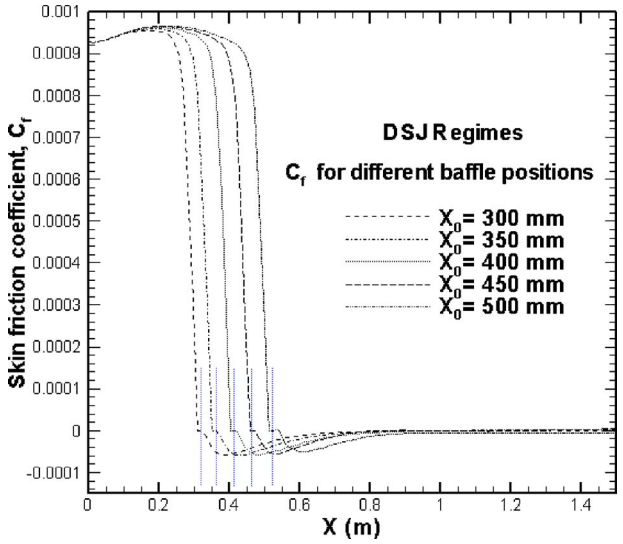

Fig. 6 Skin friction coefficient over the bed for different baffle positions (Runs 1, 2, 4, 6, and 8)

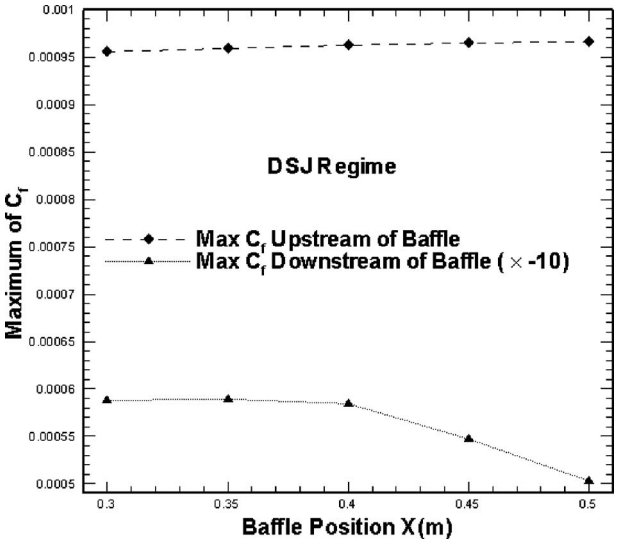

Fig. 7 Maximum skin friction coefficient (absolute value) over the bed for different baffle positions (Runs 1, 2, 4, 6, and 8)

is concerned. The second maximum is produced because of the reattachment where the flow hits the bed and produces a large skin friction coefficient, which may cause erosion downstream of the baffle.

In the deflected surface jet regime, the skin friction coefficient is smaller than that in the reattached wall jet regime in all places, except the upstream region. Because of this fact, having the RWJ regime is not desirable since it is associated with a higher likelihood for the onset of erosion. Figure 5 shows shortly downstream of the baffle that the skin friction coefficient has a large negative value (a maximum for the absolute value) for the DSJ regime. The figure also shows that if erosion were to take place in the DSJ regime, the incipient point of erosion would be the location where the skin friction coefficient is maximum. The negative maximum exists because of the presence of a sharp curvature in the streamlines in that region (see Fig. 2(*a*) in the vicinity of the corner on the downstream side of the baffle). It can therefore be concluded that if the bed is protected from erosion at the erosion incipient point of the DSJ regime, the downstream bed could be completely protected from erosion. Although the velocity has been used traditionally for predicting whether or not a particle erodes, the Shields relationship between the dimensionless shear stress (or Shields parameter) τ^* and the grain Reynolds number R^* is now recognized as a more reliable predictor for the incipient of erosion (see for example Ref. [28]). Thus, knowing the skin friction coefficient at the erosion incipient point and utilizing the well known Shields curve for incipient sediment motion along with knowledge of the bed type, it is possible to recognize where the baffle should be installed in order to protect the downstream region from erosion (this will be discussed later in the paper).

Figure 6 shows results of a series of runs for the skin friction coefficient at different baffle positions for the deflected surface jet. As can be seen, the baffle position affects the skin friction coefficient in both the upstream and downstream regions. As the baffle is located at farther distances from the inlet, a weaker circulation is produced downstream of the baffle, which is associated with the strong spread of the flow upstream of the baffle. Stronger flow spread moves less water from downstream to upstream and generates the smaller maximum value of the skin friction coefficient.

Figure 7 shows trends for a series of maxima of the absolute values of the skin friction coefficient upstream and downstream of the baffle. As can be seen, the maxima behave in opposite ways upstream and downstream for the DSJ regime. The first maxima, which occur upstream of the baffle, increase in value as the baffle locates at farther distances from the inlet. The increase of the skin friction coefficient upstream of the baffle can be explained by making two observations. First, the increase in the skin friction coefficient is related to the local acceleration of the flow caused by boundary layer growth on the bed. Second, when the baffle is located farther downstream of the inlet, the free shear layer of the upper boundary of the wall jet moves more fluid, thus produces stronger circulation upstream that causes the velocity and the skin friction coefficient to increase.

In summary, the numerical model developed in this paper has been used to provide a good estimate of the bed shear stress (see Figs. 6 and 7). This estimate can be used to calculate the Shields parameter, which helps predict erosion or incipient sediment motion for different particle sizes, baffle positions, and Reynolds numbers. Therefore, it is possible to predict the shortest distance measured from the channel inlet of the baffle in order to protect the largest area downstream of the baffle from erosion inception. It is also possible to use this information to select the most suitable bed type upstream of the baffle for purposes of maximizing protection from erosion.

3.2 Particle Trajectories. A complete study of flows containing particles should consider prediction of both erosion and deposition. The objective of this section is to provide a description of the movement of particles when they enter the flow field. First, we will predict the trajectory of particles according to their size and points of release. Second, we will introduce a diagram by which the distribution of the deposited particles could be characterized for a wide range of particle sizes. For bigger particles, the weight increases in the order of R^3, while the drag force increases in the order of R^2. Thus, for bigger particles, the effect of the weight is dominant. Therefore, it is predictable that the trajectories of bigger particles would deviate from those of the streamlines quicker than smaller particles would. The bigger particles would also settle down and deposit faster, relative to the smaller particles.

Figure 8, which pertains to particles initially released from the top of the inlet gate, shows that big particles deposit upstream of the baffle, while the flow field carries smaller particles farther downstream. One of the reasons for that is the increase of the vertical velocity component due to the flow deflection by the baffle. The large vertical velocity (see Fig. 3) produces a large drag force that pushes the particles upward to the other side of the baffle. The velocity is smaller downstream so the weight becomes more dominant there, relative to the other forces. When particles descend and reach a certain height (y=0.32 m), the reverse flow

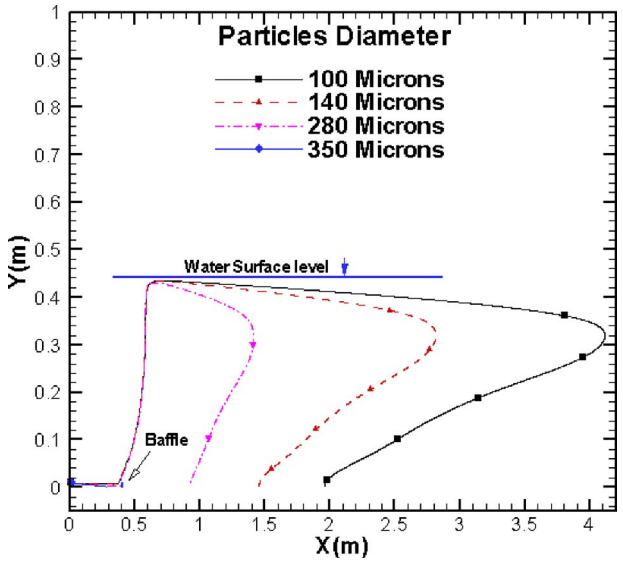

Fig. 8 Trajectories of different size particles (particle release point x_i=0, y_i=0.01, baffle position x_0=0.4 (m))

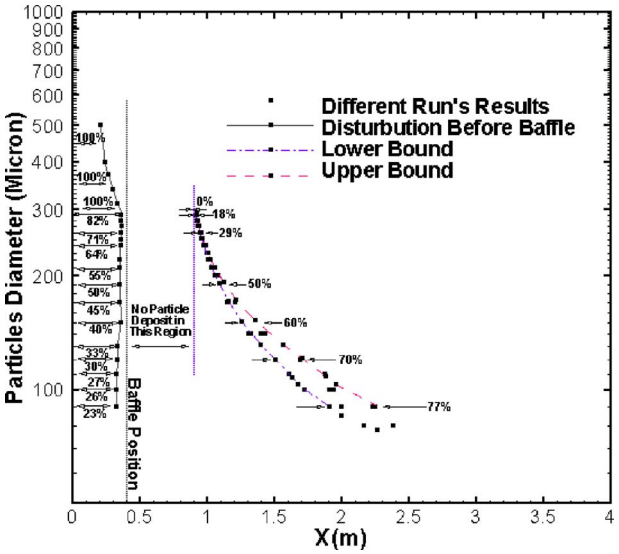

Fig. 10 Distribution of deposited particles over the bed

upstream of the baffle (for the streamlines coming from right to left in Fig. 2) provides a drag force pointing to the left-hand-side of the channel, which carries particles to the upstream region. There are three regions where no particles can be deposited, which we will label as "blind regions."

Other than the particle size, the trajectories of the particles depend on the location of the initial point of release (see Fig. 9). As can be seen, if a particle is released close to the bed, it deposits close to the inlet, while it would deposit downstream of the baffle if it is released from the top of the inlet (e.g., a particle with a 100-μ diameter released from (0, 0.0025) would deposit upstream of the baffle). The criteria used to determine what constitutes "close to the bed" will be discussed a bit later in the paper.

Since the streamlines are almost parallel to the X axis shortly downstream of the baffle, the drag force in the Y direction rapidly balances out with the particle weight, thus, particles would fall with an approximately constant velocity. Moreover, Fig. 9 shows that if a particle happens to exist in the upstream circulation region, it would rotate and descend under the actions of forces (described earlier); the most dominant of which are the weight and centrifugal forces. The radius of particle rotation typically increases as the particle descends until the particle reaches the region where the high-velocity jet exists, which would then carry the particle farther downstream. In reality, flows have numerous particles of different sizes, shapes, and points of release. Since we can only predict the trajectory of one particle at a time, many runs need to be performed in order to fully determine the distribution of particles over the whole bed.

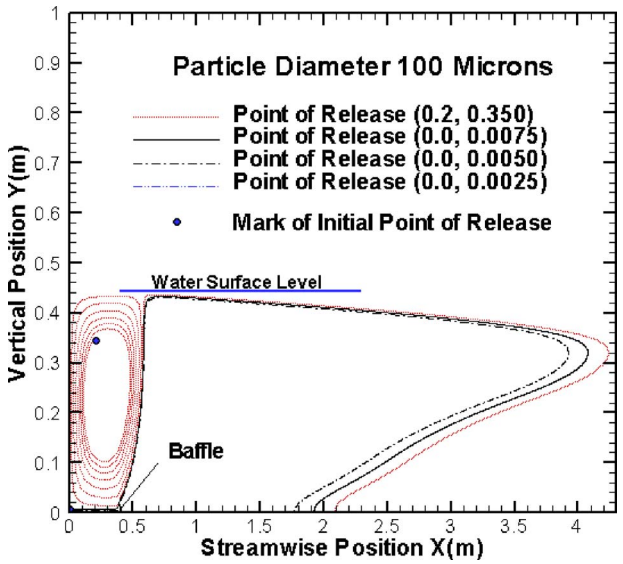

Fig. 9 Particle trajectories for several release points (particle diameter 100 μ)

Figure 9 shows that for a known particle size, there is a limit on how high from the bed the point of release should be for a particle to escape the baffle. In other words, particles released below the given limit would deposit upstream of the baffle. Figure 10 shows those limits and gives the distribution of deposited particles over the bed for different particle sizes. Three curves can be seen in the figure: The left curve, which introduces the distribution upstream of the baffle, shows that a larger fraction of the bigger particles deposit upstream. For example all of the particles bigger than a 294-μ diameter deposit upstream of the baffle, while some of the particles smaller than 294 μ deposit upstream and some deposit downstream, according to the height of their points of release from the inlet. Furthermore, the figure shows that 23% of 90-μ particles deposit upstream of the baffle, and 77% escape and deposit between x=1.82 m and 2.28 m, depending on their point of release.

Three blind regions for deposition of different size particles can be identified in Fig. 10. The first is a short region upstream of the baffle in which a small eddy with strong circulation (exactly under the deflection region) does not let particles penetrate the region. The second is a wider region downstream of the baffle. The third is a region downstream of the last deposited particle. In all regions, deposition does not take place while the potential for erosion exists due to the large bed shear stress (see Figs. 6 and 7). In order to calculate the deposition rate, we should switch from the Eulerian–Eulerian approach to the Eulerian–Lagrangian approach. In practice, the concentration of the mixture of water and particles C, along with the particle size, are known parameters. The definition of the concentration has been expressed in Eq. (19), where ρ is the mixture density, ρ_w is the water density, and ρ_p is the particle density

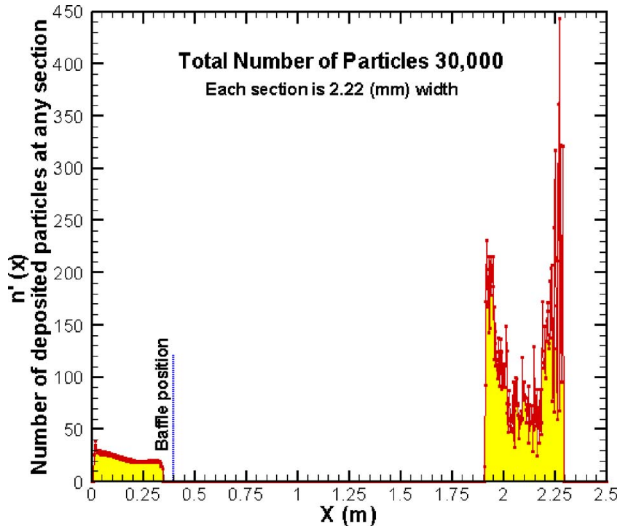

Fig. 11 Number of deposited particles at several sections of the channel (particle diameter 90 μ)

$$C = \frac{\rho - \rho_w}{\rho_p - \rho_w} \tag{19}$$

On the other hand, the mixture density ρ can be directly calculated from the volume fraction of the particles as follows:

$$\rho = \rho_w + N(m_p - \rho_w V_p)/V \tag{20}$$

where N is the number of particles in the mixture, V is the volume of any sample control volume, and m_p and V_p are the mass and volume of one particle, respectively. The number of particles in a sample control volume of the mixture N can be calculated by combining Eqs. (19) and (20). Thus, for a sample control volume of the mixture V, the number of particles can be written as

$$N = \frac{C \times V}{V_p} \tag{21}$$

As a result, the number of particles entering the flow domain can be expressed as

$$n = \dot{Q} \times \bar{N} \times t \tag{22}$$

where $\dot{Q}$ (in m^3/s) is the inlet volumetric flow rate, $\bar{N}$ is the number of particles in a unit volume of the mixture that can be determined from Eq. (21), $\bar{N} = C/V_P$, and t is the time in seconds. The thickness of the forming bed is a function of the manner with which particles deposit vis-à-vis the way particles fall on each other. Specifically, the thickness is strongly influenced by the average distance between the centers of two particles settling on each other. The empirical parameter $C'(x)$, which indicates the average distance between two centers of depositing particles can be measured based on the density of the forming bed (wet bed). Knowing the number of particles entering the domain n and the distribution of the settled particles (as determined from Fig. 10), the number of deposited particles upstream and downstream of the baffle can be calculated.

In order to have a more qualitative plot of the distribution of the settling particles along with the thickness of the forming bed at each section of the channel, numerous particles need to be released and tracked all the way through the channel. This is an extremely time consuming and costly exercise. Figure 11 shows a more accurate distribution of 30,000 particles with a 90-μ diameter uniformly released via the sluice gate. This number is equivalent to the number of particles existing in 0.381 ml of a particle-water mixture with 3% concentration (Eq. (21)). In Fig. 11, the channel has been divided into many sections whose width is 2.22 mm. The abscissa of Fig. 11 is the number of deposited particles in each section $n'(x)$. The figure shows that the deposited particles upstream and downstream are not uniformly distributed. As can be seen, the number decreases with the distance from the inlet at the upstream of the baffle. On the other hand, the number of deposited particles downstream of the baffle has two maxima near the right and left limits and has a minimum close to the middle. Figure 11 provides a good tool to calculate the thickness of the forming bed at any section of the channel as a function of time.

Using Fig. 11 and the empirical parameter $C'(x)$, the thickness of deposition over the bed can be easily calculated. If $n'(x)$ shows the number of deposited particles at a given time and location, the bed thickness $T(x)$ can be calculated as $T(x) = (1 + n'(x)) \times C'(x)$. Also, the amount of erosion can be calculated from the Shields curve, based on what was discussed in the previous sections. Therefore, the total bed formation or erosion can be described by superposing deposition and erosion.

It is important to note that the aforementioned analysis is valid, so long as the formation and erosion do not significantly alter either the flow geometry or the boundary conditions. If one or both change, we have to resort to a new mesh and time-dependent boundary conditions.

4 Conclusions

In this work, two turbulence models to study the structure of a wall jet deflected by a baffle have been compared. The baffle was used to produce a stable deflected surface jet, thereby deflecting the high-velocity stream away from the bed to the surface in order to reduce the rate of erosion downstream of the baffle. The velocity vectors and loci of maximum velocity were compared with the available experimental data. The $\overline{v^2}-f$ model was found to be more superior to the $k-\varepsilon$ model for the DSJ regime. This was the case because of the ability of the former to account for anisotropic effects in the domain and to utilize new concepts of modeling turbulence time and length scales near the impinging point. For the RWJ regime, predictions by both models were poor, mainly due to the unstable nature of this regime. Results included comparison of the skin friction coefficient of the two regimes. Results in the RWJ regime showed the maximum of the skin friction coefficient to be almost 3.3 times larger than that in the DSJ regime. Thus, producing a DSJ regime would be desired in order to reduce the likelihood of erosion inception downstream of the baffle.

A strategy of predicting the best baffle position was introduced. A diagram that predicts the effect of the baffle position on the skin friction coefficient was also developed. Even though the concept presented appears to have the potential to evolve into a design tool for energy dissipation below submerged outlets, further investigations need to be performed. In particular, we need to study the effects on the bed skin friction coefficient and the deposition rate of all the variables pertaining to submerged flows with a baffle, including the baffle height, water depth, and the inlet Froude number.

Another aspect of the work described in this paper is the prediction of the trajectory of particles using the Eulerian–Lagrangian approach. We have shown that the trajectory and accordingly, particle deposition information, are strongly dependent on the particle size, the flow field, and the location of the point of release. The study reveals the existence of three regions in which no particle deposition occurs. In one of these regions (located right downstream of the baffle), it was found that the wall shear stress is significant. It is thus recommended that the bed be structurally strengthened in this region in order to reduce the likelihood of erosion. Using numerous computational runs, a diagram providing the distribution of particles over the bed was developed. The diagram in question along with the knowledge of the manner with which particles are stacked on top of each other, the thickness of the forming bed could be calculated. In order to calculate the deposition rate more precisely, we have released 30,000 par-

ticles and tracked them all the way through their journey in the channel. It was found that the distribution of the particles upstream of the baffle is reasonably uniform, while the downstream particles deposit following a nearly parabolic pattern.

Nomenclature

$C_\mu, C_{\varepsilon 1}, C_{\varepsilon 2}$ = constants in the $k-\varepsilon$ model
C = concentration
C' = average distance between two particles
C_D = drag coefficient
C_f = bed skin friction coefficient
C_m = constant in added mass force
ε = energy dissipation rate
f_μ = damping function
f = relaxation variable
F_b = buoyancy force
F_D = drag force
F_{a1} = added mass force
F_I = inertial force
g = gravitational acceleration
y_t = water depth
h = height of baffle
K = von Karman constant
k = turbulence kinetic energy
L = length scale of turbulence
m_p = mass of a particle
$\bar{N}$ = number of particles in 1 m^3
n' = number of deposited particles at any section of the channel
n = number of particles
P_k = production term
P = pressure
P_0 = surface pressure
q = inlet flow rate
R_0 = radius of particle
S_{ij} = strain rate tensor
S = $S^2=S_{ij}S_{ij}$
T = time scale of turbulence
$T(x)$ = thickness of deposition
U_0 = inlet velocity
$\vec{V}=(u,v)$ = velocity components of x and y directions
$\overline{u_i u_j}$ = Reynolds stresses
$\overline{v^2}$ = turbulent velocity scale
$\boldsymbol{v}_p$ = particle velocity
V_p = volume of particle
x_0 = baffle position
y_0 = inlet height
ν_t = turbulence viscosity
σ_k and σ_ε = turbulence constants
ρ_w = density of water
ρ_s = density of salt solution

References

[1] Govinda Rao, N. S., and Rajaratnam, N., 1963, "The Submerged Hydraulic Jump," J. Hydr. Div., **89**, pp. 139–162.
[2] Rajaratnam, N., 1965, "Submerged Hydraulic Jump," J. Hydr. Div., **91**, pp. 71–96.
[3] Rajaratnam, N., 1965, "Flow Below a Submerged Sluice Gate as a Wall Jet Problem," Proceedings of the Second Australian Conference on Hydraulics and Fluid Mechanics, University of Auckland, New Zealand, pp. B131–B146.
[4] Long, D., Rajaratnam, N., and Steffler, P. M., 1990, "LDA Study of Flow Structure in Submerged Hydraulic Jump," J. Hydraul. Res., **28**, pp. 437–460.
[5] Ohtsue, I., Yasuda, Y., and Awazu, S., 1990, "Free and Submerged Hydraulic Jumps in Rectangular Channels," Report No. 35, Research Institute of Science and Technology, Nihon University.
[6] Wu, S., and Rajaratnam, N., 1995, "Effect of Baffle on Submerged Flows," J. Hydraul. Eng., **121**, pp. 644–652.
[7] Shams, M., Ahmadi, G., and Smith, D. H., 2002, "Computational Modeling of Flow and Sediment Transport and Deposition in Meandering Rivers," Adv. Water Resour., **25**, pp. 689–699.
[8] Zhang, H., Ahmadi, G., Fan, F.-G., and McLaughlin, J. G., 2001, "Ellipsoidal Particles Transport and Deposition in Turbulent Channel Flows," Int. J. Multiphase Flow, **27**, pp. 971–1009.
[9] Sbrizzai, F., Verzicco, R., Faraldi, P., and Soldati, A., 2004, "Interaction Between Transitional Structures and Particles in the Near-Field of a Round, Confined Jet," Proceedings of the Second International Symposium on Two-Phase Flow Modeling and Experimentation, Pisa, Italy, Sept. 22–25.
[10] Chen, X., McLaury, B. C., and Shirazi, S. A., 2005, "A Comprehensive Erosion Prediction Method for Gas/Liquid/Sand Multiphase Flow," Proceedings of the Fluids Engineering Division Summer Meeting, Houston, TX, June 19–23.
[11] Jayanti, S., and Narayanan, S., 2004, "Computational Study of Particle-Eddy Interaction in Sedimentation Tanks," J. Environ. Eng., **130**, pp. 37–49.
[12] Wang, X., Gidwani, A., Girshick, S. L., and McMurry, P. H., 2005, "Aerodynamic Focusing of Nanoparticles: II. Numerical Simulation of Particle Motion Through Aerodynamic Lenses," Aerosol Sci. Technol., **39**, pp. 624–636.
[13] Durbin, P. A., 1991, "Near-Wall Turbulence Closure Modeling Without Damping Functions," Theor. Comput. Fluid Dyn., **3**, pp. 1–13.
[14] Parneix, S., Durbin, P., and Behnia, M., 1998, "Computation of 3-D Turbulent Boundary Layer Using the $\overline{\nu^2}-f$ Model Flow," Flow, Turbul. Combust., **60**, pp. 19–46.
[15] Hermanson, K., Kern, S., Picker, G., and Parneix, S., 2003, "Prediction of External Heat Transfer for Turbine Vanes and Blades With Secondary Flow Fields," J. Turbomach., **125**, pp. 107–113.
[16] Cokljat, D., Kim, S., Iaccarino, G., and Durbin, P.A., 2003, "A Comparative Assessment of the $\overline{\nu^2}-f$ Model for Recirculating Flows," Paper No. AIAA-2003-0765.
[17] Iaccarino, G., 2001, "Predictions of a Turbulent Separated Flow Using Commercial CFD Codes," ASME J. Fluids Eng., **123**, pp. 819–828.
[18] Launder, B., and Sharma, B., 1974, "Application of the Energy-Dissipation Model of Turbulence to the Calculation of Flow Near a Spinning Disc," Lett. Heat Mass Transfer, **1**, pp. 131–137.
[19] Lien, F., and Kalitzin, G., 2001, "Computations of Transonic Flow With the $\overline{\nu^2}-f$ Turbulence Model," Int. J. Heat Fluid Flow, **22**, pp. 53–61.
[20] Sveningsson, A., and Davidson, L., 2004, "Assessment of Realizability Constraints in $\overline{\nu^2}-f$ Turbulence Models," Int. J. Heat Fluid Flow, **25**, pp. 785–794.
[21] Mehdizadeh, A., and Firoozabadi, B., 2009, "Simulation of a Density Current Turbulent Flow Employing Different RANS Models—A Comparison Study," J. of Scientia Iranica, **16**, pp. 53–63.
[22] Mehdizadeh, A., Firoozabadi, B., and Sherif, S. A., 2006, "Numerical Simulation of Submerged Flows With Baffles Using $k-\varepsilon$ and $\overline{\nu^2}-f$ Turbulence Models," ASME Paper No. IMECE2006-15403.
[23] Durbin, P. A., 1996, "On the $k-\varepsilon$ Stagnation Point Anomaly," Int. J. Heat Fluid Flow, **17**, pp. 89–90.
[24] Durbin, P. A., 1993, "A Reynolds-Stress Model for Near-Wall Turbulence," J. Fluid Mech., **249**, pp. 465–498.
[25] Magnaudet, J., and Eames, I., 2000, "The Motion of High-Reynolds Number Bubbles in Inhomogeneous Flow," Annu. Rev. Fluid Mech., **32**, pp. 659–708.
[26] Behnia, M., Parneix, S., Shabany, Y., and Durbin, P. A., 1999, "Numerical Study of Turbulent Heat Transfer in Confined and Unconfined Impinging Jets," Int. J. Heat Fluid Flow, **20**, pp. 1–9.
[27] Mehdizadeh, A., Firoozabadi, B., and Farhanieh, B., 2008, "Numerical Simulation of Turbidity Current Using $\overline{\nu^2}-f$ Turbulence Model," J. of Applied Fluid Dynamics (JAFM), **1**, pp. 45–55.
[28] Gessler, J., 1971, "Beginning and Ceasing of Sediment Motion," *River Mechanics*, H. W. Shen, ed., Water Resources Pub., Fort Collins, CO, Vol. 1, Chap. 7.

Investigation of the Flow Field in a Rectangular Vessel Equipped With a Side-Entering Agitator

C. Gómez[1]
e-mail: clara@chbe.ubc.ca

C. P. J. Bennington

F. Taghipour

Department of Chemical and Biological Engineering,
University of British Columbia,
2360 East Mall,
Vancouver, BC, V6T 1Z3, Canada

The hydrodynamics of stirred vessels with side-entering impellers, which are used in numerous process industries including petroleum, foods, and pulp and paper manufacturing, have received limited attention. In the present work, the flow in a reduced size rectangular tank equipped with a side-entering axial flow impeller, scaled down from the industrial agitation of low consistency pulp fiber suspensions, was investigated using particle image velocimetry (PIV) and computational fluid dynamics (CFD), in the laminar regime ($18 \leq Re \leq 120$). Tuning of the PIV measuring parameters for an optimum capture of valid velocity vectors within a representative portion of the vessel is described. A detailed description of the construction and refinement of the grid and quantification of the discretization error in the CFD results is also presented. The simulation predictions were extensively evaluated by comparing the measured planar flow patterns and velocity fields at various locations in the mixing vessel. Very good agreement was found between PIV measurements and computed velocities confirming the efficiency of CFD in the analysis of mixing systems. The prediction of global mixing parameters was also evaluated. The computed impeller torque and impeller power number agreed very well with experimental measurements over the range of Re studied. [DOI: 10.1115/1.4001575]

Keywords: mixing, stirred tanks, axial flow impellers, computational fluid dynamics (CFD), particle image velocimetry (PIV)

In Memoriam: Chad P. J. Bennington

Chad Bennington passed away suddenly February 14, 2010 at age 53. His untimely passing is a devastating loss for his family, colleagues, and the academic community to which he has made so many contributions. He held the Natural Sciences and Engineering Research Council of Canada (NSERC) Industrial Research Chair in Chemical Pulping Technology. From this he established a world-class research group of students and post-doctoral fellows. He was a leading expert in mixing processes in the pulp and paper industry as well as other process industries. Next to his normally easygoing nature, he was startling in his intensity and willingness to ponder our work and always ask thoughtful questions. In addition to all of his accomplishments, Chad loved the outdoors and was a devoted family man. In these very difficult times, our thoughts and prayers are with his family.

1 Introduction

Fluid mixing is a central unit operation in the chemical and biological process industries with the stirred tank being one of the most used devices. Empirical rules that rely on global operating parameters, such as the impeller power number and flow number, have been widely used to design mixing systems. However, the investigation and optimization of these processes necessitate fundamental understanding of the flow structures and velocity distributions found within the agitated vessel [1].

The quality of mixing required varies according to the specific process at hand. For the most part, bulk motion is required in order to guarantee good circulation within the mixing vessel. In addition, in suspension and dispersion operations, acceptable local velocities in regions remote from the impeller are required. Therefore the selection of an impeller for a specific duty is governed by the flow patterns and the velocity profiles that can be generated in a particular fluid.

The recent increased availability of sophisticated experimental techniques and efficient computational tools enables extensive analyses of the flow field in stirred vessels that enhance our understanding of the phenomena occurring within these systems. A wealth of literature exists on the implementation of CFD to simulate the flow fields generated in cylindrical agitated tanks with radial and axial impellers [2–8]. A number of studies have also been made in noncylindrical vessels equipped with side-entering agitators as found in industrial paper pulp mixing chests [9–12]. However, many of these computational studies have not been evaluated against sufficient experimental measurements because it is very difficult to obtain the needed data when the fluids mixed are opaque. Computational results must be validated against experimental data as their calculations depend strongly on several factors, including modeling of the system's geometry, discretization method, mesh structure, viscosity definition and rheology model in the non-Newtonian case, and turbulence model used, if any, for the momentum conservation equations.

The flow fields obtained in a stirred tank have been studied experimentally using multiple techniques including hot wire anemometry, laser Doppler anemometry, laser Doppler velocimetry (LDV), particle image velocimetry (PIV), tomography, ultrasonic Doppler velocimetry, laser induced fluorescence, etc., as reviewed by Mavros [1]. The vast majority of these experimental works have been in cylindrical vessels (baffled and unbaffled) equipped with centered top-entering agitators [3–7,13,14]. Extensive measurements of the flow induced by Rushton turbines have been reported employing both single point techniques such as LDV [14–16] and global techniques such as PIV [3–7,13,17,18]. The flow induced by centered top-entering axial flow impellers has also been measured by various investigators, using LDV [19–21]; and PIV in cylindrical vessels [17] and in square tanks [22]. To our knowledge, no work has been reported in the open literature on the combined PIV and CFD study of flow fields in mixing

[1]Formerly Ford.

Contributed by the Fluids Engineering Division of ASME for publication in the JOURNAL OF FLUIDS ENGINEERING. Manuscript received July 23, 2009; final manuscript received March 23, 2010; published online May 6, 2010. Assoc. Editor: James A. Liburdy.

vessels with side-entering agitators. Given the wide application of this configuration for blending and sediment suspension in the chemical process industries, it is important to advance our knowledge and understanding on the flow and mixing in mechanically agitated vessels of this kind.

Particle image velocimetry was selected for the investigation presented here. PIV is one of the most advanced experimental methods available to visualize the main characteristics of a flow field, providing a nonintrusive measurement of the instantaneous planar velocity field over a global domain. As the name suggests, it records the position of small tracer particles over a defined time interval to extract the local fluid velocity. PIV requires four basic components: an optically transparent test section that contains the fluid seeded with small, fluorescent, flow-following particles, an illuminating light source (laser), a recording device (a charge-coupled device (CCD) camera), and a computer algorithm to process (cross-correlate) the recorded images. Due to the complexities associated with the highly three-dimensional flow in stirred tanks, additional care must be taken in the application of PIV techniques in these configurations.

The present work focuses on the application of CFD coupled with PIV to analyze the macroscale hydrodynamics in a laboratory-scale axially agitated rectangular tank. This mixer configuration (e.g., large rectangular or cylindrical tanks equipped with side-entering mixers) is used in various industries including pulp and paper, petroleum (for crude oil and gasoline storing), and foods industry (for blending fats and oils) [23]. The fluids encountered in these applications are generally highly viscous or non-Newtonian with complex rheology. The particular configuration of the system studied here was derived from the scale-down of industrial systems for agitation of paper pulp suspensions [24]. In order to mimic the mixing occurring at the industrial process scale in this laboratory system, the operating Re number must be kept below 137 when the laboratory vessel is filled with pulp fiber suspensions [24]. However, these suspensions, like most of the industrial fluids concerned in similar mixing applications, are opaque, so that PIV cannot be implemented and therefore transparent simulant fluids must be used in laboratory studies. In the present work, we investigate the global flow field of a viscous Newtonian fluid (98 wt % glycerin solution) in a laboratory-scale system of nonconventional, yet industrially relevant geometry. Since the shear thinning behavior of pulp fiber suspensions (i.e., reduced viscosity at higher shear rates) cannot be reproduced by the glycerin solution, we decided to investigate the system under slightly lower Re numbers (i.e., $\mathrm{Re} < 120$) and cover multiple conditions under a strictly laminar regime. Thus, this work establishes the basis of future studies on the effects of non-Newtonian behavior in these mixing systems.

2 Experimental Methods

2.1 Experimental Setup. Figure 1(*a*) shows a schematic of the experimental setup used. The system consists of a plexiglass model of a 1:18 scaled mixing chest with length $L=36.5$ cm, width $W=24.5$ cm, and height $H_{\mathrm{tank}}=40$ cm. The rectangular tank is equipped with a side-entering scaled version of the Maxflo Mark II impeller (Chemineer, Inc., Dayton, OH) used industrially for paper stock agitation (three bladed; $D=10.16$ cm; pitch ratio $=0.44$), driven by a 0.33 HP motor controlled by an inverter to enable digital control of the motor speed. The impeller is centered on the z direction (corresponding to the vessel width). The impeller clearance from the side wall was $E=7.5$ ($E/W=3.2$) and clearance from the bottom wall was 7.4 cm. A shaft-mounted rotary torque transducer (Staiger Mohilo 0260DM) was used to obtain accurate measurements of the torque (± 0.002 N m). The rotation speed was varied from 59 rpm to 386 rpm with a given speed maintained to ± 4 rpm during measurements. The flow conditions were characterized by the Reynolds number Re, which was computed using measured values of viscosity and density

$$\mathrm{Re} = \frac{\rho N D^2}{\mu} \tag{1}$$

The rectangular vessel was filled with 0.98 wt % glycerin solution ($\rho=1.256$ kg/m^3) to a height of $H=30.6$ cm and left to stand overnight to allow entrained air to escape. The solution's viscosity μ of 0.68 Pa s was measured immediately after the experiments at the exact same temperature registered for the fluid in the mixing vessel, 22 °C, using a stress controlled parallel-plate rheometer (Physica MCR 501).

The flow-map 2D PIV system from Dantec dynamics Inc. (Ramsey, NJ) was used to map the velocity profiles. It consists of a dual-head Nd:YAG (neodium-doped yttrium aluminum garnet) laser (New Wave Research: Model SoloIII-15 Hz) that emits 10-ns laser pulses with energies of up to 50 mJ/pulse. The collinear frequency doubled beam (1064 nm to 532 nm) is spread into a 2 mm thick sheet through a set of cylindrical lenses attached directly to the laser head. The particle images were recorded on a high-resolution progressive-scan interline CCD camera (Hamamatsu, model HiSense MkII) having a resolution of 1344 $\times$ 1024 pixels. A 514-nm line filter was used to minimize the detection of stray light on the cells of the CCD chip. The camera and laser were connected to a PIV hub with a programmable synchronizer that controlled the timing of the laser illumination and image acquisition. The hub is connected to a personal computer (PC) where the experimental sequence is defined and the resulting data stream is captured and analyzed asynchronously.

For the PIV experiments, the glycerin was seeded with ~ 50 μm polyamide 12 seeding particles (PSP, Dantec dynamics Inc.) of density $\rho_p=1.03$ g/cm^3. The seeding was added to smaller aliquots of glycerin (~ 50 ml) and then inserted below the free surface at a low rotational speed ($N=80-120$ rpm). The impeller speed was then increased to 1200–1500 rpm to provide a uniform distribution of the seeding particles in the fluid. Nearly all of the particles remained suspended and followed the flow field closely. A small amount of particles floating on the surface were removed using a size 400 sieve.

The velocity measurements taken were phase locked with respect to the position of the impeller in order to avoid the detection of the periodic fluctuations induced by the motion of the blades. The triggering device used for this purpose consists of an inductive proximity switch (Wenglor IB40) and a thin aluminum rod (of 1 mm diameter) mounted on the impeller shaft. Each time the piece of metal passed the sensor, the image acquisition was triggered. The aluminum rod was located at an angle $\alpha=0$ deg (aligned with the y axis) with respect to the proximity switch, and at $\alpha=90$ deg (aligned with the z axis); thus two different impeller positions were studied. The accuracy with which the impeller position could be determined with this device was estimated based on the instrument delay. The inductive sensor's delay is 740 μs, which corresponds to 0.3 deg of a full impeller rotation at the minimum rotational speed tested, $N=59$ rpm, and to 1.8 deg at the maximum one, $N=386$ rpm.

2.2 Experimental Procedures. To measure the flow profiles, a 2D slice of the flow field is illuminated using a pulsing laser light sheet (pulse duration is 5–10 ns) that freezes the position of the particles. A camera is used to record the particles' position in the illuminated plane over a short time interval (Δt between laser pulses). Thus, two images of the fluid flow are obtained with a known time interval between them. Comparison of the two images by means of cross-correlation techniques allows the determination of the corresponding velocity vector map in the plane of the laser sheet [25].

Two sequential images are subsampled using square regions called interrogation areas (IAs) that define the sampling resolution. Within these sampling areas, an average spatial shift of seeding particles may be observed from the first camera image to the next, provided there is flow in the illuminated plane. Common

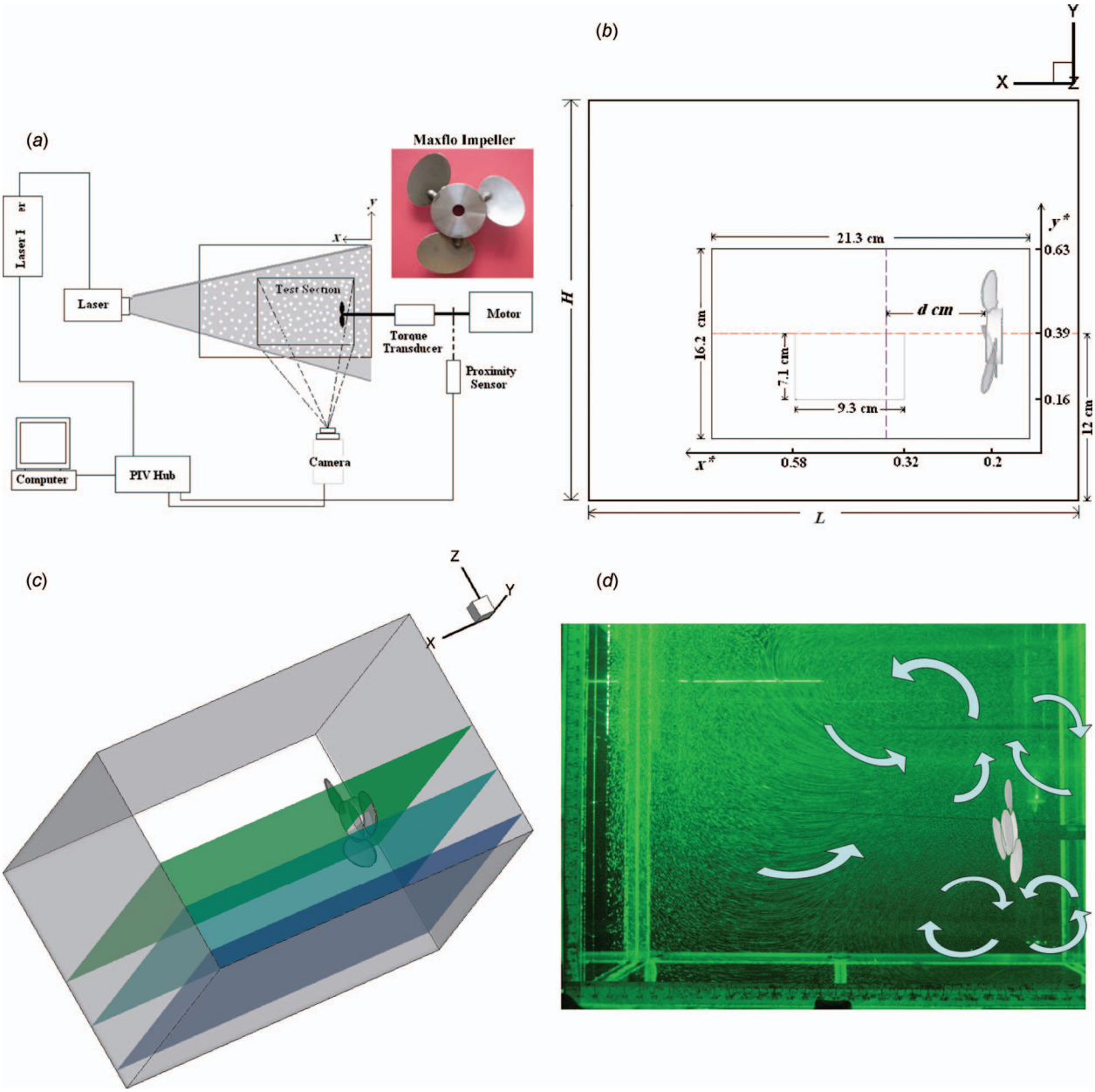

Fig. 1 (*a*) **Schematic of the experimental setup showing the front view of the mixing vessel, the PIV acquisition system, triggering device used, and photograph of the impeller (upper right corner). (*b*) Location and size of the measuring areas. The dashed lines illustrate the locations at which the velocity profiles were evaluated. The horizontal line is located at impeller height and the vertical line is located at a distance *d* cm (varied from 3 cm to 10 cm) in front of the impeller. (*c*) PIV illumination planes. (*d*) Schematic of the large-scale flow patterns over a photograph of the PIV illumination plane aligned with the impeller tip.**

particles need to exist in the IAs, which are then correlated by cross-correlation analysis using fast Fourier transform (FFT) techniques. A high cross-correlation peak is observed when many particles match up with their corresponding spatially shifted partners and small cross-correlation peaks are observed when individual particles match up with other particles entering or leaving the IA (either moving in the plane or crossing the plane), contributing to random correlations or noise. This analysis enables the calculation of the most probable particle displacement in each interrogation area. The technique is repeated at each IA thereby building the instantaneous velocity field.

A digital filter was applied to eliminate the dc component of the measurement (noise-floor) prior to the determination of the correlation peaks and subpixel interpolation. This filter removes the noise introduced by multiple particle reflections and background light. Additionally, a Gaussian window function was applied to the interrogation areas (i.e., the window width was 85% of the IA width) in order to suppress information from particles near the edges of the IA where phantom correlations are likely to dominate [26]. When window functions are used, it is recommended to increase the size of the IA [27]. Consequently, the size of the IA used was 32 pixels and a 25% overlap between adjacent IAs was applied to optimize the use of information in the image map.

An adaptive multipass cross-correlation technique was used for all velocity vector calculations in order to cover a larger area and still capture the flow details [28]. When this method is employed, the overlap of particles at small displacements is eliminated, and

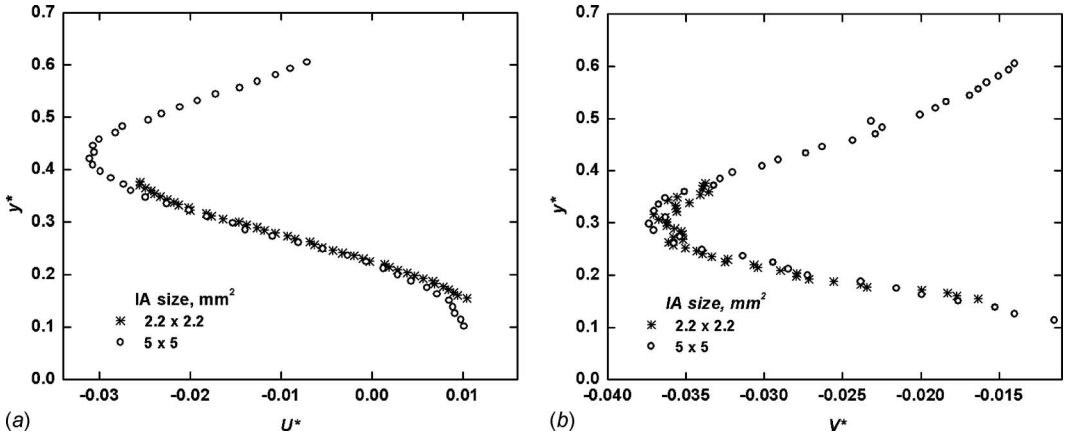

Fig. 2 Profile of the mean (*a*) axial and (*b*) vertical velocities at a line located at $x^*=0.37$; $d=6$ cm (see Fig. 1(*b*)) in the measurement plane aligned with the impeller tip ($z=-5.25$ cm), at $N=118$ rpm, Re=36

particle images that left the interrogation area during the time between the two light pulses (in-plane drop out) can be captured, thus increasing the dynamic range [25].

For each instantaneous measurement, the displacement vectors in the correlation plane for which the ratio of the signal peak to the noise peak was greater than 1.3 were rejected. No further filtering or validation was employed on the remaining valid vector map so as to truly capture any peculiarities of the flow. Only the valid vectors were accounted for in the statistical-averaging procedure.

Tests concerning the number of images or sample sets needed to get accurate time-averaged measurements were performed by taking a set of 1800 instantaneous measurement pairs at Re=36 and Re=120. Vector statistics of subsets of 1600, 1400, 1200, 1000, and 800 samples were compared against the full set of 1800 measurements. It was determined that a sample size of 1000 double-images produced a stable time-averaged result. Thereafter, all subsequent measurements were performed with 1000 measurements.

The accuracy of the velocity measurements depends on the seeding concentration, the time between laser pulses, the size of the PIV measurement area, and the spatial resolution. In order to determine the flow field in a large domain, the size of the measurement area should be as large as possible; however, the spatial resolution must be small enough so that essential velocity structures can be resolved and measured. Therefore, given our objective to investigate the global flow field in the mixing vessel, the largest possible image size that satisfied the PIV measurement criteria described by Adrian [29], Raffel et al. [25], and Dantec [27] was chosen. Accordingly, the conditions chosen to minimize error were given as follows.

- The particle seeding concentration was adjusted so that a minimum of six to ten particles per IA was attained, giving a high signal to noise ratio.
- The particle displacement was always kept below 25% of the length of the IA by selecting the appropriate time delays between laser flashes as a function of the local hydrodynamics and the parallax effects due to the through-plane motion of the particles.
- A slightly defocused camera coupled with the selected image and particle size (~ 50 μm) was used in order to obtain larger particle images (approximating two pixels in diameter)

2.2.1 Size of the PIV Measurement Area. The PIV measurement locations chosen are shown in Fig. 1(*b*). The size of the largest image in which the above mentioned criteria were fulfilled was 21.3×16.2 cm^2 (Fig. 1(*b*)). Three z planes (coordinate system or orientation is shown in Fig. 1(*c*)) were investigated: one plane located at the center of the impeller ($z=0$ cm), one plane aligned with the impeller tip (1.7 mm from the blade tip, $z=-5.25$ cm), and one plane located 2 cm away from the side wall ($z=-10.25$ cm) (these three planes are located ~ 5 cm from each

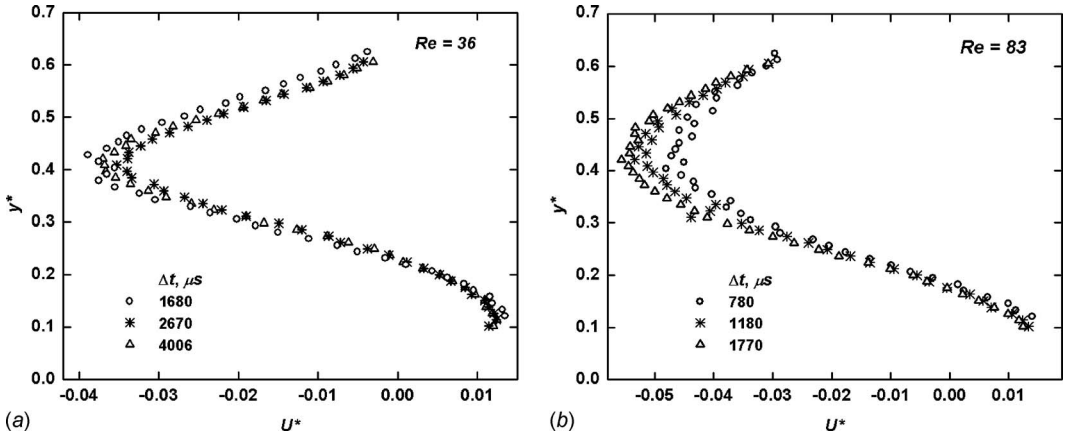

Fig. 3 Effect of Δt on the mean value of the axial velocity measured at a line located at $x^*=0.33$; $d=4.5$ cm (see Fig. 1(*b*)) in the measuring plane aligned with the impeller tip. (*a*) $N=118$ rpm, Re=36. (*b*) $N=267$ rpm, Re=83.

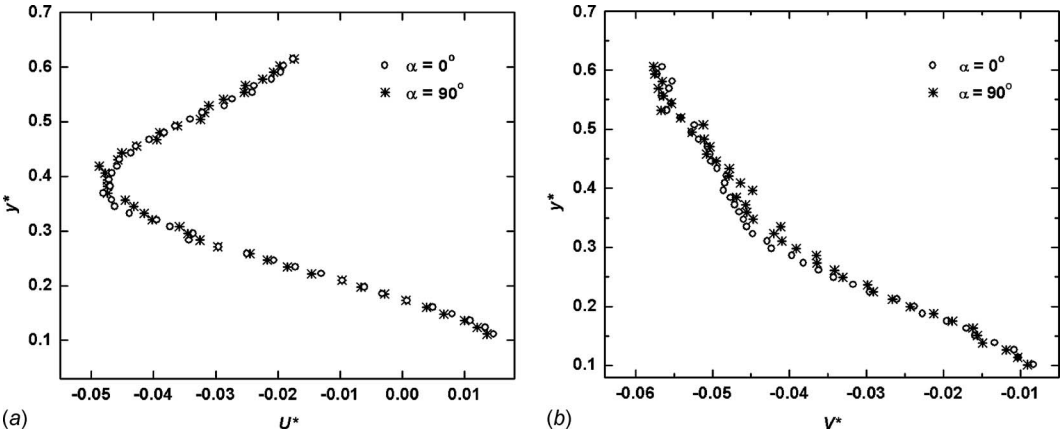

Fig. 4 Effect of the impeller angular position α (at two different angles 90 deg apart from each other) on the mean value of the axial velocity measured at a line located at $x^*=0.29$; $d=3$ cm (see Fig. 1(b)), in the measuring plane aligned with the impeller tip. $N=267$ rpm, Re=83.

other (Fig. 1(c))).

Tests with a smaller image size were performed to validate the accuracy of the global velocity measurements taken. Data were obtained with a measurement area of 9.3×7.1 cm^2 located 4.3 cm in front of the impeller and covering 7.1 cm on the negative y direction measuring from the impeller center as illustrated by the gray lines in Fig. 1(b).

The small measurement area examined is large when compared with experiments performed by Yoon et al. [7] to characterize the flow in the immediate vicinity of a Rushton turbine, but it is comparable in size to the PIV areas used in many other studies [3,6,13,17,30–32]. The large PIV measurement area covers about 60% of the tank length and 53% of the liquid height, and it is comparable to the large image PIV experiments done by Bugay et al. [17] and the standard image size used by Collignon et al. [33].

For both cases, the measuring area was divided into interrogation areas of 32×32 pixels. The size of these IAs was 5×5 mm^2 and 2.2×2.2 mm^2 for the large and the small sampling regions, respectively. The results obtained from these two experiments are compared using the profiles of the two components of the mean velocity vector. The axial and vertical velocities and the axial and vertical positions are nondimensionalized as follows:

$$U^* = \frac{U}{U_{\text{tip}}}, \quad V^* = \frac{V}{U_{\text{tip}}}, \quad x^* = \frac{x}{L}, \quad y^* = \frac{y}{H} \tag{2}$$

The vertical profiles of the axial velocity U^* and the vertical velocity V^* at Re=36 are plotted at $x^*=0.16$ ($d=6$ cm in Fig. 1(b)) in Figs. 2(a) and 2(b).

2.2.2 Time Interval Between Laser Pulses. One of the main difficulties in providing adequate velocity measurements in a large domain, like the one chosen here, lies in selection of the time interval between laser pulses (Δt) because of in-plane and out-of-plane velocity values possible in this particular configuration. For instance, the fluid velocities are much higher near the impeller but the magnitude of the velocity diminishes rapidly with most of the flow captured in the large PIV image moving at a very low velocity. Since Δt depends on the local velocities in the system, a compromise must be reached in order to enhance the number of valid velocity vectors within the image. Thus, some accuracy in the measurements may be lost both in the immediate vicinity of the impeller and far away from it.

A reliable way to capture the maximum possible number of particle pairs is to define the particle displacement as one-quarter of the IA side, L_{IA} [25,27]. The separation Δt is then given as a function of the object to image scale factor (S), L_{IA}, and the maximum velocity within the system, the impeller tip speed (U_{tip}), as follows:

$$\Delta t = \frac{0.25 L_{\text{IA}} S}{U_{\text{tip}}} \tag{3}$$

However, the through-plane movement of particles affects the accuracy of the in-plane measurements. Thus, Δt and the laser sheet thickness (z_ℓ) must be chosen in relation to the velocity perpendicular to the measurement plane (U_z), so that the following relationship is also satisfied [27]:

$$\frac{U_z \Delta t}{z_\ell} \leq 0.25 \tag{4}$$

In the immediate vicinity of the impeller, U_z also reaches the maximum velocity value given by U_{tip} at specific angles of rotation determined by the blade pitch angle. At this location, Δt given by Eq. (4) is 40% of the Δt value from Eq. (3). Considering the high viscosity of the working fluid and that a significant portion of the domain covered in the PIV measuring area is away from the impeller, the upper limit of the velocity range given by U_{tip} can be relaxed to allow for a larger Δt thus increasing the dynamic range of the measurements [29].

Previous PIV measurements with Rushton turbines in the laminar regime (Re=80) have shown that the fluid velocities reach 52% of the tip speed in the vicinity of the impeller [8]. Other PIV and LDV measurements with top-entering axial impellers in turbulent regimes [17,34] have shown that the actual fluid velocities reach 30% of the tip speed at about 5 mm below the impeller. We investigated the sensitivity of the measurements with respect to Δt by substituting $U_z=0.5U_{\text{tip}}$, $U_z=0.3U_{\text{tip}}$, and $U_z=0.2U_{\text{tip}}$ in Eq. (4). Three different Δt values were tested. For example, at Re=36, Δt values of $\Delta t_1=1680$ μs, $\Delta t_2=2670$ μs, and $\Delta t_3=4006$ μs were applied. Similarly, at Re=83, the Δt values used were $\Delta t_1=780$ μs, $\Delta t_2=1180$ μs, and $\Delta t_3=1770$ μs.

Figure 3 shows the vertical profiles of axial velocity measured at a line located at $x^*=0.33$ ($d=4.5$ cm in Fig. 1(b)) using the three different Δt values for Re=36 and 83. The major differences between measurements are found around the impeller, which is located at $y^*=0.39$. The variation between measurements was quantified in terms of the root-mean-square (rms) deviation

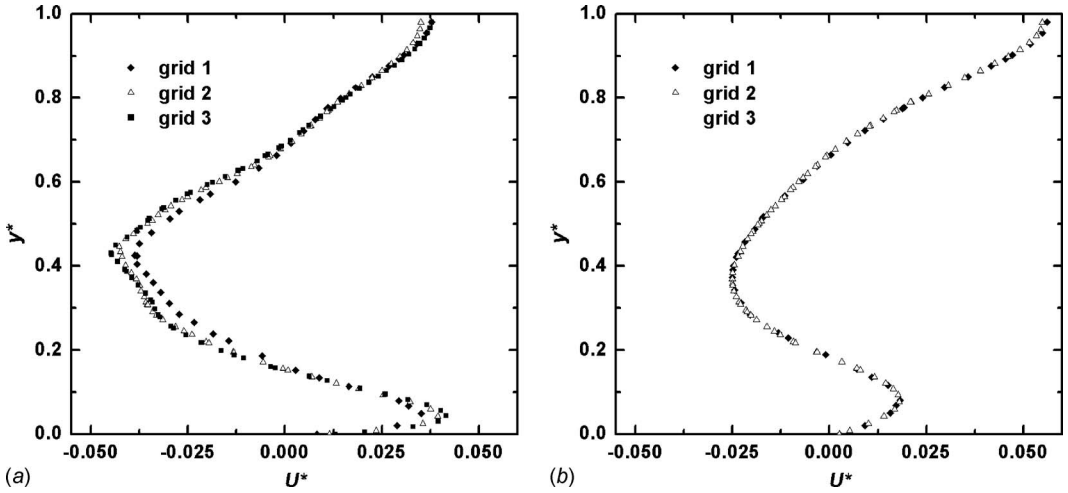

Fig. 5 Computed vertical profiles of axial velocity in a plane aligned with the blade tip (*a*) for a vertical line at $x^*=0.29$; $d=3$ cm (see Fig. 1(*b*)) and (*b*) for a vertical line at $x^*=0.48$; $d=10$ cm (see Fig. 1(*b*)). $N=327$ rpm, Re=101.

$$\text{rms} = \frac{\left[\frac{1}{N}\sum_{i=1}^{i=N}(u_{\Delta t1}-u_{\Delta t2})^2\right]^{1/2}}{\left[\frac{1}{N}\sum_{i=1}^{i=N}(u_{\Delta t2})^2\right]^{1/2}} \tag{5}$$

The deviation between measurements decreased as Δt increased. For instance, the rms deviations between the measurements made with Δt_1 and Δt_2 were 17% for Re=36 and 11.6% for Re=83. This rms deviation value decreased to 6.7% for both Re numbers when the measurements taken with Δt_2 were compared with Δt_3. Therefore, all the subsequent measurements were taken using Δt calculated from Eq. (4) with $U_z=0.3U_{\text{tip}}$ at the measurement planes near the impeller, and $U_z=0.2U_{\text{tip}}$ at the measurement plane near the wall.

2.2.3 Phase Averaging. The PIV data collected at two different impeller positions $\alpha=0$ deg and $\alpha=90$ deg were compared to determine whether the periodic fluctuations induced by the motion of the blades were significant. A location close to the impeller blade tip was chosen for the comparison of the velocity measurements. Figure 4 compares the mean values of the axial and vertical velocities, measured at the two different angles, at a line located at $x^*=0.29$ ($d=3$ cm in Fig. 1(*b*)) in a plane aligned with the impeller tip. The velocity profiles are very close to each other. The rms deviations between these two measurements were 3.8% for V^* and 4.1% for U^*. Hence, it was confirmed that phase averaging was not essential for macroscale velocity measurements of the flow induced by the Maxflo impeller used here, as suggested by Bugay et al. [17] and Weetman and Oldshue [35] for shaped, axial impellers.

Measurement reproducibility was verified by repeating the full measurement set of 1000 instantaneous velocity fields three times and comparing the mean value of the axial and vertical velocities by computing the rms deviation. Since a 25% overlap was used, the measuring plane contained 2310 vectors, and the average rms deviations calculated between identical experiments were 6.0% for U^* and 4.5% for V^*.

3 Computational Techniques

The numerical simulations of the flow field in the rectangular mixing vessel were performed using FLUENT 6.3 (Lebanon, NH). Aside from the impeller shaft and the small mounting supports of the impeller hub into the shaft, the computational model of the system represents the entire mixer geometry exactly. Re from 18 to 120 were simulated by changing the agitation rate accordingly (using the measured viscosity $\mu=0.68$ Pa s and density $\rho=1.256$ kg/m^3).

The geometry was decomposed into four blocks to allow for a more efficient hybrid mesh (generated in GAMBIT 2.4): one cylindrical volume containing the impeller, two semirectangular volumes above and below the cylinder, and one rectangular volume connected to the common left side of these three volumes. An unstructured grid of tetrahedral and prism elements, growing in size from the impeller outwards, was created within the cylindrical volume. The remaining blocks were meshed using a structured grid of hexahedral elements, with controlled size near vessel walls and surfaces around the cylindrical block, which permitted a significant reduction in the number of computational cells.

After discretization of the computational domain, the mass and momentum conservation equations for an incompressible fluid were solved. The system featured a large unbaffled vessel where interactions between the rotor (i.e., impeller) and the stator (i.e., tank walls) are weak. In such configuration, the relative orientation of the impeller blades does not have a major influence on the mean flow field as demonstrated by the PIV measurements taken at two different impeller positions shown in Fig. 4; therefore, the steady-state, multiple reference frame (MRF) approach was appropriate to model the impeller (rotating) regions [36]. Using this solution method, start-up or periodic transient flow details cannot be resolved, but calculation times and CPU expense are signifi-

Table 1 Calculations of discretization error using the GCI method

	ϕ=axial velocity at $x^*=0.08$, $y^*=0.4$	ϕ=axial velocity at $x^*=0.28$, $y^*=0.4$
r_{12}	1.65	1.65
r_{23}	1.36	1.36
p	2.5	2.3
$e_a^{23}=\left\lvert\frac{\phi_3-\phi_2}{\phi_3}\right\rvert$	2.6%	1.9%
$e_{\text{ext}}^{23}=\left\lvert\frac{\phi_{\text{ext}}^{23}-\phi_1}{\phi_{\text{ext}}^{23}}\right\rvert$	2.2%	1.9%
$\text{GCI}_{\text{fine}}^{23}=\frac{1.25e_a^{23}}{r_{23}^{p}-1}$	2.9%	2.3%

cantly reduced over those needed to provide a fully unsteady solution using a sliding mesh method. The rotating frame was defined by the cylindrical volume containing the impeller. In this region (i.e., the moving reference frame subdomain) the impeller is at rest and the momentum equation includes two additional acceleration terms: the Coriolis and the centripetal acceleration. The remaining volumes were stationary. In the solution process, the continuity of the absolute velocity is enforced at the boundaries between subdomains. A no-slip condition was set at all solid/liquid interfaces. The free surface remained flat during the experiments in the range of Re investigated, so a free-slip condition was used on the upper surface of the vessel.

The conservation equations were solved in the laminar regime using a second order upwind scheme for the convection terms. The SIMPLE pressure-velocity coupling method was used with the velocity gradients evaluated using the Green–Gauss theorem and a node-based averaging scheme to compute the velocity values at the center of the cell's faces. The convergence of the axial velocity at three different point locations in the domain (one near the impeller, one halfway to the wall opposite to the impeller, and one far away from the impeller) was continuously monitored during the computations. Iterations were continued until the change in the scaled residuals (i.e., representative of the error in the solution of the equations) for the three velocity components and the pressure fell below 1×10^{-5}. At this point, the axial velocities monitored were examined to ensure that they had reached a steady value. If this was not the case, the iterations were continued until these velocities settled. The time needed to reach a converged solution in a single PC (Intel Core 2 CPU at 2.66 GHz and 4 Gbytes of RAM) varied from 4 h at low Re to 8–10 h at the highest Re.

An initial mesh (grid 1) of 133,767 volumes, with individual cells ranging from 1.33×10^{-10} m^3 to 1.41×10^{-6} m^3, was constructed with higher mesh density near the impeller and vessel walls. The representative average cell size of grid 1, h_1, was $h_1=5.89\times10^{-3}$ m. This mesh was refined systematically in a stepwise fashion. The next finer mesh (grid 2) had 346,134 volumes, $h_2=4.29\times10^{-3}$ m, and a global refinement factor, $r_{12}=h_1/h_2$, of 1.37. The finest mesh (grid 3) was comprised of 735,121 volumes, with individual cells ranging from 3.5×10^{-11} m^3 to 3.03×10^{-7} m^3 and $h_3=3.33\times10^{-3}$ m. The global grid refinement factor r_{23} was 1.29. Figure 5 shows the computed vertical profile of axial velocity in a plane aligned with the impeller tip ($z=5$ cm), at $x^*=0.29$ and $x^*=0.48$ ($d=3$ cm and $d=10$ cm in Fig. 1(*b*)) for all grids.

In order to provide an estimation of the discretization error, the grid convergence index (GCI) method described by Celik et al. [37] was implemented. The method was applied for the axial velocity at two points within the profiles shown in Fig. 5, located near the impeller center ($y^*=0.4$) where the main differences are observed between coarse and fine grid solutions. The solution in the finest grid (grid 3) was selected for evaluation against the PIV measurements; thus we present the error estimates on this grid. Since the method was applied in nonuniform grids and for field variables, the local cell size was used in the GCI calculations. The calculated local order of accuracy (p) along with the approximate relative error (ea^{23}) and extrapolated error (e_{ext}^{23}) are summarized in Table 1. The numerical uncertainty in the fine grid solution for the axial velocities near the impeller, given by the fine grid converge index ($\text{GCI}_{\text{fine}}^{23}$), was found to be 2.9% 3 cm away from the impeller and 2.3% 10 cm away from the impeller.

4 Results and Discussion

Instantaneous velocity fields obtained from single measurements were averaged over a large number of events to determine statistical values significant to the global flow phenomena prevailing in the system. Hence, the mean "time-averaged" velocity field taken over 1000 measurements was used to reveal the prevailing macroscale flow structures inside the mixing vessel. Figure 6 gives the averaged velocity fields at the three different measurement planes (shown in Fig. 1(*c*)) for Re=101. It should be noted

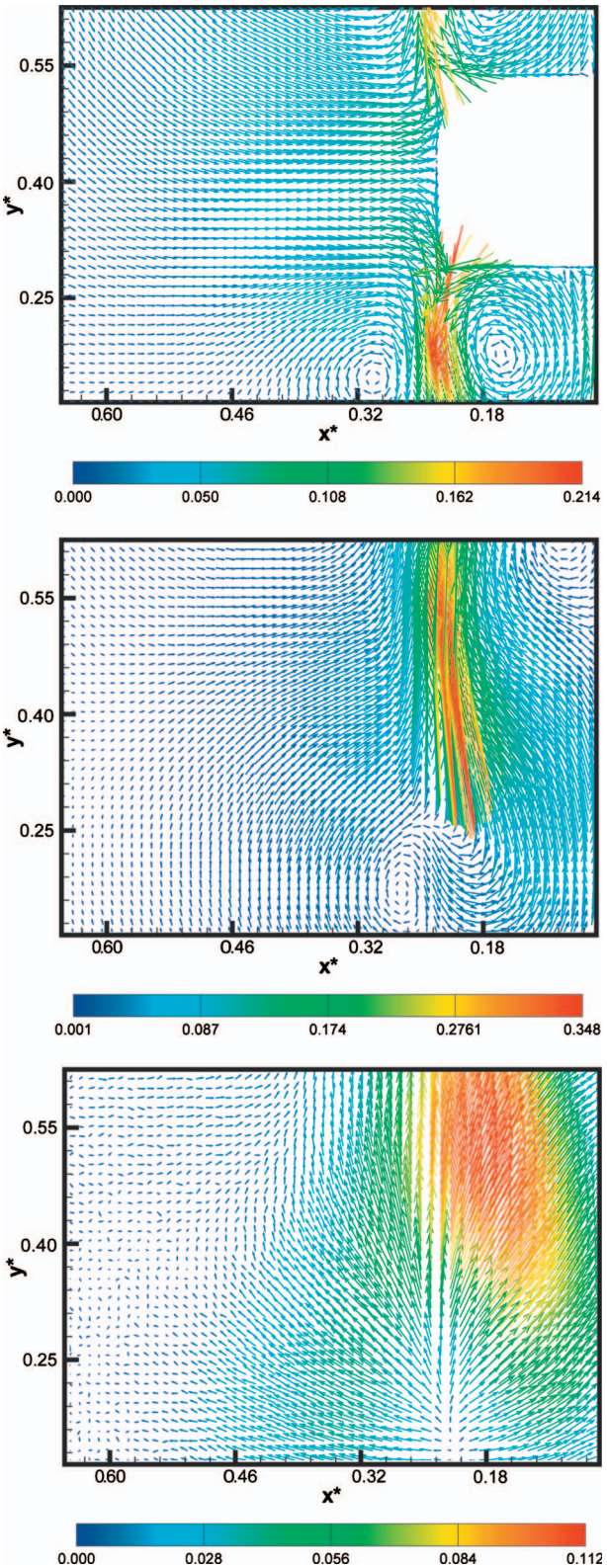

Fig. 6 Mean planar velocity fields for Re=101 in the three vertical planes of measurement: (*a*) midplane ($z=0$ cm); (*b*) plane aligned with the impeller tip ($z=-5.25$ cm) and (*c*) plane located 2 cm away from the vessel wall ($z=-10.25$ cm). Velocity vectors colored by velocity magnitude (m/s).

that measurements at the midplane exclude a portion of the image (impeller region and the area behind it) because the impeller blocks the path of the laser sheet (Fig. 6(*a*)). The length of the vectors and color coding is based on the planar velocity magnitude normalized with respect to the tip speed.

The velocity fields measured at the midplane (Fig. 6(*a*)) show four recirculation loops, two of them below the impeller region, which are created by the impingement of one of the jets, generated by the impeller, on the bottom of the vessel. The other two loops are located above the impeller, and they form as a result of the upward jet flow generated at the tip of the impeller blades at this location. The size and location of this measuring plane (Fig. 6(*a*)) limit the visibility of the upper loops, and only their bottom half can be appreciated. These main recirculation patterns evidence the axial flow structure generated by the Maxflo Mark II impeller.

For all the PIV planes studied, the velocities measured are only a fraction of the impeller tip speed (planar velocity magnitudes were below 35% of U_{tip}) due in part to the significant resistance to flow of the glycerin solution (i.e., high viscosity). The highest planar velocity magnitudes measured are located in the plane aligned with the blade tip, but this magnitude diminishes quickly away from the impeller. At this plane (Fig. 6(*b*)), the jet generated by the impeller moving upwards toward the free surface is seen. The position and shape of the recirculation loops previously iden-

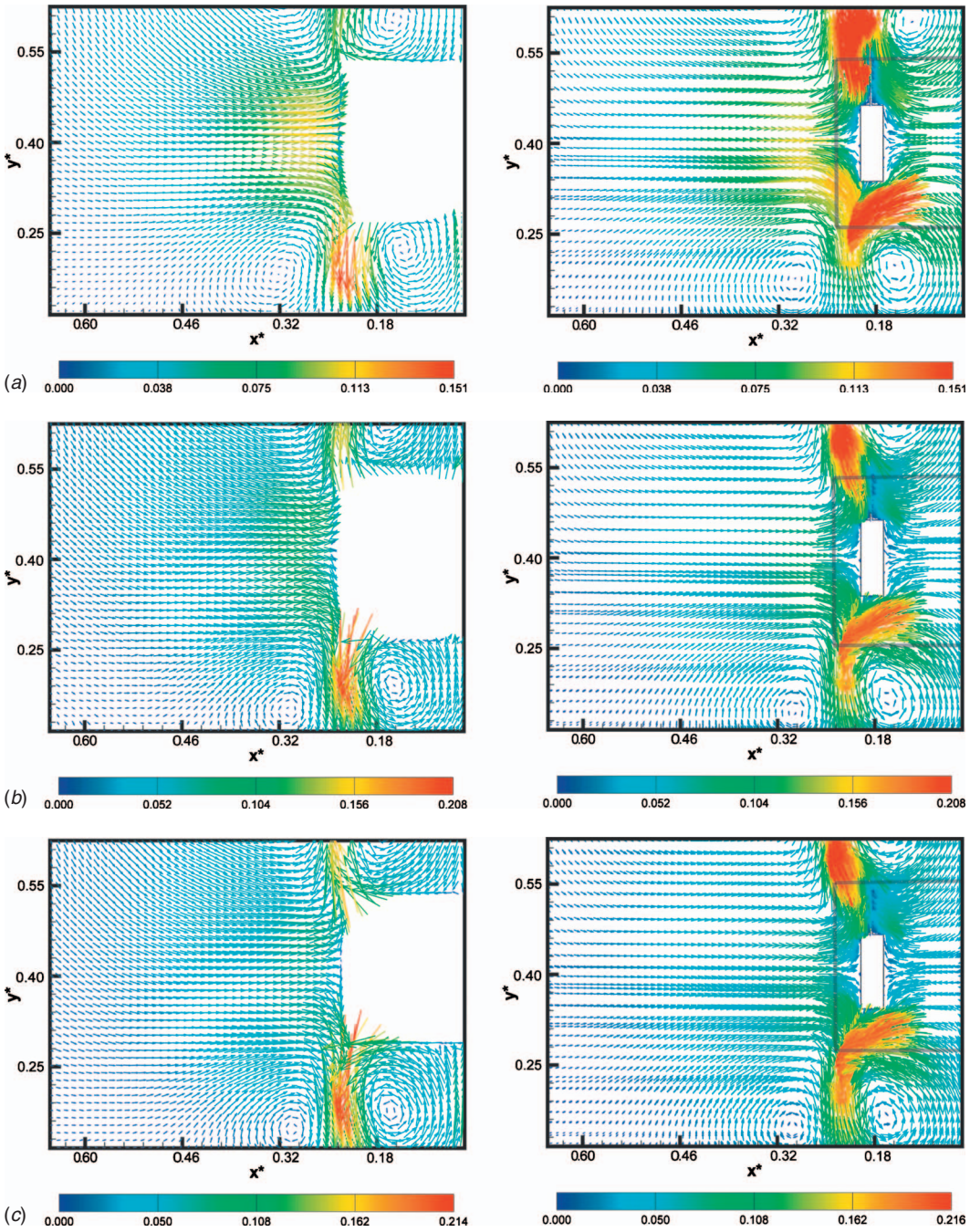

Fig. 7 Experimental (left) and CFD (right) planar velocity fields in the center plane of measurement for (*a*) Re=36, (*b*) Re=82, and (*c*) Re=101. Velocity vectors colored by velocity magnitude (m/s).

tified in the midplane measurements changed significantly from one plane to another, confirming the three-dimensional nature of the flow field.

The planar velocity field at the measurement plane located 2 cm away from the side wall (Fig. 6(*c*)) shows the evolution of the flow near the wall boundaries. The centrifugal force generated by the tangential flow of the fluid following the rotating impeller creates radial flow toward the vessel walls. Measurements at this plane show how this secondary flow becomes axial, especially near the bottom wall of the vessel, and then turns vertically inward near the impeller wall. The bifurcation of the flow captured at the lower end of the image ($x^*=0.22$ and $y^*<0.25$) at the impeller axial location provides an indication of the boundary between the two major recirculation loops below the impeller. The planar velocity magnitudes are much lower in this plane compared with the other two planes examined, and no vortices can be identified at this location.

Figure 7 compares the planar velocity vectors measured at the center plane ($z=0$ cm) for Re=36, 82, and 101 with those obtained using CFD results calculated with the fine grid. The two-dimensional CFD velocity fields on the right side of Fig. 7 were created using the axial and vertical components of the computed velocity vectors. These values were then used to calculate the planar velocity magnitude. No interpolation was applied, so the vectors and the spacing between them were determined by the mesh spacing in the CFD simulations. Note that details in the immediate vicinity of the impeller are excluded from the PIV measurements so that comparison is based on the bulk flow patterns at common areas between the two velocity fields. Also, the relative position of the impeller blades in the CFD simulations is not exactly the same as the one in the PIV images. For instance, in the computational model of the system, the relative impeller position is such that the midplane ($z=0$ cm) intersects the impeller blade above the hub, whereas in the PIV images the same plane intersects the blade below the hub. This, however, does not prevent the analysis and comparison between them, as it has been already demonstrated that phase averaging is not essential.

A number of observations can be made using these 2D-velocity fields. For all Re studied, both computational and experimental results show four recirculation loops, two above and two below the impeller (Fig. 7). The stagnation flow on the upstream faces of the blades leading to vortex flow on the downstream faces of the impeller blades can be easily appreciated from the CFD velocity fields. Very good agreement is obtained for the locations of the centers of these recirculation regions and the distribution of the planar velocity magnitude along the measurement plane. The distance between the recirculation centers and the blades decreased with Re. This trend was captured by both modeling and experi-

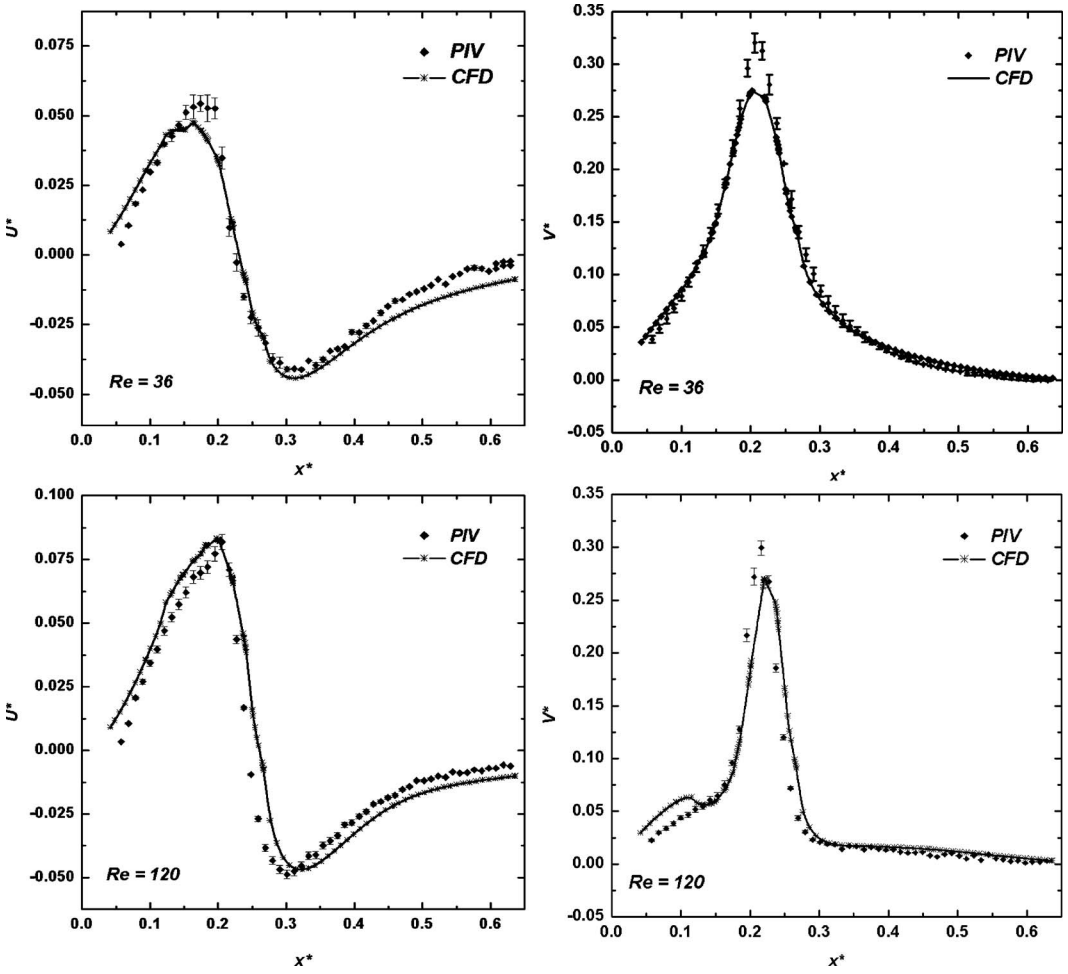

Fig. 8 CFD and PIV results for horizontal profiles of normalized axial and vertical velocity components for a horizontal line located at the impeller center (see Fig. 1(*b*)), and covering the full length of the PIV image, in a plane aligned with the blade tip ($z=-5.25$ cm). Results are shown for $N=386$ rpm, Re=120 and $N=118$ rpm, Re=36. The error bars indicate the standard deviation for a series of three measurements.

ments. The enhanced strength of the recirculation loops at higher Re was also confirmed in the measured and in the computed planar flow patterns.

The experimental and computational velocity fields can be quantitatively compared by plotting the profiles of the velocity components along sample lines (see dashed lines in Fig. 1(*b*)). Figure 8 shows the axial and vertical velocity profiles on the measurement plane aligned with the blade tip ($z=-5.25$ cm), along a horizontal line located at the impeller center, extending from $x^*=0.05$ to $x^*=0.63$ (the domain length of the PIV image). The velocity measurements show good repeatability and the associated *error bars* indicate the standard deviation for a series of three separate measurements. The CFD results show very good agreement with the experimental measurements. The local maximum and minimum normalized velocities are very similar to the measured ones. As Re increases, the maximum axial velocity increases from about 5% of the tip speed at Re=36 to 8.2% of the tip speed at Re=120. The computed local maximum for the vertical velocity is slightly lower than the measured one. A second local maximum for the vertical velocity at Re=120 was computed in the CFD simulations, but not captured by the PIV measurements. This is likely due to the limited resolution of the PIV measurements in the vicinity of the impeller, where the velocity gradients are higher [38]. In fact, the same interrogation area size (5×5 mm^2) was used in the entire image for the PIV measurements, whereas an increased mesh resolution was used in the vicinity of the impeller for the CFD simulations, with control volumes of characteristic length as low as 0.3 mm.

The evolution of the planar velocity along the length of the vessel can be examined by plotting the axial and vertical velocity profiles along vertical lines positioned at different axial distances from the impeller (i.e., varying d in Fig. 1(*b*)). Flow structures in the impeller region cannot be resolved accurately because they are smaller than the IA length. The CFD results computed using a laminar viscous model are unable to capture velocity fluctuations near the impeller due to eddies formed as a result of turbulence. Thus comparisons between PIV and CFD are made at locations where the PIV and the CFD model resolutions are both adequate.

Figure 9 shows the measured and computed vertical profiles of the axial and vertical velocities in the measurement plane aligned with the blade tip, at a line located at $x^*=0.34$ ($d=5$ cm in Fig. 1(*b*)) for Re=36 and 82. The horizontal axis represents the vertical distance along the line and the vertical axis represents the normalized velocity components. In all the cases, very good agreement is attained between the computed and measured velocities. The calculated rms deviations (measured versus computed) were 13.8% for U^* and 15% for V^* at Re=36, and 15% for U^* and 10.9% for V^* at Re=82.

In the same way, the vertical velocity profiles of the two velocity components at a line located at $x^*=0.48$ ($d=10$ cm in Fig. 1(*b*)) were examined and are shown in Fig. 10. Once again, very good agreement exists between experimental and numerical re-

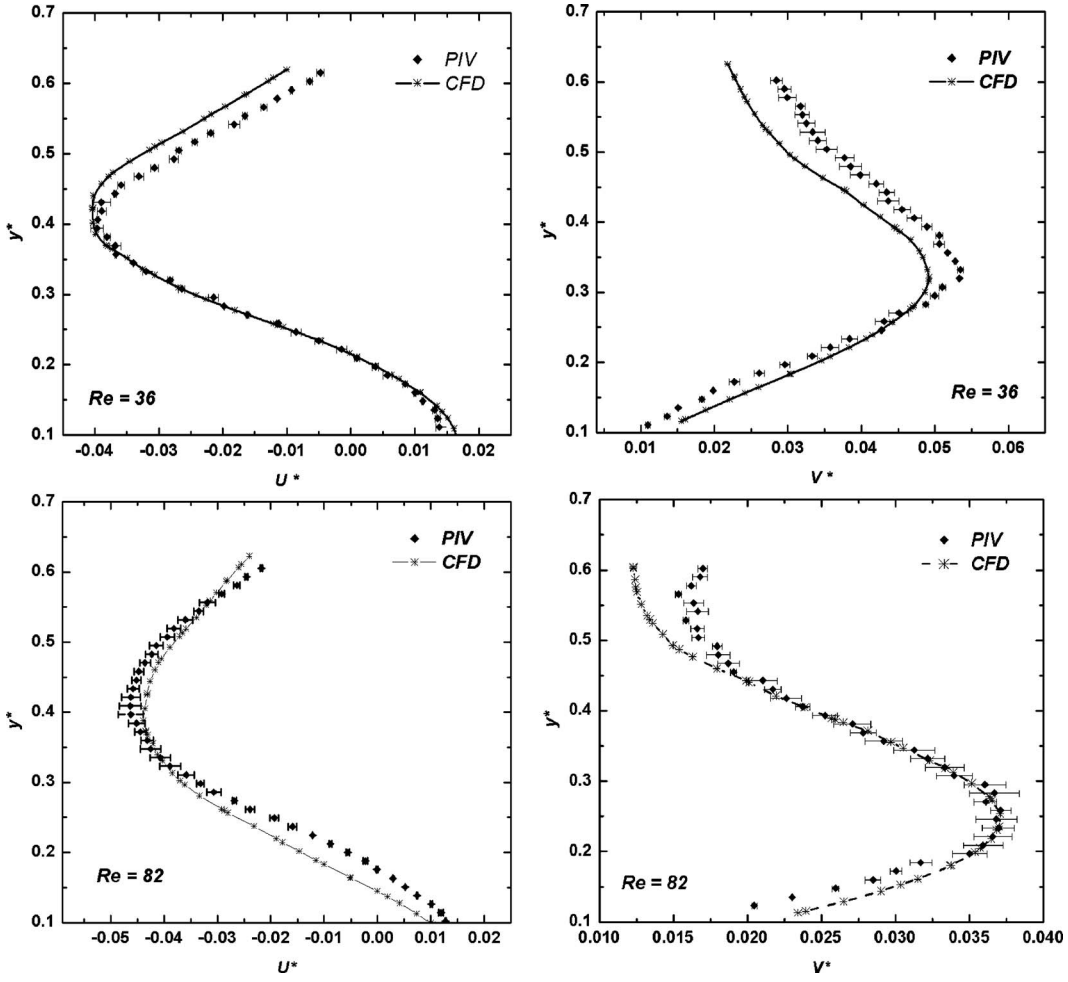

Fig. 9 CFD and PIV results for vertical profiles of normalized axial and vertical velocity components for a vertical line at $x^*=0.34$; $d=5$ cm (see Fig. 1(*b*)), spanning the PIV image height, in a plane aligned with the blade tip ($z=-5.25$ cm). Results are shown for $N=118$ rpm, Re=36 and $N=267$ rpm, Re=82. The error bars indicate the standard deviation for a series of three measurements.

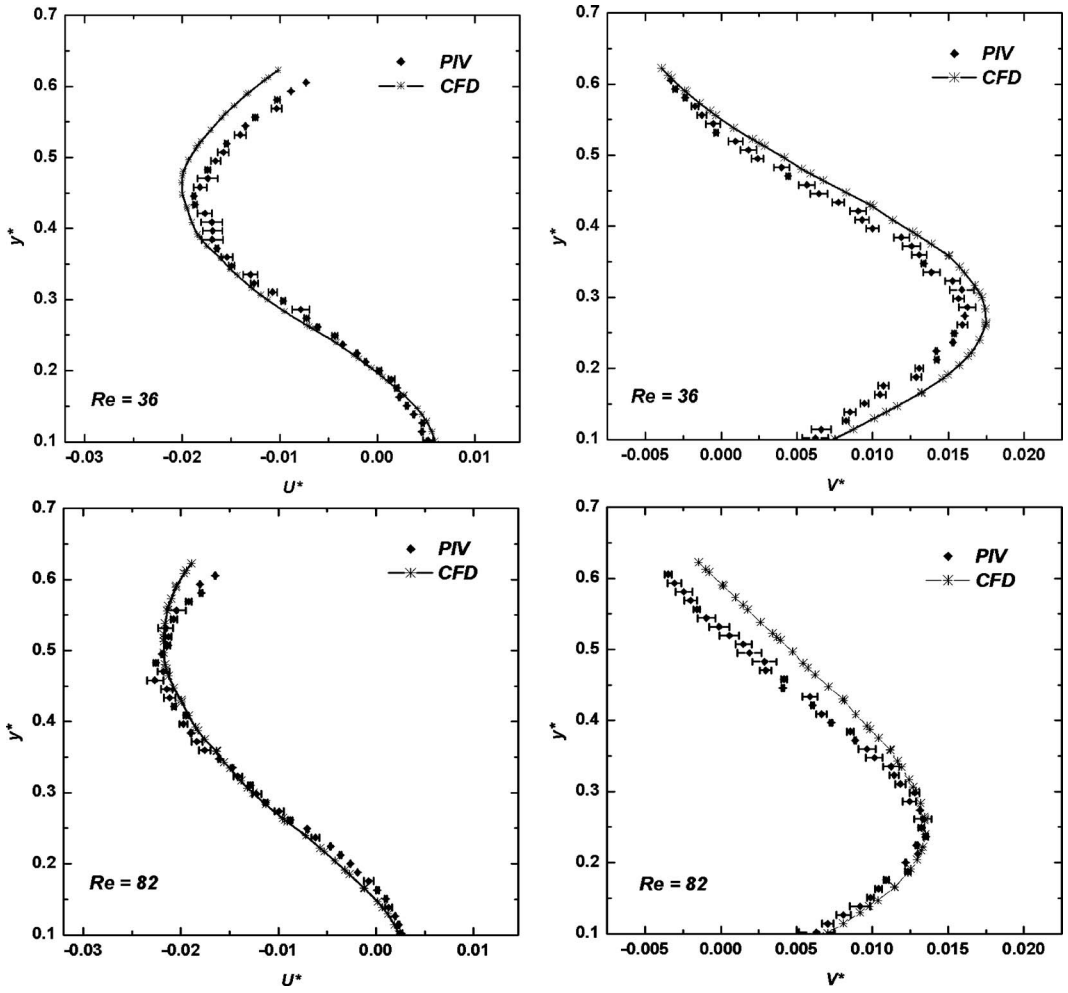

Fig. 10 CFD and PIV results for vertical profiles of normalized axial and vertical velocity components for a vertical line at $x^*=0.48$; $d=10$ cm (see Fig. 1(*b*)), spanning the PIV image height, in a plane aligned with the blade tip ($z=-5.25$ cm). Results are shown for $N=118$ rpm, Re=36 and $N=267$ rpm, Re=82. The error bars indicate the standard deviation for a series of three measurements.

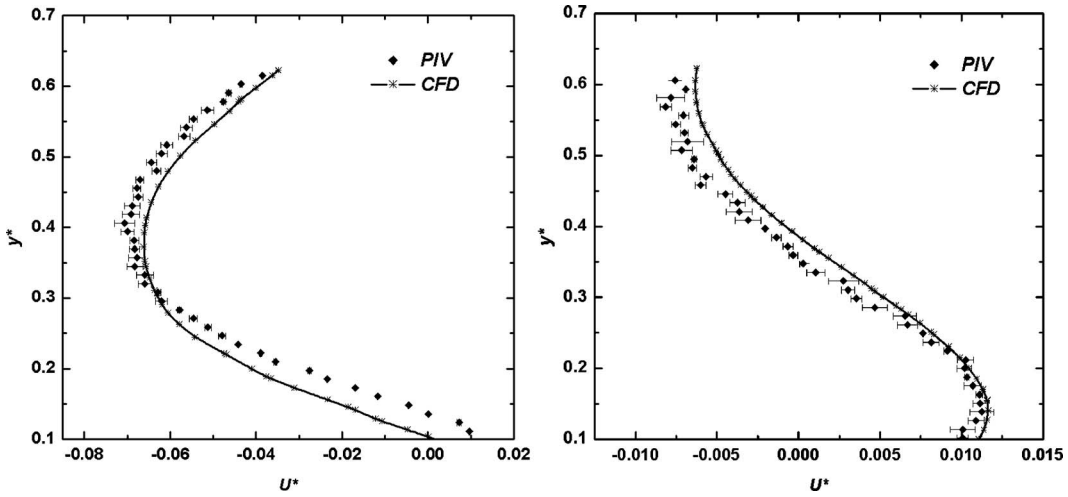

Fig. 11 CFD and PIV results for vertical profiles of normalized axial and vertical velocity components at Re=82; (*a*) for line at $x^*=0.34$; $d=5$ cm (see Fig. 1(*b*)) in the midplane of measurement ($z=0$ cm), and (*b*) for line at $x^*=0.48$; $d=10$ cm (see Fig. 1(*b*)) in the measurement plane located 2 cm away from the vessel wall ($z=-10.25$ cm). The error bars indicate the standard deviation for a series of three measurements.

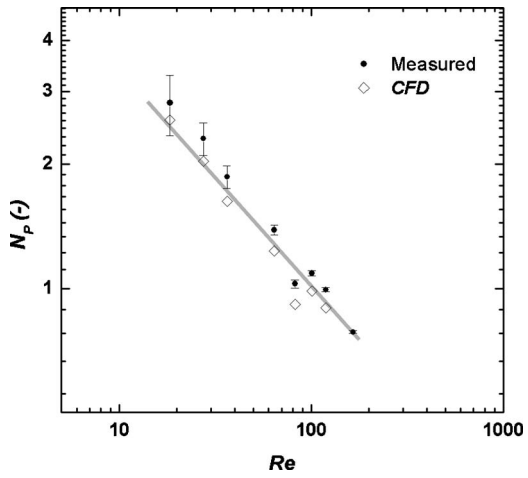

Fig. 12 Comparison of N_P versus Re for experimental and computational tests. The error bars are based on the accuracy with which the torque was measured (±0.002 N m).

sults. The calculated rms deviations were 12.4% for U^* and 16% for V^* at Re=36, and 7.2% for U^* and 20.1% for V^* at Re=82. The differences rendering this high rms deviation for V^* at Re =82 were found above the impeller ($y^* \geq 0.39$), suggesting that at this Re the deformation of the free surface (not considered in CFD) has some influence on the flow. No changes were observed on the surface during the experiments; hence the assumption of a flat upper surface was justified. Nevertheless, it is likely that a weak interaction with the surface exists, which cannot be easily observed (i.e., the free surface may rise a few millimeters).

Similar comparisons between experimental and numerical results were made at the other two measuring planes and are shown in Fig. 11 for Re=82. The calculated rms deviations were 13% for U^* at $x^*=0.34$ ($d=5$ cm in Fig. 1(b)) at the midplane of measurement and 17.2% for U^* at $x^*=0.48$ ($d=10$ in Fig. 1(b)) at the plane of measurement located 2 cm away from the vessel wall.

Global parameters such as the power number (N_P) are conventionally used to characterize the mixing process. To complement the CFD evaluation procedure, the torque was measured and computed as the axial moment on the impeller center at each Re. The power draw and N_P were then calculated and plotted against Re. Figure 12 shows a comparison of the N_P versus Re curves. The agreement between these curves is very good over the entire range of Re, with N_P being underpredicted by an average of 11%. The linear decay of N_P with increasing Re confirms the laminar flow assumption implemented in the CFD model.

5 Summary and Conclusions

The flow in a rectangular agitated vessel equipped with a side-entering axial impeller was investigated numerically and experimentally under laminar flow ($20 \leq \mathrm{Re} \leq 120$). This configuration and operating conditions were derived from scale-down of industrial mixing systems for agitation and blending of pulp fiber suspensions. By simultaneously applying CFD modeling and PIV measurements we were able to develop and validate an efficient model for the system and further demonstrate the adequacy of CFD as a valuable tool for optimization and design of mixing equipment. Experiments were conducted using PIV to characterize the flow field from time-averaged 2D-velocity maps at three different locations relative to the impeller. The PIV measurement parameters were tuned for optimum capture of the velocity fields in a representative portion of the vessel. The planar velocity fields revealed characteristic flow structures underlying the global recirculation flow patterns occurring in the vessel. The system was modeled using CFD software (FLUENT), and the PIV measurements were used to evaluate the model predictions. Special attention was directed toward building efficient and size controlled mesh structures, enabling fast and reliable computations that could be performed in one single conventional PC. The CFD predicted velocity vectors at the measurement planes agreed very well with the PIV data for global flow patterns and planar velocity magnitude. The predicted velocity profiles were examined at different positions within the measurement planes for various agitation rates in order to present an extensive evaluation of the CFD model. The experimental and computational results showed very good agreement in all cases. The N_P versus Re curve for the system was constructed from torque and rotational speed measurements and compared with the computational predictions resulting in a very adequate agreement. The accurate definition of the fluid's viscosity in the CFD simulations was crucial to reach satisfactory results. The overall results from this study indicate that the MRF steady-state approach used in CFD can effectively be used to model the mixing occurring on systems of this configuration, which is relevant in various manufacturing processes including pulp and paper, petroleum, and food industries.

Nomenclature

D = impeller diameter, cm
E = impeller clearance from the side wall, cm
L = mixing vessel length, cm
$\mathrm{GCI}_{\mathrm{fine}}^{23}$ = fine grid converge index
H_{tank} = mixing vessel height, cm
H = liquid level in the mixing vessel, cm
L_{IA} = length of the interrogation area side
N = impeller rotational speed, rpm
N_P = power number
Re = Reynolds number
S = object to image scale factor
U_{tip} = tip speed, m/s
U_z = velocity perpendicular to the measurement plane, m/s
U^* = normalized axial velocity
V^* = normalized vertical velocity
W = mixing vessel width, cm
d = axial distance in front of the impeller, cm
ea^{23} = approximate relative error between the two finest grids (grids 2 and 3)
e_{ext}^{23} = extrapolated relative error in the fine grid (grid 3)
h_i = characteristic cell size of grid i
p = apparent local order of accuracy
r_{21} = grid refinement factor from grid 1 to grid 2
r_{32} = grid refinement factor from grid 2 to grid 3
x^* = normalized axial position
y^* = normalized vertical position
z = radial position from the impeller center, cm
z_ℓ = laser sheet thickness, mm

Greek Letters

μ = fluid viscosity, kg/m s
ρ = fluid density, $\mathrm{kg/m^3}$
α = angle that defines the relative position of the impeller blades within one rotation, deg
Δt = time delay between laser flashes, s

References

[1] Mavros, P., 2001, "Flow Visualization in Stirred Vessels: A Review of Experimental Techniques," Chem. Eng. Res. Des., **79**(2), pp. 113–127.
[2] Adams, L. W., and Barigou, M., 2007, "CFD Analysis of Caverns and Pseudo-Caverns Developed During Mixing of Non-Newtonian Fluids," Chem. Eng. Res. Des., **85**(A5), pp. 598–604.
[3] Couerbe, G., Fletcher, D. F., Xuereb, C., and Poux, M., 2008, "Impact of Thixotrophy on Flow Patterns Induced in a Stirred Tank: Numerical and Experimental Studies," Chem. Eng. Res. Des., **86**(6), pp. 545–553.

[4] Khopar, A., Aubin, J., Ruibo-Atoche, C., Xuereb, C., Sauze, N. L., Bertrand, J., and Ranade, V. V., 2004, "Flow Generated by Radial Flow Impellers: PIV Measurements and CFD Simulations," Int. J. Chem. Reactor Eng., **2**(A18), pp. 1–16.
[5] Ranade, V. V., Perrard, M., Le Sauze, N., Xuereb, C., and Bertrand, J., 2001, "Trailing Vortices of Rushton Turbine: PIV Measurements and CFD Simulations With Snapshot Approach," Chem. Eng. Res. Des., **79**(1), pp. 3–12.
[6] Torré, J. P., Fletcher, D. F., Lasuye, T., and Xuereb, C., 2007, "Single and Multiphase CFD Approaches for Modeling Partially Baffled Stirred Vessels: Comparison of Experimental Data With Numerical Predictions," Chem. Eng. Sci., **62**, pp. 6246–6262.
[7] Yoon, H. S., Sharp, K. V., Hill, D. F., Adrian, R. J., Balachandar, S., Ha, M. Y., and Kar, K., 2001, "Integrated Experimental and Computational Approach to Simulation of Flow in a Stirred Tank," Chem. Eng. Sci., **56**(23), pp. 6635–6649.
[8] Zalc, J. M., Alvarez, M. M., and Muzzio, F. J., 2001, "Extensive Validation of Computed Laminar Flow in a Stirred Tank With Three Rushton Turbines," AIChE J., **47**(10), pp. 2144–2154.
[9] Bakker, A., and Fasano, J. B., 1993, "A Computational Study of the Flow Pattern in an Industrial Paper Pulp Stock Chest With a Side-Entering Impeller," AIChE Symp. Ser., **89**(293), pp. 118–124.
[10] Bhattacharya, S., Gomez, C., Soltanzadeh, A., Taghipour, F., Bennington, C. P. J., and Dumont, G. A., 2010, "Computational Modelling of Industrial Pulp Stock Chests," Can. J. Chem. Eng., **88**, pp. 295–305.
[11] Ford, C., Bennington, C. P. J., and Taghipour, F., 2007, "Modelling a Pilot-Scale Mixing Pulp Mixing Chest Using CFD," J. Pulp Pap. Sci., **33**, pp. 115–120.
[12] Ford, C., Ein-Mozaffari, F., Bennington, C. P. J., and Taghipour, F., 2006, "Simulation of Mixing Dynamics in Agitated Pulp Stock Chests Using CFD," AIChE J., **52**(10), pp. 3562–3569.
[13] Escudié, R., and Liné, A., 2003, "Experimental Analysis of Hydrodynamics in a Radially Agitated Tank," AIChE J., **49**(3), pp. 585–603.
[14] Wu, H., and Patterson, G. K., 1989, "Laser Doppler Measurements of the Turbulent Flow in Stirred Vessel to Establish Scaling Rules," Chem. Eng. Sci., **44**, pp. 2207–2221.
[15] Lee, K. C., and Yianneskis, M., 1998, "Turbulence Properties of the Impeller Stream of a Rushton Turbine," AIChE J., **44**(1), pp. 13–24.
[16] Stoots, C., and Calebrese, R. V., 1995, "Mean Velocity Field Relative to a Rushton Turbine Blade," AIChE J., **41**(1), pp. 1–11.
[17] Bugay, S., Escudié, R., and Liné, A., 2002, "Experimental Analysis of Hydrodynamics in Axially Agitated Tank," AIChE J., **48**(3), pp. 463–475.
[18] Sharp, K. V., and Adrian, R. J., 2001, "PIV Study of Small Scale Flow Structure Around a Rushton Turbine," AIChE J., **47**, pp. 766–778.
[19] Jaworski, Z., Nienow, A. W., and Dyster, K. N., 1996, "An LDA Study of the Turbulent-Flow Field in a Baffled Vessel Agitated by an Axial, Down-Pumping Hydrofoil Impeller," Can. J. Chem. Eng., **74**(1), pp. 3–15.
[20] Mavros, P., Xuereb, C., and Bertrand, J., 1996, "Determination of 3-D Flow Fields in Agitated Vessels by Laser Doppler Velocimetry. Effect of Impeller Type and Liquid Viscosity on the Liquid Flow Patterns," Chem. Eng. Res. Des., **74**(6), pp. 658–668.
[21] Schäfer, M., Yianneskis, M., Wächter, P., and Durst, F., 1998, "Trailing Vortices Around a 45° Pitched-Blade Impeller," AIChE J., **44**(6), pp. 1233–1246.
[22] Kilander, J., and Rasmuson, A., 2005, "Energy Dissipation and Macro Instabilities in a Stirred Square Tank Investigated Using an LE-PIV Approach and LDA Measurements," Chem. Eng. Sci., **60**(24), pp. 6844–6856.
[23] Oldshue, J. Y., 1983, *Fluid Mixing Technology*, McGraw-Hill, New York.
[24] Gomez, C., Derakhshandeh, B., Hatzikiriakos, S. G., and Bennington, C. P. J., 2010, "Carbopol as a Model Fluid for Studying Mixing of Pulp Fibre Suspensions," Chem. Eng. Sci., **65**, pp. 1288–1295.
[25] Raffel, M., Willert, C., and Kompehans, J., 1998, *Particle Image Velocimetry. A Practical Guide, Experimental Fluid Mechanics*, Springer, Berlin.
[26] Brown, D., Pip, J., Middlenton, J., Papadopoulos, G., and Arik, E., 2004, *Handbook of Industrial Mixing. Science and Practice*, Wiley, NJ.
[27] Dantec, 2003, "Dantec Dynamics Flow Map PIV Installation and User's Guide: General PIV Reference," Dantec Dynamics, Ramsey, NJ.
[28] Adrian, R. J., 1986, "An Image Shifting Technique to Resolve Directional Ambiguity of Double Pulsed Laser Velocimetry," Appl. Opt., **25**(21), pp. 3855–3858.
[29] Adrian, R. J., 1997, "Dynamic Ranges of Velocity and Spatial Resolution of Particle Image Velocimetry," Meas. Sci. Technol., **8**(12), pp. 1393–1398.
[30] Bujalski, J. M., Yang, W., Nikolov, J., Solnordal, C. B., and Schwarz, M. P., 2006, "Measurement and CFD Simulation of Single-Phase Flow in Solvent Extraction Pulsed Column," Chem. Eng. Sci., **61**(9), pp. 2930–2938.
[31] Escudié, R., Bouyer, D., and Liné, A., 2004, "Characterization of Trailing Vortices Generated by a Rushton Turbine," AIChE J., **50**(1), pp. 75–86.
[32] Svensson, F. J. E., and Rasmuson, A., 2006, "PIV Measurements in a Liquid-Liquid System at Volume Percentages up to 10% Dispersed Phase," Exp. Fluids, **41**(6), pp. 917–931.
[33] Collignon, M. L., Crine, M., Verdin, E., Chaubard, J. F., Peeters, L., Dessoy, S., and Toye, D., 2008, "A Study of Mixing by PIV and PLIF in Bioreactor of Cells Animals Culture," Proceedings of the Seventh International Symposium on Mixing in Industrial Processes, ISMIP VI, Niagara Falls, Canada.
[34] Myers, K. J., Ward, R. W., and Bakker, A., 1997, "A Digital Particle Image Velocimetry Investigation of Flow Field Instabilities of Axial Flow Impellers," ASME J. Fluids Eng., **119**, pp. 623–632.
[35] Weetman, R. J., and Oldshue, J. Y., 1988, "Power Flow and Shear Flow Characteristics of Mixing Impellers," Proceedings of the European Conference on Mixing, Pavia, Italy.
[36] Bakker, A., and Marshall, E., 2004, "Computational Fluid Mixing," *Handbook of Industrial Mixing. Science and Practice*, Wiley, NJ.
[37] Celik, I., Guhia, U., Roache, P. J., and Freitas, C. J., 2008, "Procedure for Estimation and Reporting of Discretization Error in CFD Applications," Technical Report: Editorial Policy of J. Fluids Eng., West Virginia University, WV.
[38] Keane, R. D., and Adrian, R. J., 1992, "Theory of Cross-Correlation Analysis of PIV Images," Appl. Sci. Res., **49**(3), pp. 191–215.

A Study of Cycle-to-Cycle Variations and the Influence of Charge Motion Control on In-Cylinder Flow in an IC Engine

Mayank Mittal
e-mail: mittalma@msu.edu

Harold J. Schock
e-mail: schock@egr.msu.edu

Department of Mechanical Engineering,
Michigan State University,
East Lansing, MI 48824

An experimental study is performed to investigate the cycle-to-cycle variations and the influence of charge motion control on in-cylinder flow measurement inside an internal combustion engine assembly. Molecular tagging velocimetry (MTV) is used to obtain the multiple point measurement of the instantaneous velocity field. MTV is a molecular counterpart of particle-based techniques, and it eliminates the use of seed particles. A two-component velocity field is obtained at various crank angle degrees for tumble and swirl measurement planes inside an optical engine assembly (1500 rpm and 2500 rpm engine speeds). Effects of charge motion control are studied considering different cases of: (i) charge motion control valve (CMCV) deactivated and (ii) CMCV activated. Both the measurement planes are used in each case to study the cycle-to-cycle variability inside an engine cylinder. Probability density functions of the normalized circulation are calculated from the instantaneous planar velocity to quantify the cycle-to-cycle variations of in-cylinder flows. In addition, the turbulent kinetic energy of flow is calculated and compared with the results of the probability density function. Different geometries of CMCV produce different effects on the in-cylinder flow field. It is found that the charge motion control used in this study has a profound effect on cycle-to-cycle variations during the intake and early compression; however, its influence reduces during the late compression. Therefore, it can be assumed that CMCV enhances the fuel-air mixing more than the flame speed. [DOI: 10.1115/1.4001617]

1 Introduction

Improvement in fuel efficiency and reduction in exhaust emissions are the two main driving forces behind the new developments in internal combustion (IC) engines. It is well known that in-cylinder flow has a fundamental influence on the combustion process, and hence, affects the engine performance. It controls the fuel-air mixing, governs the flame propagation and affects the burning rates inside an engine cylinder during the combustion process [1]. Several attempts have been made to improve the measurement techniques for velocity field and scalar properties inside an IC engine cylinder. Concerning the velocity measurements, laser doppler velocimetry (LDV) technique was used extensively in earlier studies [2–5]. Miles et al. [5] presented LDV flow measurements in a diesel engine. They compared their measured turbulent quantities with the predictions from numerical simulations at a single measurement point. Although LDV data provide excellent temporal resolution, they are limited to a single point or along a line. In IC engine research, particle image velocimetry (PIV) was the most widely used technique for velocity field measurements [6–9]. It can be used to measure two or three components of the velocity field simultaneously at multiple locations over a plane; however, the technique has a limitation for in-cylinder engine flow measurements due to the presence of solid particles. The presence of solid particles may cause complications due to mechanical interferences of the moving parts in an IC engine system. Moreover, the particle tracers may affect measurement of the highly turbulent flow field.

A molecular tagging approach overcomes these problems and offers an advantage over particle-based techniques. The technique nonintrusively maps fluid velocity simultaneously at multiple points over a plane, so properties like vorticity and strain rate can be deduced easily. Molecular tagging velocimetry (MTV) techniques are described by Gendrich and Koochesfahani [10], Hill and Klewicki [11], Zheng and Klewicki [12], and Sadr and Klewicki [13]. Note that the laser induced fluorescence is also a molecular-based technique; however, it is mainly used for the scalar quantities such as concentration and temperature measurements. Koochesfahani et al. [14] combined MTV with LIF for simultaneous measurement of the velocity and concentration fields using phosphorescent supramolecules. Stier and Koochesfahani [15] presented the two-dimensional MTV measurements in a steady flow rig model of an IC engine.

The flow inside an engine cylinder is highly transient in nature and exhibits large cycle-to-cycle variations. Schock et al. [16] and Ismailov et al. [17] investigated the cycle-to-cycle variations inside the engine cylinder. They found that probability density functions (PDFs) of normalized circulation (NC) calculated from instantaneous planar velocities are most suitable. The flow field inside the engine cylinder is affected by several factors, including engine geometry, speed, load, valve timing, and lift. In addition to these factors, the charge motion control valve (CMCV) is an important factor that affects the flow inside the engine cylinder. It is expected that the CMCV imparts an angular momentum to the charge entering the engine cylinder. The high cycle-to-cycle variations affect the fuel-air mixing, and therefore, the engine performance. Consequently, one needs to understand cycle-to-cycle variation to optimize engine design. Clarke and Stein [18] combined the variable valve timing with the charge motion control valve. Variable valve timing was obtained using the dual equal variable camshaft timing (VCT) strategy. More details about the dual equal VCT can be found in Ref. [19]. The combination of dual equal VCT with a CMCV allows an engine to be operated either at or near stoichiometry or at lean conditions, which allows

Contributed by the Fluids Engineering Division of ASME for publication in the JOURNAL OF FLUIDS ENGINEERING. Manuscript received February 23, 2009; final manuscript received April 11, 2010; published online May 13, 2010. Assoc. Editor: James A. Liburdy.

the use of a NO_x trap for the purpose of further reducing the air pollution. The authors further discussed that the synergy between the CMCV and the dual equal VCT allows the fuel consumption to be less than the fuel consumption during lean operation at standard valve timing. This is due to the fact that CMCV increases the in-cylinder charge motion, and hence improves the combustion and the ability to handle the charge dilution, which occurs from increased levels of internal exhaust gas recirculation resulting from valve timing retard. Li et al. [20] investigated the effects of swirl control valve (SCV) on in-cylinder flow characteristics using laser doppler anemometry. They found that the SCV closed condition produced both swirl and tumble motion in the cylinder, and the mean velocity was nearly doubled in comparison to the SCV open condition. Schock et al. [16] studied the effects of tumble and swirl port blockers on cyclic variations of flow in a piston cylinder assembly. They found that the swirl port blocker strengthens both tumble and swirl motions; however, the tumble port blocker only strengthens the tumble motion. Kim et al. [21] investigated the effects of injection timing and intake port flow control on fuel wetting inside the engine cylinder. They found that a tumble mixture-motion plate inside the intake port significantly reduced cylinder liner and piston top fuel wetting. This is because the use of tumble mixture-motion plate provided more turbulence, which effectively enhanced the mixing during the intake process. Lee and Heywood [22] studied the effects of CMCV on combustion characteristics and hydrocarbon emissions. The authors concluded that CMCV improved mixture preparation due to increased swirl and tumble intensities, which enhanced fuel transport, distribution, and evaporation. CMCV in the closed condition allowed reduced fuel injection and retarded spark timing strategies that reduced hydrocarbon emissions significantly during the cold start due to greater fuel evaporation and faster burning rate.

Overall, previous investigations show that a charge motion control valve is an important factor that controls the combustion process, and hence, influences the engine performance. However, studies of charge motion control valve on in-cylinder flows are limited. Therefore, an experimental study is performed to investigate the effects of charge motion control on flow measurement inside an internal combustion engine assembly. The MTV technique is used to obtain the multiple point measurement of the instantaneous velocity field over tumble and swirl measurement planes. To provide a base line for comparison, the flow results with CMCV activated are compared with the results of CMCV deactivated at various crank angle degrees (CADs). Measurements are performed at engine speeds of 1500 rpm and 2500 rpm. Cycle-to-cycle variations are presented by constructing the PDFs of NC calculated from the instantaneous planar velocity field.

2 Experimental Setup and Procedure

2.1 Experimental Setup. The optical engine assembly used for the experiments is a three-valve, two intake, and one exhaust, 0.675 l single-cylinder spark-ignited (although not fired) engine. The head includes a spark plug at the center of the cylinder and a pressure transducer to record the in-cylinder pressure data; however, not used in this study. The flat top piston is used in this study with an optical access for MTV measurements. The intake port has an elliptical shape near the intake manifold and bifurcates the flow through the two intake valves. Figure 1 shows the locations of the swirl and tumble measurement planes inside the engine cylinder [23]. Measurements with 1500 rpm engine speed are performed at 121 CAD (during the intake stroke), and at 192, 257, and 300 CADs (during the compression stroke). Similarly, the measurements are performed at 138, 171, 221, and 253 CADs with 2500 rpm engine speed. 180 CAD represents the piston position at bottom dead center (BDC) of the intake stroke. It is believed that charge motion control valves have a profound influence on the flow field, even to late compression, which affects the fuel-air mixing, and hence, the combustion process. The charge motion control valve used in this experiment is installed between

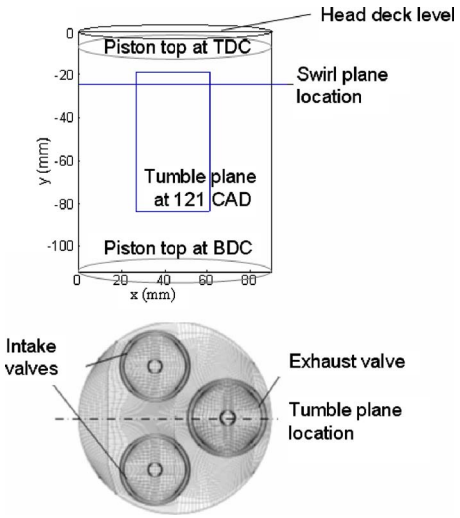

Fig. 1 Tumble and swirl measurement planes inside an IC engine cylinder

the intake manifold and the intake port. The nature of CMCV influence depends on its geometry. The CMCV used in this study reduced the port cross sectional area by about 75%, i.e., the flow area about 25%. Experiments are performed with both the conditions: CMCV deactivated and CMCV activated. It is expected that charge motion is enhanced, both in tumble and swirl measurement planes, with the activated CMCV. This study quantifies the magnitude of this enhanced motion at different CADs.

The optical setup used for MTV measurements inside the engine cylinder is shown in Fig. 2 (for tumble measurement plane). It consists of a pulsed ultraviolet laser (wavelength 308 nm), whose light beam is used to create a grid pattern in the cylinder. The laser beam passes through numerous optical elements (including a beam splitter and cylindrical lenses) that generate two light sheets propagating in the horizontal direction. Beam perforated blockers are used to transform the light sheets into sets of laser beams. One set of laser beams (horizontal) are introduced into the cylinder through the optical cylinder. The other set of laser beams are transformed into the vertical direction through a mirror, which is located below the optical piston. This is then introduced into the cylinder through the optical piston to create a grid pattern for the tumble measurement plane.

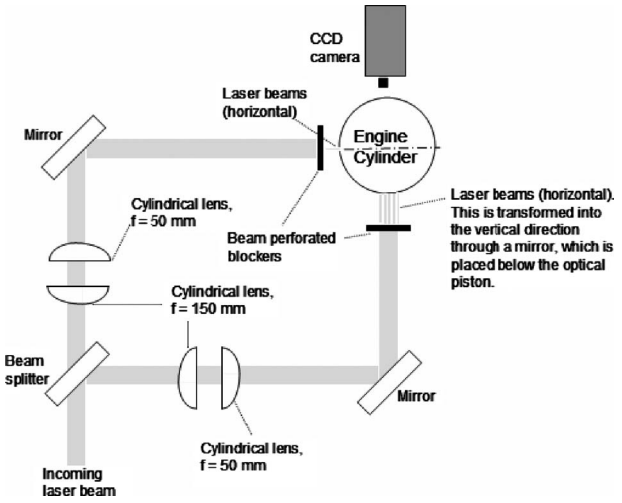

Fig. 2 Schematic of MTV optical setup for in-cylinder flow measurement

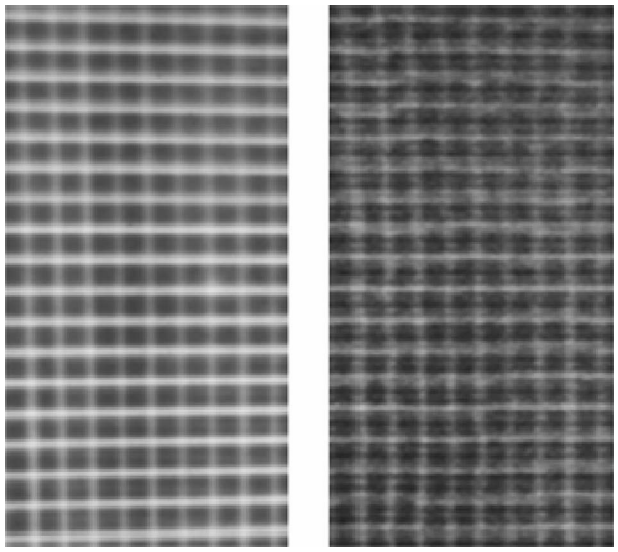

Fig. 3 Undelayed (left) and delayed (right) images for tumble measurement plane at 138 CAD

2.2 Molecular Tagging Procedure. Molecular tagging velocimetry relies on the molecules that can be turned into long lifetime tracers upon excitation by photons of an appropriate wavelength. Biacetyl is used as a tracer molecule. The working fluid in this experiment is nitrogen since the presence of oxygen quenches the phosphorescence of MTV chemicals. The MTV images at two successive time levels are recorded using a Xybion ISG intensified high spatial resolution CCD camera. Each image is an 8-bit resolution image with the size of 640×480 pixels. The reference (undelayed) image is recorded as soon as the grid pattern is written and the delayed image after a certain delay $12-35$ μs. Figure 3 shows a sample of undelayed (left) and delayed (right) images for the tumble measurement plane at 138 CAD. The grid spacing is about 4.1 mm. Similar images are obtained for the swirl measurement plane at various CADs. The optical distortion associated with the cylindrical sidewall is corrected using a calibration process, which relates the image (pixel) coordinates X, Y, to the physical space coordinates, x, y (or z), for the tumble (or swirl) measurement plane. The images are processed using a data reduction program to find the displacement at each grid point [24]. For each measured CAD, 200 undelayed and 500 delayed images are considered in this study. A spatial image correlation technique is used to obtain the displacement vectors within one pixel for the tagged region [10]. In this technique, a small window, referred to as the source window, is selected about a grid point in the tagged region in the undelayed image, and it is spatially correlated with a larger roam window in the delayed image. The two windows are centered at the same spatial location, and the roam window is large enough to encompass the grid displacement. The size of the source and roam windows (for 138 CAD measurements) is 23 pixels and 35 pixels, respectively. The subpixel accuracy is obtained using a fourth order polynomial, which requires a minimum of 15 data points from the correlation field. Since the sides of the square window have odd numbers of pixels to position the region symmetrically relative to the correlation peak, 5×5 pixels are considered for the fitting window. The location corresponding to the maximum correlation coefficient is found using a decoupled technique, as presented by Zheng and Klewicki [12].

3 Experimental Results

3.1 Swirl Measurement Plane, 1500 rpm. Measurements are performed during the intake stroke at 121 CAD and during the compression stroke at 257 and 300 CADs (load: 16.5″ Hg). Figure 4 shows the ensemble-averaged velocity vectors, $\langle u \rangle$ and $\langle v \rangle$, when the engine was operated with activated CMCV at 121 crank angle degrees. The three plots, Figs. 4(*a*)–4(*c*), are obtained considering 1–100, 101–200, and 1–500 consecutive frames, respectively. The figure shows that the mean field is quite stable when calculated with 100 consecutive frames. In general, more frames are required to calculate the higher order turbulence statistics, for example, probability density function of normalized circulation, turbulent kinetic energy. Therefore, 500 delayed frames are considered in our further investigation to obtain the instantaneous velocity field at each crank angle degree. Then the velocity statistics are calculated (Figs. 5–14).

Figure 5 shows the rms velocity contours when the engine was operated with deactivated (left) and activated (right) CMCV at 121 (upper graphs) and 300 (lower graphs) crank angle degrees, respectively. The rms values shown in the figure are the vector magnitude of the rms values of u and z velocity components. The vectors in the plots show the magnitude of ensemble-averaged velocity vectors $\langle u \rangle$ and $\langle v \rangle$. As shown in the figure, the velocity magnitudes are higher at 121 CAD (during the intake stroke) and reduce during the compression stroke. Similarly, the rms values decay during the compression stroke. Note that the rms cyclic

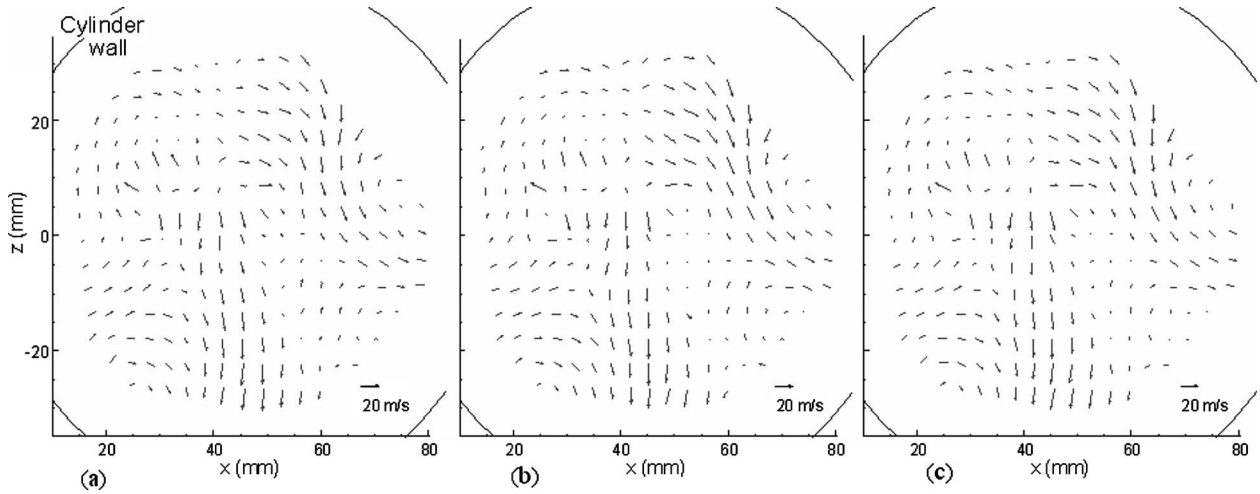

Fig. 4 Ensemble-averaged velocity vectors for activated CMCV at 121 CAD considering (*a*) 1–100, (*b*) 101–200, and (*c*) 1–500 consecutive undelayed frames; swirl measurement plane at 1500 rpm

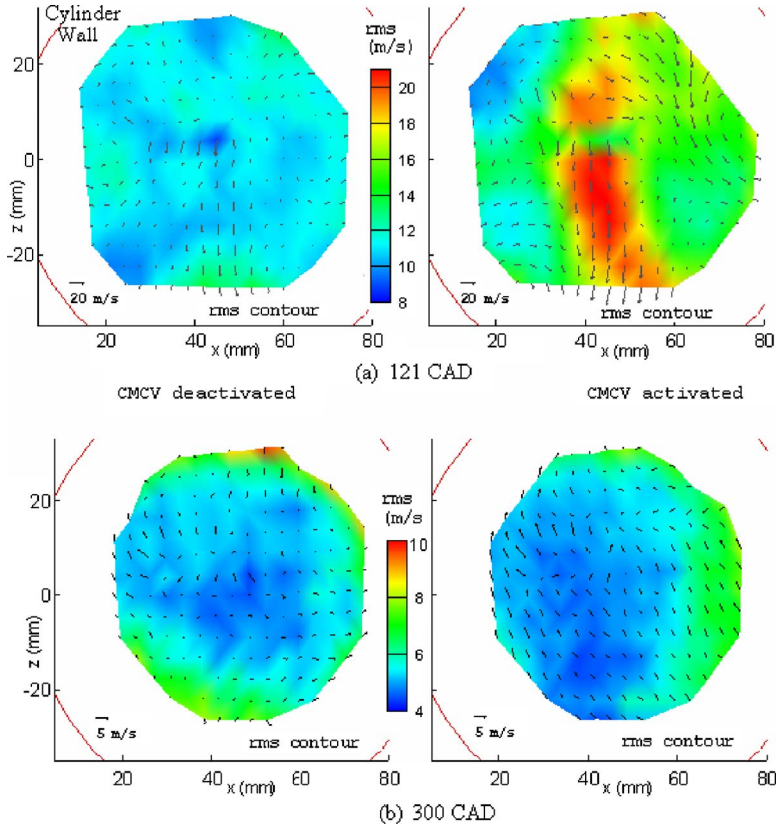

Fig. 5 Ensemble-averaged velocity vectors, contours of velocity rms for deactivated (left) and activated (right) CMCV at (*a*) 121 and (*b*) 300 CADs; swirl measurement plane at 1500 rpm

variations are considerably enhanced with the activated CMCV at 121 CAD, and they are as high as 20 m/s. The higher rms values at 121 CAD show that the flow at this crank angle is highly turbulent in nature with both the intake valves open. The cyclic variations decay during the compression stroke. These results are consistent with the earlier literature; see Ref. [9]. They found high rms values during the intake stroke at 149 CAD. These values reduce as the compression stroke is traversed. There are some counterclockwise rotations that can be observed toward the upper right half of the plane and some clockwise rotations at the bottom left half of the plane (at 121 CAD) with activated CMCV.

The circulation of the flow on a swirl or tumble measurement plane can be used as a primary parameter to characterize the rotational motion of the flow [16]. Circulation Γ is defined as follows:

$$\Gamma = \oint_C \bar{V} \cdot d\bar{l} = \int \int_A \bar{\omega} \cdot d\bar{A} \tag{1}$$

where C is a closed curve on a tumble or swirl measurement plane and A is the area enclosed by the curve C.

It is to be noticed that when the flow on the swirl or tumble measurement plane is studied at different CADs, the area of each plane is not the same. Therefore, to compare the results, the circulations of flow on different planes have to be normalized by their respective areas, which is

$$\Gamma_N = \frac{1}{A} \oint_C \bar{V} \cdot d\bar{l} = \frac{1}{A} \int \int_A \bar{\omega} \cdot d\bar{A} \tag{2}$$

Note that Γ_N, by definition, is the averaged vorticity over the computational plane, which is referred as the NC; see Refs. [16,17]. In this study, e.g., over the tumble measurement plane, vorticity ω_z, Eq. (3), for a two-component velocity field, is computed using a second order accurate finite difference technique [25], and then the spatial mean is calculated to obtain the averaged vorticity (or normalized circulation). Each frame has a different NC because of the cyclic variability. 500 frames are considered in this study to obtain the PDF plot of the normalized circulation for each case

$$\omega_z = \frac{\partial v}{\partial x} - \frac{\partial u}{\partial y} \tag{3}$$

Figure 6 shows the PDF plot of normalized circulation at different crank angle degrees with 1500 rpm engine speed. The mean value of normalized circulations gives the ensemble-averaged information for the flow inside an engine cylinder. The range of NC variation quantifies the cycle-to-cycle variability of the flow. A more representative measure to quantify the cycle-to-cycle variation inside the engine cylinder is the standard deviation (σ) of NC PDF. Almost all the change in PDF occurs within ± 3 standard deviations. As shown in the figure, for deactivated CMCV, the standard deviation (STDEV) of NC decreases from 121 CAD (σ=205.33 Hz) to 257 CAD (σ=96.76 Hz). The shift in peak shows that the negative circulations are more probable at this later crank angle. It then increases slightly at 300 CAD (σ =101.18 Hz). These results show that cycle-to-cycle variation decreases from 121 CAD to 257 CAD, and then increases slightly to CAD 300. The bin size used in PDF calculations is one-half of the standard deviation. For activated CMCV, the standard deviation decreases from 121 CAD (σ=304.37 Hz) to 300 CAD (σ =109.17 Hz). Note that CMCV effects on cycle-to-cycle variation are not significant at 300 CAD when compared with the results of deactivated CMCV.

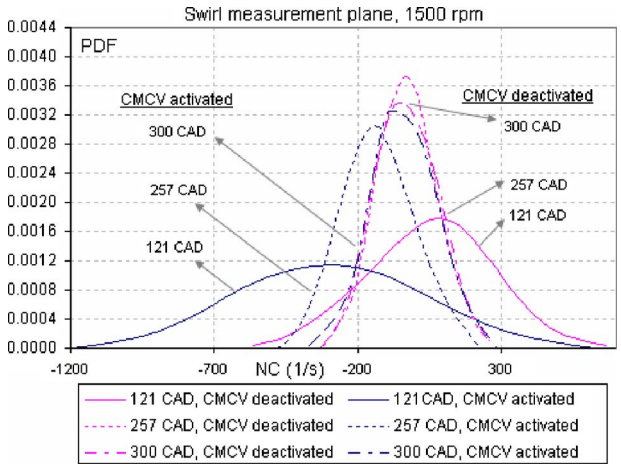

Fig. 6 PDFs of normalized circulation at different crank angle degrees; swirl measurement plane at 1500 rpm

The flow field inside an engine cylinder is highly turbulent, and thus, the flow characteristics at any point are different from cycle-to-cycle. The velocity fields are further processed to evaluate the turbulent kinetic energy (TKE). For the swirl measurement plane, the turbulent kinetic energy is calculated as follows:

$$k = \frac{1}{2}(\langle u'^2\rangle + \langle v'^2\rangle + \langle w'^2\rangle) \approx \frac{3}{4}(\langle u'^2\rangle + \langle w'^2\rangle) \tag{4}$$

where $\langle v'^2\rangle$ is estimated as $(\langle u'^2\rangle + \langle w'^2\rangle)/2$ in Eq. (4) [5]. Similarly, $\langle w'^2\rangle$ is estimated as $(\langle u'^2\rangle + \langle v'^2\rangle)/2$ when the TKE is evaluated for the tumble measurement plane. The local TKE, at each grid node, is then used to evaluate the averaged TKE over the studied plane. With N points over the plane and the local TKE k_i, the averaged TKE k_{avg} over the plane is

$$k_{\text{avg}} = \frac{1}{N}\left(\sum_{i=1}^{N} k_i\right) \tag{5}$$

Figure 7 shows the change in cycle-to-cycle variability characterized by averaged turbulent kinetic energy over the swirl measurement plane at 1500 rpm engine speed with respect to the crank angle. The values are normalized by s_p^2, where s_p is the mean piston speed. The mean piston speeds are 5.3 m/s and 8.8 m/s at 1500 rpm and 2500 rpm of engine speeds, respectively. The results are qualitatively in agreement with the PDF results, as shown in Fig. 6. CMCV effect on cycle-to-cycle variation is significant during the intake stroke; however, the effect reduces as we traverse during the compression stroke.

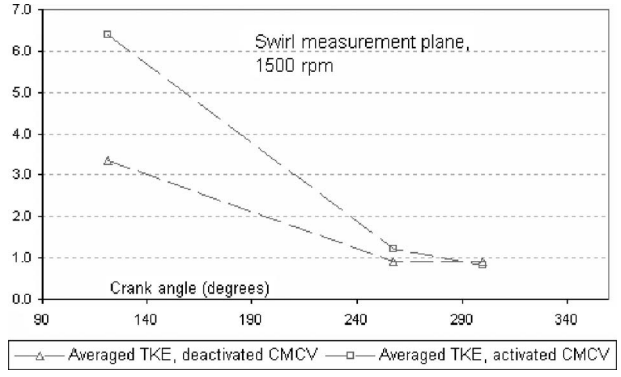

Fig. 7 Turbulent kinetic energy at different crank angle degrees; swirl measurement plane at 1500 rpm

3.2 Swirl Measurement Plane, 2500 rpm. Measurements are performed at 138, 171, 221, and 253 crank angle degrees with wide open throttle. Figure 8 shows the ensemble-averaged velocity vectors, $\langle u\rangle$ and $\langle v\rangle$, and the contours of rms velocity for deactivated (left) and activated (right) CMCV at 171 and 221 CADs, respectively. The magnitudes of ensemble-averaged velocity vectors show that CMCV enhances the flow field at 171 CAD during the intake stroke, and its effects decay during the compression stroke at 221 CAD, as expected. The rms values with activated CMCV at 171 CAD are higher than 17 m/s toward the center of the measurement plane. Some clockwise rotations can be observed at this crank angle toward the bottom left half of the measurement plane. Similarly, the rms cyclic variations are higher at 221 CAD with activated CMCV (maximum about 13 m/s). Some clockwise and counterclockwise rotations can also be observed at this crank angle.

Figure 9 shows the PDF plot of normalized circulation at different CADs for the swirl plane at 2500 rpm. As shown in the figure, the standard deviation of NC decreases from 138 CAD (σ=305.53 Hz) to 253 CAD (σ=117.11 Hz) for deactivated CMCV. These results show that cycle-to-cycle variation decreases from 138 CAD to 253 CAD with deactivated CMCV. With activated CMCV, the standard deviation decreases from 138 CAD to 221 CAD, and then increases slightly at 253 CAD. The CMCV effect shows significant enhancement in cycle-to-cycle variation at 171 CAD during the intake stroke. However, it is interesting to note that the effect is not significant at 138 CAD at this higher engine speed. Figure 10 shows the change in cycle-to-cycle variability characterized by the standard deviation of NC and averaged TKE over the plane with respect to the crank angle. The TKE with activated CMCV is only slightly higher than that of deactivated CMCV at 138 CAD, as also seen in the PDF plot (Fig. 9). The cycle-to-cycle variations are higher with activated CMCV at 171 CAD and reduce during the compression stroke.

3.3 Tumble Measurement Plane, 1500 rpm. Measurements are performed during the intake stroke at 121 CAD and during the compression stroke at 192, 257, and 300 CADs (load: 16.5″ Hg). Figure 11 shows the PDF plot of normalized circulation at different CADs. As shown in the figure, the standard deviation of NC decreases from 121 CAD (σ=219.76 Hz) to 257 CAD (σ=86.62 Hz) for deactivated CMCV. It then increases to 210.69 Hz at 300 CAD. A similar pattern is obtained when measurements are performed with activated CMCV; however, cycle-to-cycle variations are higher when compared with the deactivated CMCV. These results show that cycle-to-cycle variation decreases from 121 CAD to 257 CAD and then increases to CAD 300. Note that the CMCV effect is not significant on cycle-to-cycle variation at 300 CAD. Therefore, similar to the swirl plane measurements, CMCV has a profound effect on flow enhancement during the intake stroke; however, its effect decays during the late compression when compared with the deactivated CMCV. Figure 12 shows the cycle-to-cycle variations characterized by the standard deviation of NC and averaged TKE for this tumble measurement plane at 1500 rpm engine speed with respect to the crank angle. The TKE decays from 121 CAD to 257 CAD and then increases slightly to 300 CAD for both the cases. Joo et al. [6] also investigated the fact that the standard deviation of large- and small-scale variations was greater during the early intake and late compression when compared with the late intake and early compression processes.

3.4 Tumble Measurement Plane, 2500 rpm. Measurements are performed at 138, 171, 221, and 253 crank angle degrees with wide open throttle. Figure 13 shows the PDF plot of normalized circulation at these crank angles. For deactivated CMCV, the standard deviation of NC decreases from 138 CAD (σ=264 Hz) to 221 CAD (σ=102.15 Hz). It then increases to 253 CAD with the value of 139.38 Hz. These results show that cycle-to-cycle varia-

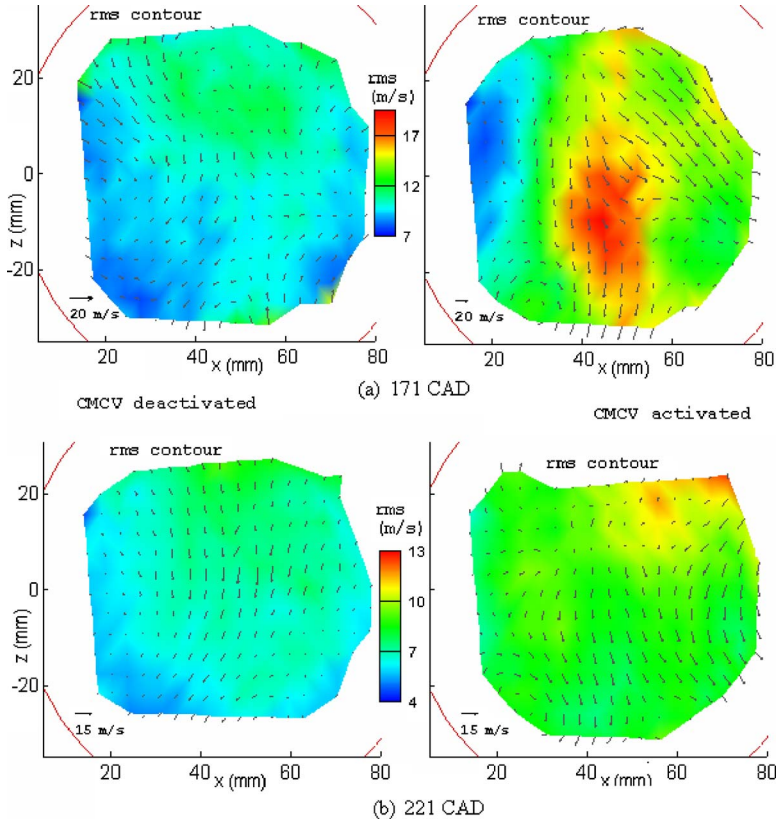

Fig. 8 Ensemble-averaged velocity vectors, contours of velocity rms for deactivated (left) and activated (right) CMCV at (*a*) 171 and (*b*) 221 CADs; swirl measurement plane at 2500 rpm

tion decreases from 138 CAD to 221 CAD and then increases to 253 CAD for deactivated CMCV. With activated CMCV, the standard deviation decreases from 138 CAD to 253 CAD. The cycle-to-cycle variations show significant difference at 138, 171, and 221 CADs (higher with activated CMCV); however, it is only slightly higher at 253 CAD with activated CMCV. Therefore, it can be assumed that the CMCV effect reduces during late compression to enhance the flow field inside an engine cylinder. Figure 14, when characterized by averaged TKE, shows consistently that cycle-to-cycle variations are higher with activated CMCV during the intake stroke, and its effect decays during the late compression.

4 Conclusions

An experimental study is performed to investigate the effects of charge motion control on flow inside an IC engine cylinder. The flow inside the engine cylinder is highly transient in nature and exhibits large cycle-to-cycle variations. PDF plots of normalized circulation are computed. This is a more representative measure to characterize the cycle-to-cycle variations. The results of the stan-

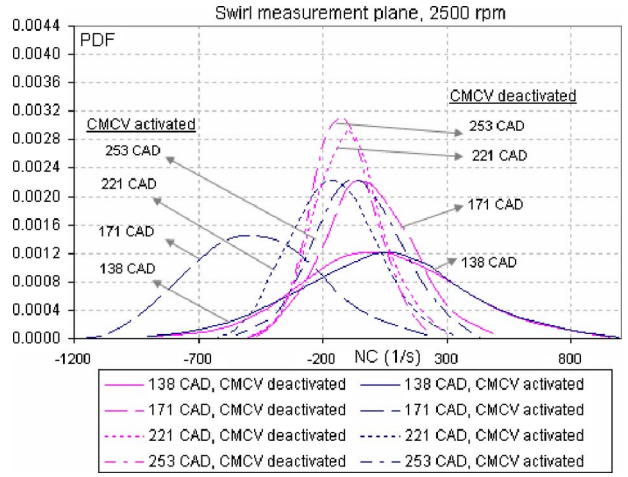

Fig. 9 PDFs of normalized circulation at different crank angle degrees; swirl measurement plane at 2500 rpm

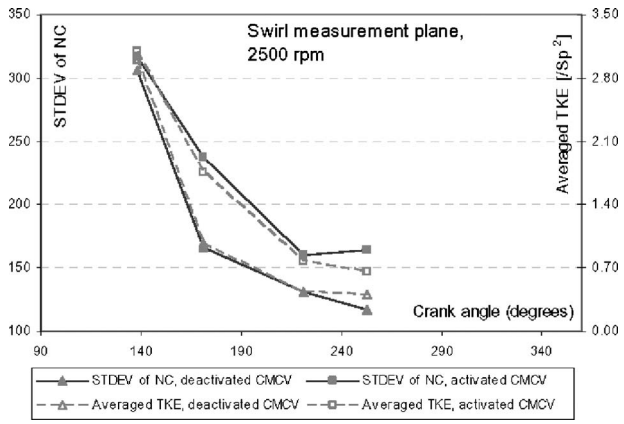

Fig. 10 STDEV of NC and turbulent kinetic energy at different crank angle degrees; swirl measurement plane at 2500 rpm

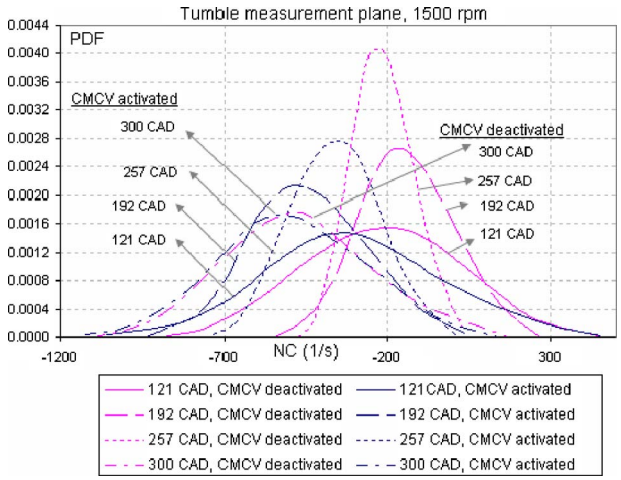

Fig. 11 PDFs of normalized circulation at different crank angle degrees; tumble measurement plane at 1500 rpm

dard deviation of NC are, in general, consistent with the turbulent kinetic energy results. Molecular tagging velocimetry is used for the experiments. This technique is superior to particle-based techniques due to the ability of the laser-tagged phosphorescent molecules that follow the flow perfectly. The effects of CMCV on in-cylinder flow measurement are summarized below.

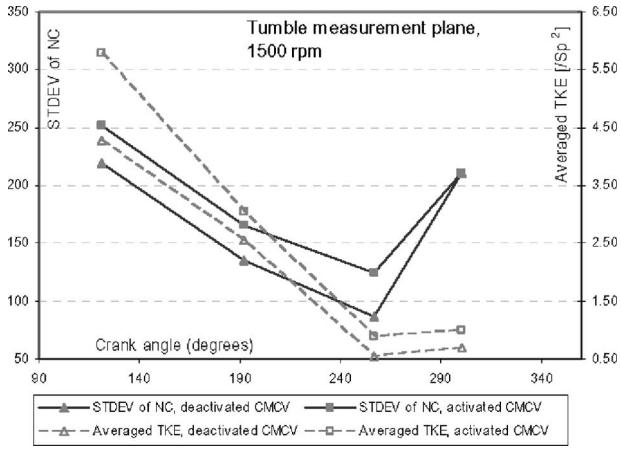

Fig. 12 STDEV of NC and turbulent kinetic energy at different crank angle degrees; tumble measurement plane at 1500 rpm

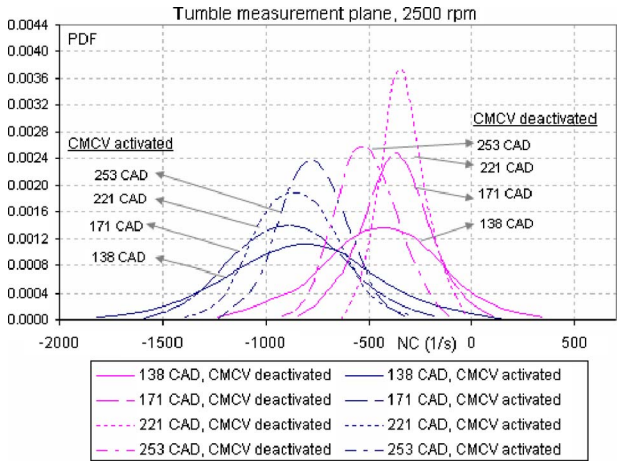

Fig. 13 PDFs of normalized circulation at different crank angle degrees; tumble measurement plane at 2500 rpm

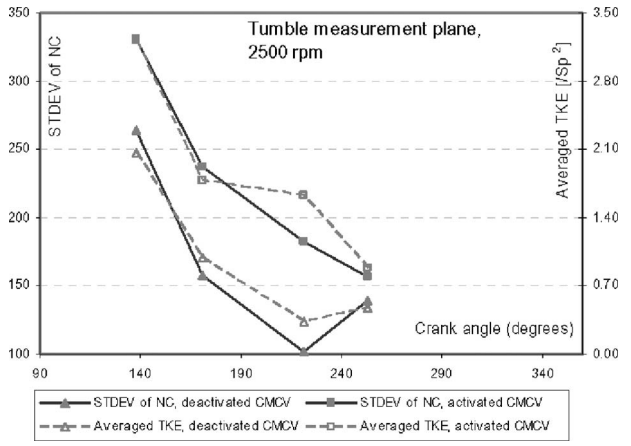

Fig. 14 STDEV of NC and turbulent kinetic energy at different crank angle degrees; tumble measurement plane at 2500 rpm

- Swirl measurement plane at 1500 rpm: Results show that cycle-to-cycle variation decreases from 121 CAD to 257 CAD. It then increases slightly at 300 CAD for deactivated CMCV. CMCV showed a considerable effect to enhance the flow field during the intake stroke; however, the effects are not significant during the compression stroke.
- Swirl measurement plane at 2500 rpm: With activated CMCV, the cycle-to-cycle variation decreases from 138 CAD to 221 CAD, and then increases, only slightly, at 253 CAD.
- Tumble measurement plane at 1500 rpm: Cycle-to-cycle variation decreases from 121 CAD to 257 CAD. It then increases at 300 CAD with both CMCV deactivated and CMCV activated. The effects of CMCV are significant to enhance the cycle-to-cycle variations, except at 300 CAD.
- Tumble measurement plane at 2500 rpm: Cycle-to-cycle variation decreases from 138 CAD to 221 CAD and then increases at 253 CAD for deactivated CMCV. With activated CMCV, the cycle-to-cycle variation decreases from 138 CAD to 253 CAD.

Insight on cycle-to-cycle variation, based on instantaneous measurements, is needed to optimize engine design. The results of this study have particular significance on fuel-air mixing, and therefore, on the combustion process. The study shows that CMCV considerably enhances the flow field during the intake; however, the effects are not significant during the late compression. Therefore, for this configuration, it can be assumed that CMCV enhances fuel-air mixing more than it enhances flame speed.

Acknowledgment

This study was supported by the Michigan Economic Development Corporation. The authors would like to thank Andrew Fedewa for his help in data acquisition. Thanks to the reviewers for their useful comments and suggestions that help improve the manuscript.

References

[1] Heywood, J. B., 1987, "Fluid Motion Within the Cylinder of Internal Combustion Engines—The 1986 Freeman Scholar Lecture," ASME J. Fluids Eng., **109**, pp. 3–35.
[2] Bicen, A. F., Vafidis, C., and Whitelaw, J. H., 1985, "Steady and Unsteady Airflow Through the Intake Valve of a Reciprocating Engine," ASME J. Fluids Eng., **107**, pp. 413–420.
[3] Kent, J. C., Haghgooie, M., Mikulec, A., Davis, G. C., and Tabaczynski R. J.,

1987, "Effects of Intake Port Design and Valve Lift on In-Cylinder Flow and Burnrate," SAE Paper No. 872153.
[4] Fraser, R. A., and Bracco, F. V., 1989, "Cycle-Resolved LDV Integral Length Scale Measurements Investigating Clearance Height Scaling, Isotropy, and Homogeneity in an IC Engine," SAE Paper No. 890615.
[5] Miles, P., Megerle, M., Nagel, Z., Reitz, R. D., Lai, M. C. D., and Sick, V., 2003, "An Experimental Assessment of Turbulence Production, Reynolds Stress and Length Scale (Dissipation) Modeling in a Swirl-Supported DI Diesel Engine," SAE Trans., **112**(3), pp. 1470–1499.
[6] Joo, S. H., Srinivasan, K. K., Lee, K. C., and Bell, S. R., 2004, "The Behavior of Small- and Large-Scale Variations of In-Cylinder Flow During Intake and Compression Strokes in a Motored Four-Valve Spark Ignition Engine," Int. J. Engine Res., **5**(4), pp. 317–328.
[7] Towers, D. P., and Towers, C. E., 2004, "Cyclic Variability Measurements of In-Cylinder Engine Flows Using High-Speed Particle Image Velocimetry," Meas. Sci. Technol., **15**, pp. 1917–1925.
[8] Bevan, K. E., and Ghandhi, J. B., 2004, "PIV Measurements of In-Cylinder Flow in a Four-Stroke Utility Engine and Correlation With Steady Flow Results," SAE Paper No. 2004-32-0005.
[9] Jarvis, S., Justham, T., Clarke, A., Garner, C. P., Hargrave, G. K., and Richardson, D., 2006, "Motored SI IC Engine In-Cylinder Flow Field Measurement Using Time Resolved Digital PIV for Characterization of Cyclic Variation," SAE Paper No. 2006-01-1044.
[10] Gendrich, C. P., and Koochesfahani, M. M., 1996, "A Spatial Correlation Technique for Estimating Velocity Fields Using Molecular Tagging Velocimetry (MTV)," Exp. Fluids, **22**(1), pp. 67–77.
[11] Hill, R. B., and Klewicki, J. C., 1996, "Data Reduction Methods for Flow Tagging Velocity Measurements," Exp. Fluids, **20**, pp. 142–152.
[12] Zheng, Q., and Klewicki, J. C., 2000, "A Fast Data Reduction Algorithm for Molecular Tagging Velocimetry: The Decoupled Spatial Correlation Technique," Meas. Sci. Technol., **11**, pp. 1282–1288.
[13] Sadr, R., and Klewicki, J. C., 2003, "A Spline-Based Technique for Estimating Flow Velocities Using Two-Camera Multi-Line MTV," Exp. Fluids, **35**, pp. 257–261.
[14] Koochesfahani, M. M., Cohn, R., and MacKinnon, C., 2000, "Simultaneous Whole-Field Measurements of Velocity and Concentration Fields Using Combined MTV and LIF," Meas. Sci. Technol., **11**(9), pp. 1289–1300.
[15] Stier, B., and Koochesfahani, M. M., 1998, "Whole Field MTV Measurements in a Steady Flow Rig Model of an IC Engine," SAE Paper No. 980481.
[16] Schock, H. J., Shen, Y., Timm, E., Stuecken, T., Fedewa, A., and Keller, P., 2003, "The Measurement and Control of Cyclic Variations of Flow in a Piston Cylinder Assembly," SAE Paper No. 2003-01-1357.
[17] Ismailov, M. M., Schock, H. J., and Fedewa, A. M., 2006, "Gaseous Flow Measurements in an Internal Combustion Engine Assembly Using Molecular Tagging Velocimetry," Exp. Fluids, **41**, pp. 57–65.
[18] Clarke, J. R., and Stein, R. A., 1999, "Internal Combustion Engine With Variable Camshaft Timing, Charge Motion Control Valve, and Variable Air/Fuel Ratio," U.S. Patent No. 5,957,096.
[19] Stein, R. A., Galietti, K. M., and Leone, T. G., 1995, "Dual Equal VCT—A Variable Camshaft Timing Strategy for Improved Fuel Economy and Emissions," SAE Paper No. 950975.
[20] Li, Y., Liu, S., Shi, S., and Xu, Z., 2000, "Effect of the Swirl Control Valve on the In-Cylinder Air Motion in a Four-Valve SI Engine," SAE Paper No. 2000-01-2058.
[21] Kim, H., Yoon, S., Xie, X. B., Lai, M. C., Quelhas, S., Boyd, R., Kumar, N., and Moran, C., 2005, "Effects of Injection Timings and Intake Port Flow Control on the In-Cylinder Wetted Fuel Footprints During PFI Engine Startup Process," SAE Paper No. 2005-01-2082.
[22] Lee, D., and Heywood, J. B., 2006, "Effects of Charge Motion Control During Cold Start of SI Engines," SAE Paper No. 2006-01-3399.
[23] Mittal, M., Schock, H. J., and Sadr, R., 2008, "Evaluating the Influence of Charge Motion Control on In-Cylinder Flow Using MTV," ASME Paper No. IMECE2008-66490.
[24] Mittal, M., Sadr, R., Schock, H. J., Fedewa, A., and Naqwi, A., 2009, "In-Cylinder Engine Flow Measurement Using Stereoscopic Molecular Tagging Velocimetry (SMTV)," Exp. Fluids, **46**(2), pp. 277–284.
[25] Cohn, R. K., and Koochesfahani, M. M., 2000, "The Accuracy of Remapping Irregularly Spaced Velocity Data Onto a Regular Grid and the Computation of Vorticity," Exp. Fluids, **29**(7), pp. S061–S069.

Bingwei Song[1]
School of Hydraulic Engineering,
Faculty of Infrastructure Engineering,
Dalian University of Technology,
Dalian 116024, China; Department of Mechanical Science and Bioengineering,
Graduate School of Engineering Science,
Osaka University,
1-3 Machikaneyama,
Toyonaka, Osaka 560-8531, Japan
e-mail: bingweisong@dl.cn

Hironori Horiguchi

Yumeto Nishiyama

Shinichiro Hata

Department of Mechanical Science and Bioengineering,
Graduate School of Engineering Science,
Osaka University,
1-3 Machikaneyama,
Toyonaka, Osaka 560-8531, Japan

Zhenyue Ma
School of Hydraulic Engineering,
Faculty of Infrastructure Engineering,
Dalian University of Technology,
Dalian 116024, China

Yoshinobu Tsujimoto
Department of Mechanical Science and Bioengineering,
Graduate School of Engineering Science,
Osaka University,
1-3 Machikaneyama,
Toyonaka, Osaka 560-8531, Japan

Fluid Force Moment on the Backshroud of a Francis Turbine Runner in Precession Motion

The fundamental characteristics of rotordynamic fluid force moment on the backshroud of a Francis turbine runner in precession motion were studied using model tests and computations based on a bulk flow model. The runner is modeled by a disk positioned close to a casing with a small axial clearance. An inward leakage flow is produced by an external pump in the model test. The effects of the leakage flow rate, the preswirl velocity at the inlet of the clearance, and the axial clearance on the fluid force moment were examined. It was found that the fluid force moment encourages the precession motion at small forward precession angular velocity ratios and the region encouraging the precession motion is affected by the preswirl velocity. Through the comparisons of the fluid force moment with and without the rotation of the disk, it was found that the normal moment without the disk rotation did not have the effect to encourage the precession motion. Thus, the swirl flow due to disk rotation was found to be responsible for the encouragement of the precession motion. [DOI: 10.1115/1.4001618]

1 Introduction

Rotordynamic forces occur in response to the shaft vibration. A severe flexural vibration of the rotor shaft of a Francis turbine runner was experienced. Reference [1] showed that the vibration was caused by the fluid forces and moments on the backshroud of the runner associated with the leakage flow through the back chamber.

For the two fundamental modes of whirling and precession motions of the rotor, many studies have been conducted to evaluate the forces and moments on the shroud of centrifugal pump impellers. For the whirling motion, the importance of the shroud forces was demonstrated in Ref. [2] and the effects of the inlet swirl of the leakage flow were examined in Ref. [3]. For the precession motion, Ref. [4] measured the fluid force moments acting on a precession impeller for the first time. It was found that rotordynamic moments on the impeller have a destabilizing effect at small angular velocity ratios. Reference [5] examined the unsteady flow in the clearance between the backshroud of the centrifugal impeller and the casing in precession motion. The effects of leakage flow in the backshroud/casing clearance and the effect of a gap between the impeller side plate and the casing on fluid force moments acting on the backshroud were investigated. Reference [6] compared the numerical results based on a bulk flow model with the experimental results of fluid force moment on a centrifugal impeller shroud in precession motion and revealed that the bulk flow model could simulate the clearance flow between the backshroud and the casing and the destabilizing fluid force moment fairly well if the resistance at the inlet of the clearance was correctly incorporated in the model. However, the effects of inlet swirl and width of the axial clearance on the fluid force moments for precession motion have not been made clear yet.

In order to study the rotordynamic vibration of the Francis turbine runner as reported in Ref. [1], the authors have measured the rotordynamic force moment on a whirling disk simulating the backshroud of a Francis turbine runner [7]. For the complete analysis of vibration composed of whirling and precession motions, we need to determine the fluid force moment caused by the precession motion. The present study examined the effects of the leakage flow rate, the preswirl velocity, and the axial clearance between the backshroud and the casing on the fluid force moment

[1]Corresponding author.

Contributed by the Fluids Engineering Division of ASME for publication in the JOURNAL OF FLUIDS ENGINEERING. Manuscript received August 2, 2009; final manuscript received April 7, 2010; published online May 13, 2010. Assoc. Editor: Edward M. Bennett.

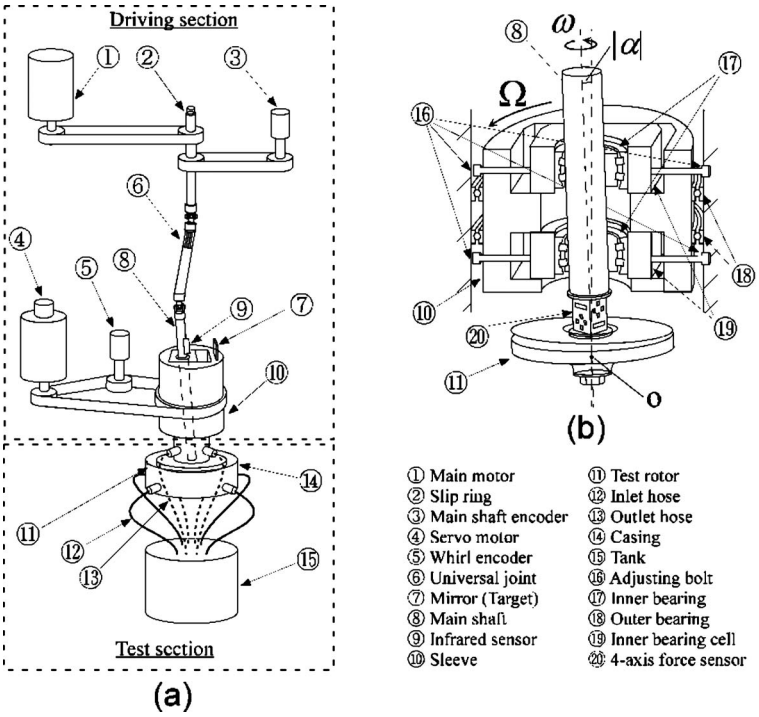

Fig. 1 Schematic of experimental facility: (*a*) overall view and (*b*) cross-section of sleeve

caused by precession motion. By comparing the results with and without the rotation of the disk, it is shown that the most important parameter is the swirl velocity relative to the minimum clearance due to precession motion.

2 Experiment Facility

Figure 1 shows the schematic of experimental facility. The overall view of the experimental facility and the cross-section of the sleeve (No. 10) are shown in Figs. 1(*a*) and 1(*b*), respectively. The disk (No. 11) simulates the backshroud of a Francis turbine runner. The main shaft (No. 8) with the disk (No. 11) is rotated by the main motor (No. 1) with an angular velocity ω. The rotational speed of the disk ω is kept at 400 ± 0.5 rpm. The shaft has an angular displacement of $|\alpha|$ around the gravity point of the disk, which is shown by "O" in Fig. 1(*b*). The rotation of the sleeve (No. 10) generates the precession motion of the disk with an angular velocity Ω. In the present study, the angular displacement $|\alpha|$ is set to be 0.48 deg. The angular velocity ratio Ω/ω is changed between -1.2 and 1.2. The uncertainty in Ω/ω is ± 0.01. The fluid forces and fluid force moments were measured by the four-axis force sensor (No. 20). The output signals were averaged over 32 times and the signals with the same frequency as the precession motion were used to obtain the fluid forces and moments.

Figure 2 shows the details of the test section. The backshroud of the runner is modeled by a disk (No. 1) set close to the back casing (No. 7) with the mean axial clearance C_2. The mean radial clearance C_1 between the disk and the outer casing (No. 8) models the seal in real turbine. The leakage flow is produced by an external pump. The working fluid is water. For the case without inlet swirl, the leakage flow is introduced into the test section from the inlet port (No. 12) radially passes through the swirl breaker (No. 11) with 36 radial vanes, the radial and the axial clearances between the stationary casing (Nos. 7 and 8) and the rotating disk

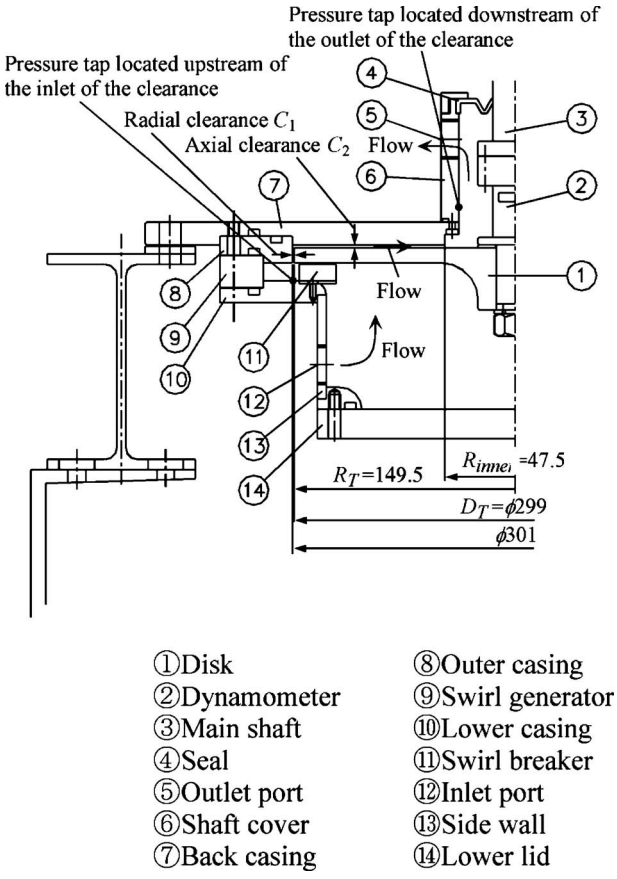

Fig. 2 Details of the test section

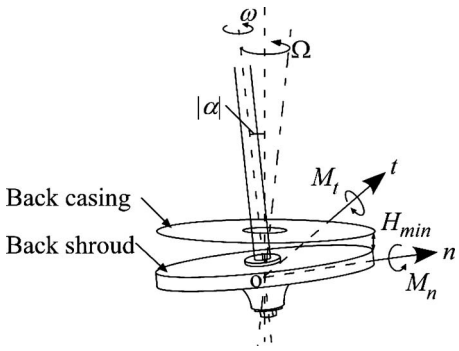

Fig. 3 Definition of the rotordynamic fluid force moments

(No. 1), and finally flows out from the outlet port (No. 5). For the case with inlet swirl, the leakage flow is supplied to the swirl generator (No. 9) composed of eight equally spaced tangential nozzles. When the swirl generator is used, the swirl breaker (No. 11) is removed and the leakage flow rate was adjusted by discharging excess flow rate from the inlet port (No. 12).

The mean radial clearance C_1 at the tip of the disk is 1 mm. The mean axial clearance C_2 between the back casing (No. 7) and the disk can be set to 2 mm, 4 mm, and 6 mm. The radius of the disk R_T is 149.5 mm. The thickness of the disk is 10 mm and hence the axial length of the radial clearance region is nearly 10 mm. The inner radius of the casing R_{inner} is 47.5 mm.

Figure 3 shows the definition of the rotordynamic fluid force moments. The n-axis is set in the direction of minimum axial clearance and the t-axis is perpendicular to it, proceeding by 90 deg from n-axis in the direction of the rotation of the disk. The angular velocity Ω of precession motion is positive when the direction of precession motion is the same as the rotation of the disk. The fluid force moment M is decomposed into normal (M_n) and tangential (M_t) components. It should be noted here when M_n has the same sign as Ω/ω, it has the effect to encourage the precession motion in the direction of Ω [6].

3 Computation Based on Bulk Flow Model

The bulk flow model was used for the computation, assuming uniform velocity and pressure distributions over the clearance and considering the wall shear and the displacement of the wall due to precession motion. Governing equations are the continuity equation and the momentum equations in radial and circumferential directions. For details, see Ref. [8].

The velocity and the pressure are divided into steady and unsteady components due to the precession motion with the angular velocity Ω. Based on the assumption that the unsteady components are much smaller than the steady components, the governing equations are linearized. The unsteady pressure and velocity are mainly caused by the oscillation of the axial clearance H_2. The seal effect of the radial clearance C_1 was taken into account simply as a constant resistance. The following boundary conditions are applied:

$$\text{inlet:} \quad P(0) = P_{\text{upstream}} - \frac{1}{2}\rho[1+\xi]\frac{H_2^2(0)}{C_1^2}U_s^2(0) \tag{1}$$

$$\text{outlet:} \quad P(1) = P_{\text{downstream}} + \frac{1}{2}\rho(C_{de}-1)[U_s^2(1)+U_\theta^2(1)] \tag{2}$$

where 0 and 1 in the parentheses mean the values at the inlet and outlet of the axial clearance, respectively. P_{upstream} and $P_{\text{downstream}}$ represent the pressure at the pressure taps located upstream of the inlet of the axial clearance and downstream of the outlet, respectively. The unsteady components of P_{upstream} and $P_{\text{downstream}}$ are assumed to be 0. As both $|\alpha|$ and the axial length of the radial clearance are small, the radial clearance C_1 is assumed to be constant. $H_2(0)$ is the width of the axial clearance at the inlet and defined as $H_2(0)=C_2-|\alpha|R_T e^{i\Omega t}$.

4 Results and Discussions

4.1 Steady Pressure Distribution in the Clearance. The distribution of the steady pressure coefficient $\psi_s=(P-P_{\text{downstream}})/(\rho U_T^2)$ in the clearance is shown in Fig. 4. The uncertainty in ψ_s is ± 0.01. Figures 4(a)–4(c) show the effects of the leakage flow rate, the preswirl velocity, and the mean axial clearance C_2, respectively. The horizontal axis shows the nondimensional coordinate $s(=S/(R_T-R_{\text{inner}}))$ along the meridional streamline and $s=0$ and 1 correspond to the inlet ($R=R_T$) and outlet of the axial clearance ($R=R_{\text{inner}}$), respectively. Locations $s=-0.2$ and 1.2 correspond to the positions upstream of the inlet of the axial clearance and downstream from the outlet, respectively.

Figure 4(a) shows the effect of the leakage flow rate on the steady pressure distribution in the clearance. The mean leakage flow velocity v_l at the inlet of the radial clearance was evaluated from the leakage flow rate. Figure 4(a) shows that the values of ψ_s decrease from the inlet ($s=0$) to the outlet ($s=1$) of the clearance. The values of ψ_s is larger for larger leakage flow velocity v_l.

Figure 4(b) shows the effect of inlet swirl. The circumferential jet velocity U_J from the swirl generator (No. 9), shown in Fig. 2,

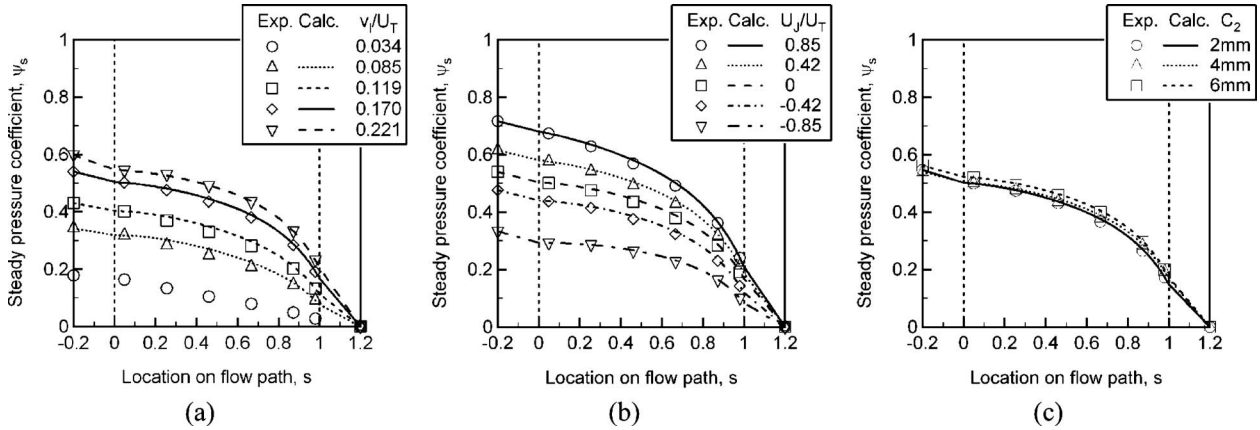

Fig. 4 Steady pressure distribution in the clearance: (*a*) effect of flow rate (C_2=4 mm and U_J=0), (*b*) effect of preswirl flow (C_2=4 mm and v_l/U_T=0.170), and (*c*) effect of clearance (U_J=0 and v_l/U_T=0.170)

Table 1 The values of $U_\theta(0)/U_T$, ξ, and C_{de} in the cases: (*a*) $U_J/U_T=0$ and $C_2=4$ mm, (*b*) $v_l/U_T=0.170$ and $C_2=4$ mm, and (*c*) $U_J/U_T=0$ and $v_l/U_T=0.170$

v_l/U_T	$U_\theta(0)/U_T$	ξ	C_{de}
0.085	0.05	5.51	1.42
0.119	0.18	2.86	1.49
0.170	0.24	1.50	1.59
0.221	0.23	1.08	1.65
U_J/U_T	$U_\theta(0)/U_T$	ξ	C_{de}
0.85	0.44	1.46	1.56
0.42	0.33	1.45	1.57
−0.42	0.22	1.54	1.43
−0.85	0.01	1.78	1.42
C_2 (mm)	$U_\theta(0)/U_T$	ξ	C_{de}
2	0.21	2.09	1.52
6	0.26	1.65	1.57

is defined positive when it is in the direction of disk rotation. Figure 4(*b*) shows that the pressure increases/decreases significantly with the increase/decrease in the jet velocity.

Figure 4(*c*) shows the effect of mean axial clearance C_2. The pressure distribution is not largely affected by the mean axial clearance C_2.

For the computation based on the bulk flow model, the values of the steady circumferential velocity $U_\theta(0)$ at the inlet ($R=R_T$) of the axial clearance, the inlet loss coefficients ξ, and the discharge coefficient C_{de} at the outlet ($R=R_{\text{inner}}$) were estimated by fitting the calculated steady pressure distributions to the experimental results. These values are listed in Table 1 and used for the calculation of unsteady components.

4.2 Normalization of the Fluid Force Moments. The fluid force moment is evaluated here to determine the representative moment to be used for normalization.

The rotation of the disk with an angular velocity of ω will produce a tangential fluid flow in the clearance between the rotating disk and stationary casing with the mean angular velocity of $(1/2)\omega$. The value of "1/2" will be changed depending on various conditions. The tangential flow velocity relative to the location of the minimum clearance is

$$R_T\left(\frac{1}{2}\omega-\Omega\right) \tag{3}$$

If we consider that the pressure distribution in the clearance is produced by the passage of this tangential flow through the minimum clearance, the magnitude of the pressure distribution might be expressed as

$$\Delta P \propto \frac{1}{2}\rho R_T^2\left(\frac{1}{2}\omega-\Omega\right)^2\left(\frac{R_T|\alpha|}{C_2}\right) \tag{4}$$

Then, the normal moment M_{ns} due to the swirl flow can be expressed as

$$M_{ns} \propto \Delta P R_T^2 R_T \propto \frac{1}{2}\rho R_T^5\left(\frac{1}{2}\omega-\Omega\right)\left|\left(\frac{1}{2}\omega-\Omega\right)\right|\left(\frac{R_T|\alpha|}{C_2}\right) \tag{5}$$

If we consider that Ω/ω is a parameter, Eq. (5) can be expressed as follows:

$$M_{ns} \propto \Delta P R_T^2 R_T \propto \frac{1}{2}\rho R_T^5\omega^2\left(\frac{R_T|\alpha|}{C_2}\right)f(\Omega/\omega) \tag{6}$$

Based on the above considerations, the following reference moment M_0 are used for the normalization of the fluid force moment:

$$M_0 = \rho R_T^5\omega^2(R_T|\alpha|/C_2) \tag{7}$$

4.3 Rotordynamic Fluid Force Moment. Figure 5 shows the normalized fluid force moments versus angular velocity ratios at various leakage flow rates in the case of $C_2=4$ mm and $U_J=0$. The velocity $U_T(=R_T\omega)$ at the tip of the disk is used for normalization. Experimental and computational results are shown in Fig. 5.

In the experimental results shown in Fig. 5(*a*), nondimensional normal moments M_n/M_0 are positive in a region with small positive precession speed ratio Ω/ω, which indicates that the normal moment encourages the precession motion in this region. This result is similar to the results of the Ref. [4]. It is also found that M_n/M_0 become larger with an increase in the leakage flow rate in $\Omega/\omega<0$. Figure 5(*b*) shows the nondimensional tangential moment M_t/M_0. The values of M_t/M_0 decrease with the increase in leakage flow rates in $\Omega/\omega<0$.

The results of computation can simulate the trend of distribution of normal and tangential fluid force moments obtained by the experiment although the values are a little different from the experimental results. The cause of this disagreement is not yet clear.

Figure 6 shows the fluid force moments versus angular velocity ratios at various preswirl velocities in the case of $C_2=4$ mm and $v_l/U_T=0.170$. As shown in Fig. 6(*a*), when the preswirl velocity increases, the normal moment increases, hence, the fluid force moments encourage the precession motion in a wider range of Ω/ω. This indicates that the suppression of the inlet swirl flow is

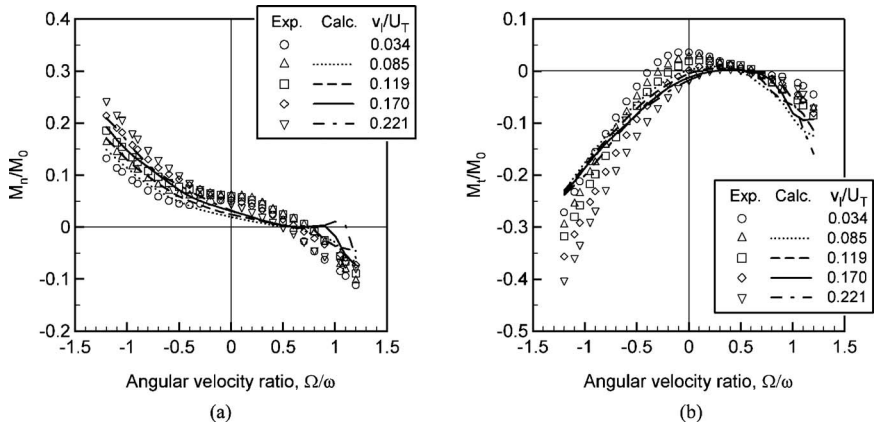

Fig. 5 Effects of leakage flow rates on fluid force moment in the case of $C_2=4$ mm and $U_J/U_T=0$: (*a*) normal moment and (*b*) tangential moment

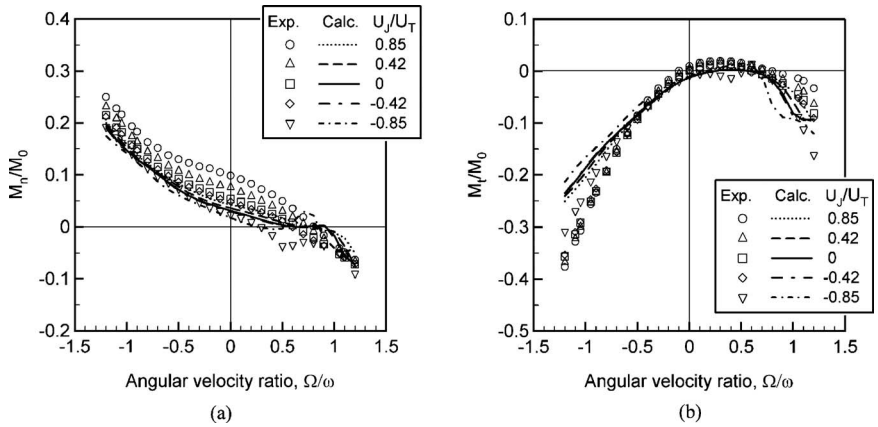

Fig. 6 Effects of preswirl velocities on fluid force moment in the case of C_2=4 mm and v_l/U_T=0.170: (*a*) normal moment and (*b*) tangential moment

effective for avoiding the precession motion. The computation can simulate the preswirl velocity effect qualitatively. However, the effect is not as large as that of the experiment. The tangential moment M_t/M_0 in Fig. 6(*b*) is almost independent of the preswirl velocity in both of the experiment and computation.

Figure 7 shows the fluid force moment in the cases of C_2 =2 mm, 4 mm, and 6 mm at v_l/U_T=0.170 and U_J/U_T=0. Figure 7(*a*) shows that the normal moment M_n/M_0 is not largely affected by the axial clearance C_2. This shows that the normalization by M_0 defined in Eq. (7) is adequate. As shown in Fig. 7(*b*), the tangential moment M_t/M_0 decreases in larger $|\Omega/\omega|$ when the axial clearance C_2 increases.

The effects of the leakage flow rate and the preswirl velocity were also examined for C_2=2 mm and 6 mm. The results are qualitatively the same as those for C_2=4 mm presented here.

4.4 Unsteady Pressure and Velocity Distributions. Figures 8–11 show the unsteady components of pressure and velocity in the clearance for Ω/ω=1.2, 0.3, −0.3, and −1.2 in the case of C_2=4 mm, v_l/U_T=0.170, and U_J/U_T=0, respectively. In each figure, the unsteady pressure component measured in the experiment is shown in (*a*). The unsteady pressure and velocity components obtained by the computation are shown in (*b*) and (*c*), respectively. The experimental and computational pressure distributions are similar. In these figures, the axial clearance is the smallest on the right.

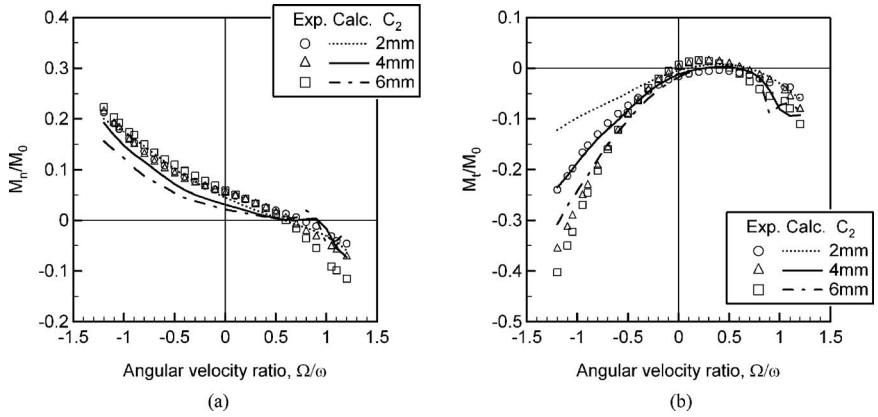

Fig. 7 Effects of axial clearance C_2 on fluid force moment in the case of v_l/U_T =0.170, U_J/U_T=0: (*a*) normal moment and (*b*) tangential moment

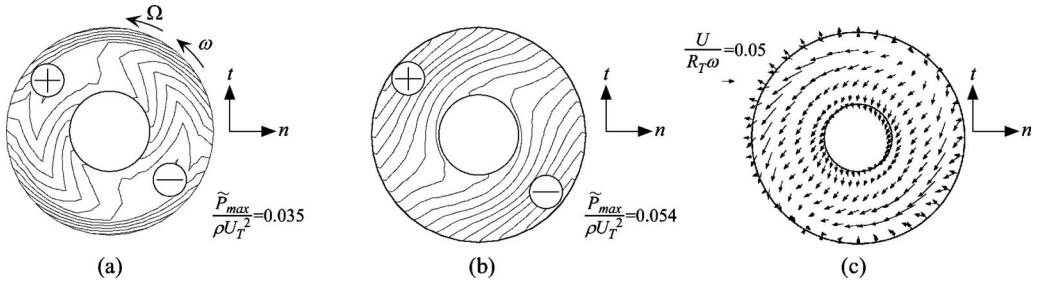

Fig. 8 Unsteady components of pressure and velocity in the clearance for Ω/ω=1.2 in the case of C_2=4 mm, v_l/U_T=0.170, and U_J/U_T=0: (*a*) pressure (exp.), (*b*) pressure (calc.), and (*c*) velocity (calc.)

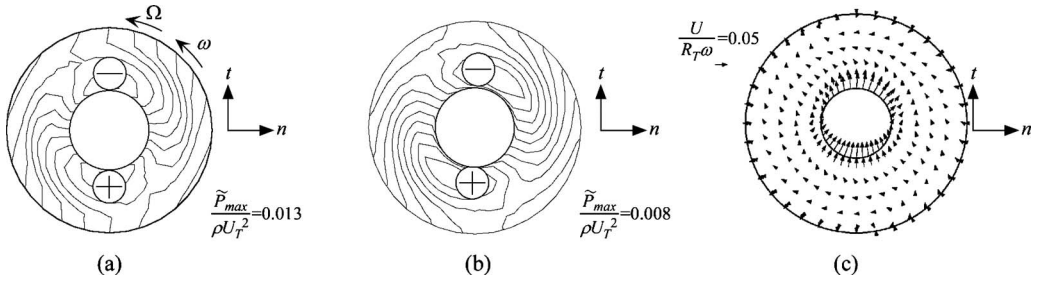

Fig. 9 The same as Fig. 8 for $\Omega/\omega=0.3$

First, we focus on the effects of Ω/ω on the unsteady pressure. We have higher pressure region in the lower part when $\Omega/\omega < 0.5$ and the maximum pressure becomes larger when $|1/2 - \Omega/\omega|$ becomes larger. On the other hand, higher pressure appears in the upper part when $\Omega/\omega=1.2>0.5$. This is caused by the relative circumferential flow with the angular velocity $\omega/2 - \Omega$ passing through the circumferential location with smaller axial clearance. The pressure distribution results in the normal moment M_n and causes the destabilizing region of $0<\Omega/\omega <0.5$.

Second, we consider the velocity disturbance. The radial velocity near the outer radius is negative on the right hand side, where the axial clearance is smaller, at all Ω/ω. This is because the leakage velocity is increased in the region with smaller axial clearance since the leakage flow rate is kept nearly constant by larger resistance of smaller radial clearance C_1, which is kept constant under precession. Near the inner radius, upward velocity is observed when $\Omega/\omega<0.5$ and the magnitude becomes larger when $|1/2-\Omega/\omega|$ becomes larger. On the other hand, downward velocity is observed at $\Omega/\omega=1.2>0.5$. The inward velocity at the inner radius occurs when the relative circumferential flow with the angular velocity $\omega/2-\Omega$ passes through the region, where the clearance decreases so that the continuity equation is satisfied. This effect does not appear at the outer radius since the radial flow there is controlled by the higher resistance of smaller radial clearance C_1 at outer periphery, as mentioned before.

4.5 Effects of Swirl Flow due to Disk Rotation. In order to clarify the contribution of swirl flow on the fluid force moment, the experiments without the rotation of the disk were conducted.

Figure 12 shows the fluid force moment under the precession motions with and without the rotation of the disk at $C_2=4$ mm, $v_l/U_T=0.170$, and $U_J/U_T=0$.

Without rotation, the moments are nearly the same for positive and negative precession, as expected. No destabilizing region is found without rotation. This shows that the destabilization is caused by the swirl flow due to disk rotation.

The disk rotation causes a swirl flow with an angular velocity of $\omega/2$. As shown in Fig. 12(*a*), the swirl flow causes the increase in the normal moment as well as the destabilizing region at small positive angular velocity ratios. The same effect occurs when we increase the preswirl velocity as shown in Fig. 6(*a*). The "difference" shown in Fig. 12 shows the results obtained by subtracting the precession moment without the disk rotation from that with the disk rotation. The values of difference in the normal moment are nearly constant while the tangential moment is proportional to Ω/ω. The constant normal moment difference can be explained from the difference of the tangential fluid velocity relative to the location of the smallest clearance. Without the disk rotation, the fluid angular velocity relative to the smallest clearance is $-\Omega$ while that with disk rotation is $-\Omega+(1/2)\omega$. The difference is $(1/2)\omega$, which does not depend on the value of Ω. The constant normal moment difference can be explained if we consider that

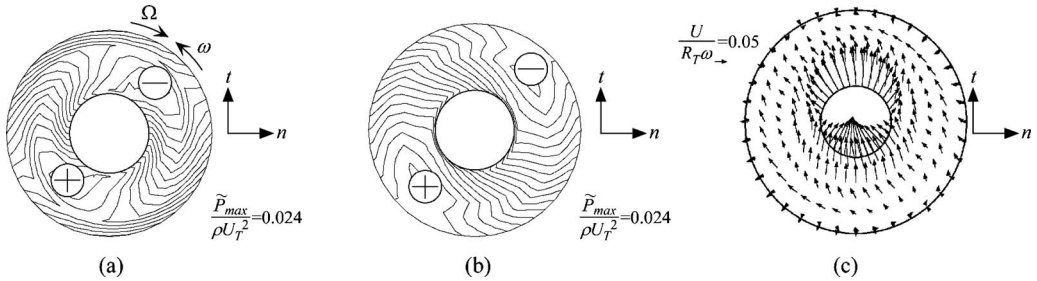

Fig. 10 The same as Fig. 8 for $\Omega/\omega=-0.3$

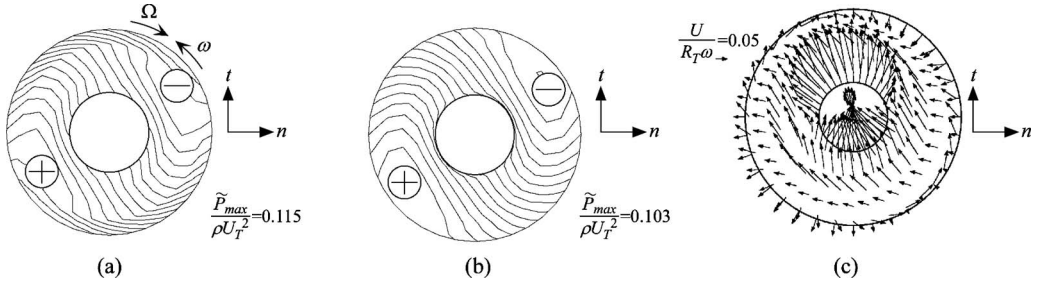

Fig. 11 The same as Fig. 8 for $\Omega/\omega=-1.2$

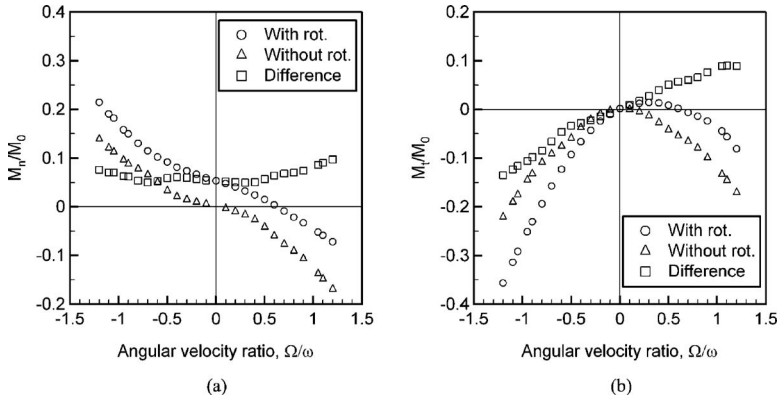

Fig. 12 Fluid force moment in the cases of precession with and without rotation at C_2=4 mm, v_l/U_T=0.170, and U_J/U_T=0: (*a*) normal moment and (*b*) tangential moment

the normal moment is proportional to the relative velocity. The difference of the tangential component can be explained if we assume that the tangential component is proportional to the square of the relative fluid velocity, $M_t=-a\Omega^2$ for the case without disk rotation and $M_t=-a(\Omega-(1/2)\omega)^2+(1/4)a\omega^2$ for the case with disk rotation, where a is a constant.

Figure 13 shows the unsteady pressure distribution under precession motion without the rotation of the disk in the case of C_2 =4 mm, v_l/U_T=0.170 and U_J/U_T=0. Nearly symmetric pattern is obtained for positive and negative precession, as expected. The pattern is quite similar to the cases with disk rotation, shown in Figs. 8–11, depending only on the sign of relative flow velocity $(-\Omega+(1/2)\omega)$.

4.6 Validity of Force Measurement. To validate the fluid force moments obtained by the four-axis force sensor, the unsteady pressure is integrated to estimate the fluid force moment acting on the rear side of the disk. Figure 14 compares the fluid force moments obtained by the force sensor and those evaluated from the unsteady pressure measurements.

As shown in Fig. 14(*a*), the normal moment obtained by the force sensor and that evaluated from the pressure are very close to each other. On the other hand, the difference in the tangential moment shown in Fig. 14(*b*) is larger although similar effect of disk rotation can be observed in both cases. With disk rotation, the calculated result is closer to the result of pressure integration. The tangential moment measured by the force sensor is negatively larger than the calculated value in the region with negative angular velocity ratio. Similar tendency is observed also in Figs. 5–7. Unfortunately, the reason of the larger difference of the tangential moment measured by the force sensor from calculated and evaluated values from the pressure measurement is not clear. However, the values measured by the force sensor can be used at least for qualitative discussions.

5 Conclusions

(1) The fluid force moment encourages the precession motion in a region with small positive angular velocity ratios.
(2) With the increase in the leakage flow rate in the clearance, the normal moment changes. However, the range of angular velocity ratios in which the normal moment encourages the precession motion is not affected largely by the leakage flow rate.
(3) With the increase in the preswirl velocity at the inlet of the radial clearance, the normal moment increases significantly and the range of angular velocity ratios in which the normal moment encourages the precession motion enlarges drastically.
(4) With the increase in the axial clearance C_2, the normal moment does not change largely.
(5) The normal moment caused by the precession motion without the rotation of the disk does not have the effect of encouraging the precession motion. So, the destabilizing moment is caused by the rotation of the disk.
(6) The rotordynamic moments can be understood reasonably by considering the swirl velocity relative to the location with minimum clearance.
(7) The bulk flow model can simulate the general characteristics of precession moment but more elaborate model might be needed for quantitative evaluation.

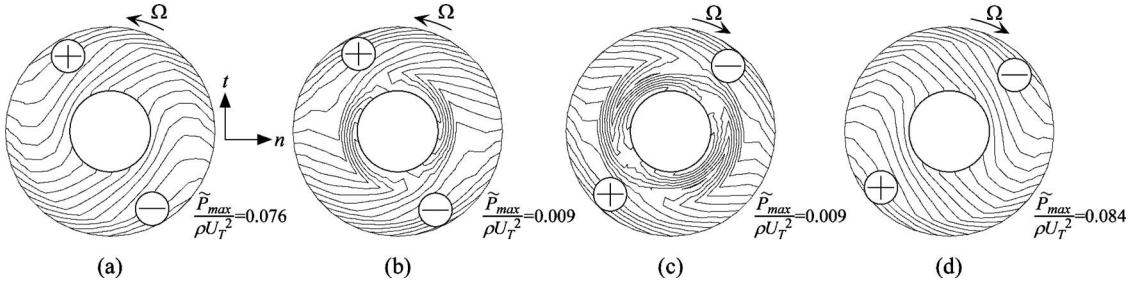

Fig. 13 Experimental unsteady components of pressure in the clearance under precession motion without rotation in the case of C_2=4 mm, v_l/U_T=0.170, and U_J/U_T=0 at (*a*) Ω/ω=1.2, (*b*) Ω/ω=0.3, (*c*) Ω/ω=−0.3, and (*d*) Ω/ω=−1.2

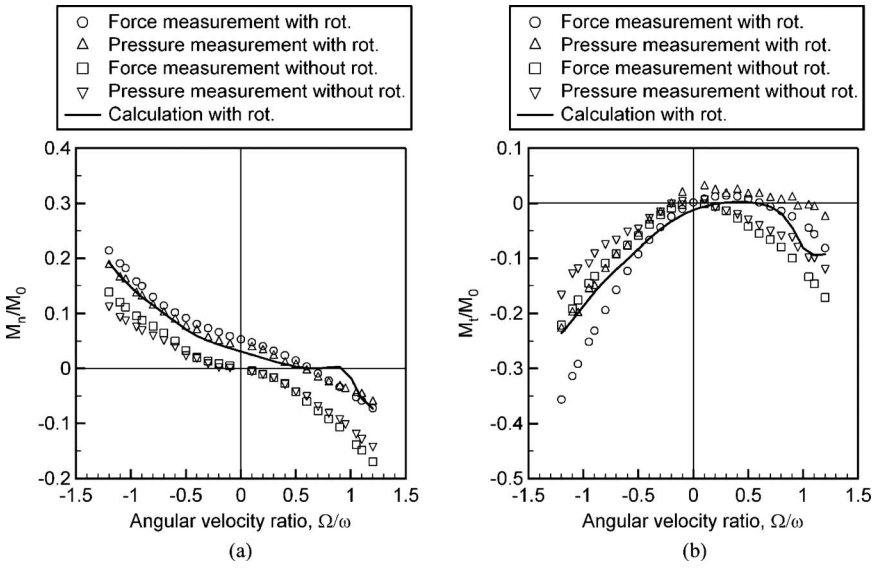

Fig. 14 Comparison of fluid force moments obtained by the force sensor, the unsteady pressure, and the computation between the conditions of precession with and without rotation in the case of C_2=4 mm, v_l/U_T=0.170, and U_J/U_T=0: (*a*) normal moment and (*b*) tangential moment

Acknowledgment

Bingwei Song would like to thank the China Scholarship Council for their financial support during his stay in Osaka University for carrying out this research. The authors would like to thank Dr. Takayuki Suzuki for his help in conducting the experiments.

Nomenclature

C_1, C_2 = radial and axial clearances
C_{de} = discharge coefficient at the outlet of the axial clearance
D_T = diameter of the disk is 0.299 (m)
$H_2(0)$ = width of axial clearance depending on time is $C_2-|\alpha|R_T e^{i\Omega t}$ at the inlet
M_n, M_t = normal and tangential fluid force moments
M_{ns} = normal moment due to swirl flow
M_0 = reference fluid moment is $\rho R_T^5\omega^2(R_T|\alpha|/C_2)$
n = coordinate directed to the minimum axial clearance
P = pressure
$P_{\text{downstream}}$ = pressure downstream of the axial clearance
P_{upstream} = pressure upstream of the axial clearance
Q = volume flow rate
R = radius
R_{inner} = inner radius of the casing is 0.0475 (m)
R_T = disk radius is 0.1495 (m)
s = nondimensional coordinate is $S/(R_T-R_{\text{inner}})$
S = coordinate along the meridional streamline in the axial clearance
t = coordinate normal to n-coordinate or time
U = velocity
U_J = jet velocity from the swirl generator
U_s, U_θ = s and θ components of the velocity
U_T = tip velocity of the disk is $R_T\omega$
v_l = mean leakage flow velocity at the inlet of the radial clearance is $Q/(\pi D_T C_1)$
$|\alpha|$ = angular displacement of the shaft is 0.48 (deg)
ρ = density of working fluid is 997.07 Kg/m^3
Ω = angular velocity of the precession motion
ω = angular velocity of the rotational shaft
ξ = loss coefficient at the inlet of the axial clearance
ψ_s = steady pressure coefficient is $(P-P_{\text{downstream}})/(\rho U_T^2)$

Superscript

$\sim$ = unsteady component

References

[1] Tomita, H., and Kawamura, M., 1965, "Self-Excited Vibration in Francis Turbines," Toshiba Review, **20**(8), pp. 787–791.
[2] Ohashi, H., Sakurai, A., and Nishihama, J., 1988, "Influence of Impeller and Diffuser Geometries on the Lateral Fluid Forces of Whirling Centrifugal Impeller," NASA CP 3026, pp. 285–306.
[3] Guinzburg, A., Brennen, C. E., Acosta, A. J., and Caughey, T. K., 1993, "The Effect of Inlet Swirl on the Rotordynamic Shroud Forces in Centrifugal Pump," ASME J. Eng. Gas Turbines Power, **115**, pp. 287–293.
[4] Ohashi, H., Imai, H., and Tsuchihashi, T., 1991, "Fluid Force and Moment on Centrifugal Impellers in Precession Motion," FED (Am. Soc. Mech. Eng.) **119**, pp. 57–60.
[5] Yoshida, Y., Tsujimoto, Y., Ohashi, H., Saito, A., and Ishizaki, S., 1997, "Measurement of the Flow in Backshroud/Casing Clearance of Precession Centrifugal Impeller," Int. J. Rotating Mach., **3**(4), pp. 259–268.
[6] Tsujimoto, Y., Yoshida, Y., Ohashi, H., Teramoto, N., and Ishizaki, S., 1997, "Fluid Force Moment on a Centrifugal Impeller Shroud in Precession Motion," ASME J. Fluids Eng., **119**, pp. 366–371.
[7] Song, B., Horiguchi, H., and Tsujimoto, Y., 2009, "Rotordynamic Moment Acting on Rotational Disk in Whirling Motion," Proceeding of the 61st Turbomachinery Society of Japan Conference, pp. 15–20.
[8] Childs, D. W., 1989, "Fluid-Structure Interaction Forces at Pump-Impeller-Shroud Surfaces for Rotor Dynamics Calculation," ASME J. Vib., Acoust., Stress, Reliab. Des., **111**, pp. 216–225.

Axial Flow Fan Tip Leakage Flow Control Using Tip Platform Extensions

Ali Aktürk
Graduate Research Assistant
e-mail: aua162@psu.edu

Cengiz Camci[1]
Professor
e-mail: cxc11@psu.edu

Department of Aerospace Engineering,
Turbomachinery Aero-Heat Transfer Laboratory,
Pennsylvania State University,
University Park, PA 16802

Performance of an axial flow fan unit is closely related to its tip leakage mass flow rate and level of tip/casing interactions. The present experimental study uses a stereoscopic particle image velocimeter to quantify the three dimensional mean flow observed near the blade tip, just downstream of a ducted fan unit. After a comprehensive description of the exit flow from the baseline fan, a number of novel tip treatments based on custom designed pressure side extensions are introduced. Various tip leakage mitigation schemes are introduced by varying the chordwise location and the width of the extension in the circumferential direction. The current study shows a proper selection of the pressure side bump location and width are the two critical parameters influencing the success of each tip leakage mitigation approach. Significant gains in the axial mean velocity component are observed when a proper pressure side tip extension is used. It is also observed that a proper tip leakage mitigation scheme significantly reduces the tangential velocity component near the tip of the axial fan blade. Reduced tip clearance related flow interactions are essential in improving the energy efficiency of ducted fan systems. A reduction or elimination of the momentum deficit in tip vortices is also essential to reduce the adverse performance effects originating from the unsteady and highly turbulent tip leakage flows rotating against a stationary casing. [DOI: 10.1115/1.4001540]

1 Introduction

The flow-field between the stationary casing and the rotor tip of an axial fan is complex because of the interaction of the leakage flow, the annulus wall boundary layer, and the rotor wake. An inherent pressure difference between the pressure and suction sides of the blade tip generates a tip leakage flow that is responsible for a substantial portion of aerodynamic losses in axial flow fans. The leakage flow also rolls into a highly three dimensional tip leakage vortex with significantly turbulent and unsteady flow features in each passage. Tip leakage vortex is a complicated flow phenomenon that is one of the dominant mechanisms of noise generation by unsteady interactions in a turbomachinery system. It is also one of the major energy loss mechanisms for the axial flow fan systems. Despite the close relation between the tip leakage flow and the performance of axial fans, there has been limited amount of information about the three dimensional flow structure of leakage vortex in open literature [1–4].

Inoue et al. [5] made detailed flow measurements before and behind an axial flow rotor with different tip clearances. In their study, they investigated the clearance effect on the behavior of the tip leakage flow. Furukawa et al. [6] also investigated the breakdown of the tip leakage vortex in a low speed axial flow compressor. Reducing the tip leakage mass flow rate improves the aerodynamic performance of axial flow fans and compressors. Implementation of treatments in the nonrotating part over the blade tip is also an efficient way of tip leakage flow reduction. References [7,8] investigate different casing treatments for axial flow compressors.

The wake developed from an axial flow fan has a strong influence on the system performance. It is a significant source of aerodynamic loss and affects the efficiency and vibration characteristics. References [9–11] deal with extensive investigations of the wake flow features such as mean velocities, turbulence, and decay characteristics on the turbomachinery performance.

Stereoscopic particle image velocimetry (SPIV) is an effective way of measuring all three velocity components of an instantaneous flow-field over a selected area [12–16]. A comprehensive discussion of the specific SPIV technique used in this paper is given by Kahveci and Camci [13–15]. Yoon and Lee [16] investigated the flow structure around an axial flow fan using the SPIV technique. The time averaged results clearly show the evolution and dissipation of tip vortices. Yen and Lin [17] analyzed the exit flow performance and properties of an axial flow fan with winglet-blades at various impeller angles using SPIV. The velocity profiles show the most stable and the best fan performance resulting from winglet-blades, which increase the lift and reduce the drag. Wernet et al. [18] made phase-locked three-dimensional digital particle image velocimetry (DPIV) measurements near the tip region of a low speed compressor rotor to characterize the behavior of the rotor tip clearance flow. A comparison of the DPIV measurements to the Navier–Stokes flow simulations was also done.

Corsini et al. [19–22] presented the results of a computational study of an axial flow fan using "improved tip concepts." The first two end-plates were with constant and variable thickness distributions, while the last two were designed by combining the end-plates with a stepped gap on the tip. The investigation was based on a finite element Navier–Stokes solver for the physical interpretation of the detailed 3D leakage flow-field. The specific fan performance experiments have shown that the improved tip concepts introduced a small performance derating, but the efficiency curves give evidence of an improvement with a better peak performance and a wider high efficiency curve toward the rotor stall margin. An aero-acoustic investigation showed a reduction in the rotor aero-acoustic signature.

The computationally predicted loss coefficients in Ref. [22] showed that the highest loss regions were always observed near the leakage vortex core. The computational comparison of mechanical energy loss within the gap showed that the tip end-plates lead to a reduction in mechanical energy loss within the gap.

The present experimental study used stereoscopic particle image velocimetry measurements at the exit of the seven-bladed

[1]Corresponding author.

Contributed by the Fluids Engineering Division of ASME for publication in the JOURNAL OF FLUIDS ENGINEERING. Manuscript received July 17, 2009; final manuscript received February 20, 2010; published online May 14, 2010. Assoc. Editor: Zvi Rusak.

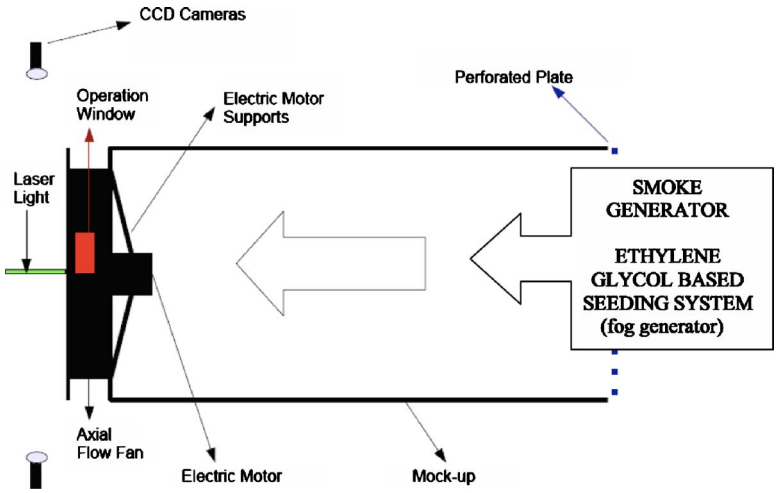

Fig. 1 Test rig and stereoscopic SPIV setup

axial fan rotor. The fan rotor used for the experiment is widely used in the air conditioning industry. All of the experiments were performed at constant rotational speed of the fan (859 rpm).

The main objectives of the current study are summarized as follows:

- to investigate the characteristics of tip leakage flow and tip vortex in an axial flow fan using a high spatial resolution and nonintrusive measurement technique; all three components of the tip region exit flow-field are measured using the SPIV technique
- to eliminate the adverse effects of the tip vortex by designing novel rotor tip geometries using pressure side extensions
- to reduce the local leakage mass flow rate and momentum deficit in tip-vortex-driven flow structures
- to increase the energy efficiency of axial flow fan systems
- to provide high quality phase-locked instantaneous flow data for further studies in aero-acoustics of tip treated axial flow fans

2 Experimental Setup

2.1 Test Rig. The test rig that consists of an axial flow fan, a mock-up unit, and an electric drive system, as shown in Fig. 1, was designed to investigate the rotor exit flow phenomena using a SPIV system. The setup also has provisions for seeding the fan flow-field with a smoke generator using a fluidized bed. The smoke generator is located near the inlet section of the mock-up unit where a perforated plate controlling the fan loading is mounted. The electric motor driving the fan rotor is speed controlled by an AC inverter unit. The current phase-locked SPIV measurements are triggered by using an optical once-per-revolution device located near the hub of the rotor inlet. An infrared beam is reflected from a highly reflective surface attached to the rotor hub. This once-per-revolution pulse provides a phase-locked triggering of the SPIV data collection system. The relative position of the rotor can be adjusted accurately in relative to the position of the laser light sheet that contains the rectangular SPIV measurement area.

2.2 Ducted Fan. Figure 2 shows a seven-bladed axial flow fan unit including the orientation of the SPIV system components. The geometric specifications are presented in Fig. 3. A perforated plate at the inlet section of the mock-up unit is used for creating realistic fan loading conditions. The tips of the blades are modified through a removable "operation window," as shown in Fig. 1. Only one blade tip out of seven blades is modified since the current SPIV system is capable of measuring in the immediate vicinity of a "selected" blade tip due to the phase-locked and instantaneous nature of the SPIV measurements. A precision machined 0.762 mm (0.030 in.) thick thermoplastic layer was used for the selected tip platform design. The tip platform design was attached to the precision machined tip area in a nonintrusive way through the operation window, as shown in Fig. 1. The modifications made on the selected tip did not cause a measurable rotor balance problem since the rotor was manufactured out of a relatively light weight thermoplastic material. The current rotor blades have serrated trailing edges for effective mixing of the blade boundary layers in the wake of each blade. The serrated trailing edges also provide an effective mixing of individual tip vortices with the wakes of the seven blades in the rotating frame of reference. It should be noted that the comparison of the flow with serrated trailing edges with a smooth trailing edge flow is not the subject of the current paper.

2.3 Fan Performance. The performance of the fan unit is measured under three different loading conditions. The first performance point (80 m^3,140 Pa) shown in Fig. 4 is obtained by using a perforated steel plate having an open area ratio of 19.6%. A second perforated plate using a slightly larger open area ratio of 42.5% provides the middle point (280 m^3/min, 88 Pa) in the performance curve, as shown in Fig. 4. The third point with the highest volumetric flow rate at 340 m^3/min is obtained when there is no perforated plate installed at the inlet section of the mock-up unit. The pressure change across the fan is measured by using pitot static holes mounted on all four sides of the mock-up unit. Wall-static pressures from all four sides are averaged. For the mass flow rate measurements, a hot-wire-based volumetric flow measurement device is used at the rotor downstream.

2.4 SPIV System. The PIV technique measures instantaneous velocity components of a flow-field over a determined area. Small particles that go with the flow are introduced into the fluid flow, and the region of interest is illuminated by the light sheet provided by subsequent Nd:YAG (yttrium aluminum garnet) laser pulses lasting as short as a few nanoseconds. The subsequent step is the recording of the displacement of particles via two high sensitivity CCD cameras.

The scattered light from the seeding particles is recorded by two different cameras for simultaneous recording on digital media. The initial position of a particle is recorded on the first frame of the camera right after the first laser pulse fires. In general, a typical duration of a laser pulse is about 30 ns in a flow-field similar to the current study. Its final position is recorded in the same way on the second frame of the same camera when the second laser pulse fires. The time interval between the two frames is usually determined by the mean flow speed in the area of in-

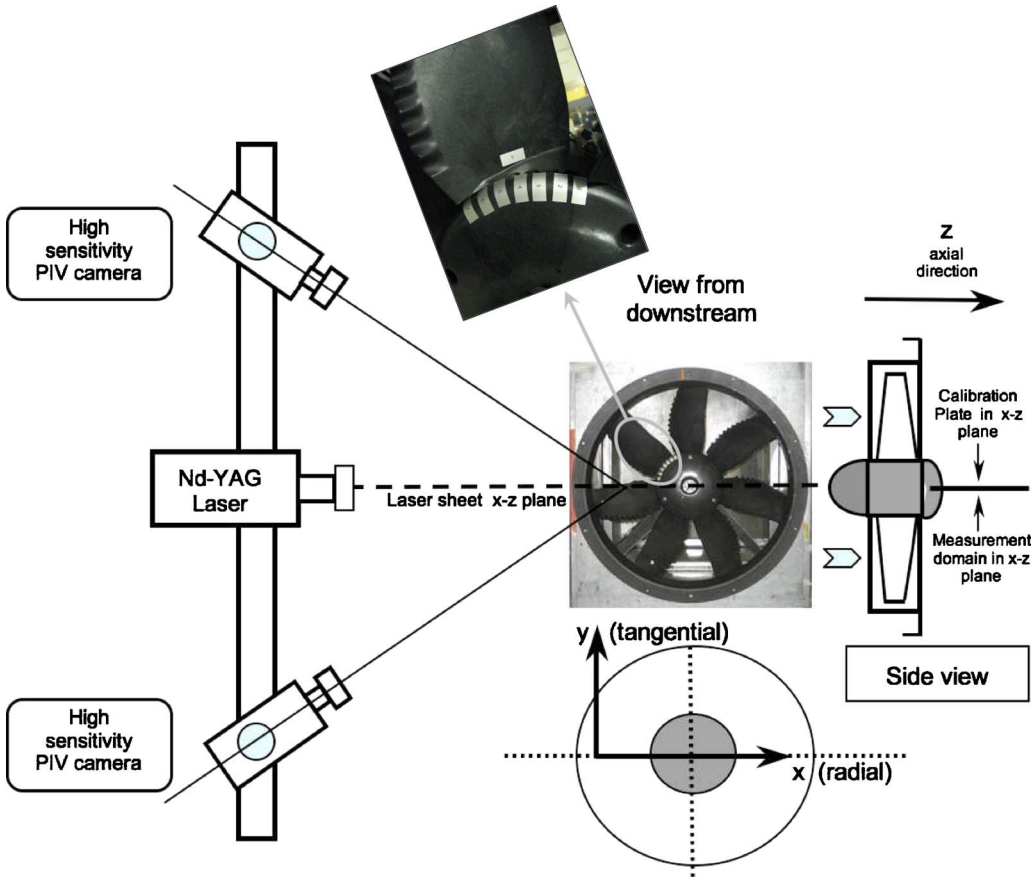

Fig. 2 Axial flow fan as seen from the exit plane and the SPIV system orientation

vestigation. The order of magnitude of this adjustable time separation between the two frames is "microseconds." Since the displacement of the particle and the time interval between the two subsequent laser pulses are known, the velocity of the particle can be calculated by the simple equation speed=distance/time. A comprehensive explanation of this technique is given in Refs. [12–16].

In 3D PIV, there is an additional camera viewing the field from a different angle. The two-dimensional image obtained by each camera is slightly different from each other, and afterwards, they are combined to produce the three-dimensional velocity information. Stereoscopic vision principles are instrumental in this process of combining the two planar images obtained from the two cameras viewing the same flow-field simultaneously. The data reduction in a SPIV system requires the processing of four independent images from the two cameras. For 3D analysis, the 2D calibration images need to be converted additionally into the 3D data by a direct linear transform (DLT) model in order to calculate the third component of the velocity. Correlation techniques are used to obtain raw vector maps out of image pairs taken during the experiments, and a number of calculation methods are used to evaluate these vector maps. In summary, the three dimensional space defined by the planar measurement area and the finite thickness of the laser sheet is analytically described in relation to the highly distorted images captured by the two CCD chips in each of the two cameras. The distortions observed on the planar CCD images are generated by the angled position of the two cameras. For example, a perfect cube in the measurement space is seen as a distorted cube in each one of the two images generated by the two cameras.

The current study uses high sensitivity cameras that are essential in high speed flow measurements. Two of the 80C60 HiSense PIV/PLIF cameras with 1024×1280 pixels are used with 80N57

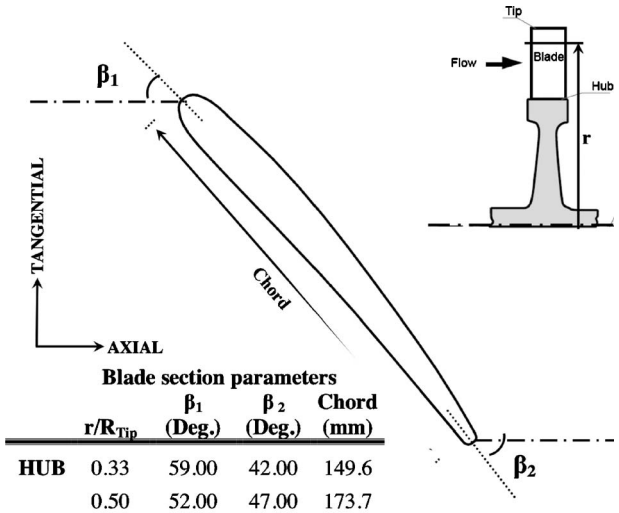

Blade section parameters

	r/R_{Tip}	β_1 (Deg.)	β_2 (Deg.)	Chord (mm)
HUB	0.33	59.00	42.00	149.6
	0.50	52.00	47.00	173.7
	0.66	46.00	54.00	161.9
	0.83	44.00	63.00	133.3
TIP	1.00	31.00	69.00	116.8

Geometric parameters of axial flow fan

Number of Blades	7
Tip Radius	384.8 mm (15.15")
Hub Radius	127.0 mm (5.00")
Rpm	859
	T =2.54 mm (0.1")
Tip Clearance	t/h=0.1"/(15.15"-5.0") ≈ 1 % relative to blade height

Fig. 3 Geometric and blade section parameters of the axial flow fan

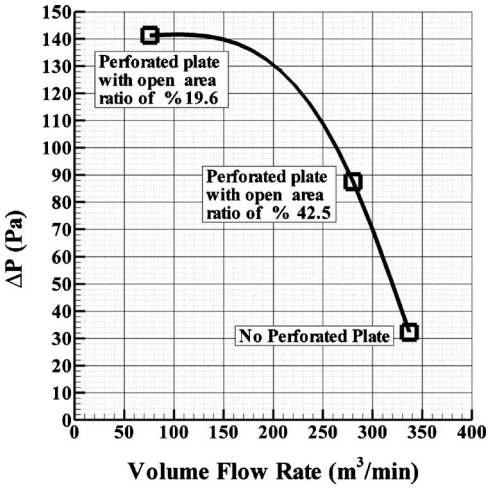

Fig. 4 Axial flow fan performance

personality module fitted to processor and a Nikon micro-Nikkor 60/2.8 objective for each camera. The calibration plate, the cameras, the Nd:YAG pulsed laser unit, and the axial fan rotor blades are shown in Fig. 2. The initial calibration procedure requires that the laser light sheet generated by the Nd:YAG laser is aligned with the calibration plate carrying a standard high precision square grid.

3 Experimental Methodology

3.1 Measurement Domain. The axial (y), radial (x), and tangential (z) components of velocity profiles were simultaneously measured near the tip region of the fan under the influence of a few novel tip platform extensions designed throughout this investigation. Figure 5 shows the measurement domain, which is a rectangle in the x-y plane located just downstream of the rotor. The x-y plane is horizontal and contains the axis of rotation. Most of the SPIV distributions covered a spanwise region from $r/R_{\text{tip}}=0.6$ to $r/R_{\text{tip}}=1.3$. This measurement area corresponds to a region covering the last three quarters of the blade height, including the tip region flow. The spanwise velocity distributions shown in Figs. 8–11 are obtained at an axial position 46 mm away from the rotor exit plane. The radial direction is also marked with r/R_{tip} in order to mark the exact position of the blade root and tip in the spanwise distributions of velocity. r/R_{tip} is approximately 0.33 at the blade root location (hub).

3.2 Specific Rotor Positions for Phase-Locked Measurements. The results from the custom designed tip platform extensions are compared with the results obtained from a baseline tip at two different tip clearance levels. All three components of the velocity vector were measured for seven circumferential positions of the rotor (with respect to the SPIV measurement plane). These locations were chosen by dividing the rotor blade pitch into seven equiangular regions. Although the measurements were performed at seven positions, only the most pertinent data from three selected positions are presented. The selected positions include blade tip leading edge, midchord, and trailing edge (locations 3, 4, and 5).

Table 1 Uncertainties of ensemble averaged velocity components

	Radial velocity	Axial velocity	Tangential velocity
$N=50$	$1.19\times10^{-1}U_a$	$1.11\times10^{-1}U_a$	$1.98\times10^{-1}U_a$
$N=100$	$7.47\times10^{-2}U_a$	$6.44\times10^{-2}U_a$	$1.28\times10^{-1}U_a$
$N=150$	$6.01\times10^{-2}U_a$	$4.85\times10^{-2}U_a$	$8.89\times10^{-2}U_a$
$N=200$	$4.77\times10^{-2}U_a$	$3.97\times10^{-2}U_a$	$7.93\times10^{-2}U_a$
$N=250$	$3.99\times10^{-2}U_a$	$3.39\times10^{-2}U_a$	$6.68\times10^{-2}U_a$

3.3 Statistical Stability of SPIV measurements. An adequate number (N) of SPIV speckle images should be recorded and processed for satisfying the statistical requirements for accurate mean velocity measurements. The ensemble average of measured velocity components approaches to a true mean as N goes to infinity. During an ensemble averaging of finite number of instantaneous velocity measurements, it should be noted that their average may have a deviation from the true mean value. This deviation is closely related to the sample size (N), which is a measure of the statistical stability of this ensemble averaging process. Table 1 shows deviations calculated from the measured data for the radial, axial, and tangential velocity components obtained by averaging 50, 100, 150, and 250 PIV speckle images. Standard errors are calculated by using the central limit theorem [23]. The central limit theorem states that uncertainty can be approximately equal to the standard deviation of measured values (σ) divided by $\sqrt{N}$ (i.e., $\epsilon=\sigma/\sqrt{N}$). The uncertainties are estimated at locations of the highest standard deviations of individual components for each sampling image size. They are normalized by using averaged axial velocity (U_a) calculated from the mass flow rate of the fan for the condition that experiments are conducted (340 m^3/min, 32 Pa). Note that the most uncertainties are smaller than 9% for the ensemble image size of more than 150 images.

Based on the examination of data convergence with the number of speckle images, the sampling image size (N) is selected to be 170. Figure 6 presents the influence of the ensemble averaging sample size on the spanwise distribution of the most significant velocity component "axial component." The baseline blade tip is used in this experiment with a nominal tip clearance of 1% of the

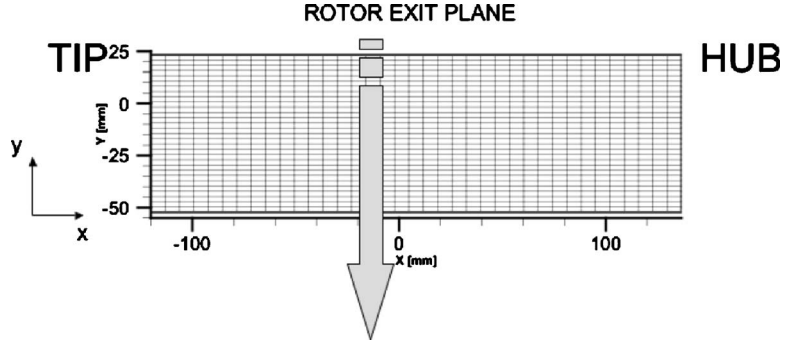

Fig. 5 SPIV measurement plane (horizontal) downstream of the rotor exit and the coordinate system

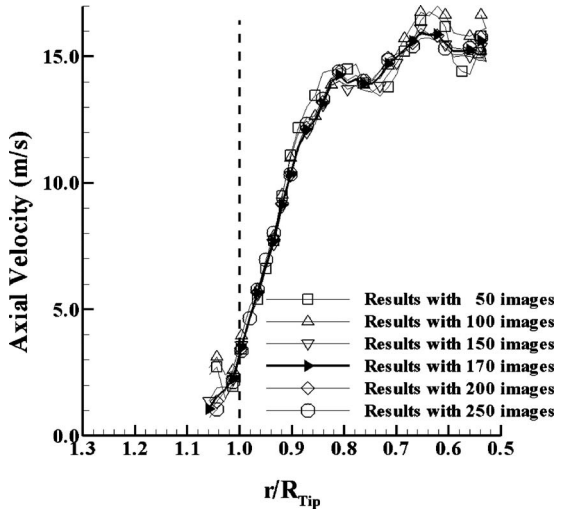

Fig. 6 Influence of the sample size on SPIV ensemble averaging

blade height. The spanwise region where $0.9 \leq r/R_{\text{tip}} \leq 1.02$ is not significantly influenced from the choice of the ensemble averaging sample size. The sample sizes of 150, 170, 200, and 250 produce very similar spanwise distributions in this region near the tip. All SPIV experiments presented in Figs. 8–13 are conducted using an ensemble averaging sample size of 170.

3.4 Tip Clearance Values. An effective control of the tip leakage flow was achieved using different tip platform extensions. The term "control of tip leakage flow" in this study could be defined as the "minimization of tip leakage flow mass flow rate." The baseline profile was evaluated at two different tip clearance values of 0.1 in. and 0.135 in., corresponding to 1% and 1.35% of the blade height. All of the "tip platform extensions" used in this study were evaluated at tip clearance values of 0.1 in., corresponding to 1% of the blade height.

3.5 The General Impact of Tip Platform Extensions. The main goal of this study is to minimize the tip leakage flow by interfering with the flow near the pressure side corner of the blade tip region. A new static pressure distribution near the blade tip section is established by the novel tip platform extension designs shown in Fig. 7.

The impact of the suggested tip platform extensions is visible in the "magnitude enhancements" of the axial velocity component downstream of the tip region. It is also highly visible that the strong tangential velocity components induced by the baseline tip

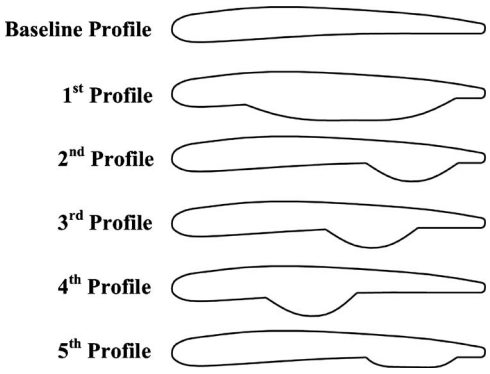

Fig. 7 Novel tip platform extensions for tip leakage mitigation

are almost eliminated by an effective tip platform design. This observation is very clear, especially near the tip diameter of the rotor exit flow.

3.6 Geometrical Definition of the Five Tip Platform Extensions. The design idea behind the present tip platform extensions is based on estimating the blade chordwise position where the tip leakage potential is the highest for a given tip profile. It is obvious that the leakage potential is represented by the static pressure differential imposed by the shape design of the blade profile. The initial computational fluid dynamics based flow prediction may be effective in finding the chordwise region where the leakage mass flow rate is maximum.

The tip platform extensions were designed by adding constant-thickness "pressure side bumps" of different designs to the base profile, as shown in Fig. 7. The thickness of the platform extended on the pressure side of the blade is about 0.030 in. (0.762 mm) for all designs used in this investigation. Initially, a wide bump between the trailing edge and the leading edge was suggested as Profile 1 in Fig. 7. The maximum width of the bump was chosen as the same as the thickness of the airfoil at the bump centerline location. Three more tip platform extensions were derived from Profile 1 by dividing the bump width of Profile 1 into three almost equal chordwise sections. The three new tip platform extensions are termed Profile 2 (near the trailing edge), Profile 3 (middle of the wide bump), and Profile 4 (almost midchord). The bump maximum widths were kept the same. Profile 5 is a derivative of the trailing edge bump named as Profile 2. Profile 5 uses a relatively small platform area when compared with all other tip platform extensions. The external contour of Profile 5 is almost parallel to the baseline profile, except the end points where blending is suggested.

Only one rotor blade at a time out of seven blades was retrofitted with a suggested design. Each experiment had six baseline blades and a seventh blade with the suggested tip platform extension. The effective clearance was kept same for all seven blades.

4 Experimental Results and Discussion

Figures 8–11 show the results of the exit flow measurements of the axial flow fan at the highest volumetric flow rate condition defined as 340 m^3/min, 32 Pa. Figure 12 complements these results from a data set obtained at the minimum mass flow rate condition where the pressure loading is maximum (80 m^3/min, 140 Pa). All the velocity profiles are plotted at 1.811 in. (46 mm) downstream of the fan.

In addition to the magnitude of the velocity vector (total velocity), the radial, tangential, and axial components of the velocity vector at the exit of the rotor are provided in function of the spanwise distance.

4.1 Baseline Tips. Near the tip, where $r/R_{\text{tip}} \geq 0.9$, the two base profiles show very similar trends in Fig. 8. The total velocity is significantly reduced in the core of the passage, where $r/R_{\text{tip}} \leq 0.9$, when the tip clearance is high at 0.135 in. level. The $t = 0.100$ in. and $t = 0.135$ in. clearance base profiles show significant momentum deficit occurring in the core of the tip vortices from the two baseline tips (without any tip platforms). The tip vortices from the baseline cases greatly influence the core flow and reduce the mean kinetic energy when they are mixed with the wake fluid. The wake fluid and the tip leakage vortex are also modified and mixed by the serrated trailing edge geometry, as shown in Fig. 2. This observation indicates that a significant momentum deficit in the core of the passage vortex exists because of the tip vortex, and this momentum deficit becomes higher when the clearance increases. The direct impact of the baseline tip vortex is visible in the measured total velocity in the core of the passage, even under strong mixing conditions induced by the wake fluid originating from the serrated trailing edges.

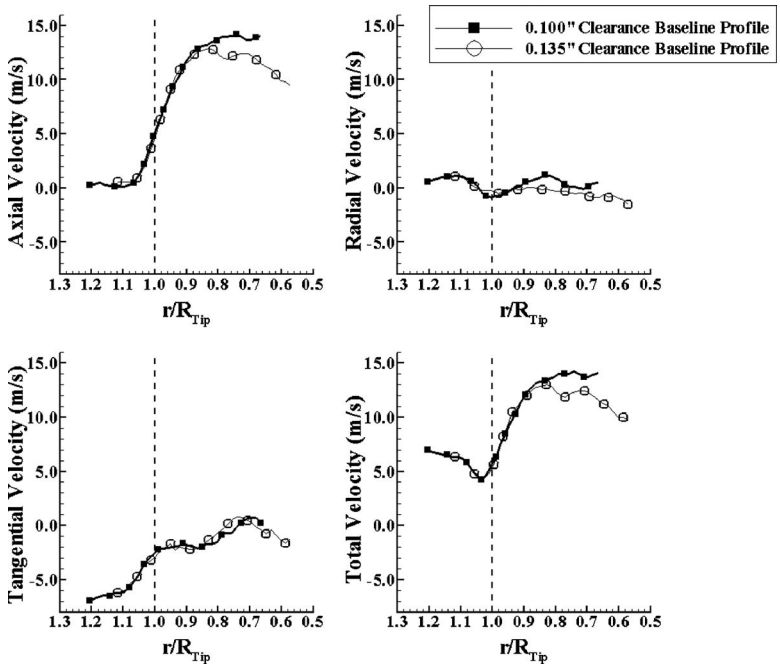

Fig. 8 Velocity profiles measured at location 3 for two different tip clearances

4.2 The Radial Component. The radial components for all cases, as shown in Figs. 8–12, are all very small magnitudes, around ± 1 m/s. There is no significant influence on the magnitude of the baseline clearance or the type of tip treatment on the magnitude of the radial component at all spanwise locations.

4.3 Influence of Tip Platform Extensions on the Tangential Component. When the axial velocity component in Fig. 9 is compared with the total velocity, a striking observation in the tip region is apparent. The total velocity for the baseline tips is much higher than the axial component, where $r/R_{\text{tip}} \geq 1.05$. However,

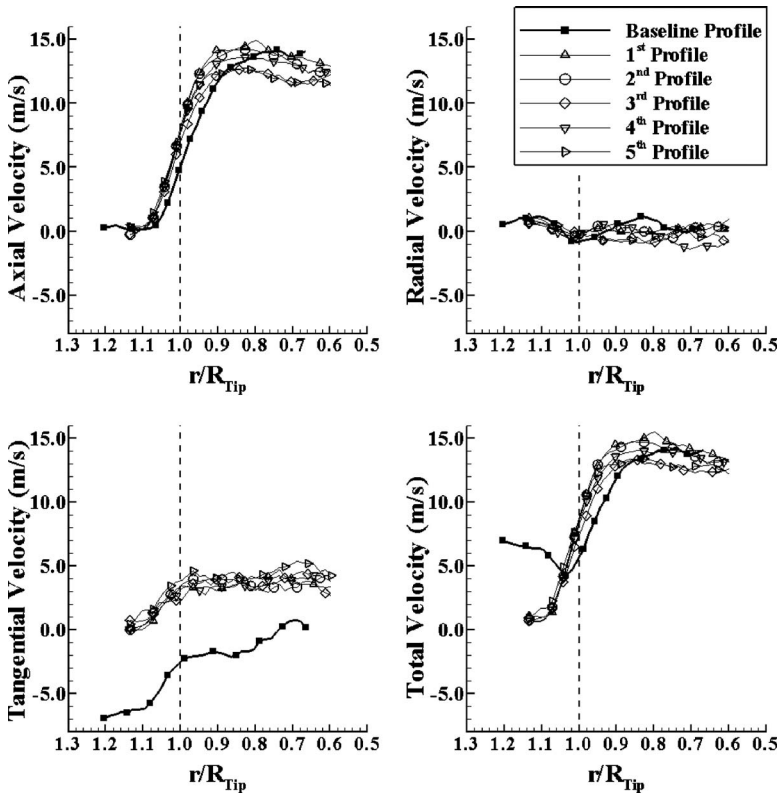

Fig. 9 Velocity profiles measured at location 3 (340 m^3/min, 32 Pa)

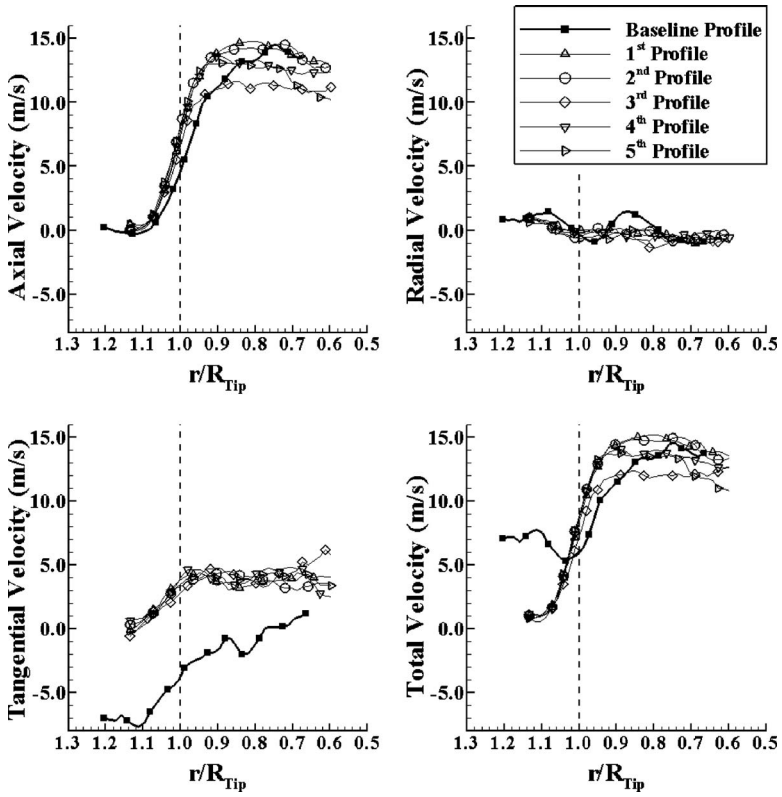

Fig. 10 Velocity profiles measured at location 4 (340 m^3/min, 32 Pa)

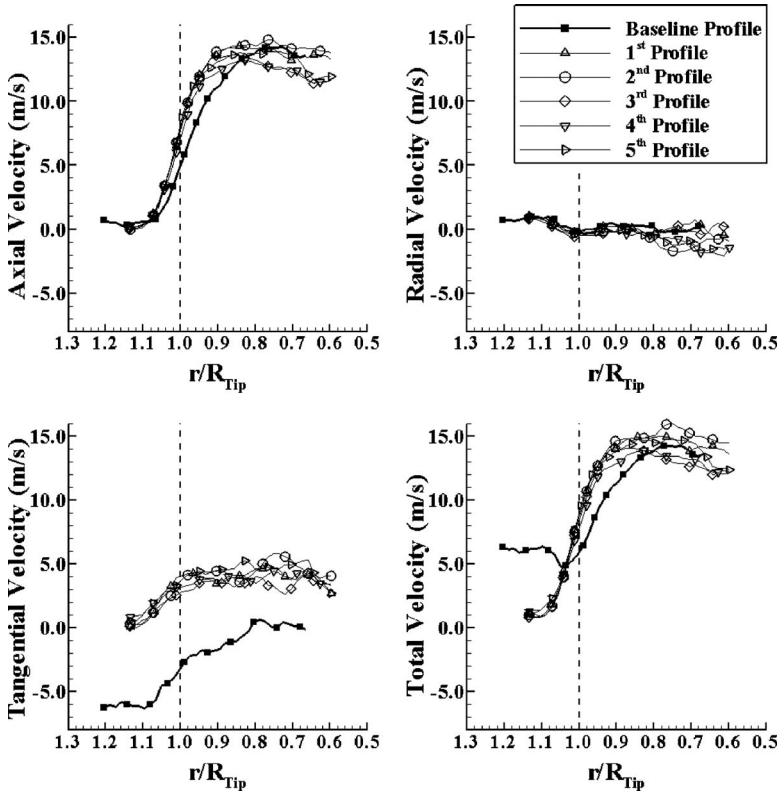

Fig. 11 Velocity profiles measured at location 5 (340 m^3/min, 32 Pa)

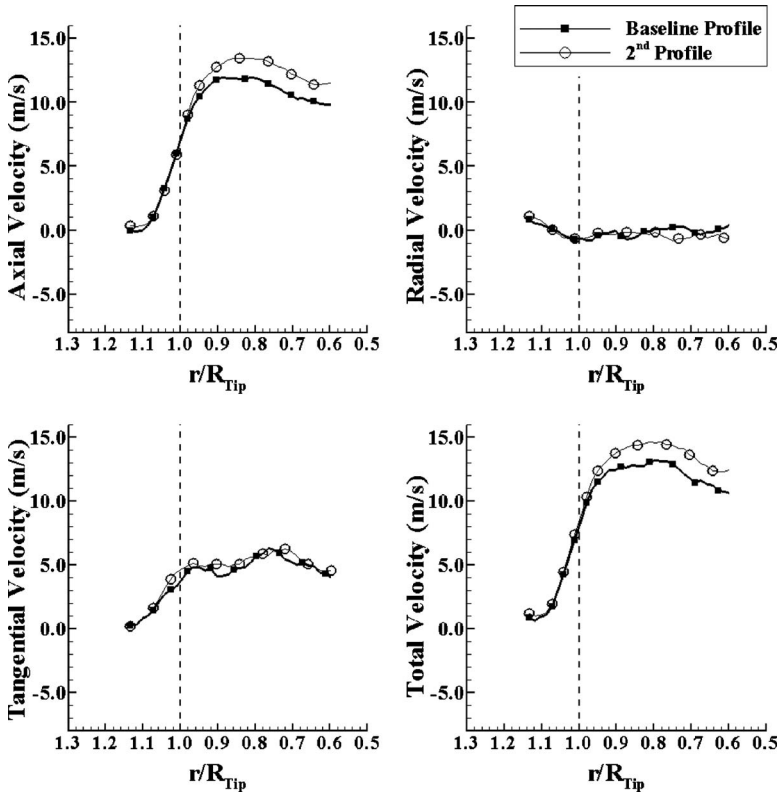

Fig. 12 Velocity profiles measured at location 3 (high ΔP with 19.6% perforated plate, 80 m^3/min, 140 Pa)

the total velocity distribution for baseline tips is about the same as the axial velocity component for the five treated tips shown in Fig. 8. Since the radial components are extremely small for all tip shapes, one can infer that the significant difference between the baseline and treated tips is due to a strong change in the tangential component of the velocity vector. The distribution of the tangential component shows a significant difference in the whole measurement region, where $r/R_{\text{tip}} \geq 0.6$.

One can conclude that there is a strong swirl component near the tip region when there is no tip treatment. The five treated tips defined in Fig. 7 provide significant reduction in the amount of swirl in the rotor exit flow. The reduction in the amount of swirl near the tip region is about 4–5 m/s, with the tip platform extensions shown in Fig. 7. The magnitude of the swirl component that is inherent to baseline tips is about one-third of the total velocity existing in the core of passage.

4.4 Tip Platform Extensions With Highest Axial Velocity at Rotor Exit. Figure 9 shows that the five new tip platform extension devices can be highly instrumental in reducing the amount of swirl coming out of the rotor. This feature is certainly a benefit in terms of the energy efficiency of the axial flow fan when the fan is operated on its high volumetric flow rate (low pressure rise) point. The tip platform extensions help to reduce the tip leakage mass flow rate and its momentum deficit via local viscous flow modifications near the tip region. Profiles 1 and 2 provide the two profiles with the highest total velocity in the core of the passage exit flow.

4.5 The Optimal Tip Platform Design. The experimental results suggest that the "maximum width" of the bump is an important parameter in designing the tip desensitization geometry. Profiles 2 and 5 cover almost the same chordwise locations. The only difference between the two is the maximum width of the bump. Figures 8–10 clearly show that the recovery of the axial velocity component and elimination of the tangential component is more effective with Profile 2 than with Profile 5. Figures 9–11 show that the features observed in Fig. 9 for location 3 repeat for other angular positions of the rotor (locations 4 and 5). Although there are slight flow-field differences at different rotor positions, the general nature of the discussion does not change.

4.6 Fan Exit Flow at the Highest Pressure Rise. An interesting tip treatment experiment could be performed by operating the fan at its highest pressure point by reducing the volumetric flow rate using a perforated steel plate at the mock-up inlet section, as shown in Fig. 1. The experiments with the specific perforated plate with an open area ratio of 19.6% indicated that measurable gains in axial velocity component at the core of the exit flow still exist with Profile 2. Figure 12 shows that the tangential and radial velocity components from Profile 2 are very similar to the baseline profile at the same effective clearance value of 0.100 in. (1%). However, the elimination of the tangential component observed in high volumetric flow rate experiments does not occur under high pressure rise conditions (140 Pa), as shown in Fig. 12. There is a consistent 2 m/s increase in axial (or total) velocity throughout the blade span when $r/R_{\text{tip}} \geq 0.6$. Under high loading conditions, the swirl component is minimal even with a baseline tip. The tip platform extensions for this case also perform their function by minimizing the tip leakage flow mass flow rate. The minimization of the tip leakage mass flow rate eventually provides the gain in axial (or total) velocity component. On the average, the gain in the total velocity magnitude at the rotor exit is about 17% throughout the blade span. This type of gain in the mean kinetic energy of the fan exit flow is expected to contribute to the energy efficiency of the fan.

4.7 Rotor Exit Total Velocity Distributions. Figures 13 and 14 show total velocity contours drawn on the axial and radial planes at the fan rotor exit for baseline tip and Profile 2, respectively. Both contours are obtained from measurements performed at a 0.1 in. tip clearance. The rotor tip ($r/R_{\text{tip}}=1.0$) is marked with

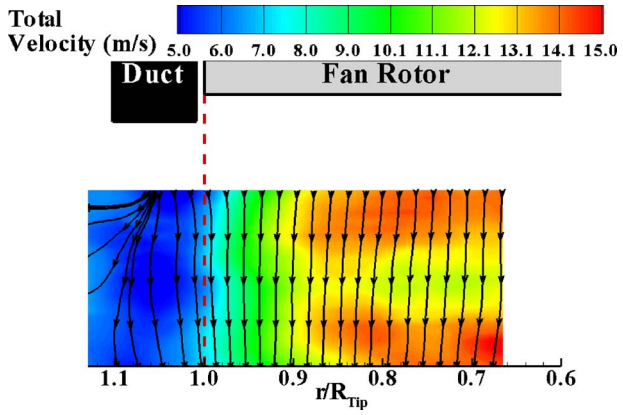

Fig. 13 Total velocity contour and streamlines at location 3 for baseline profile (340 m^3/min, 32 Pa)

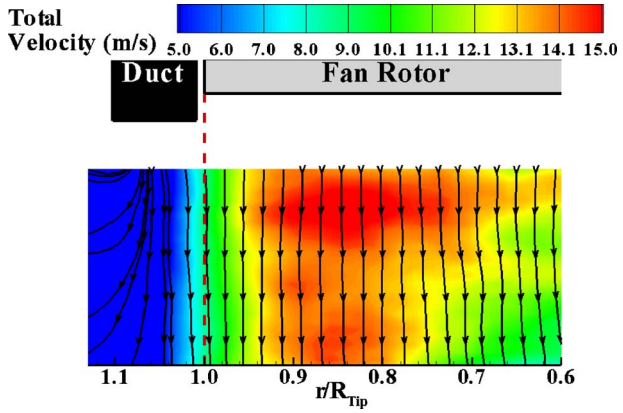

Fig. 14 Total velocity contour and streamlines at location 3 for the 2nd profile (340 m^3/min, 32 Pa)

the dashed line. An enhancement of total velocity near the tip region is observed when the tip region total velocities are compared. It is also obvious that using Profile 2 enhances the area coverage of a high momentum jet at the exit. That means the rotor blade with a tip platform Profile 2 increases the kinetic energy of the fluid flow more efficiently. It also reduces the momentum deficit near the tip due to the tip leakage flow.

4.8 Influence of Tip Platform Extensions on the Flow Coefficient. The positive effect of the five new tip platform extensions on flow coefficient of the fan rotor is shown in Fig. 15. Flow coefficient is plotted at 46 mm downstream of the fan. For $r/R_{tip} \geq 0.9$ (near the tip region), all the tip platform extensions increased the flow coefficient. This increase is related to the increase in axial velocity near the tip region due to tip treatments. Measurable reduction in the tangential velocity component resulted in a measurable increase in the flow coefficient. Profiles 1 and 2 are the two profiles with the highest flow coefficient in the core of the passage exit flow. Profiles 3, 4, and 5 slightly increase the flow coefficient near the tip region, but they provide with lower flow coefficient in the core flow region. The lower flow coefficient in the core may be attributed to the specific location of the platform extensions. On the average, the gain in the flow coefficient from Profiles 1 and 2 at the rotor exit is about 18.6% throughout the blade span.

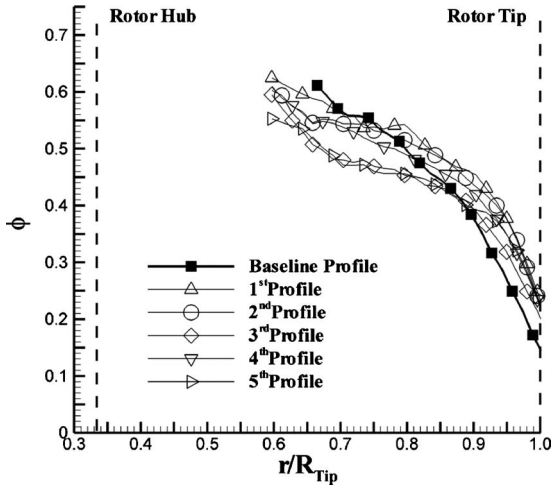

Fig. 15 Flow coefficient calculated at location 3 (340 m^3/min, 32 Pa)

5 Conclusions

Novel tip platform extensions for energy efficiency gains and aero-acoustic improvements were designed for an axial flow fan where wake mixing is already enhanced with a serrated trailing edge design.

Five different tip platform extensions were introduced especially on the pressure side of the fan blades.

It is possible to reduce the tip leakage mass flow rate using the novel tip platform extensions. Profile 2 showed the best tip treatment performance out of the five new tip platform extensions designed in this investigation.

Tip treatment experiments performed at a high volumetric flow rate/low pressure rise clearly showed the minimization of the tip vortex mass flow rate by significantly reducing the tangential components near the tip.

The tip platform extensions on the pressure side have proven to be effective swirl reducing devices at the exit of the fan. The magnitude of this reduction is about one-third of the rotor exit total velocity in the core of the passage exit.

The reduction in the tip leakage mass flow rate produced enhanced total velocity values between the midspan and the tip at the passage exit.

Tip platform experiments performed at the highest pressure point by reducing the volumetric flow rate using a perforated steel plate at the mock-up inlet section also showed a significant tip leakage control for the fan. However, the elimination of the tangential component observed in high volumetric flow rate experiments does not occur under high pressure rise conditions.

Under high loading conditions, the swirl component is minimal even with a baseline tip. With the tip platform extension "Profile 2," there is a consistent 2 m/s increase in axial (or total) velocity throughout the blade span when $r/R_{tip} \geq 0.6$.

Tip platform extensions perform their function by minimizing the tip leakage flow mass flow rate near the blade tip even under the high loading conditions. This effect eventually provides the gain in axial component.

On the average, the gain in the total velocity magnitude at the rotor exit is about 17% throughout the blade span. This type of gain in the mean kinetic energy of the fan exit flow is expected to contribute to the energy efficiency of the fan.

Acknowledgment

The authors acknowledge the major support from the Vertical Lift Rotorcraft Center of Excellence (VLRCOE) of the Department of Aerospace Engineering at Penn State University. This research is partially funded by the U.S. government under Agree-

ment No. W911W6-06-2-0008. The authors also acknowledge the technical support of Mr. H. Houtz during the experiments.

Nomenclature

β_1 = blade section inlet angle
β_2 = blade section exit angle
c = chord length
CCD = charge-coupled device
ϵ = experimental uncertainty
h = blade height
N = number of SPIV speckle images
PLIF = phosphorescence laser-induced fluoroscence
p = static pressure
ϕ = flow coefficient, $\phi = U/\omega r$
r = radial position ($r = 0.0$ at the axis of rotation)
R_{hub} = hub radius
R_{tip} = tip radius
σ = standard deviation
t = effective tip clearance in inches
U = axial velocity
V = radial velocity
W = tangential velocity
U_a = averaged axial velocity
ω = rotational speed
x = radial direction, see Fig. 2
y = axial direction, see Fig. 2
z = tangential direction, see Fig. 2

References

[1] Lee, G. H., Baek, J. H., and Myung, H. J., 2003, "Structure of Tip Leakage in a Forward-Swept Axial-Flow Fan," Flow, Turbul. Combust., **70**, pp. 241–265.
[2] Jang, C. M., Furukawa, M., and Inoue, M., 2001, "Analysis of Vertical Flow Field in a Propeller Fan by LDV Measurements and LES—Parts I, II," ASME J. Fluids Eng., **123**, pp. 748–761.
[3] Storer, J. A., and Cumpsty, N. A., 1991, "Tip Leakage Flow in Axial Compressors," ASME J. Turbomach., **113**, pp. 252–259.
[4] Lakshminarayana, B., Zaccaria, M., and Marathe, B., 1995, "The Structure of Tip Clearance Flow in Axial Flow Compressors," ASME J. Turbomach., **117**, pp. 336–347.
[5] Inoue, M., Kuroumaru, M., and Furukawa, M., 1986, "Behavior of Tip Leakage Flow Behind an Axial Compressor Rotor," ASME J. Eng. Gas Turbines Power, **108**, pp. 7–14.
[6] Furukawa, M., Inoue, M., Kuroumaru, M., Saik, K., and Yamada, K., 1999, "The Role of Tip Leakage Vortex Breakdown in Compressor Rotor Aerodynamics," ASME J. Turbomach., **121**, pp. 469–480.
[7] Fujita, H., and Takata, H., 1984, "A Study on Configurations of Casing Treatment for Axial Flow Compressors," Bull. JSME, **27**, pp. 1675–1681.
[8] Moore, R. D., Kovich, G., and Blade, R. J., 1971, "Effect of Casing Treatment on Overall and Blade-Element Performance of a Compressor Rotor," NASA Report No. TN-D6538.
[9] Reynolds, B., Lakshminarayana, B., and Ravindranath, A., 1979, "Characteristics of Near Wake of a Fan Rotor Blade," AIAA J., **17**, pp. 959–967.
[10] Ravindranath, A., and Lakshminarayana, B., 1980, "Mean Velocity and Decay Characteristics of Near and Far-Wake of a Compressor Rotor Blade of Moderate Loading," ASME J. Eng. Power, **102**, pp. 535–547.
[11] Myung, H. J., and Baek, J. H., 1999, "Mean Velocity Characteristics Behind a Forward-Swept Axial-Flow Fan," JSME Int. J., Ser. B, **42**, pp. 476–488.
[12] Adrian, R., 1991, "Particle Imaging Techniques for Experimental Fluid Mechanics," Annu. Rev. Fluid Mech., **23**, pp. 261–304.
[13] Kahveci, H. S., and Camci, C., 2006, "Flow Around Helicopter Blade Tip Sections Using 2D Particle Image Velocimeter—Part I," 11th International Symposium on Transport Phenomena and Dynamics of Rotating Machinery (ISROMAC-11), (136).
[14] Kahveci, H. S., and Camci, C., 2006, "Flow Around Helicopter Blade Tip Sections Using a (3D) Stereoscopic Particle Image Velocimeter—Part II," 11th International Symposium on Transport Phenomena and Dynamics of Rotating Machinery (ISROMAC-11), (137).
[15] Kahveci, H. S., 2004, "Implementation of a SPIV in Rotating Machinery Including Helicopter Rotor Flows," MS thesis, Pennsylvania State University, University Park, PA.
[16] Yoon, J. H., and Lee, S. J., 2004, "Exit Flow Field and Performance of Axial Flow Fans," Exp. Therm. Fluid Sci., **28**, pp. 791–802.
[17] Yen, S. C., and Lin, F. K. T., 2006, "Exit Flow Field and Performance of Axial Flow Fans," ASME J. Fluids Eng., **128**, pp. 332–340.
[18] Wernet, M. P., Van Zante, D., Strazisar, T. J., John, W. T., and Prahst, P. S., 2005, "Characterization of Tip Clearance Flow in an Axial Compressor Using 3D DPIV," Exp. Fluids, **39**, pp. 743–753.
[19] Corsini, A., Perugini, B., Rispoli, F., Kinghorn, I., and Sheard, A. G., 2006, "Investigation on Improved Blade Tip Concept," ASME Paper No. GT2006-90592.
[20] Corsini, A., Rispoli, F., and Sheard, A. G., 2006, "Development of Improved Blade Tip End-Plate Concepts for Low-Noise Operation in Industrial Fans," Proceedings of the Conference on Modeling Fluid Flows CMMF06.
[21] Corsini, A., Perugini, B., Rispoli, F., Kinghorn, I., and Sheard, A. G., 2007, "Experimental and Numerical Investigations on Passive Devices for Tip-Clearance Induced Noise Reduction in Axial Flow Fans," Proceedings of the Seventh European Conference on Turbomachinery.
[22] Corsini, A., Perugini, B., Rispoli, F., Sheard, A. G., and Kinghorn, I., 2007, "Aerodynamic Workings of Blade Tip End-Plates Designed for Low-Noise Operation in Axial Flow Fans," ASME Paper No. GT2007-27465.
[23] Ott, R. L., and Longnecker, M. T., 2000, *An Introduction to Statistical Methods and Data Analysis*, Duxbury, Los Altos, CA.

Prediction of the Nonuniform Tip Clearance Effect on the Axial Compressor Flow Field

Young-Seok Kang
Senior Engineer
Advanced Propulsion Group,
Korea Aerospace Research Institute,
Eo-Eun Dong, Yu-Seong Gu,
Daejon 305-333, Republic of Korea
e-mail: electra@kari.re.kr

Shin-Hyoung Kang
Professor
Department of Mechanical and Aerospace Engineering,
Seoul National University,
Sin-Rim Dong, Gwan-Ak Gu,
Seoul 151-742, South Korea
e-mail: kangsh@snu.ac.kr

It is well-known that nonuniform tip clearance in an axial compressor induces pressure and velocity perturbations along the circumferential direction. This study develops a numerical modeling to predict perturbed flows in an axial compressor with a nonuniform tip clearance and presents a mechanism of the flow redistribution in the axial compressor at design and off-design conditions. The modeling results are compared with CFD results (2006, "Prediction of the Fluid Induced Instability Force of an Axial Compressor," ASME FEDSM 2006, Miami, FL) not only to validate the present modeling, but also to investigate more detailed flow fields. In an axial compressor, nonuniform tip clearance varies local flow passage area and resultant axial velocity along the circumferential direction. There are small axial velocity differences between maximum and minimum clearances near the design condition, while large pressure differences are investigated according to local locations. However, contribution of the main flow region overrides the tip clearance effect as the flow coefficient deviates from the design condition. Moreover, the flow field redistribution becomes noticeably strong when the off-design effects are incorporated. In case of high flow coefficients, the low relative flow angle near the minimum clearance regions results in a large negative incidence angle and forms a large flow recirculation region and a corresponding large amount of loss occurs near the blade pressure surface. It further promotes strong flow field perturbations at the off-design conditions. The integration of these pressure and blade loading perturbations with a control volume analysis leads to the well-known Alford's force. Alford's force is always negative near the design condition; however, it reverses its sign to positive at the high flow coefficients. At the high flow coefficients, tip leakage flow effects lessen, while increased off-design effects amplify blade loading perturbations and a steep increase in Alford's force. This study enables that nonuniform flow field, and the resultant Alford's force, which may result in an unstable rotor-dynamic behavior, can be easily evaluated and assessed during the compressor, fan, or blower design process.
[DOI: 10.1115/1.4001553]

1 Introduction

Nonuniform tip clearance in an axial compressor due to rotor offset, whirling, or pitching motion can induce self-excited aerodynamic destabilizing rotor-dynamic forces. It was first announced by Thomas [1] and Alford [2] in axial flow turbines with statically offset rotors to elucidate the tangential destabilizing reaction force, the so-called Alford or Thomas force. In turbine stages, Alford supposed that work extraction from the fluid to the blade is more efficient near the minimum clearance region (high blade loading) and less efficient near the maximum clearance region (low blade loading). Then the resultant Alford's force due to the shaft offset makes the shaft rotate in the rotor rotational direction. Sometimes it stimulates a whirl motion of the turbine rotor rows in the direction of rotation (positive or forward whirl) because Alford's force has a positive value at most operating conditions in the turbine stages. For this reason, it is necessary to have opposite directions in the compressor stages to stabilize or neutralize the rotor-dynamic behavior of the shaft.

For the compressor stages, a similar theory is proposed by Alford. He formed the hypothesis that the compressor blade needs less work in the minimum clearance region (low blade loading) and that it requires a large amount of work in the maximum clearance (low blade loading). Therefore, the resultant Alford force has the direction of rotation similar to that of turbines. On the contrary, Ehrich [3] approached Alford's force from a different point of view. He focused on the local tip clearance performance when the tip clearance is not uniform in a compressor stage. He assumed that the blade sustains high pressure difference near the minimum clearance region and low pressure difference near the maximum clearance region. Therefore, Alford's force has an opposite direction of the rotation (negative or backward whirl) based on Ehrich's theory.

Consequently, some researches began to take an interest in resolving this disparity in Alford's force direction between Alford's and Ehrich's theories. There are several prediction methods developed to predict the nonuniform tip clearance effects on Alford's force of axial compressors. Colding-Jorgensen [4] predicted Alford's force in a compressor stage using an actuator disk model. They assumed a tip clearance penalty on the stage efficiency and implemented it in governing equations. They predicted Alford's force is positive at most operating conditions except at low flow coefficients. Ehrich [3] developed a parallel compressor model to predict Alford's force in the compressor stages. He assumed that Alford's force is induced by the local tip clearance performance. He put experimentally measured pressure rise and blade torque for two tip clearance heights into the modeling. The parallel compressor model divides the blade row into two parts: half for the small clearance region and half for the large clearance region. He assumed that half of the compressor follows the compressor performance curve of the compressor with a small clearance and the other half follows the performance curve of the compressor with a large clearance. Then pressure perturbation along the circumfer-

Contributed by the Fluids Engineering Division of ASME for publication in the JOURNAL OF FLUIDS ENGINEERING. Manuscript received August 12, 2009 final manuscript received April 5, 2010 published online May 14, 2010. Assoc. Editor: Chunill Hah.

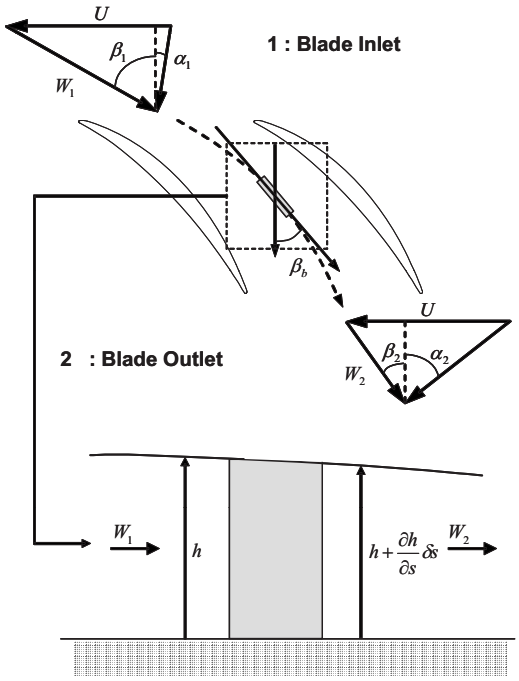

Fig. 1 Control volume of a rotor row with a nonuniform tip clearance distribution

ential direction was evaluated, and Alford's force was obtained. Song et al. [5] developed the two-coupled actuator disk (2CAD) model, which originated from the actuator disk model. The advantage of the 2CAD model is that it does not require any experimental data. Flow redistribution around the compressor row was calculated with local tip clearance effects on the underturning of the tip leakage flow incorporated with the main flow. Spazkovsky [6] presented the two-sector parallel compressor (2SPC) model by further investigating flow field perturbation based on a control volume analysis.

These prediction models were applied to the low speed research compressor developed by GE Aviation [7,8]. The results showed that the low speed research compressor (LSRC) has negative Alford's forces over the most flow coefficient. It is totally different from the result of Colding-Jorgensen [4].

Most previous researches have showed that the flow redistribution and Alford's force variation are largely dependent on the flow coefficient. However, the mechanism of the flow redistribution and Alford's force variation when the operation conditions are off-design conditions are not fully understood. They are associated with a reliable estimation of the rotor-dynamic response at the off-design condition to guarantee stable operation of the turbomachine. Also there are some shortcomings in previous analysis methods; it is hard to implement or require experimental results to predict a nonuniform tip clearance effect. Therefore, in this study, we developed a simple method to assess nonuniform tip clearance effects on flow field perturbations without any empirical formulations at the design and off-design conditions. In assistance with numerical simulation results [9], we could validate the prediction method and analyze the flow distribution mechanism in the axial compressor with nonuniform tip clearances.

2 Model Derivation

The flow fields at the inlet and outlet of the rotor row can be predicted by integrating the governing equations along the streamline, as shown in Fig. 1. The analysis method requires the following assumptions to simplify complicated 3D flow to 2D flow at the inlet and outlet of an axial compressor:

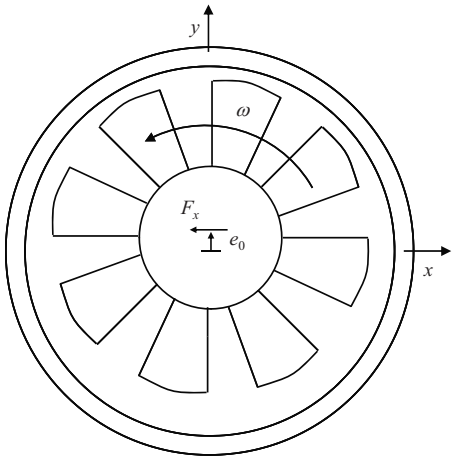

Fig. 2 Schematic of an offset rotor model

1. Nonuniform tip clearance has a sinusoidal distribution when the rotating axis is offset from the casing center.
2. The deviation and underturned angles from the tip leakage flow of the axial compressor are evaluated from Howell's compressor cascade theory.
3. There are three major total pressure loss sources: incidence loss due to incidence or attack angle, tip clearance loss from tip leakage flow and its mixing with the main flow, and profile loss due to flow dissipation; incidence pressure loss due to large or negative incidence has an important role in this modeling; and tip clearance loss is varied along the circumferential direction due to nonuniform tip clearance distributions. In this modeling, the total pressure loss including these three losses is incorporated as a source term.
4. There is an effective flow area change according to the blade inlet incidence at the off-design condition. It is implemented as an equivalent eccentricity from the casing center.

2.1 Continuity Equation. The rotor row schematic, in which the rotating center is offset by e_0, is illustrated in Fig. 2. Then the tip clearance has a nonuniform distribution along the circumferential direction, and the blade height h at the local coordinate is dependent on time, as shown in Fig. 1. Then, the continuity equation is written as follows:

$$\frac{1}{h}\frac{\partial h}{\partial t}+\frac{\partial W}{\partial s}=0 \tag{1}$$

$$h=h_0-(e_0+e_b)\sin\,\theta \tag{2}$$

where e_0 is a statically offset distance and e_b is an equivalent offset distance due to flow blockage effect. This means that the relative velocity along the streamline accelerates or decelerates according to the local blade height. It is convenient to convert the continuity equation into a velocity dimension. The tip equivalent velocity q is defined as

$$q=\omega h \tag{3}$$

The continuity equation can be rewritten as follows:

$$\frac{\partial q}{\partial t}+q\frac{\partial W}{\partial s}=0 \tag{4}$$

2.2 Momentum Equation. The streamwise momentum equation includes a source term, which includes the total pressure loss between the inlet and outlet of the rotor row

$$\frac{\partial W}{\partial t} + W\frac{\partial W}{\partial s} = -\frac{1}{\rho}\frac{\partial p}{\partial s} - s \tag{5}$$

Adding Eq. (4) to Eq. (5) and integrating the equation from the inlet to the outlet will solve the equation

$$\int_1^2 \left(\frac{\partial W}{\partial t} + \frac{\partial q}{\partial t} + W\frac{\partial W}{\partial s} + q\frac{\partial W}{\partial s}\right)ds = -\int_1^2 \left(\frac{1}{\rho}\frac{\partial p}{\partial s} + s\right)ds \tag{6}$$

The first term of the integrated equation is modified in the form

$$\int_1^2 \frac{\partial W}{\partial t}ds = \frac{1}{\cos\beta_b}\frac{\partial C_{m2}}{\partial t}\int_1^2 \frac{A}{A_2}ds = \frac{1}{\cos\beta_b}\left(\frac{\partial C_{m2}}{\partial t'} + \omega\frac{\partial C_{m2}}{\partial \theta}\right)L_e \tag{7}$$

where β_b is the mean blade angle and L_e is an equivalent stream line length between the inlet and outlet. As investigating a flow field in the global coordinate is convenient in this study, conversion into the global coordinates is required for the time derivate terms in Eq. (7)

$$\frac{dC_{m2}}{dt} = \frac{\partial C_{m2}}{\partial t'} + \frac{\partial \theta}{\partial t'}\frac{\partial C_{m2}}{\partial \theta} = \frac{\partial C_{m2}}{\partial t'} + \omega\frac{\partial C_{m2}}{\partial \theta} \tag{8}$$

Throughout the remainder of this study, the dot at the right hand side of Eq. (8) will be omitted for convenience. In a similar manner, the forth term of Eq. (6) becomes

$$\frac{\partial q}{\partial t} = \omega\frac{\partial q}{\partial \theta} = -(e_0 + e_b)\omega^2\cos\theta \tag{9}$$

As q is the function of θ, there is no necessity for a time derivate in the global coordinate. From the velocity triangle, the third term of Eq. (6) becomes

$$\int_1^2 W\frac{\partial W}{\partial s}ds = -U(C_{t2} - C_{t1}) + \frac{1}{2}(C_2^2 - C_1^2) \tag{10}$$

With the mean blade angle, last part of the left-hand side of Eq. (6) becomes

$$\int_1^2 q\frac{\partial W}{\partial s}ds = q\frac{1}{\cos\beta_b}\int_1^2 \frac{\partial C_m}{\partial s}ds \approx q\frac{C_d}{\cos\beta_b} \tag{11}$$

C_d in Eq. (11) is the axial velocity difference between the control volume inlet and outlet. Then, the final equation becomes

$$\frac{\partial C_{m2}}{\partial t} + \omega\frac{\partial C_{m2}}{\partial \theta} = \frac{\cos\beta_b}{L_e}\left\{U(C_{t2} - C_{t1}) - \frac{1}{\rho}(p_{02} - p_{01}) - qC_d - S_l\right\} + (e_0 + e_b)\omega^2\cos\beta_b\cos\theta \tag{12}$$

2.3 Inflow Incidence Effect. Kang and Kang [9] showed that a large reverse flow region appears at the pressure side of the rotor blade as the flow coefficient increases. In this study, the blocked flow area at a high flow rate is assumed to be imposed on the casing radius for convenience

$$A - \delta A_b = \pi((r_o - e_b)^2 - r_i^2) = \pi(r_o^2 - r_i^2) - 2\pi r_o e_b \tag{13}$$

$$\frac{\delta A_b}{A} = \frac{2\pi r_o e_b}{\pi(r_o^2 - r_i^2)} = \frac{2\frac{e_b}{r_o}}{\left(1 - \left(\frac{r_i}{r_o}\right)^2\right)} \tag{14}$$

where δA_b is the flow area decrease due to the blockage and e_b means the equivalent offset due to the flow blockage. To determine δA_b in Eq. (14), a simple correlation developed by Roelke [10] is used

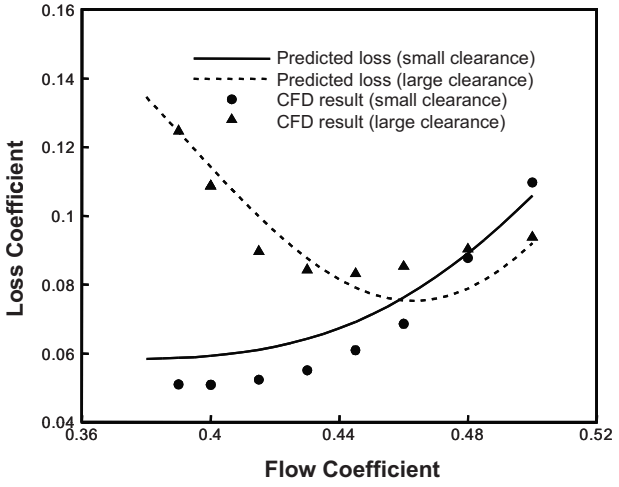

Fig. 3 Total pressure loss coefficient from CFD and loss model

$$\frac{\delta A_b}{A} = \frac{|\sin i|}{|\sin i| + \cos i} \tag{15}$$

Then, the final form of the flow blockage becomes

$$e_b = \frac{r_0}{2}\frac{|\sin i|}{|\sin i| + \cos i}\left(1 - \left(\frac{r_i}{r_o}\right)^2\right) \tag{16}$$

2.4 Deviation Angle and Underturned Flow Due to the Tip Clearance. Fluid flow leaving the rotor blade deviates from the exit blade angle due to the pressure difference between the pressure and suction surfaces. The tip leakage flow, which results in underturned flow relative to the main flow, is another source that affects the outlet flow angle. As the tip clearance height and flow area varies along the circumferential direction, the blade loading and tip clearance flow also changes, corresponding to the local location. In this study, it is assumed that blade loading and the corresponding deviation angle follow Howell's cascade theory [11,12]

$$m = 0.23(2 \times a/l)^2 + \beta_2^*/500 \tag{17}$$

$$\delta = \theta m(s/l)^{1/2} \tag{18}$$

With Eqs. (17) and (18), the deviation angle at the nominal flow condition is evaluated. Deviation angles at the other flow coefficients are evaluated based on Howell's empirical formulations. The lift coefficient can be evaluated using Eq. (19)

$$c_l = 2\frac{s}{l}\cos\beta_b(\tan\beta_1 - \tan\beta_2) - c_d\tan\beta_b \tag{19}$$

where c_d is an empirical formulation of the drag coefficient of the compressor cascade suggested by Howell [13]. Since the tip clearance flow in the axial compressor is usually assumed to be inviscid flow [14], the speed of tip clearance flow can be evaluated from the pressure difference between the pressure and suction surfaces

$$W_{\text{gap}} = \sqrt{2\frac{p_{\text{ps}} - p_{\text{ss}}}{\rho}} \tag{20}$$

The underturned flow angle can be predicted as

$$\theta_t = \tan^{-1}\frac{W_{\text{gap}}}{W} = \tan^{-1}\sqrt{c_l} \tag{21}$$

Evaluated underturned flow angles are used to predict the averaged circumferential velocity at the rotor outlet in Eq. (29).

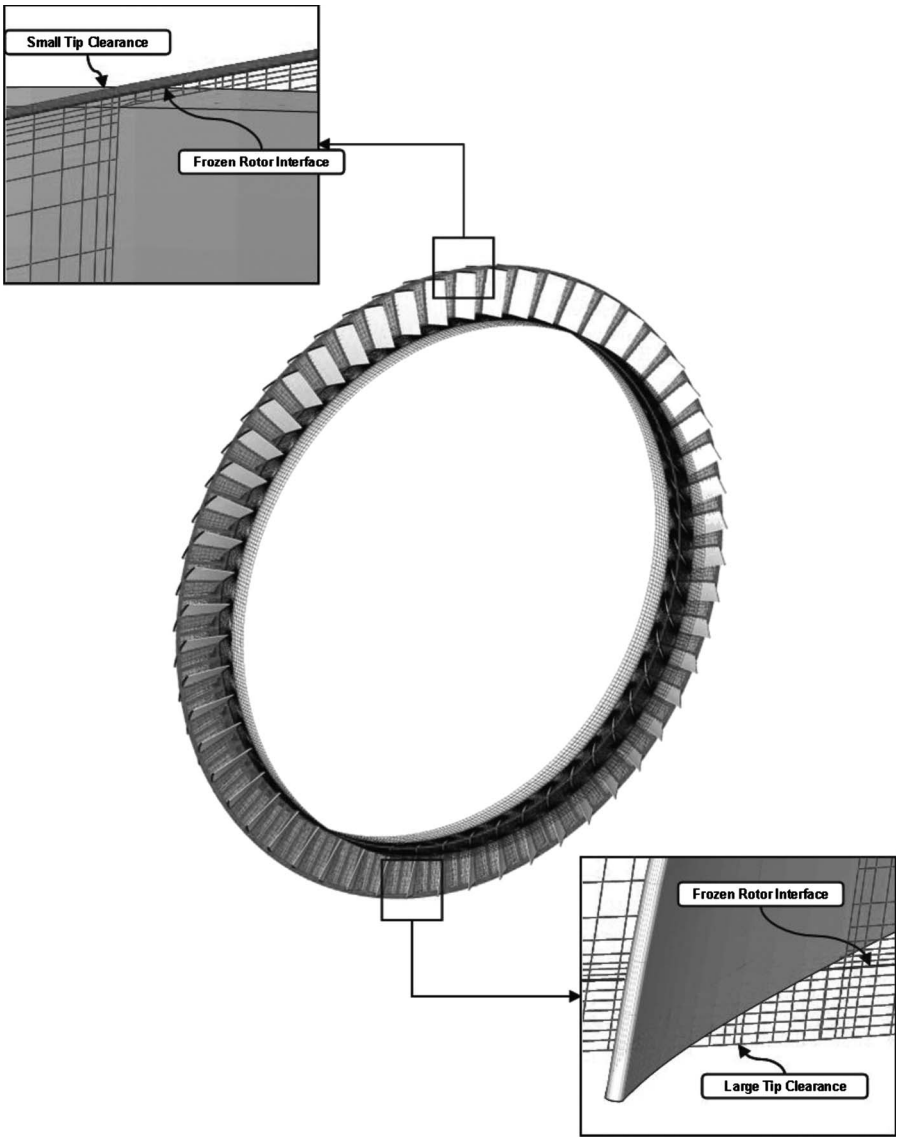

Fig. 4 Computational grid of the statically offset rotor row

2.5 Loss Model. In this study, the model employs the tip leakage, incidence and resultant secondary flows, and profile losses in Eq. (12) for reasonable predictions of the flow fields in the rotor row. Tip clearance loss is modeled by modifying Storer's modeling [15] for compressor cascades

$$L_t = \phi^2 \chi \sin \theta_t \left\{ \frac{2 + \chi \sin \theta_t - 2 \cos \theta_t}{(1 + \chi \sin \theta_t)^2} \right\} \frac{1}{\cos \beta_2^2} \tag{22}$$

where χ is the tip clearance area to flow area ratio. Incidence loss follows Roelke's simple suggestion [10] that the kinetic energy normal to blade passage becomes loss

$$L_i = \left(\frac{W}{U} \right)^2 \sin^2 i \tag{23}$$

Profile loss is assumed to be proportional to the kinetic energy in the flow passage

$$L_p = K_p \left(\frac{W}{U} \right)^2 \tag{24}$$

where K_p is the drag coefficient suggested by Howell [13], which has a value of around 0.02. It varies according to the blade incidence angle.

Figure 3 compares the total pressure loss coefficients of the rotor for this study. CFD results and predicted losses in the rotor blades with a small clearance (1.2% of the blade span) and large clearance (4.8% of the blade span). At the large clearance, loss reduces as the flow coefficient increases. However, as the loss reaches a certain point, it increases again, and the overall loss distribution forms a U shape. In the meanwhile, loss at the small clearance increases gradually, and as the flow coefficient increases, the total amount of loss increases steeply and overtakes that of the large clearance.

2.6 Solving Equation. Equation (12) is a first-order hyperbolic equation to solve for C_{m2}

$$\frac{\partial C_{m2}}{\partial t} + \omega \frac{\partial C_{m2}}{\partial \theta} = S \tag{25}$$

To discretize Eq. (12), the Lax–Wendroff scheme is used, which is first-order in time and second-order in space. The discrete form of Eq. (12) is obtained as follows:

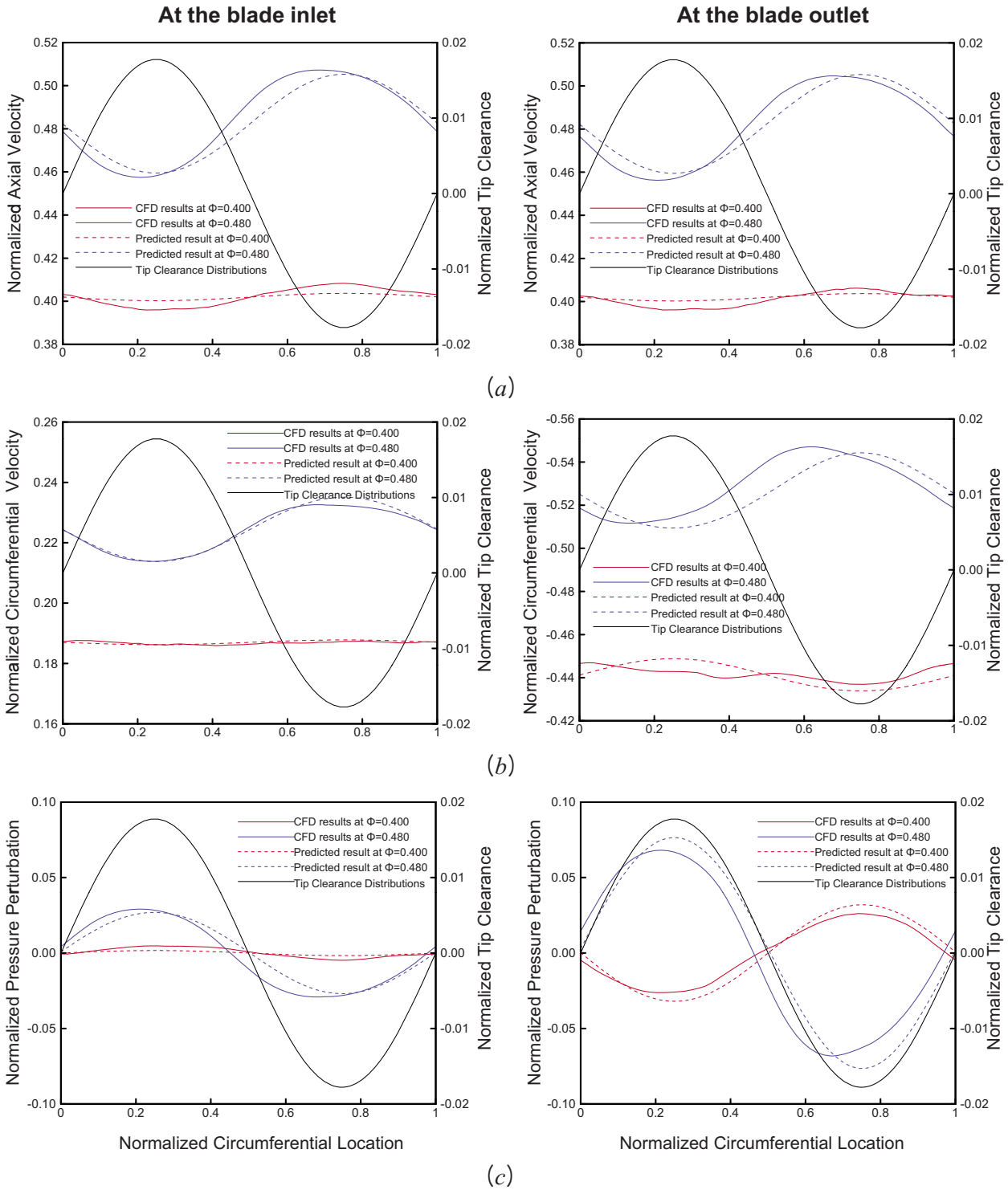

Fig. 5 Distributions of normalized (*a*) axial velocity, (*b*) circumferential velocity, and (*c*) pressure perturbations at the blade inlet and outlet

$$C_{m2,i}^{k+1} = C_{m2,i}^{k} - \frac{\mathrm{CFL}}{2}(C_{m2,i+1}^{k} - C_{m2,i-1}^{k}) + \frac{\mathrm{CFL}^2}{2}(C_{m2,i+1}^{k} - 2C_{m2,i}^{k} + C_{m2,i-1}^{k}) + S \tag{26}$$

where $\mathrm{CFL} = \omega \Delta t / \Delta \theta$. To solve Eq. (26), computational grids are given at the rotor inlet and outlet at every 1 deg. Axial velocity at the inlet is obtained from

$$C_{m1,i}^{k+1} = C_{m2,i}^{k+1} \tag{27}$$

The inlet circumferential velocity is evaluated from the velocity triangle. It is assumed that the tip clearance region and main flow region contributions are separated according to the tip clearance height

$$C_{t1,i}^{k+1} = C_{m1,i}^{k+1} \tan \alpha_1 \tag{28}$$

$$C_{t2,i}^{k+1} = U - C_{m1,i}^{k+1}\left(\frac{h_i}{h_0}\sin(\beta_b + \theta_{t,i}) + \frac{h_0 - h_i}{h_0}\sin(\beta_b + \delta_i)\right) \quad (29)$$

Subtracting dynamic pressure from the total pressure becomes static pressure at the inlet and outlet

$$p_{s1,i} = p_{01} - \frac{1}{2}\rho(C_{m1,i}^2 + C_{t1,i}^2) \quad (30)$$

$$p_{s2,i} = \rho U(C_{t2,i} - C_{t1,i}) - \frac{1}{2}\rho(C_{m1,i}^2 + C_{t1,i}^2) - s_l \quad (31)$$

3 Modeling Results

The prediction method is applied to an analysis of the third stage rotor row of a low speed research compressor in the Seoul National University. The predicted results are compared with computationally calculated results by Kang and Kang [9]. They carried out numerical simulations for the rotor row with a static offset from the casing center. The inlet and outlet flow fields are available for comparison with the modeling results. Figure 4 shows the computational grids of the rotor row with an eccentricity that consists of approximately 4.5×10^6 nodes. Refer to Ref. [9] for details of the numerical simulation process. The design flow coefficient of the LSRC is 0.41. The flow coefficient varies from 0.400 to 0.480. The minimum, nominal, and maximum clearances are defined as 1.2%, 3%, and 4.8% of the rotor blade span, respectively. Both the predicted and numerical simulation results show obvious difference between the design flow coefficient (0.400) and high flow coefficient (0.480). For this reason, the flow field at flow coefficients of 0.400 and 0.480 are discussed at first.

3.1 Velocity and Pressure Distributions. Figure 5 shows the velocity and pressure distributions at the inlet and outlet at flow coefficients of 0.400 and 0.480. Both the CFD and predicted results show a good agreement in the velocity and pressure distributions. This means that proper assumptions are integrated in the present prediction method. When comparing with the tip clearance distribution, both the predicted and numerical simulation results show that the axial velocity is high near the minimum clearance region and small near the maximum clearance region. The axial velocity difference between the maximum and minimum clearances is mainly influenced by local tip clearance heights. However, as the flow coefficient increases, the flow incidence amplifies the axial velocity variation when the flow coefficient is 0.480; it also affects the circumferential velocity distribution. Figure 5(*c*) shows normalized static pressure perturbations at both flow coefficients. The overall trend of the predicted pressure agrees well with the CFD result. However, the reason of pressure variation is different for each case. As shown in Fig. 5(*a*), a large axial velocity variation occurs at high flow coefficients, while a relatively small amount of velocity difference occurs at the design condition. Figure 6 compares pressure rise coefficient distributions with those of uniform tip clearances. One can easily notice that the nonuniform tip clearance has no penalty on the pressure rise coefficient. It is thought that the pressure reduction at the large clearance is compensated by the pressure gain at the small clearance. As shown in Fig. 5(*a*), there is little axial velocity variation around the rotor row when the flow coefficient is 0.400. It is reasonable that pressure has its maximum near the minimum clearance region (① in Fig. 6), and its minimum near the maximum clearance region (③ in Fig. 6). If so, the averaged outlet pressure becomes ② in Fig. 6.

On the other hand, as the flow coefficient becomes 0.480, large axial velocity variation occurs due to the flow incidence. The local normalized axial velocity by the blade tip speed at the minimum clearance is 0.500, and that of the maximum clearance is 0.460, as shown in Fig. 5(*a*). Thus, the small clearance region undergoes a low pressure rise (④ in Fig. 6), and the large clearance region

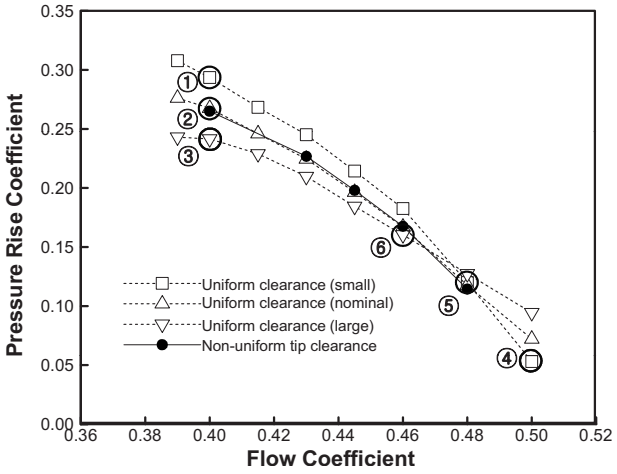

Fig. 6 Pressure rise coefficients at different tip clearance heights

suffers relatively high pressure rise (⑥ in Fig. 6). If there were no off-design effects, such as flow blockage effect, incidence angle effect, tip leakage flow effect, and so on, there would be less pressure variation around the rotor row. This process occurs progressively as the flow goes through the rotor blade.

Figure 7 illustrates pressure rise coefficient distributions through the rotor row from CFD results. There is little difference in pressure distribution patterns at the blade inlet in Fig. 7(*a*). The pressure contours start to differ greatly as the flow goes through mid-chord of the blade in Fig. 7(*b*). This pressure redistribution pattern clearly appears at the blade outlet in Fig. 7(*c*). The tip clearance region has a dominant effect on the pressure redistribution at the design condition.

When the flow coefficient is 0.480, the tip clearance effect becomes smaller, while the main flow region effect grows due to the large amount of axial velocity variations. The pressure and blade loading perturbations are major sources of Alford's force.

3.2 Alford's Force Distributions. Figure 8 compares Alford's force distributions evaluated from the CFD and predicted results. Alford's force is evaluated by integrating the circumferential force and spool pressure perturbations.

In both CFD and predicted results, Alford's forces are negative at the design condition. Both Alford's forces reverse their signs as the flow coefficient approaches 0.445. Alford's force prediction without the off-design effects is also compared in Fig. 8. Predicted Alford's force shows negative value at the all flow coefficient, if the off-design effects are not influential.

If there is no area difference between the minimum and maximum clearance regions, there would be no axial velocity difference. However, the local flow area according to the local tip clearance height varies local axial velocities along the circumferential direction. If the axial velocity variation does not change according to the flow coefficient, pressure rises at the minimum and maximum clearances vary, as shown in Fig. 9(*a*). In this case, the rotor row experiences high blade loading near the minimum clearance region and low blade loading near the maximum clearance region except for very high flow coefficients.

The pressure difference becomes small as the flow coefficient increases. When the flow coefficient reaches a certain point, there is no difference in the pressure, and the difference between the small and large clearances disappears. At the point, there is no pressure perturbation around the rotor row, and the resultant Alford's force becomes zero. When the flow coefficient is higher than this "threshold flow coefficients," little difference in the pressure rise occurs between the small and large clearances. In opposition to the low flow coefficients, the pressure rise pattern reverses; low pressure rise occurs near the minimum clearance and

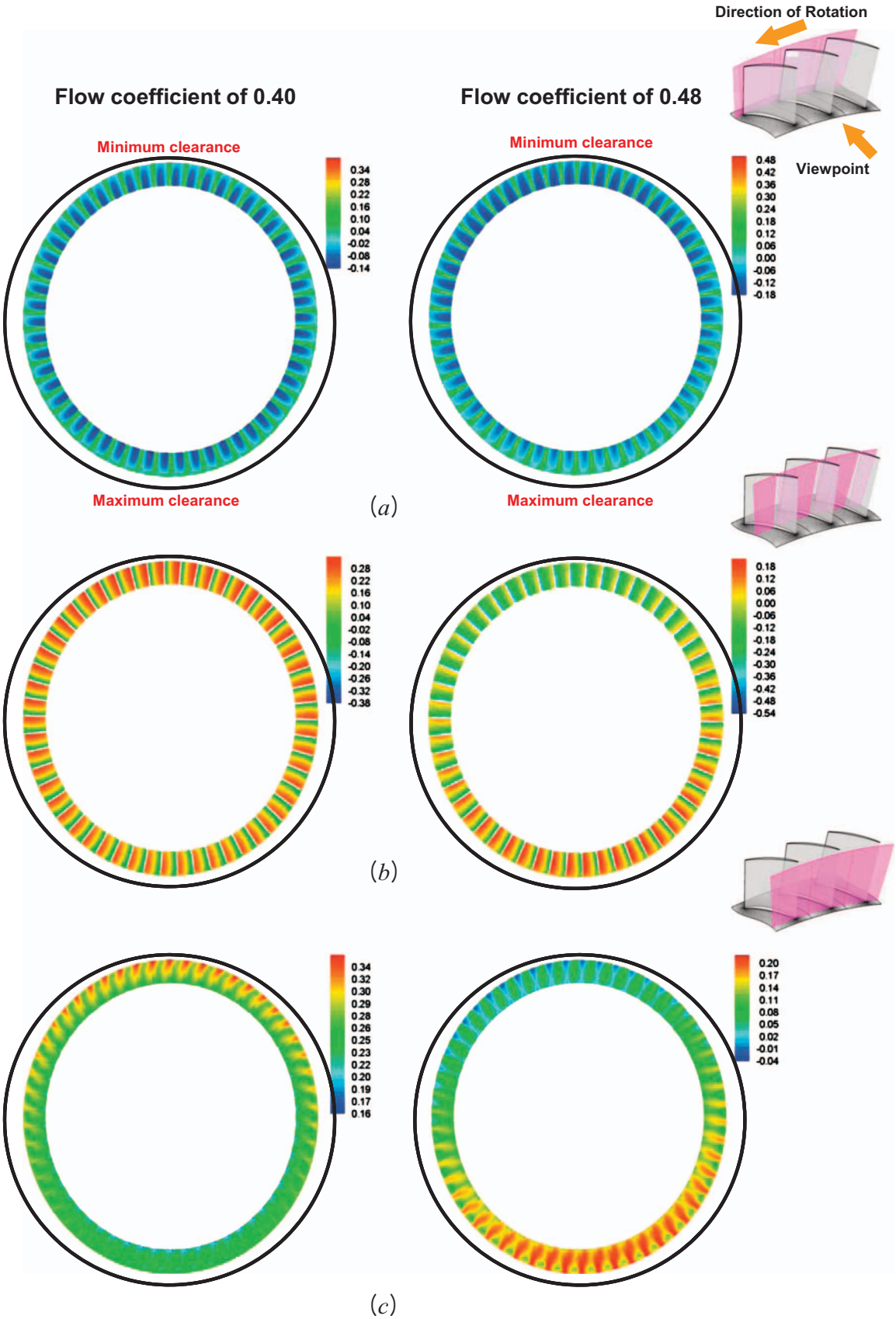

Fig. 7 Distributions of pressure coefficient at the (*a*) blade inlet, (*b*) mid-chord, and (*c*) blade outlet

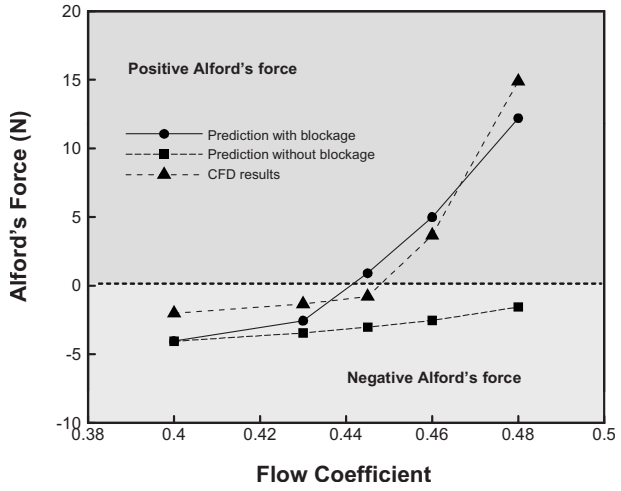

Fig. 8 Alford's force distributions from CFD and modeling

high pressure rise occurs near the maximum clearance. Therefore, the sign of Alford's force reverses when the flow coefficient is higher than the thresholds flow coefficient.

When the incidence blockage at the off-design conditions is introduced in the model, the axial velocity difference becomes wider as the flow coefficient increases, as shown in Fig. 9(*b*). Therefore the threshold flow coefficient becomes a smaller value than that in Fig. 9(*a*). Large axial velocity difference and a smaller threshold flow coefficient induce higher pressure difference or blade loading, as shown in Fig. 9(*b*). The resultant Alford's force increases rapidly at the high flow coefficient region. It explains well why the through flow region is more influential than the tip clearance region in redistributing the velocity and pressure field around the rotor row in both the numerical simulation and predicted results.

The results show that conventional axial compressors may have negative Alford's force at the design condition. In the meanwhile, the axial flow turbomachine, of which design point is determined at the high flow coefficient, such as the fan or blower, may have positive Alford's force, because it does not require high blade loading and the local tip clearance has less sensitive effect than that of the highly loaded compressors. From this point of view, Alford's theory holds because it is based on the idea that enthalpy rise along the circumferential direction is almost uniform, regardless of the local tip clearance. Moreover, incidence effect at the off-design condition promotes velocity and pressure perturbations along the circumferential direction. In this case, the resultant Alford's force steeply increases and it may cause severe rotor-dynamic instability. Therefore, predictions of Alford's force at the operating condition as well as those at the off-design conditions are very important to guarantee stable operation of the whole system.

4 Conclusions

A numerical modeling was developed to predict a nonuniform tip clearance effect on an axial compressor rotor row. The predicted results agreed well with the CFD results of Kang and Kang [9]. Not only the statically offset distance, but also other off-design factors such as the flow incidence or tip leakage flow have important roles on the reasonable prediction of the nonuniform tip clearance effects at the off-design conditions. This means it is hard to assess the nonuniform tip clearance effects with geometry information alone when these factors have noticeable contributions.

When the flow coefficient is low, the velocity and pressure redistributions are largely dependent on the local tip clearance performance. As the tip clearance effect according to tip clearance

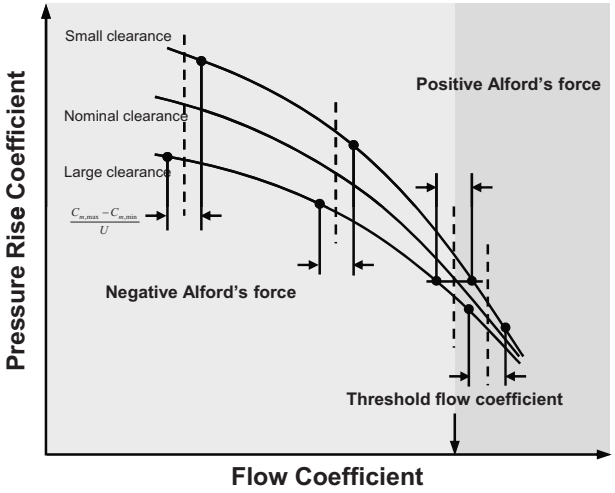

(*a*)

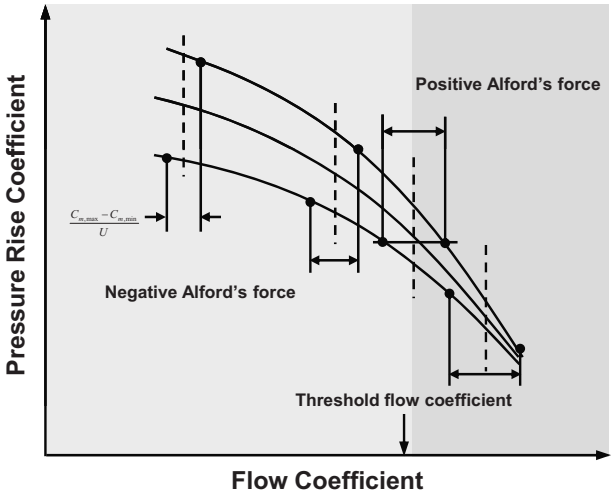

(*b*)

Fig. 9 Schematics of nonuniform tip clearance effects on pressure rise (*a*) without and (*b*) with off-design effects

heights becomes very small at the high flow coefficient, the determinant factor determining the redistribution of the flow field around the rotor row is local through the flow performance according to the local axial velocity.

As with previous researches, Alford's force has negative value at the design and low flow coefficients. However, with the flow incidence effects, the threshold flow coefficient where the Alford's force changes its sign moves to the low flow coefficient region. It also promotes a steep increase in Alford's force at the high flow coefficient.

One of the contributions of this study is the consideration of off-design effects for predicting more reliable nonuniform flow fields. This study offers a simple but reliable method to predict rotor-dynamic behavior at off-design conditions, especially for the turbomachine, which has variable operating conditions or very sensitive to the flow incidence, corresponding secondary flow, and total pressure loss such as high speed compressors or fans.

Acknowledgment

This study was, in part, financially supported by 'Next Generation Highly-loaded Axial Compressor Development Program' of the Korea Aerospace Technology Research Association (KATRA) and the Ministry of Knowledge Economy, Republic of Korea.

Nomenclature

A = flow passage area
A_b = flow area blocked
C = absolute velocity
c_P = pressure coefficient
e_0 = eccentricity of the nonuniform tip clearance
e_b = equivalent eccentricity due to the flow blockage
i = incidence angle
h = blade height
l = blade chord length
L = loss coefficient
F_T = tangential force acting on blades
q = tip equivalent velocity
p = pressure
R = radius
s = streamwise direction, source term
U = rotor tip velocity
W = relative velocity
α = absolute flow angle
β = relative flow angle
β_b = mean blade angle
ϕ = flow coefficient
ρ = density
θ = circumferential coordinate
θ_t = underturned flow angle due to the tip clearance
ω = rotational speed

Subscript

0 = nominal value, total condition
1 = rotor inlet
2 = rotor outlet
gap = tip clearance
m = axial direction
s = static condition
t = circumferential direction
ps = pressure side
ss = suction side

References

[1] Thomas, H. J., 1958, "Unstable Natural Vibration of Turbine Rotors Induced by the Clearance Flow in Glands and Blading," Bull. de l'A.I.M., **71**(11/12), pp. 1039–1063.
[2] Alford, J., 1965, "Protecting Turbomachinery From Self-Excited Rotor Whirl," ASME J. Eng. Power, **87**, pp. 333–344.
[3] Ehrich, F. F., 1993, "Rotor Whirl Forces Induced by the Tip Clearance Effect in Axial Flow Compressors," ASME J. Vibr. Acoust., **115**, pp. 509–515.
[4] Colding-Jorgensen, J., 1992, "Prediction of Rotordynamic Destabilizing Forces in Axial Flow Compressors," ASME J. Fluids Eng., **114**, pp. 621–625.
[5] Song, S. J., and Cho, S. H., 2000, "Non-Uniform Flow in a Compressor Due to Asymmetric Tip Clearance," ASME/IGTI TurboExpo 2000, Munich, Germany.
[6] Spakovszky, Z. S., 2000, "Analysis of Aerodynamically Induced Whirling Forces in Axial Flow Compressors," ASME/IGTI TurboExpo 2000, Munich, Germany.
[7] Storace, A. F., Wisler, D. C., Shin, H. W., Beacher, B. F., Ehrich, F. F., Spakovszky, Z. S., Martinez-Sanchez, M., and Song, S. J., 2000, "Unsteady Flow and Whirl-Inducing Forces in Axial-Flow Compressors. Part I—Experiment," ASME/IGTI TurboExpo 2000, Munich, Germany.
[8] Ehrich, F. F., Spakovszky, Z. S., Martinez-Sanchez, M., Song, S. J., Wisler, D. C., Storace, A. F., Shin, H. W., and Beacher, B. F., 2000, "Unsteady Flow and Whirl-Inducing Forces in Axial-Flow Compressors. Part II—Analysis, ASME/IGTI TurboExpo 2000, Munich, Germany.
[9] Kang, Y. S., and Kang, S. H., 2006, "Prediction of the Fluid Induced Instability Force of an Axial Compressor," ASME FEDSM 2006, Miami, FL.
[10] Roelke, R. J. 1994, ""Miscellaneous Losses"," A. J. Glassman, ed., *Turbine Design and Applications*, NASA, Chap. 8, p. SP-290.
[11] Howell, A. R. 1945, "Design of Axial Compressor," Proc. Inst. Mech. Eng., **153**, pp. 452–462.
[12] Howell, A. R. 1945, "Fluid Dynamics of Axial Compressors," Proc. Inst. Mech. Eng., **153**, pp. 441–452.
[13] Howell, A. R. 1942, "The Present Basis of Axial Flow Compressor Design: Part I, Cascade Theory and Performance," ARC R and M, Report No. 2095.
[14] Eum, H. J., Kang, Y. S., and Kang, S. H., 2004, "Tip Clearance Effect on Through-Flow and Performance of a Centrifugal Compressor," KSME Int. J., **18**(6), pp. 979–989.
[15] Storer, J. A., and Cumsty, N. A., "An Approximate Analysis and Prediction Method for Tip Clearance Loss in Axial Compressors," ASME Paper No. 93-GT-140.

Flow and Dipole Source Evaluation of a Generic SUV

Jonas Ask
Department of Environment and Fluid Dynamics Centre,
Volvo Car Corporation,
SE-405 31 Göteborg, Sweden

Lars Davidson
Professor
Department of Applied Mechanics,
Division of Fluid Dynamics,
Chalmers University of Technology,
SE-412 96 Göteborg, Sweden

Accurately predicting both average flow quantities and acoustic sources at the front window of today's ground vehicles are still a considerable challenge to automotive companies worldwide. One of the most important aspects in terms of obtaining not only trustworthy results but also the most tedious one and therefore perhaps overlooked, is the control and outcome of the mesh generation process. Generating unstructured volume meshes suitable for large eddy simulations with high level representation of geometrical details is both a time consuming and an extremely computer demanding activity. This work investigates two different mesh generation processes with its main aim to evaluate their outcome with respect to the prediction of the two dominating dipole sources in a temporal form of the Curle's equation. Only a handful of papers exists that report a high level representation of the vehicle geometry and the aim of predicting the fluctuating exterior noise sources. To the author's knowledge no studies have been conducted in which both these source terms are evaluated quantitatively against measurements. The current paper investigates the degree to which the amplitude of these two source terms can be predicted by using the traditional law-of-the-wall and hex-dominant meshes with isotropic resolution boxes for a detailed ground vehicle geometry. For this purpose, the unstructured segregated commercial FLUENT finite volume method code is used. The flow field is treated as incompressible and the Smagorinsky–Lilly model is used to compute the subgrid stresses. Mean flow quantities are measured with a 14 hole probe for 14 rakes downstream of the side mirror. The dynamic pressure sensors are distributed at 16 different positions over the side window to capture the fluctuating pressure signals. All measurements in this work were conducted at Ford's acoustic wind tunnel in Cologne. All three simulations accurately predict the velocity magnitude closest to the window and downstream of the mirror head recirculation zone. Some variations in the size and shape of this recirculation zone are found between the different meshes, most probably caused by differences in the detachment of the mirror head boundary layer. The Strouhal number of the shortest simulation was computed from the fundamental frequency of the drag force coefficient. The computed Strouhal number agrees well with the corresponding results from similar objects and gives an indication of an acceptable simulation time. The dynamic pressure sensors at 16 different locations at the vehicle side window were also used to capture the levels of the two dipole source terms. These results are compared with the three simulations. With the exception of three positions, at least one of the three simulations accurately captures the levels of both source terms up to about 1000 Hz. The three positions with less agreement as compared with measurements were found to be in regions sensitive to small changes in the local flow direction. [DOI: 10.1115/1.4001340]

1 Introduction

Flow induced noise or wind noise in ground vehicles caused by flow passing the vehicle exterior at cruising speed is undesirable noise as experienced by the driver and passengers. A reduction in and knowledge of the underlying mechanisms of this noise generation and aspiration into the compartment represent a research field of great importance to the world's automotive companies. This flow induced noise can arise from one or several of the following, according to Stapleford and Carr [1]:

- unpitched noise caused by air rushing past the vehicle surface
- monotone noise due to sharp edges and gaps at the vehicle surface
- acoustic resonance caused by flow excitation of vehicle openings such as side windows or sunroofs

This work treats the first item, namely, air rush noise, which has been addressed in wind tunnel measurements and "on road" tests from the mid-1960s until the last decade.

Some examples are given here. In 1964, Thomson [2] conducted road tests to investigate which of the two attributes, aerodynamic shape or seal design, is the most important property in the prevention of wind noise. His study led to the conclusion that the shape of the vehicle is not as important as air leakages caused by poor seal designs. The most critical region in his study was the sealing in the vicinity of the A-pillar, followed by the C-pillar region close to the beltline (see Fig. 1), and the front door region close to the driver or passenger.

A two part study was initiated in 1971 by Stapleford and coworker [1,3] to associate different flow regimes with aerodynamic noise levels for generic objects and production vehicles. They found that high aerodynamic noise levels were highly associated with different forms of flow separation, particularly from spiral vortex flows. A direct consequence of this finding was that aerodynamic shape is an important factor because minimizing flow separation will help to reduce the wind noise.

Further insight into important parameters for reducing air rush noise was described in Watanabe et al. [4] in 1978. As in Stapleford and co-worker [1,3], they stated that the fundamental cause

Contributed by the Fluids Engineering Division of ASME for publication in the JOURNAL OF FLUIDS ENGINEERING. Manuscript received November 14, 2007; final manuscript received January 18, 2010; published online May 14, 2010. Assoc. Editor: Rajat Mittal.

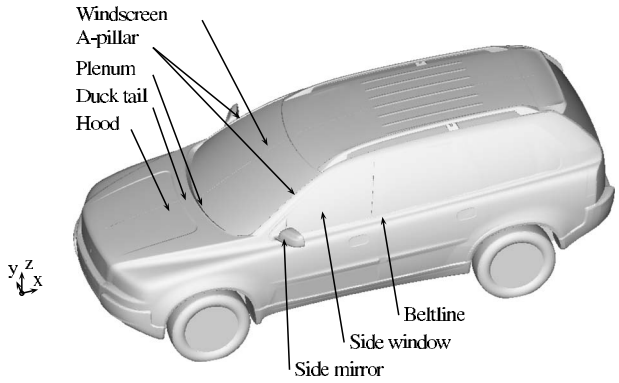

Fig. 1 Vehicle geometry

of air rush noise is flow separation. They also identified the fact that the relationship between the rain gutter height and the side window recess depth is an important parameter in the reduction in noise levels. They wrote that a third way to decrease air rush noise is to reduce local flow velocities. In their work, this was investigated by mounting a wind deflector on the hood, reducing the flow speed at the A-pillar.

The important aspects of aerodynamic noise in ground vehicles were reviewed in 1990 by George [5]. He stated that surface pressure fluctuations caused by flow separations are the most important source of air rush noise. He also presented an approach to tackling the complete aerodynamic noise problem based on the following four steps:

- Understanding the flow field including the separations.
- Finding the surface pressure fluctuations based on this information.
- Finding the external sound radiation from the pressure fluctuations.
- Finally, finding how these pressure fluctuations excite the vehicle structure to generate internal noise.

Numerical attempts to solve these four steps have been made in the last decade and much effort is now directed toward improving and refining existing techniques. The two dominating techniques for predicting separation dynamics as a starting point for wind noise predictions are by the traditional finite volume method (FVM) and the Lattice Boltzmann method (LBM).

Starting with the FVM approach, one of the first papers in which accurate large eddy simulations (LES) of the flow around simplified ground vehicles were made in order to understand the aerodynamics, including flow separation by LES, i.e., point 1, is the work of Krajnović and co-workers [6–9].

Rung et al. [10] conducted a flow and noise radiation study of a generic side mirror in comparisons of unsteady Reynolds averaged Navier–Stokes (URANS) and detached eddy simulations (DES). They compared fluctuating wall pressure and radiated sound computed by the Ffowcs Williams and Hawkings analogy [11] with corresponding measured results. They covered the first three steps in George's list. Their findings showed a major improvement in the predicted acoustic sources and the radiated sound using the DES model for most surface mounted sensors and microphones as compared with the URANS results.

Posson and Pérot [12] took the geometry complexity one step further by mounting a production mirror on top of a plate and exposing it to a freestream velocity of 40 m/s. Both mean and fluctuating velocity components from the finest resolved case were compared with PIV measurements, showing well predicted trends for all the regions evaluated. Furthermore, fluctuating pressure spectra in the wake were compared with measurements and showed good agreement at one location but underpredicted the decibel levels in the frequency range of 100–1000 Hz at a point farther downstream. One interesting observation is that two grids of approximately 6×10^6 cells and 5×10^6 cells gave approximately a 10 dB offset in the fluctuating wall pressure spectra.

Several authors [13–15] have also described the use of the LBM approach to estimating aeroacoustic noise sources in flow separated regions. Duncan et al. [13] conducted a simulation past the Ahmed body and used signal processing to visually identify noise sources restricted to different frequency bands.

Senthooran et al. [14] conducted a 0 deg and a 10 deg yaw angle simulation to validate simulated surface pressure spectra over the front side window as compared with measurements for a sedan type vehicle. The probes closest to the beltline and B-pillar showed promising agreement up to about 1000 Hz when compared with the measurements for both yaw angles evaluated.

Gaylard [15] used a similar approach for a full vehicle including side mirrors and rails at a 0 deg yaw angle. His results showed fair predictions of the surface pressure for some of the probes over the side window but an almost 40 dB offset at most at another location.

It appears from the above studies as though the accuracy of the fluctuating surface pressure spectra is dependent more on the location of the dynamic pressure sensors in relation to the local flow than on the methodology used. In other words, the dynamic pressure sensors located in regions with high spatial gradients of the source rms levels are more likely to deviate as compared with sensors located in a more diffuse region.

The third step in George's list has partly been covered by some of the above mentioned authors but is further discussed here. The most straightforward way is to compute the sound radiation directly. With this approach it is possible to evaluate sound emissions at any point within the computational domain. This technique however puts enormous constraints on both numerical schemes and boundary conditions in order to capture the wide range of scales present in any turbulent flow field. If the interest instead is in finding the emissions at points outside the computational domain or from an incompressible flow field, a different strategy must be used. For flows where walls are present, a feasible method is to use either the analogy of Ffowcs William and Hawking [11] or the analogy of Curle [16]. These analogies convert the governing momentum and continuity equations to an inhomogeneous wave equation. Studies of the incompressible assumption combined with a time formulation of Curle's analogy were reported in Ask and Davidson [17,18]. Discrepancies in the sound directivity were caused by a phase mismatch of the sources in the incompressible flow as compared with the compressible flow cause by a sudden change in the geometry. The main conclusion of their work was that the incompressible treatment, even at a Mach number of ($\mathrm{Ma}<0.15$), can be unsuitable when predicting sound radiation based on acoustic analogies since the flow has no possibility to expand or compress. Even though this compression/expansion of the flow is small compared with the gross characteristics of the flow, the radiated sound will be a consequence of a more or less complete cancellation of large source regions, which amplifies subtle details of the flow. Even at low Mach number, a compressible treatment of the flow is therefore more appropriate for flows, for example over, cavities, rear, and forward facing steps, where the flow takes a sudden change in direction. However, the incompressible flow field could accurately predict the levels of the two dominating dipole source terms. This was the chief motivation for the present work, where both flow and geometrical complexity are significantly increased. The time formulation of Curle's analogy, Eq. (1), uses the temporal derivatives inside the integral instead of keeping the spatial derivatives outside the integral, as Curle's [16] original formulation states.

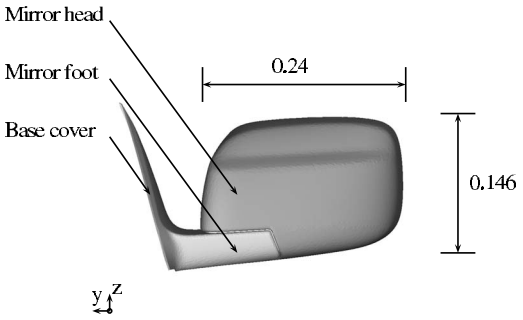

Fig. 2 Mirror geometry, front view

$$p(\mathbf{x},t)-p_\infty=\frac{1}{4\pi}\int_V\left[\frac{l_il_j}{a_\infty^2 r}\ddot{T}_{ij}+\frac{3l_il_j-\delta_{ij}}{a_\infty r^2}\dot{T}_{ij}+\frac{3l_il_j-\delta_{ij}}{r^3}T_{ij}\right]dV(\mathbf{y})$$
$$+\frac{1}{4\pi}\int_S l_in_j\left[\frac{\dot{p}\delta_{ij}-\dot{\tau}_{ij}}{a_\infty r}+\frac{p\delta_{ij}-\tau_{ij}}{r^2}\right]dS(\mathbf{y}) \quad (1)$$

In Eq. (1), the acoustic pressure fluctuation at an observer located at **x** is evaluated from a forward time projection of two integrals evaluated at the source location **y**. The first integral contains the volume contribution, where $T_{ij}=\rho u_iu_j-\tau_{ij}+(p-a_\infty^2\rho)\delta_{ij}$ is commonly referred to as the Lighthill tensor. The dot(s) above T_{ij}, τ_{ij}, and p denote time derivative(s) and l_j is the unit vector pointing from the source to the observer; the terms in this integral are often referred to as quadrapole terms. The second integral contains the surface integral and consists mainly of the fluctuating pressure and the fluctuating pressure temporal derivative. These terms are commonly referred to as dipole terms and are often regarded as the dominating terms for low Mach number wall bounded flows. The derivation of the expression above can be found in Ref. [19].

The text is organized in the following way. The Sec. 2 describes the object. This is followed by a description of the methodology used for the different simulations and a brief description of the measurement techniques (Sec. 3). The flow field results are given in Sec. 4 followed by the acoustic source results (Sec. 5). Section 6 concludes the results and is followed by the acknowledgment.

2 Case Description

The object in the present study is a side mirror mounted on a simplified sport utility vehicle. Both the underbody and wheel geometry are simplified as compared with a production vehicle due to their low impact on the flow above the beltline. The vehicle geometry at the present state is shown in Fig. 1 together with the identification of different parts used in the text.

Some parts in Fig. 1 are self explanatory, such as the front and side windows, the side mirror, and the hood but the remaining parts require additional description. The A-pillar is the roof support structure separating the front and side windows. The duck tail is an elevation of the rearmost part of the hood that has the purpose of screening the washer nozzles and wipers both visually and aerodynamically. The plenum is the space between the rearmost part of the hood and the windscreen and, finally, the beltline refers to the topmost horizontal line of the vehicle before reaching the glazed-in greenhouse region. A close-up of the mirror geometry is shown in Fig. 2. The mirror head width and height are 0.24 m and 0.146 m, respectively, and the projected area including both head and foot is 0.034 m^2. The Reynolds number based on the mirror height is $Re_H\approx 3.8\times 10^5$. In the following text, the mirror head refers to the darker part in this figure and the mirror foot is the support structure between the vehicle exterior and the mirror head, here identified as the lighter of the two.

The coordinate system is defined as follows: the x-axis follows the streamwise direction, the y-axis originates at the vehicle symmetry plane and is directed out of the domain, and the z-axis is normal to the ground surface.

3 Methodology

Two mesh generation processes are investigated and will be explained briefly here. In the first process, ICEM 5.1 grid generator is used to generate the volume mesh. Resolution boxes are here used for increased resolution in the investigated regions. In the first step of this process, an isotropic grid is generated with a Cartesian cell structure. Each Cartesian cell is built of 12 tetrahedral cells and is restricted to the off-wall region. This is also the main drawback of the present approach due to an initial mesh determined by the memory size of the front-end computer. In the second step, two prism layers are generated closest to the solid walls; in the final step, the grouped 12 tetrahedral cells are converted into one hexahedral cell if the quality restriction for the hexahedral cells is kept. This process took about 30 h (man time and CPU time) for each case on a double processor 32 GB HPC8000 computer but gives the user full control of both the mesh quality and the near-wall resolution.

In the second process, HARPOON 2.4 is used with resolution boxes similar to those in the ICEM process. The advantage of this code is first that the algorithm skips the mesh subdivision and generates a hexahedral dominant mesh directly and second that the whole mesh process took slightly more than 1 h (man time and CPU time). A drawback of this approach is that the prism generation is not sufficiently stable for this version and is therefore in this work partly compensated for by both a slower cell growing ratio close to the wall and a higher resolution.

Three different grids were investigated based on the above processes, two with ICEM and one mesh based on the HARPOON process. The two ICEM meshes are called GSM1I and GSM2I with grid sizes corresponding to 6.6×10^6 cell and 8×10^6 cells, respectively. The third grid based on the HARPOON mesh is called GSM3H and consists of 19.6×10^6 cells. The three cases are summarized in Table 1.

The first column in Table 1 gives the case identifications used in the following text. The second column gives the number of prism layers in the different cases. The third and fourth columns show the maximum cell size for the two most important resolution boxes. The fifth column gives the average n^+ over the A-pillar, mirror foot, and the mirror head, where n^+ refers to the wall normal direction. The final column gives the average number of cells

Table 1 Description of the three meshes

	Grid definitions				
ID	No. of prism layers	Cell size mirror wake (mm)	Cell size A-pillar region (mm)	Avg. n^+ A-pillar/mirror foot/mirror head	No. of cells resolving the mirror sail log-layer
GSM1I	2	4	8	50/72/70	6
GSM2I	2	4	4	53/70/70	6
GSM3H	0	2.5	2.5	40/111/102	5

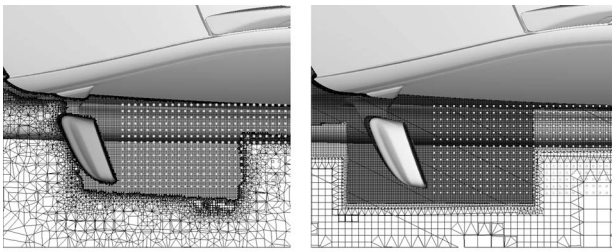

(a) (b)

Fig. 3 Mesh cut planes for GSM2I and GSM3H: (*a*) cut through the mesh of case GSM2I and (*b*) cut through the mesh of case GSM3H

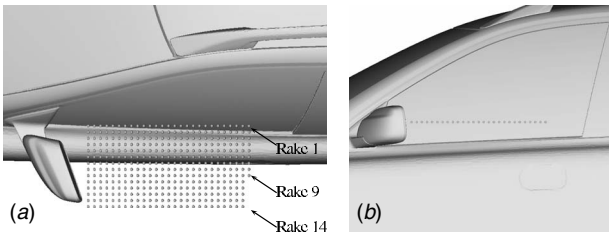

Fig. 4 Positions of the 14 hole probe: (*a*) probe location, top view and (*b*) probe location, side view

used for resolving the mirror sail log-layer ($n^+ < 500$). A cut-plane of the mesh is shown in Figs. 3(*a*) and 3(*b*) for cases GSM2I and GSM3H, respectively. The code used in this paper is the FLUENT 6.2.16 unstructured solver. It is based on a control volume formulation to convert the governing equations to a solvable algebraic set of equations. The code uses a collocated scheme with cell-centered storage of both scalars and vectors. The freestream velocity for the current simulation is 39 m/s, resulting in an ambient Mach number of 0.11, which implies that the incompressible assumption is justified. The bounding domain extends from the inlet located 20 m upstream of the front bumper to the outlet located 24.8 m downstream of the rear bumper. The farfield boundaries are located 9 m above the ground and 4.7 m from the symmetry plane. The vehicle is symmetric about the $y=0$ plane and, thus, only half the geometry is computed. The symmetry boundary condition is generally not recommended for LES due to its physical restriction for the three dimensionality of turbulent structures. However, the aim of the present work is to study the separated flow downstream of the A-pillar and side mirror, which is believed to have a small impact on the boundary condition at $y=0$.

The spatial discretization scheme used in the present work is a bounded central differencing scheme, which is essentially a second-order central scheme with a wiggle detector for wavelengths of $2\Delta x$ or less. For these occasions it blends to a second-order upwind scheme or, in the worst case, a first-order upwind scheme. The discretization in time follows an implicit second-order scheme, and at least five subiterations were conducted for each time step. The subgrid-scale stresses are computed by the Smagorinsky–Lilly model, where the eddy viscosity is modeled as

$$\nu_t = \rho L_s^2 |\bar{S}| \tag{2}$$

where S is the magnitude of the strain-rate tensor and L_s is the mixing length for subgrid scales and is defined as

$$L_s = \min(\kappa d, C_s V^{1/3}) \tag{3}$$

In Eq. (3), κ is the von Karman constant, d is the distance to the closest wall, C_s is the Smagorinsky constant, and V is the cell volume. In the present work, $C_s=0.1$. At solid boundaries, the log-law is applied for cells located in the range of $30 < n^+ < 300$, and a linear velocity relation is assumed for cells located at $n^+ < 5$. A blending of the wall shear stress is carried out in the intermediate region. The freestream velocity is applied at the inlet. Other boundary conditions used in the present work are a pressure boundary condition at the outlet and symmetry conditions at the farfield boundaries. The ground surface is modeled as a wall boundary and moves at the same speed as the freestream velocity.

The following simulation procedure was used. After a total simulation time of $160H/U$, an extraction of statistics and wall pressures was initiated and case GSM1I was run for a further $160H/U$. Here, H is the mirror head maximum height, see Fig. 2, and U is the freestream velocity. An interpolated solution field was then created as an initial solution for the other two cases. Case GSM2I was run from this solution for a further $53H/U$ before initiating extraction of the statistics. The simulation was then run for a further $160H/U$. GSM3H was initiated from the same solution as GSM2I and was run $77H/U$ before extracting statistics. After a total simulation time of $184H/U$, this final simulation was terminated. The time step for all cases was $\Delta t = 2 \times 10^{-5}$ s.

The flow measurements downstream of the side mirror were made by Ford Merkenich through scans at discrete points with a T-shaped 14 hole probe at their acoustic wind tunnel. The streamwise length of the probe is 14 mm and it has a cross-flow diameter of 4 mm; the locations of these points are shown in Fig. 4. The distance from the innermost rake to the side window varies between 25 mm at the farthest upstream point to 3 mm for the point located farthest downstream. A grid spacing of 20 mm in both the streamwise and spanwise directions was used for these measurements. The measurements of the mirror wake are grouped into 14 streamwise rakes, where the first rake is located closest to the window and the last rake is the most distant measured from the $y=0$ plane.

The two acoustic source terms evaluated in this work are

$$p_w^{\text{rms}} \quad \frac{\dot{p}_w^{\text{rms}}}{a_\infty} \tag{4}$$

where the first refers to source term 1 and the second refers to source term 2, see Eq. (1). In Eq. (4), the dot represents a time derivative and $a_\infty = 343$ m/s. The dynamic surface pressure was measured through ten integrated circuit piezoelectric type 103B01 acoustic pressure sensors from PCB Piezotronics Inc., mounted on the inside of a 5 mm thick polycarbonate window by an adhesive mounting ring. A 3.0 mm hole through the window connected the microphone with the external flow. The dynamic pressure was measured in two sequences to obtain a total of 16 measurement points. These locations are shown in Fig. 5. The fluctuating pressure sequence was then used to reconstruct the second source term.

4 Flow Field Results

Freestream air is accelerated above the hood starting from the grille stagnation line, see Fig. 1. The duck tail close to the rear edge of the hood affects the flow by lifting the windscreen stag-

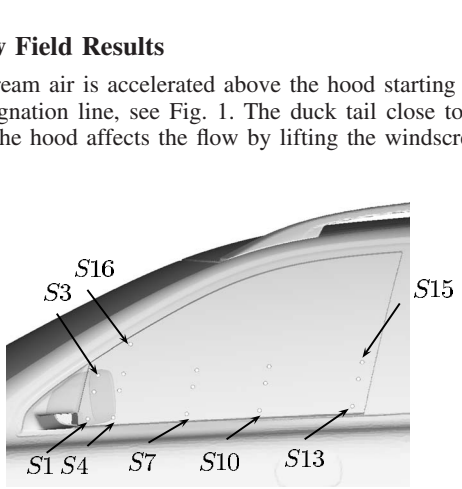

Fig. 5 Positions of the dynamic pressure sensors

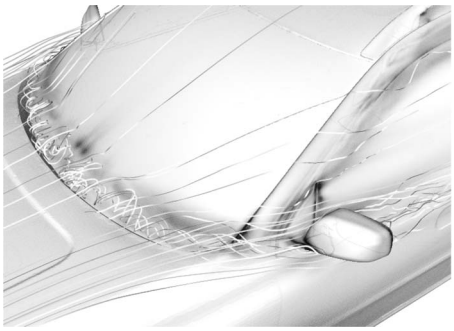

Fig. 6 Flow field for case GSM2I. Contours denote p_{rms}. Black corresponds to high values (150 Pa) and white is $p_{rms}=0$.

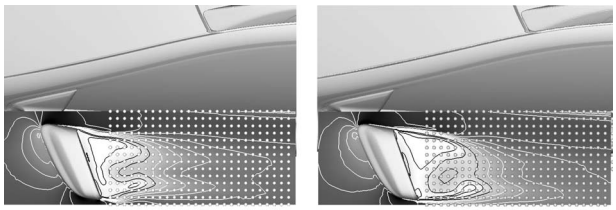

(*a*) (*b*)

Fig. 7 Velocity magnitude for cases GSM3H and GSM2I: (*a*) velocity magnitude for case GSM3H and (*b*) velocity magnitude for case GSM2I

nation line. This stagnation line divides the flow into one vortical structure within the plenum excited by flow passing above the plenum and a boundary layer flow at the hood directed toward the roof and the A-pillar, Fig. 6. Depending on the shape and angle of the A-pillar, the flow passing the A-pillar can be more or less well controlled. The A-pillar angle and radius also determine the shape and strength of the spiral vortex at the front door frame. At the lower part of the A-pillar, the flow separates due to the adverse pressure gradient and is directed either below or above the mirror foot, see Fig. 2. Between the base cover and the inner side of the mirror head, the flow is initially accelerated as a result of the converging flow path.

Downstream of this point, the flow decelerates and separates at the downstream part of the base cover, causing high levels of

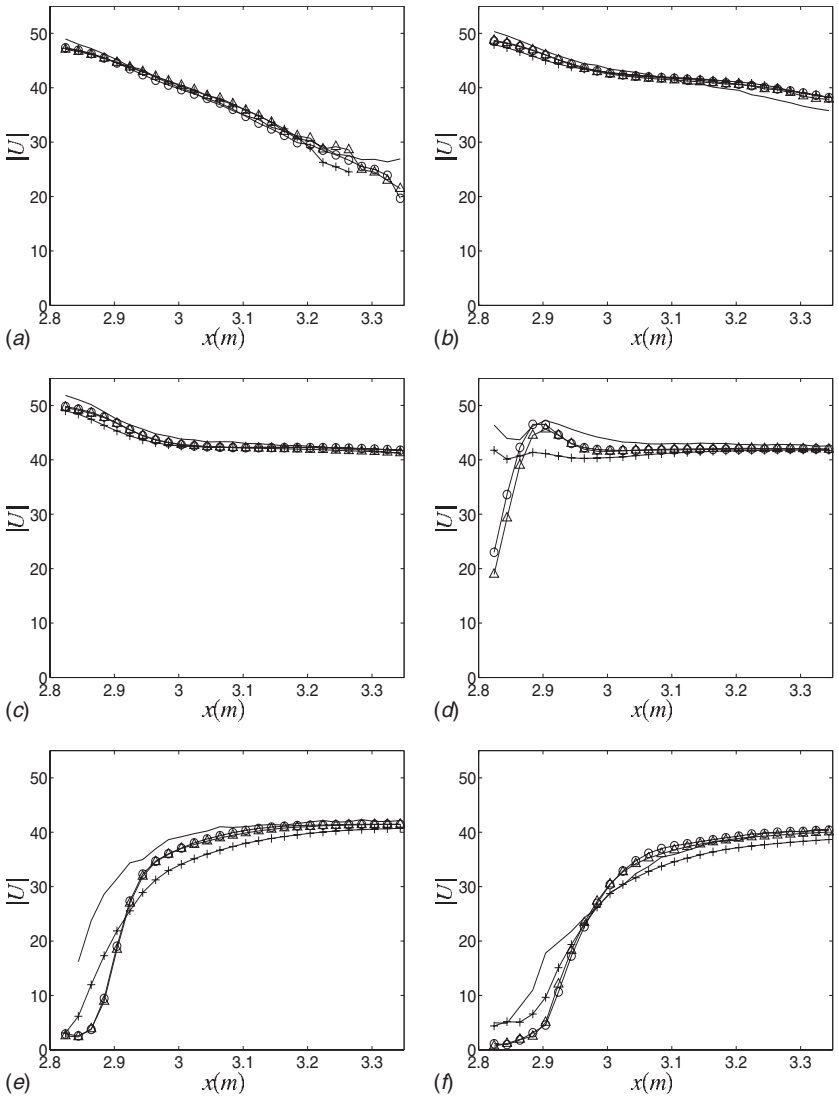

Fig. 8 $|U|$ along rakes 1–6, GSM1I (△), GSM2I (○), and, GSM3H (+) measured (−): (*a*) $|U|$ along rake 1, (*b*) $|U|$ along rake 2, (*c*) $|U|$ along rake 3, (*d*) $|U|$ along rake 4, (*e*) $|U|$ along rake 5, and, (*f*) $|U|$ along rake 6

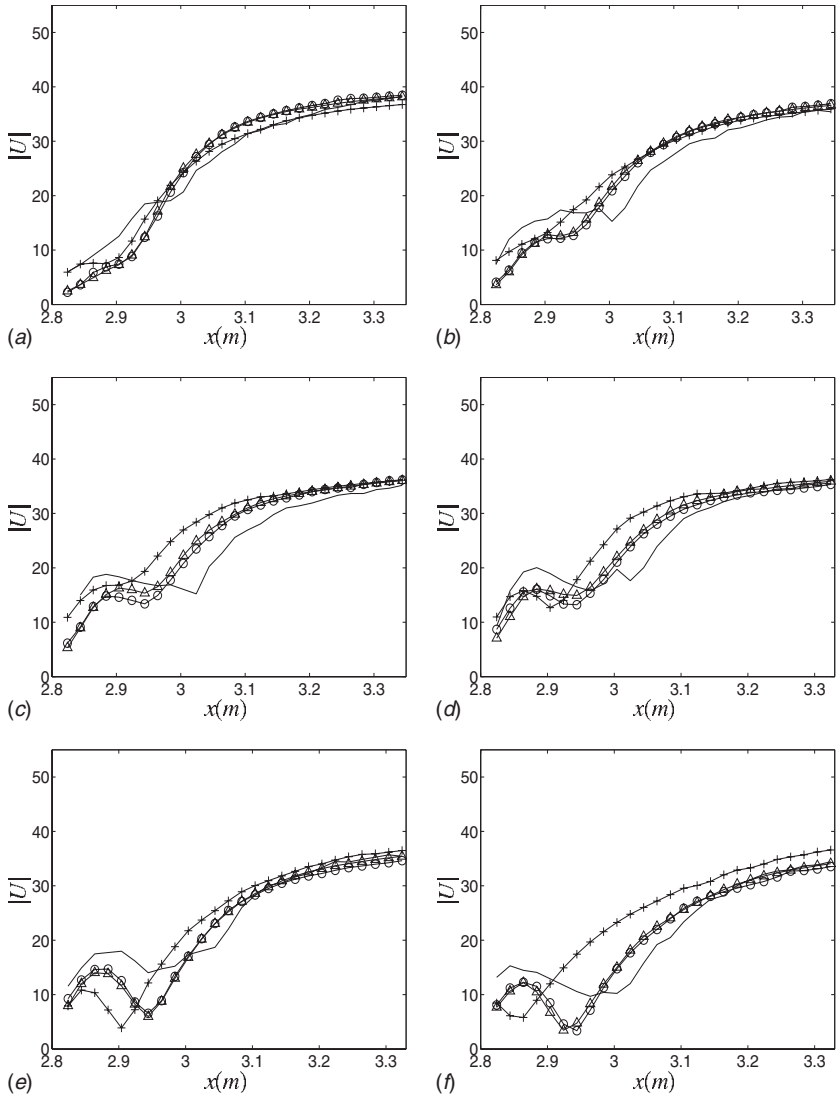

Fig. 9 $|U|$ along raked 7–12, GSM1I (△), GSM2I (○), and, GSM3H (+) measured (−): (*a*) $|U|$ along rake 7, (*b*) $|U|$ along rake 8, (*c*) $|U|$ along rake 9, (*d*) $|U|$ along rake 10, (*e*) $|U|$ along rake 11, and, (*f*) $|U|$ along rake 12

pressure fluctuations at the foremost part of the front side window. The vortex within the plenum is ejected at the junction between the plenum, the hood and the A-pillar root. Depending on the position and shape of the side mirror, this flow is either directed beneath the mirror foot, which is the case in the present work, or can be directed above the foot. This is the general description of the flow past the A-pillar and the side mirror region; below follows a comparison of the flow in the mirror wake.

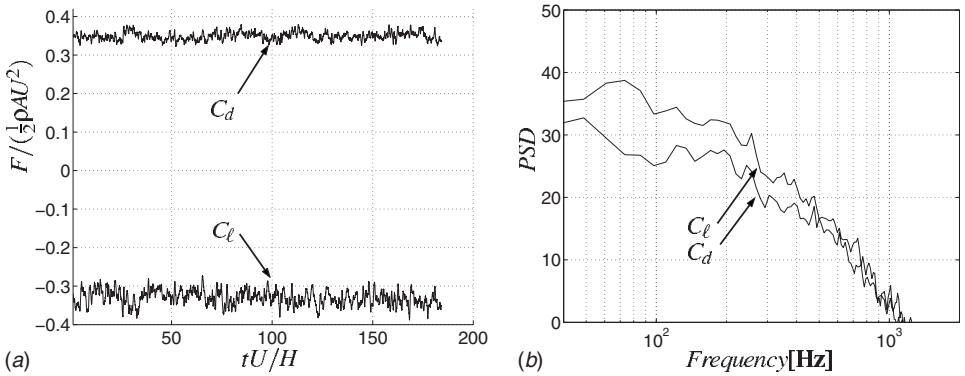

Fig. 10 C_d and C_ℓ for GSM3H: (*a*) mirror streamwise and floor normal force coefficient and (*b*) PSD of the force coefficients

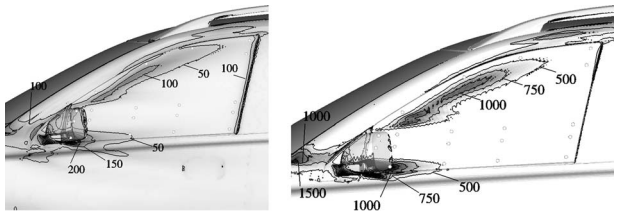

(*a*) (*b*)

Fig. 11 Contours of the two dipole source terms: (*a*) contours of source term 1 and (*b*) contours of source term 2

Figure 7 compares the mean velocity magnitude at the plane at which the 14 hole probe measurements were made.

For the inner rake adjacent to the window, Fig. 8(*a*), the distance to the window decreases with an increased streamwise position. This is also reflected in the mean velocity magnitude, which decreases slowly along the rake. For the last four points in this rake, a more rapid decay of the velocity magnitude can seen for all the simulations, which is explained by the proximity of the window. Again, the last point is located only 3 mm from the window. The measurements break this trend where the velocity magnitude is seen to level out and even increases for the point located farthest downstream in this rake. It appears here as though the probe induces an increased flow speed by blocking the near-wall flow and thus inducing a higher outer flow speed. For rakes 2 and 3, Figs. 8(*b*) and 8(*c*), the velocity magnitude shows good agreement between the three simulations and the measurements. A jetlike flow is created between the mirror head and A-pillar with a direction determined mainly by the angle of the mirror head. The presence of this jet is indicated in the points located farthest upstream in rake 2 but is more pronounced for rake 3. Rake 4 shows a slightly different result than the first three rakes, where case GSM3H seems to catch the trend even though the levels are too low for the upstream part of this rake. One way to interpret this result is that the flow has separated from the inner side of the mirror head in both the measured flow field and in case GSM3H, as is indicated in Fig. 7(*a*). This gives a slightly narrower wake as compared with cases GSM1I and GSM2I, where an attached flow leaves the mirror trailing edge. The streamwise velocity gradients identified in these two cases are therefore caused by the shear

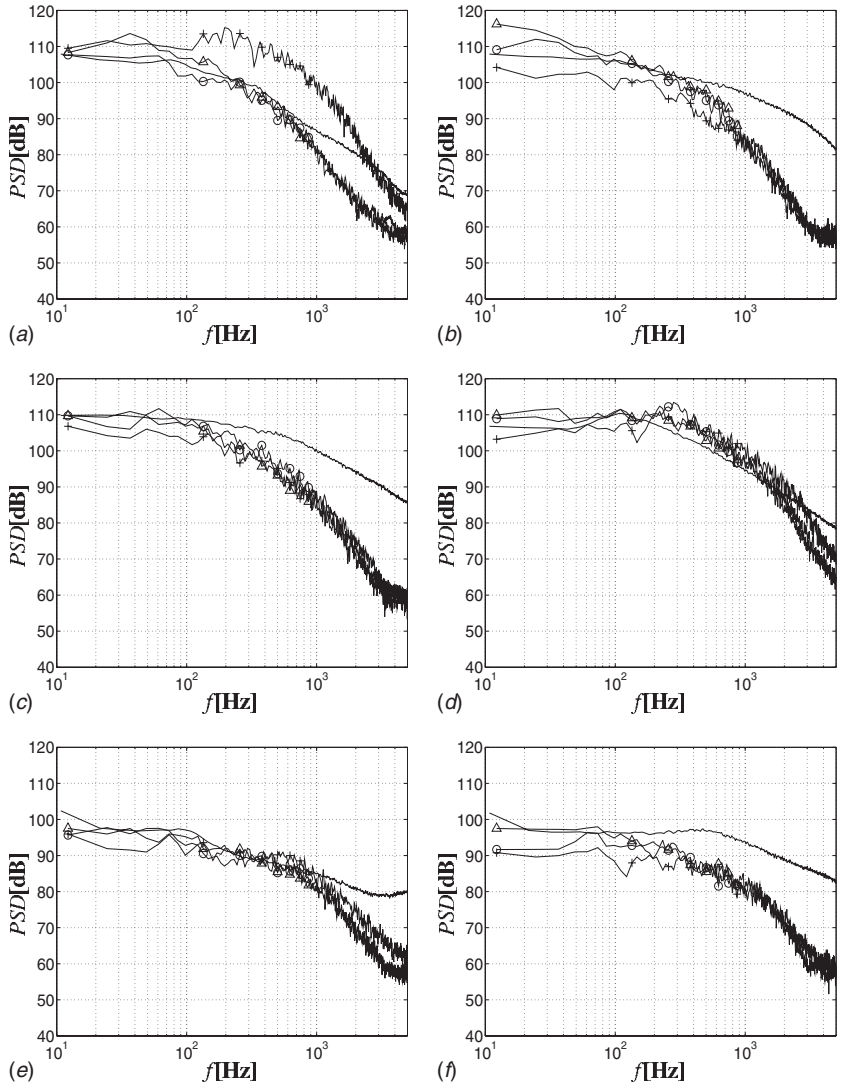

Fig. 12 Power spectral density of source term 1 for cases GSM1I (△), GSM2I (○), and, GSM3H (+) measured (−), where $p_{ref}=2e^{-5}$ Pa: (*a*) PSD of source term 1 at position 1, (*b*) PSD of source term 1 at position 2, (*c*) PSD of source term 1 at position 3, (*d*) PSD of source term 1 at position 4, (*e*) PSD of source term 1 at position 5, and, (*f*) PSD of source term 1 at position 6

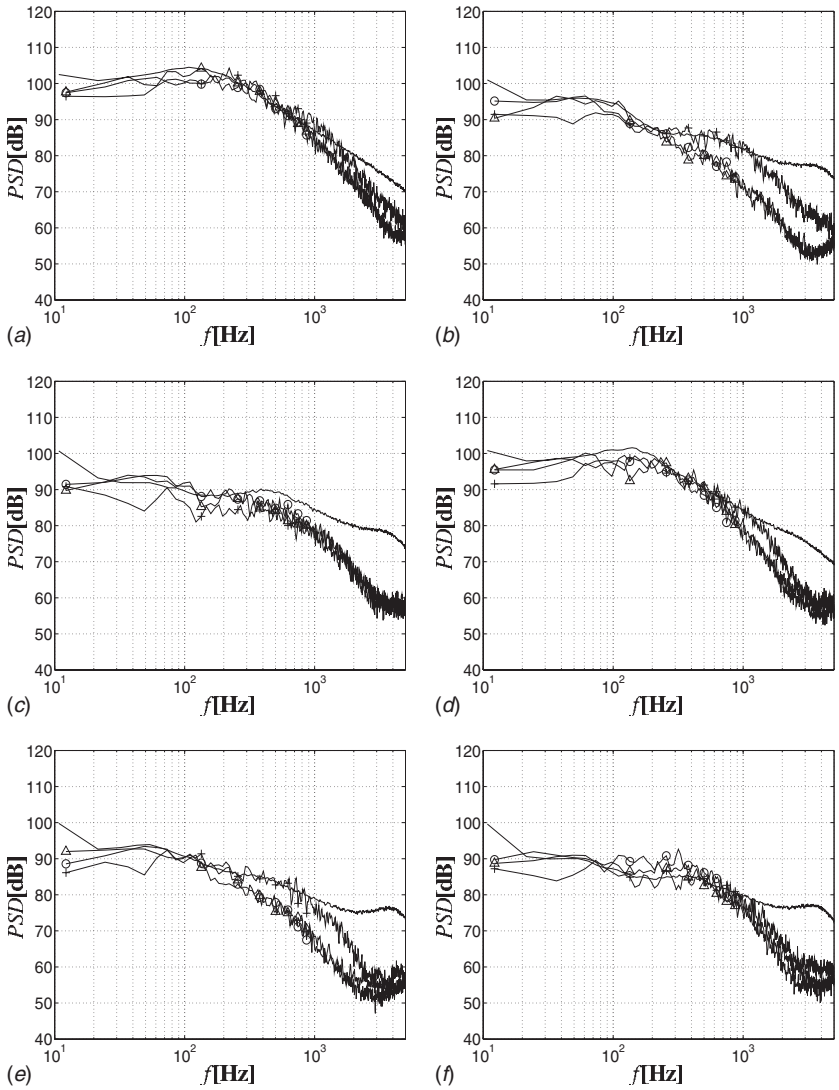

Fig. 13 Power spectral density of source term 1 for cases GSM1I (△), GSM2I (○), and, GSM3H (+) measured (−), where $p_{ref}=2e^{-5}$ Pa: (*a*) PSD of source term 1 at position 7, (*b*) PSD of source term 1 at position 8, (*c*) PSD of source term 1 at position 9, (*d*) PSD of source term 1 at position 10, (*e*) PSD of source term 1 at position 11, and (*f*) PSD of source term 1 at position 12

layer, which is located closer to the side window compared with case GSH3H. In rake 5 the farthest upstream point is located in the mirror wake and the next point along the rake cuts through the shear layer. Judging from Fig. 8(*e*) it appears as though all simulations overpredict the streamwise extent of the mirror recirculation zone but a small difference in the spanwise location of the shear layer can very well cause this effect. In the final rake in this series, Fig. 8(*f*), the agreement between the simulations and measurements is again better. The 14 hole probe gives smooth and continuous profiles up to rake 4 when traversed downstream but shows a tendency from rake 5 and higher to give a shaky profile, for example, for rake 6, point 5.

In Fig. 9(*a*), case GSM3H agrees well with the measured results and a small underprediction of the velocity magnitude can be seen for the other two simulations in the upstream part of the mirror wake. Rake 8, Fig. 9(*b*), starts in the recirculation zone in the mirror wake where the velocity magnitude slowly increases downstream. At point 6 in this rake, the maximum level is found in the case of the measurements while the corresponding peak is found for point 5 in cases GSM1I and GSM2I. The level decreases downstream of this peak until the end of the recirculation zone is reached, where the level again increases. Figure 9(*c*) shows the rake located approximately in the center of the mirror and, from this rake to the end, i.e., rake 14, cases GSM1I and GSM2I show slightly better agreement with the measurements than case GSM3H. The recirculation zone in the upstream part of rake 3 is both more distinguished and located farther upstream as compared with rake 8. Even though case GSM3H has the highest resolution in the mirror wake region, the results deviate to a greater extent with higher rake number as compared with the other two simulations. One possible explanation is the insufficient near-wall resolution.

The mean streamwise force coefficient of the mirror is as follows: $\bar{C}_{d,\mathrm{GSM1I}}=0.3624$, $\bar{C}_{d,\mathrm{GSM2I}}=0.3648$ and $\bar{C}_{d,\mathrm{GSM3H}}=0.349$. The lift force coefficient was also extracted for case GSM3H for which the time sequences of the two force components are presented in Fig. 10(*a*). To determine the fundamental frequency of the mirror, the power spectral density (PSD) was computed for both components, Fig. 10(*b*).

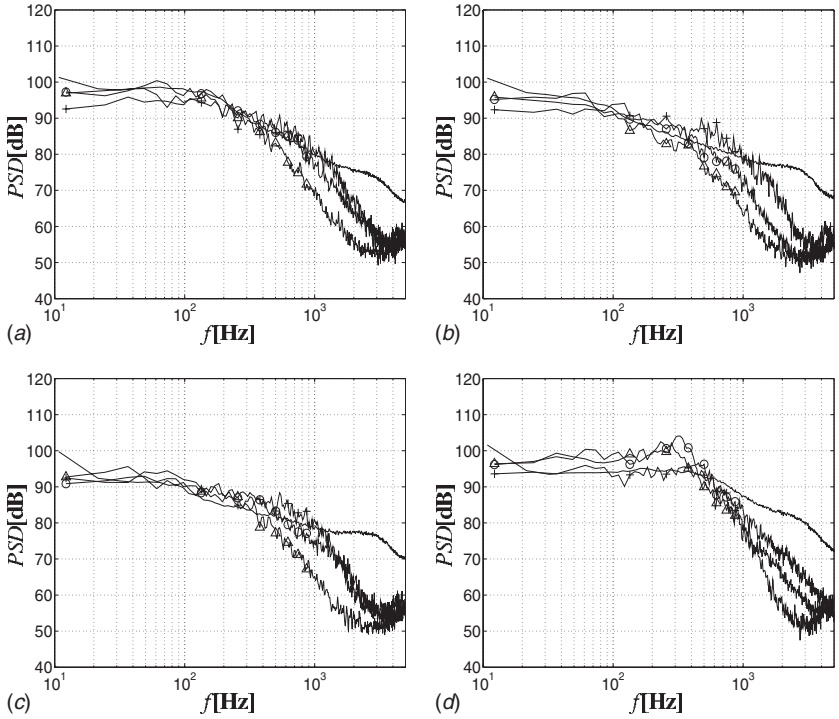

Fig. 14 Power spectral density of source term 1 for cases GSM1I (△), GSM2I (○), and GSM3H (+) measured (−), where $p_{ref}=2e^{-5}$ Pa: (*a*) PSD of source term 1 at position 13, (*b*) PSD of source term 1 at position 14, (*c*) PSD of source term 1 at position 15, and (*d*) PSD of source term 1 at position 16

The peak levels from Fig. 10(*b*) were found at $f_n(\text{lift})=73$ Hz and $f_n(\text{drag})=49$ Hz, which determined the fundamental frequency. The Strouhal number could then be computed according to

$$\text{St}=\frac{f_n(\text{drag})H}{U_\infty} \tag{5}$$

In Eq. (5), St is the Strouhal number, H is the mirror head height and U_∞ is the freestream velocity. The Strouhal number was then computed to be St=0.18, which is close to other bluff body objects, such as cylinders and spheres. This means that one period is covered within $4.37H/U$ and the shortest simulation, GSM3H, contains approximately 24 periods of this frequency.

5 Acoustic Results

Figure 11 shows contours of the two source terms investigated (see Eqs. (1) and (4)) together with the location of the dynamic pressure sensors (shown in Fig. 5). Figure 11(*a*) shows the rms level of source term 1 at the front part of the greenhouse. The effect of the A-pillar vortex is clearly marked in this figure by a thin region close to the door frame. Still, the highest level of this source term is found at the lee side of the lower part of the mirror foot caused by the sudden change in the geometry of the mirror foot combined with high local velocities for this region. Source term 2 represents the temporal variation in the first term. This means that the highest levels will be found in regions with short time scales. Figure 11(*b*) shows a high correlation with source term 1 but it must be kept in mind for this term that the two terms cannot be compared quantitatively as they represent sources to Curle's equation with different dependencies with respect to the distance to an observer (r and r^2, respectively, see Eq. (1)). However, both terms show maximum levels in the vicinity of the mirror foot and the second highest levels at the root of the A-pillar. The two pictures can also give a hint of the difficulties associated with the comparison of different data sets for a coarse measurement grid, as in the present case. A small shift in the location of the present unsteady structures will have a great effect on the PSD spectra because of the sharp gradient that exists, for example, at the sensors located closest to the base cover.

Position 1, Fig. 12(*a*), is located at the lee side of the mirror foot. Cases GSM1I and GSM2I agree well with measured levels up to about 1000 Hz, and case GSM3H shows a clear overprediction for the whole resolved frequency range for this position. The reason is primarily that, in this case, the shear layer is directed slightly more downward when leaving the trailing edge of the mirror foot as compared with the other two cases. In addition, the flow stays attached for a greater distance downstream of the junction between the mirror foot and the base cover. This has the effect of directing the flow to the window in this case, generating high fluctuation levels. At position 2, Fig. 12(*b*), the flow separates smoothly from the trailing edge of the base cover, similar to the flow at position 1 in cases GSM1I and GSM2I. All simulations predict this up to 300 Hz, where the levels decay rapidly as compared with the measured signal. The resolution here is apparently insufficient to capture the turbulent structures. Comparing the measured results at positions 1 and 2, there are significantly higher levels for the intermediate frequencies at the latter position. At position 3, Fig. 12(*c*), the flow follows the curvature of the base cover trailing edge and again directs the flow toward the window in all simulations. The measured level increases also at this point in the intermediate frequency range, and the simulations have clear problems predicting these levels accurately.

The findings thus far in the most upstream part of the window are mainly determined by the flow passing between the mirror house and the base cover. The variation in the position that captures the unsteady dynamics of this region primarily affects the frequency range between 100 Hz and 5000 Hz, judging from the measurements. The next three points are positioned further downstream at the side window. The measurements at position 4, Fig. 12(*d*), indicate a small peak at 100 Hz while GSM2I indicates a peak close to 250 Hz. The other two cases exhibit a more broad-

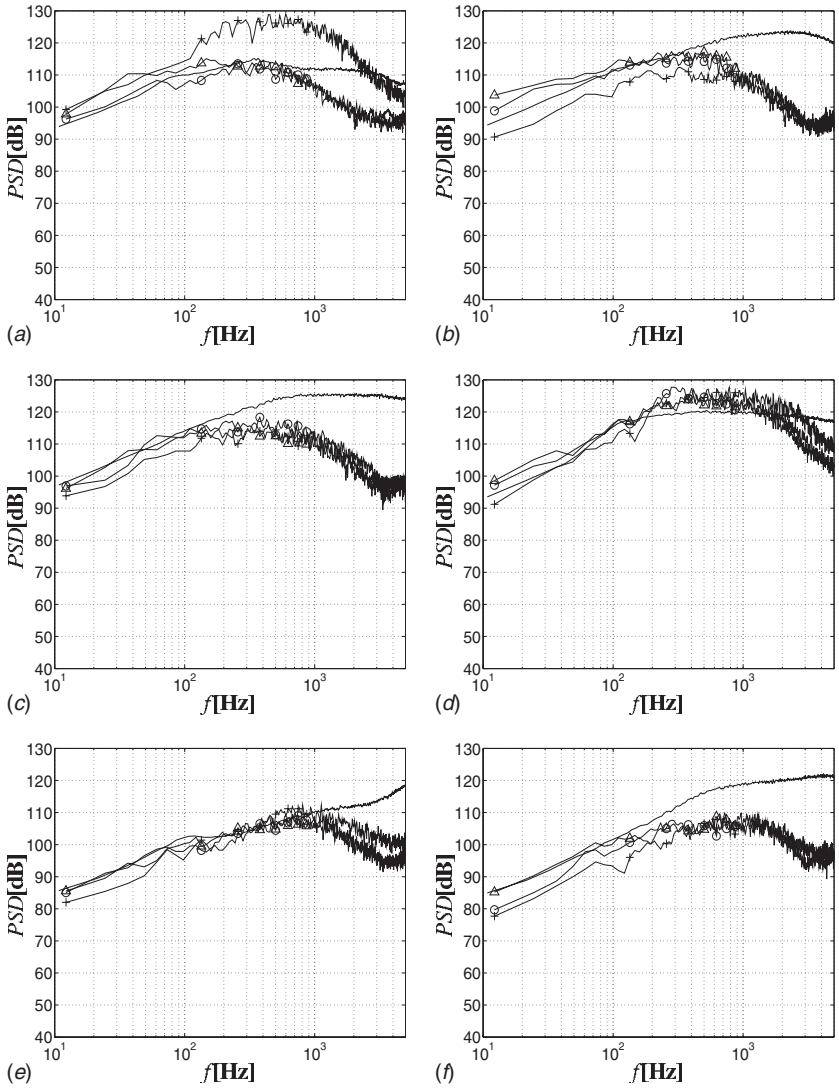

Fig. 15 Power spectral density of source term 2 for cases GSM1I (△), GSM2I (○), and GSM3H (+) measured (−), where $p_{ref}=2e^{-5}$ Pa: (*a*) PSD of source term 2 at position 1, (*b*) PSD of source term 2 at position 2, (*c*) PSD of source term 2 at position 3, (*d*) PSD of source term 2 at position 4, (*e*) PSD of source term 2 at position 5, and (*f*) PSD of source term 2 at position 6

banded character, and, except for the peak, all simulations follow the measurements up to about 2000 Hz. The peak is caused by vortex shedding downstream of the mirror and leaves a rather broad footprint in Fig. 11(*a*). The levels are significantly reduced at position 5 as compared with the first four positions because of a more steady flow field. The levels here are well predicted up to about 1000 Hz in all the cases, Fig. 12(*e*). For position 6, Fig. 12(*f*), a flat level can be seen all the way up to 600 Hz in the measurements. The three simulations capture this trend up to about 300 Hz, where the decay starts and they rapidly begin to lose energy. The spiral A-pillar vortex is located between positions 6 and 16, Fig. 14(*d*), and the measured results of these two points are fairly similar.

For position 7, Fig. 13(*a*), the agreement in levels for the measured results and for case GSM3H matches up to almost 2000 Hz. This position and downstream of position 15 are characterized by a smaller spatial gradient of source term 1. This is also reflected in the results with a generally higher correlation between measured and simulated results. The resolution zone has ended in case GSM1I for the last positions at the lower part of the window, and the effect is clearly reflected in Figs. 14(*a*)–14(*c*) with a much earlier decay in source levels. The last result for source term 1 is shown for position 16, located closer to the door frame than the other points, Fig. 14(*d*). The only case with a sufficient grid resolution in this region is GSM3H, which predicts the measured frequencies perfectly up to about 700 Hz.

Source term 2 is somewhat more difficult to analyze than the first source term because of its more abstract interpretation. This source increases with short time scales, however, and is comparatively smaller for the more slowly varying flow structures even if the magnitude of their fluctuation is large. This is typically the case for the subsequent results at the same positions, as previously investigated for source term 1. Here the level increases with increased frequency instead of the opposite. There is of course an upper limit at which dissipation takes place but that maximum is not always present in the results or at least not in the frequency range investigated. Even though the physical interpretation of source term 2 is different than that of source term 1, the trends are still very similar to what was found in the previous text. For example, at position 1, Fig. 15(*a*), the levels in case GSM3H were significantly overpredicted due to a mismatch of the upstream flow field. The other two cases, GSM1I and GSM2I, accurately

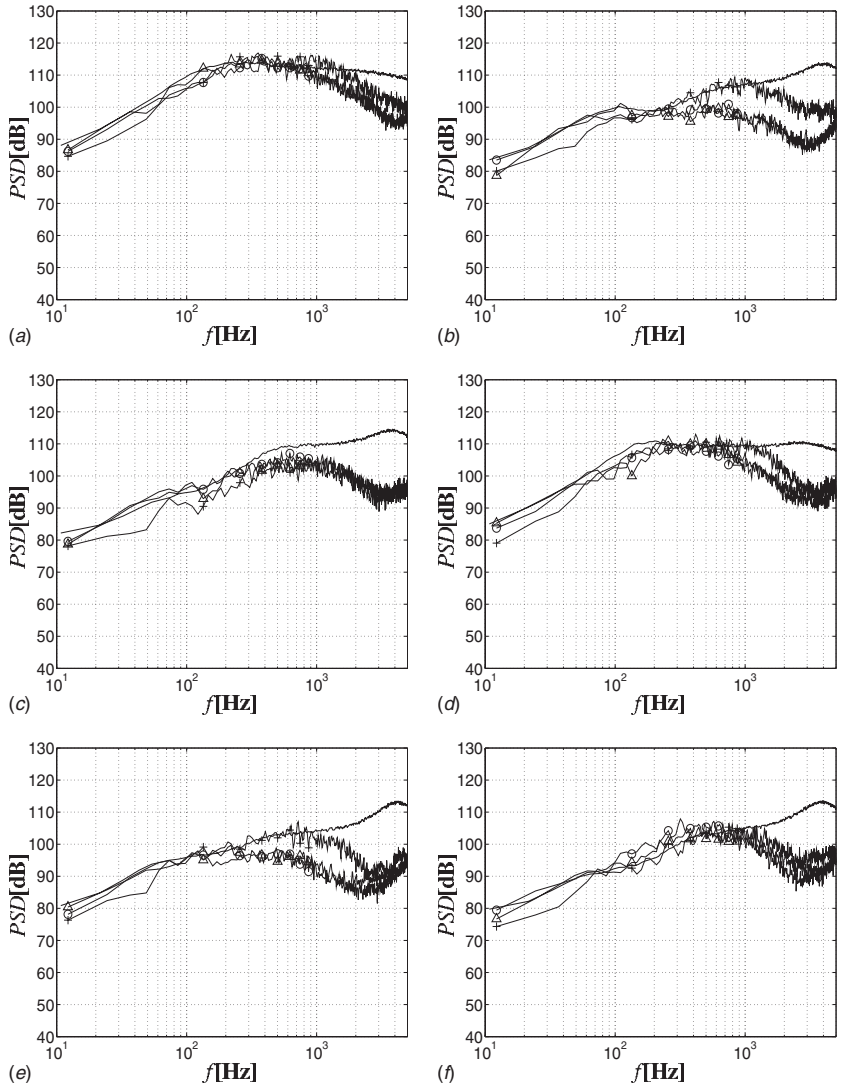

Fig. 16 Power spectral density of source term 2 for cases GSM1I (△), GSM2I (○), and GSM3H (+) measured (−), where $p_{ref}=2e^{-5}$ Pa: (*a*) PSD of source term 2 at position 7, (*b*) PSD of source term 2 at position 8, (*c*) PSD of source term 2 at position 9, (*d*) PSD of source term 2 at position 10, (*e*) PSD of source term 2 at position 11, and (*f*) PSD of source term 2 at position 12

predicted the levels up to about 1000 Hz, and similar results are found for this source term. One striking thing about the results is that it appears as though the numerical cut-off is much more pronounced in these results than in the results for source term 1. Of all the positions investigated, the highest levels measured are found at position 3, followed by position 2. This is interesting because it shows the importance and potential of better aerodynamic design of this region of the vehicle, see Figs. 16 and 17. As mentioned in the text above, the flow in this region is extremely complex and involves several geometrical parameters. Except for positions 2, 3, and 6, the results are seen to be very well predicted in at least one of the three cases.

6 Conclusion

This paper reports an investigation of the degree to which the amplitude of the two dominating dipole source terms in Curle's equation can be predicted by using the traditional law-of-the-wall and hex-dominant meshes with isotropic resolution boxes for a detailed ground vehicle geometry.

Three simulations were made using the Smagorinsky–Lilly model combined with the law-of-the-wall for the near-wall region. Two different mesh strategies were investigated, both with hex-dominant meshes and with the use of local resolution boxes. Two different meshes were investigated in the first process with different resolution zones and employing two prism layers at the solid walls. The second strategy contains no prism layers but these are partly compensated for by higher resolution. Although the size mesh of the GSM3H is three time more than two other cases (GSM1I and GSM2I) there is no significant changes in results can be seen. The main reason is probably the prism layer, which is used for cases GSM1I and GSM2I but not for case GSM3H.

The flow field results containing the velocity magnitude are compared for the three simulations and the 14 hole probe measurement made at the acoustic wind tunnel in Ford Merkenich at 14 rakes located in the mirror wake. Closest to the window and downstream of the mirror head recirculation zone, all three simulations accurately predict the velocity magnitude. Some variation in the size and shape of this recirculation zone is found between the different meshes, most probably caused by differences in the detachment of the mirror head boundary layer.

The Strouhal number of the shortest simulation case, GSM3H, was computed from the fundamental frequency of the ground nor-

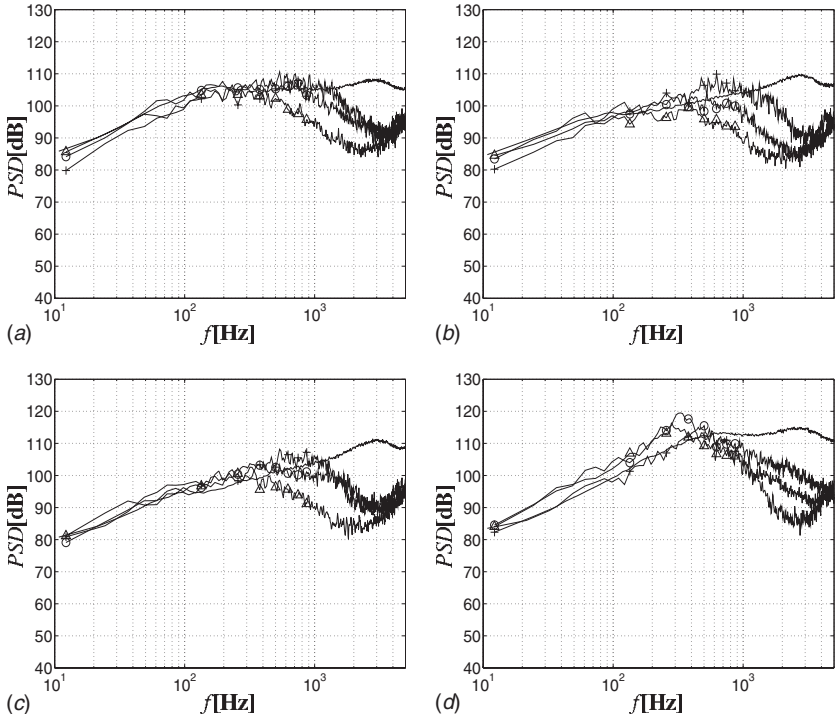

Fig. 17 Power spectral density of source term 2 for cases GSM1I (△), GSM2I (○), and GSM3H (+) measured (−), where $p_{ref}=2e^{-5}$ Pa: (*a*) PSD of source term 2 at position 13, (*b*) PSD of source term 2 at position 14, (*c*) PSD of source term 2 at position 15, and (*d*) PSD of source term 2 at position 16

mal force component. The computed Strouhal frequency agrees well with the flow past similar objects and gives indications of an acceptable simulation time.

In addition, dynamic pressure sensors at 16 different locations at the vehicle side window were used to capture the levels of the two dipole source terms. These results are compared with the three simulations. Except for at three positions, at least one of the three simulations accurately captures the levels of both source terms up to about 1000 Hz. The three positions with poorer agreement with measurements were found in regions sensitive to small changes in the local flow direction.

Acknowledgment

This work was supported by the Volvo Car Corporation and the Swedish Agency for Innovation Systems (VINNOVA).

References

[1] Stapleford, W., and Carr, G., 1970, "Aerodynamic Noise in Road Vehicles, Part 1: The Relationship Between Aerodynamic Noise and the Nature of the Airflow," The Motor Industry Research Association, p. 1971/2.
[2] Thomson, J., 1964, "Wind Noise—A Practical Approach," Society of Automotive Engineers, Mar. 30–Apr. 3, p. 840B.
[3] Stapleford, W., 1970, "Aerodynamic Noise in Road Vehicles, Part 2: A Study of the Sources and Significance of Aerodynamic Noise in Saloon Cars," The Motor Industry Research Association, p. 1972/6.
[4] Watanabe, M., Harita, M., and Hayashi, E., 1978, "The Effect of Body Shapes on Wind Noise," Society of Automotive Engineers, p. 780266.
[5] George, A., 1990, "Automobile Aerodynamic Noise," Society of Automotive Engineers, Feb. 26–Mar. 2, p. 900315.
[6] Krajnović, S., and Davidson, L., 2003, "Numerical Study of the Flow Around the Bus-Shaped Body," J. Fluids Eng., **125**, pp. 500–509.
[7] Krajnović, S., and Davidson, L., 2005, "Flow Around a Simplified Car. Part I: Large Eddy Simulations," J. Fluids Eng., **127**(5), pp. 907–918.
[8] Krajnović, S., and Davidson, L., 2005, "Flow Around a Simplified Car. Part II: Understanding the Flow," J. Fluids Eng., **127**(5), pp. 919–928.
[9] Krajnović, S., 2002, Large-Eddy Simulations for Computing the Flow Around Vehicles, Ph.D. thesis, Chalmers University of Technology.
[10] Rung, T., Eschricht, D., Yan, J., and Thiele, F., 2002, "Sound Radiation of the Vortex Flow Past a Generic Side Mirror," Eighth AIAA/CEAS Aeroacoustics Conference, Breckenridge, CO, Jun. 17–19, Paper No. AIAA-2002-2340.
[11] Ffowcs Williams, J., and Hawkings, D., 1969, "Sound Generation by Turbulence and Surfaces in Arbitrary Motion," Philos. Trans. R. Soc. London, Ser. A, **264**(1151), pp. 321–342.
[12] Posson, H., and Pérot, F., 2006, "Far-Field Evaluation of the Noise Radiated by a Side Mirror Using LES and Acoustic Analogy," 12th AIAA/CEAS Aeroacoustics Conference, Cambridge, MA, May 8–10, Paper No. AIAA-2006-2719.
[13] Duncan, B., Sengupta, R., Mallick, S., Shock, R., and Sims-Williams, D., 2002, "Numerical Simulation and Spectral Analysis of Pressure Fluctuations in Vehicle Aerodynamic Noise Generation," SAE Paper No. 2002-01-0597.
[14] Senthooran, S., Crouse, B., Noelting, S., Freed, D., Duncan, D., Balasubramanian, G., and Powell, R., 2006, "Prediction of Wall Pressure Fluctuations on an Automobile Side-Glass Using a Lattice-Boltzmann Method," AIAA/CEAS Aeroacoustics Conference and Exhibit, Cambridge, MA, May 8–10, Paper No. 2006-2559.
[15] Gaylard, A., 2006, "CFD Simulation of Side Glass Surface Noise Spectra for a Bluff SUV," SAE Paper No. 2006-01-0137.
[16] Curle, N., 1955, "The Influence of Solid Boundaries Upon Aerodynamic Sound," Proc. R. Soc. London, Ser. A, **A231**, pp. 505–514.
[17] Ask, J., and Davidson, L., 2005, "An Acoustic Analogy Applied to the Laminar Upstream Flow Over an Open 2D Cavity," C. R. Mec., **333**(9), pp. 660–665.
[18] Ask, J., and Davidson, L., 2009, "Sound Generation and Radiation of an Open Two–Dimensional Cavity," AIAA J. **47**, 1337–1349.
[19] Larsson, J., 2002, "Computational Aero Acoustics for Vehicle Applications," Chalmers University of Technology.

Flows and Their Stability in Rotating Cylinders With a Porous Lining

M. Subotic[1]
Graduate Research Assistant

F. C. Lai
Professor
Fellow ASME

School of Aerospace and Mechanical Engineering,
University of Oklahoma,
Norman, OK 73019

Flow fields in an annulus between two rotating cylinders with a porous lining have been numerically examined in this study. While the outer cylinder is stationary, the inner cylinder is rotating with a constant angular speed. A homogeneous and isotropic porous layer is press-fit to the inner surface of the outer cylinder. The porous sleeve is saturated with the fluid that fills the annulus. The effects of porous sleeve thickness and its properties on the flows and their stability in the annulus are numerically investigated. Three-dimensional momentum equations for the porous and fluid layers are formulated separately and solved simultaneously in terms of velocity and vorticity. The solutions have covered a wide range of the governing parameters ($10^{-5} \leq Da \leq 10^{-2}$, $2000 \leq Ta \leq 5000$, $0.8 \leq \bar{b} \leq 0.95$). *The results obtained show that the presence of a porous sleeve generally has a stabilizing effect on the flows in the annulus.* [DOI: 10.1115/1.4001541]

1 Introduction

There are many engineering applications, which involve rotational concentric cylinders. These include, for example, catalytic chemical reactors, filtration devices, liquid-liquid extractors, drilling in oil and gas wells, and journal bearings. For the latter application, the inner cylinder (shaft) is rotating while the outer cylinder remains stationary. One way to keep a bearing lubricated is the use of porous bearings in which a porous layer is press-fit to the inner surface of the outer cylinder and serves as a lubricant storage. Depending on the application, this feature can totally or partially eliminate the need for an external source of lubricant. Another advantage of these bearings is that very high production rates are possible due to the short sintering times required. However, one issue that has not been considered so far is the effects of porous layer properties on the hydrodynamic stability of the fluid flow in the annulus. It is well known when cylinders rotate at high speeds, the originally two-dimensional rotational flow in the annulus will become three-dimensional due to the appearance of toroidal vortices. This issue has become very important because the change of flow structure in journal bearings can cause uneven pressure distribution inside the annulus and therefore uneven lubricant distribution. This can leave certain metal areas "lubricant free" and metal to metal contact may occur between the rotating shaft and the bearing, which is highly undesirable.

For flows without the involvement of a porous layer, Lord Rayleigh was the first to study the stability of circular Couette flows but his study was limited to inviscid flows [1]. Taylor extended this study to include viscous effects and he observed that instabilities led to a steady secondary flow in the form of toroidal vortices, which were regularly spaced along the axis of the cylinder [2,3]. Numerous studies have been followed [4–8], which also include Newtonian [9,10] as well as non-Newtonian fluids [11]. The presence of a porous layer makes the problem more complicated and challenging. This also brings up the questions of how the porous layer properties and dimensions will affect the flow in the annulus and the onset of instability. To the authors' knowledge, these questions have only received limited attention. Most previous studies have assumed two-dimensional flows. In a related study, Channabasappa et al. [12] investigated the linear stability of viscous flow in a porous annulus bounded by two concentric circular cylinders in which the inner cylinder was stationary and the outer was rotational. Their results revealed that the critical Taylor number increases with a decrease in permeability of the porous medium. Chang [13] also investigated the hydrodynamic stability of Taylor–Dean flow in a porous annulus between rotating cylinders with radial flow. He considered both inward and outward radial flows. He found that the superimposed radial flow can produce either stabilizing or destabilizing effect depending heavily on the ratio between the average pumping velocity and the rotation velocity.

It has been shown that the presence of a porous layer alters the angular velocity profiles in the annulus [14]. Therefore, it is reasonable to expect that the critical Taylor number, which reported for pure fluid flows would be modified as well. Thus it is the objective of the present study to investigate the effects of porous sleeve thickness and its properties on the flows and their stability in such configuration.

2 Formulation and Numerical Method

One approach, which is commonly used in the study of flow stability, is the linear stability analysis. However, when using this approach, it is usually assumed that the gap between the cylinders is very small [15]. This assumption is equivalent to say that $1 - \eta \ll 1$. Indeed, the value of η is usually limited to 0.9 when a linear stability analysis is applied. Although this assumption leads to a great simplification of the problem, the above condition is not always met. Evidently, a gap width can be much greater in real applications. Although it is possible to apply a linear stability analysis without resorting to the small-gap approximation as explained by Chandrasekhar [16] but this would lead to greater mathematical difficulties.

To determine the critical Taylor number and the onset of flow instability, a novel approach has been proposed and validated by Coronado-Matutti et al. [17]. This approach is adopted for the present study. This approach avoids the need to derive and solve the linearized perturbation equations, which ultimately lead to an eigenvalue problem. With the complexity imposed by the presence of porous lining (as evident from the interface conditions discussed in the following section), the solution for the resulting eigenvalue problem becomes extremely difficult if not impossible. With the new approach proposed [17], one tracks the solution path

[1]Present address: Mechanical Engineer, Schlumberger Oilfield Services, Sugar Land, TX 77478.

Contributed by the Fluids Engineering Division of ASME for publication in the JOURNAL OF FLUIDS ENGINEERING. Manuscript received March 12, 2009; final manuscript received March 6, 2010; published online April 27, 2010. Assoc. Editor: Dimitris Drikakis.

of three-dimensional equations of motion with respect to Taylor number instead and then the value of Taylor number at which the growth rate of velocity field in the R-Z plane has the highest value is determined as the critical Taylor number.

To this end, the governing equations are formulated separately for the fluid and porous regions and solved simultaneously. To avoid the complications involving the pressure terms [18–21], the vorticity-velocity method has been adopted for the present study. This method is also reported to be more numerically stable for high Reynolds number flows. Thus the dimensionless governing equations are formulated below in terms of velocity and vorticity for fluid and porous regions separately.

2.1 Fluid Region.

$$V_{R1}\frac{\partial V_{\theta 1}}{\partial R}+\frac{V_{\theta 1}}{R}\frac{\partial V_{\theta 1}}{\partial \theta}+V_{Z1}\frac{\partial V_{\theta 1}}{\partial Z}+\frac{V_{R1}V_{\theta 1}}{R}=\frac{1}{Re}\left[\frac{1}{R}\frac{\partial}{\partial R}\left(R\frac{\partial V_{\theta 1}}{\partial R}\right)+\frac{1}{R^2}\frac{\partial^2 V_{\theta 1}}{\partial \theta^2}+\frac{\partial^2 V_{\theta 1}}{\partial Z^2}+\frac{2}{R^2}\frac{\partial V_{R1}}{\partial \theta}-\frac{V_{\theta 1}}{R^2}\right] \tag{1}$$

$$\frac{\partial^2 V_{R1}}{\partial R^2}+\frac{1}{R}\frac{\partial V_{R1}}{\partial R}+\frac{\partial^2 V_{R1}}{\partial Z^2}-\frac{V_{R1}}{R^2}=\frac{\partial \zeta_1}{\partial Z}-\frac{\partial}{\partial R}\left(\frac{1}{R}\frac{\partial V_{\theta 1}}{\partial \theta}\right) \tag{2}$$

$$\frac{\partial^2 V_{Z1}}{\partial R^2}+\frac{1}{R}\frac{\partial V_{Z1}}{\partial R}+\frac{\partial^2 V_{Z1}}{\partial Z^2}=-\frac{\partial \zeta_1}{\partial R}-\frac{\zeta_1}{R}-\frac{1}{R}\frac{\partial^2 V_{\theta 1}}{\partial Z\,\partial \theta} \tag{3}$$

$$V_{R1}\frac{\partial \zeta_1}{\partial R}+\frac{V_{\theta 1}}{R}\frac{\partial \zeta_1}{\partial \theta}+V_{Z1}\frac{\partial \zeta_1}{\partial Z}+\frac{\partial V_{R1}}{\partial R}\zeta_1+\frac{\partial V_{Z1}}{\partial Z}\zeta_1+\frac{1}{R}\left(\frac{\partial V_{\theta 1}}{\partial Z}\frac{\partial V_{R1}}{\partial \theta}-\frac{\partial V_{\theta 1}}{\partial R}\frac{\partial V_{Z1}}{\partial \theta}\right)+\frac{V_{\theta 1}}{R^2}\frac{\partial V_{Z1}}{\partial \theta}-\frac{2V_{\theta 1}}{R}\frac{\partial V_{\theta 1}}{\partial Z}=\frac{1}{Re}\left[\frac{\partial^2 \zeta_1}{\partial R^2}+\frac{\partial}{\partial R}\left(\frac{\zeta}{R}\right)+\frac{1}{R^2}\frac{\partial^2 \zeta_1}{\partial \theta^2}+\frac{\partial^2 \zeta_1}{\partial Z^2}+\frac{2}{R^3}\frac{\partial^2 V_{Z1}}{\partial \theta^2}-\frac{2}{R^2}\frac{\partial^2 V_{\theta 1}}{\partial Z\,\partial \theta}\right] \tag{4}$$

2.2 Porous Region.

$$V_{R2}\frac{\partial V_{\theta 2}}{\partial R}+\frac{V_{\theta 2}}{R}\frac{\partial V_{\theta 2}}{\partial \theta}+V_{Z2}\frac{\partial V_{\theta 2}}{\partial Z}+\frac{V_{R2}V_{\theta 2}}{R}=\frac{\phi}{Re}\left(\frac{1}{R}\frac{\partial}{\partial R}\left(R\frac{\partial V_{\theta 2}}{\partial R}\right)+\frac{1}{R^2}\frac{\partial^2 V_{\theta 2}}{\partial \theta^2}+\frac{\partial^2 V_{\theta 2}}{\partial Z^2}+\frac{2}{R^2}\frac{\partial V_{R2}}{\partial \theta}-\frac{V_{\theta 2}}{R^2}\right)-\frac{\phi^2}{Re\,Da}\frac{V_{\theta 2}}{} \tag{5}$$

$$\frac{\partial^2 V_{Z2}}{\partial R^2}+\frac{1}{R}\frac{\partial V_{Z2}}{\partial R}+\frac{\partial^2 V_{Z2}}{\partial Z^2}=-\frac{\partial \zeta_2}{\partial R}-\frac{\zeta_2}{R}-\frac{1}{R}\frac{\partial^2 V_{\theta 2}}{\partial Z\,\partial \theta} \tag{6}$$

$$\frac{\partial^2 V_{R2}}{\partial R^2}+\frac{1}{R}\frac{\partial V_{R2}}{\partial R}+\frac{\partial^2 V_{R2}}{\partial Z^2}-\frac{V_{R2}}{R^2}=\frac{\partial \zeta_2}{\partial Z}-\frac{\partial}{\partial R}\left(\frac{1}{R}\frac{\partial V_{\theta 2}}{\partial \theta}\right) \tag{7}$$

$$V_{R2}\frac{\partial \zeta_2}{\partial R}+\frac{V_{\theta 2}}{R}\frac{\partial \zeta_2}{\partial \theta}+V_{Z2}\frac{\partial \zeta_2}{\partial Z}+\frac{\partial V_{R2}}{\partial R}\zeta_2+\frac{\partial V_{Z2}}{\partial Z}\zeta_2+\frac{1}{R}\left(\frac{\partial V_{\theta 2}}{\partial Z}\frac{\partial V_{R2}}{\partial \theta}-\frac{\partial V_{\theta 2}}{\partial R}\frac{\partial V_{Z2}}{\partial \theta}\right)+\frac{V_{\theta 2}}{R^2}\frac{\partial V_{Z2}}{\partial \theta}-\frac{2V_{\theta 2}}{R}\frac{\partial V_{\theta 2}}{\partial Z}=\frac{\phi}{Re}\left[\frac{\partial^2 \zeta_2}{\partial R^2}+\frac{\partial}{\partial R}\left(\frac{\zeta_2}{R}\right)+\frac{1}{R^2}\frac{\partial^2 \zeta_2}{\partial \theta^2}+\frac{\partial^2 \zeta_2}{\partial Z^2}+\frac{2}{R^3}\frac{\partial^2 V_{Z2}}{\partial \theta^2}-\frac{2}{R^2}\frac{\partial^2 V_{\theta 2}}{\partial Z\,\partial \theta}\right]-\frac{\phi^2}{Re\,Da}\zeta_2 \tag{8}$$

It should be noted that the above governing equations for flows in the porous region are based on Brinkman-extended Darcy law [22]. Also in the above equations, ϕ and $Da(=K/c^2)$ are the porosity and the Darcy number of the porous medium, respectively/. The Darcy number represents a relative measure of the permeability of the porous sleeve.

The solutions of the above governing Eqs. (1)–(8) depend on the boundary and interface conditions imposed. For the present study, no-slip boundary conditions are applied to the surfaces of the inner and outer cylinders while continuities of velocity, vorticity, and shear stress are imposed on the interface between the fluid and porous regions. The dimensionless boundary and interface conditions are presented below.

$$R=\bar{a},\quad V_{\theta 1}=1,\quad V_{R1}=0,\quad V_{Z1}=0 \tag{9a}$$

$$R=1,\quad V_{\theta 2}=0,\quad V_{R2}=0,\quad V_{Z2}=0 \tag{9b}$$

$$Z=0,\quad V_{\theta 1}=V_{\theta 2}=0,\quad V_{R1}=V_{R2}=0,\quad V_{Z1}=V_{Z2}=0 \tag{9c}$$

$$Z=L,\quad V_{\theta 1}=V_{\theta 2}=0,\quad V_{R1}=V_{R2}=0,\quad V_{Z1}=V_{Z2}=0 \tag{9d}$$

$$R=\bar{b},\quad V_{\theta 1}=V_{\theta 2},\quad V_{R1}=V_{R2},\quad V_{Z1}=V_{Z2},\quad \zeta_1=\zeta_2 \tag{9e}$$

$$\frac{\partial V_{Z1}}{\partial R}+\frac{\partial V_{R1}}{\partial Z}=\frac{\partial V_{Z2}}{\partial R}+\frac{\partial V_{R2}}{\partial Z} \tag{9f}$$

$$R\frac{\partial}{\partial R}\left(\frac{V_{\theta 1}}{R}\right)+\frac{1}{R}\frac{\partial V_{R1}}{\partial \theta}=R\frac{\partial}{\partial R}\left(\frac{V_{\theta 2}}{R}\right)+\frac{1}{R}\frac{\partial V_{R2}}{\partial \theta} \tag{9g}$$

$$\frac{\partial V_{\theta 1}}{\partial Z}+\frac{1}{R}\frac{\partial V_{Z1}}{\partial \theta}=\frac{\partial V_{\theta 2}}{\partial Z}+\frac{1}{R}\frac{\partial V_{Z2}}{\partial \theta} \tag{9h}$$

Taylor number has taken various forms in the literature. For the present study, the following form is adopted.

$$Ta=\frac{R_1(R_2-R_1)^3\omega^2}{\nu^2} \tag{10}$$

In the above form, the following correlation for the critical Taylor number has been proposed [3]:

$$Ta_c=1708\left\{1+0.652\frac{1-\omega_2/\omega_1}{1+\omega_2/\omega_1}(1-\eta)\right\} \tag{11}$$

for $0\leq\omega_2/\omega_1\leq 1$ and $1-\eta\ll 1$. Clearly, the critical Taylor number depends on the gap width between the cylinders and the ratio of rotational speeds of outer and inner cylinders. For the present study, the outer cylinder is stationary and thus the speed ratio is reduced to zero. Also, it is easy to show the relation between the Taylor number and Reynolds number for the present geometry and which is given by

$$Re=6.6376\sqrt{Ta} \tag{12}$$

To determine the critical Taylor number numerically, one needs to track the solution path as Taylor number varies. For computations involving each Taylor number, the ratio of the norm of the axial velocity field to the norm of the tangential velocity field is calculated after solution converged.

$$\frac{\|V_Z\|}{\|V_\theta\|}=\frac{\sum_{i=1}^{nodes}|V_Z|_i}{\sum_{i=1}^{nodes}|V_\theta|_i} \tag{13}$$

The critical value is determined based on the derivative of the norm ratio with respect to the Taylor number, which is defined below in Eq. (14). The critical Taylor number is set to the point where the derivative has its maximum value.

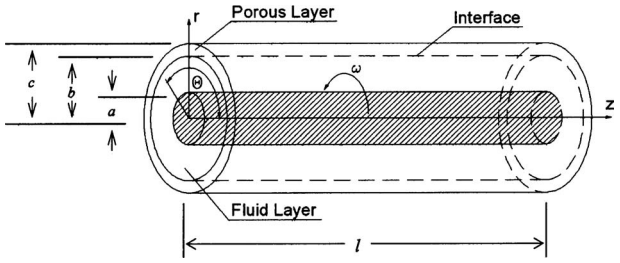

Fig. 1 Flow between two rotating cylinders with a porous lining

$$\text{Rate of growth} = \frac{d\left(\frac{\|V_Z\|}{\|V_\theta\|}\right)}{dTa} \tag{14}$$

Finite difference method was used to solve the governing equations and boundary conditions derived above. The governing equations and boundary condition were discretized using central-difference except for the convective terms, which were discretized by the upwind scheme. Strictly speaking, the accuracy of the numerical solutions obtained is of the first order because of the implementation of upwind scheme. For the present study (Fig. 1), the length of the cylinders is fixed at L=5 and the radius of the inner cylinder $\bar{a}=0.74375$, which correspond to a case examined by Taylor [3] in which $R_1=3$ cm and $R_2=4.035$ cm. It has been determined through a systematic grid refinement test that the computational domain with the grid of $321\times1601\times181$ in the direction of R, Z, and θ, respectively (that is, a grid size of 0.003125 in both radial and axial directions) is best suited for the present study. Since only the annular space is considered, that reduces the actual computational grid in the radial direction to $321-239=83$ nodes. Still the grid with $83\times1601\times181=24{,}051{,}823$ nodes was extremely large. It required a very long computational time even when the calculations were performed on a supercomputer, which has 1024 Intel Xeon 64 bit single core CPUs at 3.2 GHz, 2176 GB of RAM, a Data Direct SAN of 14 TB of disk running the Lustre high performance parallel filesystem and an additional RAID of 8 TB. The supercomputer has a peak performance of 6.5536 TFLOPs. The average CPU time ranges from 47 h for the cases with a low Taylor number (lower than the critical Taylor number) to more than 111 h for the cases with a higher Taylor number (close to and above the critical Taylor number) with the usage of up to four cores in computation.

To validate the code thus developed, it has been first tested against analytical solutions derived by the authors [14] for the cases in which the two-dimensionality of flow fields was preserved (i.e., the cases with lower Taylor number). The agreement in velocity profiles was excellent, indicating that the interface boundary conditions were implemented correctly and the equations were solved properly. Computations have also been performed for the case reported in the study of Taylor [3]. Figure 2 shows the evolution of the vortex patterns as the Taylor number increases. At Ta=2600, in addition to the vortices at the end of the cylinders, there are weak secondary vortices just beginning to form (Fig. 2(*a*)). The vortices at the end of the cylinders are due to the end effects, which represent a combined action of shearing forces at the solid surfaces of the inner and outer cylinders, as well as the end wall. Other than this, there is no additional vortex propagating toward the center of the annulus. Thus it indicates that the flow is rather stable and remains mostly two-dimensional. With an increase in the Taylor number, secondary cell grows at a very slow rate (Figs. 2(*b*) and 2(*c*)). However, one observes a much sudden increase in the vortex strength at $3000<Ta<3100$.

A further increase in the Taylor number produces additional cell, which indicates propagation of instability deeper into the midsection of the annulus. The cells being formed are counter-rotating and of the same size. The aspect ratio of each recirculating cell is about 0.98, which agrees well with the results reported by Chandrasekhar [16] and with experimental observations of Taylor [3]. To determine the critical Taylor number, the solution path is shown in Fig. 3. Calculations were first performed with an increment of 100 in Taylor number and then reduced to 20 when the range of the critical value was identified. Central-difference scheme was used in the calculation of the growth rate of norm ratio (Eq. (14)). As observed, at small Taylor numbers, the norm of the axial velocity is a very small fraction of the tangential velocity. As the Taylor number increases, the value of the axial velocity increases as well. When Taylor number is close to 3000, there is a sudden change in the growth rate of the norm of the axial velocity. This behavior indicates the onset of instability and growth of toroidal vortices. Through further refinement, the criti-

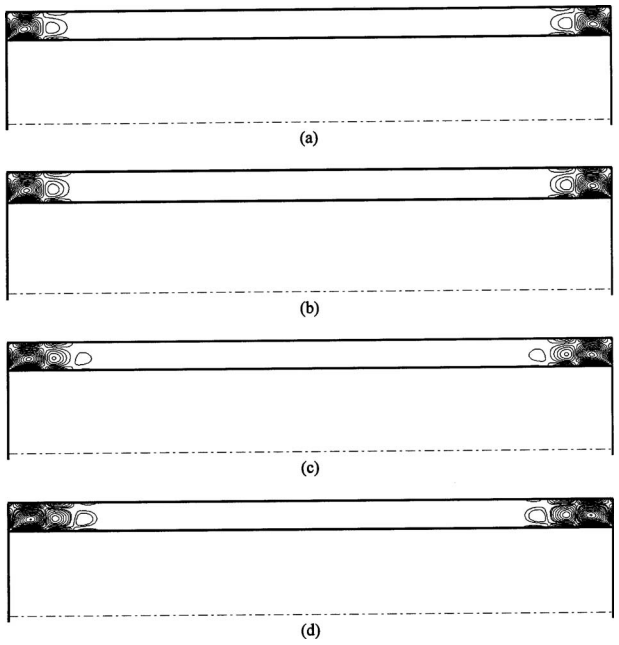

Fig. 2 Evolution of vortex patterns with the Taylor number ($\bar{a}=0.74375$, L=5 and $\Delta\zeta=0.2$): (*a*) Ta=2600, (*b*) Ta=2800, (*c*) Ta=3000, and (*d*) Ta=3100

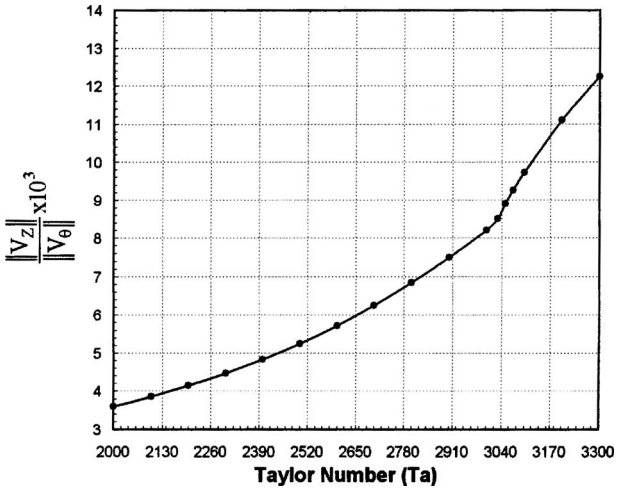

Fig. 3 Solution path for a pure fluid flow in the rotating cylinders ($\bar{a}=0.74375$ and L=5)

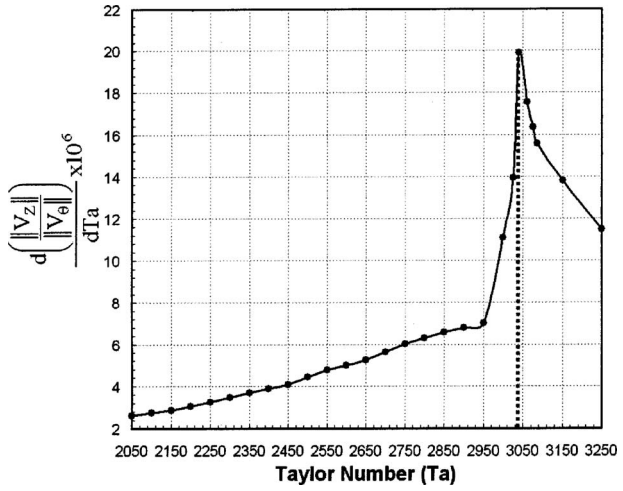

Fig. 4 Growth rate of the relative flow intensity in the axial direction for a pure fluid flow in the rotating cylinders ($\bar{a}$ =0.74375 and L=5)

cal Taylor number is determined to be Ta=3040 (Fig. 4), which is in very close agreement with the value of 3053.7 reported by Taylor [3].

3 Results and Discussion

3.1 Effects of the Presence of Porous Sleeve. The presence of a porous sleeve has a significant influence over the flow field in the annulus and which can be observed in Fig. 5. Since the flow field is symmetric to the centerline, only half of the annular space is shown. The dashed line in the figure indicates the location of

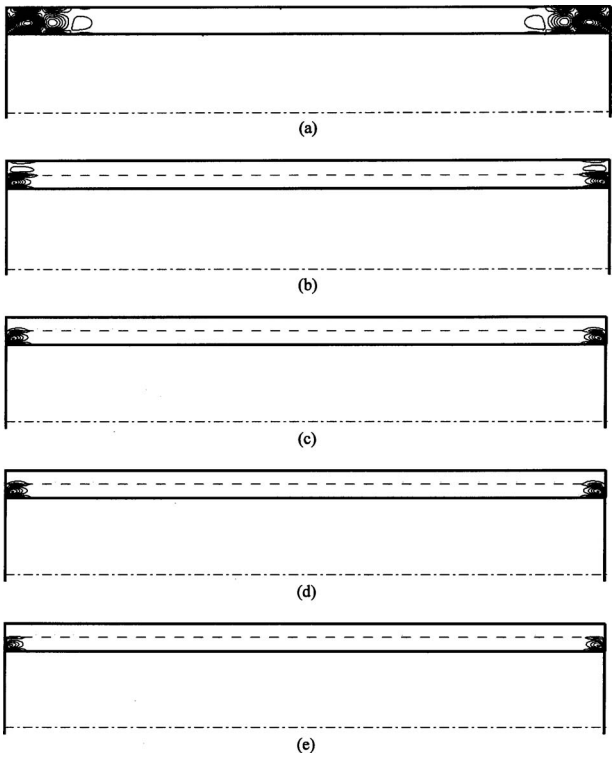

Fig. 5 Effect of the presence of a porous sleeve on the distribution of vorticity ($\bar{a}$=0.74375, $\bar{b}$=0.875, L=5, ϕ=0.25, Ta =3040, and $\Delta\zeta$=0.2): (*a*) without porous sleeve, (*b*) Da=10^{-2}, (*c*) Da=10^{-3}, (*d*) Da=10^{-4}, and (*e*) Da=10^{-5}

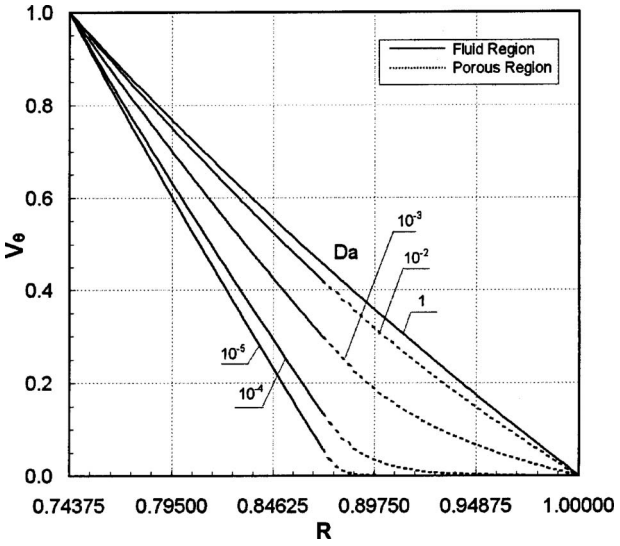

Fig. 6 Effects of the presence of a porous sleeve on the flow tangential velocity at the midsection of the annulus, Z=2.5 ($\bar{a}$ =0.74375, $\bar{b}$=0.875, L=5, ϕ=0.25, and Ta=3040)

the interface between fluid region and porous sleeve. Notice that the Taylor number for the case shown is 3040, which marks the transition to three-dimensional flows. As one observes, the size and strength of the vortices are greatly reduced with the addition of a porous sleeve in the annulus. In addition, the strength of the vortices decreases as the porous sleeve becomes less permeable (i.e., a decrease in the Darcy number). Thus it is clear that the presence of a porous sleeve has a stabilizing effect on the flow in the annulus, which delays the transition to three-dimensional flows. This can be examined from the tangential velocity profile of the flows (Fig. 6). In the figure, the case with Da=1, which represents a limiting case involving only pure fluid is also included for comparison. First, one notices that the tangential velocity profiles shown are similar to those reported in the previous study, which assumes two-dimensional flows [14], which further confirms the above observation. Second, one notices that the slip velocity at the interface decreases as the Darcy number decreases. However, the velocity gradient at the surface of the inner cylinder (i.e., R=0.74375) becomes steeper with a decrease in the Darcy number, which has a significant influence on the shear stress (and eventually the torque) on the surface of the inner cylinder (Fig. 7).

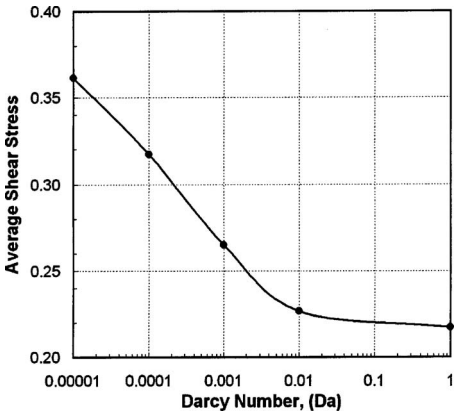

Fig. 7 Effects of the presence of a porous sleeve on the average shear stress at the surface of the inner cylinder: ($\bar{a}$ =0.74375, $\bar{b}$=0.875, L=5, ϕ=0.25, and Ta=3040)

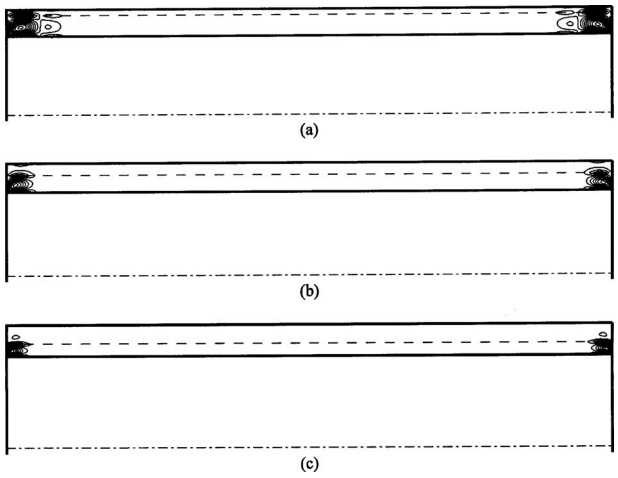

Fig. 8 Effect of porous sleeve thickness on the distribution of vorticity ($\bar{a}$=0.74375, L=5, ϕ=0.25, Da=10^{-3}, Ta=3040, and $\Delta\zeta$=0.2): (*a*) $\bar{b}$=0.95, (*b*) $\bar{b}$=0.9, and (*c*) $\bar{b}$=0.85

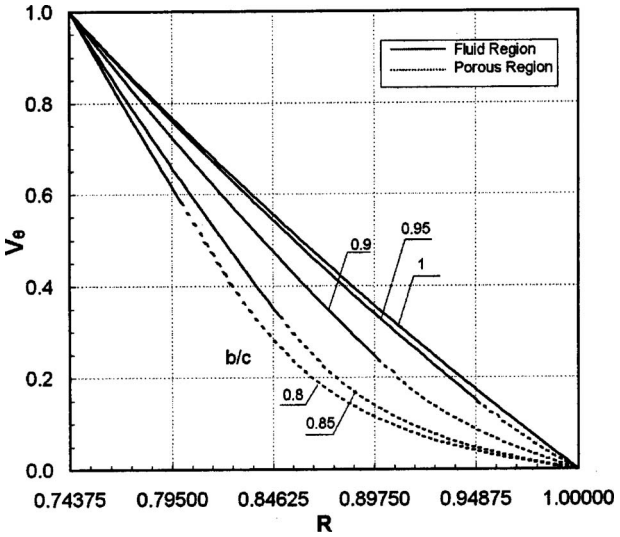

Fig. 9 Effects of porous sleeve thickness on the tangential velocity profile at the midsection of the annulus, Z=2.5 ($\bar{a}$=0.74375, L=5, ϕ=0.25, Da=10^{-3}, and Ta=3040)

To calculate the average shear stress, the stress is integrated and averaged over the entire surface of the inner cylinder, which is shown below.

$$\bar{\tau} = \frac{-1}{2\pi \mathrm{aL}} \int_0^L \int_0^{2\pi} \left[\mathrm{R} \frac{\partial}{\partial \mathrm{R}} \left(\frac{\mathrm{V}_\theta}{\mathrm{R}} \right) + \frac{1}{\mathrm{R}} \frac{\partial \mathrm{V_R}}{\partial \theta} \right] \mathrm{Rd}\theta \mathrm{dZ} \qquad (15)$$

From Fig. 7, one observes that the average shear stress increases with a decrease in the Darcy number. Especially, the rate of change of the shear stress increases significantly as the Darcy number reduces from 10^{-2} to 10^{-5}. This suggests that an additional decrease in the Darcy number past the value of 10^{-2} while doing little with regard to the onset of flow instability will significantly increase the shear stress exerted upon the surface of the inner cylinder, which in turn will require a larger torque to maintain operation at the constant rotational speed.

3.2 Effects of Porous Sleeve Thickness. The effects of porous sleeve thickness can be examined from the flow fields shown in Fig. 8. When compared with that of pure fluid (Fig. 5(*a*)), one can see that the difference is rather evident. When the porous sleeve is thin (Fig. 8(*a*)), there are recirculating cells forming at the ends of the cylinders due to the end effects. There are also two secondary cells forming at the interface, which extends half-way into the porous region. Their strength is considerably weaker than those without a porous sleeve. With a further increase in the porous sleeve thickness, recirculating cells become even weaker, which clearly demonstrates the damping (and thus stabilizing) effect due to the presence of a porous sleeve.

The angular velocity profiles are presented in Fig. 9 for the further examination of the effects of porous sleeve thickness on the flow between the cylinders. It can be seen that the present results display the same trend and agree very well with those reported in the previous study with a two-dimensional analysis [14]. Both results show that the slip velocity and velocity gradient at the interface increase as the thickness of the porous sleeve increases, which has significant effects on the torque applied at the inner cylinder as discussed in the previous study [14]. Consistent with the trend observed above, the average shear stress on the surface of the inner cylinder also increases with an increase in the porous sleeve thickness (Fig. 10). It is interesting to note that the shear stress increases only slightly when the porous sleeve thickness initially increases from $\bar{b}$=1 to 0.95. But, it increases in a much greater rate when the porous sleeve becomes thicker. This trend needs to be considered carefully in the design involving this kind of geometry because it means a greater torque is required to maintain the operation and greater viscous heating is produced.

3.3 Effects of Darcy Number on the Flow Stability. To examine the effects of Darcy number on the flow stability between rotating cylinders with a porous lining, computations have been performed for a fixed system with $\bar{a}$=0.74375, $\bar{b}$=0.95, and L=5 as well as the Darcy number varying from 10^{-2} to 10^{-5}. For each Darcy number, Taylor number has been varied from 2000 to 5000 or until the critical Taylor number is identified, whichever comes first.

For Da=10^{-5}, the vorticity contours are shown in Fig. 11 for various Taylor numbers. As one observes, there is a sudden growth of vortices when Taylor number increases from 4300 to 4400. This is further confirmed by examining the rate of growth of the velocity norm ratio shown in Fig. 12. It shows that the rate of growth reaches a maximum at 4375, where the critical Taylor number lies. For other Darcy numbers, their corresponding critical Taylor number has been determined in the same fashion. The critical Taylor numbers are listed in Table 1 for all Darcy numbers considered. As one observes, the presence of a porous sleeve leads to a critical Taylor number greater than that without, which clearly demonstrates the stabilizing effects provided by a porous sleeve.

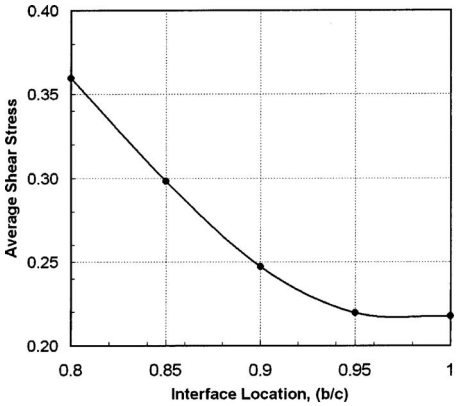

Fig. 10 Effects of porous sleeve thickness on the average shear stress at the surface of the inner cylinder ($\bar{a}$=0.74375, L=5, ϕ=0.25, Da=10^{-3}, and Ta=3040)

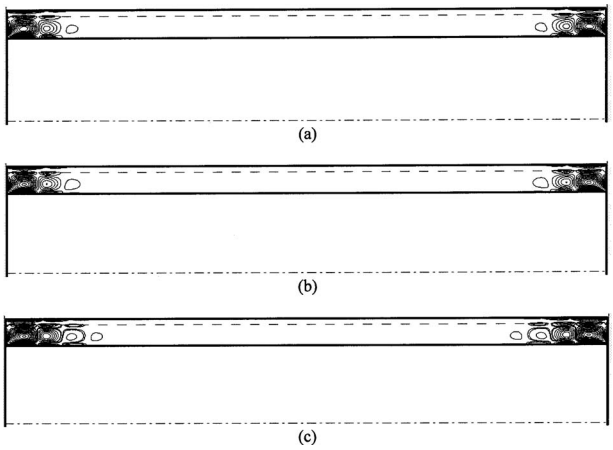

Fig. 11 Development of vorticity profiles with Taylor number (Da=10^{-5}, $\bar{a}$=0.74375, $\bar{b}$=0.95, L=5, ϕ=0.25 and $\Delta\zeta$=0.2): (*a*) Ta=4200, (*b*) Ta=4300, and (*c*) Ta=4400

However, with a reduction in the permeability of the porous sleeve, the critical Taylor number also decreases. A further reduction in the permeability of the porous sleeve eventually leads to an impermeable solid layer. Therefore, for the system considered in the present study, one can conclude that the critical Taylor number would vary between two limiting cases involving only pure fluid. One limiting case corresponds to an annulus with a radius ratio of a/b and the other with a radius ratio of a/c.

4 Conclusion

Flows and their stability in rotating cylinders with a porous lining have been numerically evaluated in the present study. It has been found that the presence of a porous sleeve in general has a stabilizing effect on the flow in the annulus. In other words, the inclusion of a porous sleeve in the annulus maintains the flow field predominantly two-dimensional. When the Taylor number is lower than the critical value, the three-dimensional flow effect is confined to a very small region near the ends and thus the flow field can be largely treated as two-dimensional. In addition, it has been found that an increase in the porous sleeve thickness leads to an increase in the critical Taylor number as well. The results also show that with the inclusion of a very coarse porous sleeve, there is a large increase in the critical Taylor number (for example, when the Darcy number decreases from 1, a limiting case of pure fluid, to 10^{-2}). However, a further decrease in the permeability leads to a gradual reduction in the value of the critical Taylor number. Thus, it is recognized that the critical Taylor number of rotating cylinders with a porous sleeve varies between two limiting cases involving only pure fluid. One corresponds to an annulus with a radius ratio of a/b and the other with a radius ratio of a/c. It is also understood that, as the Darcy number decreases, the flow resistance increases and so does the shear stress exerted upon the surface of the inner cylinder. This in turn requires an increase in the torque to maintain the same rotational speed of the inner cylinder.

While the present study has examined a fundamental problem in fluid flow involving rotating cylinders with a porous sleeve, the results obtained not only help to identify critical parameters for design consideration but also have important implications for many engineering applications. However, one issue, which has not been addressed in the present study, is the effect of viscous heating. As the present results have shown, with the inclusion of a porous sleeve, it usually leads to a larger velocity gradient in the flow field, which can produce considerable amount of viscous heating. Although viscous heating and temperature-dependent fluid properties may impose additional challenges on the already complicated problem, which await further investigation in the future, it may bring out more complete and useful information for the design of such systems.

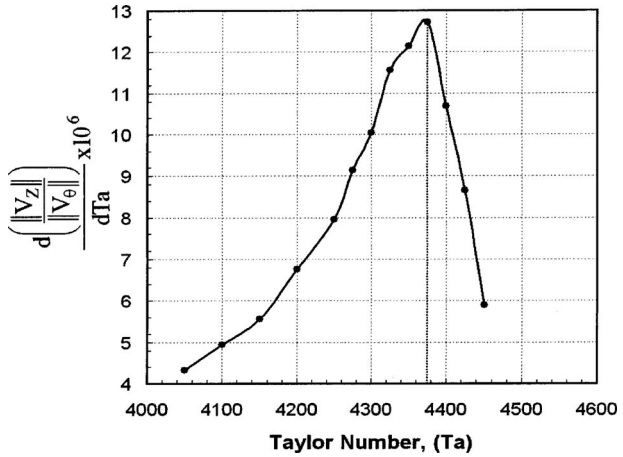

Fig. 12 Growth rate of the relative flow intensity in the axial direction with respect to the Taylor number (Da=10^{-5}, $\bar{a}$=0.74375, $\bar{b}$=0.95, L=5, and ϕ=0.25)

Table 1 Critical Taylor numbers for various Darcy numbers ($\bar{a}$=0.74375, $\bar{b}$=0.95, L=5, and ϕ=0.25)

Darcy number, Da	Critical Taylor number, Ta_{cr}
1	3040
10^{-2}	4625
10^{-3}	4575
10^{-4}	4425
10^{-5}	4375

Acknowledgment

The support of this work through GAANN fellowship program provided by the Department of Education is gratefully acknowledged. The authors also sincerely acknowledge the excellent support received from the Supercomputer Center at the University of Oklahoma administered under Dr. Henry Neeman.

Nomenclature

- a = radius of the inner cylinder (m)
- $\bar{a}$ = dimensionless radius of the inner cylinder, a/c
- b = radial distance of the interface (m)
- $\bar{b}$ = dimensionless radial distance of the interface, b/c
- c = radius of the outer cylinder (m)
- Da = Darcy number (K/c^2)
- K = permeability (m^2)
- l = length of the cylinder (m)
- L = dimensionless length of the cylinder, l/c
- r = radial distance (m)
- R = dimensionless radial distance, r/c
- Re = Reynolds number, Uc/ν
- Ta = Taylor number, defined in Eq. (10)
- U = tangential velocity at the surface of the inner cylinder, $a\omega$, (m/s)
- u_r = velocity in the radial direction (m/s)
- u_z = velocity in the axial direction (m/s)
- u_θ = velocity in the angular direction (m/s)
- V_θ = dimensionless velocity in the angular direction, u_θ/U
- V_R = dimensionless velocity in the radial direction, u_r/U

V_Z = dimensionless velocity in the axial direction, u_z/U

Greek Symbols

ζ = dimensionless vorticity
η = radius ratio, R_1/R_2
ν = kinematic viscosity of fluid, (m^2/s)
$\bar{\tau}$ = dimensionless average shear stress, defined in Eq. (15)
ϕ = porosity
ω = angular velocity, (rad/s)

Subscripts

1 = fluid
2 = porous medium

References

[1] Rayleigh, L., 1879, "On the Stability, or Instability, of Certain Fluid Motions," Proc. London Math. Soc., **s1-11**, pp. 57–72.
[2] Taylor, G. I., 1921, "Experiments With Rotating Fluids," Proc. Cambridge Philos. Soc., **20**, pp. 77–99.
[3] Taylor, G. I., 1923, "Stability of a Viscous Liquid Contained Between Two Rotating Cylinders," Philos. Trans. R. Soc. London, Ser. A, **223**, pp. 289–343.
[4] Walowit, J., Tsao, S., and DiPrima, R. C., 1964, "Stability of Flow Between Arbitrarily Spaced Concentric Cylindrical Surfaces Including the Effect of a Radial Temperature Gradient," ASME J. Appl. Mech., **31**, pp. 585–593.
[5] Davis, S. H., 1969, "On the Principle of Exchange of Stabilities," Proc. R. Soc. London, Ser. A, **310**, pp. 341–358.
[6] Yih, C.-S., 1972a, "Spectral Theory of Taylor Vortices," Archive for Rational Mechanics and Analysis, **46**, pp. 218–240.
[7] Yih, C.-S., 1972b, "Spectral Theory of Taylor Vortices Part II. Proof of Nonoscillation," Archive for Rational Mechanics and Analysis, **47**, pp. 288–300.
[8] Al-Mubaiyedh, U., Sureshkumar, A. R., and Khomami, B., 2002, "The Effect of Viscous Heating on the Stability of Taylor-Couette Flow," J. Fluid Mech., **462**, pp. 111–132.
[9] Muller, S. J., Larson, R. G., and Shaqfeh, E. S. G., 1989, "A Purely Elastic Transition in Taylor-Couette Flow," Rheol. Acta, **28**, pp. 499–503.
[10] White, M. J., and Muller, S. J., 2002, "Experimental Studies on the Stability of Newtonian Taylor-Couette Flow in the Presence of Viscous Heating," J. Fluid Mech., **462**, pp. 133–161.
[11] Lockett, T. J., Richardson, S. M., and Worraker, W. J., 1992, "The Stability of Inelastic Non-Newtonian Fluids in Couette Flow Between Concentric Cylinders: A Finite Element Study," J. Non-Newtonian Fluid Mech., **43**, pp. 165–177.
[12] Channabasappa, M. N., Ranganna, G., and Rajappa, B., 1984, "Stability of Viscous Flow in a Rotating Porous Medium in the Form of an Annulus: The Small-Gap Problem," Int. J. Numer. Methods Fluids, **4**, pp. 803–811.
[13] Chang, M.-H., 2003, "Hydrodynamic Stability of Taylor–Dean Flow Between Rotating Porous Cylinders With Radial Flow," Phys. Fluids, **15**, pp. 1178–1188.
[14] Subotic, M., and Lai, F. C., 2008, "Flows Between Rotating Cylinders With a Porous Lining," ASME J. Heat Transfer, **130**, p. 102601.
[15] Drazin, P. G., and Reid, W. H., 1991, *Hydrodynamic Stability*, Press Syndicate of the University of Cambridge, Cambridge.
[16] Chandrasekhar, S., 1961, *Hydrodynamic and Hydromagnetic Stability*, Oxford University Press, Oxford.
[17] Coronado-Matutti, O., Souza Mendes, P. R., and Carvalho, M. S., 2004, "Instability of Inelastic Shear-Thinning Liquids in a Couette Flow Between Concentric Cylinders," ASME J. Fluids Eng., **126**, pp. 385–390.
[18] Fusegi, T., and Farouk, B., 1986, "Predictions of Fluid Flow and Heat Transfer Problems by the Vorticity–Velocity Formulation of the Navier–Stokes Equations," J. Comput. Phys., **65**, pp. 227–243.
[19] Orlandi, P., 1987, "Vorticity-Velocity Formulation for High Re Flows," Comput. Fluids, **15**, pp. 137–149.
[20] Speziale, C. G., 1987, "On the Advantages of Vorticity–Velocity Formulation of the Equations of Fluid Dynamics," J. Comput. Phys., **73**, pp. 476–480.
[21] Dennis, S. C. R., and Hudson, J. D., 1995, "Methods of Solution of the Velocity-Vorticity Formulation of the Navier-Stokes Equations," J. Comput. Phys., **122**, pp. 300–306.
[22] Neale, G., and Nader, W., 1974, "Practical Significance of Brinkman Extension of Darcy's Law. Coupled Parallel Flow Within a Channel and a Bounding Porous Medium," Can. J. Chem. Eng., **52**, pp. 475–478.

Active Control of Flow Separation in a Radial Blower

David Greenblatt

Guy Arzuan

Faculty of Mechanical Engineering,
Technion–Israel Institute of Technology,
Haifa 32000, Israel

An experimental investigation was undertaken as a proof-of-concept study for active separation control in a radial blower. Acoustic perturbations were introduced into the impeller housing of a small radial blower with fully stalled blades. Increases in the plenum pressure of 35% were achieved and, based on tuft-based flow visualization, it was concluded that the pressure increases were brought about due to excitation and deflection of the leading-edge separated shear layer. Within the parameter range considered here, the optimum dimensionless control frequencies were found to be O(0.5), irrespective of the blade orientation or number of blades. Moreover, the maximum pressure rise was achieved with an investment of only 2% of the fan input power. Backward bladed impeller blades exhibited slightly larger increases in pressure coefficients when compared with their forward bladed counterparts. The dependence of blower performance on reduced frequency was remarkably similar to that seen on flat plate airfoils at similar Reynolds numbers under periodic excitation. [DOI: 10.1115/1.4001446]

1 Introduction

It has been known for several decades that flow separation from solid surfaces can be controlled by the introduction of periodic perturbations. Initial demonstrations were made on airfoils by introducing acoustic signals into the test sections of wind tunnels. This was typically achieved using conventional acoustic loudspeakers or specialized acoustic drivers [1]. Typically, significant post-stall lift coefficient increases are observed on airfoils; as much as 50% of the post-stall lift coefficient value. Two basic mechanisms were identified for lift enhancement: forcing of laminar-turbulent transition, and direct control of the separated shear layer [2]. In recent years, investigators have dispensed with acoustic drivers and prefer to use actuators that are mounted on, or within, the airfoil or wing itself. This approach is far more effective and efficient because the perturbations can be applied only where they are needed, and much larger hydrodynamic perturbations are possible with a much smaller power input. Common methods of actuation include surface mounted actuators and zero mass-flux blowing. An extensive review of modern techniques can be found in Ref. [3].

Despite the rapid increase in active separation control studies, coupled with advances in actuation, control of separation on rotating machinery has received very little attention. This is surprising because blade stall is a major factor leading to reduced efficiency, as well as increased vibrations, noise and damage. Moreover, fans and blowers consume approximately 20% of the industrial energy in the European Union and in the U.S. [4]. It is therefore clear that the effective control of blade stall would impact dramatically on performance, potentially leading to large energy savings. In the context of rotating machinery, all studies appear to be confined to stationary simulated turbomachinery flows [5,6]. In fact, active separation control on turbine blades invariably involves a simulated static pressure gradient or studies performed in linear cascades. This is because considerable technical difficulties are encountered when attempting to apply active control on rotating fan blades. First, it is difficult to establish, a priori, where to place actuators on the blades when very little is known about the nature of stall. Second, the implementation of actuators would require either electrical or pneumatic modification to the blading system. Third, the actuators themselves would be subjected to significant centrifugal forces.

The objective of this technical brief was to assess the viability of separation control on the blades of a radial blower. The difficulties associates with actuating the flow were circumvented by introducing high-amplitude acoustic perturbations ($\sim$120 dB) into the impeller housing by means of a loudspeaker. This novel approach avoided the abovementioned problem of actuator location as the entire flowfield was perturbed periodically. Furthermore, the problem of physically attaching actuators to the blade surfaces was avoided. This novel approach and experimental arrangement facilitated the proof-of-concept study that is described in the following sections.

2 Experimental Setup

A 550-W O.ERRE industrial squirrel-cage-type blower was modified by removing the original squirrel-cage impeller and replacing it with a custom back-plate and adjustable blades. Straight blades (chord length $c=58$ mm; span $s=70$ mm) were used with the option of either two-bladed or four-bladed configurations. The blades could be deployed in backward-bladed configurations and forward bladed configurations from -45 deg to $+45$ deg in steps of 15 deg. A photograph of the four-bladed configuration, installed in the blower, is shown in Fig. 1, where the holes drilled along the periphery of the back-plate were used for changing the blade angles mentioned above.

In order to enforce separated flow at the blade leading-edges (innermost part of the impeller), the blades were constructed from thin (2 mm thick) plates. A grating and photovoltaic diode were attached to the motor shaft in order to measure rpm via a frequency counter. The blower was attached to a variable transformer, and the supply voltage (V_{ac}) and current (I_{ac}) were monitored. Power supplied to the blower was calculated according to the relation: $\dot{W}_b = V_{ac} \times I_{ac}$.

A plenum, constructed from wood, was attached to the outlet of the blower. The plenum was equipped with four circumferentially distributed static pressure ports. A fine wire mesh was located between the outlet and plenum to equilibrate the plenum pressure. A side view schematic of this assembly is shown in Fig. 2.

The pressure ports were joined and connected to an inclined alcohol-based U-tube manometer, measuring the plenum pressure p_p. The manometer was referenced to the atmospheric pressure p_∞, and hence, a standard pressure coefficient

Contributed by the Fluids Engineering Division of ASME for publication in the JOURNAL OF FLUIDS ENGINEERING. Manuscript received October 20, 2009; final manuscript received March 4, 2010; published online April 28, 2010. Assoc. Editor: Zvi Rusak.

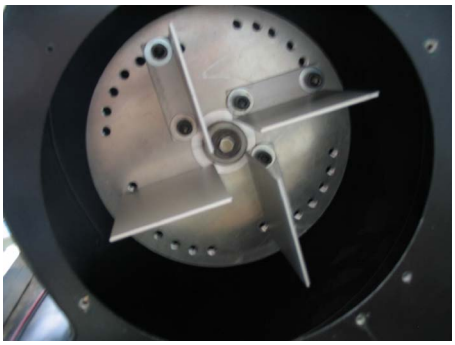

Fig. 1 The four-bladed impeller configuration shown installed in the blower housing

$$C_P \equiv \frac{p_p - p_\infty}{\frac{1}{2}\rho(\omega_b R_i)^2} \tag{1}$$

was defined, where ρ is the air density, ω_b is the rotational frequency (c.f. rpm) of the impeller blades $2\pi f_b$, and R_i is the impeller inner radius. A 100 mm circular hole was drilled into the downstream end of the plenum and a 60 W-rated "woofer" acoustic speaker was placed over the hole (see Fig. 2).

A function generator and amplifier were used to drive the speaker at frequencies ranging between 20 Hz and 200 Hz. The excitation voltage supplied to the speaker (V_e) was measured using a hand-held digital voltmeter; the speaker impedance Z was measured directly, and thus, the excitation power was calculated using $\dot{W}_e = V_e^2/Z$. Thus, the blower blades were driven in a fully stalled state, while simultaneously periodic perturbations were introduced in an attempt to control stall. No integer relationship, and hence, no phase relationship, was enforced between the blower frequency and speaker excitation frequencies. Initial experiments showed that, for a wide range of speaker frequencies, the pressure within the plenum corresponding to the stalled fan blades increased with increasing speaker power input. Following this, a systematic parametric study was conducted, and this is described in Sec. 4. The maximum sound level in the plenum was recorded using a calibrated microphone at 123 dB.

The main parameter governing the control of separation from a stationary airfoil or blade in a two-dimensional flow is the dimensionless frequency

$$F^+ \equiv \frac{f_e X}{U_\infty} \tag{2}$$

where f_e is the excitation (or forcing) frequency, X is the distance from the position of actuation to the trailing-edge of the wing or blade (here, blade chord c), and U_∞ is the free-stream velocity [7]. A wide range of different investigations indicate that the reduced frequencies that produce improvements in airfoil lift coefficient

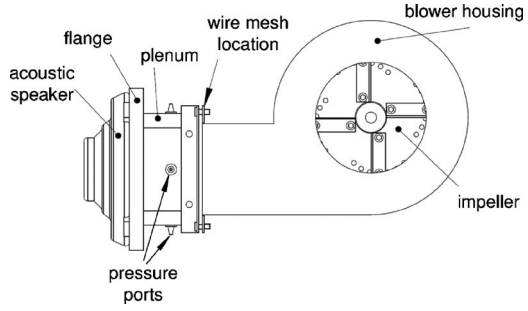

Fig. 2 A schematic of the experimental setup, showing the blower, plenum, and speaker

C_L are mainly in the approximate range of $0.3 \leq F^+ \leq 2$ [7]. For separation control on flat plate airfoils at low Reynolds numbers with leading-edge separation, the optimum reduced frequency is $F^+_{\text{opt}} \sim 0.5$ [8]. This optimum reduced frequency is achieved both for airfoils and finite span wings [8], as well as curved flat plate airfoils [9].

In the case of blades within a radial blower, the characteristic velocity is a vector combination of the rotation speed $\omega_b R_i$ and the flow velocity though the blades Q/A, where Q is the volumetric flowrate through the blower and A is the impeller inlet area. For the purposes of this investigation, as shown in Sec. 1, we enforced the conditions of zero flow rate ($Q=0$), and hence, Eq. (2) can be written as

$$F^+ \equiv \frac{f_e X}{\omega_b R_i} \tag{3}$$

For the present investigation, the length-scale X was defined as the blade chord length c. This was done in order to be consistent with wind tunnel investigations conducted on airfoils subjected to acoustic perturbations [1,10,11], as well as flat plate airfoil investigations employing leading-edge excitation [8,9].

Acoustic forcing of the flow using a speaker, as opposed to a localized hydrodynamic perturbation on the blades themselves, was employed for purely practical reasons. It was assumed that the "global" control that produces disturbances throughout the flowfield has a similar effect to acoustic control of separated flows over airfoils in wind tunnels. Namely, that the acoustic perturbations mainly excite the separated free-shear layer above the airfoil, enhancing momentum transfer across the shear layer, and thereby forcing reattachment. In these investigations [1,10,11], the length-scale between the actuator and airfoil was not considered, but rather, the chord length yielding the parameter $f_e c/U_\infty$. Despite the fact that the blades are rotating in the present investigation, it is assumed that the mechanism of control is similar to that observed in wind tunnels on stationary airfoils. This is discussed further in Sec. 4.2.

3 Experimental Method

Following initial observations described in Sec. 2, a systematic parametric study was carried out in the following manner.

1. Fan blades were set in a 45 deg backward-bladed configuration.
2. The fan was driven using a variable transformer at its design speed, namely, $f_b = 2760$ rpm ($\omega_b = 289$ rad/s).
3. The voltage (V_{ac}) and current (I_{ac}) supplied to the blower were recorded.
4. Using Eq. (3), a speaker excitation frequency f_e was selected, corresponding to a value in the reduced frequency range of $0.3 \leq F^+ \leq 2$.
5. At this frequency, the power supplied to the speaker was gradually increased from zero until 40 W (rms). This was ascertained from a direct voltage measurement described above.
6. Steps 1 to 3 were repeated for different frequencies in the range described in item 4 above.
7. Full selected experiments were repeated for the following conditions:
   - blower rotation speed $f_b = 1680$ rpm
   - two impeller blades instead of four
   - fan blades set in a 30 deg forward bladed configuration
7. Tuft-based flow visualization was carried out using a high speed camera. This is described in Sec. 4.3 below.
8. Additional experiments were performed for a wide range of perturbation frequencies, and these are discussed in Sec. 4.2.

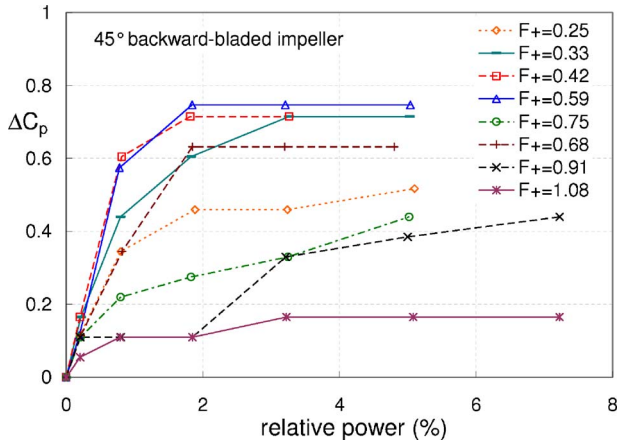

Fig. 3 Change in the plenum pressure coefficient as a function of the relative actuator excitation power input $\dot{W}_e/\dot{W}_b$ for a backward-bladed impeller; rotational speed=2760 rpm. Uncontrolled C_p=2.1.

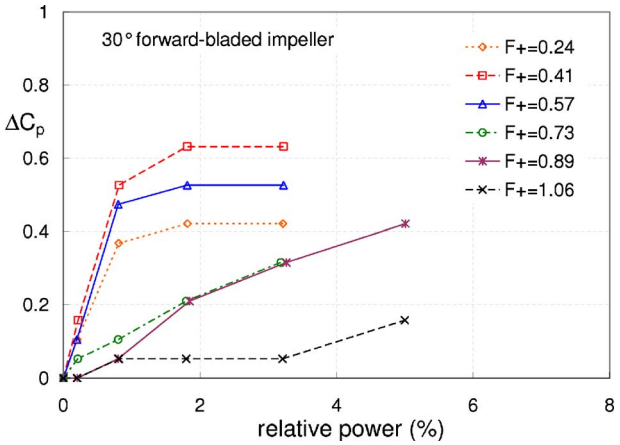

Fig. 4 Change in the plenum pressure coefficient as a function of the relative actuator excitation power input $\dot{W}_e/\dot{W}_b$ for a forward bladed impeller; rotational speed=2760 rpm. Uncontrolled C_p=1.74.

4 Discussion of Results

4.1 Effect of Actuator Power. Based on the procedure described in items 1–6 above, the plenum pressure was considered as a function of power supplied to the speaker. All data show the same basic trend: namely, that the plenum pressure increases with increasing excitation power and then saturates. The maximum overall pressure rise is 33–35% above the uncontrolled state and occurs at reduced frequencies in the range of $0.33 \leq F^+ \leq 0.59$. At lower and higher reduced frequencies, smaller plenum pressure increases are observed. To illustrate this, the relative pressure rise $\Delta C_p \equiv C_p(\text{controlled}) - C_p(\text{uncontrolled})$ is plotted as a function of the relative actuator power, i.e., $\dot{W}_e/\dot{W}_b$ (see Fig. 3). The graph shows that the 35% pressure rise due to control is achieved with an increase of only 2% of the fan power input. For the present case, the flowrate Q is zero, and hence, the air power is also zero. However, for small Q, similar results may be expected, and hence, the air power pQ will also increase by approximately 35% with an increase in actuator power of only 2%. Moreover, because the actuator power is so low, the overall fan efficiency is also expected to show an improvement of the same order. As Q increases further, the velocity vector relative to the blade changes in direction and magnitude, and it may be expected that the nature of stall will change. Therefore, no clear conclusions can be drawn regarding the pressure increase due to control at significant Q because it is not clear how excitation will affect the flowfield at a different operating point. Although the significant increase in fan pressure under fully stalled conditions as presented here is very encouraging, the characterization of the p versus Q throughout the stalled region is considered a priority for future work.

The possibility that the pressure rise was caused by an acoustic standing wave was ruled out, due to the fact that the acoustic wavelength $\lambda = a/f_e$ was always very much larger than the largest blower dimension (a is the isentropic speed of sound). Nevertheless, to confirm this, data was acquired for the entire excitation frequency range with no fan blade rotation ($\omega_b = 0$), and no measurable effect was observed on the plenum pressure. This was true, irrespective of the stationary position of the blades.

The identical procedure was followed for the impeller blades oriented in a 30 deg forward bladed configuration and the data are shown in Fig. 4. The overall trends are similar with some relatively minor differences. The forward bladed configuration achieves a similar lower maximum plenum pressure without control, and when control is applied, the plenum pressure increase is smaller. The net result therefore is a similar percentage increase, namely, 36%. Despite the different stalling characteristics of backward and forward bladed impellers [12], the basic control mechanism seems to be the same.

4.2 Effect of Reduced Frequency. Based on the above results, additional data were acquired for a range of perturbation frequencies corresponding to $0.2 \leq F^+ \leq 2$. At each frequency, the saturation pressure was acquired, i.e., the pressure at which no further increases are observed with additional speaker power. Changes in the pressure coefficient, as a function of reduced frequency for the backward-bladed impeller at two fan speeds, is shown in Fig. 5. The data indicate that there is clearly an optimum frequency in the approximate range $0.3 \leq F^+ \leq 0.6$ and that this optimum appears to be independent of the fan speed within the limited range tested here. At higher frequencies, a reduction in pressure is observed for $F^+ > 1$ at the lower fan speed. The uncertainty intervals shown in Fig. 5 are based on repeated runs with a 95% confidence level.

The identical experiment was performed, but this time, with the forward bladed configuration at the maximum rpm, and the data are shown, together with the backward-bladed impeller, in Fig. 6. The dependence of the pressure coefficient on reduced frequency is similar, but seems to exhibit a sharper peak at $F^+ \sim 0.4$. Nevertheless, the data for $F^+ > 0.7$ is almost indistinguishable, within experimental uncertainty, for the backward and forward bladed configurations. The figure also shows data acquired with only two blades. In general, the pressure rise is slightly smaller, but the

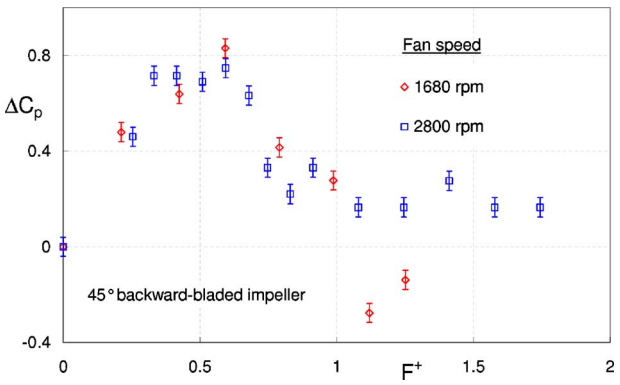

Fig. 5 Pressure coefficient rise as a function of reduced frequency for the backward-bladed impeller at two different fan speeds

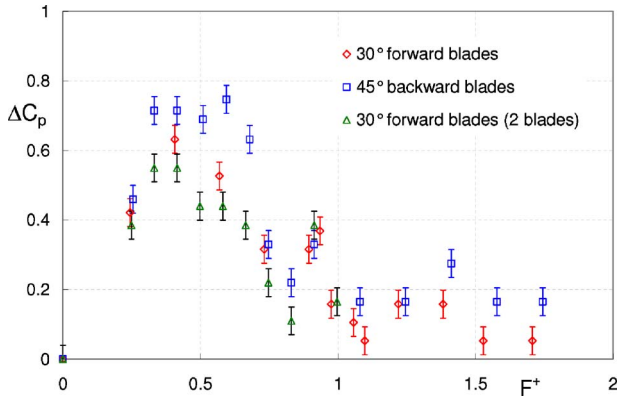

Fig. 6 Pressure coefficient rise as a function of reduced frequency for the backward-bladed and forward bladed impellers at 2760 rpm

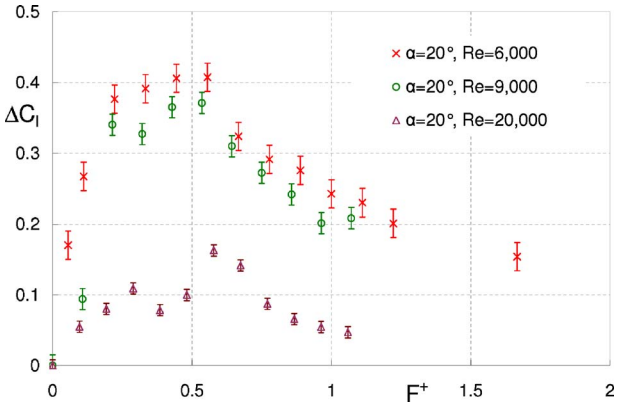

Fig. 7 Flat plate airfoil lift data as a function of reduced excitation frequency. Perturbations are supplied by plasma-based actuators at the airfoil leading-edge [8]. α represents the airfoil angle of attack.

overall trend as a function of reduced frequency is similar. This suggests that the pressure increases are not dependent on the internal geometry of the blower impeller, but rather that the perturbations are interacting with the shear layer over the blades. Further evidence of this is presented in Sec. 4.3 below.

A representative Reynolds number for the blower is based on the conditions at boundary layer separation, i.e., at the inner radius R_i. Hence, the Reynolds number is

$$\mathrm{Re}_b = \frac{\rho \omega_b R_i c}{\mu} \tag{4}$$

On the basis of this definition, representative Reynolds numbers at 1680 rpm and 2760 rpm are 13,600 and 22,400, respectively.

Furthermore, it is evident from Eq. (3) that the reduced excitation frequency F^+ and the dimensionless frequency f_e/f_b are linearly related by the factor $X/2\pi R_i$. Therefore, for a given blower geometry, an optimum physical excitation frequency can be established that is only a function of the rotation speed. This result could be used to establish relatively simple feed-forward control in order to maximize blower pressure. Clearly, a feedback loop could also be introduced to automate and optimize the system fully.

It is instructive to compare the pressure rise of the blower with the pressure difference (lift) across a flat plate airfoil (two-dimensional section) at similar Reynolds numbers [8]. The basis for this is the geometric similarity between the flat plate airfoil and the flat plate impeller blades. Airfoil data acquired by Greenblatt et al. [8], indicating lift coefficient as a function of reduced frequency, is shown in Fig. 7. In this instance, perturbations were supplied at the leading-edge of the airfoil by means of a plasma-based body-force. Notwithstanding the different methods of perturbation, the similarities between the pressure rise (Figs. 5 and 6) with the lift coefficient increase (Fig. 7) are remarkable, with both showing an optimum around $F^+ \sim 0.5$. This similarity suggests that the global flowfield excitation produced by the acoustic speakers acts predominantly to excite the leading-edge separated shear layer on the impeller blades. This mechanism is discussed further below by means of flow visualization with regard to the airfoil data, as well as flow visualization on the impeller blades, discussed in Sec. 4.3.

The similarity between the pressure rise in the blower and the lift enhancement on the flat plate airfoil as a function of reduced frequency facilitates a tentative explanation of the impeller flowfield that is based on flat plate flow visualization. This has been done by examining smoke-based flow visualization over a stalled flat plate (α=20 deg) for both baseline and controlled conditions (Figs. 8(*a*)–8(*c*)) [8] that correspond to the data of Fig. 7. The uncontrolled (baseline) airfoil case (Fig. 8(*a*)) clearly shows separation from the leading-edge and subsequent rollup of the shear layer into distinct vortices. Flow separation from the trailing-edge also appears to generate vortical structures with a longer wavelength. Pulsed control at the airfoil leading-edge near optimal conditions at F^+=0.42 (Fig. 8(*b*)) shows that the detached leading-edge shear layer is forced to roll-up into a vortex (or bubble) that attaches to the airfoil surface. Downstream of this vortex, the previously generated vortex is in the process of being shed into the wake. A clockwise trailing-edge vortex can also be seen that arises as a result of the low pressure now present on the airfoil upper surface. It is believed that the strong adverse pressure gradient existing on the upper surface of the airfoil is responsible for the dramatic upward distortion of the streamlines. Repeated photographs throughout the phase of the excitation showed that, at any instant, there were at least two vortices present on the airfoil surface. Further increases in control frequency produced rolled-up

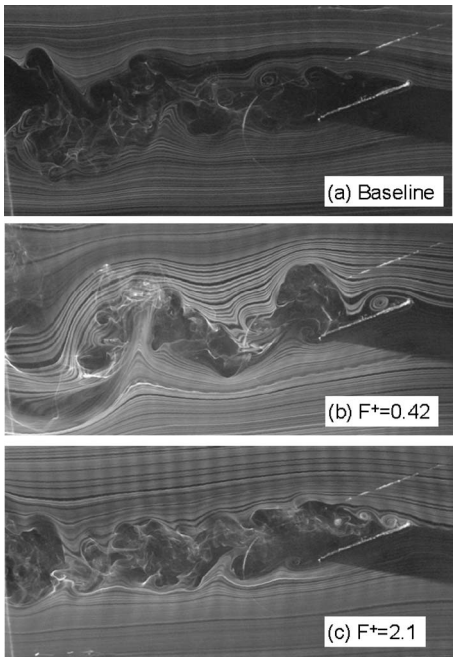

Fig. 8 Flat plate airfoil flow visualization for the baseline case and two reduced excitation frequencies (flow from right to left). Perturbations are supplied by plasma-based actuators at the airfoil leading-edge [8]. (*a*) Baseline, (*b*) F^+=0.42, and (*c*) F^+=2.1.

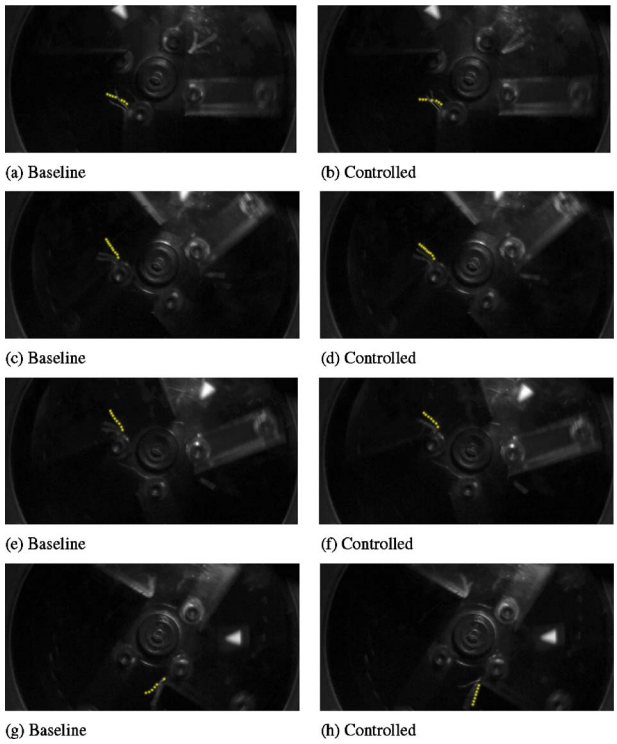

Fig. 9 Individual frames of high speed photographs of the impeller leading-edge region. Tuft number 3, the furthest inboard, is highlighted. Phases 1 to 4 correspond to the four rows. Left hand column is the baseline (uncontrolled) case; right hand column is the controlled case.

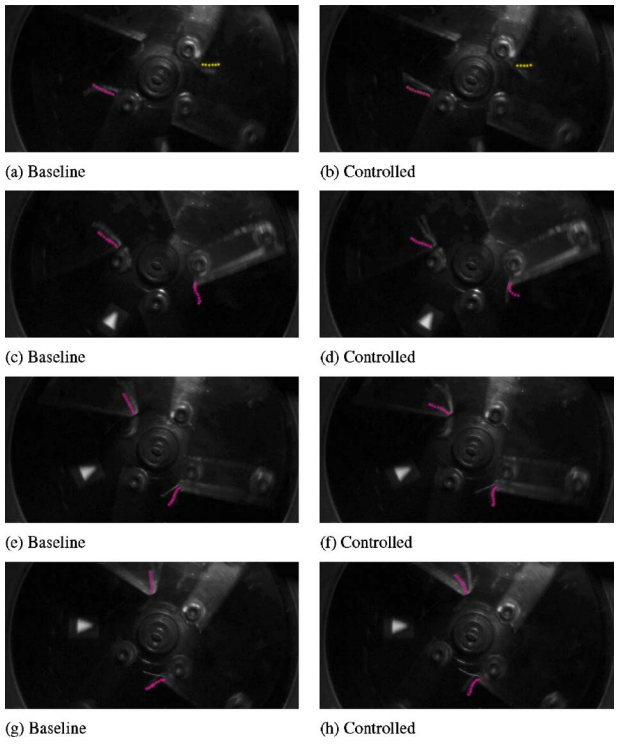

Fig. 10 Individual frames of high speed photographs of the impeller leading-edge region. Tuft number 3, the furthest inboard, is highlighted in on the right; opposite blade: tuft number 1, closest to the tip, highlighted in the left. Phases 5 to 8 correspond to the four rows. Left hand column is the baseline (uncontrolled) case; right hand column is the controlled case.

vortices, successively closer to the leading-edge. For example, an increase in frequency by a factor of 5, to $F^+=2.1$ (Fig. 8(*c*)), is only effective in transporting momentum toward the airfoil surface at $x/c<0.1$. Immediately downstream of this, the small vortices are not effective in transporting high momentum fluid to the surface. Control at $F^+<0.1$ resulted in large lift and drag oscillations. It is tentatively concluded here that the mechanism responsible for lift enhancement on the airfoil of Ref. [8] is also responsible for the plenum pressure rise observed in the blower. Direct tuft flow visualization on the impeller blades are shown in Sec. 4.3 below.

4.3 Blower Flow Visualization. Due to the similarity between the blower pressure rise and airfoil performance as a function of F^+ (Sec. 4.2), it was believed that the measured increases in plenum pressure were due to excitation of the separated shear layer over the leading-edges of the blades. In order to investigate this, three 1.5 cm long white cotton tufts were glued to two opposite blade leading-edges (inboard, midspan, and outboard). To provide a contrast, the back-plate and impeller blades were painted matt-black. The fan was run at 2760 rpm and filmed under two conditions: (1) no excitation frequency introduced (baseline case) and (2) a control frequency of 70 Hz corresponding to $F^+=0.6$ introduced (controlled case). The leading-edge region of the blades was then filmed for both cases with a high speed digital camera (4 kHz) that was triggered by the photovoltaic diode via the grating mounted on the motor shaft (described in Sec. 2). A white triangle was placed on the impeller back-plate to indicate the relative phase position for comparisons.

Eight representative phases of the rotation are shown in Figs. 9 and 10. Initial observations indicated that the phase-dependent tuft direction was significantly affected by the perturbations. Before describing the effects, it is important to note that the blades tested here are essentially low aspect ratio semispan wings and not two-dimensional airfoils. In stationary flows over large aspect ratio wings ($AR>4$), only the inboard flow, not too close to the tunnel wall or vehicle body, can be considered quasi-two-dimensional. In such cases, control deflects the shear layer closer to the wall. For the present experiments where the blades have an equivalent aspect ratio of 2.4, the flow can be expected to be highly three-dimensional. On stationary low aspect ratio wings, the tip flow is dominated by a strong vortex. The vortex strengthens when control perturbations are introduced [13]. It should thus be appreciated that the present flowfield is far more complex than a simple two-dimensional flow due to the low aspect-ratio blades coupled with the rotation.

It is convenient to discuss the first three phases together (Figs. 9(*a*)–9(*f*)) as they show a similar tuft behavior. Here, we initially consider tuft furthest inboard (number 3—yellow highlight) in order to obtain a qualitative sense of the effect of control. A visual comparison of the baseline and controlled cases shows that the tuft is deflected closer to the wall by the perturbations. The inherent stiffness of the thread does not allow it to bend fully in the direction of the flow, but the observed deflection indicates that, in a mean sense, the flow must be deflected closer to the wall. In contrast, the tuft located close to the tip is deflected further from the surface, while the midspan tuft shows no meaningful change. Clearly, the effect of control is not uniform along the span, and in this sense, it is very different from our principal experiences in two-dimensional nonrotating flows. The differences between corresponding tufts of the controlled and uncontrolled cases become successively smaller as the tufted blade moves to the top of the blower housing. This is because the acoustic perturbations are weaker in this region, being further from the speaker and not directly impacted by the plane acoustic wave being introduced at the blower outlet.

In the fourth phase (Fig. 9(*g*) and 9(*f*)), the opposite-bladed outboard tuft is highlighted, and in the fifth phase (Fig. 10(*a*) and 10(*b*)), the tufts on both sides are highlighted. In this instance, the tuft near the tip is deflected closer to the blade, while the opposite is true for the inboard tufts. This trend continues from phase 4 to 8. This observation is difficult to explain because it is precisely the opposite trend observed on the opposite blade when it was in the same physical location, and indicates a lack of symmetry in the inertial frame within the blower casing. Simultaneously, on the opposite blade in the outboard tuft is closer to the blade with control, while the inboard tufts are further from the blade.

5 Concluding Comments

The present investigation established the viability of using periodic perturbations to improve performance in radial blowers whose blades are stalled.

The following specific conclusions were drawn.

1. Within the limited parameter space considered here, the optimum reduced control frequencies were found to be $F^+ \sim 0.5$, irrespective of the blade orientation, number of blades or fan speed.
2. At optimum control frequencies, the control effect (pressure rise) saturated at relatively low relative power, typically around 2%.
3. Under fully stalled or close to fully stalled conditions, air power, and fan efficiency can be expected to increase by up to 35%.
4. The effect of control on backward and forward bladed impeller blades was similar in percentage terms.
5. The dependence of blower performance on reduced frequency was remarkably similar to that seen on flat plate airfoils subject to periodic excitation at similar Reynolds numbers.
6. Tuft-based flow visualization showed a significant effect of control at the blade leading-edges. However, this effect did not appear to be symmetric in the absolute frame.

To the best of our knowledge, these data are the first and only demonstration of shear layer or separation control on the blades of a radial blower. They show great promise for more sophisticated control techniques. These more advanced techniques can then be exploited to achieve significant energy savings on large industrial machines. This could have a major impact on the control of separation on axial fans, which also suffer from debilitating blade stall, as well as axial turbines where advanced techniques could be used to reduce compressor stages. On the basis of this investigation, it is recommended to conduct a more detailed study where the flowrate Q is added as a parameter. It would also be advantageous to perform optical measurements on the impeller blades, for example, using laser Doppler anemometry or particle image velocimetry.

References

[1] Zaman, K. B. M. Q., McKinzie, D. J., and Rumsey, C. L., 1989, "A Natural Low-Frequency Oscillation of Flow Over an Airfoil Near Stalling Conditions," J. Fluid Mech., **202**, pp. 403–442.

[2] Greenblatt, D., and Wygnanski, I., 2009, "Chapter 2: Physical Concepts Underlying the Application of Modern Flow Control," *Fundamentals and Applications of Modern Flow Control, Progress in Astronautics and Aeronautics Series*, R. D. Joslin and D. Miller, eds., AIAA, Vol. 231, pp. 21–57.

[3] Joslin, R. D., and Miller, D., 2009, *Fundamentals and Applications of Modern Flow Control, Progress in Astronautics and Aeronautics Series*, AIAA, Vol. 231.

[4] Cory, W. T. W., 2004, "Fans—Just How Mature Are They," Proceedings of the IMechE International Conference on Fans, One Birdcage Walk, London, UK, Nov. 9–10, Paper No. C631/100/2004.

[5] Hultgren, L. S., and Ashpis, D. E., 2003, "Demonstration of Separation Delay With Glow-Discharge Plasma Actuators," Proceedings of the 41st AIAA Aerospace Sciences Meeting and Exhibit, Reno, NV, Jan. 6–9, AIAA Paper 2003-1025.

[6] Ramakumar, K., and Jacob, J. D., 2007, "Low Pressure Turbine Blade Separation Control Using Plasma Actuators," Proceedings of the 45th AIAA Aerospace Sciences Meeting and Exhibit, Reno, NV, Jan. 8–11, AIAA Paper 2007-371.

[7] Greenblatt, D., and Wygnanski, I., 2000, "The Control of Separation by Periodic Excitation," Prog. Aerosp. Sci., **36**(7), pp. 487–545.

[8] Greenblatt, D., Göksel, B., Rechenberg, I., Schüle, C., and Romann, D., 2008, "Paschereit, Dielectric Barrier Discharge Flow Control at Very Low Flight Reynolds Numbers," AIAA J., **46**(6), pp. 1528–1541.

[9] Schüle, C. Y., Greenblatt, D., and Paschereit, C. O., 2008, "Combined Plasma and Gurney Flap Flow Control at Very Low Flight Reynolds Numbers," Proceedings of the Second International Conference on Jets, Wakes and Separated Flows, Technical University Berlin, Berlin, Germany, Sept. 16–19.

[10] Ahuja, K. K., and Burrin, R. H., 1984, "Control of Flow Separation by Sound," AIAA Paper No. 84-2298.

[11] Zaman, K. B. M. Q., and McKinzie, D. J., 1991, "Control of Laminar Separation Over Airfoils by Acoustic Excitation," AIAA J., **29**(7), pp. 1075–1083.

[12] McQuiston, F. C., Parker, J. D., and Spitler, J. D., 2004, *Heating, Ventilating, and Air Conditioning: Analysis and Design*, 6th ed., Wiley, New York.

[13] Greenblatt, D., and Washburn, A. E., 2008, "Influence of Finite Span and Sweep on Active Flow Control Efficacy," AIAA J., **46**(7), pp. 1675–1694.

Spectral Linear Stochastic Estimation of the Turbulent Velocity in a Square Three-Dimensional Wall Jet

Joseph W. Hall
Department of Mechanical Engineering,
University of New Brunswick,
Fredericton, NB, E3B 5A3, Canada
e-mail: jwhall@unb.ca

Daniel Ewing
Toronto, ON, Canada

The instantaneous turbulent velocity field in a three-dimensional wall jet was estimated from the fluctuating wall pressure using a spectral linear stochastic estimation technique. The wall jet investigated issued from a long square channel with Reynolds number of 90,000. Two downstream positions in the intermediate field were examined, $x/h=10$ and $x/h=20$, owing to the rapid changes in wall jet development over this region. The results indicate that the passage of the large-scale structures cause large, coherent lateral sweeps of fluid across the entire span of the wall jet. These sweeps are caused by the passage of half horseshoe-like structures and appear to be responsible for the larger lateral development of this flow. [DOI: 10.1115/1.4001490]

1 Introduction

Wall jets are formed when a jet of fluid is directed at, or along a wall, as shown in Fig. 1. One of the most noteworthy features of turbulent, three-dimensional wall jets is that the lateral spread rate along the wall is roughly 5–8 times the vertical growth rate normal to the wall [1–7]. It is generally accepted that this behavior is related to the passage of organized vortical structures in the flow [8–11]. The present investigation examines the development of these organized motions in a three-dimensional wall jet formed using a long square channel to determine what feature, or features, of the coherent structures cause the large lateral growth of this flow.

Most previous investigations of the coherent structures in three-dimensional wall jets focused on jets formed using round outlets [8–11]; for example, Matsuda et al. [9] used conditionally averaged velocity measurements to investigate the structures in the near field of a three-dimensional wall jet formed using a round contoured nozzle. They proposed that the lateral growth in the three-dimensional wall jet was caused by the passage of horseshoe vortex structures formed by the interaction of the ring structures at the jet nozzle with the wall. The passage of these horseshoe structures was thought to drive the flow into the wall and outward. Ewing and Pollard [10] later examined the development of a three-dimensional wall jet close to the wall and identified additional, smaller horseshoe structures that formed when the bottom of the ring structures at the nozzle exit interacted with the wall. Using similar types of measurements, Sun and Ewing [11] noted that the outer structures appeared to incline more relative to the mean flow as the structures evolved further downstream. They believed that the increased inclination enhanced the lateral ejection of fluid, and in turn, enhanced the lateral development of the wall jet.

The coherent structures in three-dimensional wall jets formed using square or rectangular outlets has received considerably less attention than wall jets formed using round outlets. Like the aforementioned investigations [10,11], Sullivan and Pollard [12] examined the inclination of the structures in detail for a wall jet emanating from an $A_r=W_c/h=10$ sharp-edged orifice. Recently, Hall and Ewing [13,14] measured the fluctuating wall pressure laterally across a three-dimensional wall jet exiting from $A_r=1$ and 4 channels to examine the instantaneous lateral symmetry of the pressure fluctuations in the jet. They found that the instantaneous pressure fluctuations were strongly laterally asymmetric in both flows, similar to the time averaged velocity measurements reported by Sun and Ewing [11]. In a companion study, Hall and Ewing [15] demonstrated that the instantaneous turbulent velocity field estimated from the wall pressure field using spectral linear stochastic estimation (LSE) in the $A_R=4$ wall jet was also asymmetric. The results indicated that the flow was dominated by a horseshoe structure, much like that proposed by Matsuda et al. [9], although asymmetric about the jet centerline.

The present investigation will use the pressure velocity correlation database measured by Hall and Ewing [13,14] to examine instantaneous reconstructions of the velocity field in an $A_r=1$ wall jet. The velocity reconstructions will be performed at two measurement locations in the intermediate field, $x/h=10$ and $x/h=20$, roughly the start of the intermediate field where the rapid lateral spread rate of the wall jet increases rapidly [16].

2 Experimental Facility

The air flow to the wall jet was initially conditioned in a settling chamber equipped with three air filters, a flow straightener, and a wire mesh, as described by Hall and Ewing [13–15]. The flow entered a rectangular channel of variable width W through a bellmouth. The width of the jet could be varied from 0 cm to 25 cm, while the inside height of the channel h was fixed at 2.54 cm, and the length was 2.5 m. The measurements were performed with the aspect-ratio of the channel set to 1. The wall jet flowed over a horizontal plate with a width of 2.4 m and a length of 1.8 m. The base of the channel was mounted flush with the wall so that the jet interacted with the wall immediately after it exited the channel. A 1.2 m high by 2.4 m wide plate was mounted at the channel exit to block the entrainment of air from behind the channel exit. The centerline velocity U_{cl} of the jet was set to 55.0 m/s, corresponding to a Reynolds number based on channel height and centerline velocity of $Re_h=89{,}600$.

The fluctuating wall pressure was measured using a specially constructed 16 channel, Panasonic WM-61B electret microphone system. The response of these microphones was flat from 20 Hz to 5000 Hz. The microphones were mounted directly in the wall to improve the frequency response and sensed the flow through a 0.8 mm hole, and were calibrated using a B&K pistonphone with the

Contributed by the Fluids Engineering Division of ASME for publication in the JOURNAL OF FLUIDS ENGINEERING. Manuscript received June 8, 2009; final manuscript received March 16, 2010; published online April 28, 2010. Assoc. Editor: Pavlos P. Vlachos.

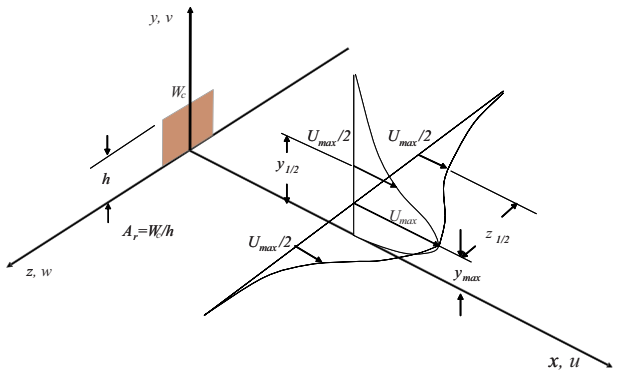

Fig. 1 Schematic of a three-dimensional wall jet

microphones mounted in-situ. One hole was drilled at the jet centerline and seven additional holes were equally spaced on either side of the jet centerline so that the entire flow was spanned. For the $x/h=10$ case, the microphones were evenly spaced from $-3.9h$ to $3.9h$, whereas for $x/h=20$, the microphones spanned from $-6.125h$ to $6.125h$; in both cases, the measurements spanned 3 lateral half widths on either side of the centerline.

The velocity field in the wall jet was measured using an Auspex $u-w$ boundary layer cross-wire probe that was traversed vertically above each microphone so the cross-spectra of the fluctuating wall pressure and the streamwise and lateral velocity could be obtained. The hot-wire probe was connected to an eight channel, specially constructed, in-house anemometry system. The probe was positioned over each of the 15 microphones, and the pressure velocity cross-spectra were computed at 21 points above each microphone. For the $x/h=10$ case, the measurements spanned from the wall to $2.88h$, whereas for the $x/h=20$ case, the measurements spanned from $0h$ to $3.45h$ above the wall. The ambient room temperature was also monitored and the hot-wire probe response was corrected for changes in the room temperature using the scheme suggested by Beuther [17]. The voltage signals from the hot-wires, the microphones, and the thermistor were simultaneously sampled at 10,000 Hz using a 14 bit Microstar 5600a board. At each point, 100 independent blocks of 0.25 s duration were recorded for each channel. Thus, the uncertainty in the cross-spectra computed between the pressure and the fluctuating velocity at the 95% confidence interval was $\pm 20\%$.

3 POD-Based Spectral LSE

The proper orthogonal decomposition (POD) represents the pressure fluctuations using a set of orthogonal basis functions determined by maximizing the normalized projection of the fluctuating pressure onto these functions. The POD technique was used here to spatially filter the pressure fluctuations before the instantaneous velocity field was estimated using linear stochastic estimation. This increases the correlation of the pressure with the velocity field, and thus improves the estimate of the large-scale structures as the contribution of the small-scale motions (to the pressure) is removed.

The POD was applied here after the pressure was Fourier transformed in time so that the POD basis functions are solutions to the integral eigenvalue problem given by [18,19]

$$\int_{-\infty}^{\infty} \phi(z,z',f)\psi(z',f)dz' = \lambda^{(n)}(f)\psi(z,f) \tag{1}$$

where $\psi(z,f)$ are the eigenvectors, $\lambda^{(n)}(f)$ are the eigenspectra of the n modes, and $\phi(z,z'f)$ is the cross-spectral tensor given by

$$\frac{\overline{\hat{p}(z,f)\hat{p}^*(z',f)}}{T} = \phi(z,z',f) \tag{2}$$

where $\hat{p}(z,f)$ represents the Fourier transform in time

$$\hat{p}(z,f) = \int_{-T/2}^{T/2} p(z,t)e^{-i2\pi ft}dt \tag{3}$$

and the asterisk denotes the complex conjugate. In this investigation, all variables are computed from finite record length segments of length T. The Fourier transformed pressure field can be reconstructed using

$$\hat{p}^{\text{rec}}(z,f) = \sum_{n=1}^{\infty} \hat{a}_n(f)\psi^{(n)}(z,f) \tag{4}$$

where the coefficients of each POD mode are given by

$$\hat{a}^{(n)}(f) = \int \hat{p}(z,f)\psi^{(n)*}(z,f)dz \tag{5}$$

A low-dimensional description of the fluctuating pressure field can be reconstructed by including only a limited number of modes. The resulting field is then inverse Fourier transformed back to the time domain.

The POD was applied to the 15 simultaneous pressure measurements across the jet at each downstream location. Before applying the POD, the pressure field was symmetrized across the centerline of the jet using

$$p(z,t) = \frac{p(z,t)}{p_{\text{rms}}(z)}\frac{p_{\text{rms}}(z)+p_{\text{rms}}(-z)}{2} \tag{6}$$

The blocks were then Fourier transformed in time via a complex FFT, and were used to determine the cross-spectral tensor. The discretized eigenvalue problem was solved using a trapezoidal weighting scheme [20]. The POD coefficients for the various modes were determined by projecting the instantaneous pressure field onto the POD modes, allowing the contribution from the individual modes to be determined.

The streamwise u and lateral w components of the fluctuating velocity, defined as

$$u = \tilde{u} - U \tag{7}$$

and

$$w = \tilde{w} - W \tag{8}$$

where U and W are the mean velocities, were estimated from the 15 simultaneous measurements of the fluctuating wall pressure using the spectral LSE technique proposed by Ewing and Citriniti [21], and used previously by Hall and Ewing [15] and Tinney et al. [22]. Hall and Ewing [15] demonstrated that the spectral approach was superior to typical one-time LSE techniques (i.e., Refs. [23–26]) in the three-dimensional wall jet. In particular, single time LSE techniques were not capable of capturing the inclination in the structures in the wall jet because it could not properly capture the phase information [15].

Using the spectral LSE technique, the estimates of the Fourier coefficients of the streamwise and lateral fluctuating velocity at a single point are written as a linear combination of the fluctuating pressure associated with each individual POD mode at the ith pressure tap

$$\hat{u}_{\text{est}}^{(n)}(y,z,f) = \sum_{i=1}^{M} A(y,z_i,f)\hat{p}^{\text{rec},n}(z_i,f) \tag{9}$$

and

$$\hat{w}_{\text{est}}^{(n)}(y,z,f) = \sum_{i=1}^{M} B(y,z_i,f)\hat{p}^{\text{rec},n}(z_i,f) \tag{10}$$

where

$$\hat{p}^{\text{rec},n}(z,f) = \hat{a}_n(f)\psi^{(n)}(z,f) \tag{11}$$

is the pressure field associated with each POD mode.

The mean square error can be minimized at each frequency yielding a linear system of equations

$$\overline{\hat{p}^{\text{rec},n}(z_i,f)\hat{p}^{\text{rec},n*}(z_j,f)}A(y,z_i,f) = \overline{\hat{u}(y,z,f)\hat{p}^{\text{rec},n*}(z_j,f)} \tag{12}$$

and

$$\overline{\hat{p}^{\text{rec},n}(z_i,f)\hat{p}^{\text{rec},n*}(z_j,f)}B(y,z_i,f) = \overline{\hat{w}(y,z,f)\hat{p}^{\text{rec},n*}(z_j,f)} \tag{13}$$

where summation is implied over the repeated index. These equations are solved for A and B at each frequency and velocity measurement location. Once A and B are determined, Eqs. (9) and (10) are used to estimate the Fourier coefficients of the velocity field. These coefficients are then inverse Fourier transformed back into time so that the streamwise and lateral fluctuating velocity can be determined at the location of each velocity measurement.

Finally, the estimated velocity field from the individual POD modes are added together to yield an accurate low-dimensional description of the fluctuating velocity field, that is

$$u_{\text{est}}(y,z,t) = \sum_{n=1}^{N} u_{\text{est}}^{(n)}(y,z,t) \tag{14}$$

and

$$w_{\text{est}}(y,z,t) = \sum_{n=1}^{N} w_{\text{est}}^{(n)}(y,z,t) \tag{15}$$

Here, only the estimate from the first two POD modes are retained in the reconstruction so that $N=2$.

4 Experimental Results

Contours of the normalized mean flow field and turbulent velocity field in the three-dimensional wall jet at $x/h=10$ are shown in Figure 2. Both the streamwise and lateral components of velocity are shown, and in all cases are normalized by the local maximum streamwise velocity $U_{\max}$. The contours of $U/U_{\max}$ indicate that the mean flow has begun to spread mostly near the wall at this location. Consistently, the lateral velocity is largest near the wall and oriented away from the jet centerline. There are strong turbulent fluctuations in both the streamwise and lateral components of the fluctuating velocity at the center of the jet, whereas a region of high w fluctuations exist near the wall at the jet centerline. There is no evidence of this region in the u fluctuations.

Similar contours of the velocity field are shown in Figure 3 at $x/h=20$. The rapid lateral development of the jet from $x/h=10$ to 20 is readily apparent upon comparison of Figs. 2 and 3. In particular, the mean flow contours at $x/h=10$ indicate that the wall jet has begun to spread only slightly at the wall, whereas by $x/h=20$, the jet is significantly wider and resembles contours expected in the far field (as discussed in more detail by Hall and Ewing [16]). The wider contours at $x/h=20$ are accompanied by stronger mean lateral velocities (relative to $U_{\max}$) near the wall, and correspondingly larger turbulence intensities than at $x/h=10$.

The POD was applied to the fluctuating wall pressure before performing the spectral LSE technique, so a brief overview of the POD results are given here. More details from the POD investigation of the pressure field can be found in Ref. [14]. The relative and cumulative amount of energy recovered by each POD pressure mode integrated over all frequencies is shown in Fig. 4. The POD quickly converges, indicating that the pressure fluctuations are reasonably organized in this flow. At both locations, three POD modes recover at least 75% of the variance of the fluctuating

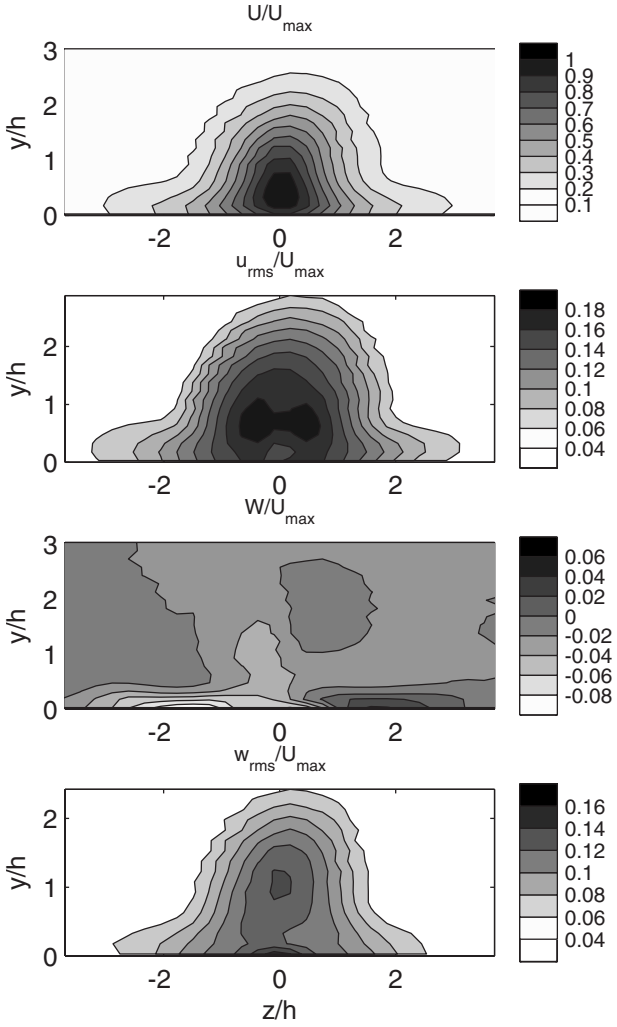

Fig. 2 Contours of (*a*) $U/U_{\max}$, (*b*) $u_{\text{rms}}/U_{\max}$, (*c*) $W/U_{\max}$, and (*d*) $w_{\text{rms}}/U_{\max}$ at $x/h=10$

pressure, and in both cases, the first two POD modes capture at least 65% of the energy. In the present analysis, only the combination of the first two POD modes will be used to estimate the velocity field, since together, they contain the majority of the flow energy.

The eigenspectra of the first two POD modes and the real part of the mode-shapes at $x/h=10$ and 20 are shown in Figs. 5 and 6, respectively. The real part of the mode-shapes are plotted at various frequencies yielding information about both the variation in magnitude and sign of the mode-shape across the jet. The eigenspectra of the first two POD modes at $x/h=10$ have distinct peaks at $fh/U_{\max}=0.18$, indicating that the majority of the pressure fluctuations associated with the large-scale structures are centered at this frequency. For higher frequencies, the pressure fluctuations associated with the large-scale structures quickly decay as expected since these frequencies are associated with smaller-scale structures. Similar behavior can be observed in the eigenspectra at $x/h=20$, although here, the peak is at a slightly lower frequency, $fh/U_{\max}=0.1$. This lower frequency may be attributed to the structures passing over the wall more slowly or becoming longer in the streamwise direction.

At $x/h=10$, the mode-shapes for the first POD mode are antisymmetric about the jet centerline for frequencies near the peak in the eigenspectra (for example, $fh/U_{\max}=0.12$) and symmetric for all other frequencies. The second POD mode-shapes behave in the opposite manner. Integrating the portions of the eigenspectra as-

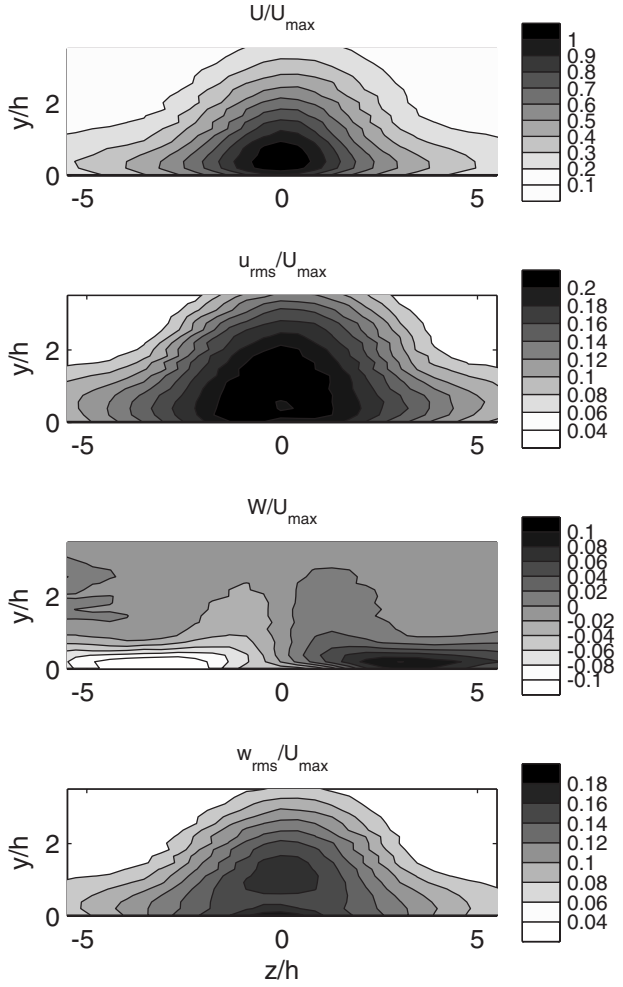

Fig. 3 Contours of (*a*) U/U_{max}, (*b*) u_{rms}/U_{max}, (*c*) W/U_{max}, and (*d*) w_{rms}/U_{max} at $x/h=20$

sociated with the symmetric and antisymmetric mode-shapes separately reveals that the antisymmetric mode is more prominent. Downstream, at $x/h=20$, the first POD mode is symmetric and the second mode is antisymmetric for all frequencies. The mode-shapes show a distinct narrowing at the higher frequencies (for example at $fh/U_{max}=0.34$). Hall and Ewing [14] attributed this behavior to a second narrower inner structure at the core of the jet. Hall and Ewing [14] also demonstrated how the first two symmetric and antisymmetric POD modes combine to instantaneously recover asymmetrical pressure fluctuations that are correlated over one-half of the lateral span of the wall jet. The relationship between the pressure POD modes and the turbulent velocity field, however, has not been investigated.

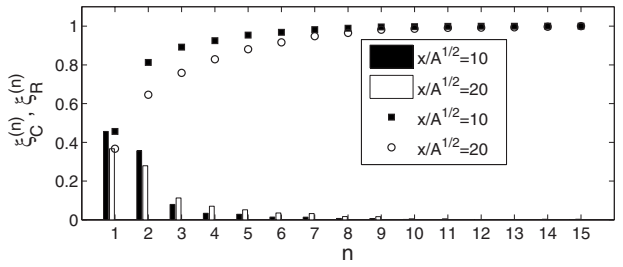

Fig. 4 Relative and cumulative pressure energy recovered using the POD integrated over all frequencies

The streamwise and lateral components of the estimated velocity field at $x/h=10$ are compared in Fig. 7. The estimate from the first POD mode, the second POD mode, the combined contribution from the first and second POD modes, and the combined contribution from the first and second POD modes with the mean added are all shown at the same instant. The streamwise and lateral components of the velocity field estimated from the first POD mode are antisymmetric about the jet centerline, in both cases, consistent with Hall and Ewing's [14] assertion, based upon pressure measurements only. The estimated lateral velocity component from the first POD mode is in phase across the entire lateral span of the wall jet, and is considered to be antisymmetric because w does not change sign with z. The estimate from the second POD mode is significantly weaker than the estimate from the first POD mode for both components. In fact, only u is detectable at the given contour levels ($0.05U_{max}$). Inspection of this figure and the full data set reveals that the estimated velocity field from the second POD mode is symmetric in both u and w. When the estimate from the two modes are combined, the instantaneous estimate of the velocity field becomes slightly larger and somewhat more irregular. When the mean flow field is added to the estimate, the role of the antisymmetric velocity field becomes clear; in particular, the antisymmetric streamwise fluctuations cause the streamwise velocity on one side of the jet centerline to increase, and the streamwise velocity on the opposite side to decrease. This causes the maxima in the streamwise velocity field to be directed to one side of the jet. The antisymmetry associated with the lateral velocity fluctuations causes a coherent velocity sweep across the span of the wall jet. The estimated direction of the lateral velocity field is consistent with that expected from the streamwise velocity estimate, confirming the accuracy of the estimation technique as both velocity components are estimated independently.

The behavior of the velocity field estimated from a symmetric POD pressure mode can be better observed at $x/h=20$, as shown in Fig. 8. In this case, the symmetric POD pressure mode (mode 1) is more dominant than the antisymmetric mode. The highest streamwise velocity fluctuations associated with this mode appear at the center of the jet and the corresponding lateral velocity components are oriented to oppose each other, causing the flow to be swept away from the jet centerline. When this mode changes signs, the estimate of the lateral velocity from mode 1 caused the flow to be directed inwards towards the jet centerline. The turbulent velocity estimated from the antisymmetric POD pressure mode is quite similar to the estimate at $x/h=10$; the streamwise velocity is out of phase across the jet centerline, whereas the lateral component is in phase across the jet. When the velocity fields estimated from the two modes are combined, their role also appears to be similar to $x/h=10$; the antisymmetric mode causes large lateral sweeps of fluid across the entire span of the wall jet and the side to side translation of the streamwise flow.

The streamwise and lateral components of the fluctuating velocity field estimated from the first two POD modes with the mean included at $x/h=10$ and $x/h=20$ are plotted in sequence in Figs. 9 and 10, respectively. These two figures are plotted on the same axis, with the same contour levels, and are normalized by U_{max} to allow comparison of the flow at the two streamwise positions. Initially, at $x/h=10$, a region of large negative lateral velocity forms at the center of the jet away from the wall. From $tU_{max}/h=3.9$ to 5.2, this region becomes wider and moves downwards towards the wall. This strong lateral sweep of fluid causes the streamwise velocity profile to become strongly distorted to the left. These sweeps are in excess of 20% of U_{max}. At $tU_{max}/h=6.5$, a region of strong positive lateral velocity forms at the center of the jet and away from the wall that causes the top half of the streamwise velocity profile to begin to shift to the right. The resulting shear caused by the oppositely signed lateral velocities at the center of the jet is likely, at least partially responsible for the region of high turbulence at the center of the jet shown in Fig. 2. At later instants, the lateral velocity grows in strength, moves

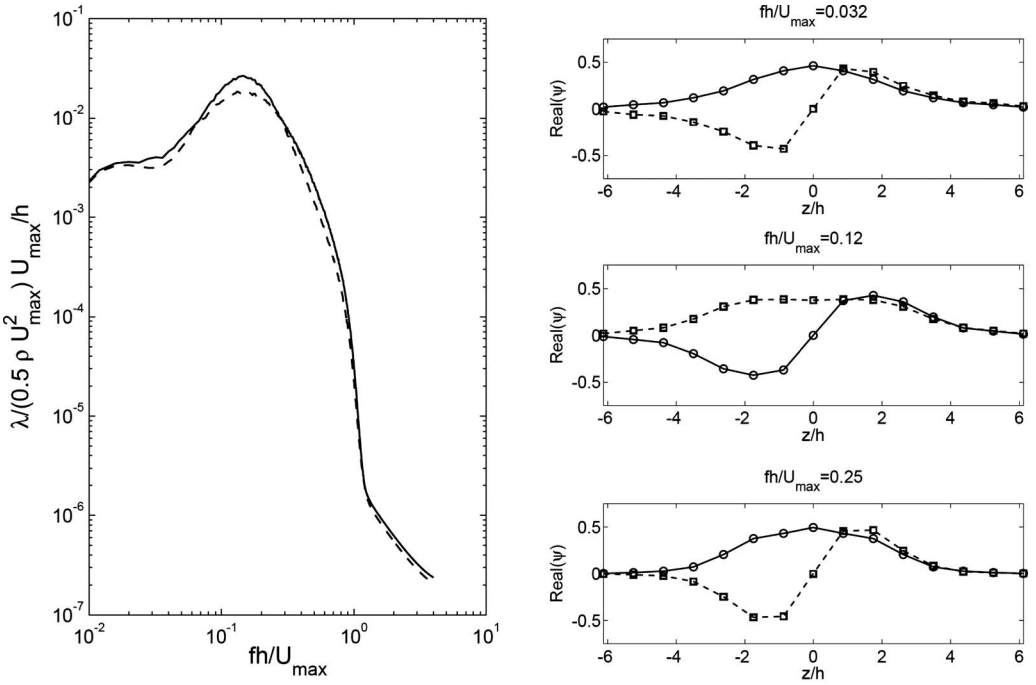

(a) EIGENSPECTRA, $-$ $n=1$, $---$ $n=2$. (b) MODE-SHAPES, $\circ$ $n=1$; AND $\square$ $n=2$.

Fig. 5 POD results at *x/h*=10

towards the wall, and the region grows in size. This causes the streamwise velocity field to be directed strongly to the left. A similar series of events can be observed in the estimate of the flow field downstream at $x/h=20$. In this case, large regions of lateral velocity initially develop away from the wall above the jet centerline, and again, move towards the wall. The lateral fluctuations here however, are wider than at $x/h=10$, and persist across the entire lateral span of the jet. This causes the streamwise velocity field to be strongly distorted to the left or right. In this case, the deviation from the mean contours is greater here than at $x/h=10$.

To better characterize the spatial character of the coherent structures in the flow, the instantaneous streamwise vorticity was ap-

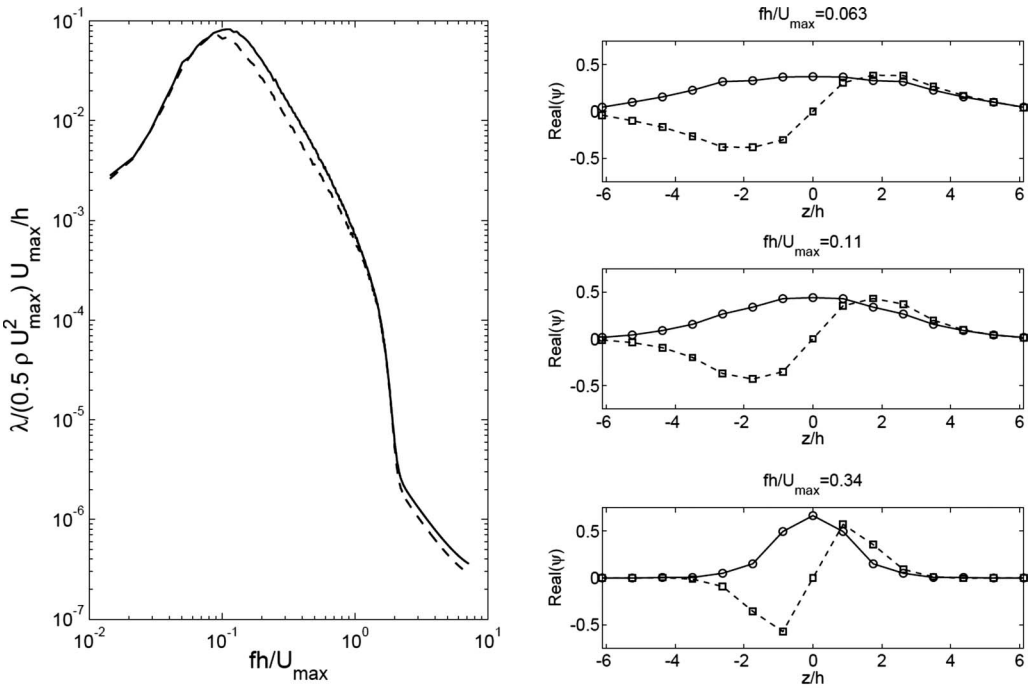

(a) EIGENSPECTRA, $-$ $n=1$, $---$ $n=2$. (b) MODE-SHAPES, $\circ$ $n=1$; AND $\square$ $n=2$.

Fig. 6 POD results at *x/h*=20

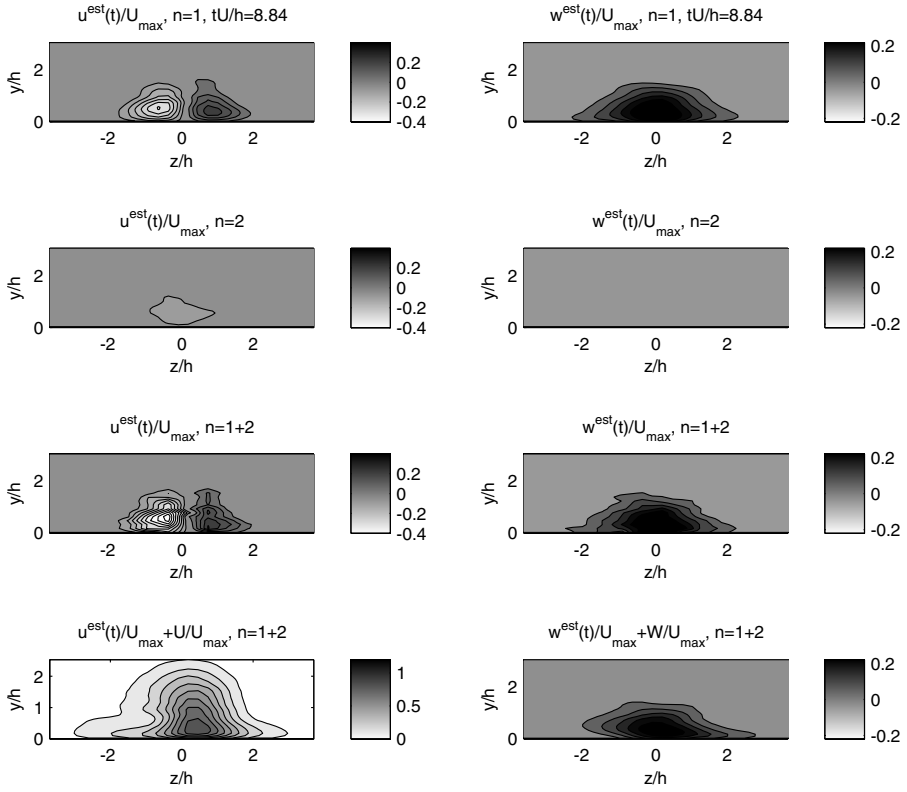

Fig. 7 Estimate of the streamwise (left) and lateral (right) component of the velocity in the *y*–*z* plane at *x*/*h*=10. The streamwise direction is into the page.

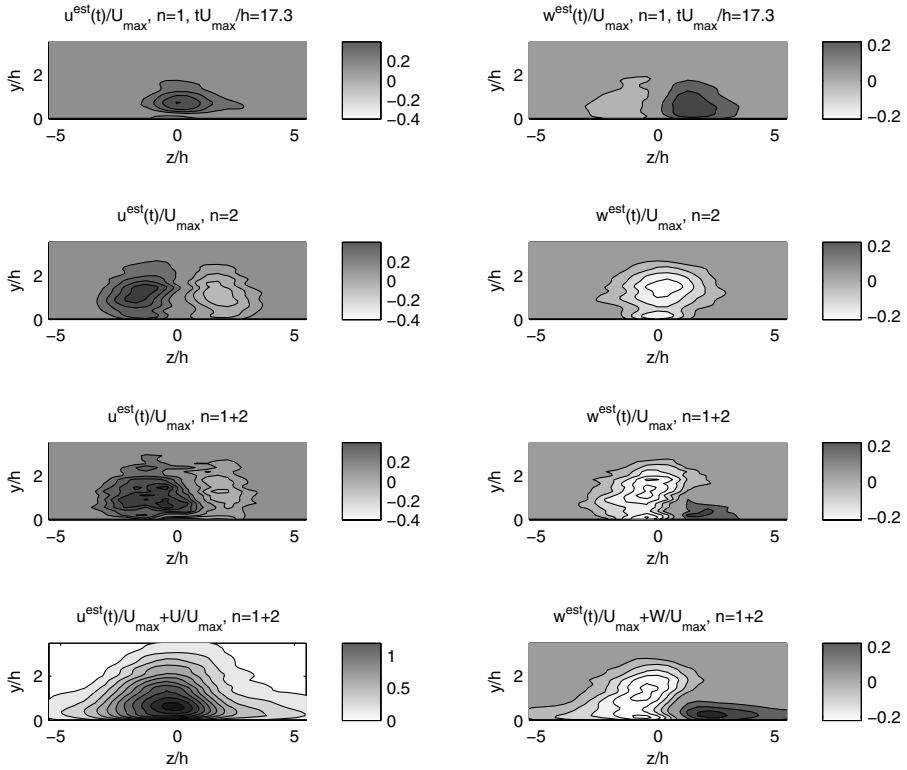

Fig. 8 Estimate of the streamwise (left) and lateral (right) component of the velocity in the *y*–*z* plane at *x*/*h*=20. The streamwise direction is into the page.

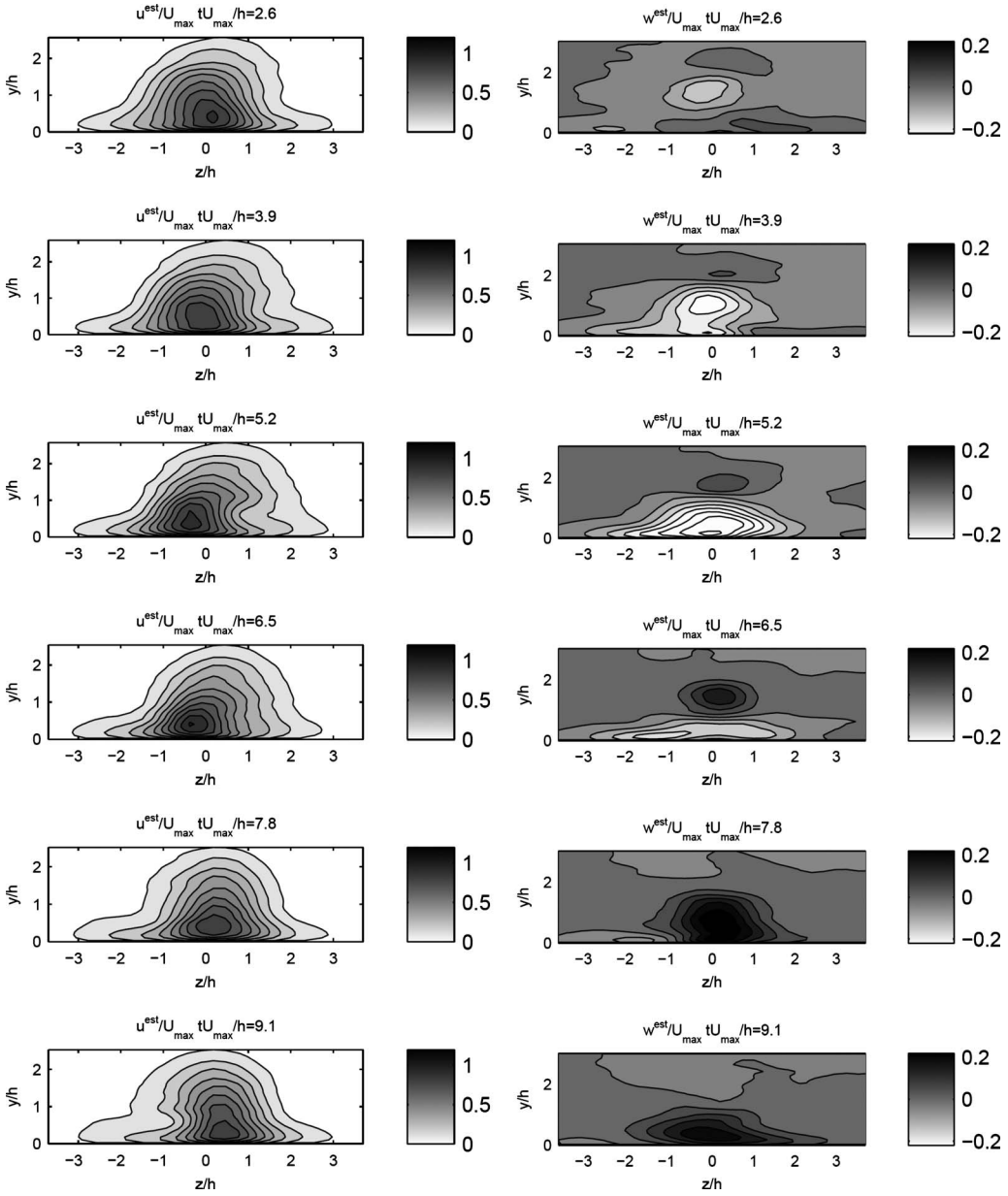

Fig. 9 A typical sequence of the streamwise (left) and the lateral (right) velocity estimates from first two POD modes including mean in the $y-z$ plane at $x/h=10$. The streamwise direction is into the page.

proximated by computing one component of the mean streamwise vorticity from the estimated lateral velocity, $\partial(w_{\text{est}}+W)/\partial y$. Isosurfaces of both positive and negative vorticity values are shown in Fig. 11. Even though only one component of the streamwise velocity is used, the structure looks remarkably similar to the horseshoe structures proposed by Matsuda et al. [9], with the notable exception that the positive and negative signed portions of vorticity on either side of the jet centerline seem to be offset in the temporal direction. As noted in previous investigations [11,12], there is some inclination of the structure away from the wall at the center of the jet. The structures at $x/h=20$ (Fig. 12) appear similar to the half horseshoe structure observed at $x/h=10$, with the notable exception that the near wall leg of the vortex structure at $x/h=20$ persists for a longer duration. This is consistent with the lower peak frequency observed in the eigenspectra at this location than at $x/h=10$. Although not shown here, inspection of the associated unsteady velocity fields indicate that the legs of the horseshoe structure are associated with the strong, unsteady lateral velocity sweeps observed in Figs. 9 and 10. The longer leg of the vortex-structure observed at $x/h=20$ than at $x/h=10$ causes these lateral velocity sweeps to persist for a longer duration and contributes to the large lateral growth of the three-dimensional wall jet at this location and likely into the far-field.

5 Concluding Remarks

A spectral LSE using the spatially filtered pressure was performed to examine the instantaneous velocity field associated with the large-scale structures in a three-dimensional wall jet exiting a long square channel. Estimates were performed in the intermediate field of the wall jet at $x/h=10$ and $x/h=20$, the region where the jet quickly develops. The coherent structures in the wall jet appear to be similar to one-half of the larger outer horseshoe structure proposed by Matsuda et al. [9], with the notable excep-

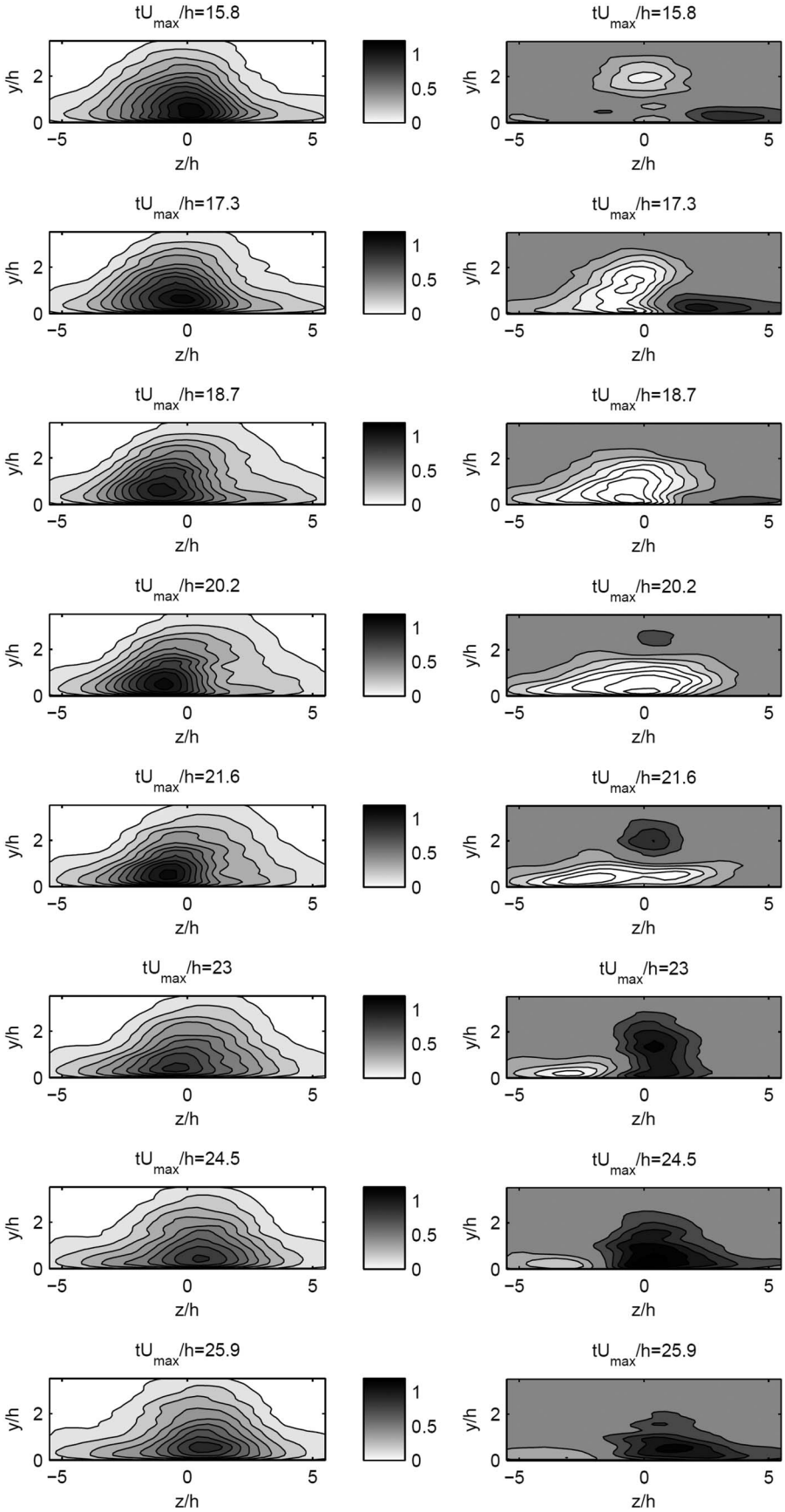

Fig. 10 A typical sequence of the streamwise (left) and the lateral (right) velocity estimates from first two POD modes including mean in the $y-z$ plane at $x/h=20$. The streamwise direction is into the page.

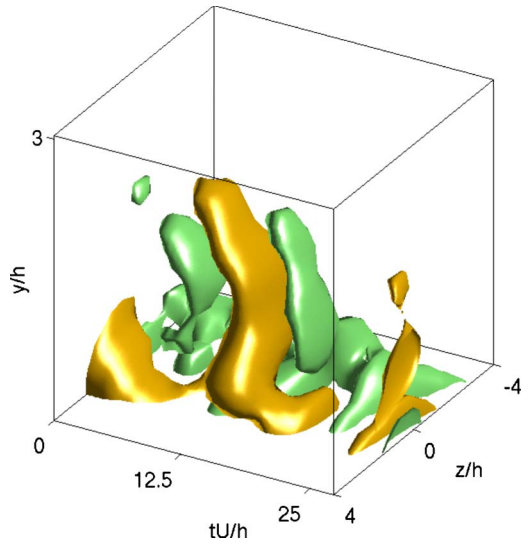

Fig. 11 Isosurface at ±1 for $\partial(W+w_{est})/\partial y$ for wall jet at $x/h=10$

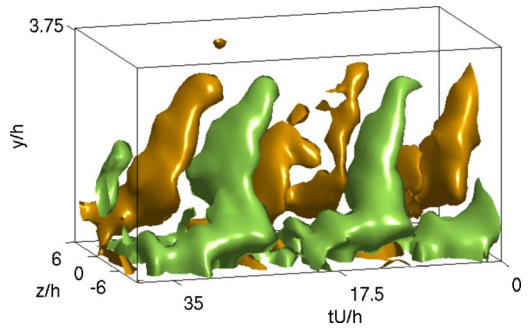

Fig. 12 Isosurface at ±1 for $\partial(W+w_{est})/\partial y$ for wall jet at $x/h=20$

tion that the oppositely signed regions are not symmetric about the jet centerline and are staggered across the jet. The passage of this structure causes large lateral sweeps of fluid that persist across the entire span of the wall jet and induces the streamwise velocity field to shift from side to side. As the structures evolve downstream to $x/h=20$, the lower legs of the outer vortex structures become longer and produce strong lateral sweeps of fluid that persist across the entire span of the jet. At both locations, there was no evidence of the energetic smaller inner structure proposed by Ewing and Pollard, however, it is unclear if it was just obscured by the larger velocity fluctuations. As the asymmetry of the velocity and pressure field has been noted to be a feature of three-dimensional wall jets formed using round contoured nozzles [11], long rectangular channels [14], and now, long square channels, it is likely that the staggered vortex structures noted here are common to all three-dimensional wall jets. Work is presently underway to examine whether these inner structures are present using the band-pass filtered spectral LSE technique proposed by Hall and Ewing [15].

Acknowledgment

The authors are grateful for the support of the Natural Sciences and Engineering Research Council of Canada. The help of Professor Nan Gao in the experimental phase of this investigation is also gratefully acknowledged.

References

[1] Abrahamsson, H., Johansson, B., and Lofdahl, L., 1997, "The Turbulence Field of a Fully Developed Three-Dimensional Wall Jet," Technical Report No. 91-1, Chalmers University of Technology, Sweden.
[2] Davis, M. R., and Winarto, H., 1980, "Jet Diffusion From a Circular Nozzle Above a Solid Plane," J. Fluid Mech., **101**, pp. 201–221.
[3] Launder, B. E., and Rodi, W., 1979, "The Turbulent Wall Jet," Prog. Aerosp. Sci., **19**, pp. 81–128.
[4] Launder, B. E., and Rodi, W., 1983, "The Turbulent Wall Jet-Measurements and Modelling," Annu. Rev. Fluid Mech., **15**, pp. 429–459.
[5] Hall, J. W., and Ewing, D., 2005, "The Rectangular Wall Jet—Part I: The Effect of Varying Aspect Ratio," *Proceedings of the 43rd AIAA Aerospace Sciences Meeting and Exhibit*, Reno, NV, Jan. 10–13, AIAA Paper No. AIAA2005-0115.
[6] Sun, H., and Ewing, D., 2002, "Effect of Initial and Boundary Conditions on the Development of Three-Dimensional Wall Jet," *Proceedings of the AIAA Winter Meeting*, Tahoe, AIAA Paper No. AIAA 2002-0733.
[7] Padmanabham, G., and Gowda, B., 1991, "Mean and Turbulence Characteristics of a Class of Three-Dimensional Wall Jets—Part 1: Mean Flow Characteristics," ASME J. Fluids Eng., **113**, pp. 620–628.
[8] Iida, S., and Matsuda, H., 1988, "An Experimental Study of Circular Turbulent Wall-Jet Along a Convex Wall," Trans. Jpn. Soc. Mech. Eng., Ser. B, **54**, pp. 354–360.
[9] Matsuda, H., Iida, S., and Hayakawa, M., 1990, "Coherent Structures in Three-Dimensional Wall Jet," ASME J. Fluids Eng., **112**, pp. 462–467.
[10] Ewing, D., and Pollard, A., 1997, "Evolution of the Large-Scale Motions in a Three-Dimensional Wall Jet," *Proceedings of the 28th AIAA Fluid Dynamics Conference/Fourth AIAA Shear Flow Control Conference*, Paper No. 97-1964.
[11] Sun, H., and Ewing, D., 2002, "Development of the Large-Scale Structures in the Intermediate Region of the Three-Dimensional Wall Jet," ASME Paper No. FEDSM2002-31414.
[12] Sullivan, P., and Pollard, A., 1996, "Coherent Structure Identification From the Analysis of Hot-Wire Data," Meas. Sci. Technol., **7**, pp. 1498–1516.
[13] Hall, J. W., and Ewing, D., 2005, "Investigation of the Large-Scale Structures in Large Aspect Ratio Three-Dimensional Wall Jets," ASME Paper No. FEDSM2005-77272.
[14] Hall, J. W., and Ewing, D., 2007, "The Asymmetry of the Large-Scale Structures in Turbulent Three-Dimensional Wall Jets Exiting Long Rectangular Channels," ASME J. Fluids Eng., **129**, pp. 929–941.
[15] Hall, J. W., and Ewing, D., 2006, "A Combined Spatial and Temporal Decomposition of the Coherent Structures in the Three-Dimensional Wall Jet," *Proceedings of the 44th AIAA Aerospace Sciences Meeting and Exhibit*, Reno, NV, Jan. 9–12, AIAA Paper No. AIAA2006-308.
[16] Hall, J. W., and Ewing, D., 2007, "The Development of Three-Dimensional Turbulent Wall Jets Issuing From Moderate Aspect Ratio Rectangular Channels," AIAA J., **45**(6), pp. 1177–1186.
[17] Beuther, P. D., 1980, "Experimental Investigation of the Axisymmetric Turbulent Bouyant Plume," Ph.D. thesis, SUNY, Buffalo.
[18] Lumley, J. L., 1967, "The Structure of Inhomogeneous Turbulence Flows," *Atmospheric Turbulence and Wave Propagation*, A. M. Yaglom and V. I. Tatarsky, eds., Nauka, Moskau.
[19] Holmes, P., Lumley, J. L., and Berkooz, G., 1996, *Turbulence, Coherent Structures, Dynamical Systems and Symmetry*, Cambridge University Press, New York.
[20] Glauser, M. N., Leib, S. J., and George, W. K., 1987, "Coherent Structures in the Axisymmetric Mixing Layer," *Turbulent Shear Flows 5*, F. Durst, ed., Springer-Verlag, Berlin, pp. 4.21–4.26.
[21] Ewing, D., and Citriniti, J. H., 1999. "Examination of a LSE/POD Complementary Technique Using Single and Multi-Time Information in the Axisymmetric Shear Layer," *Proceedings of the IUTAM Symposium on Simulation and Identification of Organized Structures in Flows*, J. Sorensen, E. J. Hopfinger, and N. Aubry, eds., Lyngby, Denmark, May 25–29, pp. 375–384.
[22] Tinney, C. E., Coiffet, F., Delville, J., Hall, A. M., Jordan, P., and Glauser, M. N., 2006, "On Spectral Linear Stochastic Estimation," Exp. Fluids, **41**(5), pp. 763–775.
[23] Taylor, J., and Glauser, M., 2004, "Towards Practical Flow Sensing and Control via POD and LSE Based Low-Dimensional Tools," ASME J. Fluids Eng., **126**(3), pp. 337–345.
[24] Naguib, A., Hudy, L., and Humphreys, W., 2002, "Stochastic Estimation and Non-Linear Wall-Pressure Sources in a Separating/Reattaching Flow," American Society of Mechanical Engineers, New York, Vol. 257, pp. 1211–1216.
[25] Ukeiley, L., and Murray, N., 2003, "Estimation of the Flowfield From Surface Pressure Measurements in an Open Cavity," AIAA J., **42**, pp. 969–972.
[26] Picard, C., and Delville, J., 2000, "Pressure Velocity Coupling in a Subsonic Round Jet," Int. J. Heat Fluid Flow, **21**, pp. 359–364.

Weiguo Gu
School of Mechanical Engineering,
Shanghai Jiao Tong University,
Shanghai 200240, China
e-mail: guweiguo@sjtu.edu.cn

Yasuo Kawaguchi
Professor
Member of JSME,
Faculty of Science and Technology,
Tokyo University of Science,
Noda, Chiba 278-8510, Japan
e-mail: yasuo@rs.noda.tus.ac.jp

Dezhong Wang
Professor
School of Mechanical Engineering,
Shanghai Jiao Tong University,
Shanghai 200240, China
e-mail: dzwang@sjtu.edu.cn

Saito Akihiro
Mitsubishi Heavy Industry,
Kobe, Hyogo 654-0153, Japan

Experimental Study of Turbulence Transport in a Dilute Surfactant Solution Flow Investigated by PIV

Drag-reducing flow of dilute surfactant solution in the two-dimensional channel is investigated experimentally by using particle image velocimetry (PIV) system. Five hundred instantaneous velocity frames of u-v in the x-y plane are taken by PIV for every condition. Fluctuation intensity and instantaneous velocity distributions are discussed in order to study the turbulence transport in the drag-reducing flow. As compared with water, the results show that wall-normal velocity fluctuations in the drag-reducing flow are suppressed significantly, and instantaneous velocity distributions display different features. Moreover, the drag-reducing flow exhibits the reduced inclination angle of turbulence transport and appearance of "zero Reynolds shear stress." High shear dissipation also appears in some solutions. Based on the analysis of the balance of mean and mean turbulent kinetic energies, it is found that the complex rheology, i.e., the elasticity and viscosity of the solution, is considered as the main factor that change the characteristics of turbulence transport. [DOI: 10.1115/1.4001631]

1 Introduction

It is well known that the presence of small amounts of certain additives (such as polymers or surfactants) in water can result in a considerable reduction in the drag in the turbulent flow, which was named "Toms effect" because this phenomenon was first reported by Toms in 1948 [1]. Li et al. [2,3] even reported that the frictional drag reduced by 60–80%, appearing in the very dilute aqueous solution of cetyltrimethyl ammonium chloride (CTAC) and sodium salicylate (NaSal) with a concentration of only 30 ppm. Moreover, surfactant solutions has increasingly received the significant attention during the past 2 decades because of the strong self-repairing ability after the mechanical degradation.

In order to clarify the drag-reduction mechanism of the surfactant solution flow, a lot of experiments and simulations seen in Refs. [4–6] have been carried out. The dynamic characteristics of the drag-reducing flow were summarized by Gyr and Tsinober that the small scale part of the flow (both in time and space) was suppressed, and the streamwise velocity fluctuations remained approximately the same level, whereas the transverse one was strongly reduced. Moreover, the anisotropy of the turbulent flow increased, and the Reynolds stress was strongly reduced because of less correlation between the two components of the velocity fluctuations [7]. In the wall-bounded turbulent flow, the turbulent bursting phenomenon and Reynolds shear stress are important to clarify the turbulence transportation. It was found in the surfactant solution flow that the cyclic turbulent bursts were inhibited and the vortex structures were modified [8,9]. Kawaguchi et al. [10] found that the penetration of the fluid from the low-speed fluid region into the high-speed region almost disappeared, and the strong fluctuations of spanwise vorticities near the wall also disappeared in the experiments by using particle image velocimetry (PIV) to measure the velocity field in the streamwise and wall-normal plane in the surfactant solution channel flow. Furthermore, Li et al. [11,12] found that the inclination angle of the low-momentum region below the hairpin vortices decreased and the frequency of bursts was reduced, which indicated the inhibition of bursting events by surfactant additives. The decrease in the turbulence transportation also led to the decrease in the heat transfer because the wall-normal turbulent heat flux was depressed at the same time [13,14].

One of our present researches aims at the modification of turbulence transportation in the channel flow by the complex rheology of surfactant solutions. The rheology of surfactant solutions depends on the mass concentration, and strong viscoelasticity will appear when the mass concentration increases [15]. Most of the abovementioned studies focused on the very dilute solution with the concentration normally less than 50 ppm. As the authors know, surfactant additives added into the water will form the cross-linked micellar networks under a proper shear stress, which will modify the turbulent structures and is regarded as the cause of drag reduction [16,17]. The investigation by Cryo-TEM proved that the solution with wormlike micellar displayed rich rheological behaviors such as drag-reducing agents and viscosity enhancers [18]. Shear thickening phenomenon was usually found in low concentration surfactant solutions, and many experiments exhibited that the nonequilibrium shear-induced phase transition happened accompanying the shiftup of viscosity during the course of shear thickening [19]. Our present rheology measurement on one surfactant solution proved the presence of shear thickening and showed the almost fixed range of shear rate between 10 and 20 when the apparent viscosity started to be raised at 25°C. Such shear rates are comparatively low and normally within the range across the whole channel flow, so different rheology behaviors of the flow will appear in sequence from the wall to the middle of the channel. In this paper, PIV is used to measure the velocity in streamwise-wall-normal plane. The dynamic characteristics of the surfactant solution flow are studied based on the statistic results and instantaneous velocity distribution.

2 Experimental Facility

The experiments are performed on a closed-circuit water loop shown in Fig. 1 in order to measure the two-dimensional velocity distribution in the channel, which is made of transparent acrylic

Contributed by the Fluids Engineering Division of ASME for publication in the JOURNAL OF FLUIDS ENGINEERING. Manuscript received February 20, 2009; final manuscript received April 9, 2010; published online May 13, 2010. Assoc. Editor: Hassan Peerhossaini.

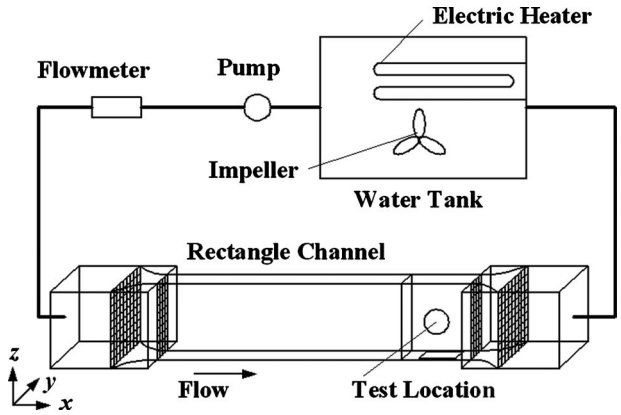

Fig. 1 Schematic diagram of the experimental facility

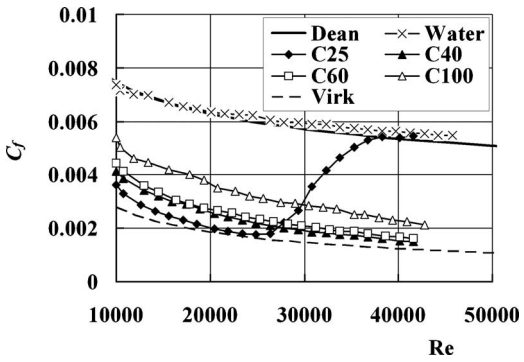

Fig. 3 Frictional factor versus Reynolds number

resin with a length of more than 10 m, height of 0.5 m, and width of 0.04 m. A honeycomb rectifier with a length of 0.15 m is set at the channel entrance in order to remove large eddies. The segment for test is located at 6 m downstream from the entrance of the channel. An electromagnetic flow meter with an uncertainty of ± 0.01 m^3/min is installed upstream of the channel to measure the flow flux. The solution in the water tank is heated by electric heaters at an identical temperature (25 °C in this experiment) with an uncertainty of ± 0.1 °C. The wall shear stress is estimated from the static pressure gradient, which is tested with an uncertainty of ± 0.1 Pa between two tabs located on the vertical side wall of the channel at a distance of 1.5 m.

The additives added into the water in this experiment are CTAC and NaSal with the same mass concentration. The impeller driven by the electric motor is installed in the water tank as the stirrer to keep the additives uniformly distributed. Because it is found that many small bubbles are difficult to be eliminated in the solution with a concentration of more than 100 ppm, the concentration is selected to be less than 100 ppm in the experiment to ensure taking clear particle images.

The PIV system consists of a double-pulsed laser, laser sheet optics, charge-coupled device (CCD) camera, timing circuit, image-sampling computer, and image-processing software. The double-pulsed laser is a combination of a pair of Nd-YAG lasers, as shown in Fig. 2. The timing circuit, communicating with the CCD camera and computer, generates pulses to control the double-pulsed laser. The CCD camera has a resolution of 2048×2048 pixels. PIV tests the velocities within a streamwise and wall-normal (x-y) plane, which the laser sheet covered with having a height of 250 mm from the channel bottom. One kind of white coating of waterbased synthetic resins is added into the flow as the seed particles with a diameter of $0.1-1$ μm. The concentration of seed particles is adjusted to ensure an average of at least ten particle pairs observed in every interrogation window.

Five hundred of dual frames are acquired in every measurement condition. The photograph acquisition rate is 4 Hz. The pictures taken by PIV cover the full width of the channel with an area of about $x \times y = 58 \times 42$ mm^2. The interrogation area is set to 32×32 pixels with 75% overlap in each direction. As a result, about 127×90 vectors are got respectively in x- and y-directions with 0.45 mm spacing between adjacent vectors.

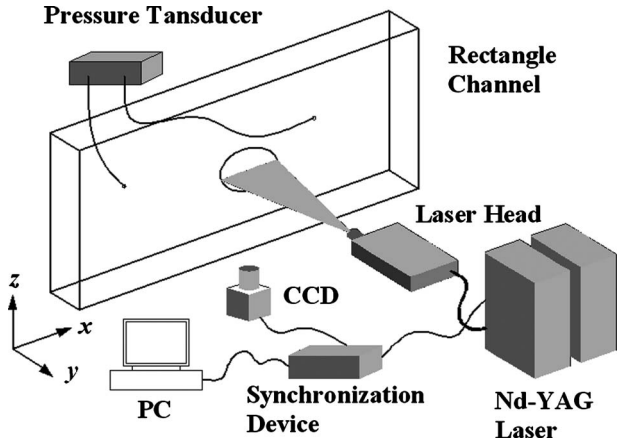

Fig. 2 Optical configuration for the PIV measurement

3 Results and Discussion

3.1 Frictional Drag Factor and Drag Reduction Rate. Fanning friction factor and drag reduction (DR) are defined in the following equations:

$$C_f = \tau_w/(1/2\rho U_b^2) \tag{1}$$

$$\mathrm{DR} = (C_{f,W} - C_{f,S})/C_{f,W} \times 100\% \tag{2}$$

The profiles of the friction factor and DR for 25 ppm, 40 ppm, 60 ppm, and 100 ppm surfactant solutions are presented in Figs. 3 and 4, respectively.

Dean's correlation of friction factor for a Newtonian fluid in a two-dimensional channel [20]

$$C_f = 0.073\ \mathrm{Re}^{-0.25} \tag{3}$$

and Virk ultimate correlation of friction factor for polymers solution [21]

$$C_f = 0.58\ \mathrm{Re}^{-0.58} \tag{4}$$

are also included in Fig. 3 for comparison. Reynolds number is defined as $\mathrm{Re} = \rho U_b W/\mu$.

As shown in Fig. 3, the friction factors of water obeys Dean's equation and decrease smoothly when the Reynolds number in-

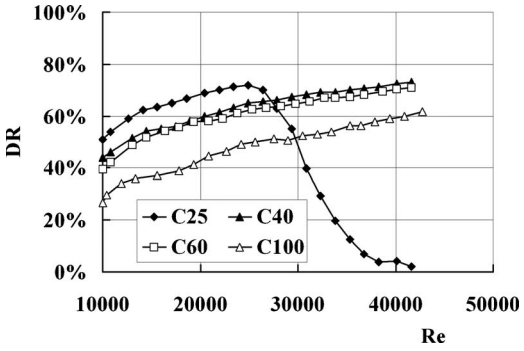

Fig. 4 Drag reduction versus Reynolds number

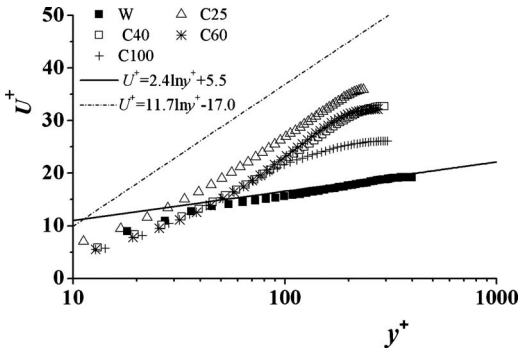

Fig. 5 Profiles of U^+ at Re=15,000

creases. In contrast, the friction factors of the four types of surfactant solutions are markedly smaller than water. At the same time, the solution with the low concentration exhibits the small friction factors; for example, the profile of 25 ppm is the smallest one, which nearly reaches the profile of Virk's ultimate friction factor. But its profile of friction factors rises quickly when the Reynolds number is larger than 25,000 and ultimately reach the friction level of water after Re=38,000. Accordingly, the largest DR appears in the 25 ppm surfactant solution and reaches more than 70%. The surfactant solutions of 40 ppm and 60 ppm show almost the same DR within the whole range of Reynolds number, and DR of 100 ppm is the smallest. According to the division of DR state [22], the Reynolds number at which DR reaches the maximum is called as first critical Reynolds number and at which DR disappears completely is called as second critical Reynolds number. Based on this division, Re=25,000 is the first critical Reynolds number of 25 ppm surfactant solution.

3.2 Statistic Results. The statistic calculation is performed based on the ensemble average of 500 instantaneous velocity fields for one flow at the same Reynolds number. Mean velocity profiles are presented in Figs. 5 and 6 at Re=15,000 and 40,000, respectively, where the superscript "+" indicates nondimensionalization by the friction velocity u_τ. The log law equation of the mean velocity for the Newtonian turbulent flow

$$U^+ = 2.4 \ln y^+ + 5.5 \tag{5}$$

and the ultimate velocity profile of polymeric solution flow suggested by Virk

$$U^+ = 11.7 \ln y^+ - 17.0 \tag{6}$$

are included in the figures.

The profiles of water are in close agreement with the profile of Eq. (5), as shown in Figs. 5 and 6. In addition, the solution of 25 ppm at Re=40,000 exhibits a similar distribution of the mean velocities with the water flow accompanying its absolute disappearance of DR. In contrast, drag-reducing flows show the upward distribution of the mean dimensionless streamwise velocity. The profiles of drag-reducing flows are below the profile of the water, where y^+ is approximately less than 50, and then rise increasingly and exceed the water accordingly as y^+ increases. Moreover, the distributed profiles are dependent on DR, i.e., the profiles of the higher drag reduction are closer to the line of Eq. (6).

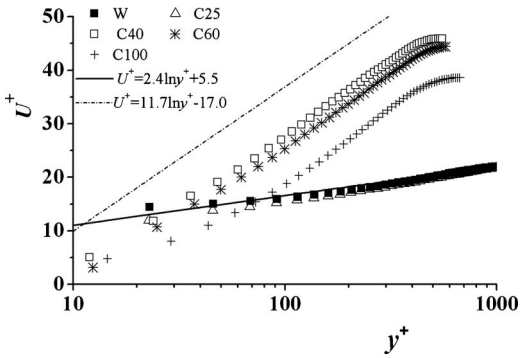

Fig. 6 Profiles of U^+ at Re=40,000

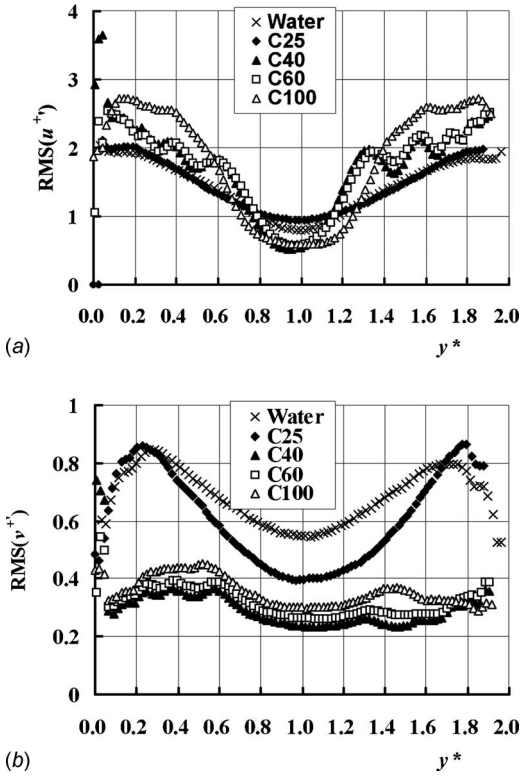

Fig. 7 Profiles of RMS of velocity fluctuations at Re=40,000: (*a*) RMS of $u^{+\prime}$ and (*b*) RMS of $v^{+\prime}$

Root mean square (RMS)

$$\mathrm{RMS} = \sqrt{\frac{1}{N}\sum_{i}^{N} (u_i^+ - U^+)^2} \tag{7}$$

is usually represented by the turbulence intensity, where N is the total number of vectors at one identical y-position.

As seen in Fig. 7, the RMS of the streamwise velocity fluctuations in drag-reducing flow is appreciably larger than that of the water in the major region of the channel. At the same time, the wall-normal fluctuations exhibit the significant suppression across the whole channel section. For the 25 ppm surfactant solution, the distribution of wall-normal velocity fluctuations are similar with water at Re=40,000. The suppression of wall-normal velocity fluctuations will result in the decrease in the turbulence transportation and Reynolds shear stress. But a different phenomenon appears in Fig. 8 at Re=15,000 when the fluctuations of both streamwise and wall-normal velocities in the 100 ppm surfactant solution flow become the smallest, whereas at Re=40,000 the RMS of fluctuations are larger than that of 40 ppm and 60 ppm. In addition, it is surprising to find that DR does not correspond with the change in the fluctuations. Besides, the similar phenomenon also appears in 60 ppm CTAC solution at Re=10,000 which is shown in Fig. 9. This phenomenon indicates that the relationship between the friction factor and velocity fluctuations is not identical.

When the concentration of the solution is given, small differences are found among the RMS-$u^{+\prime}$ profiles of 40 ppm surfactant

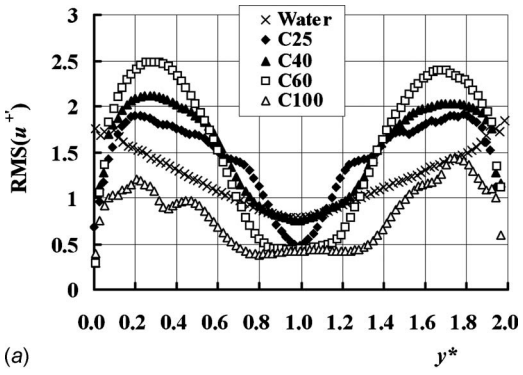

(*a*)

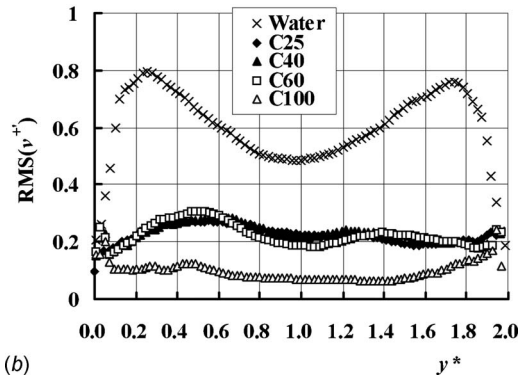

(*b*)

Fig. 8 Profiles of RMS of velocity fluctuations at Re=15,000: (*a*) RMS of $u^{+\prime}$ and (*b*) RMS of $v^{+\prime}$

solutions under different Reynolds numbers, which are shown in Fig. 10. Moreover, Fig. 11 displays the similar distributions for the solution of 60 ppm other than the case of Re=10,000. Thus, it can be clearly seen that only three cases, i.e., 60 ppm at Re

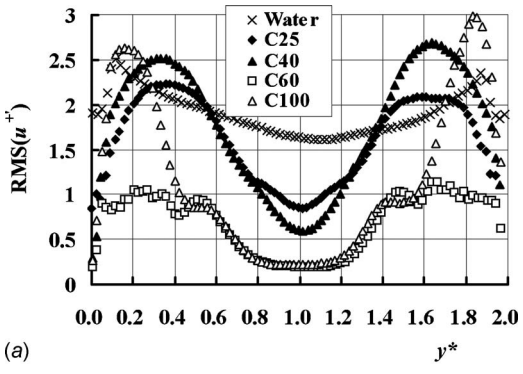

(*a*)

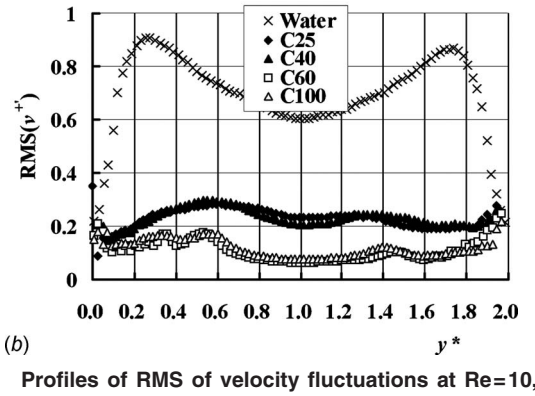

(*b*)

Fig. 9 Profiles of RMS of velocity fluctuations at Re=10,000: (*a*) RMS of $u^{+\prime}$ and (*b*) RMS of $v^{+\prime}$

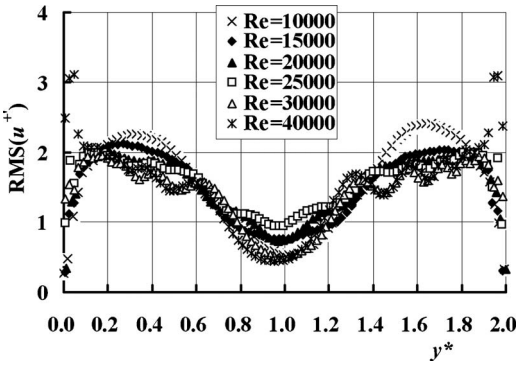

Fig. 10 Profiles of RMS-$u^{+\prime}$ of the 40 ppm CTAC solution

=10,000, and 100 ppm at Re=10,000 and 15,000, show the unusual decline of velocity fluctuations, whereas DR maintains the usual trend. The small friction factors of the three cases indicate that the flow does not transfer to the laminar state, but the decline of velocity fluctuations will imply the unusual turbulence transportation in surfactant solution flows.

3.3 Instantaneous Distribution of Streamwise Velocity Fluctuations. The two-dimensional instantaneous distributions of streamwise velocity fluctuations nondimensionalized by the bulk velocity (u'/U_b) in the x-y plane are shown in Fig. 12. The superscript "$*$" in the axis label indicates the nondimensionalization by half the width of the channel ($W/2$). The direction of the bulk flow in the figures is from the left to the right with an increase in the x-coordinates.

Figure 12(*a*) exhibits the typical pattern of turbulence in wall-bounded water flow that almost the whole channel is occupied by the high-fluctuation blocks, which is randomly distributed and has complicated edges. In contrast, the drag-reducing flows exhibit the different distributions of the streamwise velocity fluctuations. The significant difference is that the distribution in the drag-reducing flow appears as horizontal stripes instead of the block feature in the water flow, e.g., in Figs. 12(*b*) and 12(*c*). Moreover, the stripe feature can also be found in 60 ppm and 100 ppm surfactant solution flows in Figs. 12(*g*) and 12(*h*) besides 25 ppm and 40 ppm. The stripes developed in the streamwise direction indicate that the turbulent structures that transferred from the wall toward the bulk flow are modified so that the additives not only suppress the wall-normal velocity fluctuations, but also change the inclination angle of turbulence transportation.

The distributions of 60 ppm at Re=10,000, and 100 ppm at Re=10,000 and 15,000 are shown in Figs. 12(*e*)–12(*g*). All the fluctuations exhibit the uniform distribution of the fractus pattern and decreased intensity. Furthermore, there seems to be little fluc-

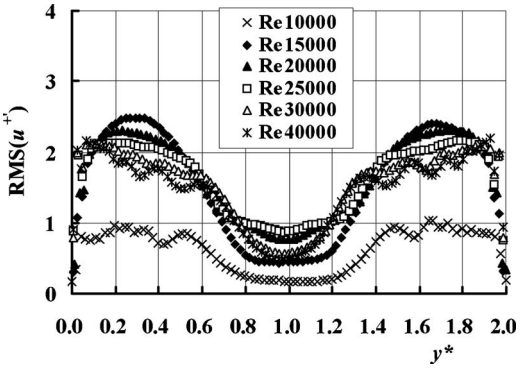

Fig. 11 Profiles of RMS-$u^{+\prime}$ of the 60 ppm CTAC solution

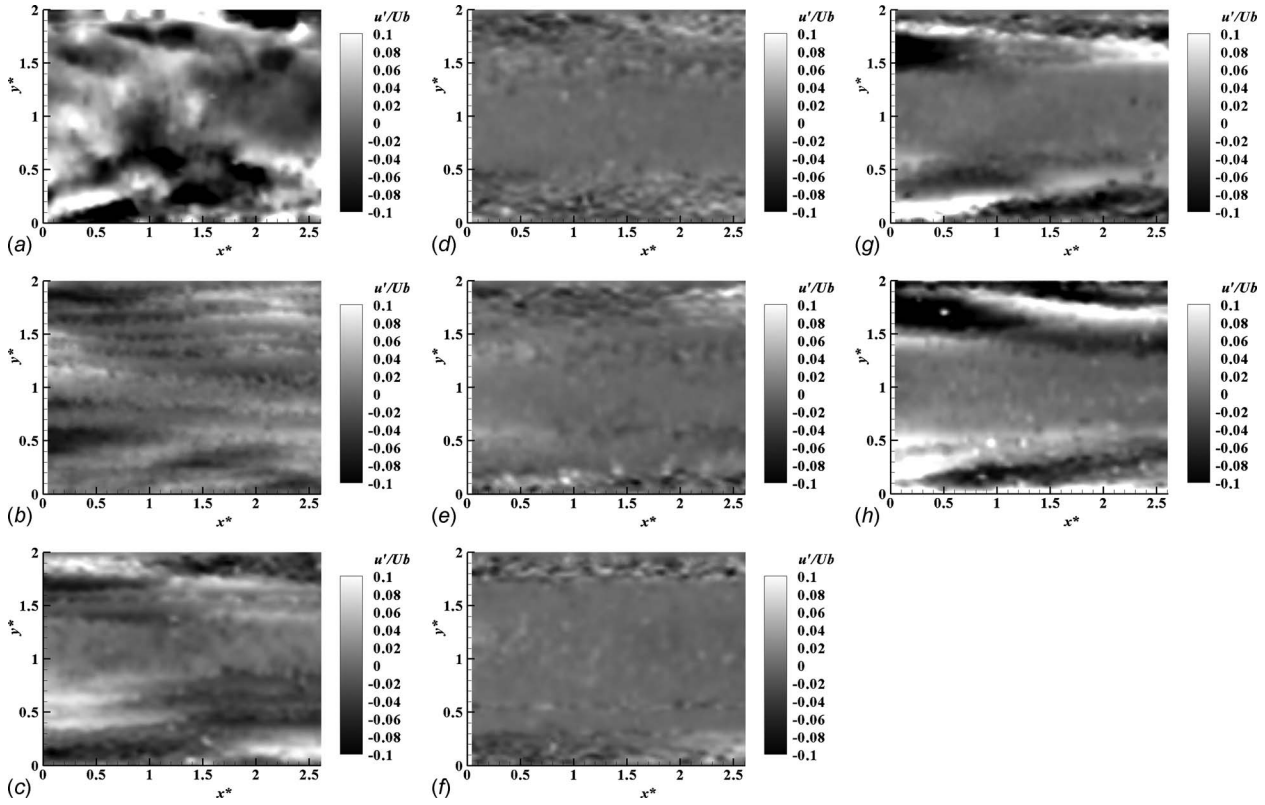

Fig. 12 Instantaneous distribution of streamwise velocity fluctuations in the *x-y* plane: (*a*) water at Re=10,000; (*b*) 25 ppm at Re=10,000; (*c*) 40 ppm at Re=10,000; (*d*) 60 ppm at Re=10,000; (*e*) 100 ppm at Re=10,000; (*f*) 100 ppm at Re=15,000; (*g*) 60 ppm at Re=15,000; and (*h*) 100 ppm at Re=40,000

tuation appearing in the areas around the centerline of the channel. The fluctuations and the turbulence transportation are damped in the three cases.

3.4 Discussion. The balance of the mean and mean turbulent kinetic energies in the fully developed turbulent flow are given in the following equations [23]:

$$0 = \underbrace{-U\frac{\partial P}{\partial x}}_{P_U} + \underbrace{\frac{\partial}{\partial y}\left(-\rho\overline{u'v'}U + \mu\frac{\partial U}{\partial y}U + \tau_{xy}U\right)}_{T_U} - \left(\underbrace{-\rho\overline{u'v'}\frac{\partial U}{\partial y}}_{D_U} + \underbrace{\mu\frac{\partial U}{\partial y}\frac{\partial U}{\partial y}}_{V_U} + \underbrace{\tau_e\frac{\partial U}{\partial y}}_{E_U}\right) \tag{8}$$

$$0 = \underbrace{-\rho\overline{u'v'}\frac{\partial U}{\partial y}}_{P_k} + \underbrace{\frac{\partial}{\partial y}\left(-\overline{v'p'} - \rho\overline{kv'} + \mu\frac{\partial\overline{k}}{\partial y} + \overline{u_i'\tau_e'}\right)}_{T_k} - \underbrace{\mu\overline{\frac{\partial u_i'}{\partial x_j}\frac{\partial u_i'}{\partial x_j}}}_{\varepsilon_s} - \underbrace{\overline{\tau_e'\frac{\partial u_i'}{\partial x_j}}}_{\varepsilon_e} \tag{9}$$

In Eq. (8), P_U is the product item of the mean kinetic energy produced by the streamwise pressure gradient, T_U represents the energy transportation and exhibits the zero contribution to the energy balance when integrated over the channel cross section, D_U is normally regarded as the deformation work by the Reynolds shear stress, which is also the product of the turbulent kinetic energy in Eq. (9), V_U and E_U are the deformation work by the viscous and elastic shear stresses, respectively. In Eq. (9), T_k is similar to T_U, and ε_s and ε_e are the viscous and elastic dissipations of the turbulent kinetic energy.

In the water flow, the mean kinetic energy exhibit the balance among the items of P_U, D_U, and V_U. But in the drag-reducing flow, "zero Reynolds shear stress" appears in Fig. 13, which leads to the "shear stress deficit." However, the Reynolds shear stress will not be replaced by the elastic shear stress completely. As a result, the decrease in D_U will cause the decline of the pressure gradient, and then the occurrence of the drag reduction. In addition, the item of E_U depends on the rheology, especially the viscoelasticity of the solution. The high mass concentration will enhance the viscoelasticity, which will lead to the increase in E_U and the decrease in DR if little difference appears in the velocity gradients at the same Reynolds number.

In the turbulent kinetic energy equation, there is a balance between the production (P_k) and the dissipation (ε_s and ε_e). But the

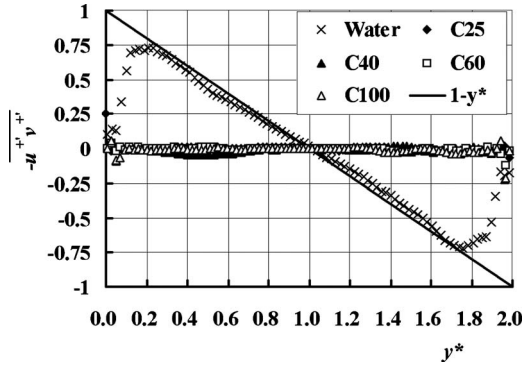

Fig. 13 Profiles of the Reynolds shear stress at Re=10,000

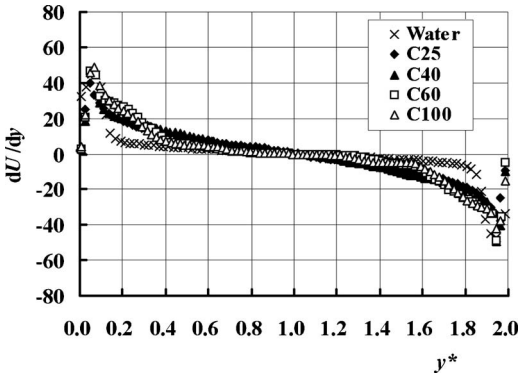

Fig. 14 Profiles of *dU/dy* at Re=10,000

zero production in the drag-reducing flow will cause no turbulent kinetic energy being dissipated, which is called as "turbulent kinetic energy deficit." In fact, the item of ε_e will be negative, indicating that the pulsation of the elastic stress will generate the velocity fluctuations and contribute the turbulence.

However, the rheology of the solution is not uniform across the channel because it depends on the shear rate of the flow. The high shear rates near the wall cause the complete formation of shear-induce structures (SIS) of the additives, which provide the strong elasticity to suppress the Reynolds turbulence transportation and cause them to develop in the streamwise direction. It is different with the viscosity, in that the elasticity will not dissipate but store the kinetic energy. Although the wall-normal velocity fluctuations are damped, the longitudinally inclined distribution of fluctuations will drive the wall-normal pulsation of elasticity at the same time, and then fluctuations are generated again. This assumption will be the other reason for the appearance of stripe features of the velocity fluctuations in the surfactant solution flow.

For the unusual appearance of the fluctuation distributions in 60 ppm and 100 ppm surfactant solutions under comparatively low Reynolds number, the weak turbulence intensity, especially in the middle of the channel, implies that the turbulence transportation decreases or even disappears completely. Compared with the other surfactant solutions, stripe features disappear and only small fluctuations appear near the wall with the fractus feature. It is indicated that the strong viscosity instead of the elasticity dissipates the fluctuations for a very large degree. As previously reported, surfactant solutions with the concentration larger than 200 ppm exhibited the phenomenon of shear thickening during which the apparent viscosity rose quickly by several times normally within the identical rage of the shear rate between 20 and 50 when the temperature is 20°C. Moreover, the maximum DR occurs when the concentration is 120 ppm using the same additives in the abovementioned rheology measurement. By analogy, shear thickening will probably happen in 60 ppm or 100 ppm surfactants in the present experiments. When the Reynolds number is 10,000, small shear rates appear even near the wall; for example, the largest one is less than 60, as seen in Fig. 14. In this case, shear thickening will happen in the near-wall region accompanying the very large viscosity, which leads to the high shear dissipation and the low of actual Reynolds number. If the actual Reynolds number reaches critical Reynolds number, the decline of burst events will cause the small fluctuations, but the high shear dissipation produces the large skin friction. As a result, the complex and nonuniform rheology of the surfactant solutions results in the unusual characteristics.

4 Conclusions

The turbulence transport in dilute CTAC surfactant solution in a two-dimensional channel has been studied experimentally by using a PIV system. It is found that the complex rheology of the surfactant solution has effects on the turbulence transport. The following conclusions are drawn from the present study.

(1) Drag reduction in surfactant solutions in this experiment depends on the Reynolds number and mass concentration. Large DR usually appears in the case of comparatively high Reynolds number or low mass concentration when below the first critical Reynolds number.
(2) Compared with the water flow, statistic results showed that wall-normal velocity fluctuations in the drag-reducing flow are suppressed significantly. Moreover, the instantaneous velocity distribution displays the streamwise-developed regions with high velocity fluctuations, which indicate the reduced inclined angle of turbulence transportation. The appearance of zero Reynolds shear stress indicates the shear stress and turbulent kinetic energy deficits. It is considered that the strong elasticity of the solution plays the key role in damping fluctuations and at the same time generates fluctuations again, which leas to the stripes distribution.
(3) Surfactant solutions of 60 ppm and 100 ppm exhibit the unusual characteristics that fluctuations are diminished with the smallest intensity, whereas no change appears in the DR trend when the Reynolds number is only approximately at 10,000. By analogy with the rheology measurement, it is considered that shear thickening has happened and the increasingly high viscosity leads to the high shear dissipation near the wall. As a result, skin friction maintains a high level and turbulence transportation is diminished.

Acknowledgment

This research is supported by National Natural Science Foundation of China (Grant No. 50476016), NSFC-JSPS Scientific Cooperation Program (Grant No. 50611140359), and China Scholarship Council.

Nomenclature

H = height of the channel (m)
W = wall-normal width of the channel (m)
C_f = friction factor
U = mean streamwise velocity (m/s)
u_τ = friction velocity (m/s)
u = streamwise velocity (m/s)
v = wall-normal velocity (m/s)
ρ = density of the solvent (kg/m^3)
τ_w = wall shear stress (Pa)
τ_e = elastic shear stress (Pa)
μ = dynamic viscosity of the solvent (Pa s)

Subscripts

W = water
C = CATC solution
b = bulk flow

Superscripts

$'$ = fluctuations
$+$ = nondimensionalization by the friction velocity
$*$ = nondimensionalization by half the width of the channel

References

[1] Toms, B. A., 1948, "Some Observations on the Flow of Linear Polymer Solutions Through Straight Tubes at Large Reynolds Numbers," Proceedings of the International Congress on Rheology, Vol. 2, pp. 135–138.
[2] Li, P. W., Kawaguchi, Y., and Yabe, A., 2001, "Transitional Heat Transfer and Turbulent Characteristics of Drag-Reducing Flow Through a Contracted Channel," J. Enhanced Heat Transfer, **8**, pp. 23–40.
[3] Li, P., Kawaguchi, Y., Daisaka, H., Yabe, A., Hishida, K., and Maeda, M., 2001, "Heat Transfer Enhancement to the Drag-Reducing Flow of Surfactant Solution in Two-Dimensional Channel With Mesh-Screen Inserts at the Inlet," ASME J. Heat Transfer, **123**, pp. 779–789.
[4] Cruz, D. O. A., and Pinho, F. T., 2003, "Turbulent Pipe Flow Predictions With

a Low Reynolds Number $k-\varepsilon$ Model for Drag Reducing Flow," J. Non-Newtonian Fluid Mech., **114**, pp. 109–148.
[5] Yu, B., and Kawaguchi, Y., 2005, "DNS of Fully Developed Turbulent Heat Transfer of a Viscoelastic Drag-Reducing Flow," Int. J. Heat Mass Transfer, **48**, pp. 4569–4578.
[6] Li, C.-F., Sureshkumar, R., and Khomami, B., 2006, "Influence of Rheological Parameters on Polymer Induced Turbulent Drag Reduction," J. Non-Newtonian Fluid Mech., **140**, pp. 23–40.
[7] Gyr, A., and Tsinober, A., 1997, "On the Rheological Nature of Drag Reduction Phenomena," J. Non-Newtonian Fluid Mech., **73**, pp. 153–162.
[8] Fukagata, K., Iwamoto, K., and Kasagi, N., 2002, "Contribution of Reynolds Stress Distribution to the Skin Friction in Wall-Bounded Flows," Phys. Fluids, **14**, pp. L73–L76.
[9] Hetsroni, G., Zakin, J. L., and Mosyak, A., 1997, "Low-Speed Streaks in Drag-Reducing Turbulent Flow," Phys. Fluids, **9**, pp. 2397–2404.
[10] Kawaguchi, Y., Segawa, T., Feng, Z., and Li, P., 2002, "Experimental Study on Drag-Reducing Channel Flow With Surfactant Additives-Spatial Structure of Turbulence Investigated by PIV System," Int. J. Heat Fluid Flow, **23**, pp. 700–709.
[11] Li, F. C., Kawaguchi, Y., Hishida, K., and Oshima, M., 2006, "Investigation of Turbulence Structures in a Drag-Reduced Turbulent Channel Flow With Surfactant Additive by Stereoscopic Particle Image Velocimetry," Exp. Fluids, **40**, pp. 218–230.
[12] Li, F.-C., Kawaguchi, Y., Yu, B., Wei, J.-J., and Hishida, K., 2008, "Experimental Study for Drag-Reduction Mechanism for a Dilute Surfactant Solution Flow," Int. J. Heat Mass Transfer, **51**, pp. 835–843.
[13] Li, F.-C., Kawaguchi, Y., and Hishida, K., 2005, "Structural Analysis of Turbulent Transport in a Heated Drag-Reducing Channel Flow With Surfactant Additives," Int. J. Heat Mass Transfer, **48**, pp. 965–973.
[14] Li, F. C., Wang, D. Z., Kawaguchi, Y., and Hishida, K., 2004, "Simultaneous Measurements of Velocity and Temperature Fluctuations in Thermal Boundary Layer in a Drag Reducing Surfactant Solution Flow," Exp. Fluids, **36**, pp. 131–140.
[15] Zhang, H.-X., Wang, D.-Z., Gu, W.-G., and Chen, H.-P., 2008, "Effects of Temperature and Concentration on Theological Characteristics of Surfactant Additive Solution," J. Hydrodynam., **20**, pp. 603–610.
[16] Clausen, T. M., Vinson, P. K., Minter, J. R., Davis, H. T., Talmon, Y., and Miller, W. G., 1992, "Viscoelasitc Micellar Solution: Microscopy and Rheology," J. Phys. Chem., **96**, pp. 474–484.
[17] Lu, B., Li, X., Scriven, E., Davis, H. T., Talmon, Y., and Zakin, J. L., 1998, "Effect of Chemical Structure on Vicoelasticity and Extensional Viscosity of Drag-Reducing Cationic Surfactant Solution," Langmuir, **14**, pp. 8–16.
[18] González, Y. I., and Kaler, E. W., 2005, "Cryo-TEM Studies of Worm-Like Micellar Solutions," Curr. Opin. Colloid Interface Sci., **10**, pp. 256–260.
[19] Hu, Y. T., and Boltenhagen, P., 1998, "Shear Thickening in Low-Concentration Solution of Wormlike Micelles. I. Direct Visualization of Transient Behavior and Phase Transitions," J. Rheol., **42**(5), pp. 1185–1208.
[20] Dean, R. B., 1978, "Reynolds Number Dependence of Skin Friction and Other Bulk Flow Variables in Two-Dimensional Rectangular Duct," ASME J. Fluids Eng., **100**, pp. 215–223.
[21] Virk, P. S., Mickley, H. S., and Smith, K. A., 1970, "The Ultimate Asymptote and Mean Flow Structure in Tom's Phenomenon," ASME J. Appl. Mech., **37**, pp. 488–493.
[22] Kawaguchi, Y., Daisaka, H., and Yabe, A., 1997, "Turbulent Characteristics in Transition Region of Dilute Surfactant Drag Reducing Flow," Proceedings of the 11th International Symposium on Turbulent Shear Flows, Grenoble, France, Vol. 9, pp. 49–54.
[23] Zhang, H., Wang, D., Chen, H., and Wang, Y., 2007, "Development Characteristics of Velocity Transports in an Isothermal Heated Drag-Reducing Surfactant Solution Flow," AIP Conf. Proc., **914**, pp. 566–573.

Hiroshi Yamaguchi
Department of Mechanical Engineering,
Energy Conversion Research Center,
Doshisha University,
Kyoto 630-0321, Japan

Xin-Rong Zhang[1]
Department of Energy and Resources Engineering,
College of Engineering,
Peking University,
100871, P.R. China;
Department of Mechanical Engineering,
Energy Conversion Research Center,
Doshisha University,
Kyoto 630-0321, Japan
e-mail: scho@mail.doshisha.ac.jp

Xiao-Dong Niu

Yuta Ito

Department of Mechanical Engineering,
Energy Conversion Research Center,
Doshisha University,
Kyoto 630-0321, Japan

Flow Characteristics of Microglass Fiber Suspension in Polymeric Fluids in Spherical Gaps

An experimental study is carried out to investigate the effects of microglass fiber suspensions in the non-Newtonian fluids in a gap between an inner rotating sphere and an outer whole stationary sphere. In the experiments, the microglass fibers with different aspect ratios are mixed with a macromolecule polymeric fluid to obtain different suspension fluids. For comparison, a Newtonian fluid and the non-Newtonian polymeric fluid are also studied. The stationary torques of the inner sphere that the test fluids acted on are measured under conditions of various concentric spherical gaps and rotational Reynolds numbers. It is found that the polymeric fluid could be governed by the Couette flow at a gap ratio of less than 0.42 and the Reynolds number of less than 100, while the fiber-suspended polymeric fluids could expand the Couette flow region more than the Reynolds number of 100 at the same gap ratios. [DOI: 10.1115/1.4001491]

Keywords: fiber suspension, sphere Couette flow, viscoelastic fluid

1 Introduction

Generally, a system wherein the solid particles are dispersed in liquid is called suspension. Research on the rheology of the suspension has a long history. However, due to various shapes, sizes, distributions, and complex interactions between the suspended particles, the properties of the suspension rheology are far from understood. Recently, as a tendency to rheology research of the suspensions, a concept of using suspension to control the complicated flow behaviors becomes popular due to its important applications in various industry fields [1].

On the other hand, a variety of composite materials have been developed in recent years. Particularly, due to merits of light weight, superior strength, and low-cost of fibers, the fiber suspensions in macromolecule liquids have been extensively applied in fields of aerospace, medical equipment, motor parts, and so on. Unlike Newtonian fluids, flow behaviors of fiber suspension fluids are very complicated and behave as non-Newtonian fluids [2]. To understand characteristics of these complicated suspension fluids, this study focuses on studying rheology and the flow behaviors of microglass fiber suspensions experimentally and theoretically.

In addition, nowadays in industries, there are a lot of mechanical parts in a machine having various gaps filled with fluids. These gaps control the flow behaviors of the fluids, and the flow behaviors also affect the motion of the mechanical parts, which further affect the lifetime of the whole machine. In practice, it is very desirable to control the operating condition that the flows in the gaps are of the Couette flows. This is because that the Couette flow has simple fluid properties and can make the mechanical parts avoid vibration and move stable [3]. In the past decades, various researches have been reported to claim merits of the Couette flows [4–9].

For the viscoelastic macromolecule fluids in the spherical gap [10–12], there are torque characteristics based on two co-axis spheres, with the inner sphere rotating and the outer sphere stationary. Results [10–12] show that the viscoelastic spherical Couette flows are symmetric to the equatorial plane at low Reynolds numbers regardless of rotating the inner or the outer sphere. In a case of the inner rotated hemisphere and the stationary outer sphere, where the flow symmetry related to the equatorial plane is broken, Yamaguchi and Morishita [12] measured the torques and thrusts of the inner hemisphere, and reported that the flow structures gradually change from the Couette flow pattern to a vortex array called the Taylor–Görtler (T–G) [5], with the Reynolds number increasing over a critical value. Besides the macromolecule fluids, Yamaguchi and Hikaru [13,14] also carried out some basic investigations of the rheology of the fiber suspensions.

In this study, the fluid characteristics and rheology of microglass fiber suspensions in the gaps of two concentric spheres, with the inner sphere rotating and the outer sphere stationary, are further studied. The glass fiber suspensions, which have high viscosity and elasticity, are simply modeled as viscoelastic fluids. In this study, the stationary torques of the inner sphere acted on by the polymeric fluids or the glass fiber-suspended polymeric fluids are measured in a wide range of the spherical gaps and the rotational Reynolds numbers.

2 Experiment

2.1 Experimental Apparatus. In Fig. 1 a schematic diagram of the apparatus used in the experiments is shown. The outer sphere shell ② is made of a transparent acrylic resin to allow the measurement of the flow velocity by laser Doppler velocimetry (LDV). The inner sphere ① is made of a vinyl chloride resin. The surfaces of both spheres are smoothed by waterpower to keep the roughness effects as minimum as possible. The outer sphere is

[1]Corresponding author.

Contributed by the Fluids Engineering Division of ASME for publication in the JOURNAL OF FLUIDS ENGINEERING. Manuscript received June 27, 2009; final manuscript received March 17, 2010; published online May 13, 2010. Assoc. Editor: Theodore Heindel.

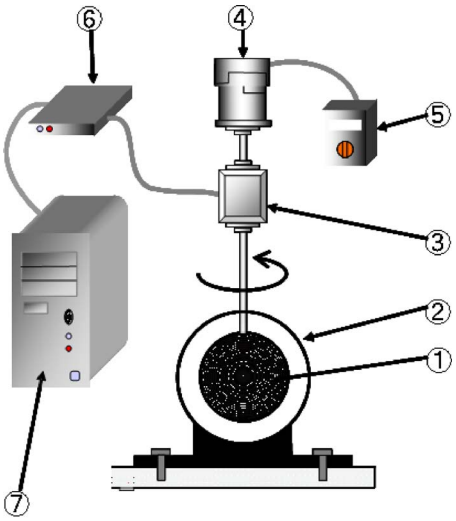

Fig. 1 A schematic diagram of the apparatus used in the experiments

arranged concentrically with the inner spheres at different gap ratios $\alpha=(r_2-r_1)/r_1$ (see Table 1, where r_1 and r_2 are the radius of the inner and outer spheres, respectively) on the same $\phi 10$ mm aluminum axis, and the test fluids are enclosed inside the gaps of the two spheres. The accuracy of the radius measurement is $\pm 0.1\%$.

Keeping the outer sphere shell stationary, the inner sphere is given a rotational speed from 0 rpm to 360 rpm by a driving motor ④. The rotational speed is changed by a speed controller ⑤ by a step of 10 rpm with an accuracy of $\pm 0.1\%$. When the inner sphere is rotating, the static frictional torque exerted on the inner sphere by the fluids inside the gaps is measured at each number of rotation by a torque detector ③ connected directly to the shaft (axis) of the inner sphere. The accuracy of the torque detector is $\pm 0.1\%$. Output signals from the torque detector are performed analog to digital (A/D) conversion with the sensor interface ⑥. A computer ⑦ is used for data processing. During the experiment, the two major sources of experimental error are as follows: (1) radius, speed, torque, viscosity, first normal stress difference, and shear rate measurement accuracy; and (2) errors resulting from data logging and reading by the computer. The error of data logging and reading were analyzed, and their values are listed as follows: $\pm 0.1\%$ for the radius, $\pm 0.1\%$ for the speed, $\pm 0.2\%$ for the torque, $\pm 0.2\%$ for the viscosity, $\pm 0.2\%$ for the first normal stress difference, and $\pm 0.1\%$ for the shear rate. Based on the above accuracies, the accuracies of all the parameters defined in this paper are calculated to be less than $\pm 1.0\%$ using the following equation:

Table 1 Experimental conditions

Forming error:under±0.1% Room temperature:22°C	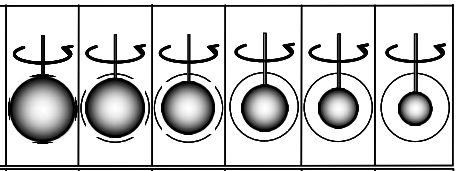					
Radius of Inner Sphere r_1 [mm]	65	65	65	55	35	35
Radius of Outer Sphere r_2 [mm]	70	75	78	78	70	83
Gap ratio $\alpha=\frac{r_2-r_1}{r_1}$	0.077	0.154	0.200	0.418	1.000	1.371

Table 2 Typical properties of polyacrylamide

Name	Appearance	Ionicity	pH range for effective use	
SANFLOC AH-210P	White powder	Anionic(m)	6–12	
Viscosity of the aqueous solution (mPa s) at 30°C				
0.1 wt %	0.2 wt %	0.3 wt %	0.5 wt %	1.0 wt %
280	960	1800	3500	7500

$$\bar{x}=\sqrt{\frac{x_1^2+x_2^2+\ \ldots\ +x_n^2}{n}}=\sqrt{\frac{\sum_{i=1}^{n}x_i^2}{n}} \tag{1}$$

where $\bar{x}$ is the average of the parameter x, x_i is the accuracy of every parameter involved in the calculation equation of x, and n is the number of the parameters in the calculation equation of x.

Considering that the flow behaviors are influenced by rotational acceleration [4], thus in the present experiment, the revolution increase in the inner sphere is adjusted quasi-statically. The torque measurement for a given rotational speed is made only when the flow becomes stable after an increase in the rotational speed. Stabilization was determined by continuous visual observation of the flow and by monitoring the continuous torque signals, ensuring that the appearing flow state did not change with time for a given rotational speed. The representative torque data are then calculated for a given rotational speed by a mean value of 20,000 measurements, which are taken at 10 s intervals. Friction and thrust forces on the bearings are carefully minimized, and the remaining friction torque due to bearings is subtracted from the measured torque.

All experiments are conducted at 22.0°C in a temperature-controlled room. The temperature rise due to the friction is monitored by an inserted thermocouple. The resultant temperature rise is well below 1.0°C for all experiments, and no temperature correction for thermophysical parameters is necessary.

2.2 Test Fluids

2.2.1 Newtonian Fluid. In this study, the glycerin water solution with concentration 70% (made by Miyishi Yushi Co. Ltd., Japan and denoted as glycerin70%) is used as the Newtonian fluid because the glycerin solution has a high viscosity, is safe to the environment, and is easy to take care of.

2.2.2 Viscoelastic Fluid. The polyacrylamide water solution (made by Sanyo Kase Co. Ltd., Japan) is also easy to take care of, and its rheology characteristic is similar to that of the viscoelastic fluid with dilute solutions; thus, in this research, the polyacrylamide water solution with a concentration of 2000 ppm (denoted as the PAA2000) is used, and its properties are shown in Table 2.

2.2.3 Suspensions. Mixtures of the PAA2000 with the micro-glass fibers (denoted as PG*xxx-y*, with *xxx* and *y* representing the length and volume ratio of the suspended glass fiber, respectively) are used to study the fiber suspension effects. The glass fibers are usually used as a reinforcing material and are easily obtained.

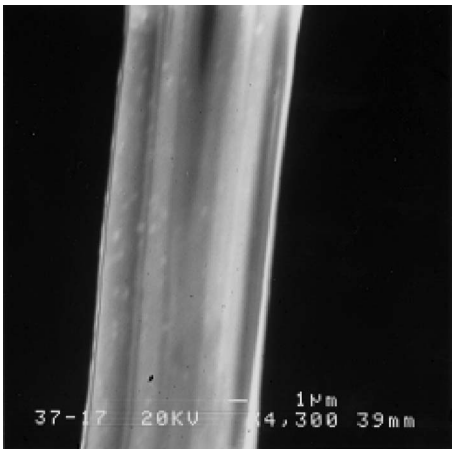

Fig. 2 Visualization of the glass fiber

Figure 2 shows a visualization of the microglass fiber.

Since shapes and volume fractions of the fibers have significant effects on the fluid properties, six kinds of glass fiber-suspended polyacrylamide water solutions are used in the present study, and they are given in Table 3 with their respective denotations for convenience.

2.3 Rheology Characteristic of the Test Fluids. The rheological characteristics of the PAA2000 and the PG*xxx-y* solutions are shown in Figs. 3(*a*) and 3(*b*), in which the shear viscosity η and the first normal stress difference N_1 for the shear rates of $1 \leq \dot{\gamma} \leq 2000$ are plotted, respectively. The accuracies of the shear rate, viscosity, and first normal stress difference are $\pm 0.1\%$, $\pm 0.1\%$, and $\pm 0.2\%$, respectively. For clearly observing the effects of the fiber suspensions and their non-Newtonian effects, the rheology of the fiber suspensions with a volume fraction 0.4% are displayed.

As shown in Fig. 3(*a*), the viscosity of glycerin70% is constant and is independent of the shear rate. From Fig. 3(*a*), it is rationally confirmed that glycerin70% can be used as a model of for Newtonian fluid. For the PAA2000 and the PG*xxx-y* solutions. Figure 3(*a*) displays clearly that their viscosities increase at a very small shear rate, and then linearly decrease to that of glycerin70% as the shear rate is increased. This finding generally agrees with the prediction of Batchelor [15], which predicts the effect of spherical particle suspensions on the viscosity of the non-Newtonian fluid by the formula $\eta/\eta_{\text{non-Newtonian fluid}} = 1 + 5\phi/2 + (7.6 \mp 0.8)\phi^2$ (ϕ represents the volume ratio of the suspension). Since in our present study the measured viscosities of the non-Newtonian fluid of PAA2000 and the PG100-0.4 at zero shear rate are 0.9541 Pa s and 1.002 Pa s, respectively, therefore their ratio is about 1.05, which is very close to Batchelor's prediction of 1.01, if we neglect the effects of the aspect ratio of the glass fiber itself in the present study. In the PG*xxx-y* solutions, the fiber suspensions are in the form of three-dimensional (3D) network structures. When the shear rate is increased, those 3D structures will be destroyed, and the rheology properties will be changed as a consequence. Those phenomena can be observed from Figs. 3(*a*) and 3(*b*), where the viscosities and first normal shear stress are shown to slightly deviate from those of the PAA2000 solutions. From Fig. 3(*b*), the first normal shear stress differences N_1 between the PAA2000 and PG solutions are linearly increased with the shear rate increasing. All the PAA2000 and PG solutions exhibit obvious viscoelastic non-Newtonian behaviors.

Table 3 The test PG*xxx-y* solutions

Test fluids	Fiber volume ratio (%)	Aspect ratio of the fiber (length/diameter) (mm/μm)
PG100-0.2	0.2	100 (0.6/6)
PG100-0.4	0.4	100 (0.6/6)
PG500-0.2	0.2	500 (3/6)
PG500-0.4	0.4	500 (3/6)
PG2000-0.2	0.2	2000 (12/6)
PG2000-0.4	0.4	2000 (12/6)

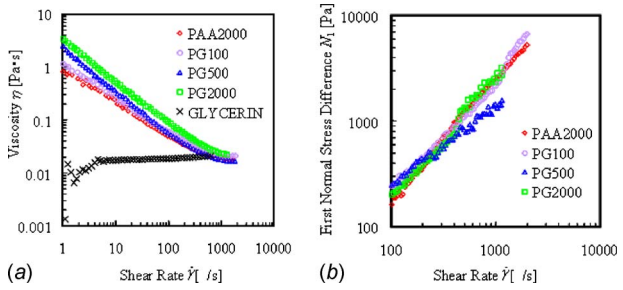

Fig. 3 The rheological characteristics of the test fluids: (*a*) shear viscosity for the test fluids; (*b*) the first normal stress difference for the test fluids

Table 4 Rheological constants of *m* and *n* in Eq. (2) obtained by fitting the measured experimental data in Fig. 4(*a*)

Test fluids	*m*	*n*
Glycerin70%	0.02	1.00
PAA2000	0.83	0.38
PG100-0.2	1.05	0.37
PG100-0.4	1.03	0.37
PG500-0.2	1.38	0.34
PG500-0.4	1.95	0.34
PG2000-0.2	1.55	0.31
PG2000-0.4	2.04	0.31

3 Theoretical Background

Regardless of the rotation of the inner or outer sphere, the flow behaviors in the spherical gap are dependent on the shear force generated by the test fluids, and the Couette flow is usually dominant in the Reynolds number ranging from zero to the value of the first laminar flow transition. The static friction torque exerted by the shear force on the inner sphere can be measured experimentally and calculated theoretically, and the flow behaviors in the spherical gap can be learned by comparing with the experimental and theoretical values. For the sake of comparison and theoretical analysis in the following results and discussions based on the nondimensional parameters related to the static friction torque, the rheological shear viscosity plotted in Fig. 3(*a*) are fitted by a well-known power-law model [16]

$$\tau = m\dot{\gamma}^n \tag{2}$$

where τ is the shear stress, and m and n are the rheological constants. In Table 4 we list the rheological constants of m and n obtained by fitting the measured experimental data in Fig. 3(*a*) to Eq. (2) for the test fluids.

In order to calculate the static friction torque exerted on the inner rotating sphere by the test fluids, a simple spherical Couette flow, in which the circumferential velocity distribution in the radial direction is only considered, is assumed for the low generalized rotational Reynolds numbers $(\text{Re}^* = \rho(r_1\omega)^{2-n}(r_2 - r_1)^n/m$, where ρ is the density of the test fluids and ω is the rotational angular velocity of the inner sphere) before the onset of the hydrodynamic instability. The characteristic of torque is governed by the shear stress exerted on the inner spheres. The respective radial

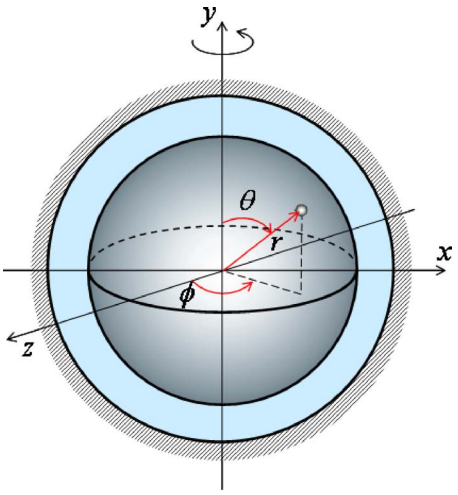

Fig. 4 The spherical coordinate system

and circumferential torques T_r and T_θ of the sphere are thus obtained as follows for simple spherical Couette flow:

$$T_r = 2\pi r_1^3 \int_0^\pi \tau_{r\phi} \sin^2 \theta d\theta \tag{3}$$

$$T_\theta = 2\pi \int_0^\pi \tau_{\theta\phi} r^2 dr \tag{4}$$

where r and ϕ represent the radial and circumferential directions of the spherical coordinates defined in Fig. 4, respectively, and $\tau_{r\phi}$ and $\tau_{\theta\phi}$ are the shear stress on the surface element of the inner sphere in the radial and circumferential directions, respectively, and are expressed in the power-law model as follows:

$$\tau_{r\phi} = m\left\{ r\frac{\partial}{\partial r}\left(\frac{v_\phi}{r}\right)\right\}^n \tag{5}$$

$$\tau_{\theta\phi} = m\left\{ \frac{\omega r}{\sqrt{r_2^2 - r^2}}\right\}^n \tag{6}$$

where v_ϕ is the circumferential velocity obtained analytically from the Cauchy momentum equation and is given as

$$v_\phi = \frac{\omega r}{(1+\alpha)^{3/n} - 1}\left\{\left(\frac{r_1(1+\alpha)}{r}\right)^{3/n} - 1\right\} \tag{7}$$

With Eqs. (3)–(7) and the definition of the Reynolds number, we can define the following dimensionless radial, circumferential, and total torque coefficients Cm_r, Cm_θ, and Cm_{sphere} of the inner sphere in the present study as

$$Cm_r = \frac{T_r}{\rho r_1^5 \omega^2} = \frac{2\pi}{\mathrm{Re}^*}(1+\alpha)^3\left\{\frac{(3/n)\alpha}{(1+\alpha)^{3/n} - 1}\right\}^n \int_0^\pi \sin^{2+n}\theta d\theta \tag{8}$$

$$Cm_\theta = \frac{T_\theta}{\rho r_1^5 \omega^2} = \frac{2\pi}{\mathrm{Re}^*}\frac{\alpha^n}{r_1^3}\int_0^{r_1} r^{2+n}\left(\frac{1}{\sqrt{r_2^2 - r^2}}\right)^n dr \tag{9}$$

and

$$Cm_{\text{sphere}} = Cm_r + Cm_\theta \tag{10}$$

respectively.

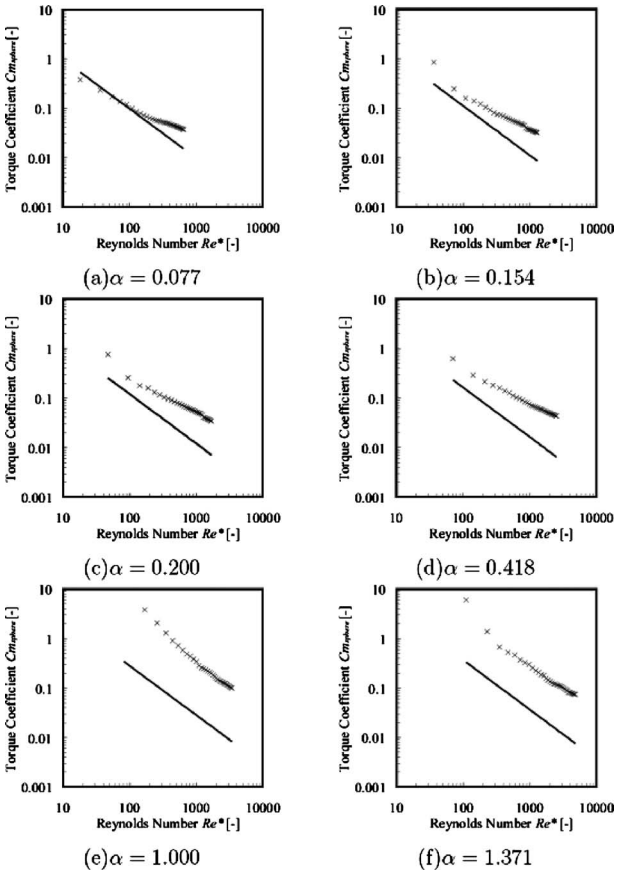

Fig. 5 Torque coefficients versus Reynolds numbers for glycerin70% with rotating inner sphere

4 Result and Discussion

For each test fluid, the friction torque coefficients are compared between the experimental measurements and the theoretical predictions by Eq. (10) in Sec. 3. The figures shown below are plotted by the torque coefficient versus the generalized rotational Reynolds number Re^*, and the theoretical predications and experimental data of the test fluids of glycerin70%, PAA2000, PG100, PG500, and PG2000 are represented by solid lines and the symbols × (black), ◇ (red), ○ (purple), △ (blue), and □ (green), respectively.

In the earlier experiment with the inner rotational hemisphere [17], the suspension fluids of the PG*xxx-y* in narrow gap ratios of α=0.08–0.42 is more advantageous to be the Couette flow than glycerin70% and PAA2000. To see whether the PG*xxx-y* fluids behave the Couette flow or not at the high gap ratios, gap ratios of α=1.00 and 1.37 are also tested in this study.

4.1 Results

4.1.1 Glycerin70%. The torque coefficients Cm_{sphere} of the inner sphere of glycerin70% are depicted in Fig. 5 as the relationship of Re^*. Figures 5(*a*)–5(*f*) show the results at gap ratios of α=0.08, 0.15, 0.20, 0.42, 1.00, and 1.37, respectively.

As shown in Fig. 5(*a*), at the most narrow gap (α=0.08) and low Reynolds number region ($\mathrm{Re}^* \leq 100$), the experimental value linearly decreases with increasing Reynolds numbers, and is consistent with the theoretical calculation of Eq. (10) based on the power law. This observation implies that the flow of the glycerin70% solution as the Newtonian fluid in the gap of two spheres is a unique simple spherical Couette flow at small Re^* [10]. However, when the Reynolds number is further increased, the experimentally measured value deviates slightly from the theoretical

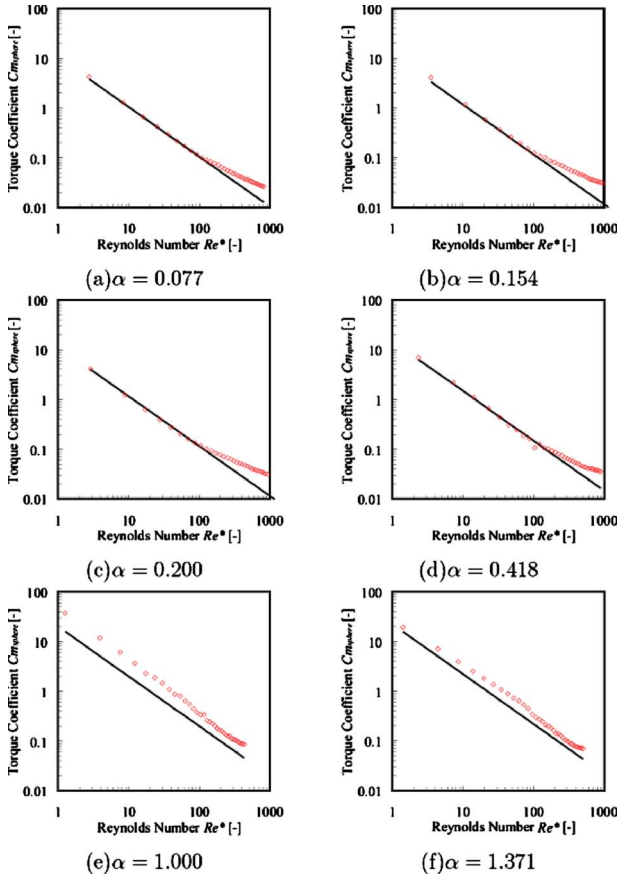

Fig. 6 Torque coefficients versus Reynolds numbers for PAA2000 with rotating inner sphere

value, suggesting that the Couette flow is never dominant.

Figures 5(*b*)–5(*f*) show that there are large differences between the theoretical and experimental values in the given Reynolds number region at gap ratios of α=0.15, 0.20, 0.42, 1.00, and 1.37, respectively. With the gap ratio increasing, those differences are also increased, denoting that the flows in the gap are not Couette flow.

4.1.2 PAA2000. The torque coefficients Cm_{sphere} of the inner sphere of the PAA2000 are depicted in Fig. 6 as the relationship of Re^* at gap ratios of α=0.08, 0.15, 0.20, 0.42, 1.00, and 1.37, respectively. As shown in Figs. 6(*a*)–6(*d*), for all gap ratios, the experimental data demonstrate linearly decreasing features when $\text{Re}^* \leq 100$. However, with the increase in the Reynolds number, the linearity of Cm_{sphere} to Re^* breaks down, and Cm_{sphere} slightly increases.

In addition, due to the assumption of the Couette flow in the gap of the inner and outer spheres used in the theoretical analyses in Sec. 3, the present experimental data have been shown to agree well with the theoretical predictions by Eq. (10) at $\text{Re}^* \leq 100$ for α=0.08, 0.15, 0.20, and 0.42 from Figs. 6(*a*)–6(*d*), implying that the flow states are also simple spherical Couette flows in a gap ratio of less than 0.418 at small Re^*. Differences between the measured Cm_{sphere} and the theoretical prediction by Eq. (10) at α=1.00 and 1.37 are observed from Figs. 6(*e*) and 6(*f*). However, these differences are smaller than those of glycerin70%. Comparing to glycerin70%, in the region of the Reynolds numbers $\text{Re}^* \leq 100$, Figs. 6(*a*)–6(*f*) show that the Couette flows of the PAA2000 solution can be easily realized at larger gap ratios of $0.08 < \alpha \leq 0.42$.

4.1.3 The PG*xxx-y Suspension Solutions*. The earlier research

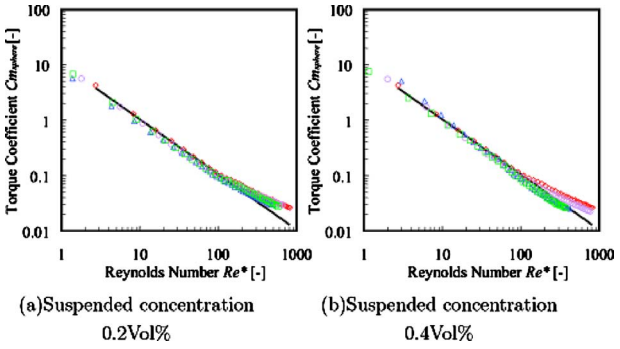

Fig. 7 Torque coefficients versus Reynolds numbers for glass fiber-suspended polymeric fluids for α=0.08 with rotating inner sphere

based on flows in the spherical gap with the inner rotating hemisphere showed that the glass fiber suspension fluids is easier to be the Couette flow than the PAA2000. In Sec. 4.1.2, for the PAA2000 fluid, we have shown that, at gap ratios of $\alpha \leq 0.42$, the rotary mainstream Couette flow dominates the flow field for $\text{Re}^* \leq 100$, and breakdown due to the Taylor vortexes occurring when $\text{Re}^* \geq 100$. To further show the fiber suspension effects on the PAA2000 fluids, the glass fibers with different aspect ratios r_a is added in the PAA2000 solutions with volume ratios of 0.2 vol % and 0.4 vol %, respectively. Since Figs. 6(*a*)–6(*d*) show a similar trend of the sphere torque characteristics for the PAA2000 at a gap ratio of $\alpha \leq 0.42$, in this study, the mixture solutions of the PG*xxx-y* are only tested at gap ratios of α=0.08, 0.42, 1.00, and 1.37.

Figures 7(*a*) and 7(*b*) show the sphere torque characteristic results of the (a) PG*xxx*-0.2 and (b) PG*xxx*-0.4 suspensions at α =0.08, respectively. For comparisons, the power-law prediction and the experimental values of PAA2000 are also included in these figures. As shown in Figs. 7(*a*) and 7(*b*), good agreement between the theoretical predictions by Eq. (10) and the experimental data for the PG500 and PG2000 solutions is up to $\text{Re}^* \approx 120$, while for the PAA2000 and PG100 solutions, it is up to $\text{Re}^* \approx 100$. These observations imply that the generalized rotational Reynolds numbers of the PG*xxx-y* solutions, at which the rotary Couette flow dominates, increase due to the glass fiber adding, and increasing the aspect ratio and volume ratio of the glass fibers, the Couette flow Reynolds numbers relationships are also shown to increase slightly. Similar observations can also be found in Figs. 8(*a*) and 8(*b*), in which the sphere torque characteristic results of the PG*xxx*-0.2 and PG*xxx*-0.4 suspensions at α =0.42 are shown, respectively, while comparing with the power law and PAA2000 results. The results in Fig. 8 confirmed again

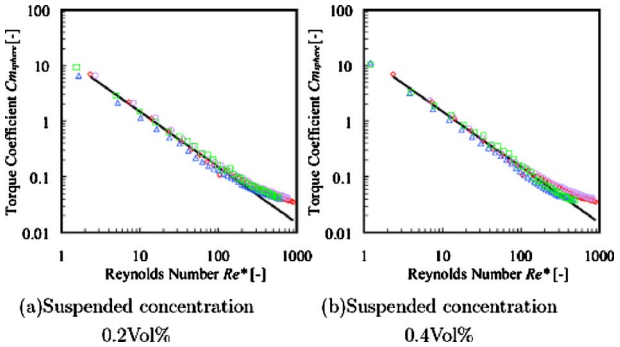

Fig. 8 Torque coefficients versus Reynolds numbers for glass fiber-suspended polymeric fluids for α=0.42 with rotating inner sphere

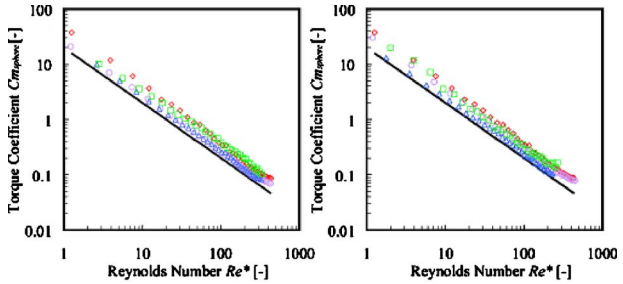

Fig. 9 Torque coefficients versus Reynolds numbers for glass fiber-suspended polymeric fluids for α=1.00 with rotating inner sphere

that the Couette flow Reynolds numbers of the PG*xxx-y* solutions increase compared with that of the PAA2000 solutions; also, increasing the fiber aspect ratio greatly reduces the flow instability, and the Couette flow can be realized at high Reynolds numbers.

Figures 9 and 10 show the torque properties for the PG*xxx-y* suspensions at gap ratios α=1.00 and 1.37, respectively. From all the results shown in Figs. 9 and 10, consistency between the theoretical values and experimental data are not observed. However, some interesting phenomena are still found from these figures. In Figs. 9 and 10, regardless of the volume fraction of the fibers suspended in the PAA2000 solutions, almost the same results are observed. The results of the PG*xxx-y* suspensions have shown to be closer to the theoretical predications of Eq. (10) than those of PAA2000, implying that the Couette-like flow can be realized more easily for the PG*xxx-y* suspensions than PAA2000, specifically at a large fiber aspect ratio.

4.2 Discussions. One common observation from Figs. 5–10 is that, for Cm_{sphere} versus Re^* relationships, the differences between theoretical predictions and experimental values increase with increasing Reynolds number. This finding is not surprising and can be well attributed to the T–G vortex that occurred inside the spherical gap [5]. As for the flow in the gap between the rotated inner sphere and the static outer sphere, it is known well that, with the Reynolds number increasing over a critical value, the steady Couette flow abruptly becomes the steady vortex flow with four vortices symmetric to the equatorial plane (Fig. 11(*a*)). After that, a spiral flow path along the θ direction occurs and it evolves in the ϕ direction (Figs. 11(*b*) and 11(*c*)). When the Reynolds number further increases, the flow becomes unstable due to the rootless oscillating wave occurring in the ϕ direction [9,18–22]. The T–G vortex occurring in the spherical gap depends on the generalized rotational Reynolds number Re^* and the gap ratio α. The present

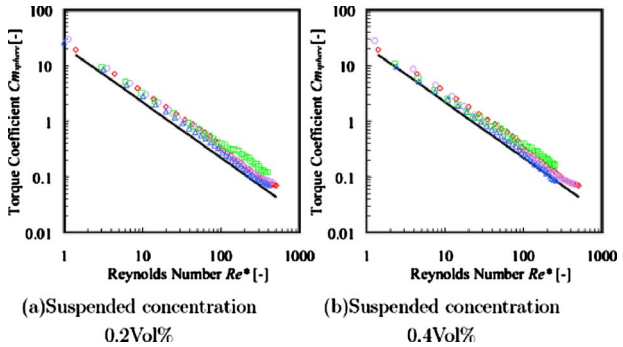

Fig. 10 Torque coefficients versus Reynolds numbers for glass fiber-suspended polymeric fluids for α=1.37 with rotating inner sphere

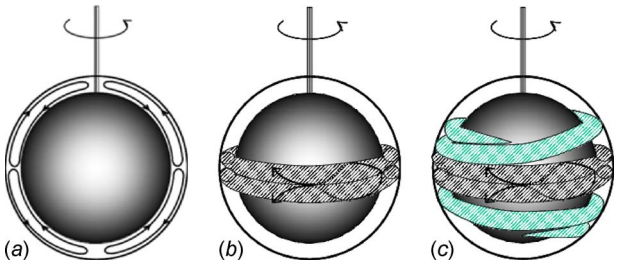

Fig. 11 Sketch of evolutions of the T–G vortex: (*a*) four symmetric vortices; (*b*) Taylor–Görtler vortex; and (*c*) spiral Taylor–Görtler vortex

study has shown that the suspension fluids can delay the T–G vortex occurrence compared with the general viscoelastic and Newtonian fluids.

4.2.1 Glycerin70%. For glycerin70% at a gap ratio of α =0.08 (Fig. 5(*a*)), due to the Couette flow dominating the flow field when $Re^* \leq 100$, the experimental values are agree well with the theoretical prediction. With increasing Re^*, the spiral T–G vortex occurs at the equator of the inner sphere, which causes the velocity gradients in the r and θ directions to increase suddenly [4]. As a result, the static friction torque increases abruptly, and hence, it makes the experimental values deviate from the theoretical predictions.

When the gap ratio increases (Figs. 5(*b*)–5(*f*) for α =0.15–1.37), glycerin70% flows inside the spherical gaps are changed from the static state to the quasi-static state (see Fig. 12, flow visualizations of the test fluids at two gap ratios), which causes the large differences between the experimental values and the theoretical predictions at all ranges of Reynolds numbers.

4.2.2 PAA2000. As shown in Figs. 6(*a*)–6(*d*) for the PAA2000 solution at gap ratios of α=0.08, 0.15, 0.20, and 0.42, such as the one displayed in Fig. 5(*a*) for glycerin70% at α=0.08, the actual measured experimental data agree consistently with the theoretical values in the range of $Re^* \leq 100$ due to the dominant Couette flows inside the spherical gaps, and deviate themselves from the theoretical values due to the T–G vortex occurring when the Reynolds number further increases. In a viewpoint of the viscoelas-

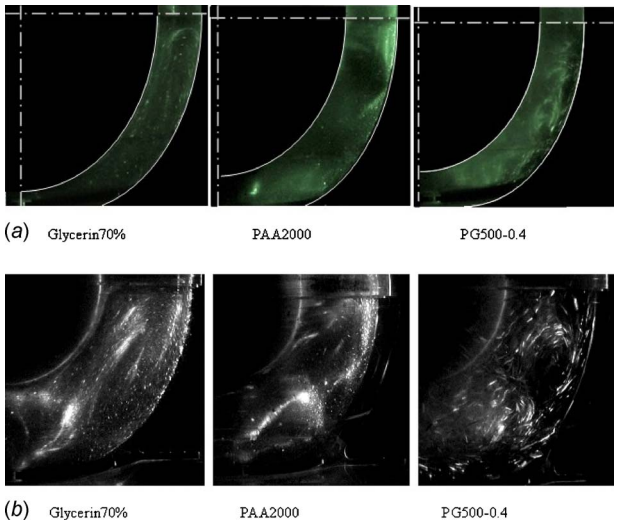

Fig. 12 Flow visualizations of the test fluids in two gap ratios: (*a*) static flow at the gap ratio α=0.42; (*b*) quasi-static flow at the gap ratio α=1.00

Table 5 Calculated $Re^{\star}_{\dot{\gamma}=800}$ for glycerin70% and PAA2000 at different gap ratios

Test fluid gap ratio α	Glycerin70%	PAA2000
0.08	1.11×10^3	1.56×10^3
0.15	4.44×10^3	6.22×10^3
0.20	7.51×10^3	1.05×10^4
0.42	2.35×10^4	3.29×10^4
1.00	5.44×10^4	7.62×10^4
1.37	1.02×10^5	1.43×10^5

ticity, the above findings can be well explained from Fig. 3(*a*).

As shown in Fig. 3(*a*), at a shear rate of $\dot{\gamma}\approx800$, the viscosity η of the PAA2000 has the same value with that of glycerin70%. Based on the measured viscosity at a shear rate of $\dot{\gamma}\approx800$, the corresponding $Re^{*}_{\dot{\gamma}=800}$ can be calculated for glycerin70% and PAA2000 at different gap ratios from Eqs. (2) and (6) with m and n obtained from the power-law fitting to the experimental data. The calculated $Re^{\star}_{\dot{\gamma}=800}$ for glycerin70% and PAA2000 at different gap ratios are given in Table 5. As shown in Table 5, at all gap ratios the calculated $Re^{\star}_{\dot{\gamma}=800}$ of the PAA2000 is shown to be always higher than that of Glycerin70%, implying that the viscosity or the parameter m for PAA2000 is always larger than that for glycerin70% at the same Reynolds numbers. This conclusion is consistent with the experimental results displayed in Fig. 3(*a*) and the power-law fitting data in Table 4. High viscosity of PAA2000 means high viscoelastic effects. These high viscoelastic effects generate an attraction force to the particles in the PAA2000 fluids, and make the PAA2000 flow inside the spherical gap more stable. Therefore, at gap ratios of $\alpha=0.15$, 0.20, and 0.42, the PAA2000 solution is shown to more easily be the Couette flows (Figs. 6(*b*)–6(*d*)) compared with glycerin70%. In other words, the viscoelastic PAA2000 solution has a more relaxed condition to be the Couette flow and to be used for suppressing the T–G vortex than glycerin70% in practical operations. However, as shown in Fig. 12 for PAA2000, the influences of the quasi-static three-dimensional flows are still large, and cause inconsistency between the experimental values and the theoretical predictions at all range of the Reynolds numbers (Figs. 6(*e*) and 6(*f*)), although the viscoelasticity of the PAA2000 reduces the differences as compared to those of glycerin70%.

4.2.3 The PG*xxx-y Suspension Solutions*. When the glass fibers are added in the PAA2000 solutions, as shown in Figs. 7–10 for the PG*xxx-y* solutions, it is observed that the generalized rotational Reynolds number at which the T–G vortex occurs is increased to about 120. This denotes that adding the glass fiber into PAA2000 can suppress the occurrence of the Taylor vortices at the same experimental conditions. The reason is due to the glass fiber not liking the streamline curvature. To align the glass fiber to the streamline curvature, an additional torque will be needed, implying that the generalized rotational Reynolds number at which the T–G vortex occurs in the suspensions is higher than that of pure polymer solutions [22]. This above finding can also be explained by the constituent equation of the Newtonian fluids with slightly heavy suspension proposed by Dinh and Armstrong [23].

The constituent equation of suspension in the present study can be written as follows:

$$\tau=\tau_P+\tau_f \tag{11}$$

where the term τ_P is the stress tensor for the polymeric fluid, and τ_f is stress tensor for the glass fiber, which can be given by the constituent equation of Dinh and Armstrong [23] as

$$\tau_f=\frac{1}{2}\eta_s\beta\dot{\gamma}:\langle PPPP\rangle \tag{12}$$

where $\langle PPPP\rangle$ is an orienting distribution function, η_S is the viscosity for the Newtonian fluid, $\dot{\gamma}$ is the shear rate, and β is the fiber parameter, which can be calculated by

$$\beta=\frac{\pi l^3 n_f}{6\ln\left(\frac{2h}{d}\right)} \tag{13}$$

where n_f is the number of fiber per unit volume, depending on the volume fraction of the fiber, l is the fiber length, d is the fiber diameter, and h is the average distance between the fibers.

Equation (12) can be simplified as follows:

$$\tau_f=\frac{1}{2}\eta_S\beta S\langle S:\dot{\gamma}\rangle \tag{14}$$

where $S=\langle PP\rangle$ is an oriented tensor, which can be described by the oriented tensor equation given as follows:

$$\frac{DS}{Dt}=\omega\cdot S-S\cdot\omega+\frac{1}{2}\frac{r_a^{\,2}-1}{r_a^{\,2}+1}(\dot{\gamma}\cdot S+S\cdot\dot{\gamma}-2\dot{\gamma}:SS) \tag{15}$$

where ω is the vorticity tensor.

Since $(r_a^{\,2}-1)/(r_a^{\,2}+1)\approx1$ when the aspect ratio $r_a=100$, 500, and 2000 in this study, the influence of the aspect ratio to S is very small and can be neglected in the present analysis. In addition, the value of $S(S:\dot{\gamma})$ in Eq. (15) is almost the same for the present test fluids at the same gap ratio. Therefore, from Eq. (15), at the same gap ratio, one can find that the parameter directly influencing the stress tensor τ_f is the fiber parameter β. Equation (13) shows that as the fiber length becomes shorter and the volume fraction of the fibers becomes lower, the value of the fiber parameter β becomes smaller.

Since the stress tensor τ acting on the inner sphere is close to the shear stress for the polymeric fluid τ_P when the aspect ratio r_a of the fibers is 100 and the volume fraction of the fibers is 0.2%, the torque properties of PAA2000 and PG100-0.2 at $\alpha=0.08$ and 0.42 have been shown to have similar behaviors (Figs. 7(*a*) and 8(*a*)). However, as the fiber parameter β increases with increasing aspect ratio ($r_a\geq500$) and volume fraction of the fibers, the shear stress tensor τ_f contributed from the added glass fibers increases, and this increment causes the obvious differences in the static friction coefficients between PG*xxx-y* and PA2000 (Figs. 7–10). The increased stress tensor τ due to adding glass fibers into the PAA2000 solutions implies that the torque needed to drive the PG*xxx-y* solutions is larger than that of the PA2000 solution. As a result, a higher rotational speed will be needed to generate the T–G vortex, implying that the generalized rotational Reynolds number of the onset of the T–G vortex increases. Therefore, the instabilities of the viscoelastic fluids are suppressed by adding the glass fiber, and the Couette flow can be realized for the PG*xxx-y* solutions.

However, due to the large influences of the quasi-static three-dimensional flows at gap ratios of $\alpha=1.00$ and 1.37 (Fig. 12), the differences between the experimental values and the theoretical predictions at all ranges of the Reynolds numbers are still large (Figs. 9 and 10), although the fiber suspension reduces the differences as compared to those of PAA2000.

5 Conclusions

Experiments have been carried out to study the effects of glass fiber suspensions in non-Newtonian fluids in the gap of the inner rotating sphere and the outer stationary sphere. The following conclusions are obtained:

1. Glycerin70% can be governed by the spherical Couette flow at a gap ratio of $\alpha\leq0.08$ and $Re^{*}\leq100$.

2. The polymeric fluids (PAA2000) could be also governed by the Couette flow at $\alpha \leq 0.42$ and $Re^* \leq 100$.
3. The polymeric fluids, in which the longer glass fibers are suspended with a concentration 0.4 vol %, could be governed by the Couette flow at $\alpha \leq 0.42$ and $Re^* \geq 100$.
4. At large gap ratios, the flows of the test fluids in the spherical gap are difficult to become Couette flows due to the effects of the quasi-static three-dimensional flow, but the suspension fluids have better performances than the polymeric solutions and the Newtonian fluids on this point.

Acknowledgment

This work was supported by a grant-in-aid for Scientific Research (C) from the Ministry of Education, Culture, Sports, Science, and Technology of Japan.

References

[1] Nawab, M. A., and Mason, S. G., 1958, "The Viscosity of Dilute Suspensions of Thread-Like Articles," J. Phys. Chem., **62**, pp. 1248–1253.
[2] Goto, S., Nagazono, H., and Kato, H., 1986, "The Flow Behavior of Fiber Suspensions in Newtonian Fluids and Polymer Solutions. I. Mechanical Properties," Rheol. Acta, **25**, pp. 119–129.
[3] Ito, Y., and Yamaguchi, H., 2007, "Characteristics of Fiber-Suspension Macromolecule Fluid Flows in the Spherical Gaps," Japan Society of Mechanics, Engineering Fluidics Lecture Memoirs, **16**, pp. 137–142.
[4] Wimmer, M., 1976, "Experiments on a Viscous Flow Between Concentric Rotating Spheres," J. Fluid Mech., **78**, pp. 317–335.
[5] Bartels, F., 1982, "Taylor Vortices Between Two Concentric Rotating Spheres," J. Fluid Mech., **119**, pp. 1–25.
[6] Yavorskaya, I. M., and Belyaev, Y. N., 1986, "Hydrodynamic Stability in Rotating Spherical Layers: Application to Dynamics of Planetary Atmosphere," Acta Astronaut., **13**, pp. 433–440.
[7] Nakabayashi, K., 1978, "Frictional Moment of Flow Between Two Concentric Spheres, One of Which Rotates," ASME J. Fluids Eng., **100**, pp. 97–106.
[8] Nakabayashi, K., and Thuchida, Y., 1988, "Spectral Study of the Laminar-Turbulent Transition in Spherical Couette Flow," J. Fluid Mech., **194**, pp. 101–132.
[9] Nakabayashi, K., and Thuchida, Y., 1988, "Modulated and Unmodulated Traveling Azimuthal Waves on Toroidal Vortices in a Spherical Couette System," J. Fluid Mech., **195**, pp. 495–522.
[10] Yamaguchi, H., Fujiyoshi, J., and Matsui, H., 1997, "Viscoelastic Fluid in Spherical Couette Flow Part I: Experimental Study for the Inner Sphere Rotation," J. Non-Newtonian Fluid Mech., **69**, pp. 29–46.
[11] Yamaguchi, H., and Matsui, H., 1997, "Viscoelastic Fluid in Spherical Couette Flow Part II: Numerical Study for the Inner Sphere Rotation," J. Non-Newtonian Fluid Mech., **69**, pp. 47–70.
[12] Yamaguchi, H., and Morishita, M., 2000, "Viscoelastic Fluid Flow in Co-Axis Hemispherical Gaps," J. Soc. Rheol., Jpn., **28**(3), pp. 105–112.
[13] Yamaguchi, H., and Hikaru, H., 2002, "Viscoelastic Fluid Flow in Hemispherical Gaps," Japan Society of Mechanics, Annual Conference Lecture Memoirs, **3**, pp. 9–13.
[14] Yamaguchi, H., and Hikaru, H., 2003 "A Study About Bamboo/Glass Fiber Suspension Macromolecule Fluid Flows in Hemispherical Gaps," Japan Society of Mechanics, Annual Conference Lecture Memoirs, **2**, pp. 253–260.
[15] Batchelor, G. K., 1974, "Transport Properties of Two-Phase Materials With Random Structure," Annu. Rev. Fluid Mech., **6**, pp. 227–255.
[16] Bird, R. B., Armstrong, R. C., and Hassager, O., 1987, *Dynamics of Polymeric Liquids*, 2nd ed., Wiley-Interscience, New York, Vol. 1.
[17] Yamaguchi, H., Zhang, X. R., Niu, X., and Ito, Y., 2009, "Experimental Study of Rheological Behaviors of Glass-Fiber-Suspended Polymeric Fluids Based on the Spherical Couette Flows With the Inner Hemisphere Rotation," J. Non-Newtonian Fluid Mech., submitted.
[18] Egbers, C., and Rath, H. J., 1995, "The Existence of Taylor Vortices and Wide-Gap Instabilities in Spherical Couette Flow," Acta Mech., **111**, pp. 125–140.
[19] Mullin, T., and Benjamin, B., 1980, "Transition to Oscillatory Motion in the Taylor Experiment," Nature (London), **3288**, pp. 567–569.
[20] Wereley, S. T., and Lueptow, R. M., 1998, "Spatial-Temporal Character of Non-Wavy and Wary Taylor–Couette Flow," J. Fluid Mech., **364**, pp. 59–80.
[21] Schrauf, G., 1986, "The First Instability in Spherical Taylor-Couette Flow," J. Fluid Mech., **166**, pp. 287–303.
[22] Larson, R. G., 1992, "Instabilities in Viscoelastic Flows," Rheol. Acta, **31**, pp. 213–263.
[23] Dinh, S. M., and Armstrong, R. C., 1984, "A Rheological Equation of State for Semiconcentrated Fiber Suspensions," J. Rheol., **28**(3), pp. 207–227.

Hyeongkeun Kim
School of Mechanical Engineering,
and Center for Human Interface Nanotechnology (HINT),
Sungkyunkwan University,
300 Cheoncheon-dong, Jangan-gu, Suwon,
Gyeonggi-do 440-746, Korea
e-mail: faithkim99@skku.edu

Dongmin Choi
School of Mechanical Engineering,
Sungkyunkwan University,
300 Cheoncheon-dong, Jangan-gu, Suwon,
Gyeonggi-do 440-746, Korea

Youngjin Kim
School of Mechanical Engineering,
SKKU Advanced Institute of Nanotechnology (SAINT),
Sungkyunkwan University,
300 Cheoncheon-dong, Jangan-gu, Suwon,
Gyeonggi-do 440-746, Korea

Seunghyun Baik
Department of Energy Science,
School of Mechanical Engineering,
SKKU Advanced Institute of Nanotechnology (SAINT),
Sungkyunkwan University,
300 Cheoncheon-dong, Jangan-gu, Suwon,
Gyeonggi-do 440-746, Korea

Hyungpil Moon[1]
School of Mechanical Engineering,
Sungkyunkwan University,
300 Cheoncheon-dong, Jangan-gu, Suwon,
Gyeonggi-do 440-746, Korea
e-mail: hyungpil@me.skku.ac.kr

Shape Optimization of Symmetric Cylinder Shape on Buoyancy Using Fourier Series Approximation

The hydrophobicity of water striders and fisher spiders shows the geometrical property of microsetae with elaborate nanogrooves. Studying such geometrical morphology naturally leads to the question: what is an optimal shape for buoyancy? In this paper, we present a methodology to find suboptimal shapes for star-shaped cross-sectional rods, which maximizes the buoyant force by modeling the cross-sectional shapes with Fourier series representation in the polar coordinate. We provide four suboptimal cross-sectional shapes and their experimental results. Our results support the importance of the geometrical shape for buoyant force and might be helpful in designing water repelling devices. [DOI: 10.1115/1.4001493]

Keywords: Fourier series, hydrophobicity, buoyant force, contact angle, multiwalled carbon nanotubes, shape optimization

1 Introduction

The importance of the geometrical morphology in hydrophobicity such as microstructures of lotus leaves [1–3], butterfly wings [4], rice leaves [5], nanosized grooves of water strider legs [6–12], and mosquito legs [13] was actively investigated recently. Inspired by such biosystems, material scientists synthesized artificial superhydrophobic surfaces by various methods: wax solidification, lithography, vapor deposition, plasma technique, sol-gel process, electrospinning, and so on [3,14]. However, there has been little attempt to find optimal shapes for better hydrophobicity or larger buoyant force.

Shape optimization or topology optimization [15] is a very important concept in the design of mechanical components. The basic approach is to consider an initial truss structure or a grid-map structure of material distribution and iterate the shape by adding or eliminating a small element based on the response of the cost function. In this paper, we present a methodology that represents the profile of a cross-sectional geometrical shape in a polar coordinate (the profile radius is represented by a function of orientation), and approximates the profile function with the Fourier series. To the best of our knowledge, we are the first group introducing the shape optimization methodology using the Fourier series to design shapes with maximum buoyant force.

The Fourier series representation of shape profiles is first obtained, and then the Fourier series coefficients are searched to maximize the buoyant force. Design constraints and cost functions may vary depending on the application. Therefore, unlike the design optimization in the engineering perspective whose goal is to find the best solution (global optimal) for given constraints and a cost function, we are more interested in searching for suboptimal shapes to investigate the effect of shapes on buoyant force. Our approach is to generate a large number of cross-sectional designs and use a simple search method to find several suboptimal shapes. The meniscus profile at sinking condition is obtained using the Young–Laplace equation model [16,17], and the buoyant force is calculated using the total volume of the displaced water and the submerged part of the shape [18–21]. The major focus of this work is shape optimization, and the surface contact angle (CA) is maintained constant at 105 deg, where the volume criterion is the dominant sinking condition [16]. Note that the maximal volume condition is equivalent to the maximum buoyant force condition when these values are normalized. We first provide the comparison result of computing buoyant force for the Fourier series representations of an equilateral triangular shape with the exact solu-

[1]Corresponding author.

Contributed by the Fluids Engineering Division of ASME for publication in the JOURNAL OF FLUIDS ENGINEERING. Manuscript received August 11, 2009; final manuscript received March 6, 2010; published online May 14, 2010. Assoc. Editor: Steven T. Wereley.

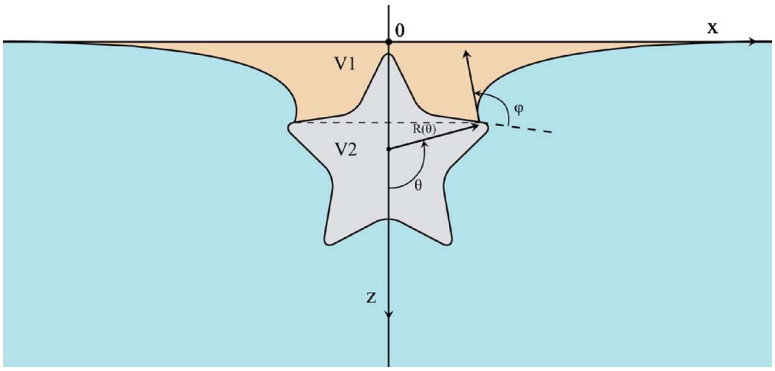

Fig. 1 Coordinate system for a star shape cross section floating on a liquid. The liquid meniscus is also shown as a solid line. V1 is the replaced volume of water due to the meniscus formation and V2 is the volume of the immersed rod.

tion to validate our approach. Then, we present two theoretically optimal cross-sectional shapes that maximize the buoyant force, but may not be entirely practical for manufacturability, as well as two practical suboptimal cross-sectional shapes with experimental verifications.

2 Experimental Procedure

2.1 Modeling Methodology. To find (sub)optimal shapes for larger buoyant force, we need to first compute the buoyant force at the critical sinking condition for the given specific cross-sectional shape rods, which requires the analytic function of the meniscus and integration of the area of the displaced water and submerged part of the shape. Second, we need to iterate the shapes in the direction of maximizing the buoyant force. For the first part, we adopt the modeling process from Feng's work in study of buoyant force and sinking conditions of thin rods [16], and summarize it here for the sake of readability of this letter.

We consider a rod with a star-shaped cross section floating on a liquid surface. The mathematical definition of a star shape is as follows: A planar shape S is star-shaped if and only if there is a point $c \in S$, such that, for any point $p \in S$, the line segment $\overline{cp}$ is contained in S. The coordinate system is depicted in Fig. 1. The equation of the meniscus can be obtained from the Laplace equation

$$\frac{x''}{\sqrt{(1+x^2)^3}} = \kappa^2 z \tag{1}$$

where $\kappa^2 z = \sqrt{\gamma/\rho_L g}$ is the capillary length, γ is the surface tension of the liquid, ρ_L is the density of the liquid, and g is the gravity. The boundary conditions at the free surface and the contact angle lead the analytic solution of Eq. (1)

$$x = \kappa^{-1} \cosh^{-1}\left(\frac{2}{z\kappa}\right) - \sqrt{4\kappa^{-2} - z^2} + c_2 \tag{2}$$

where $c_2 = R(\theta)\sin\theta - \kappa^{-1}\cosh^{-1}(2\kappa^{-1}/h) + 2\kappa^{-1}\sqrt{1-\kappa^2 h^2/4}$ and h denotes the height difference between the contact point and the surface of the liquid at $x=\infty$.

Note here that $R(\theta)$ is the radial profile function of the star shape in the polar coordinate. The buoyant force can be computed from the area of the submerged part of the shape object and the area of the replaced water. In this paper, we consider the normalized buoyant force

$$\tilde{F}_b = \frac{F_b}{\gamma} = \frac{F_b \kappa^2}{\rho_L g} = -2\sin(\theta+\phi) + 2\sqrt{2}\kappa R(\theta)\sin\theta\sqrt{1+\cos(\theta+\phi)} + \kappa^2 R(\theta)^2(\theta - \sin\theta\cos\theta) \tag{3}$$

where F_b is the buoyant force, $\tilde{F}_b$ is the normalized buoyant force with respect to the surface tension, and ϕ is the contact angle of the floating material.

To find (sub)optimal shapes that maximize the normalized buoyant force based on the volume criterion [16], we represent the radial profile function in the Fourier series

$$R(\theta) = a_0 + \sum_{n=1}^{\infty}\left(a_n \cos\frac{2\pi n}{T}\theta + b_n \sin\frac{2\pi n}{T}\theta\right) \tag{4}$$

Thus, the normalized buoyant force is a function of the Fourier series variables (a_n, b_n, T). Due to the computational complexity, a finite set of Fourier series variables in Eq. (4) are considered in optimization. As symmetric shapes are sufficient in consideration, only the constant term and first three cosine terms are considered in the Fourier series representations. The numerical parameters that are considered in this paper are provided in Table 1. The appropriateness of this approach will be discussed shortly.

2.2 Experimental Methodology. Experimental investigations are carried out to verify buoyant forces calculated by the modeling approach. Four different cross-sectional shapes, designed by the Fourier series modeling, are fabricated using cylindrical aluminum rods (Al-6061) by electrical discharge machining (EDM), as depicted in Fig. 2. The cross-sectional area and length of the rod were identical for all four shapes (cross-sectional area: 50.26 mm^2, length: 40 mm).

The surface is coated by Teflon (DuPont, PTFE-30) after the EDM process to increase hydrophobicity [14]. The contact angle is increased from 60 deg to 105 deg, as shown in the inset of Fig. 2. The measurements are carried out five times and the variability is smaller than 1 deg (SEO 300A). A schematic of the experimen-

Table 1 Fourier series variable values

Variable	Values
a_0	0, 1/5, 2/5, 3/5, 4/5, 1
a_1	−1, −3/4, −1/2, −1/4, 0, 1/4, 1/2, 3/4, 1
a_2	−1, −3/4, −1/2, −1/4, 0, 1/4, 1/2, 3/4, 1
a_3	−1, −3/4, −1/2, −1/4, 0, 1/4, 1/2, 3/4, 1
Period (T/n)	1, 2, 3, 4, 5, 6, 7, 9

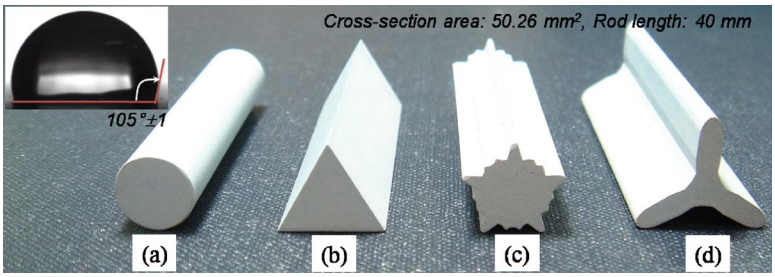

Fig. 2 Digital images of the PTFE coated rods. The aluminum block was processed using EDM followed by the PTFE coating. The contact angle is 105 deg as shown in the inset image. The rod of (*a*) circular, (*b*) triangular, (*c*) star, and (*d*) Y-shaped cross section.

tal setup to measure the buoyant force of thin rods with different cross-sectional shapes is shown in Fig. 3. Water is contained in a transparent cubic bath (acryl, $100\times100\times100$ mm^3). Blue dye is introduced in water (0.1 vol %) to visualize meniscus around the sample clearly. The sample is stationary and the bath is placed on a translation stage. The immersion distance is changed from 0 mm to 15 mm at a step of 0.5 mm. The distance is measured using a digital micrometer (Mitutoyo 547). The rods with different cross-sectional shapes are placed 1 mm away from the frontal panel of the acrylic bath to investigate two-dimensional meniscus shapes with an assumption of an infinitely long rod. The interaction of the frontal panel with water results in a change in the meniscus shape due to surface tension. The acrylic bath is hydrophilic with a contact angle of 68 deg. As shown in Fig. 4, this deformation is represented as a thin band at the top surface of water. Due to the light scattering, the thin band color is dark as compared with the rest of the water in the bath. The shape of the water meniscus is imaged using a digital camera (Sony DSC-T3). Figure 4 also shows the shape of the water meniscus of four rods as a function of the immersion distance. The reading of the digital micrometer is set to zero when the sample is in contact with the top surface of the water. Note that we incrementally raised the bath for the sequence of images shown in Fig. 4. Figure 5 shows the photographs of the water meniscus around the cylindrical rod at the maximum immersion distance. The thin band with transient color, induced by the water interaction with the frontal panel, is disregarded for the calculation of buoyant force. The photographic image (step 1) is processed with SOLIDWORKS® to calculate buoyant force, as shown in Fig. 5. The displaced area of water and body

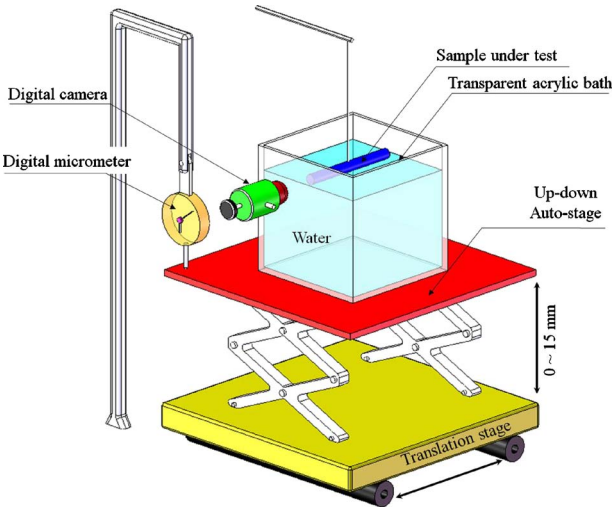

Fig. 3 Schematic of the experimental setup to estimate buoyant force

was used to calculate the buoyant force [18–21]. Water density of 998.2 kg/m^3 (at 20°C) is used for the calculation.

3 Results and Discussion

Normalized buoyant forces of thin rods with different cross-sectional shapes such as ellipses with aspect ratios of 0.8, 1.0, and 1.5, equilateral triangle, annulus, and hexagon are studied recently [16]. Among these cross-sectional shapes, an equilateral triangular rod shows the maximal buoyant force. To validate our methodology, we first show the comparison result of the normalized buoyant force for a rod with an equilateral triangular cross-sectional shape. Figure 6 depicts the normalized buoyant forces for the exact triangular shape, which has discontinuity of the profile at each vertex, and for the third and seventh order approximations of the Fourier series representation. Although the maximum buoyant force results of Fourier series approximations are lower than the exact solution by 8.3% and 6.5%, respectively, for the third order and the seventh order approximations, the overall response validates our methodology. The differences in maximum buoyant forces are due to our approximation of the shape with continuous functions at ideally discontinuous vertices. Note that it is not desirable to increase the order of the Fourier series to reduce the modeling error when approximating discontinuous functions because of the ripple effect. Hereafter, we use the shape models of the third order Fourier series approximations to find optimal shapes.

The two resultant shapes from brute-force search are shown in Fig. 7, which are suboptimal shapes among 34,992 sampling shapes that are represented by the third order Fourier series. The maximal buoyant forces for each suboptimal shape are 6.41 and 6.55, respectively, where their nondimensional cross-sectional areas are all 5.73 mm^2. Each of these values is 23.9% and 25.6% higher than that of the equilateral triangular cross-sectional shape, which is reported as the optimal shape among ellipse, annulus, and hexagon [16]. However, the optimal shapes in Fig. 7 may not be entirely practical for manufacturability, because of the extremely thin neck of each limb at the center of the body part. Because we did not consider the constraints on the minimal thickness of the part in the search process, we obtained such unpractical results. Considering fabrication constraints such as minimum thickness and material properties in finding optimal shapes for larger buoyancy and optimal microstructure for better hydrophobicity need to be carried out in the future.

In this paper, instead of considering such unpractical ideal shapes, we searched other suboptimal shapes that can be manufactured and experimentally validated: star and Y-shaped cross-sectional shapes. Figure 8 depicts the variation in nondimensional buoyant force with respect to the angular location of the water contact point for circular, triangular, star, and Y-shaped cross-sectional rods along with experimental results. Note that the graph of the nondimensional buoyant force is plotted with respect to the angular location of the water contact point. As shown in Fig. 8,

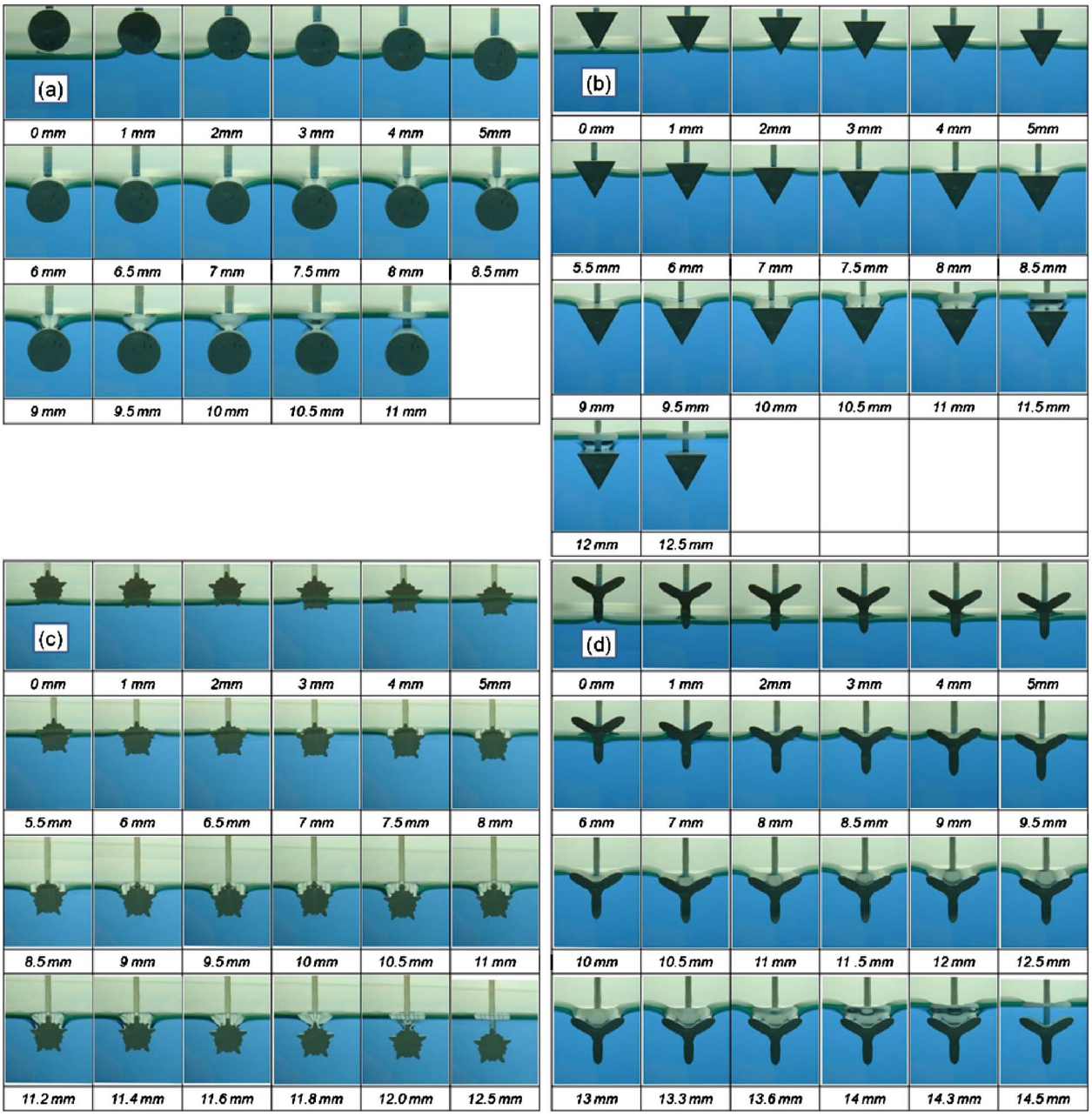

Fig. 4 The photographic images of water meniscus around samples: (*a*) circular, (*b*) triangular, (*c*) star, and (*d*) Y-shaped cross sections

the buoyant force is not a monotonic function with increasing contact point angle, even for the circular cross-sectional rod. The maximum buoyant force for the circular cross-sectional rod is obtained at the angular location of 148 deg, which is the maximal dimple-volume condition rather than a meniscus contact condition, as discussed in a reference by Liu et al. [16]. The trend of the experimentally obtained data shows a good agreement with the theoretical prediction. Notice that the change in the measured buoyant force for the triangular cross-sectional rod shown in Fig. 8(*b*) appears different from the theoretical results shown in Fig. 6, because the measured force is plotted as a function of the angular location of the water contact point in Fig. 8, as opposed to a function of the depth in Fig. 6. Also, note that the tangent angle of the meniscus at the contact point in the case of the Fourier series model is not constant. Remark that the relatively low contact angle (105 deg) makes the meniscus become concave at the contact point, as shown in Fig. 4(*b*). However, when the contact lines

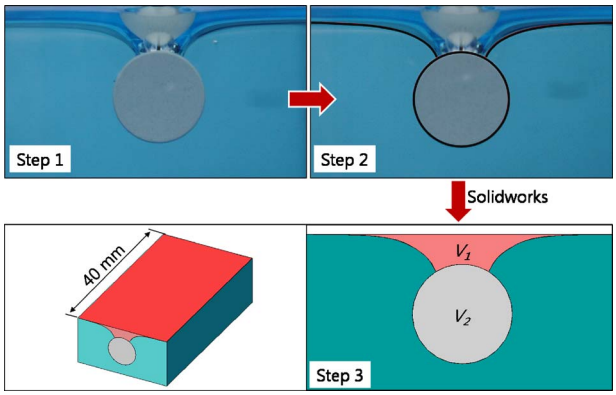

Fig. 5 Calculation of the buoyant force. Step 1: photographic image. Step 2: outline of water meniscus. Step 3: processed two-dimensional and three-dimensional images.

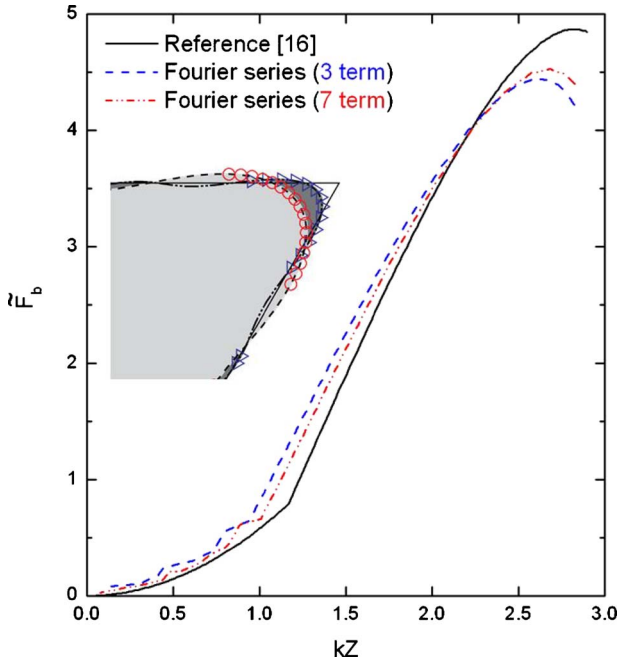

Fig. 6 Comparison of the nondimensional buoyant force with respect to the nondimensional depth for an equilateral triangular rod, the exact solution [16], the third order, and the seventh order Fourier series approximations (k^{-1} is the capillary length)

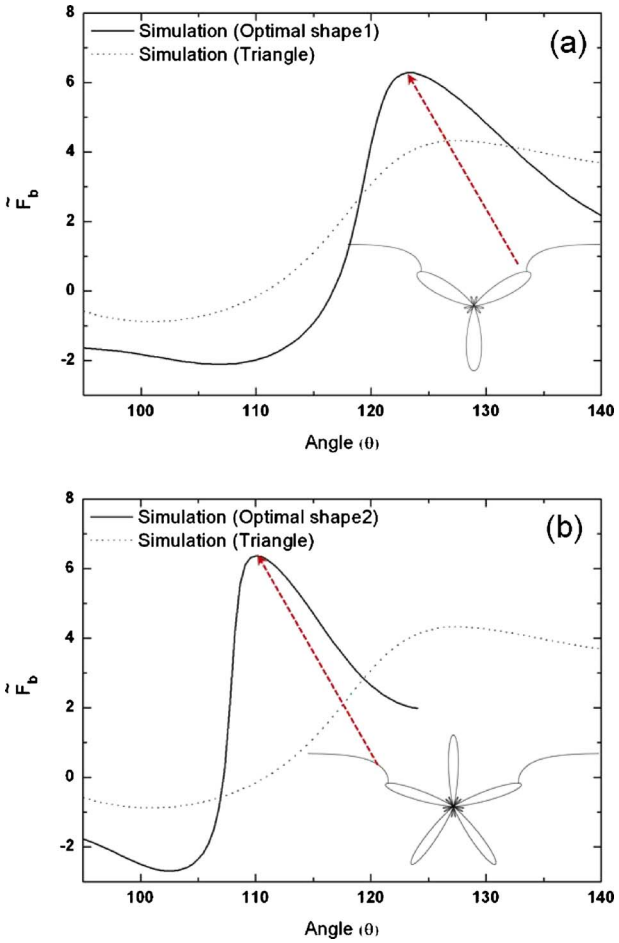

Fig. 7 Shape optimization for buoyancy using Fourier series approximation. Comparisons of the buoyant force of rods with different cross-sectional shapes: (*a*) optimal shape 1 and (*b*) optimal shape 2 (cross-sectional area: 5.73 mm^2); with respect to equilateral triangle

are pinned at the vertex, the measured buoyant force values are very close to the theoretical ones, as shown in Fig. 8(*b*). In the case of the star shape shown in Fig. 8(*c*), the profile of the manufactured sample rod is the Fourier series function itself. This means that the wavy characteristics of the force change is not an error, but due to complexity of the profile itself. There are three peaks and two valleys in the region of the contact location angle between 60 deg and 120 deg in Fig. 8(*c*). Note that the buoyant force becomes negative at some valley points when the meniscus shape becomes concave. One of the reasons that cause this variation is that the submerging depth of the rod is not monotonically increasing as the contact location angle increases for the star shape cross-sectional rod. An interesting part in Fig. 8(*c*) is where the buoyant force increases from near zero, at a CA of 100 deg, to reach the maximum value around at a CA of 112 deg. This corresponds to Fig. 4(*c*), where the contact line of the meniscus is pinned at the tip of one of the five large limbs and the rod keeps submerging. When the Y-shaped cross-sectional rod was submerging into the water, it made two contact points, as shown in Fig. 4(*d*) (6 mm), and there was a sudden jump of the contact point. At this moment, the shape of the meniscus changed from concave to convex abruptly. However, this region is represented by a convex region around the CA between 80 deg and 100 deg in Fig. 8(*d*). In this graph, we considered plausible meniscus contact conditions, which is the concave contact. The buoyant force increases suddenly near the contact point angle of 120 deg, where the meniscus contact lines are pinned at the limb of the Y-shaped cross-sectional rod.

The theoretically computed maximal buoyant force of the star-shaped cross-sectional rod is 13.3% higher than that of the circular rod, and that of the Y-shaped is 21.5% higher than that of the equilateral triangle. The quantitative comparisons of the maximal buoyant forces are summarized in Fig. 9. The Fourier series analysis data are compared with experimental results, as depicted in Fig. 9. We observed that the maximum deviation is about 10.9%. This deviation is mainly due to the error in the measurement setup. However, the trend of the theoretical calculation shows a good agreement with the experimental data. The experimental result for a circular cross-sectional shape agrees with the theoretical result with 5.9% deviation. This result validates our Fourier series method in computing the buoyant force for a given cross-sectional shape. However, in case that the edge effect is critical such as for triangular, star, and Y-shaped cross-section shapes, the deviations go up to about 10%. The plausible sources of the error are (1) a measurement error in detecting the contact point due to edge effect and finiteness of the rod length, (2) the difference between manufactured shape and the computed shape from the Fourier series approximation, and (3) limited incremental depth resolution of the translational stage in the z direction.

Although the manufacturing constraint restrained us from using smaller cross-sectional rods, the effectiveness of the optimal shape would not be deteriorated because normalized dimensions are used throughout the work. The verification of the theoretical modeling is carried out at a CA of 105 deg, which is a relatively small contact angle. Figure 10 shows normalized maximum buoyant forces as a function of CA. The surface of the triangular rod was coated with multiwalled carbon nanotubes (MWCNTs) to demonstrate the effect of CA on water meniscus and buoyant force. Vertically aligned MWCNTs with an average nanotube diameter of 15 nm and a tube length of 10 mm was grown by a thermal chemical vapor deposition method [22,23]. Magnified scanning electron microscope (SEM; JEOL, JSM7500F) and high-resolution transmission electron microscope (HRTEM; JEOL, JEM2100F) images of the carbon nanotubes are shown Fig. 10. The forest was cut into thin films with an average thickness of

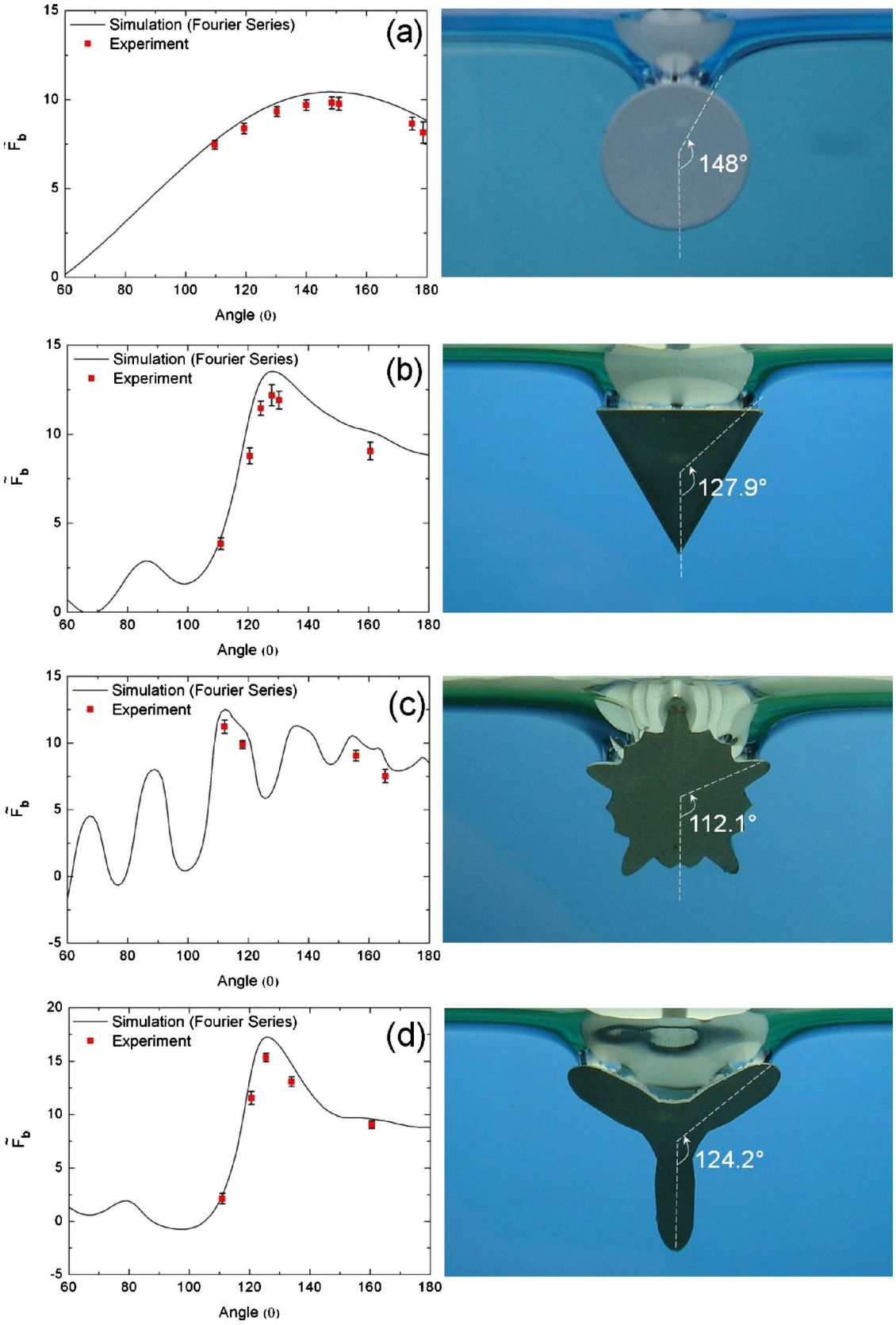

Fig. 8 Normalized buoyant force, obtained theoretically and experimentally, as a function of the angle θ for (*a*) circular, (*b*) triangular, (*c*) star, and (*d*) Y-shaped cross sections with corresponding digital images obtained experimentally (cross-sectional area: 50.26 mm^2)

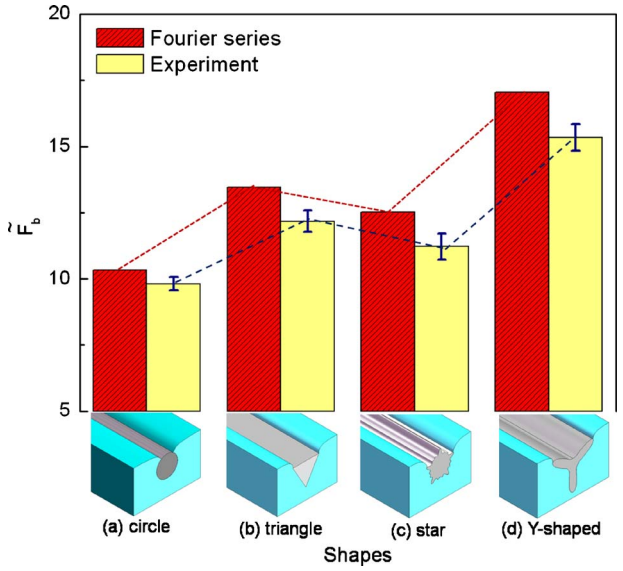

Fig. 9 Comparison of the buoyant force between theoretical predictions (Fourier series) and experimental results

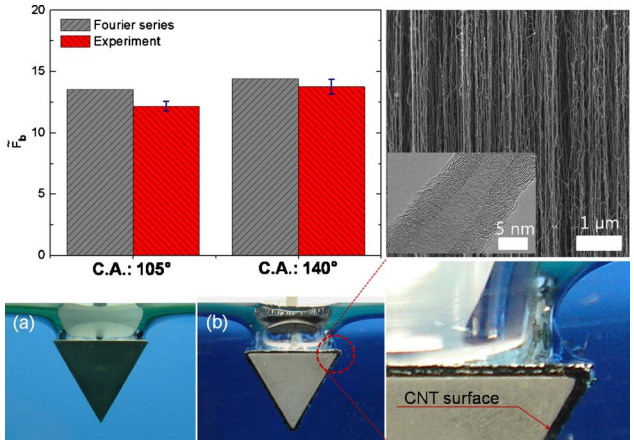

Fig. 10 Normalized buoyant force, obtained theoretically and experimentally, as a function of CA: (*a*) Teflon coated triangular cross section (CA 105 deg), and (*b*) carbon nanotube (CNT) coated triangular cross section (CA 140 deg)

150 μm using a multiangle slicer (JASCO HW-1). Then, the films were attached to the surface of the triangular rod using a carbon tape with a thickness of 120 μm. An increase in CA from 105 deg to 140 deg leads to an increase in buoyant force by 6.1%. Direct growth of vertically aligned MWCNTs on the surface of shaped-optimized rods will be carried out as future work.

4 Conclusions

The importance of the geometrical morphology in buoyancy is investigated. We propose a theoretical methodology to find optimal cross-sectional shapes that maximize the buoyant force using Fourier series representation, and experimental validations are also performed. The optimized design with a Y-shaped cross section, obtained by a brute-force search, demonstrated 21.53% larger buoyant force compared with that of an equilateral triangle. In engineering perspective, the optimality in the average sense of the buoyant forces at all dipping orientations of the rod needs to be studied because the sinking direction of the leg in real applications such as water strider robots would be varying as the robots locomote on the water surface. Also, practical design constraints such as manufacturability, part strength, and stress concentration need to be incorporated in the modeling effort. We believe that our finding in optimal cross-sectional shapes of rods will aid in designing of microstructures for better hydrophobic parts if combined with other surface treatments to obtain larger contact angles.

Acknowledgment

This research was supported by the Ministry of Knowledge Economy (MKE) and Korea Institute for Advancement in Technology (KIAT) through the Workforce Development Program in Strategic Technology and WCU (World Class University) program through the Korea Science and Engineering Foundation funded by the Ministry of Education, Science and Technology (Grant No. R31-2008-000-10029-0).

Nomenclature

x, z = Cartesian coordinates axes
κ^{-1} = capillary length
γ = surface tension of the liquid
ρ_L = density of liquid
g = gravity
h = the height difference between the contact point and the surface of the liquid at $x=\infty$
θ = the angle between z axis and contact point direction
F_b = buoyant force
$\tilde{F}_b$ = normalized buoyant force
ϕ = the microscopically effective contact angle
$R(\theta)$ = the radial profile function

References

[1] Marmur, A., 2004, "The Lotus Effect: Superhydrophobicity and Metastability," Langmuir, **20**9), pp. 3517–3519.
[2] Spori, D. M., Drobek, T., Zürcher, S., Ochsner, M., Sprecher, C., Mühlebach, A., and Spencer, N. D., 2008, "Beyond the Lotus Effect: Roughness Influences on Wetting Over a Wide Surface-Energy Range," Langmuir, **24**(10), pp. 5411–5417.
[3] Zhang, J., Sheng, X., and Jiang, L., 2009, "The Dewetting Properties of Lotus Leaves," Langmuir, **25**(3), pp. 1371–1376.
[4] Xia, F., and Jiang, L., 2008, "Bio-Inspired, Smart, Multiscale Interfacial Materials," Adv. Mater., **20**(15), pp. 2842–2858.
[5] Feng, L., Li, S., Li, Y., Li, H., Zhang, L., Zhai, J., Song, Y., Liu, B., Jiang, L., and Zhu, D., 2002, "Super-Hydrophobic Surface: From Natural to Artificial," Adv. Mater., **14**(24), pp. 1857–1860.
[6] Feng, X. Q., Gao, X. F., Wu, Z., Jiang, L., and Zheng, Q. S., 2007, "Superior Water Repellency of Water Strider Legs With Hierarchical Structures: Experiments and Analysis," Langmuir, **23**(9), pp. 4892–4896.
[7] Hu, D. L., Chan, B., and Bush, J. W., 2003, "The Hydrodynamics of Water Strider Locomotion," Nature (London), **424**, pp. 663–666.
[8] Hu, D. L., and Bush, J. W., 2005, "Meniscus-Climbing Insects," Nature (London), **437**, pp. 733–736.
[9] Bush, J. W., and Hu, D. L., 2006, "Walking on Water: Biolocomotion at the Interface," Annu. Rev. Fluid Mech., **38**, pp. 339–369.
[10] Cheng, L., 1973, "Marine and Freshwater Skaters: Differences in Surface Fine Structures," Nature (London), **242**, pp. 132–133.
[11] Dickinson, M., 2003, "Animal Locomotion: How to Walk on Water," Nature (London), **424**, pp. 621–622.
[12] Shi, F., Niu, J., Liu, J., Liu, F., Wang, Z., Feng, X. Q., and Zhang, X., 2007, "Towards Understanding Why a Superhydrophobic Coating Is Needed by Water Striders," Adv. Mater., **19**(17), pp. 2257–2261.
[13] Wu, C. W., Kong, X. Q., and Wu, D., 2007, "Micronanostructures of the Scales on a Mosquito's Legs and Their Role in Weight Support," Phys. Rev. E, **76**(1), p. 017301.
[14] Zhang, X., Shi, F., Niu, J., Jiang, Y., and Wang, Z., 2008, "Superhydrophobic Surface: From Structure Control to Function Application," J. Mater. Chem., **18**, pp. 621–633.
[15] Nishiwaki, S., Frecker, M., Min, S., and Kikuchi, N., 1998, "Topology Optimization of Compliant Mechanisms Using the Homogenization Method," Int. J. Numer. Methods Eng., **42**, pp. 535–559.
[16] Liu, J. L., Feng, X. Q., and Wang, G. F., 2007, "Buoyant Force and Sinking Conditions of a Hydrophobic Thin Rod Floating on Water," Phys. Rev. E, **76**(6), p. 066103.
[17] Bhatnagar, R., and Finn, R., 2006, "Equilibrium Configurations of an Infinite Cylinder in an Unbounded Fluid," Phys. Fluids, **18**, p. 047103.
[18] Vella, D., Lee, D. G., and Kim, H. Y., 2006, "The Load Supported by Small Floating Objects," Langmuir, **22**(14), pp. 5979–5981.

[19] Hesla, T. I., and Joseph, D. D., 2004, "The Maximum Contact Angle at the Rim of a Heavy Floating Disk," J. Colloid Interface Sci., **279**(1), pp. 186–191.
[20] Rapacchietta, A. V., Neumann, A. W., and Omenyi, S. N., 1977, "Force and Free-Energy Analyses of Small Particles at Fluid Interfaces: I. Cylinders," J. Colloid Interface Sci., **59**(3), pp. 541–554.
[21] Singh, P., and Joseph, D. D., 2005, "Fluid Dynamics of Floating Particles," J. Fluid Mech., **530**, pp. 31–80.
[22] Kim, H. K., Lee, C. S., Choi, J. B., Chun, K. Y., Kim, Y. J., and Baik, S. H., 2009, "Effects of a Sandwich-Like Catalyst on the Vertical Growth of Carbon Nanotubes Synthesized by Using Chemical Vapor Deposition," J. Korean Phys. Soc., **54**(3), pp. 1006–1010.
[23] Kim, H. K., Chun, K. Y., Choi, J. B., Kim, Y. J., and Baik, S. H., 2010, "Effects of Catalyst on the Super-Growth of Multi-Walled Carbon Nanotubes," J. Nanosci. Nanotechnol., **10**(5), pp. 3362–3365.

F. Sanchez-Silva
LABINTHAP-SEPI-ESIME,
UPALM,
National Polytechnic Institute of Mexico,
Avenue IPN s/n, Edificio 5,
Colonia Lindavista, Delegacion GAM,
Mexico City D.F. 07738, Mexico
e-mail: fsnchz@yahoo.com.mx

V. Hernandez-Perez
School of Chemical Environmental and Mining Engineering,
University of Nottingham,
University Park NG7 2RD, UK
e-mail: hepv@yahoo.com.mx

I. Carvajal-Mariscal[1]
e-mail: icarvajal@ipn.mx

J. G. Barbosa-Saldaña
e-mail: jgabriel_bs@yahoo.com.mx

LABINTHAP-SEPI-ESIME,
UPALM,
National Polytechnic Institute of Mexico,
Avenue IPN s/n, Edificio 5,
Colonia Lindavista, Delegacion GAM,
Mexico City D.F. 07738, Mexico

J. A. Cruz-Maya
Department of Advanced Technologies,
SEPI-UPIITA,
National Polytechnic Institute of Mexico,
Avenue IPN 5209,
Laguna Ticoman,
Mexico City D. F. 07340, Mexico
e-mail: jcmaya@ipn.mx

Separation of a Two-Phase Slug Flow in Branched 90 deg Elbows

Novel experimental data for phase separation of air-water mixtures in horizontal 90 deg branched elbows are presented in this work. The branched elbows were formed by attaching a pipe to a 90 deg elbow on the side of maximum radius of curvature, and halfway between the inlet and outlet sections of the elbow. All three arms coming from the junction were in the horizontal plane. Both the branch orientation and branch diameter were varied. Three different branch/elbow diameter ratios were tested, as well as three different branch inclination angles. In addition, the static pressure was monitored at different points along the ramified elbow using a set of pressure transducers in order to analyze and associate the pressure drop with the phase separation. At the inlet section of the elbow, the two-phase flow pattern was mainly slug flow. Based on the experimental data, a correlation for the liquid phase separation is proposed. Finally, the volume-weighted phase separation in the branched elbow was compared with the phase separations on the T-junction, and it was found that in some cases the branched elbows have a similar performance to that of the T-junctions. [DOI: 10.1115/1.4001488]

Keywords: slug flow, elbow, phase separation, two-phase flow

1 Introduction

In industrial practices, the distribution of a gas-liquid mixture through a pipe network containing ramifications is a very common task. Normally, the objective is to divide the mixture in a uniform way, that is, the same mass fraction flowing through each branch as in the power generation industry. Nevertheless, in many other situations, it is required to separate the phases from the mixture, as in oil-gas production, where natural gas pipelines often contain important amounts of liquids that can interfere with the proper operation of the pipeline and related equipment. In both applications, it is necessary to be able to predict the two-phase flow behavior in the branched conduit in order to handle the flow properly.

In addition, in pipe networks for conduction of both single- and two-phase flows, elbows are accessories absolutely necessary to provide changes in the flow direction and therefore, they also give more flexibility to the system. However, in the past, little attention has been paid to study the two-phase flow separation phenomenon taking place in these fittings, and nor has the extra service they can provide as phase separators been explored.

The splitting of gas-liquid mixtures flowing through branched conduits both horizontally and vertically has been studied during the last 3 decades by several authors [1–8]. It was the work by Oranje [1] on gas pipelines that first reported, to the best of our knowledge, an irregular distribution of phases at the pipe junctions. Later, the main focus has been in the nuclear and power industry due to the potential loss of coolant accidents (LOCAs). However, most of these experimental works have been carried out using T-junctions.

One of the factors that strongly influences the flow split and associated pressure drops is the geometry of the junction. In this sense, different geometric configurations have been tested by different authors in an attempt to enhance the phase separation. For instance, Van Gorp et al. [2] employed reduced T-junctions, whereas Hwang et al. [3] used impacting Y- and T-junctions. More recently, Baker [4] employed T-junctions in series and developed a T-piece separator by means of a combination of two horizontal T-junctions, one with the side arm upwards and one with the side arm downwards. The report of Azzopardi et al. [5] outlines the design and installation of a T-junction partial phase separator within an operational plant.

[1]Corresponding author.

Contributed by the Fluids Engineering Division of ASME for publication in the JOURNAL OF FLUIDS ENGINEERING. Manuscript received March 19, 2009; final manuscript received March 9, 2010; published online April 27, 2010. Assoc. Editor: Theodore Heindel.

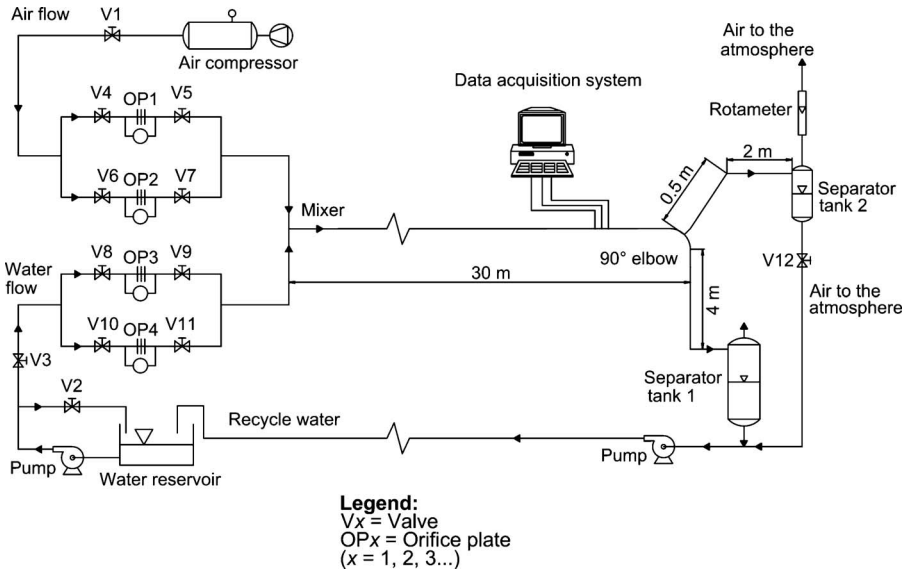

Fig. 1 Experimental setup

A few attempts have been made to model the phase separation phenomenon in the junctions. Most available models are presented in terms of the flow pattern approaching the junction. These methods for predicting the flow split are either wholly empirical in nature or based on one-dimensional analysis, still relying on empirical correlations. For instance, the initial work of Azzopardi and Whalley [6] focused on vertical 90 deg T-junctions with annular flow. Other models have been reported in Ref. [7], as well as in Ref. [8]. However, since the phase separation in a branched conduit is a quite complex phenomenon, the quality of the prediction of the flow separation by these models is not satisfactory. This is the main motivation to experimentally study the behavior of gas-liquid mixtures flowing through a junction.

As for elbows, Hernández-Ruíz [9] and Sánchez-Silva et al. [10] studied single-phase flow through horizontal 90 deg elbows with different curvature radii to determine experimentally the radial pressure distribution for metrology purposes. They found that the largest radial pressure difference in an elbow depends on the elbow curvature radius as well as on the Reynolds number. Nevertheless, the point of maximum radial pressure difference was located between 18 deg and 55 deg with respect to a line from the center of curvature of the elbow to its inlet. Vera-Arenas et al. [11] explored these results numerically, finding a good agreement between the model and the previous experimental data. They also studied the effect of the separation distance between two horizontal elbows on the flow behavior, finding that there is no influence when the separation-diameter ratio is greater than 8 ($L/D > 8$).

The literature review reveals that no effort has been made to study two-phase flow separation in branched bends. Hernández-Pérez [12], taking advantage of the above mentioned results for T-junctions and single bend, performed an experimental campaign in order to explore the curvature effect on the phase separation using a branched elbow.

In an effort to boost the liquid phase separation reported in the literature using T-junctions, an experimental study on the phase separation performance of branched elbows, when a gas-liquid mixture under slug flow conditions passes through them, has been carried out, and the results are reported in the present paper. The experimental results will be useful for developing a mathematical model, which aims at predicting the phase separation in branched elbows.

2 Experimental Setup

The experimental setup used in this research is shown in Fig. 1. It is made up of six sections; air supply, water supply, flow rate measurement, experimental section, phase separation section, and data acquisition system.

A 10 hp reciprocating compressor was used for the air flow supply; the air was stored in a 1 m^3 tank at 6 bar. Before being measured, the air flow passed through a pressure regulating valve (V1), where the pressure was reduced to 2 bar, so that sonic flow was attained and the air flow stability in the experiments was warranted. At the pressure regulating valve (V1), sonic gas flow usually occurs, and stable gas flow velocity is achieved when the downstream to upstream pressure ratio is kept below the critical value of 0.528. In that case, mass flow rate basically depends on the valve (V1) opening.

The water supply section included a 0.50 m^3 storage tank and a 5 hp centrifugal pump. Also, a recirculation system was used in order to avoid overcharge and maintain stable the flow selected for each experiment.

The arrangements employed to measure the flow rates of both air and water were similar. Each arrangement used a couple of orifice plate (OP) gauges that were mounted on two similar 52.8 mm diameter pipes connected in parallel. Each gauge covers a different range of flow rates. The orifice plates and their pressure taps were installed and calibrated according to the ISO-5167 standard [13].

Once the flow rate of each individual phase had been measured, they both were mixed in a Y-mixer, then the resulting two-phase mixture traveled along a 30 m long horizontal pipe line before reaching the elbow. This pipeline was made up mainly of steel pipe sections, but a 3 m long acrylic pipe section was incorporated for flow visualization purposes. Downstream was located the test section, which is made up of the 90 deg elbow and the data acquisition system, as presented in Fig. 1.

The data acquisition system consisted of an 11 channel data acquisition card, and ten pressure transducers. All the data were stored in a personal computer memory.

In the branched elbow, the gas flow rate going through the branch was measured with a calibrated rotameter, whereas the corresponding water flow rate was measured by using the graduated tank-2 together with a stop watch. The diameter of the separator was 304.8 mm, and the scale to measure the liquid height was graduated in millimeter. The rest of the mixture, which continued through the elbow, was finally collected in a cyclone separator. At the end of the process, the separated water was returned to the main water reservoir, whereas the air was discharged to the atmosphere.

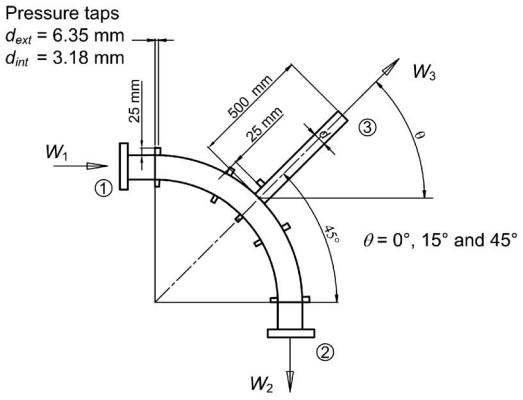

Fig. 2 Main parameters of the branched elbow in the horizontal plane

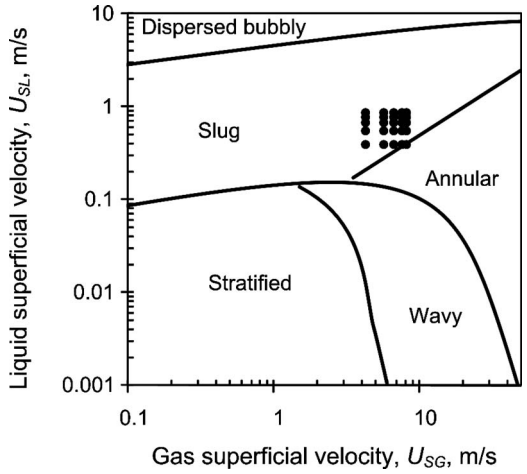

Fig. 3 Experimental flow conditions (●)—25 combinations of gas and liquid superficial velocities

A schematic representation of the elbow is shown in Fig. 2, where d_3 is the branch pipe diameter, d_1 is the elbow diameter, and θ is the inclination angle of the branch with respect to a line parallel to the flow at the inlet of the elbow. Three branch inclination angles were tested: 0 deg, 15 deg, and 45deg. For the branch diameter (d_3) three values were also tested; 12.7 mm, 25.4 mm, and 50.8 mm, giving three diameter ratios (d_3/d_1), namely, 0.25, 0.5, and 1.0. The branch pipe was welded on the side of the maximum radius of curvature and midway between the inlet and outlet sections of the elbow. The elbow had a curvature radius $r=6d$ at the center of the bend. Both the elbow and the branch were in the horizontal plane, as shown in Fig. 2. By combining all these geometric parameters, a matrix of nine test combinations was obtained, and five of them were selected to run the experiments.

In order to select the number of geometric combinations ($\theta, d_3/d_1$) for the experimentation, initially, a set of experiments was run for $d_3/d_1=0.25$ and $\theta=0$ deg, 15 deg, and 45 deg, for each of the flow rate conditions reported in Table 1.

In practice the most common way to predict the flow pattern that will occur under specified flow conditions, fluids, pipe diameter, and inclination angle is to use a flow pattern map. In a horizontal, gas-liquid, two-phase flow, the most widely used model to predict the flow pattern transitions is that of Taitel and Dukler [14], which is based on a semimechanistic approach. The model is quite general and accounts for the fluid properties, pipe diameter, pipe inclination, and fluid velocities by using five dimensionless groups. In this model, the stratified-nonstratified (intermittent or annular) transition is ascribed to the onset of the Kelvin–Helmholz instability, and an inviscid form of this instability to the prediction of the transition is applied. The stratified-wavy transition is considered to occur when the pressure and shear stress can overcome the viscous dissipation in the waves. The slug-annular transition was assumed to occur if the equilibrium liquid level at the onset of the Kelvin–Helmholz instability was less than half of the channel diameter. Slug-dispersed bubble transition is ascribed to the capability of the turbulence in the liquid phase to suspend the bubbles; when the bubbles cannot be suspended, then they agglomerate to form the gas bubble regions in the slug flow.

The flow conditions reported in Table 1 together with the flow pattern boundaries predicted by Taitel and Dukler [14], for the system used in this work, are plotted in Fig. 3. According to this figure, it was evident that the experiments realized were run for conditions of slug flow.

For $d_3/d_1=0.25$, the configuration that best performed the liquid separation was the one with $\theta=15$ deg. Hence, for the subsequent experiments, θ was kept constant at 15 deg, and values of 0.5 and 1 were tested for d_3/d_1. In all cases an elbow with 50.8 mm internal diameter and dimensionless radius of curvature $r/d_1=6$ at the center of the bend was used. This geometry was tested for a combination of five superficial gas velocities (horizontal axis, U_{SG1}) and five superficial liquid velocities (vertical axis, U_{SL1}), as summarized in Fig. 3.

3 Measurements Uncertainty

In order to estimate the uncertainty of the measurements, the method of repeating measurements with a trust limit of 95% was employed for the monitored variables, whereas for the controlled and separated flow rates in the experiment, the method of minimum count of the instrument was used. Bias uncertainties have a relatively small contribution to the overall uncertainty. For instance, the pressure transducers were calibrated with a column of water, whose minimum reading count was 1 mm (10 Pa). This represents an uncertainty level of ±5 Pa. The propagation of uncertainty has been calculated using the root-sum-square combination, as described in Moffat [15]. The maximum values estimated are reported in Table 2. The highest measurement uncertainty was for the gas flow rate in the branch. This is due to the fact that

Table 1 Experimental flow conditions—25 combinations of gas and liquid superficial velocities

	U_{SG1} (m/s)				
U_{SL1} (m/s)	4.283	5.710	6.696	7.610	8.128
0.388	1	2	3	4	5
0.547	6	7	8	9	10
0.668	11	12	13	14	15
0.769	16	17	18	19	20
0.859	21	22	23	24	25

Table 2 Uncertainty of the experimental measurements

Measurement	Uncertainty (±%)
P_1	10
P_2	8
P_3	15
W_{G1}	5
W_{L1}	2.5
W_{G3}	20
W_{L3}	5
W_{L3}/W_{L1}	5.6
W_{G3}/W_{G1}	20.62

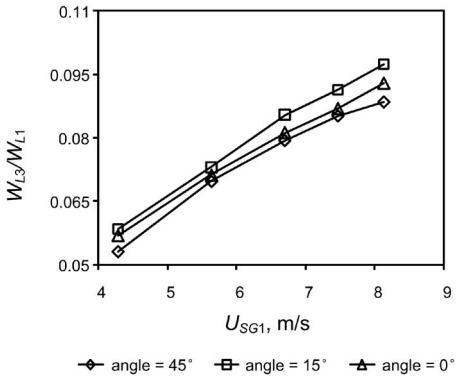

Fig. 4 Effect of the branch inclination. Elbow with d_3/d_1 =0.25 and U_{SL1}=0.64 m/s

when slugs arrived to the elbow there were oscillations in the test section. Additionally, a rotameter was employed in a low pressure region.

4 Results and Discussion

Phase separation results are usually reported in plots of fraction of liquid taken off F_L against the fraction of gas taken off F_G. Alternatively, a graph of x_3/x_1 versus W_3/W_1 is also frequently used. In this work, the geometry of the branched elbow is such that the liquid is expected to be diverted along the branch pipe. Therefore, the way of evaluating the phase separation is based on the fraction of the inlet liquid flow rate extracted through the branch pipe W_{L3}/W_{L1}. This fraction is a function of several parameters such as the diameters ratio d_3/d_1, the inclination angle of the branch pipe θ, and the inlet liquid and gas superficial velocities U_{SL1} and U_{SG1}. In this work, these parameters were considered as the main independent variables, and their effects on the phase separation is discussed below.

5 Effect of the Branch Inclination

The first parameter whose effect on the phase separation was investigated was the branch inclination angle. For the sake of simplicity, this parameter was studied only for a diameter ratio of 0.25. Although the effect of the branch inclination might not be the same at any diameter ratio, the data obtained at $d_3/d_1=0.25$ do provide valuable information and can be taken as a starting point for further investigations. In Fig. 4, W_{L3}/W_{L1} was plotted as a function of the gas superficial velocity U_{SG1} for three different angles, and U_{SL1} was kept constant. These results reveal that similar trends are obtained in the plots of the W_{L3}/W_{L1} for all the three angles tested, with only a slight variation in their magnitudes. It can be observed that the inlet liquid fraction extracted by the branch W_{L3}/W_{L1} is 12% superior for the branch inclined at 15 deg, with respect to the one inclined at 45 deg and around 8% with respect to that at 0 deg. These results suggest an agreement with the available numerical and experimental data [9,10], in terms of the position of the point of higher static pressure in a 90 deg elbow, and the direction of the velocity in this region of the elbow.

6 Effect of the Diameter Ratio

Based on the results of the effect of the branch inclination angle on the phase separation, as described in Sec. 4, a branch inclination angle of 15 deg was selected, and as it was mentioned previously, three ratios of diameters were studied, namely, d_3/d_1 =0.25, 0.5, and 1.0. As it could be expected, the largest water fraction W_{L3}/W_{L1} was extracted using the ratio $d_3/d_1=1.0$. Because this diameter ratio offered a larger branch cross sectional area for the extraction, more liquid flow rates were allowed to enter through the branch. Also, due to the way in which the phases were distributed inside the elbow as a result of the effect of the curvature, it was the liquid that was more directly influenced by the diameter ratio. It is important to highlight that the results corresponding to $d_3/d_1=1.0$ are around an order of magnitude higher than those of $d_3/d_1=0.25$, as shown in Fig. 5(*a*). As for the gas fraction extracted by the branch W_{G3}/W_{G1}, it can be observed in Fig. 5(*b*) that it also increased with the diameter ratio. Also, such as the case of W_{L3}/W_{L1}, W_{G3}/W_{G1} at $d_3/d_1=1$ is around an order of magnitude higher than at $d_3/d_1=0.25$, particularly at the lowest gas superficial velocities. This suggests that the extracted liquid was accompanied by a proportional amount of gas.

7 Effect of the Inlet Gas Superficial Velocity

The effect of the inlet gas superficial velocity is plotted in Fig. 6. It can be observed that within the range of inlet flow conditions of gas and liquid superficial velocities employed in this work, an increment of the inlet gas superficial velocity U_{SG1}, maintaining the inlet liquid flow rate constant, produces higher W_{L3}/W_{L1} ratios. This is accompanied by a small increase in W_{G3}/W_{G1}. The reason for this behavior is mainly due to the liquid inertia and the centrifugal force induced by the curvature of the elbow, as well as the inlet gas superficial velocity. One interesting fact to observe in

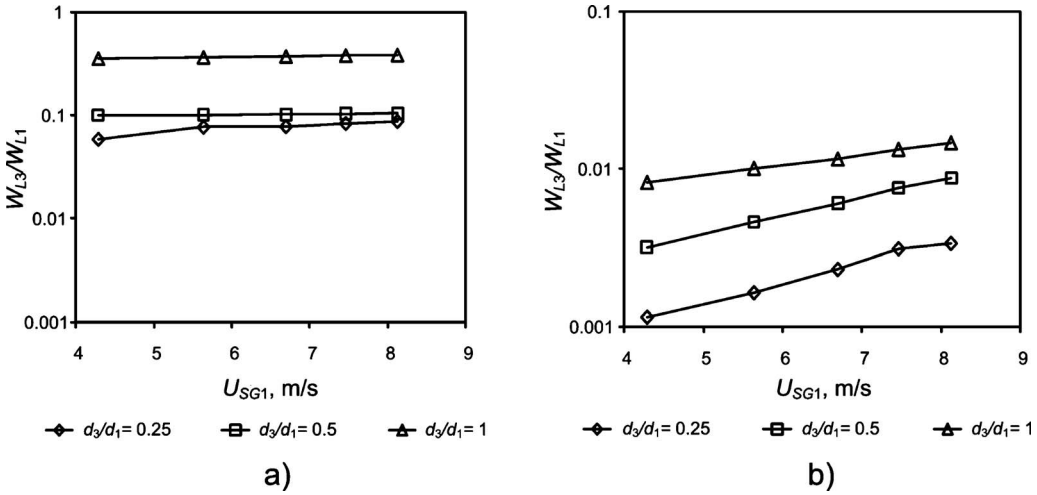

Fig. 5 Effect of the diameters ratio (d_3/d_1), θ=15 deg, and U_{SL1}=0.64 m/s: (*a*) on the liquid splitting W_{L3}/W_{L1}; (*b*) on the gas splitting W_{G3}/W_{G1}

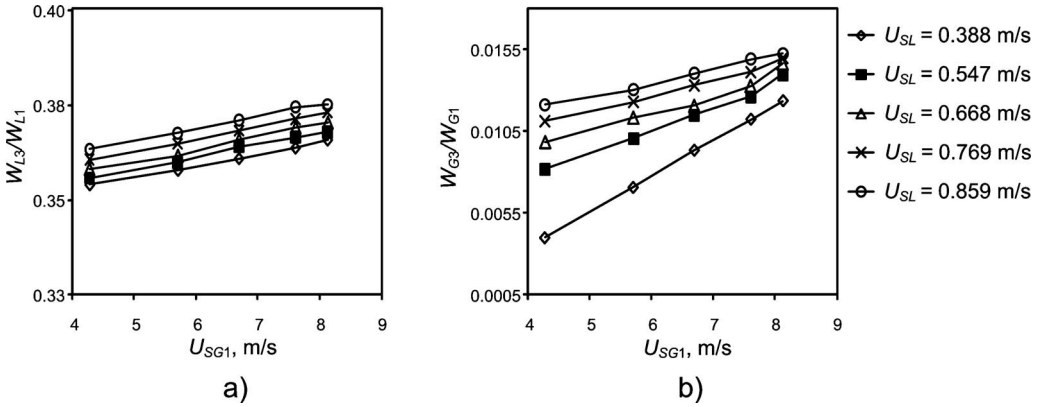

Fig. 6 Effect of the U_{SG1} for different U_{SL1}: (*a*) on the liquid splitting W_{L3}/W_{L1}; (*b*) on the gas splitting W_{G3}/W_{G1}. Elbow with $d_3/d_1=1$ and $\theta=15$ deg.

the experimental results reported in Fig. 6(*a*) is that, by increasing U_{SG1}, the liquid flow ratio W_{L3}/W_{L1} exhibits a slight growth in a linear fashion over the range of gas superficial velocities employed. This slight growth can be attributed to a reduction in the higher inertia of the liquid slugs at larger velocities due to the fact that the liquid slugs become highly aerated when the gas superficial velocity is increased. The transition to annular flow is still far, according to Taitel and Dukler [14], as can be seen in Fig. 3. The flow pattern predicted by the flow pattern map of Taitel and Dukler [14] was observed through a visualization section located 60 pipe diameters before the elbow. Since a flow development distance of 600 pipe diameters was provided, which is more than the one recommended by Penmatcha et al. [16], the flow pattern was maintained down to the elbow. However, the flow patterns obtained after the junction point were not investigated. This is beyond the scope of this work.

As a whole, the gas flow ratio that is extracted by the branch W_{G3}/W_{G1} increased when U_{SG1} was augmented (Fig. 6(*b*)); this particular behavior is expected, since the supply of more gas at the inlet results in an increase in the different slug flow parameters, such as the void fraction in the liquid slug body and the total slug unit length. In fact, the slope of the curve of W_{G3}/W_{G1} versus U_{SG1} displayed an increase as well. However, for a particular flow condition, it was found that W_{L3}/W_{L1} was around 25 times bigger than W_{G3}/W_{G1}, which means that the branch extracted mainly water.

8 Effect of Inlet Liquid Superficial Velocity

When the inlet liquid superficial velocity U_{SL1} was increased, maintaining the inlet gas superficial velocity U_{SG1} constant, it was found that there was an increment in both W_{L3}/W_{L1} and W_{G3}/W_{G1}, as shown in Figs. 7(*a*) and 7(*b*). However, it can be recognized that there is a tendency for the W_{L3}/W_{L1} versus U_{SL1} slope to become slightly larger at larger U_{SL1}. The way W_{L3}/W_{L1} and W_{G3}/W_{G1} are affected by the inlet liquid superficial velocity is similar to that of the inlet gas flow rate above mentioned (Fig. 6(*a*)). However, the increment of W_{G3}/W_{G1}, due to U_{SG1}, has a slope that is almost constant, and the increment of the W_{G3}/W_{G1}, due to U_{SL1}, is smaller than that due to U_{SG1}, as it could be expected since the gas supply was maintained constant.

The effects of U_{SL1} and U_{SG1} on W_{L3}/W_{L1} and W_{G3}/W_{G1} can be thought of as a result of the higher centrifugal force that the liquid phase undergoes, compared with that undergone by the gas phase. The centrifugal force of the phases is a function of the density and velocity of the phases themselves. As a result, it is expected that the liquid is forced to flow, inside the elbow, along the section of bigger curvature radius, where the branch is attached. Moreover, in the region around 45 deg with respect to a line from the center of the curvature to the inlet of the elbow [9,10], the static pressure reaches a maximum, which also suggests that the liquid is more likely to occupy the side near the branch and leave through the branch. The larger centrifugal force of the liquid phase is due to two factors: the first one is its higher density, which is around 1000 times the density of the air under the test conditions, and the second one is its high velocity, which, for the case of the slug flow pattern employed in the experiments, can be comparable to that of the gas.

9 Pressure Drop

The liquid and gas mass flow rates deviated toward the branch can also be affected by the pressure drop between the inlet and the run arm Δp_{1-2}, and the pressure drop (or rise) through the branch

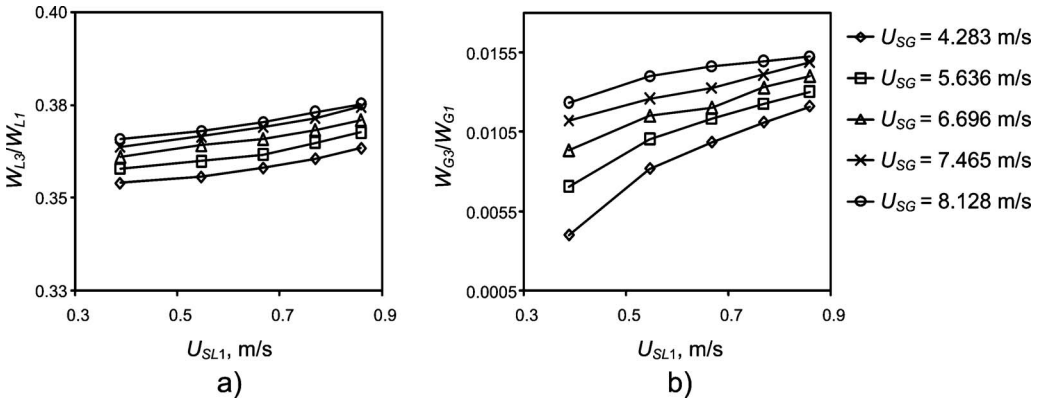

Fig. 7 Effect of the inlet liquid superficial velocity on splitting of (*a*) liquid and (*b*) gas. Elbow with $d_3/d_1=1$ and $\theta=15$ deg.

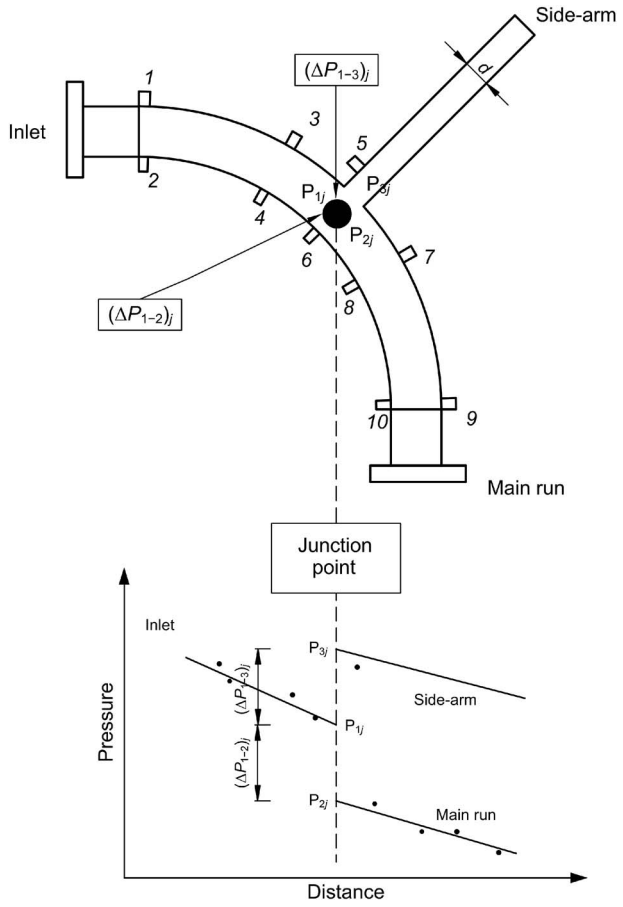

Fig. 8 Pressure drop measurement technique in the branched elbow

Δp_{1-3}. The pressure was not fixed to a particular value either at the inlet section or at both exit sections of the branched bend. On the other hand, both exit sections discharged to the atmosphere, so the action taken was monitoring the pressure at different positions along the elbow by means of a calibrated pressure transducers connected to a 100 Hz frequency data acquisition system (Figs. 2 and 8).

Following a well-known methodology by Buell et al. [17], and Saba and Lahey [8], the pressure immediately before the junction point P_{1j} was calculated by extrapolating the pressures upstream of this point (pressure taps 1–4). Similarly, the pressure just after the junction point P_{2j} was calculated by extrapolating the pressures downstream the junction point (pressure taps 7–10).

There was only one pressure tap installed in the branch arm and thus, it was taken as the value for P_{3j} (see Fig. 8). This reading was taken at a location close enough to the junction point to give an appropriate pressure value, but at a sufficient distance from the junction point in order to avoid errors in the readings due to the flow turbulence. The values for the pressure drop ΔP_{1-2} and pressure rise ΔP_{1-3} are obtained by subtracting the corresponding pressures.

A set of the pressure drop values for the elbow with $d_3/d_1=1$ and $\theta=15$ deg is plotted in Fig. 9. Here, the liquid superficial velocity was kept constant, and the gas superficial velocity was increased, as shown in Fig. 3; for other liquid superficial velocities, similar trends were obtained. In general the trend of the pressure drop is upwards.

Figure 10 shows both pressure drops Δp_{1-2} and Δp_{1-3} as a function of the total mass flow rate ratio W_3/W_1 for the experimental case of $d_3/d_1=0.25$ and 15 deg. For both the elbow and the branch, there is a relationship between the mass flow rate and

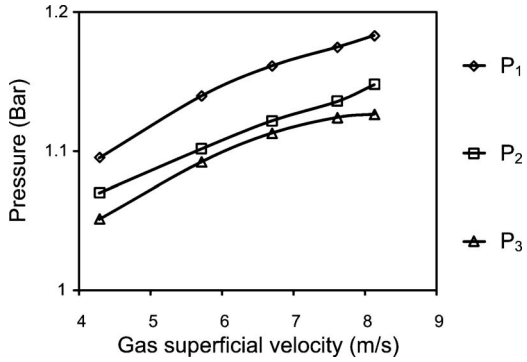

Fig. 9 Pressure and pressure drop for the elbow with $d_3/d_1=1$ and $\theta=15$ deg

the pressure drop. In this sense, the pressure drop is also an important factor related not only with the extracted flow rate but also with the phase distribution in the separation region. For this case, the pressure drop through the branch is larger than the one through the elbow, and it might be associated with the fact that for $d_3/d_1=0.25$, there is a reduction in the diameter from the elbow inlet to the branch. In addition, it can be observed in Fig. 10 that as W_3/W_1 increases, pressure drop also augments; in fact, there is more dispersion in the data when W_3/W_1 grows. The dispersion in the data is understandable due to the transient nature of the flow pattern under consideration. Slug flow features, such as its length and frequency, behave in an unsteady manner.

10 Comparison Between the Elbow and a T-Junction as Phase Separators

Results of phase separation, mainly for T-junctions, have been published in the literatures [1–8,16,17]. In most of the situations reported, the gas tends to leave mainly through the branch, and the W_{G3}/W_{G1} ratio varies from zero to values close to 1. However, W_{L3}/W_{L1} is almost proportional to W_{G3}/W_{G1}, which tends to reduce the performance of the T-junctions as phase separators. Nevertheless under certain conditions T-junctions are able to distribute the flow evenly between both discharge points, which is one of their applications in industries.

In order to compare the phase separation efficiency, the results of this work were plotted in a similar manner to that used by other authors, such as Azzopardi and Whalley [6]. This involves a plot where the abscissa is the fraction of the gas extracted by the branch pipe F_G, and the ordinate is the separated fraction of liquid F_L (Fig. 11).

$$F_G = \frac{W_{G3}}{W_{G1}} \tag{1}$$

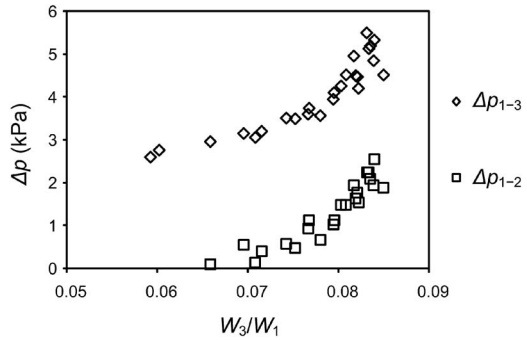

Fig. 10 Pressure drop Δp_{1-2} and Δp_{1-3} for the case $d_3/d_1=0.25$ and $\theta=15$ deg

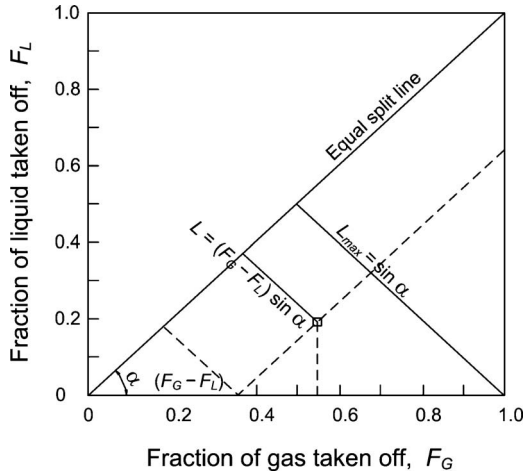

Fig. 11 Conventional expressions of the phase split results [18]

$$F_L = \frac{W_{L3}}{W_{L1}} \tag{2}$$

There are several situations that could occur: (a) If the experimental point lies on the diagonal line $F_L = F_G$, it means that the same proportion of liquid and gas is extracted by the branch; (b) if $F_L = 1$ and $F_G = 0$, the efficiency is equal to 1 because all the liquid is extracted by the branch and all the gas continues through the main line (this situation is the one we are looking for); (c) if $F_G = 1$ and $F_L = 0$, all the gas is extracted by the branch and all the liquid continues through the main line; this case is certainly similar to case (b) because the liquid is all separated; and (d) when $F_L = 1$ and $F_G = 1$, it means that all the liquid and all the gas exits through the branch nothing goes through the main line, this is not a normal situation because it requires that the main line is closed.

The actual situation is that all data have a couple of values (F_L, F_G) different from 0 and 1, which means that they can be found in two regions: in the region where $F_G > F_L$, and in the region where $F_L > F_G$. Of course the interest is the region where $F_L > F_G$ and trying to increase F_L and reduce F_G in order to obtain the best performance of the elbow as a phase separator.

The farther the data are away from the equal split line, the better the phase separation. The maximum distance $L_{\max}$ from the equal split line to either of the two corners, which represents a complete separation, can be expressed as

$$L_{\max} = \sin \alpha \tag{3}$$

where α is the angle between the diagonal line and the abscissa (45 deg). The distance L from the equal split line to a practical experimental point, which correspondingly stands for the actual separation, is as reported by Yang and Azzopardi [18]

$$L = (F_G - F_L) \sin \alpha \tag{4}$$

The separation efficiency η can be defined as the ratio of the actual separation to the ideal or complete separation of the water. In other words, this definition must include the gas fraction accompanying the water; the less gas is associated with the separated water, the better. So the efficiency can be represented by

$$\eta = \frac{|F_L - F_G|}{|F_L - F_G|_{\max}} = |F_L - F_G| \tag{5}$$

That is, when $|F_L - F_G|_{\max} = 1$, it means that $F_L = 1$ and $F_G = 0$.

The absolute value is used because the experimental data may fall on either side of the equal split line, depending on which phase dominates the extraction. Equation (5) reveals that the separation efficiency equals the difference of the fractions extracted of both phases. As a result, when $F_L \gg F_G$, the elbow performs better as a phase separator. The separation efficiency ranges from 0% to 100%, i.e., from no separation to complete liquid separation.

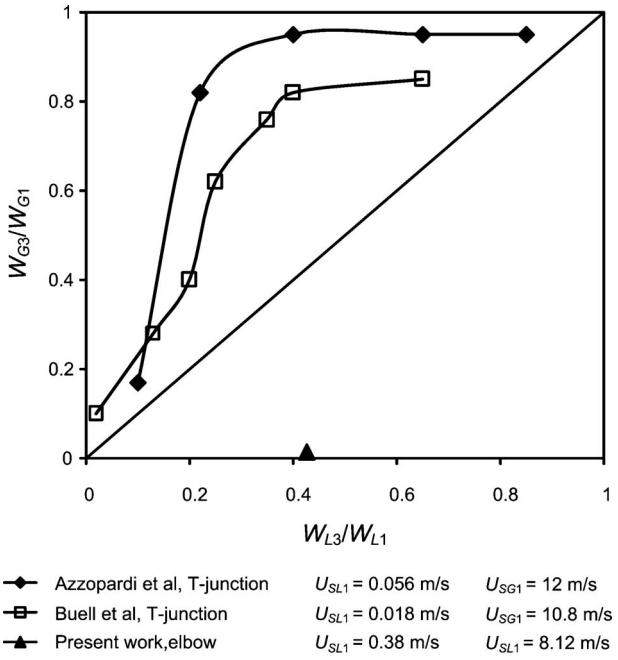

Fig. 12 Comparison between a T-junction and the branched elbow with a branch inclination of 15 deg, as phase separators, for $d_3/d_1 = 1$

Figure 12 shows a comparison between a T-junction and the branched elbow, as phase separators, with similar ratio of diameters. It was difficult to find similar flow conditions and flow pattern to compare with the literature. However, flow conditions were chosen as close as possible to those used in the present work.

The results of the present work indicate that, as expected, the branch pipe mainly extracts liquid phase. However, in the best scenario, W_{L3}/W_{L1} reached a value of 0.4, which means that 40% of the inlet water flow was separated by the branch. This result was for the largest diameter ratio tested $(d_3/d_1 = 1.0)$. Meanwhile, the gas fraction W_{G3}/W_{G1} accompanying this separated water reached a maximum of 0.015, that is, only 1.5% of the inlet air flow rate W_{G1} went through the branch, which means that W_{L3}/W_{L1} is approximately 26 times the W_{G3}/W_{G1} value, or the separation efficiency is $\eta = (0.4 - 0.015)/1 = 0.385$. A calculation of the separation efficiency for the T-junction data in Fig. 12 gives a maximum value of $\eta = (0.82 - 0.22)/1 = 0.6$, which occurs for the point that is more distant from the diagonal line. The data of Buell et al. [17] have separation efficiencies in a range from 0.08 to 0.42. This suggests that in some cases the branched elbow has a separation efficiency similar to that of a T-junction.

11 Correlation for the Phase Separation in the Elbow

The parameters that can affect the phase separation in a branched elbow are the liquid and gas superficial velocities, geometry, fluid properties, and pressure drop. Unfortunately, in this work, the discharge pressure was not controlled, and all the discharges were done to the atmosphere, so the correlation suggested in Eq. (8) only considers the liquid and gas superficial velocities at the inlet section of the elbow and the diameter ratio (U_{SL1}, U_{SG1}, and d_3/d_1 respectively). The fraction of liquid extracted F_L is a function of all of these parameters and can be correlated with them. In order to simplify the process of developing the correlation, the independent parameters were grouped into a single variable b in such a way that b is dimensionless. Several ways of grouping the parameters were tested. Finally, b was put in terms of the quality and the diameters ratio, as described in Eq. (6)

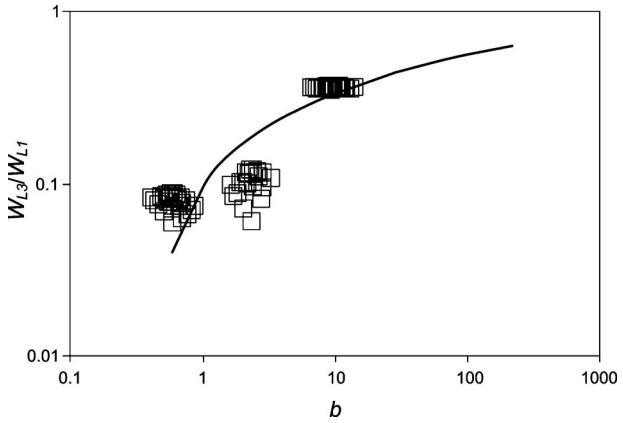

Fig. 13 Curve of adjustment of the phase separation data

$$b = x_1^{-0.5}\left(\frac{d_3}{d_1}\right)^2 \tag{6}$$

where x_1 is the inlet mass fraction of the gas or quality, which is defined as

$$x_1 = \frac{W_{G1}}{W_{G1} + W_{L1}} \tag{7}$$

Then the least-squares method of curve fitting was applied to all the experimental data obtained in order to develop the correlation (Eq. (8)). A logarithmic function was selected. This function exhibits a gradual growth of F_L within the interval [0 1] over a wide range of values for b, which is dimensionless, and fits the data with a regression coefficient of 0.83

$$F_L = 0.1017 \ln(b) + 0.0996 \tag{8}$$

So the liquid phase separated can be expressed as a function of the parameter b

$$F_L = f(b) = f\left(U_{SL1}, U_{SG1}, \frac{d_3}{d_1}\right) \tag{9}$$

The correlation curve and the experimental data points are plotted in Fig. 13. Not surprisingly, it can be observed that a higher value of F_L is obtained, that is, the liquid separation is better when the parameter b is increased. This happens particularly at low values of b. For high values of b, the increase in F_L is small. The maximum F_L attainable in the experiments was around 40%, which is not bad considering the device simplicity.

12 Conclusions

The results of an experimental investigation of the phase separation performance of a horizontal branched 90 deg elbow with an air-water mixture have been reported. From the above it can be concluded that:

For a given inlet liquid flow rate and when the flow is a slug flow at the elbow inlet, an increment of U_{SG1} produces an increment in the inlet liquid fraction extracted by the branch pipe. It was found that for the flow conditions employed in this work, U_{SL1} produced a linear increase in F_L.

The fraction of the inlet liquid extracted through the branch is slightly bigger for the branch inclined at 15 deg, compared with the cases of 0 deg and 45 deg inclination; thus, the best angle producing better extractions of liquid must be near to the 15 deg inclination. On the other hand, the bigger is the ratio of the diameter branch/elbow, the bigger is the fraction of liquid extracted by the branch.

When comparing the results of this work with those obtained by other investigators using T-junctions, based on Eq. (5), it can be concluded that elbows in some cases have a similar performance as a phase separator for two-phase flows as a T-junction.

Nomenclature

b = group of variables that affect the phase separation (dimensionless)
d_1 = elbow diameter (m)
d_3 = branch pipe diameter (m)
F_L = fraction of liquid taken off (%)
F_G = fraction of gas taken off (%)
ΔP_{1-2} = pressure rise along the elbow (kPa)
ΔP_{1-3} = pressure drop (or rise) between the elbow inlet and branch pipe (kPa)
P_j = pressure next to the junction (Pa)
r = radius of curvature (m)
U_{SL} = liquid superficial velocity (m/s)
U_{SG} = gas superficial velocity (m/s)
U_M = mixture velocity (m/s)
W_1 = inlet total mass flow rate (kg/s)
W_3 = branch total mass flow rate (kg/s)
W_{G1} = inlet gas mass flow rate (kg/s)
W_{L1} = inlet liquid mass flow rate (kg/s)
W_{G3} = branch gas mass flow rate (kg/s)
W_{L3} = branch liquid mass flow rate (kg/s)
x_1 = inlet mass quality (%)
x_3 = branch mass quality (%)
η = phase separation efficiency (%)
θ = branch inclination angle (deg)

References

[1] Oranje, L., 1973, "Condensate Behavior in Gas Pipelines is Predictable," Oil Gas J., **32**, pp. 39–44.
[2] Van Gorp, C. A., Soliman, H. M., and Sims, G. E., 2001, "The Effect of Pressure on Two-Phase Flow Dividing at a Reduced Tee Junction," Int. J. Multiphase Flow, **27**(3), pp. 571–576.
[3] Hwang, S. T., Soliman, H. M., and Lahey, R. T., 1989, "Phase Separation in Impacting Wyes and Tees," Int. J. Multiphase Flow, **15**(6), pp. 965–975.
[4] Baker, G., 2003, "Separation and Control of Gas-Liquid Flows at Horizontal T-Junctions," Ph.D. thesis, Department of Fluid Mechanics, University of Nottingham, UK.
[5] Azzopardi, B. J., Colman, D. A., and Nicholson, D., 2002, "Plant Application of a T-Junction as a Partial Phase Separator," Chem. Eng. Res. Des., **80**(1), pp. 87–96.
[6] Azzopardi, B. J., and Whalley, P. B., 1982, "The Effect of Flow Patterns on Two Phase Flow in a T-Junction," Int. J. Multiphase Flow, **17**(3), pp. 481–507.
[7] Seeger, W., Reimann, J., and Mueller, U., 1986, "Two-Phase Flow in a T-Junction With a Horizontal Inlet, Part I: Phase Separation," Int. J. Multiphase Flow, **12**(4), pp. 575–585.
[8] Saba, N., and Lahey, R. T., 1983, "The Analysis of Phase Separation Phenomena in Branching Conduits," Int. J. Multiphase Flow, **10**(1), pp. 1–20.
[9] Hernández-Ruiz, J., 1998, "Study About the Flow Field Behavior in Curved Pipes for Metrology Applications," M.Sc. thesis, Graduate Studies and Research Section, ESIME-IPN, México.
[10] Sánchez-Silva, F., Gómez, A., Toledo, M., Quinto, P., and Zurita, V., 2003, "Experimental and Numerical Curved Flow Study for Metrology Purposes," J. Appl. Res. Tech., **1**(2), pp. 114–126.
[11] Vera-Arenas, V., Sánchez-Silva, F., Pysmennyy, Y., Polupan, G., and Barbosa-Saldaña, J. G., 2007, "Numerical Analysis of the Flow Velocity Regions in an Array of Three Horizontal 90° Elbows Conducting Water," *Proceedings of the Fifth International Conference on Heat Transfer, Fluid Mechanics and Thermodynamics, HEFAT 2007*, J. Meyer ed., University of Pretoria Press, Sun City, South Africa, pp. 1–6
[12] Hernández-Pérez, V., 2003, "90° Elbows Performance as Phase Separators in Two-Phase Air-Water Flows," M.Sc. Thesis, Graduate Studies and Research Section, ESIME-IPN, México.
[13] 1991, "Measurement of Fluid Flow by Means of Pressure Differential Devices. Part1: Orifice Plates, Nozzles and Venturi Tubes Inserted in Circular Cross-Section Conduits Running Full," Ref. No. ISO5167-1:1991(E).
[14] Taitel, Y., and Dukler, A. E., 1976, "A Model for Predicting Flow Regime Transition in Horizontal and Near Horizontal Gas-Liquid Flow," AIChE J., **22**(1), pp. 47–55.
[15] Moffat, R. J., 1988, "Describing the Uncertainties in Experimental Results," Exp. Therm. Fluid Sci., **1**(1), pp. 3–17.
[16] Penmatcha, V. R., Ashton, P. J., and Shoham, O., 1996, "Two-Phase Stratified Flow Splitting at a T-Junction With an Inclined Branch Arm," Int. J. Multiphase Flow, **22**(6), pp. 1105–1122.
[17] Buel, J. R., Soliman, H. M., and Sims, G. E., 1994, "Two Phase Pressure Drop and Phase Distribution at a T Junction," Int. J. Multiphase Flow, **20**(5), pp. 819–836.
[18] Yang, L., and Azzopardi, B. J., 2007, "Phase Split of Liquid-Liquid Two-Phase Flow at a Horizontal T-Junction," Int. J. Multiphase Flow, **33**(2), pp. 207–216.

Microbubble Drag Reduction Downstream of Ventilated Partial Cavity

Eduard Amromin
Mechmath LLC,
Prior Lake, MN 55372-1283

The effect of air flux from ventilated partial cavities on drag of bodies was studied. An integral equation method for estimation of air bubble effects on drag was employed and validated with earlier known experimental data for flat plates and bodies. The qualitative difference in the effects of flow speed and air supply rate on drag of flat plates and bodies was numerically confirmed and explained as a combined effect of the boundary layer density decrease and the increase in its displacement thickness. The numerical analysis shows reduction in the total drag of ventilated bodies with increasing air flux rate up to an optimum, but the drag rise for greater rates. A synergy of friction reduction under attached ventilated cavity and microbubble drag reduction downstream of it was shown. [DOI: 10.1115/1.4001489]

1 Introduction

Ventilated partial cavitation is the proven drag reduction technique for bodies and hydrofoils (see Refs. [1–3], etc.). The employed design concept (described in Ref. [4], for example) allows stabilization of the attached cavity and suppression of drag penalty caused by cavity tail pulsation, but the ventilated cavities always require an air supply for their maintenance.

The permanently supplied air escapes from cavities to the boundary layer and drifts downstream of it. This escape has multiple effects on the efficiency of drag reduction by air cavitation. First, some energy must be spent to provide air to the cavity and, consequently, any increase in air flux (supply) increasing the total energy spent for body motion. Second, an excessive air flux may disturb the smooth flow reattachment behind the cavity and cause some cavitating drag penalty. Third the air flux enriches the boundary layer by bubbles and may give some microbubble drag reduction in the wetted surfaces downstream of the cavity, but this enrichment also increases the wake thickness and tends to increase the body form resistance. However, is there some effect compensation or an effect synergy associated with air flux from cavity?

A theoretical analysis of such synergy must include an analysis of microbubble drag reduction, but state-of-the art in its theory makes it difficult to find a comprehensive numerical technique for such analysis. The recent studies have been emphasized either on quite delicate aspects of turbulent mixing [5,6] (though there are old data on microbubble drag reduction in laminar flows [7] and significance of the turbulent mixing detail for drag reduction is unclear) or on bubble mutual interaction [8] (though a little effect of bubble shape and size was reported in Refs. [9,10]). Validation of the employed approaches by known experimental data (as data published in Ref. [11]) has not been sufficient in known studies. No successful validation was mentioned in the most recent review on microbubble drag reduction (by Ceccio et al. [12]). The simple qualitative information (such as existence of a linear dependency of the drag reduction rate on the mixture density in channel flows [13]) did not induce related numerical studies able to clarify the microbubble drag reduction mechanism. Moreover, a simple comprehensive analysis of microbubble drag reduction with boundary layer integral equations was not reported yet.

Contributed by the Fluids Engineering Division of ASME for publication in the JOURNAL OF FLUIDS ENGINEERING. Manuscript received March 31, 2009; final manuscript received March 19, 2010; published online May 13, 2010. Assoc. Editor: Steven Ceccio.

Such analysis is described below, with its validation by the flat-plate large Reynolds number experiments [11]. The elaborated and validated numerical tools and computer code are then applied to analyze the flow around the buttock of a ship model similar to that earlier [4] designed for a study of drag reduction by partial ventilated cavitation.

2 Integral Equations for Bubbly Boundary Layers and Method Validation With Flat-Plate Experimental Data

The integral boundary layer equations have been broadly used in the past and generally described in many known books (Refs. [14,15] and others). However, for the air-water mixture, the medium compressibility must be taken into account in such equations and the displacement and momentum thicknesses $\delta^*=\int_0^\delta(1-ru/U)dy$ and $\delta^{**}=\int_0^\delta ru/U(1-u/U)dy$ depend on r. Here δ is the boundary layer thickness, the coordinate x is directed along this layer, the coordinate y is directed across it, and $u(x,y)$ is the profile of tangential velocity within the boundary layer. Although the density profile can be also introduced, only the average across the layer ratio r of mixture density to the water density is used here. This simplified description of the ratio r makes it possible to define the thicknesses of the mixture boundary layer directly with the water boundary layer thicknesses and include this ratio only as a factor to integrals in these definitions. Therefore, for the mixture, $\delta^*=(1-r)\delta+r\delta_W^*$, $\delta^{**}=r\delta_W^{**}$, and momentum equation are rewritten from Eq. (10.92) of Ref. [14] as

$$\frac{d(r\delta_W^{**})}{rdx}+\frac{2\delta_W^{**}+\delta_W^*+\left(\frac{1}{r}-1\right)\delta-\delta_W^{**}\mathrm{M}^2}{U}\frac{dU}{dx}=\frac{v^{*2}}{U^2} \tag{1}$$

Here M is the mixture Mach number, and subscripts W relate to mixture or water. The profile $u(x,y)=F(x,\eta)+C_U(x)F_P(x,\eta)$ conventional for turbulent boundary layers is employed here, $\eta=y/\delta$, $\eta_+=\eta\delta v^*/\nu$, $F=2.5v^*(\ln|\eta_+|+B^*)$, $F_P=3\eta^2-2\eta^3$, $C_U=U(x)-F(x,\delta)$, and $B^*(x)$ is a function depending on the surface roughness; the local Mach number M can be presented as $\mathrm{M}=\sqrt{(1-\beta)[\mathrm{M}_W^2(1-\beta-\beta\varepsilon)+\mathrm{M}_a^2\beta/\varepsilon]}/(1-\varepsilon\beta)$, the ratio of air density to water density ε is computed with employment of Poisson adiabatic law, and M_a is the Mach number computed with the sound speed in air.

The mass conservation law for this boundary layer is written with an empirical coefficient K^* as

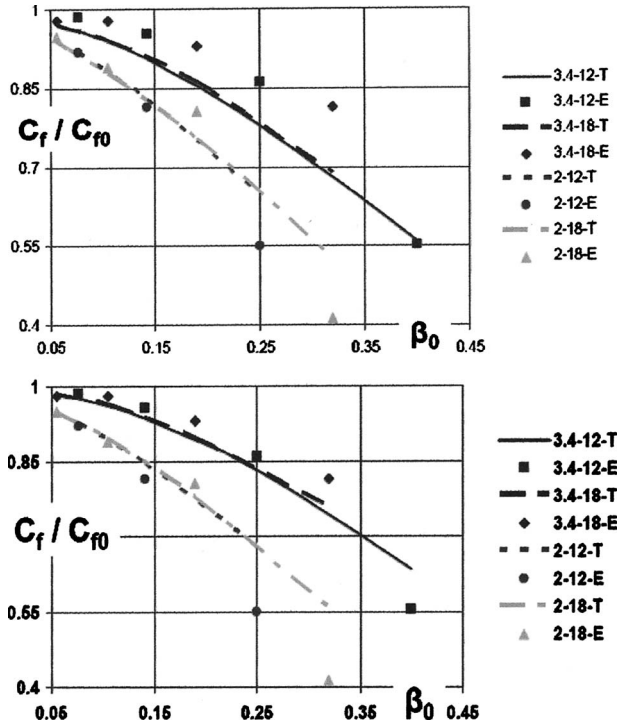

Fig. 1 Comparison of computed (lines) and measured (symbols, after Ref. [11]) effects of air volumetric ratio at the slot β_0 on the drag ratio C_f/C_{f0} for two measurement points and two speeds. The upper plot presents computations without air diffusion account in Eq. (2). The lower plot presents computation with air diffusion described by the law $d\beta/dx=-0.0025\beta/\delta$ tuned to the experimental data [11]. The first numbers in the legend indicate the distance from the plate leading edge to the point (in m). The second numbers indicate flow speed (in m/s). Letter T means theory (our computation) and E means experimental data.

$$\frac{d[U(\delta-\delta_W^*)r]}{dx} = UK^* \tag{2}$$

The integration of Eqs. (1) and (2) provides the functions $\delta(x)$ and $v^*(x)$ and allows computation of the friction coefficient.

It is important to point out initial conditions to these first-order ordinary differential equations. At the bubble ejection point, the boundary layer thickness has a jump of $\beta o \times \delta$ and δ^* also has some jump there, but there is no jump of the momentum thickness δ^{**}, which continuity can be kept with a v^* drop only.

The proven recommendation for K^* as a function of the ratio $(\delta-\delta^*)/\delta^{**}$ for the single phase flows [15] is used here, but air diffusion from the boundary layer must be also taken into account in definition of K^*. Comparison of the drag rates $C_f(\beta_0)/C_f(0)$ in two points of the flat plate with measurements [11] shown in two parts of Fig. 1 manifests that neglecting by such diffusion, one will underestimate this rate and overestimate the drag reduction. The friction coefficient is defined here as $C_f=(4r-2)v^{*2}$; this definition, first, corresponds to the known [14,15] $C_f=2v^{*2}$ for one-phase media ($r=1$) and, second, corresponds to implicit hypothesis [16] of air-free flow out of the boundary layer.

The air supply took place at $x=1.3$ m in the experiments [11] and the error bars were indicated in the range from $\pm 10\%$ to $\pm 20\%$ (one can read Refs. [11,16] for more details on these experiments). The dependency of the drag rate on the distance from the leading edge in Fig. 2 is computed with taking into account the air diffusion from the boundary layer.

The agreement of solutions of these boundary layer integral equations with the experimental data looks reasonably good. The

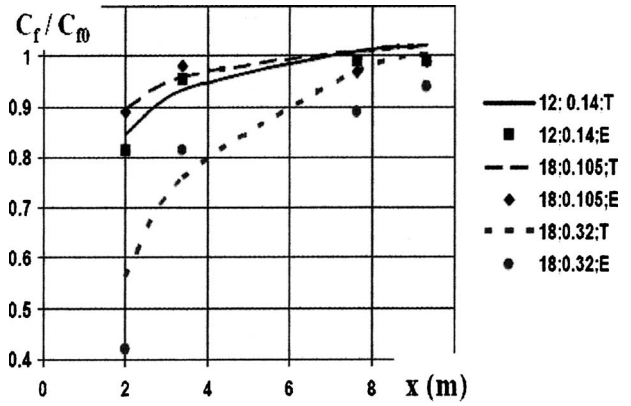

Fig. 2 Comparison of computed and measured (after Ref. [11]) distributions of the drag ratio C_f/C_{f0} along the flat plate. The first numbers in the legend indicate the flow speed (in m/s). The second numbers indicate the value of β_0. Letter T means theory (our computation) and E means experimental data.

nominal flow speed used in computations is lower than the actual flow speed in the water tunnel experiments [11] (by $\approx 8\%$), and the slight overprediction of drag reduction with the numerical method may be caused also by this speed difference. Of course, there is a possibility to augment the accuracy of computations by introducing some dependencies of the mixture density profiles and air diffusion coefficients on Froude number (buoyancy effects), etc. However, the set of available experimental data on the mixture density profiles does not look to be sufficient for the confident augmentations yet.

3 Estimation of the Body Total Drag

The objective of this work is to find the influence of air flux from partial cavity (as shown in Ref. [3], occurring mainly in the form of small bubbles affecting the wake turbidity) on the body total drag. As evident from Eq. (1), the dependency of drag on air supply (on air concentration in the boundary layer) can be influenced by the body shape. Such an influence was already reported and the experimental data from the review [9] are copied to Fig. 3.

There is a qualitative difference of experimental data for plates and bodies: Both top and bottom sides of a flat plate exhibit

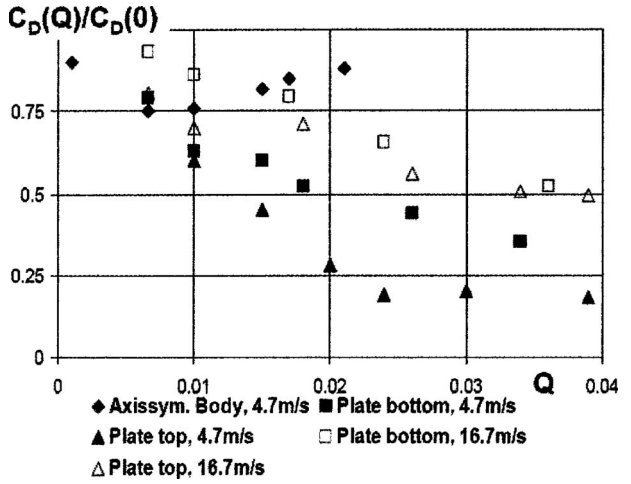

Fig. 3 Effect of air supply on the ratio of drag coefficients for plates with air ejections on their different sides and for an axisymmetric body with air ejections (after Ref. [9]; the abscissa axis is graduated by a parameter Q proportional to β_0, but with an undetermined factor)

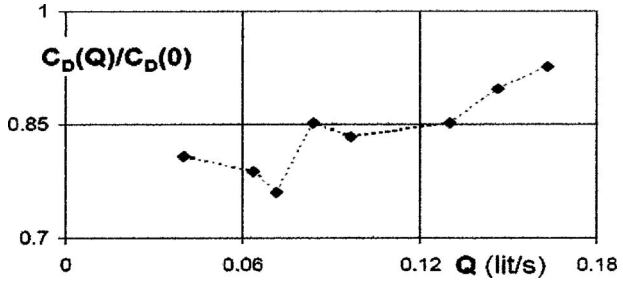

Fig. 4 Dependency of drag rate on the air flux Q for the ventilated hydrofoil OK-2003 [3]

gradual drag decreases with the increase in air supply at any flow speed U_∞, but there is a minimum of drag at some intermediate $\boldsymbol{\beta_0}$ for a body. Further, the air supply effect on drag similar to described for axisymmetric body was also observed [3] for ventilated hydrofoil OK-2003. As shown in Fig. 4, the drag decreases with the increase in air flux from $Q=4$ liter/min (from the minimum of air supply/flux noted in Ref. [3] as necessary to maintain a cavity) up to $Q=8$ liter/min, where the reverse trend started.

It was supposed that the body shape effect is indeed the pressure distribution effect on the boundary layers with air-water mixtures. Therefore, the same Eqs. (1) and (2) were applied to the bodies with microbubbles in their boundary layer. Moreover, there is also no difference between a bubble ejecting slot and a cavity tail for these equations: For both cases, it is an initial point with given δ, δ^{**}, and βo (the selected body shape with cavities is shown in Fig. 5). The numerical methods employed for computation of the cavity shape were described in Ref. [4], but it would be appropriate to recall that the ideal fluid theory can be used for determination of such cavity shape because it has the fixed cavity detachment. However, the Froude number effect becomes important for such cavities and the pressure constancy condition for the cavity must be written as $U^2+2z\ \mathrm{Fr}^{-2}=1+\sigma$ and cavitation number σ has usually negative values ($P_C>P_\infty$). The numerical method employed for boundary layer characteristics over cavity is also an integral method. This method was also already described [17], but it is similar to the method employed below for the wake.

One can see in Eqs. (1) and (2) that the pressure gradient effect is coupled with the medium compressibility effects there. As a result, correlation between dependencies $C_f(x)$ and $\mathrm{Cp}(x)$ in Fig. 6 looks unusual for a body in a water flow: Variations of friction coefficient are in the same phase with variations of pressure coefficient. The phase coincidence occurs (for a sufficiently great $\boldsymbol{\beta_0}$) because of air compressibility: The increasing pressure compresses the boundary layer, reduce δ, etc. On the other hand, the effect of M itself in Eq. (1) is small: For the speed of 10.5 m/s, omitting the term proportional to M gives less than 1% of change in drag.

Additionally to the friction, the total drag of any body includes also the form resistance, and the wake analysis is necessary to estimate this drag component. For the wake computation, the velocity profile $u(x,y)=w+(U-w)F_P$ is selected and the momentum equation on the wake axis is employed instead of Eq. (2) at $x>L$ as follows:

$$w\frac{dw}{dx}=\frac{a}{\delta^*}(U-w)^2+\frac{U}{r}\frac{dU}{dx} \tag{3}$$

Here $a=0.015$ is the Clauser empirical constant [14]. Integration of two pairs of equations is carried out with conservation of δ, δ^*, δ^{**}, and β at $x=L$ (at the transition from boundary layer to the wake). The initial value of w is determined from the condition of δ^{**} continuity.

Also, an air diffusion law is necessary to introduce in the wake. Because of free surface influence, the air flux from the ship wake is more intensive than from its boundary layer: Having a vertical speed component due to buoyancy, some bubbles are lost across the free surface while they are not across the solid surface. The formula $\beta(x)=\beta(L)\delta(L)[x/L]^{-m}$ was used for the wake here. Replacement of $m=1$ by $m=1.5$ does not affect qualitatively the major results, and $m=1$ was used below. All presented results for the body were obtained with taking into account the inverse effect of δ^* on pressure distribution along the boundary layer and wake, but for this particular buttock shape, this effect is quite small because of flat pressure distribution over the stern at $x>0.9L$ shown in Fig. 6.

The total drag can be determined by values of δ^* in the far wake, where δ^{**} achieves its constant value (but the Squire–Young formula [14] is not applicable to drag estimation in two-phase media!). The examples of the computed effect of air concentration at the cavity tail on the viscous drag of the body are given in Fig. 7 for different body lengths L (Reynolds numbers proportional to $L^{3/2}$). The curves are marked by values of Froude number Fr because the Fr effect on the cavity shape was taken into account in 2D cavity computations. The comparisons of the provided computations with the available experimental data for bodies (in Figs. 3 and 4) manifested the complete qualitative agreement. Both predicted speed effect and air concentration effect coincide with observed effects.

The nature of the difference in dependencies of C_f on $\boldsymbol{\beta_0}$ for plates and bodies is clarified by computational results presented in Fig. 8. The form resistance depends mainly on the δ^* distribution around the stern, and this distribution is significantly affected by $\boldsymbol{\beta_0}$. Thus, the microbubble drag reduction can be explained as a result of variation of the boundary layer thickness and its density

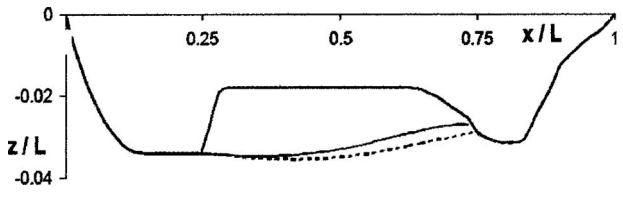

Fig. 5 Buttock of a ship hull with cavities in a recess/niche (the dotted curve shows the cavity surface for Fr=0.54, and the solid curve shows the cavity surface for Fr=0.48). Flow goes from the left, and z is the vertical coordinate; $z=0$ corresponds to the free surface.

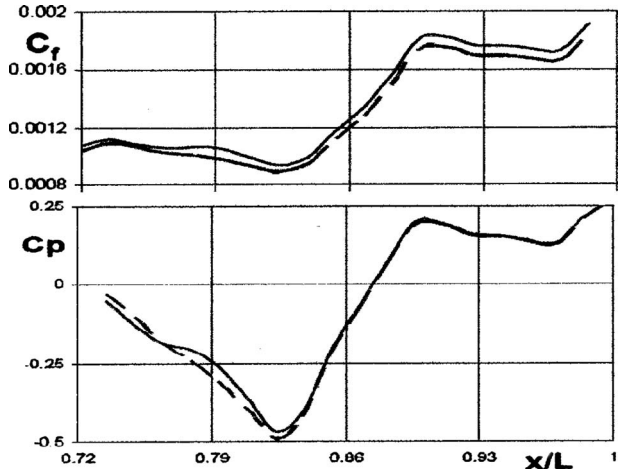

Fig. 6 Comparison of friction coefficient and pressure coefficients along the buttock shown in Fig. 5 at Fr=0.54 (solid line) and Fr=0.48 (dashed line) for $\beta_0=0.2$

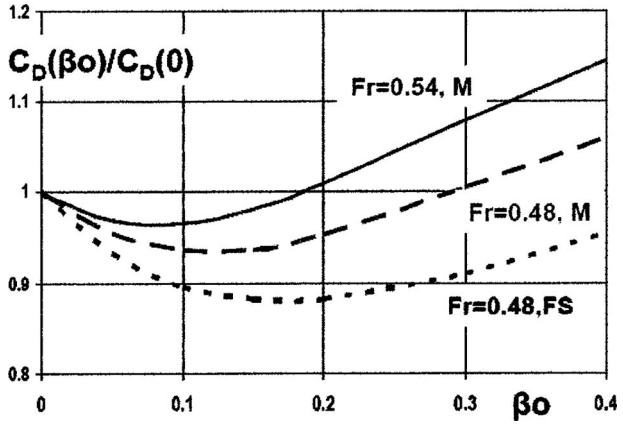

Fig. 7 Ratio of drag coefficient versus air concentration for the buttock shown in Fig. 5. The index M at the curves relates to the buttock of the 5.5 m length, and the index FS relates to 50 m length.

(as should be expected because stresses are proportional [14] to $\rho\delta^{-2}$). No substantial contributions of other physical factors are necessary for this reduction.

Finally, let us employ Fig. 7 for predictions of the combined effect of cavitation and microbubble drag reduction. First of all, regardless of the air flux, the attached cavity covers the same body surface area and provides the same friction reduction. Only distributions of friction and pressure downstream of it are influenced by this flux and will therefore influence the total drag. However, a ship drag includes also the Fr-dependent wave resistance. This drag component was not included in C_D here (therefore, C_D in Fig. 7 represents only the sum of friction and form resistance computed in 2D approach).

For the prediction of the above-mentioned combined effect, the air flux values $Q(L,U_\infty)$ was extrapolated from the water tunnel test data for a similar body [18] with the formula $Q=\alpha LbU_\infty$, where b is the beam and α is a constant found from this extrapolation. After computation of the boundary layer thickness $\delta(Xc)$ at the end of cavity $x=Xc$ and its comparison with Q/bU, one can calculate $\boldsymbol{\beta_0}\approx 0.18$ for the model at Fr=0.48. This concentration would give a 5% of the positive interaction effect for the model buttock shown in Fig. 5. However, taking into account the 3D ship geometry (with no recess for cavity on the hull side surfaces and, correspondingly, a significant fraction of streamlines without friction reduction by air), as well as the share of the wave resistance in the total drag, one may expect a 2% positive effect for the model total drag only. One can also see in Fig. 7 that the value $\boldsymbol{\beta_0}=0.18$ is greater than the optimum and a negative effect will appear with its 50% increase.

For the full scale ($L\approx 50$ m in these computations), the corresponding concentration is $\boldsymbol{\beta_0}\approx 0.14$ and a positive effect of bubbly boundary layer on the stern may go up to 12% for this buttock. As a result, the total drag reduction for the ship would be 4–5% of the total drag. According to Fig. 7, some positive effect will be kept even up to $\boldsymbol{\beta_0}\approx 0.4$.

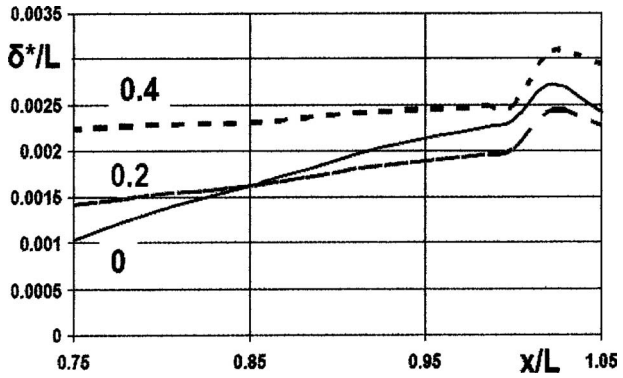

Fig. 8 Distributions of thickness displacement along the part of the buttock shown in Fig. 4 and in the wake near the stern at Fr=0.48 and different values of β_0 (shown at the curves)

4 Conclusions

A simple and comprehensive numerical method for estimation of microbubble effects on boundary layers was developed and successfully validated with the known experimental data on drag reduction for flat plates and bodies.

The qualitative difference in the effects of flow speed and air supply rate on drag of flat plates and bodies was explained. It was shown that microbubble drag reduction takes place mainly due to the density decrease and the thickness increase in the boundary layer with the air concentration (air flux) increase, whereas other physics effects can play additionally roles in this drag reduction phenomenon. On the other hand, this thickness increase augments the body form resistance. Therefore, there are two opposite effects of the air flux increase on the body drag, whereas the second effect does not exist on the flat plates.

A synergy of cavitation drag reduction and microbubble drag reduction was manifested for an example of the body with the partial ventilated cavity maintained in a surface recess. This synergy exists up to some threshold value of air flux from cavity. A more extensive air flux will increase the total drag.

Acknowledgment

The author is grateful to NAVSEA for support of this study (program manager G. Karafiath).

Nomenclature

C_D = total drag coefficient
C_f = friction coefficient
Cp = pressure coefficient
Fr = Froude number
L = body length
M = Mach number
P_C = air pressure in cavity
P_∞ = ambient water pressure
r = ratio of mixture density to water density
Re = Reynolds number
U = velocity on the line separating boundary layer and inviscid flow
U_∞ = freestream speed
u = velocity within the boundary layer (wake)
v^* = friction velocity
w = velocity on the wake axis
x = coordinate counted along the boundary layer (wake)
y = coordinate counted across the boundary layer (wake)
β = air volumetric concentration in the boundary layer
β_0 = value of β at the ejection slot or at the cavity tail
ε = ratio of air density to water density
δ = boundary layer thickness
δ^* = displacement thickness
δ^{**} = momentum thickness
ν = water kinematical viscosity
σ = cavitation number

References

[1] Butuzov, A. A., Gorbachev, Y. N., Ivanov, A. N., Kaluzhny, V. G., and Pavlenko, A. N., 1990, "Ship Drag Reduction by Artificial Gas Cavities," Sudostroenie, **11**, pp. 3–6, in Russian.

[2] Sverchkov, A. V., 2005, "Prospects of Artificial Cavities in Resistance Reduction for Planning Catamarans With Asymmetric Demihulls," International Conference on Fast Sea Transport FAST'2005, St. Petersburg, Russia.

[3] Kopriva, J., Amromin, E. L., and Arndt, R. E. A., 2008, "Improvement of Hydrofoil Performance by Partial Ventilated Cavitation in Steady Flow and Periodic Gusts," ASME J. Fluids Eng., **130**, p. 031301.

[4] Amromin, E. L., 2007, "Design of Bodies With Drag Reduction by Partial Cavitation as an Inverse Ill-Posed Problem for Velocity Potential," NMSH2007 Conference, Ann Arbor, MI.

[5] Kunz, R. F., Deutsch, S., and Lindau, J. W., 2003, "Two Fluid Modeling of Microbubble Turbulent Drag Reduction," ASME Paper No. FEDSM2003-45640.

[6] Kawamura, T., and Nakatani, T., 2006, "Direct Numerical Simulation of Homogeneous Turbulent Shear Flow Containing Bubbles," ASME Paper No. FEDSM2006-98405.

[7] Ichikawa, Y., Sugiyama, K., and Mastumoto, Y., 1995, "Characteristics of Bubbly Flow Around a Circular Cylinder," Symposium on Multiphase Flow-95, Kyoto, Japan, p. 132.

[8] Xu, J., Maxey, M. R., and Karniadakis, G. E., 2002, "Numerical Simulation of Turbulent Drag Reduction Using Micro-Bubbles," J. Fluid Mech., **468**, pp. 271–281.

[9] Merkle, C. L., and Deutsch, S., 1992, "Microbubble Drag Reduction in Liquid Turbulent Boundary Layers," Appl. Mech. Rev., **45**, pp. 103–127.

[10] Kodama, Y., 2003, "On the Skin Friction Reduction Mechanisms of Microbubbles," ASME Paper No. FEDSM2003-45643.

[11] Sanders, W. C., Winkel, E., Dowling, D. R., Perlin, M., and Ceccio, S. L., 2006, "Bubble Friction Drag Reduction in a High Reynolds Number Flat Plate Turbulent Boundary Layer," J. Fluid Mech., **552**, pp. 353–380.

[12] Ceccio, S. L., 2010, "Friction Drag Reduction of External Flows With Bubble and Gas Injection," Annu. Rev. Fluid Mech., **42**, pp. 183–203.

[13] Moriguchi, Y., and Kato, H., 2002, "Influence of Microbubble Diameter and Distribution on Frictional Resistance Reduction," J. Mar. Sci. Technol., **7**, pp. 79–85.

[14] Schlichting, H., and Gersten, K., 1999, *Boundary Layer Theory*, Springer, New York.

[15] Cebeci, T., and Bradshaw, P., 1984, *Physical and Computational Aspects of Convective Head Transfer*, Springer-Verlag, Berlin.

[16] Sanders, W. C., Ivy, I. M., Ceccio, S. L., Dowling, D. R., and Perlin, M., 2003, "Microbubble Drag Reduction at High Reynolds Numbers," ASME Paper No. FEDSM2003-45649.

[17] Amromin, E. L., and Kovinskaya, S. I., 2006, "Numerical Analysis of Reynolds Number Effects on Sheet Cavitation," Sixth International Symposium on Cavitation, Wageningen, The Netherlands.

[18] Arndt, R. E. A., Hambelton, W. T., Kawakami, E., and Amromin, E. L., 2009, "Creation and Maintenance of Cavities Under Horizontal Surfaces in Steady and Gust Flows," ASME J. Fluids Eng., **131**(11), p. 111301.

Mitigation of Damage to Solid Surfaces From the Collapse of Cavitation Bubble Clouds

Parag V. Chitnis[1]
e-mail: pchitnis@rri-usa.org

Nicholas J. Manzi

Robin O. Cleveland

Ronald A. Roy

R. Glynn Holt

Department of Aerospace and Mechanical Engineering and Department of Mechanical Engineering,
Boston University,
110 Cummington Street,
Boston, MA 02215

The collapse of transient bubble clouds near a solid surface was investigated to test a scheme for mitigation of cavitation-induced damage. The target was a porous ceramic disk through which air could be forced. Transient cavitation bubbles were created using a shock-wave lithotripter focused on the surface of the disk. The dynamics of bubble clouds near the ceramic disks were studied for two boundary conditions: no back pressure resulting in surface free of bubbles and 10 psi (0.7 atm) of back pressure, resulting in a surface with a sparse (30% of area) bubble layer. Images of the cavitation near the surface were obtained from a high-speed camera. Additionally, a passive cavitation detector (3.5 MHz focused acoustic transducer) was aligned with the surface. Both the images and the acoustic measurements indicated that bubble clouds near a ceramic face without a bubble layer collapsed onto the boundary, subsequently leading to surface erosion. When a sparse bubble layer was introduced, bubble clouds collapsed away from the surface, thus mitigating cavitation damage. The erosion damage to the ceramic disks after 300 shock waves was quantified using micro-CT imaging. Pitting up to 1 mm deep was measured for the bubble-free surface, and the damage to the bubble surface was too small to be detected. [DOI: 10.1115/1.4001552]

Keywords: cavitation, cavitation erosion, fluid structure interaction, water hammer

1 Introduction

The dynamics of bubbles in fluids have been studied for over a century. When subjected to tension, bubbles grow and subsequently collapse often, resulting in damage to adjacent surfaces. This phenomenon has been studied extensively starting with Lord Rayleigh's investigation of cavitation damage to ship propellers [1]. Two main sources of physical damage associated with cavitation are recognized. The first, and likely dominant mechanism of cavitation damage, is the asymmetric collapse of bubbles in the immediate vicinity of a hydrodynamically rigid boundary, which results in a microjet of fluid, whose impact leads to surface erosion [2–5]. In addition, symmetrically collapsing bubbles produce pressure pulses of large amplitude [6–8], which could lead to stress-induced damage. These cavitation effects present themselves in many medical and industrial applications [9].

Our work is motivated by the potential for cavitation in a vessel of liquid mercury employed in the spallation neutron source (SNS) at Oak Ridge National Laboratory (ORNL). In the SNS, a proton beam is absorbed by the vessel of mercury. The interaction of the protons with the mercury results in a spallation reaction that yields the desired neutrons but also produces megapascal acoustic pulses due to rapid heating and the resulting thermo-elastic expansion of the mercury. The large stresses can drive cavitation in the mercury, which could then damage the walls of the target vessel and require more frequent target replacement [10,11].

We propose a mitigation technique based on altering the dynamics of cavitation in the vicinity of the walls of the vessel. This work was inspired by the study of cavitation dynamics performed by Blake and Gibson [12], where they showed that the direction of the fluid microjet resulting from a cavitating bubble is reversed when the bubble collapses near a free surface. Here, the feasibility of using a bubble wall positioned along a porous surface in order to approximate a hydrodynamically pressure release surface is investigated. We present initial results from a series of experiments designed to demonstrate the reduction in the cavitation activity and erosion damage afforded by the introduction of a "bubble shield." A detailed quantitative analysis and comparison with theoretical predictions will be presented in a companion paper to follow.

2 Experimental Setup

The description of the experimental instrumentations and methods employed is divided into four sections: the electrohydraulic lithotripter used to replicate the cavitation damage in the SNS, the ceramic samples used for producing the different boundary conditions, the diagnostic tools used for monitoring cavitation and characterizing damage, and the experimental protocol.

2.1 Shock Wave Source. Prior studies indicate that cavitation damage induced by the large stress waves in the spallation neutron source is similar to that observed from other mechanical and acoustic devices capable of generating large stress waves including shock-wave lithotripters [10]. The present study employed an electrohydraulic shock-wave lithotripter for generating a cavitation bubble cloud. The GALCIT lithotripter referred to in Ref. [13] is now located at Boston University and was used for these studies. Briefly, an 80 nF capacitor is charged to 20 kV, and then discharged through a spark gap underwater. The high-voltage spark results in the vaporization of water surrounding the electrode. The supersonic expansion of this vapor bubble produces a predominantly compressive, spherically spreading shock wave (SW) that is focused by means of a hemi-ellipsoidal reflector. The negative tail is principally generated by a diffraction from the edge of the reflector [14]. The reflector-electrode assembly was oriented at a 14 deg angle from the vertical to avoid bubbles resulting from the spark discharge from interfering with the propagation of the SW. Figure 1 shows a representative waveform measured at the focus of the lithotripter with a fiber-optic probe hydrophone (FOPH 500, RP Acoustics, Leutenbach, Germany) after

[1]Corresponding author. Also at F. L. Lizzi Center for Biomedical Engineering, Riverside Research Institute, 156 William Street, 9th Floor, New York, NY 10038.

Contributed by the Fluids Engineering Division of ASME for publication in the JOURNAL OF FLUIDS ENGINEERING. Manuscript received April 20, 2009; final manuscript received March 30, 2010; published online May 14, 2010. Assoc. Editor: Steven Ceccio.

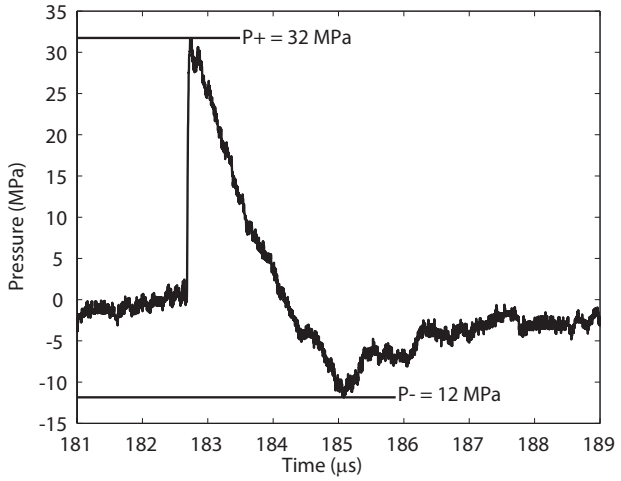

Fig. 1 A representative waveform of the SW measured at the focus of the electrohydraulic lithotripter using a fiber-optic probe hydrophone. The peak positive pressure was 32 MPa and the peak negative pressure was −12 MPa.

deconvolution of the hydrophone's response and calibration [15]. The lithotripter generated a SW with a peak positive pressure of 32 MPa and a peak negative pressure of −12 Mpa. It takes the SW about 175 μs to travel from the spark, to the reflector and then to the focus. The free-field focal region was cigar-shaped, with −6 dB dimensions of 60 mm along the axis of sound propagation and 10 mm in the lateral direction [13]. The 5-μs long SW generates a bubble cloud, which undergoes unstable growth, followed by inertially driven collapse (on both the individual bubble and cloud scales) with a life time ranging from 300 μs to 600 μs in the free field [16]. The shot-to-shot variability of over 25% in the amplitude of the SWs produced by the electrohydraulic lithotripter is the primary reason for the variability in the cavitation life time.

2.2 Damage Target. Porous ceramic disks (0604D00.5-B0.5M2, Soil Moisture, Santa Barbara, CA), which are completely submerged in water, were used for evaluating damage inflicted by cavitation on the boundary. The ceramic disks were 25.4 mm in diameter and 12.8 mm thick. The reported volume porosity, effective pore size, and mass density of the ceramic samples were 50%, 6 μm, and 1092 kg/m^3, respectively. The boundary condition of the ceramic samples was altered by forcing air through the ceramic. Two boundaries were investigated: one with bubbles at the surface and one without. In order to force air through the ceramic disks they were bonded to a polyvinyl chloride (PVC) housing, as shown in Fig. 2, and connected to a compressed air supply. The back pressure was controllable between 0 psi and 30

Fig. 2 The porous ceramic disk was mounted in a PVC housing to facilitate the gas flow through the ceramic disk

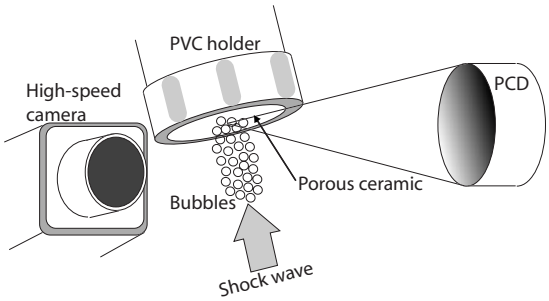

Fig. 3 The schematic of the experimental setup

psi by means of a regulator (VWR Scientific 55850-150). The sample and housing were submerged underwater at an angle of 14 deg such that the propagation axis of the incident SW was normal to the face of the ceramic sample.

For the case of no back pressure (regulator in the "off" position), the pores were partially saturated with water. When a back pressure of 0.7 atm (10 psi) was maintained, active bubbling occurred at the front face of the disk. Photographs of the front face indicated that approximately 30% of the ceramic face was covered with bubbles (on average) and the bubble layer comprised of bubbles ranging from 0.5 mm to 1 mm in diameter and was approximately 1 mm thick.

2.3 Cavitation Diagnostics. The dynamics of cavitation bubbles clouds near the ceramic surface, with and without a sparse bubble layer, was observed using a high-speed digital camera (Imacon 200, DRS Data and Imaging Systems, Inc., Oakland, New Jersey) capable of recording up to 14 images with a resolution of 1200×980 pixels and a maximum frame-rate of 100 $\times 10^6$ frames per second. Backlit images were obtained at 80 μs intervals with an exposure time of 100 ns for each frame.

Cavitation activity was also monitored using a passive cavitation detector (PCD) [17,18] consisting of a 3.5 MHz focused transducer (Panametrics/Olympus-NDT, Waltham, MA). The PCD had a radius of curvature of 50.8 mm, an aperture diameter of 25.4 mm, and a −6 dB focal beam diameter of 1.3 mm in the free field. The PCD was confocally aligned to the lithotripter focus, as shown in Fig. 3. For every SW fired, a corresponding PCD measurement was acquired at a sampling rate of 25 MHz. PCD traces were recorded for a 2 ms time window, where 0 ms corresponded to the firing of the spark. The PCD was expected to detect two signatures: a signal corresponding to the scattering of the incident SW at the ceramic face and transients corresponding to the subsequent inertial collapse of the bubbles, provided that the collapsing bubbles were in the detection volume, i.e., the focal beam of the PCD.

2.4 Experimental Protocol. A total of ten ceramic disks were investigated. A back pressure of 10 psi (0.7 atm) was applied to five samples, resulting in a protective bubble layer, while the remaining were maintained at 0 psi (0 atm) to provide control samples without a bubble layer. Before each experiment, the water in the lithotripter tank was filtered and degassed for 1 h (dissolved O_2 content reduced to under 5 ppm) to enhance the likelihood of producing inertial cavitation. Because the bubbles resulting from gas-injection through the porous ceramic ranged in size from 0.5 mm to 1 mm, these bubbles, once released from the ceramic surface, rose to the water surface and were expelled. Therefore, gas-injection should have had a minimal effect on the quality of the water or its propensity to host inertial cavitation.

The PVC holder with the ceramic sample was positioned in the water with the front face of the ceramic disk aligned at the lithotripter focus normal to the acoustic axis and also providing an acoustic path for cavitation signals to travel to the PCD. The back pressure was then adjusted to either 0 psi (0 atm) or 10 psi (0.7

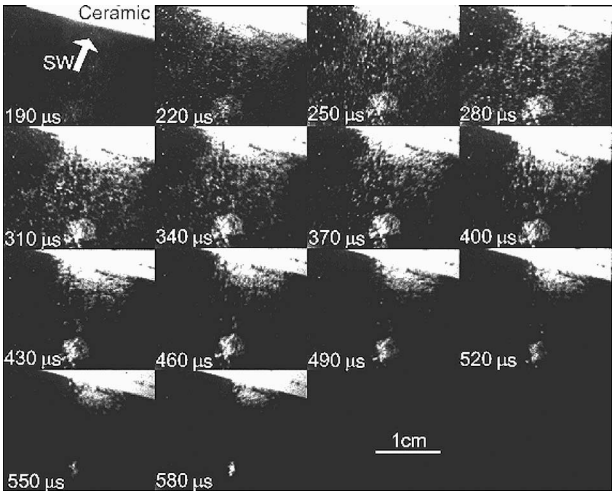

Fig. 4 A sequence of high-speed camera images for a bubble cloud collapsing near a ceramic face without a bubble layer (0 psi (0 bars) back pressure). The SW is normally incident at the ceramic face and time=0 μs represents the firing of the SW.

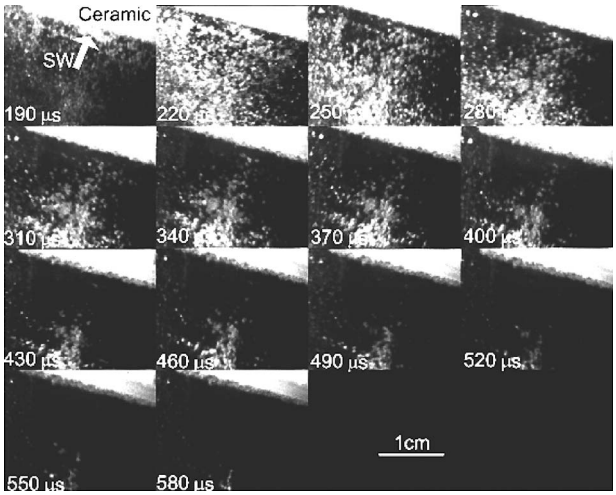

Fig. 5 A sequence of high-speed camera images for a bubble cloud collapsing near a ceramic face with a sparse bubble layer (10 psi (0.7 bars) back pressure). The SW is normally incident at the ceramic face and time=0 μs represents the firing of the SW.

atm). Each sample was treated with 300 SWs fired at a rate of 1 Hz. After the SWs had been delivered, the disk and housing were removed from the tank and allowed to dry overnight. The ceramic disks were then removed from the PVC housing, and a 15 mm core piece, corresponding to the region exposed to cavitation, was cut from the disk. The excised sample was then scanned using a X-ray microcomputed tomography (CT) (Scanco 40, Scanco USA, PA) to produce a 3D map of the sample with an isotropic voxel size of 20 μm. The resulting 3D data sets were processed and analyzed using MATLAB (The Mathworks, Inc., Natick, MA). Three parameters associated with the damage were extracted from the processed images: maximum depth or penetration, the net cross-sectional area of erosion, and the net volume of erosion.

3 Results

The results will be presented in three sections. First, the qualitative details of the cavitation dynamics observed using the high-speed camera will be discussed. Second, PCD measurements of emissions resulting the cavitation collapses will be presented. Third, quantitative results describing the damage induced by cavitation acquired using the X-ray computed tomography will be shown.

3.1 High-Speed Camera. The high-speed camera was used to observe the bubbles clouds growing and collapsing in the vicinity of the surface in response to the lithotripter SW. Figure 4 shows a representative sequence of images for a bubble cloud collapsing near a porous ceramic sample without a bubble layer. The time that the SW is fired was designated as 0 μs, and the SW arrived at the sample at approximately 175 μs. The tensile phase of the SW led to the growth of bubbles. At 220 μs (i.e, 45 μs after the SW was incident on the disk), a large number of small bubbles were visible near the boundary. The bubbles continued to grow in size, while the bubble cloud appeared to remain attached to the proximal face of the ceramic sample, as seen in the frame captured at 340 μs. At 490 μs, the bubble cloud started to diminish in size. The bubble cloud eventually collapsed, and the convergence of the implosion remained in close proximity of the ceramic disk as evident from the frame captured at 580 μs. This manner of bubble cloud growth and collapse in the vicinity of a surface is known to result in the formation of liquid microjets that can induce surface erosion [19]. These jets are not explicitly visible in the image due to the relatively low resolution of the camera. The visual observations of cavitation dynamics in the vicinity of this sample confirmed that in the absence of a bubble layer, the proximal face of the porous ceramic disk acts like a hydrodynamically rigid boundary. This is a situation where cavitation clouds collapse toward the boundary, leading to jetting toward the surface and pitting damage.

Figure 5 shows a representative sequence of images, showing the bubble cloud dynamics near a porous ceramic sample with a sparse bubble layer at the proximal face when air was forced through the ceramic at 0.7 atm. At 190 μs a large number of small bubbles were observed near the boundary, significantly more than for the case of no back pressure. Gas injection through the porous ceramic likely increased the number of cavitation nuclei, leading to the larger bubble cloud. However, unlike the case with no bubble layer, the SW-induced bubble cloud separated from the ceramic face. The bubble cloud remained detached from the ceramic sample as it collapsed. The convergence of the imploding bubble cloud was almost 10 mm away from the proximal face of the ceramic disk as observed from the frame captured at 580 μs. These images indicated that the sparse bubble layer anchored to an otherwise hydrodynamically rigid surface changed the overall behavior of the cavitation cloud near the boundary. Because the collapse occurred away from the ceramic boundary, SW-induced cavitation, in this case, was not expected to produce damage typically associated with fluid microjets resulting from cavitating microbubbles, and the surface was thus protected from fluid-microjet-induced erosion. High-speed camera observations for ceramic disks with a bubble layer and those without were reproducible and consistent with the proposed hypothesis.

3.2 Passive Cavitation Detection. Measurements of acoustic transients resulting from cavitation collapse induced by the incident SWs were measured using a PCD consisting of a 3.5 MHz focused transducer. Representative measurements (overlaid PCD traces corresponding to each of the 300 SWs) for a ceramic sample in each category are shown in Fig. 6. The PCD traces exhibited two distinct signals. The signal arriving at about 175 μs corresponded to the SW scattered from the ceramic face and forced collapse of any pre-existing bubbles due to the large compressive pressure of the SW. The signal arriving between 600 μs and 1000 μs can be attributed to acoustic emissions resulting from the inertial collapse of bubble clouds induced by the incident SW. These signatures and their time scales are consistent with what has been reported in lithotripsy [16]. Since the proximal surface of the ceramic samples was aligned at the lithotripter fo-

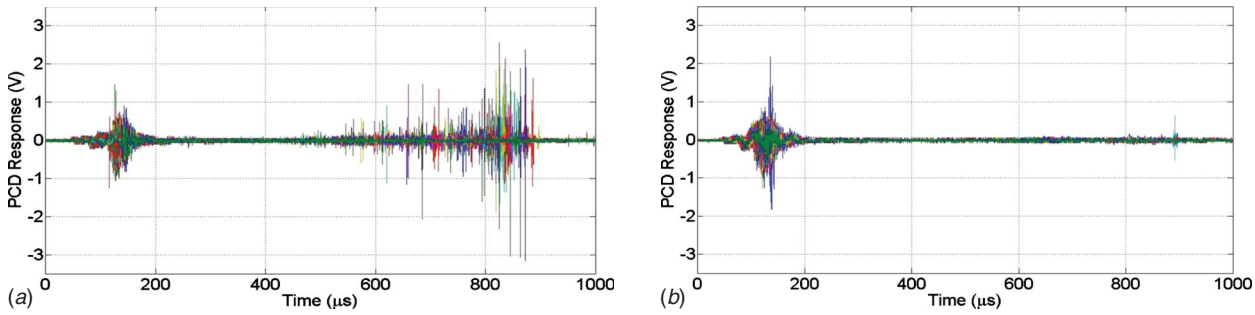

Fig. 6 Measurements of the acoustic emissions acquired using a passive cavitation detector (a focused 3.5 MHz transducer) confocal to the lithotripter: (*a*) no bubble layer, 0 psi (0 bar); (*b*) sparse bubble layer, 10 psi (0.7 bar). Both (*a*) and (*b*) depict all 300 waveforms acquired for each ceramic sample. Acoustic emissions detected between 600 μs and 1000 μs represent noise from inertial cavitation collapses within or near the sensing volume of the PCD, which is positioned confocal with the lithotripter focus.

cus and the PCD has a narrow −6 dB beam diameter of 1.3 mm, the acoustic signals detected by the PCD are limited to those originating at the portion of the ceramic face in the lithotripter focus. For the ceramic sample without a bubble layer, 293 out of 300 incident SWs resulted in detectable acoustic transients resulting from inertial cavitation. The time of the inertial collapse varied from 615 μs to 985 μs. For the ceramic sample with a sparse bubble layer, detectable transients that could be attributed to an inertial cavitation collapse was detected at the face of the sample for only two out of 300 incident SWs. The PCD measurements consistently indicated an acoustic emission corresponding to the inertial cavitation collapse of the bubble cloud at the surface of the ceramic samples without a protective bubble layer. Conversely, the PCD consistently failed to detect the signatures associated with inertial cavitation at the surface of the ceramic samples with a protective bubble layer.

The strength of the inertial cavitation observed by PCD was characterized by the following: number of detected events, amplitude (A) of acoustic emission detected, and the characteristic time (T_c) defined as the duration from the growth until the collapse of the bubble cloud. Table 1 shows the number of cavitation events detected at the ceramic face using the PCD, the corresponding mean amplitude of the acoustic emissions, and the corresponding mean characteristic times for each ceramic sample. These PCD measurements are consistent with the high-speed camera images and indicate that the sparse bubble layer inhibits inertial cavitation collapses at the proximal face of the ceramic sample. The PCD traces also indicate that the bubbles injected through the ceramic sample, though likely serve as nuclei for inertial cavitation, do not lead to inertial collapse at the surface of the ceramic sample.

3.3 Damage Characterization. The damage resulting from cavitation induced by incident SWs was quantified using X-ray microcomputed tomography. Each of the ten ceramic samples (five samples without a bubble layer and five samples with a sparse bubble layer) were scanned.

Figure 7 depicts surface renderings of two representative samples: one that was not protected by a bubble layer (Fig. 7(*a*)) and one that was (Fig. 7(*b*)). Here, the undamaged surface defines the x-y plane, and the z-coordinate is projected into the ceramic; positive i corresponds to surface erosion. The surface rendering shows that cavitation induced a significant erosion crater on the front surface of the unprotected ceramic sample. After 300 SWs, the resulting damage had a maximum depth of 0.87 mm, a surface area of 3.81 mm^2, and a volume of 0.73 mm^3. In stark contrast, the surface of the sample possessing a sparse bubble layer displayed no detectable damage down to the resolution of the micro-CT (20 μm).

Table 2 shows the summary of damage parameters obtained from the microCT scans for the ten samples. For all ceramic samples without a bubble layer, significant damage was observed. The damage characterization indicated sample to sample variations, which could be attributed to shot-to-shot variation in the incident SWs and variations within the ceramic samples. Of the five ceramic samples with a sparse bubble layer at the proximal surface, only one sample showed quantifiable indication of cavitation-induced damage. This damage was an order of magnitude less than the samples with no bubble layer.

4 Discussion

The results presented here demonstrate that a sparse bubble layer (30% area coverage) with large bubbles (0.5–1 mm in diameter) alters the dynamics of inertially collapsing bubble clouds and could be used to mitigate cavitation-induced surface damage. Because of their relatively large size, the majority of the injected bubbles rose to the water surface and were expelled from the fluid. Therefore, injection of air should have had a minimal effect on the

Table 1 Cavitation parameters obtained from PCD measurements; # events: number of cavitation events detected by the PCD, A: amplitude, and T_c: characteristic time. A and T_c values are given as mean ±1 standard deviations for cases with more than two detected events.

	No bubble layer			Sparse bubble layer		
Trial	# events	A (V)	T_c (μs)	# events	A (V)	T_c (μs)
1	293	0.36 ± 0.19	662 ± 97	2	0.22	304
2	180	0.34 ± 0.18	578 ± 120	1	0.14	360
3	189	0.18 ± 0.05	615 ± 77	1	0.24	312
4	292	0.38 ± 0.20	632 ± 102	9	0.18 ± 0.05	501 ± 173
5	229	0.23 ± 0.11	652 ± 67	1	0.16	325

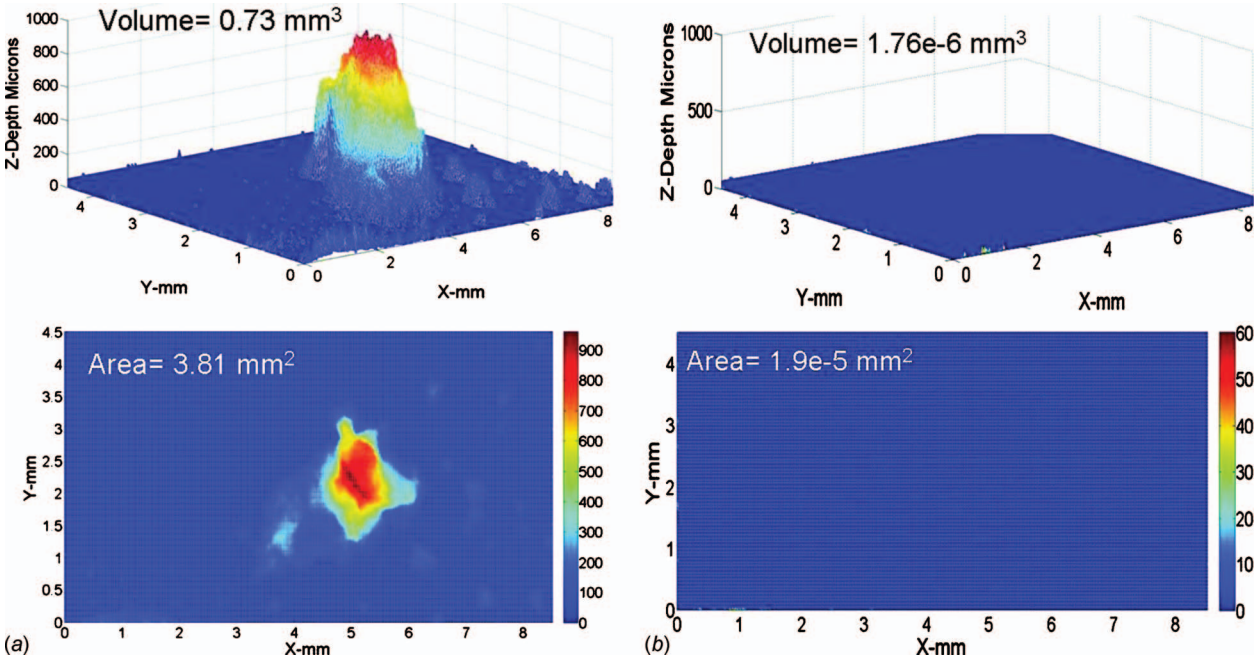

Fig. 7 Representative X-ray tomography scans acquired after SW treatment for ceramic samples with hydrodynamically rigid and hydrodynamically compliant boundaries. The *Z*-coordinate is normal to the undamaged surface and projected inwards toward the ceramic. (*a* no bubble layer, 0 psi (0 bar)) Cavitation induced by the incident SWs resulted in significant quantifiable damage to the ceramic sample. (*b* sparse bubble layer, 10 psi (0.7 bar)). The ceramic sample with a sparse bubble layer did not suffer any cavitation-induced damage.

water quality or the nature of cavitation at the ceramic surface. The bubbles resulting from SW-induced inertial cavitation were considered to be predominantly vapor bubbles with similar potential for cavitation-induced damage in both cases.

The high-speed camera images indicated that the presence of the bubble shield resulted in the bubble cloud collapse with a convergence point roughly 10 mm from the ceramic face. Measurement of acoustic emissions from the surface indicated that less than 1% of the SWs produced cavitation that collapsed on the surface. Erosion studies demonstrated that the ceramic samples with the bubble shield did not suffer any detectable cavitation-related damage. However, in the absence of a protective bubble shield, millimeter size craters were formed on all the ceramic samples. Although damage mitigation was achieved by reducing the occurrence of violent inertial cavitation collapse at the ceramic face, merely the presence of the gas bubbles on the surface is insufficient to explain this effect. The injected bubbles do not cover the entire ceramic face, and the SW-induced growth of the cavitation bubble cloud in cases with and without a bubble layer start at the ceramic surface. Based on the visual observations and the collapse times of the bubble clouds, the violence or the strength of the cloud collapses in both cases are comparable. Therefore, the difference in the damage inflicted by the bubble cloud in the two cases could be attributed to the change in dynamics of the bubble cloud similar to that observed for a single bubble collapse near a rigid (ceramic face with no bubble layer) and a compliant (ceramic face with a bubble layer) boundary [12].

The bubble wall was created by bubbling gas through the porous ceramic. One possible concern is that by producing bubbles right at the wall one, could result in greater cavitation damage as these bubbles could grow and collapse in response to the incident SW. The video images suggest that these injected bubbles did in fact serve to nucleate cavitation during the rarefaction portion of the incident SW. However, the governing hydrodynamics caused the collapsing bubble cloud to translate away from the boundary and outside the sensing volume of the PCD. The net result was a cessation of both detected cavitation collapse noise and surface damage. Furthermore, bubbles created at the ceramic surface were relatively large (>200 μm), and numerical simulations of single bubbles in response to a incident SW indicate that the injected gas bubbles in this size range do not collapse violently [20,21], and therefore, should not induce damage. It may be that a bubble layer consisting of small bubbles (less than 10 μm) may respond inertially to a SW, and so would not provide the protection reported here.

Table 2 Parameters for damage characterization from X-ray computed tomography; *D*: depth, *A*: surface area, and *V*: volume

	No bubble layer			Sparse bubble layer		
Trial #	*D* (mm)	*A* (mm^2)	*V* (mm^3)	*D* (mm)	*A* (mm^2)	*V* (mm^3)
1	0.87	3.81	0.73	0	0	0
2	0.99	16.9	7.90	0	0	0
3	0.39	1.62	0.14	0.06	0.18	0.01
4	0.42	2.94	0.15	0	0	0
5	0.90	4.09	0.91	0	0	0

5 Conclusion

The concept of mitigating cavitation-induced damage by employing a protective bubble layer was inspired by the studies of Blake and Gibson [12], which had shown that single bubbles collapsing near a rigid boundary result in a microjet toward the boundary, whereas single bubbles near a free-surface jet away from the boundary. Ongoing studies at Boston University indicate that single bubbles collapsing near a boundary consisting of a sparse bubble layer also jet away from the surface. In the data reported here the cavitation consisted of bubble clouds rather than single bubbles; however, the same qualitative trends were observed. Using a high-speed camera and a micro-CT imaging system, we determined that a bubble cloud near the otherwise bubble-free surface collapsed toward the surface and resulted in extensive surface erosion. Conversely, a bubble cloud collapsing near a sparse bubble layer collapsed away from the surface and did not result in surface erosion. Using a passive cavitation detector configured to sense inertial cavitation noise emanating from the region where the SW impacts the surface, it was possible to correlate the absence of surface cavitation noise with the absence of surface damage.

In conclusion we have shown that a sparse bubble cloud can protect a surface from cavitation damage. Further investigations are necessary to determine the optimal parameters for damage mitigation, for example, the portion of the surface that needs to be covered and the sizes of the bubbles that should be present.

Acknowledgment

This work was supported by the ORNL Spallation Neutron Source, which is managed by UT-Battelle, LLC, under Contract No. DE-AC05-00OR22725 for the U.S. Department of Energy. The authors would like to thank Bernie Riemer of ORNL for many helpful discussions, Dr. Elise Morgan and Zach Mason for providing access to X-ray computed tomography scanner, and Dr. Michael Bailey for providing access to the high-speed camera.

References

[1] Rayleigh, L., 1917, "On the Pressure Developed in a Liquid During the Collapse of a Spherical Cavity," Philos. Mag., **34**, pp. 94–98.
[2] Plesset, M. S., and Chapman, R. B., 1971, "Collapse of an Initially Spherically Vapour Cavity in the Neighborhood of a Solid Boundary," J. Fluid Mech., **47**(2), pp. 283–290.
[3] Crum, L. A., 1988, "Cavitation Micro-Jets as a Contributory Mechanism for Renal Calculi Disintegration in ESWL," J. Urol., **140**, pp. 1587–1590.
[4] Vogel, A., and Lauterborn, W., 1988, "Acoustic Transient Generation by Laser-Produced Cavitation Bubbles Near Solid Boundaries," J. Acoust. Soc. Am., **84**(2), pp. 719–731.
[5] Coleman, A. J., Saunders, J. E., Crum, L. A., and Dyson, M., 1987, "Acoustic Cavitation Generated by an Extracorporeal Shock Wave Lithotripter," Ultrasound Med. Biol., **13**(2), pp. 69–76.
[6] Coleman, A. J., Choi, M. J., Saunders, J. E., and Leighton, T. G., 1992, "Acoustic Emission and Sonoluminescence Due to Cavitation at the Beam Focus of an Electrohydraulic Lithotripter," Ultrasound Med. Biol., **18**(3), pp. 267–281.
[7] Xi, X., and Zhong, P., 2001, "Dynamic Photoelastic Study of the Transient Stress Fields in Solids During Shock Wave Lithotripsy," J. Acoust. Soc. Am., **109**(3), pp. 1226–1239.
[8] Chitnis, P. V., and Cleveland, R. O., 2006, "Quantitative Measurements of Acoustic Emissions From Cavitation at the Surface of a Stone in Response to a Lithotripter Shock Wave," J. Acoust. Soc. Am., **119**(4), pp. 1929–1932.
[9] Leighton, T., 1997, *The Acoustic Bubble*, Academic, Boston, MA.
[10] Haines, J. R., Riemer, B. W., Felde, D. K., Hunn, J. D., Pawel, S. J., and Tsai, C. C., 2005, "Summary of Cavitation Erosion Investigations for the SNS Mercury Target," J. Nucl. Mater., **343**, pp. 58–69.
[11] Futakawa, M., Kogawa, H., Hasegawa, S., Ikeda, Y., Riemer, B., Wendel, M., Haines, J., Bauer, G., Naoe, T., and Tanaka, N., 2006, "Cavitation Erosion by Proton Beam Bombarding Mercury Target for Spallation Neutron Source-Damage Potential Evaluation by Measuring Acoustic Vibration," *Proceedings of the Sixth International Symposium on Cavitation*, Wageningen, The Netherlands.
[12] Blake, J. R., and Gibson, D. C., 1981, "Growth and Collapse of a Vapor Cavity Near a Free Surface," J. Fluid Mech., **111**, pp. 123–140.
[13] Cleveland, R. O., Bailey, M. R., Fineberg, N., Hartenbaum, B., McAteer, J. A., and Sturtevant, B., 2000, "Design and Characterization of a Research Electrohydraulic Lithotripter Patterned After Dornier HM3," Rev. Sci. Instrum., **71**(6), pp. 2514–2524.
[14] Averkiou, M. A., and Cleveland, R. O., 1999, "Modeling of an Electrohydraulic Lithotripter With the KZK Equation," J. Acoust. Soc. Am., **106**(1), pp. 102–112.
[15] Staudenraus, J. and Eisenmenger, W., 1993, "Fiber-Optic Probe Hydrophone for Ultrasonic and Shock-Wave Measurements in Water," Ultrasonics, **31**(4)267–273.
[16] Bailey, M. R., Blackstock, D. T., Cleveland, R. O., and Crum, L. A., 1999, "Comparison of Electrohydraulic Lithotripters With Rigid and Pressure-Release Ellipsoidal Reflectors. II. Cavitation fields," J. Acoust. Soc. Am., **106**(2), pp. 1149–1160.
[17] Coakley, W. T., 1971, "Acoustical Detection of Single Cavitation Events in a Focused Field in Water at 1 MHz," J. Acoust. Soc. Am., **49**, pp. 792–801.
[18] Cleveland, R. O., Sapozhnikov, O. A., Bailey, M. R., and Crum, L. A., 2000, "A Dual Passive Cavitation Detector for Localized Detection of Lithotripsy-Induced Cavitation In Vivo," J. Acoust. Soc. Am., **107**(3), pp. 1745–1758.
[19] Pishchalnikov, Y. A., Sapozhnikov, O. A., and Bailey, M. R., 2003, "Cavitation Bubble Cluster Activity in the Breakage of Kidney Stones by Lithotripter Shock Waves," J. Endourol, **17**, pp. 435–446.
[20] Gilmore, F. R., 1952, "The Growth or Collapse of Spherical Bubble in a Viscous Compressible Liquid," Report No. 26-4, Office of Naval Research.
[21] Church, C. C., 1989, "A Theoretical Study of Cavitation Generated by an Extracorporeal Shock Wave Lithotripter," J. Acoust. Soc. Am., **86**(1), pp. 215–227.

Shape Optimization of a Multi-Element Foil Using an Evolutionary Algorithm

Yu-Tai Lee
Naval Surface Warfare Center,
Carderock Division,
West Bethesda, MD 20817
e-mail: yu.lee@navy.mil

Vineet Ahuja

Ashvin Hosangadi

CRAFT Tech,
Pipersville, PA 18947

Michael Ebert
Naval Surface Warfare Center,
Carderock Division,
West Bethesda, MD 20817

A movable flap with a NACA foil cross section serves as a common control surface for underwater marine vehicles. To augment the functionality of the control surface, a tab assisted control (TAC) surface was experimentally tested to improve its performance especially at large angles of operation. The advantage of the TAC foil could be further enhanced with shape memory alloy (SMA) actuators to control the rear portion of the control surface to form a flexible tab (or FlexTAC) surface. Hybrid unstructured Reynolds averaged Navier–Stokes (RANS) based computational fluid dynamics (CFD) calculations were used to understand the flow physics associated with the multi-element FlexTAC foil with a stabilizer, a flap, and a flexible tab. The prediction results were also compared with the measured data obtained from both the TAC and the FlexTAC experiments. The simulations help explain subtle differences in performance of the multi-element airfoil concepts. The RANS solutions also predict the forces and moments on the surface of the hydrofoil with reasonable accuracy and the RANS procedure is found to be critical for use in a design optimization framework because of the importance of flow separation/turbulent effects in the gap region between the stabilizer and the flap. A systematic optimization study was also carried out with a genetic algorithm (GA) based design optimization procedure. This procedure searches the complex design landscape in an efficient and parallel manner. The fitness evaluations in the optimization procedure were performed with the RANS based CFD simulations. The mesh regeneration was carried out in an automated manner through a scripting process within the grid generator. The optimization calculation is performed simultaneously on both the stabilizer and the nonflexible portion of the flap. Shape changes to the trailing edge of the stabilizer strongly influence the secondary flow patterns that set up in the gap region between the stabilizer and the flap. They were found to have a profound influence on force and moment characteristics of the multi-element airfoil. A new control surface (OptimTAC) was constructed as a result of the design optimization calculation and was shown to have improved lift, drag, and torque characteristics over the original FlexTAC airfoil at high flap angles. [DOI: 10.1115/1.4001343]

1 Introduction

Multi-element airfoils are commonly used as control surfaces in underwater marine vehicles. At high angles of attack the torque required to operate the control surface increases significantly thereby limiting the functionality of these systems. Several design concepts have been considered to alleviate these operational difficulties with the multi-element airfoils. One such solution is the tab assisted control (TAC) foil, shown in Fig. 1(*a*), where a rigid tab was added to the flap section of the foil. The reason for adding a tab to the control surface is to enhance the capabilities of the foil through significant modification of lift and torque on the control surface. However, inclusion of the tab introduces other challenges that stem from the inclusion of an additional moving part and its drive and control mechanism. Most significantly, the tab control produces another gap between the flap and the tab. A second concept involved the utilization of shape memory alloy (SMA) actuator [1], as shown in Fig. 2, for obtaining a flexible foil configuration that could adapt to the flow and operating conditions. Employing SMA actuator enables the use of electric power to manipulate the control surface and eliminates the need for hydraulic systems and the gap between the flap and the tab. These advantages led to the development of the flexible tab assisted control (FlexTAC) surface, which has an integrated flap, i.e., no gap exists between the flap and the tab, for the current application.

To understand the operation of the TAC and FlexTAC foil concepts detailed water-tunnel tests were carried out. The TAC airfoil was tested in the 24 in. water tunnel at the Naval Surface Warfare Center, Carderock Division (NSWCCD) in 1998 [2]. The test TAC foil contained (1) a pedestal to minimize the water-tunnel bottom-wall boundary-layer effect on the measured forces and moments and (2) gudgeons to connect the stabilizer, the flap, and the tab and to control their relative motions. These gudgeons affected the gap flowfields, which in turn affected the torque and lift performance of the TAC airfoil. The FlexTAC foil tests [3] were conducted in 2002 at the NSWCCD's 36 in. water-tunnel and did not have the pedestal and gudgeons, as shown in Fig. 3. The length of the flexible tab, accounting for 20% of the flap foil chord, was determined based on early optimization studies [4]. However, the stabilizer for the FlexTAC experiment was installed with a turbulent-flow stimulator near the foil's leading edge. Although the two experiments deal with a similar foil shape, which have the similar augmentation capability in enhancing the forces, they show subtle differences in the torques produced.

Sung and co-workers [5,6] used CFD simulations to predict forces and moments on the TAC foil. The agreement of their CFD results with the measured data was good but the comparisons were restricted to the linear portion of the data. Although three relative angular settings between the stabilizer, flap, and tab were studied experimentally, the numerical investigations [6] were limited to only one angular position for their comparisons. In addition, the

Contributed by the Fluids Engineering Division of ASME for publication in the JOURNAL OF FLUIDS ENGINEERING. Manuscript received September 17, 2009; final manuscript received February 19, 2010; published online April 28, 2010. Assoc. Editor: Paul Durbin.

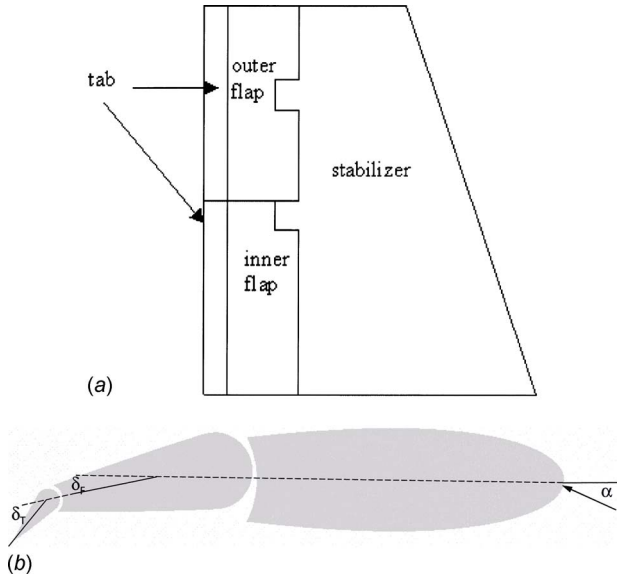

Fig. 1 Schematics of TAC foil tested in the 0.61m (24 in) water-tunnel (*a*) overall foil (*b*) a cross section with defined angles

effects of the gaps between the stabilizer and the flap and between the flap and the tab were neglected in Ref. [5] and not addressed in Ref. [6]. In this paper high fidelity unstructured Reynolds averaged Navier–Stokes (RANS) simulations [7–9] were used to predict flowfields associated with both TAC and FlexTAC foils. The predictions were compared with the measured data obtained from both experiments. The comparisons not only lead to the identification of the differences that existed between the two data sets but also provide the validation that demonstrates the predicted forces and moments acting on the foil are of adequate accuracy. Furthermore, our understanding of the operation of this class of multi-element foils was supplemented by design optimization studies, where RANS based CFD computational framework was used to evaluate the fitness of the designs generated by the optimizer.

Early work [4] with optimization calculations for the multi-element foil provided guidelines in choosing the length for the flexible tab in constructing the FlexTAC foil shape. The resulting

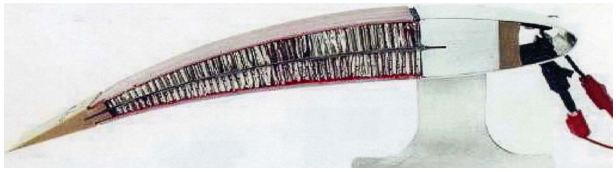

Fig. 2 Foil instrumented and actuated with SMA wires

foil shapes [4] were, however, not realistic due to the deficiency in locating the global maximum or minimum with a gradient scheme used in the search process. In the present paper, an evolutionary algorithm is coupled with the CFD calculations in seeking an optimal configuration. This evolutionary scheme is based on a GA based search procedure. It has the advantage of easily handling complex constraints and objectives and avoiding local extremes. The utilization of the hybrid unstructured CFD methodology provides flexibility in incorporating large changes in shape. The mesh regeneration was carried out in an automated manner through a scripting process within the grid generator. The optimization calculation was performed simultaneously on both the stabilizer and the flap since the flow in the gap region is critical to the performance of the multi-element airfoil. The resultant shapes selected from the knowledge base of the optimization landscape are compared. A 3D OptimTAC control surface was constructed from the results of the 2D design optimization study and was extensively evaluated with CFD and compared against the FlexTAC experiments.

In the following sections, we discuss CFD validation of the FlexTAC and TAC multi-element airfoils. This is followed by a discussion of our design optimization framework and results of the design optimization studies. CFD simulations on the 3D OptimTAC airfoil are discussed next after which we conclude with a summary of the salient features of our optimized design and lessons learned through the design process.

2 Validation Studies of TAC and FlexTAC Foils

In this section we discuss CFD simulations of both the TAC and FlexTAC foils and compare these against detailed water-tunnel measurements. The CFD simulations were performed utilizing multi-element unstructured grids using the incompressible RANS approach [7–9] with a finite-volume formulation and a two-

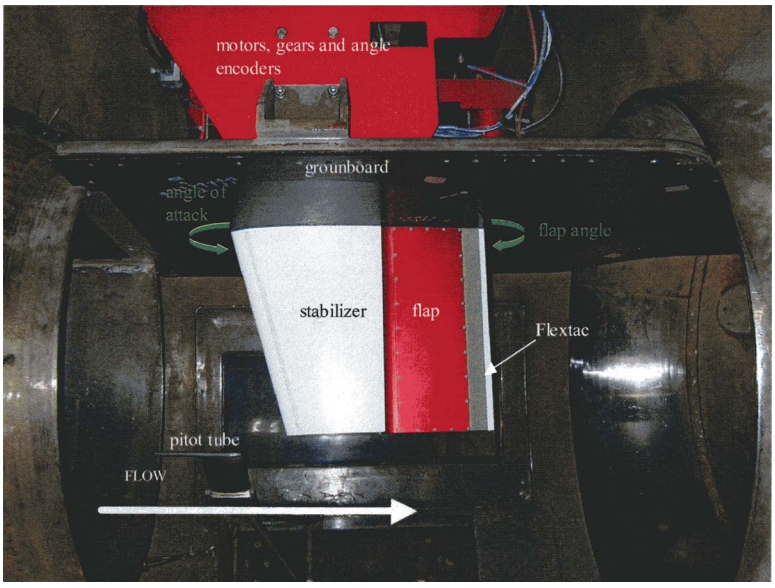

Fig. 3 FlexTAC foil in the 0.91m (36 in) water-tunnel

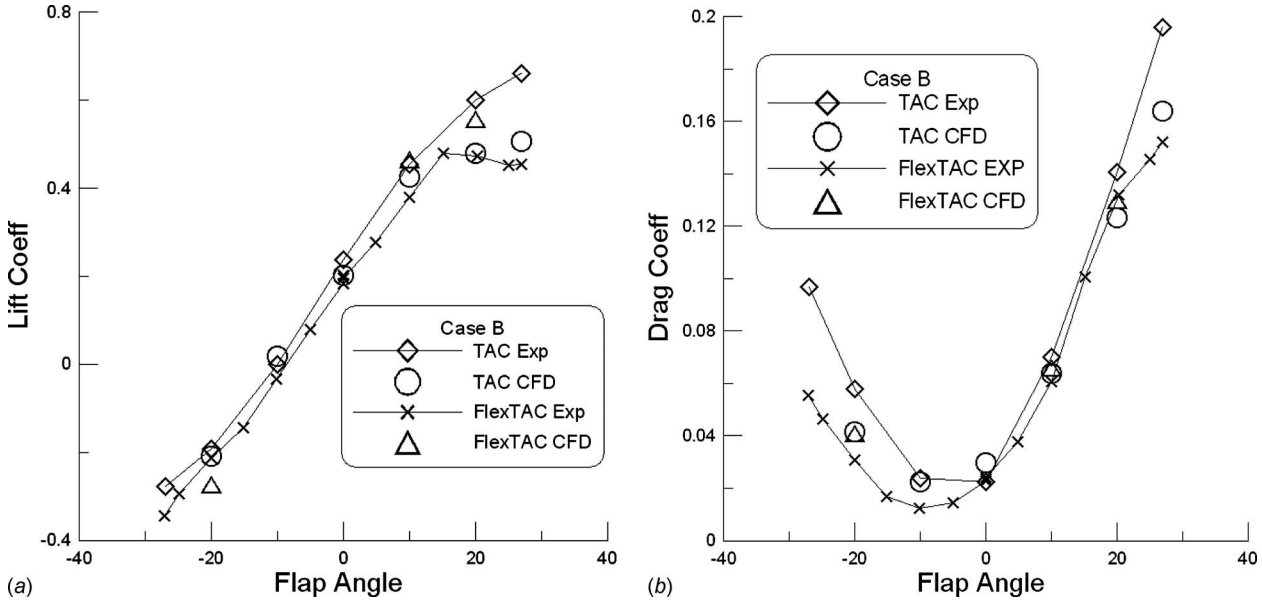

Fig. 4 Force comparisons for TAC and FlexTAC foils

equation turbulence model. The CFD codes utilize second-order spatial discretization and implicit generalized minimal residual, Gauss–Seidel schemes for numerical integration. They are suitable for parallel processing using massage-passing interface for interprocessor communication and automated load balancing for domain decomposition. The computational domains typically used in these simulations extend five chord lengths upstream and ten chords downstream of the foils, five chord lengths in the transverse direction and seven chord lengths in the spanwise direction. The computational domains were judiciously chosen such that the pressure distribution on the foil is grid independent. A typical grid used in the validation study was approximately 3.5×10^6 cells. A symmetry boundary condition was applied on the plane formed by the root section of the foil and a far-field boundary condition was employed at the outer boundaries, which are located at sufficient distances away from the foil to avoid any influence on the solution. A nonslip condition was used on the foil surfaces. Far-field turbulence level was assumed to be less than 0.1%.

The TAC foil has a tip chord of 0.213 m (8.40 in.), base chord of 0.271 m (10.66 in.), and span of 0.214 m (8.44 in.). Both the flap and tab gaps are 0.159 cm (1/16 in.) with the flap gap widened at both ends. The computational grid is nondimensionalized by the mean chord length at midspan, which is 0.242 m (9.526 in.). The Reynolds number based on the mean chord and a flow speed of 3.392 m/s (11.13 ft/s) is 9.7×10^5. The hinge points for the torque calculations are located at $x=0.3085$ for the stabilizer, $x=0.8011$ for the flap, and $x=1.0186$ for the tab in the nondimensional units. The origin of the coordinate is at the leading edge of the stabilizer. Note that the experimentally installed pedestal and the gudgeons are not modeled. The deflection angles, shown in Fig. 1(*b*), for the stabilizer (α), the flap (δ_F), and the tab (δ_T) are measured with respect to the incoming flow, the stabilizer and the flap, respectively. The measured ranges of α, δ_F, and δ_T varied from -15 deg to 15 deg, from -27 deg to 27 deg, and from -60 deg to 60 deg, respectively. For the FlexTAC foil, the dimensions are normalized by the mean chord of 0.503 m (19.791 in.). Due to slightly different construction, the FlexTAC hinge point for the stabilizer torque calculation is at $x=0.3572$. The hinge point for the FlexTAC flap is, however, the same as the TAC flap. The pretest calculations were performed at a nominal speed of 3.048 m/s (10 ft/s) and a Reynolds number of 1.833×10^6. The test was later performed at a lower speed of 2.59 m/s (8.5 ft/s) due to limitations of the SMA wire actuation at the higher flow speed.

Multiple flow conditions were simulated and rigorous validation studies were performed to predict the flow features especially the secondary flow structures in the gap regions (see Lee et al. [10]). For the case of brevity, in this paper we limit ourselves to the discussion of the following case:

Case B: $\alpha=6$ deg, $\delta_T=0$ deg, δ_F varying between -27 deg and 27 deg.

This case is representative of the range of operation of the control surface. It includes an angle of attack for the stabilizer and relative motion between the stabilizer and the flap. It should be noted that there is no exact correspondence between the FlexTAC and TAC foils in δ_T, thus it is set to zero.

The 24 in. water-tunnel measurements [2] for the TAC foil include overall lift and drag on the foil and torques acting on the stabilizer, the flap with the tab, and the tab, respectively. These measured quantities are compared with the predictions in a nondimensional form based on the mean chord (c_m) and the water-tunnel speed V_∞. They include lift and drag coefficients (normalized by $\frac{1}{2}\rho V_\infty^2 c_m^2$) and stabilizer, flap, and tab torque coefficients (normalized by $\frac{1}{2}\rho V_\infty^2 c_m^3$).

The 36 in. water-tunnel tests [3] for the FlexTAC foil measured similar quantities as for the TAC foil. Since the profile shapes of the flexible portion of the FlexTAC foil were not known a priori, the pretested predictions were done with the assumption that the foil was rigid.

The comparisons are plotted in Figs. 4 and 5. The measured FlexTAC lift and drag are lower than the measured TAC values, particularly for the flap angles less than 0 deg and greater than 18 deg. The predicted FlexTAC lift and drag values are generally higher than the measured values. This suggests that the measured FlexTAC forces may have been overcorrected for the water-tunnel blockage effect [3], particularly for the flap angles smaller than 0 deg. For the flap angles larger than 18 deg, the FlexTAC test has shown that the foil is stalled. Although the blockage correction is perhaps too large, the measured FlexTAC drag at $\alpha=\delta_F=\delta_T=0$ is 0.0162 and is 35% higher than the measured TAC drag of 0.01202. This is believed to be from the contribution of the turbulent stimulator installed in the FlexTAC experiments. Figure 5 shows the stabilizer and flap torque comparisons. There are clearly different trends between the FlexTAC and the TAC foils due to the differences in the test setups. The RANS calculations predict the trend of the FlexTAC experiments correctly. The ef-

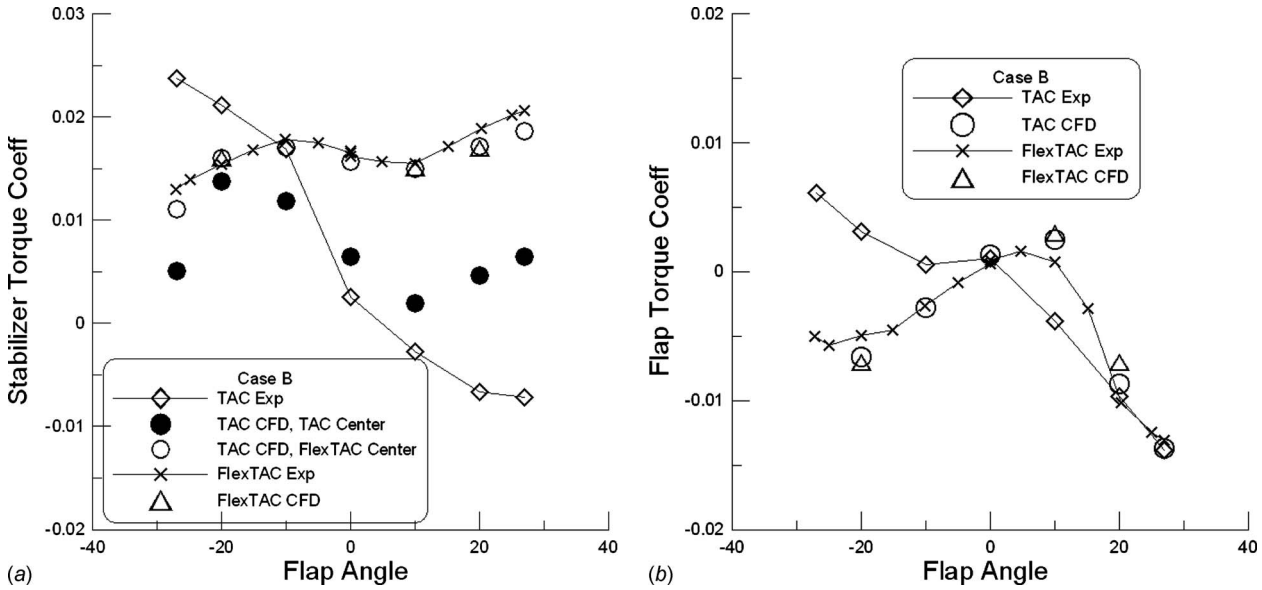

Fig. 5 Moment comparisons for TAC and FlexTAC foils

fects of the gap flow and the gudgeons on the torque calculations are obvious from the differences between the two measured data sets with and without the gudgeons. For the stabilizer torques, the difference of the torque centers contributes further in the sparseness of the comparisons. Thus a recalculation of the TAC stabilizer torque based on the TAC solutions but using the FlexTAC torque center, was performed and plotted in Fig. 5(*a*) labeled as "TAC CFD, FlexTAC Center." This latter prediction in the stabilizer torque agrees well with the "FlexTAC Exp" and the "FlexTAC CFD" shown in Fig. 5(*a*) since both the FlexTAC and TAC CFDs were predicted without gudgeons and are similar to the FlexTAC Exp. Therefore the gudgeons effects can be estimated as the differences between the "TAC CFD, TAC Center" and the "TAC Exp" in the stabilizer torque of Fig. 5(*a*), and between TAC Exp and FlexTAC Exp in the flap torque of Fig. 5(*b*).

A flow visualization at $\alpha=6$ deg, $\delta_F=10$ deg, and $\delta_T=0$ deg was also made for the FlexTAC foil to further validate the CFD predictions in the foil tip region. Figure 6 shows pressure side paint traces (Figs. 6(*a*) and 6(*b*)) compared with the predicted particle traces (Fig. 6(*c*)) on the pressure side surface. The two paint trace photos zoom in at the flap tip portion in order to see the detailed streamline pattern. The installation of the sand-grain turbulent stimulator is clearly shown on the stabilizer. The tip flow from the pressure side to the suction side is also visible in both traces. The stagnation line at the leading edge of the flap is shown in the prediction but was difficult to capture in the experiment due to the high viscosity of the paint.

3 Design Optimization Methodology

Evolutionary algorithms encompassing genetic algorithms [11], evolutionary strategies [12], and swarm algorithms [13] are beginning to see widespread use in design optimization methods across various disciplines. In the field of fluid dynamics, in particular, such stochastic optimization methods are attractive because they search the design landscape in a global manner and are particularly effective in nonlinear landscapes defined by discontinuous and/or multimodal functional. The fitness evaluations in such problems are usually performed with lower-order methods such as potential-flow formulations, empirical relationships, etc. [14,15]. However, such methods usually preclude resolving essential viscous, turbulent, and nonlinear flow phenomena and are not appropriate for the shape optimization of multi-element airfoils, where viscous turbulent effects dominate the gap region of the control surfaces and greatly influence the lift and torque. For such problems, it becomes imperative to use RANS based simulation for fitness evaluation during the design/optimization iterations. However, incorporating a RANS solver in the population based stochastic optimization methods can be prohibitively expensive in terms of turnaround time and cumbersome to implement because of grid updating issues. Such issues arise because of the global changes to geometries during the design iteration that preclude the use of grid movement type methodologies for the geometry changes. Evolutionary algorithms require a procedure for the mesh regeneration to be embedded in the design/optimization cycle since large/important changes to the shape/geometry have to be incorporated. Our approach in the shape optimization effort is geared toward coupling a GA based evolutionary optimization procedure with a multi-element unstructured RANS framework, as shown in Fig. 7. The RANS based CFD solvers have been validated with experiments as discussed earlier. The grids used in the design optimization loop are generated through an automated scripting process coupled to the grid generator GRIDGEN [16]. Details of our design optimization framework are discussed in the following sections.

3.1 GA. GAs are based on the principles of Darwin's theory of evolution and natural selection. The key ideas of how design unfolds in nature in an efficient, parallel, and multimodular manner satisfying a complex network of constraints, variables, and objectives are embodied in the workings of GAs. Formal presentation of the ideology is based on seminal work of Holland [17] that structures based on chromosome-like string of binary switches could trigger more favorable characteristics in systems if the chromosomes were permitted to interact with other similar structures based on some measure of fitness, thereby, reproduce and mutate leading to offspring systems that were better adapted to the environment.

The design procedure is started by taking a stochastic representation of possible designs from the design space and carrying out fitness evaluations utilizing CFD analyses concurrently on all the designs. Designs evolve with the use of the selection, crossover and mutation operators on the design space in a manner analogous to evolution in nature. Particulars of our GA implementation are provided below.

3.1.1 Method of Representation. In our implementation of the GA, the chromosomes utilize binary encoding. Although many

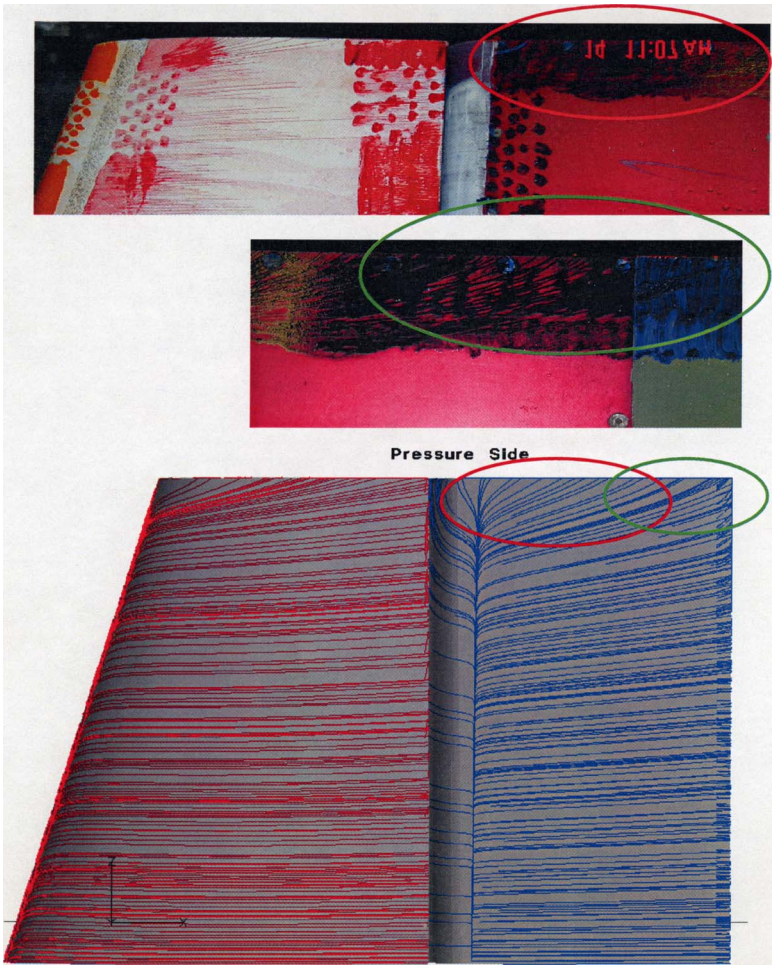

Fig. 6 Comparison of (*a*) water-tunnel paint traces and (*b*) closed-up traces with (*c*) predicted surface particle traces

engineering applications use real coded chromosomes, the lower cardinality binary encoding replicates evolutionary processes closely (for example, four types of nucleotide encode an alphabet in the human genome). Fundamental GA theory also postulates that alphabets of lower cardinality provide greater flexibility during crossover and are not blocked in their search for a global extreme in certain complex landscapes [11].

3.1.2 Selection. The simple GA implementation [11] incorporated a roulette-wheel selection, which stipulated that an individual's probability of selection is directly proportional to its relative fitness in the population. The tournament selection procedure used in our GA is also based on a proportionate fitness philosophy. However, in our case subsets of the population are chosen and members of the subset compete with each other and one indi-

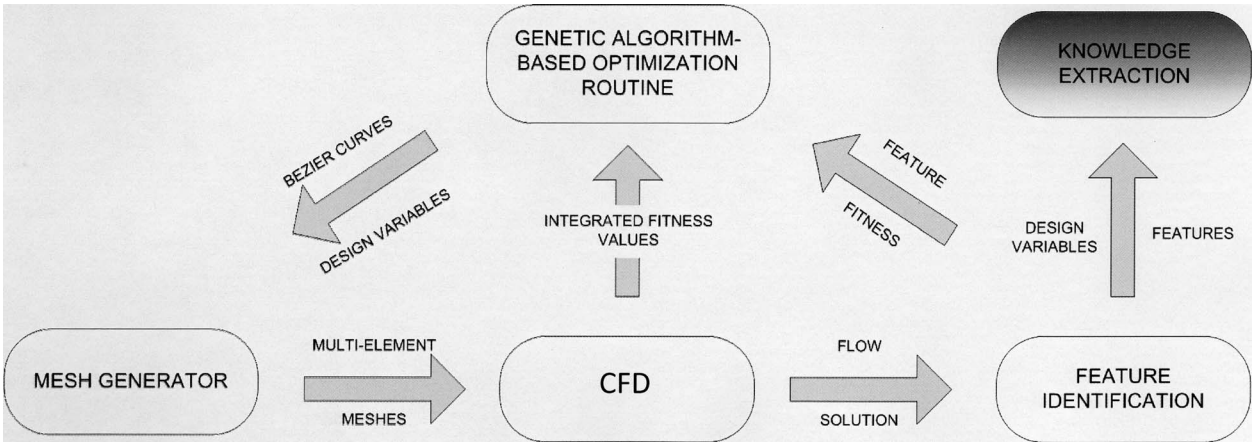

Fig. 7 Flow of information in the design optimization loop

vidual from each subset advances to the next generation. Furthermore, we also incorporate an elitist strategy, which ensures that the fittest member of each generation always advances to the next generation.

3.1.3 Crossover. Many different crossover techniques exist including single point, multipoint and uniform crossover. The simple GA utilizes a single point crossover, where a random location is chosen as the point of exchange between two parent chromosomes.

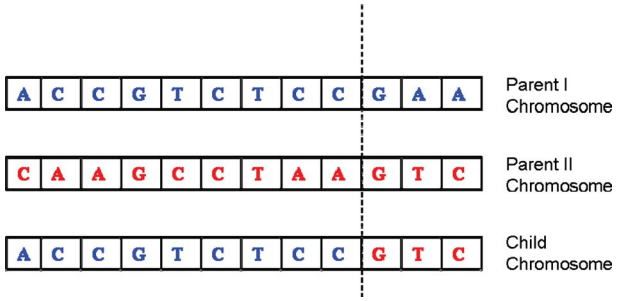

Illustration of Single Point Cross-over

Multipoint crossover is very popular and improves on the single point crossover technique by utilizing multiple sites of exchange between the parent chromosomes. Multipoint crossover can accelerate convergence of the GA. However, it is also disruptive in terms of schema (genetic patterns) preservation. The limiting case of multipoint crossover is uniform crossover or the utilization of a crossover mask for the entire chromosome. Based on the value of the crossover mask at a certain location in the chromosome, the corresponding genetic information is extracted from the relevant parent chromosome. The following schematic depicts the working of the uniform crossover operator. A "0" at a certain location in the mask indicates that that particular location in the child chromosome is filled with the value in the chromosome of Parent 1. Similarly, a "1" in the mask indicates the value will be extracted from the chromosome of parent 2. The uniform crossover operator is found to be very efficient in searching complex landscapes especially with small populations (e.g., problems utilizing CFD for fitness evaluations usually have small population sizes due to the expense involved with fitness calculations).

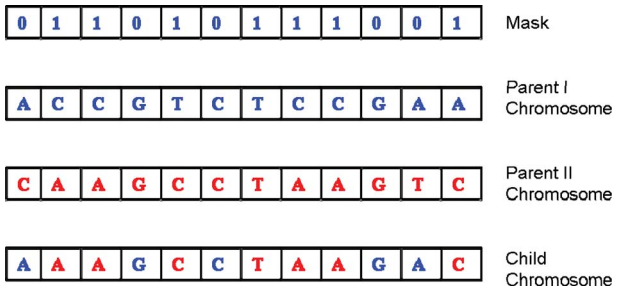

Illustration of Uniform Crossover

3.1.4 Mutation. In our implementation the mutation operator is assigned a small probability that one or more of the chromosomes of the offspring will be altered. In our implementation this mutation operator ensures that at any given location in the chromosome the value flips between a 0 and a 1. In the simple genetic algorithm [11] mutation played a dominant role in avoiding premature convergence in multimodal design landscapes. However, placing undue reliance on the mutation is inefficient because mutation usually results in designs with lower fitness.

Preservation of diversity in the design population is ensured by niching or fitness sharing by subpopulations that define a certain niche in a multimodal design space. In particular, following the lead of Carroll [18], we have used Goldberg's multidimensional phenotypic sharing scheme with a triangular sharing function. For multi-objective optimization problems we follow the ranking scheme of Fonseca and Fleming [19] and Deb [20] in obtaining the Pareto optimal set of solutions.

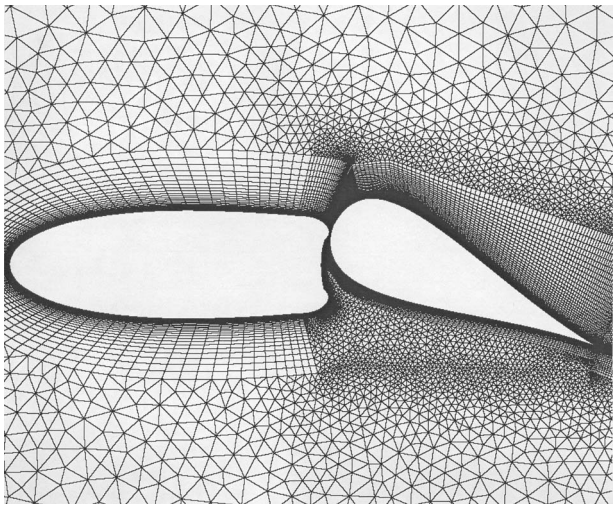

Fig. 8 A typical multi-element unstructured grid used in design optimization studies

3.2 Automated Grid Generation. The CFD simulations are used for fitness evaluations. Since GAs effectively search the entire design space, the geometry can undergo radical changes, thereby requiring a new grid to be generated. For each design, a new grid is generated through a semi-automated grid generation procedure utilizing the scripting language in GRIDGEN. A scripting language TCL/TK interfaces with the grid generator that permits various facets of the grid generation topology such as grid points, shapes of curves, control points, clustering to be specified as variables. Shape deformation in the form of Bezier control points is passed from the GA to the TCL/TK script that invokes the grid generation process. The success of the scripted grid generation process is dependent on the use of the same topology for mesh generation of all the designs involved. Multi-element hybrid meshes used by the CFD code and its dynamic gridding capability [21] provide significant flexibility to achieve this without any conflicts or distorted grids, as shown in Fig. 8. Meshes for the new designs are verified for skewness and positive volumes. The topology is modified to accommodate any cellular distortions automatically.

In our studies, the trailing edge of the stabilizer is defined as a cubic Bezier curve with the coordinates of the control points being defined as design variables. Furthermore, the entire curve representing the upper section of the flap is defined as a combination of piecewise Bezier cubic curves. The control points of the Bezier representation also serve as design variables. In all, a combination of seven design variables was considered. Two design variables defined the control points of the Bezier curve representing the trailing edge of the stabilizer and the remaining five variables represented the control points of the piecewise Bezier cubic curves defining the entire surface of the symmetric flap. The curves were defined in such a manner that special emphasis was put on the leading edge (nose thickness) and the trailing edges of the flap and the stabilizer. Since the flap geometry is constrained to be symmetric, the lower section is extracted as a mirror image of the redefined upper section. Since the aim of the control surface optimization is the torque reduction at a large operating angle, the objective function is defined to be the torque at the largest flap angle of operation (i.e., 25 deg). In order to eliminate designs that show a reduction in torque with a substantial reduction in lift, penalty functions were applied to all designs, where the flap lift was less than 20% of the baseline flap lift. The other important

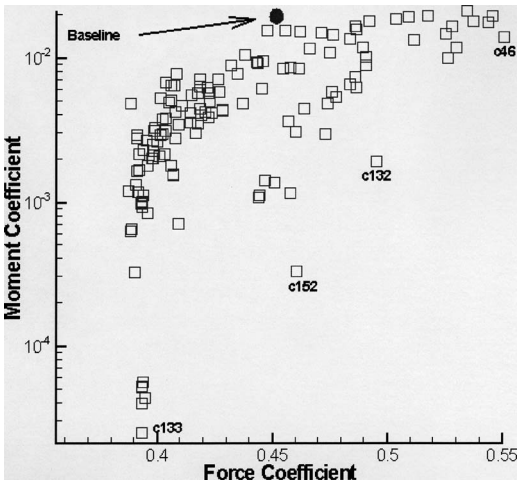

Fig. 9 Design landscape showing relative performance of flap characteristics for all shapes utilized by the GA

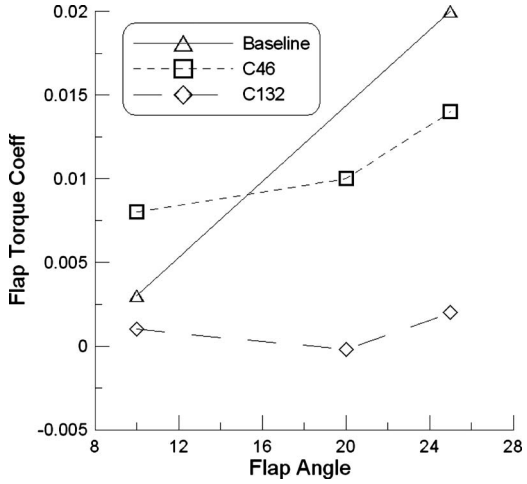

Fig. 11 Flap torque comparison for C132 and C46

constraint taken into consideration was preserving the direction of the torque. Penalty functions were also utilized to discard any designs that changed the direction of the torque from the baseline design. Simulations pertaining to fitness evaluations were performed with a Reynolds number of 1.8×10^6 and a characteristic velocity of 3.05 m/s. Flow was assumed to be incident on the multi-element foil at 6 deg and the flap angle was set at 25 deg.

4 Results of Design Optimization Process

A population size of 16 designs was considered for the GA based optimization procedure. All design variables were binary coded for an efficient calculation. The resulting fitness function, based on the torque of the flap asymptotes after the fifth generation of a total of 16 generations calculated, converged to torque values that are more than three orders of magnitude smaller than the baseline flap section. Although the optimized design reduced the flap torque by almost three orders of magnitude, the resulting flap lift coefficient on the optimized design reduced from 0.45 to 0.39 (13.3% drop) labeled as C133 in Fig. 9, which is a survey of the entire design landscape. From a practical standpoint, a more attractive design point would be one that provided a reduction in flap torque with an increase in the flap (or flap and stabilizer combined) lift characteristics. Furthermore, sustaining such favorable characteristics over the entire operational range would yield a design far superior to the baseline design. Figure 9 indicates a Pareto frontier (including all the labeled points) of potential design candidates that simultaneously show better force and moment characteristics. The first of these potential candidates labeled C132 has a torque coefficient that is an order of magnitude lower than the baseline design and a flap force coefficient indicates more than 10% increase in flap force coefficient. The second potential candidate labeled C46 in Fig. 9 shows a 30% reduction in flap torque while providing more than 20% increase in flap lift. Such a design is useful because it provides an avenue for operating at a lower flap angle to achieve the same lift generated by a 25 deg flap angle in the case of the baseline design. It should be noted that the design landscape shown in Fig. 9 represents the database of simulations performed for all the design points during the genetic algorithm based optimization for minimizing the flap torque.

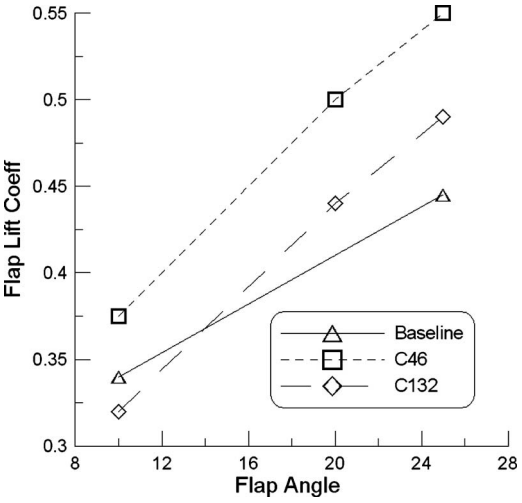

Fig. 10 Flap lift comparison for C132 and C46

Parametric simulations were performed on the cases identified above (C132 and C46) at three different flap angles (25 deg, 20 deg, and 10 deg) and the performance was compared against the baseline design (see Fig. 10). Consistent with the findings for the 25 deg cases, the flap lift was found to be either vastly improved or close to the baseline flap design lift. In particular, the design for the C46 case consistently proved to show improved flap lift coefficients over the baseline design (improvements ranged from 15% to 22%) throughout the operating range. The multi-element foil design pertaining to C132 showed improvement in flap lift by about 10% over the baseline design at the higher angle, however, it deteriorated at the lower flap angles. This deterioration is primarily due to the smaller nose region of the flap, which changes the flow blockage characteristics on the suction side leading to a smaller pressure drop (see Figs. 13 and 14 for the geometry differences). Although, the flap for C46 has a similar nose, the taper in that design from the midchord to the trailing edge dramatically increases the lift at lower angles for that case. The increase in lift at the higher flap angles is accentuated for both the C132 and C46 stabilizer and flap designs. This increase is primarily due to the improvement in the suction side performance on the stabilizer at the higher flap angles. Similarly, the flap torque for the three designs as a function of flap angle is shown in Fig. 11. The flap torque dramatically increases for the baseline design at the higher flap angles of operation. By contrast, the C46 design increases only slightly with flap angle, although it shows an increased flap torque at a flap angle of 10 deg over the baseline design. Interestingly, the C132 design shows a flat torque profile with variation in flap angle. Moreover, the flap torque is orders of magnitude smaller than the torque of the other two designs. This is a highly desirable feature since it indicates that the power required by the motor to change the flap operating angle is substantially less during the entire operating regime.

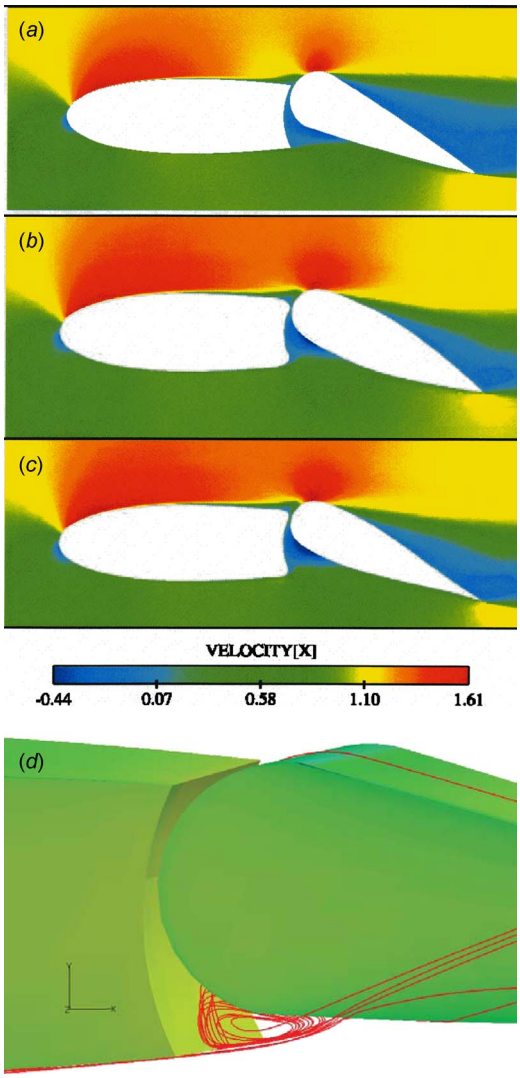

Fig. 12 Comparison of the axial velocity distributions among (*a*) baseline, (*b*) C132 and (*c*) C46 designs with (*d*) the shed vortex in the flap nose region, which links with the reverse axial velocity distributions

A detailed discussion of the C132 and C46 designs and associated flowfields is provided here. Figures 12(*a*)–12(*c*) depicts a back-to-back comparison of the axial velocity distributions in the flowfields related to the baseline, C132 and C46 designs at a flap angle of 25 deg. The gap flow separation is linked to the negative axial velocity distribution, as illustrated in Fig. 12(*d*). The three designs show significant variation in geometry of the stabilizer and the flap. The baseline design has sharp trailing edges on the stabilizer and the stabilizer and flap together represent a NACA airfoil shape. The C132 design comprises of a stabilizer with well-rounded trailing edges and a flap with a relatively smaller nose region. The C132 flap design, however, is more bulbous (increased thickness) than the baseline design for most of its chord. The C46 design is representative of a stabilizer that is slightly rounded and a flap that is, like the C132 design, smaller in the nose region. However, unlike the C132 design, the C46 flap tapers toward the trailing edge of the flap, thereby showing a reduction in thickness compared with the baseline flap design. A comparison of the axial velocity distributions of the three designs reveals a smooth transition between the flap and stabilizer on the suction side for the C132 and C46 designs. This is primarily due to a combination of the rounding of the stabilizer trailing edge and the smaller nose of the flap. As a consequence of the smooth transition through the gap region on the suction side, the pressure distribution on both the flap and the stabilizer are altered considerably. For example, the pressure on the suction side of the stabilizer is lowered throughout the length of the stabilizer for both the C132 and C46 designs (see Figs. 13 and 14) and the strong adverse pressure gradient close to the suction side trailing edge seen in the baseline design is to a large extent alleviated. This leads to the enhanced combined (stabilizer+flap) lift for the two designs. Furthermore, the velocity distributions in Fig. 12 also indicate that both the C132 and C46 designs have a smaller wake region behind their respective flaps. On the pressure side of the flap the velocity recirculation in the gap region is much smaller for the C132 and C46 designs as the flow comes off smoothly over the rounded stabilizer trailing edges. This causes the high pressure

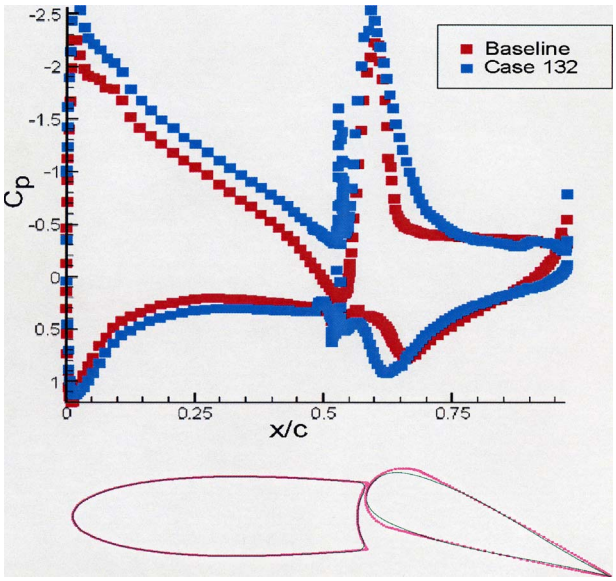

Fig. 13 Comparison of the Cp distribution and shape profile of the C132 and baseline designs

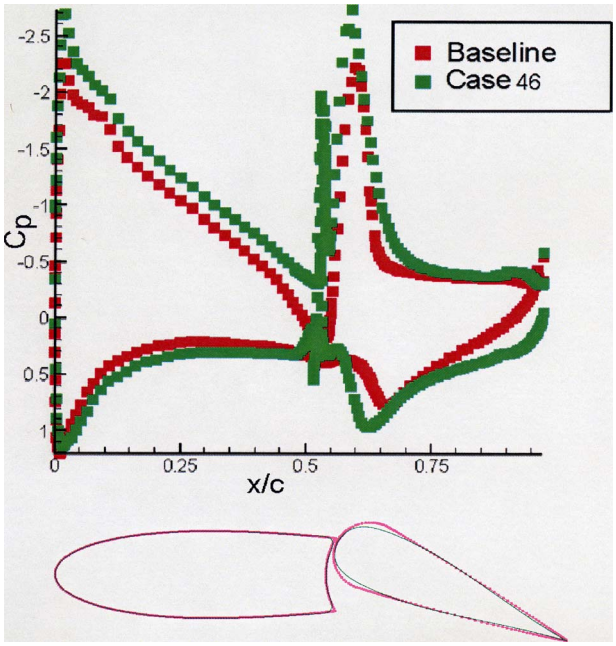

Fig. 14 Comparison of the Cp distribution and shape profile of the C46 and baseline designs

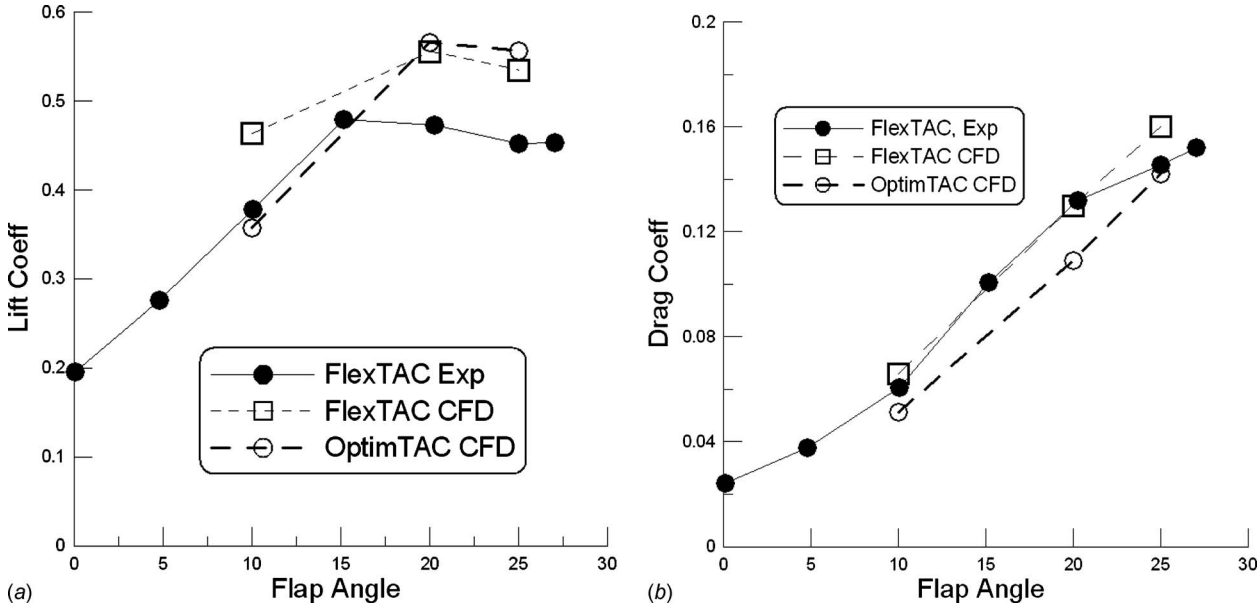

Fig. 15 Comparison of forces between FlexTAC and OptimTAC foils (*a*) lift and (*b*) drag

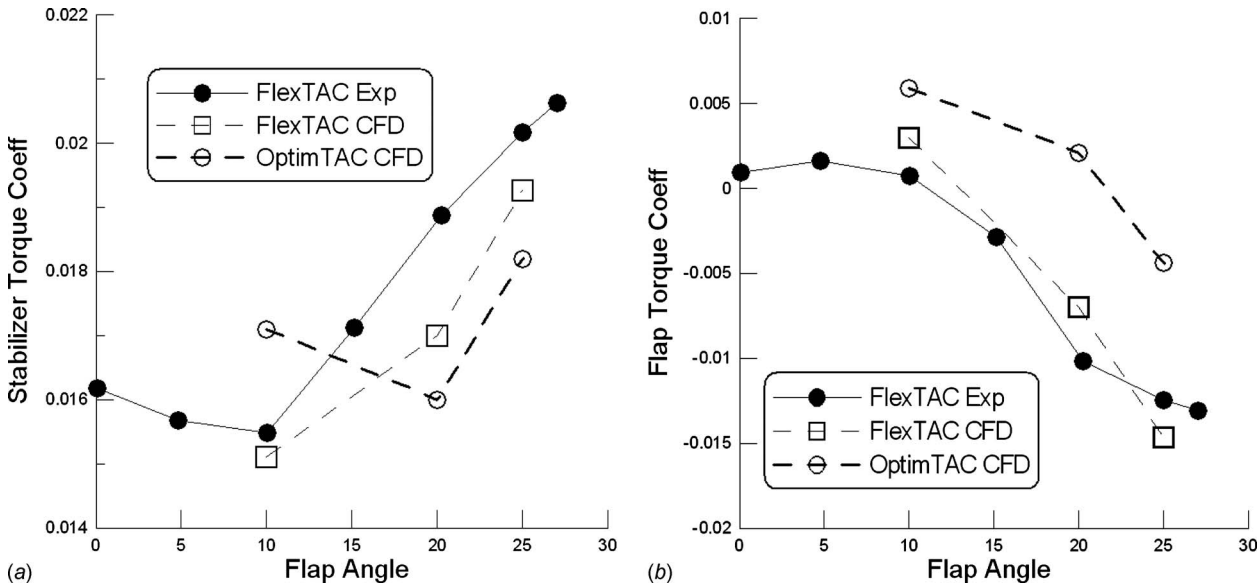

Fig. 16 Comparison of moments between FlexTAC and OptimTAC foils (*a*) stabilizer torque and (*b*) flap torque

stagnation region to shift forward in the C132 and C46 cases and is primarily responsible for the improved torque characteristics of the two designs. The surface pressure distributions on the stabilizer and flap for the C132 and C46 design cases are plotted against the baseline design in Figs. 13 and 14. The trends in these plots corroborate the findings discussed above: (a) better suction side performance on both the stabilizer and the flap (b) shift in the peak pressure location resulting in a reduction in torque (c) change in gap pressure distribution and (d) significant increase in lift provided by the tapering close to the trailing edge in the C46 design case.

5 Validation of Optimized Shape

The current objective of the optimization calculations is to design the multi-element foil with a minimum torque under the large

Table 1 Force changes between OptimTAC and FlexTAC

Flap angle	FlexTAC lift coeff	OptimTAC lift coeff	Lift change (%)	FlexTAC drag coeff	OptimTAC drag coeff	Drag change (%)
10	0.4640	0.3576	−22.9	0.0660	0.0514	−22.1
20	0.5560	0.5660	1.8	0.1300	0.1091	−16.1
25	0.5348	0.5570	4.2	0.1601	0.1420	−11.3

Table 2 Moment changes between OptimTAC and FlexTAC

Flap angle	FlexTAC stab torq coeff	OptimTAC stab torq coeff	Stab torq change (%)	FlexTAC flap torq coeff	OptimTAC flap torq coeff	Flap torq change (%)
10	0.0151	0.0171	13.2	0.0030	0.0059	96.7
20	0.0170	0.0160	−5.9	−0.0070	0.0021	−130.0
25	0.0193	0.0182	−5.6	−0.0147	−0.0044	−70.0

flap angle of 25 deg. We therefore adapt C132 (used to construct the OptimTAC) for further numerical validation even through the computed lift force is slightly smaller than the original foil at smaller flap angles (Fig. 10).

The aforementioned optimization calculations were performed for the 2D cross sections since the design optimization process is very computationally expensive, requiring a large number of CFD calculations. The successful 2D designs from the optimization process were extrapolated in the spanwise direction to generate an analogous 3D OptimTAC foil and compared with the original FlexTAC foil. The force and moment curves of the OptimTAC foil are compared with the baseline FlexTAC foil in Figs. 15 and 16 for $\alpha=6$ deg. The percentage changes in forces and moments between the two foils are listed in Tables 1 and 2 along with their values, where negative percents imply reductions in the parameters compared. The predicted FlexTAC foil lift in Fig. 15(*a*) is higher than the measurements as it was shown in Fig. 5(*a*) due to the overcorrection of the FlexTAC data for the water-tunnel blockage effect [3]. The OptimTAC foil lift is 4.2% higher than the FlexTAC at the 25 deg flap angle but it is about 23% lower at the 10 deg flap angle. The drag in Fig. 15(*b*) for the OptimTAC is between 22% and 11% lower than the FlexTAC for all flap angles. The stabilizer and flap torques in Fig. 16 show the OptimTAC foil again has 5.6% and 70%, respectively, lower values at the 25 deg flap angle than the FlexTAC foil. At the 10 deg flap angle, the OptimTAC foil encounters larger torques for both the stabilizer and the flap but these torques are smaller than the peak torques at the 25 deg flap angle. The general trends for forces and moments are consistent with the results (shown in Figs. 10 and 11) obtained through 2D calculations. However, the near constant torque curve for the 2D OptimTAC flap torque (Fig. 11) has been replaced with a monotonically decrease in curve (Fig. 16(*b*)) with the flap angle in the 3D results.

6 Conclusions

The TAC and FlexTAC foils are conceptual designs for marine vehicle control surfaces. The TAC foil has a rigid tab attached to the stabilizer and the flap while the FlexTAC foil has a flexible tab connected to the flap without a gap. The CFD validation calculations using the hybrid unstructured RANS based CFD codes were performed to compare with the water-tunnel TAC and FlexTAC measured data. The force predictions agree well with both TAC and FlexTAC data except the predicted FlexTAC lift at larger flap angles, where the data have been overcorrected for the tunnel blockage and have shown that the foil was stalled during the measurements. The CFD torque predictions agree well with the FlexTAC data. From the CFD predictions and the measurements on both TAC and FlexTAC, the gudgeons effects were identified and estimated. The CFD validation implies the FlexTAC calculation is able to be adapted for optimization calculations.

The validated CFD calculation was coupled with a GA based optimization procedure to evaluate the fitness function. The evolutionary algorithm permits global search of the design landscape in a robust manner and encompasses a complex array of design variables and constraints to be specified. The optimization procedure includes an automated grid generation, which is able to account for large deformations of the stabilizer and the flap configurations. The RANS based CFD was necessary for this problem because of strong viscous/turbulent effects in the gap region between the stabilizer and flap, particularly at large flap angles. The study finds that a simultaneous modification to the stabilizer and flap geometries is necessary to ensure the close coupling of the two elements. The optimization calculations with an objective to reduce the flap torque at a high flap angle provide multiple designs, which show both the enhanced overall lift and the reduced flap torque. At an extreme, the flap torque can be reduced three orders of magnitude but with a 13% loss in lift. An OptimTAC was selected from the Pareto frontier for further CFD evaluations, which show 11.3%, 70%, and 5.6% reductions in the drag, the flap, and the stabilizer torques, respectively, along with a 4.2% increase in the overall lift when comparing to the FlexTAC. However, the performance of the OptimTAC drops at a lower flap angle of 10 deg. Further investigation indicates that the lift enhancement is mostly achieved by the modification of the flow in the gap region between the stabilizer and the flap. On the other hand, the torque reduction on the flap is related to the shifted peak pressure location on the flap. The modification of the stabilizer's trailing edges contributes to both lift enhancement and torque reduction.

Acknowledgment

The computer resources for computations described in this paper were provided by the DoD High Performance Computing Modernization Program. Additional computer resources were provided by the United States Navy's SEATECH Center located at Naval Surface Warfare Center Carderock Division. The work was funded by the Naval Sea Systems Command.

Nomenclature

- C132, C46 = foils named during optimization calculations
- c_m = mean chord
- k = turbulent kinetic energy
- NACA = National Advisory Committee for Aeronautics
- OptimTAC = 3D foil with C132 cross section
- q = $(k)^{1/2}$
- TCL/TK = scripting language
- V_∞ = freestream velocity
- x, y, z = Cartesian coordinates
- α = inflow angle to multi-element foil
- ε = rate of dissipation of turbulent kinetic energy
- δ_F = flap angle
- δ_T = tab angle
- ρ = fluid density
- ω = ε/k

References

[1] Carpenter, B., and Nguyen, T., 1999, "Shape Memory Alloy Actuator for Tab Assisted Control Surface Application," Proceedings of SPIE Conference on Smart Structures and Materials 1999, Newport Beach, CA, Vol. 3674, March 2–4.

[2] Nguyen, T. D., Gowing, S., and Bochinski, D., 1999, "Tab-Assisted Control Surface for Marine Application," Proceedings of the International Symposium on Warship '99 Naval Submarines.

[3] Gowing, S., Lee, Y. T., Carpenter, B., Atsavapranee, P., and Hess, D., 2004, "FlexTAC: An Advanced Submarine Control Surface and Actuation System," AIAA Paper No. 2004-902.

[4] Lee, Y. T., Ahuja, V., Ebert, M., and Hosangadi, A., 2003, "Flow Predictions and Shape Optimization of A Multi-Element Airfoil," Proceedings of the

Eighth International Conference on Numerical Ship Hydrodynamics, Busan, Korea (South), pp. 22–25.
[5] Sung, C. H., and Rhee, B., 1999, "Prediction of Forces and Moments of Rudders With Flap and Tab, Part I. 2D Airfoil with Flap and Tab," Proceedings of the Seventh International Conference on Numerical Ship Hydrodynamics, Nantes, France, Jul. 19–22.
[6] Sung, C. H., Rhee, B., and Koh, I.-Y., 2000, "Validation of Tab Assisted Control Surface Computation," Proceedings of the 23rd Symposium on Naval Hydrodynamics, Bassin D'essair Des Carenes, Val De Reuil, France, Sep. 17–22.
[7] Hosangadi, A., Lee, R. A., York, B. J., Sinha, N., and Dash, S. M., 1996, "Upwind Unstructured Scheme for Three-Dimensional Combusting Flows," J. Propulsion Power, **12**(3), pp. 494–502.
[8] Hyams, D. G., Sreenivas, K., Sheng, C., Nichols, S., Taylor, L. K., Briley, W. R., Marcum, D. L., and Whitfield, D. L., 2002, "An Unstructured Multielement Solution Algorithm for Complex Geometry Hydrodynamic Simulations," Proceedings of the 24th Symposium on Naval Hydrodynamics, Fukuoka, Japan, Jul. 8–13.
[9] Ahuja, V., Hosangadi, A., and Arunajatesan, S., 2001, "Simulations of Cavitating Flows Using Hybrid Unstructured Meshes," ASME J. Fluids Eng., **123**(2), pp. 331–340.
[10] Lee, Y. T., Ebert, M. P., and Hosangadi, A., 2002 "Flow Predictions for Multi-Element Control Surface," NSWCCD Report No. NSWCCD-50-TR-2002/061.
[11] Goldberg, D. E., 1989, "Genetic Algorithms in Search," *Optimization, and Machine Learning*, Addison-Wesley, Reading, MA.
[12] Sbalzarini, I. F., Muller, S. D., Koumoutsakos, P. D., and Cottet, G.-H., 2001, "Evolutionary Strategies for Computational and Experimental Fluid Dynamic Applications," Proceedings of the Genetic and Evolutionary Computation Conference, San Francisco, CA, Jul. 7–11.
[13] Ray, T., and Tsai, H. M., 2004, "Swarm Algorithm for Single- and Multiobjective Airfoil Design Optimization," AIAA J., **42**(2), pp. 366–373.
[14] Obayashi, S., and Takanashi, S., 1996, "Genetic Optimization of Target Pressure Distributions for Inverse Design Methods," AIAA J., **34**(5), pp. 881–886.
[15] Jones, B. R., Crossley, W. A., and Lyrintzis, A. S., 1998, "Aerodynamic and Aeroacoustic Optimization of Airfoils via a Parallel Genetic Algorithm," AIAA Paper No. 98-4811.
[16] Pointwise Inc., 2003, GRIDGEN User's Manual, Version 15.
[17] Holland, J. H., 1992, *Adaptation in Natural and Artificial Systems*, MIT Press, Cambridge, MA.
[18] Carroll, D. L., 1995, "Modeling High Pressure Chemical Oxygen-Iodine Lasers," AIAA J., **33**(8), pp. 1454–1462.
[19] Fonseca, C. M., and Fleming, P. J., 1995, "An Overview of Evolutionary Algorithms in Multi-Objective Optimization," Evol. Comput., **3**, pp. 1–16.
[20] Deb, K., 2002, *Multi-Objective Optimization Using Evolutionary Algorithms*, Wiley, New York.
[21] Cavallo, P. A., Hosangadi, A., Lee, R. A., and Dash, S. M., 1997, "Dynamics Unstructured Grid Methodology With Application to Aero/Propulsive Flowfields," AIAA Paper No. 97-2310.

A Serendipitous Application of Supercavitation Theory to the Water-Running Basilisk Lizard

Eric R. White

Timothy F. Miller

Applied Research Laboratory,
Pennsylvania State University,
State College, PA 16804

The classic study of the water entry of a body has applications ranging from hydroballistics to behavior of basilisk lizards. The availability of Russian supercavitation theory in recent years has allowed for an even greater understanding, and was used to develop a model to predict the dynamic size, shape, and pressure of a naturally or artificially produced underwater cavity. This model combines supercavitation theory, rigid body dynamics, and hydrodynamic theory into a comprehensive model capable of determining the motional behavior of underwater objects. This model was used as the basis for modeling the vertical water entry of solid objects into a free water surface. Results from simulation of water entry of various-sized thin disks compared favorably with published experimental data from the technical literature. Additional simulated data support a disk radius dependence on a relative object depth at cavity closure that was not previously recognized. Cavity closure times are also presented.
[DOI: 10.1115/1.4001487]

1 Introduction

The entrance of a solid object into a free water surface is a classical problem that has been studied since the start of the 1900s [1]. Despite its long history, the study of water entry is still of interest today for such wide ranging applications as hydroballistics [2], missile water entry [3], and the water-running behavior of basilisk lizards [4–6]. A water-running robot based on the basilisk lizard is under development [7]. Experimental work and numerical models [8–10] are also being developed and refined to better our understanding of the topic. More recent work by Duclaux et al. [11] has contributed to this literature and will be discussed more in the context of the present work.

The cavity formation from a solid object entering the water surface at high speed has a strong similarity to the artificial cavity generated from a high-speed underwater vehicle [12]. Supercavitation, as it pertains to underwater vehicles, is a method by which the vehicle can drastically reduce its drag by traveling in a naturally generated or an artificially generated gas cavity. The formation, stability, and control of this supercavity have been the topic of many studies [13–15]. A large body of literature generated in countries that made up the former Soviet Union exists, which specifically addresses the cavity formation in relatively high-speed flows. The present work was initially undertaken to determine the applicability of the theory of supercavitation and the modeling of dynamic high-speed cavities to the cavity formation and closure aspects of water entry at relatively low speeds.

A serendipitous application of this theory was an examination of the physics behind the water-striding behavior of basilisk lizards [4–6]. These lizards are able to generate enough upward impulse as their feet plunge through the water surface that they are able to keep above (and thus run on) the surface. In particular, the dependence of foot size (taken here as an equivalent disk diameter) and lizard weight on their ability to run is of keen interest to their researchers. Glasheen and McMahon [5] advanced the theory that the relationship between the size of a lizard's foot and its weight, and the lizards' ability to run on the water surface is key to the effective allocation of resources in the lizards' ecosystem. Specifically, younger (and generally smaller) lizards run more easily on water and thus populate a location in the ecosystem that is distinct and presumably noncompetitive with older (and generally larger) lizards that have a much more difficult time staying on the surface.

2 Mathematical Formulation

2.1 Supercavitation. Supercavitating flows are flows of liquids, past solid bodies, that involve large trailing cavities; these cavities are filled by the vapor of the surrounding liquid or by a noncondensible foreign gas. The metric used to describe supercavitating flow is the cavitation number

$$\sigma = \frac{2(P_\infty - P_{\text{cav}})}{\rho u^2} \tag{1}$$

where P_∞ is the ambient pressure (the sum of atmospheric and hydrostatic components), P_{cav} is the pressure within the cavity, ρ is the fluid density, and u is the flow (or object) velocity. The supercavitating regime is characterized by small values of the cavitation number, $\sigma < 0.1$. Small cavitation numbers occur when the flow velocity is high (natural cavitation) or the pressure difference is low. The pressure difference can be lowered by a decrease in ambient pressure (also natural cavitation) or by an increase in cavity pressure (ventilation with a noncondensable gas).

The expansion of a dynamic, axisymmetric cavity can be described by the following second-order, partial differential equation described by Serebryakov [16,17], Paryshev [18], and Epshtein [19]:

$$\frac{\partial^2 S(\tau,t)}{\partial t^2} = \frac{-4\pi(P_\infty - P_{\text{cav}})}{A^2 \rho} \tag{2}$$

This equation is the mathematical formulation of the principle of "independence of cavity expansion" formulated by Logvinovich [20]. In the above equation, S is the cross section of the cavity at a given instant in time t and at a given position along the axis of the cavity indirectly indicated by τ, which is the time of each cavity section formation. The parameter designated by A is a unitless empirical constant, and is typically set equal to 2 (see Refs. [16,17]) and has been well validated with experimental data for a typical range of cavitational flows. Equation (2) derives from the generalized Bernoulli equation in cylindrical coordinates. There is a term produced in the cylindrical equation form $\ln(R_{\text{infinity}}/R)$, which requires an approximation. Duclaux et al. [11] approximated that term by unity. The supercavitation community approximates it with the value of 2, and consequently, the results obtained from Eq. (2) may be expected to differ from those of Duclaux et al. [11]. Cor and Miller [21] described some of the empirical and theoretical rationales for the use of 2 instead of unity.

Physically, the above equation describes the act of an object passing a fixed fluid plane at time $t = \tau$ represented by the dashed line in Fig. 1. When this occurs, the object creates a space in that plane equal to the object's area by displacing the fluid. The energy imparted to that fluid is proportional to the square of the object's velocity on impact with the plane and results in high radial velocities in the fluid. The space expands due to inertia overcoming the pressure difference $P_\infty - P_{\text{cav}}$ until a maximum area is reached. After that, the space decreases and ultimately closes again. The variable t represents the present time and defines the values of ambient pressure, cavity pressure, and disk velocity that determine

Contributed by the Fluids Engineering Division of ASME for publication in the JOURNAL OF FLUIDS ENGINEERING. Manuscript received August 5, 2008; final manuscript received March 25, 2010; published online April 27, 2010. Assoc. Editor: Theodore Heindel.

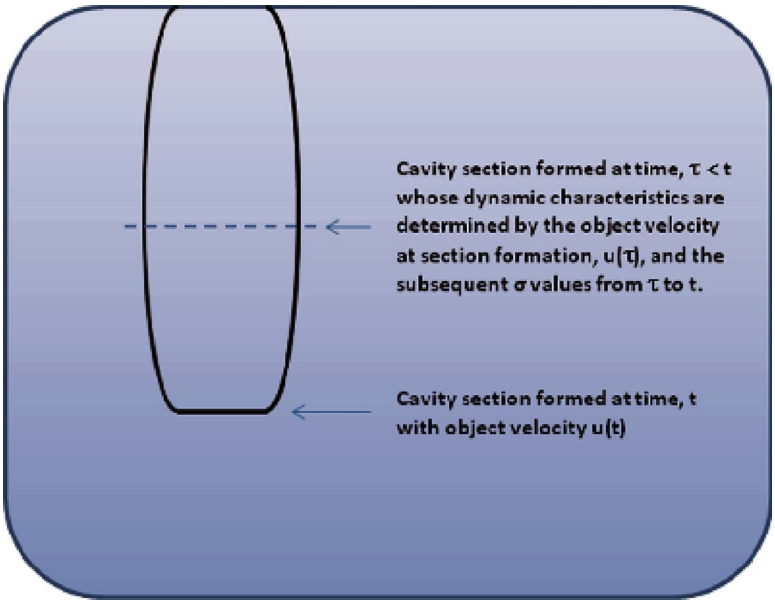

Fig. 1 The dynamic cross sectional area of a cavity section is determined by the condition at the time of cavity formation τ, and in part by the cumulative effect of cavitation number

the cavity formation at the disk. The variable τ represents the past time at which a downstream portion of the cavity was formed at the disk. The behavior of this section is assumed to be defined by the parameter values that existed at its time of formation (which to the stationary observer occurred at $dt=t-\tau$ before the current time). For the case of the water entry problem, the cavity formation at the disk depends on an external pressure equal to the sum of atmospheric and hydrostatic pressures that occurs at the depth of the disk. The section of the cavity partway between the current disk location and the water surface was determined by an external pressure equal to the sum of atmospheric and hydrostatic pressures that existed at the partway depth (i.e., at a location that the disk passed $t-\tau$ earlier).

The initial conditions for this differential equation are

$$S_o = \frac{\pi D^2}{4} \quad \text{and} \quad \frac{\partial S_o}{\partial t} = \dot{S}_o = \frac{\pi}{A} D u \sqrt{C_D} \tag{3}$$

Here, S_o is the initial cavity section area and is determined by the effective diameter of the water entry object D. $\dot{S}_o$ is the initial rate of change in the cavity section area and is dependent on the object's effective diameter, the instantaneous velocity u, and the object drag coefficient C_D.

Double integration of Eq. (2) with the given initial conditions of Eq. (3) yields

$$S(\tau,t) = \frac{\pi D^2}{4} + \frac{\pi}{A^2} u(\tau) \left(AD\sqrt{C_D}(t-\tau) - 2u(\tau) \int_\tau^t (t-\xi)\sigma(\xi) d\xi \right) \tag{4}$$

Here, $\tau \leq t$ is the time of the section formation. The variable $u(\tau)$ is the instantaneous velocity at the time of the section formation. Fundamental to this equation is Logvinovich's notion of section independence [20], which states that a cavity section, once initiated, is not dependent on the past conditions of the object, but will expand based on the values of the instantaneous velocity of the object when the section was formed. In light of Logvinovich's treatment, each cavity section travels at the speed the object had when that section was formed, indicated by the $u(\tau)$ factor outside the time integral.

For the case of water entry before cavity closure, cavity pressure is the atmospheric pressure less the hydrodynamic head (adjusted by a Bernoulli effect)

$$P_{\text{cav}} = P_{\text{atm}} - \tfrac{1}{2}\rho_{\text{gas}} u^2 \tag{5}$$

where ρ_{gas} is the density of the gas or vapor in the cavity. This effect results in a lower effective cavity pressure as air enters into the open end of the cavity to fill the additional volume due to cavity growth as the object descends. The substitution of Eq. (5) into Eq. (1) shows that $\sigma \sim \rho_{\text{gas}}/\rho_{\text{water}}$ ($\ll 1$) if $P_\infty \sim P_{\text{atm}}$ (as is nearly the case for water entry) and satisfies the supercavitation criteria. For the case of water entry after cavity closure (or for the general case of artificial cavitation), the cavity pressure and thus the cavitation number are unknown. This can be found by performing a mass balance around the cavity

$$\frac{dm_g}{dt} = \dot{m}_{\text{in}} - \dot{m}_{\text{out}} \tag{6}$$

Here, m_g is the mass of the gas in the cavity, $\dot{m}_{\text{in}}$ is the mass flow rate of the gas entering the cavity through artificial ventilation means, and $\dot{m}_{\text{out}}$ is the mass flow rate of the gas being carried away from the cavity. Our interest here is solely in the behavior of the cavity up to the closure point; consequently, Eq. (6) does not play a role, but is given for completeness since it is mostly used in other supercavitation applications. Also, note that the supercavitation equations described here are only valid if surface tension effects are not significant, which is the case for large Weber numbers We; i.e.,

$$\text{We} = \frac{\rho u^2 D}{2\gamma} \gg 1 \tag{7}$$

where γ is the liquid surface tension.

2.2 Object Dynamics. A general, nonsymmetric object experiences forces and moments for three translational and three rotational degrees of freedom. The forces considered were those originating from weight, buoyancy, and hydrodynamic forces. Calculations were done in a body-centered reference frame using

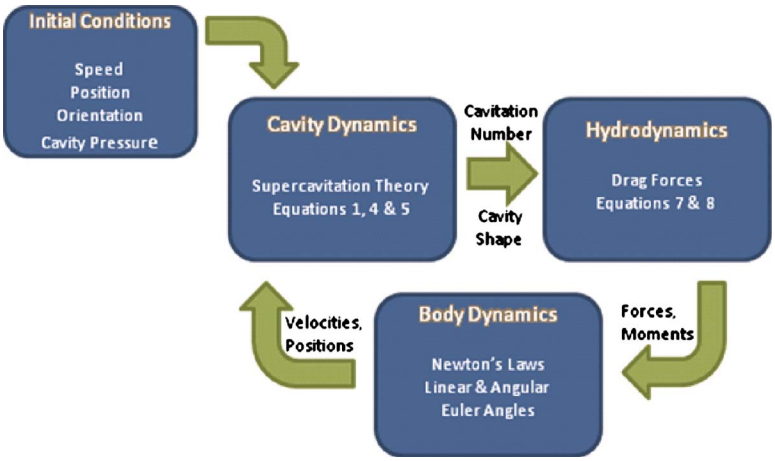

Fig. 2 Computational flow of the SIMULINK numerical implementation of the water entry model

the center of buoyancy as the origin. Newton's first law is solved for the six degrees of freedom model resulting in translational positions and orientations in both the body-centered reference frame and inertial coordinates. For the vertical water entry case, only the axial (body-centered x-axis) force is considered.

$$\sum F_x = (m + m_{\text{added}})g - (F_{\text{drag}} + F_{\text{skin}} + F_{\text{buoyancy}}) \tag{8}$$

where $(m+m_{\text{added}})g$ is the effective weight of the object including added mass, F_{drag} is the "nose" pressure drag, F_{skin} is the skin friction based on the wetted portion of the object as the cavity collapses, and F_{buoyancy} is the buoyancy force experienced by the object as the cavity collapses.

The added mass term is an additional inertia added to the system due to the fact that an accelerating or decelerating body must displace some volume of surrounding fluid as it moves. This type of term is prominent in oscillatory applications where the moving body nearly always has a changing velocity. The added mass term used in this application is a value of the mass of water that occupies half the spherical volume with a diameter equal to the disk diameter as advocated elsewhere [22–24].

The pressure drag is calculated [25] using

$$F_{\text{drag}} = \tfrac{1}{2}\rho u^2 A_{\text{nose}} C_{d0}(1 + \sigma) \tag{9}$$

where ρ is the density of water, u is the flow or object velocity, A_{nose} is the frontal area of the object, C_{d0} is the drag coefficient of the basic body, and σ is the cavitation number. Note that the term $C_{d0}(1+\sigma)$ is equivalent to the C_D term in Eqs. (3) and (4) and is widely used by the supercavitation community [15–20,25]. As the object slows and the cavity begins to collapse, the cavitation number σ starts to increase. At the point when supercavitation is no longer applicable (i.e., $\sigma > 0.1$), the $(1+\sigma)$ term is dropped from the calculation. For this work, when the cavity pinches off, we are no longer interested in the solution. However, if the simulation is continued and the cavity followed underneath the surface, Eq. (6) would then be used to determine the proper value for σ, thus preventing the occurrence of a discontinuity. Also, as the cavity collapses on the moving object, additional terms such as skin friction would have to be added to account for the additional wetted surface.

3 Numerical Implementation

The dynamics of both the cavity and the water entry objects, described by Eqs. (1) and (4)–(9), were modeled within the commercial SIMULINK [26] environment. The execution flow of the model is shown in Fig. 2. The model uses the initial conditions to seed the cavity dynamics portion of the model. This portion of the model uses the previously described supercavitation theory and numerically integrates Eq. (4) for each cavity section from the time of the cavity inception (τ) to the current simulation time (t) resulting in an amalgamated axisymmetric cavity profile and a cavitation number.

The forces and moments on the water entry object are calculated in the hydrodynamics portion of the model using Eqs. (8) and (9) and the information obtained from the cavity dynamics portion. For the thin disk, the vertical entry case such as described later in this paper, all forces are in the object axis (vertical) direction. Also, since the simulation is terminated at the time of cavity closure, there is no skin friction or buoyancy force, which results in an axial force due solely to the weight and the normal pressure drag. However, if an object longer than a thin disk were used with an oblique water entry scenario in an extended simulation where the cavity partially collapses on the object, the single axial force becomes a force/moment matrix, which is calculated by the hydrodynamics section.

The body dynamics portion of the model determines the body-centered accelerations from Newton's laws given the forces and moments calculated from the hydrodynamics section and a time invariant mass matrix. These linear and angular accelerations are integrated to determine velocities and ultimate positions. This information is also used to determine the directional cosine matrix and ultimately the Euler angles to indicate orientation. Again, the thin disk, vertical water entry scenario described in this paper, tends to greatly simplify the necessary equations, but the model contains the ability to handle any axisymmetric object shape following any complex trajectory. The resultant velocity information is then used by the cavity dynamics portion of the model to begin the next iteration.

The model also has the capability to inject gas into the cavity to simulate an artificially induced cavity. The model can also estimate a gas leakage flow rate for a steady state cavity that has closed upon itself. There are various observed gas leakage mechanisms for supercavities [17,27] such as portion leakage, vortex shedding, and pulsation cavity breakoff. A simplified gas leakage rate based on a cavitation number is used in this model. During a simulation, when the cavity is open to the ambient as is the case of water entry, cavity pressure is held at ambient (atmospheric) pressure reduced by Eq. (5) to account for Bernoulli's effect until cavity closure, at which time the dynamics of the system determine the cavity pressure.

The limitations of this model originate from the assumptions inherent in the supercavitation theory. The object creating the cavity must be an axisymmetric body. Because of this, the cavity

sections generated by the simulation are necessarily circular. Also, it is assumed that the pressure within the cavity is uniform and there are no localized pressure fluctuations.

When the model is used for simulations involving object dynamics (Eq. (8)) or the determination of cavity pressure and cavitation number (Eq. (6)), as well as the cavity shape (Eq. (4)), then the solution of coupled ordinary differential equations (ODEs) is required. For these cases, the simulations are accomplished using a variable-step ode45 (Dormand–Prince) solver in the SIMULINK environment, which optimally orders and solves the dynamic equations. In any numerical simulation, convergence is never guaranteed. If the dynamics of the system change faster than the smallest time step, then the model will fail to converge and the SIMULINK modeling environment will indicate such. It is important to note, however, that for the water entry problem of interest here, the cavity pressure and object speed are not determined by Eqs. (6) and (8). Instead, the cavity pressure is determined from the ambient pressure and Bernoulli effect (Eq. (5)), and the object speed is constant due to the choice of disk masses by Glasheen and McMahon. The significance of this simplification is that the cavity dynamics are obtained by the solution of Eq. (4), which only requires a numerical integration to be performed at every time step. Hence, stability concerns such as the Courant–Frederick–Levy number are not applicable here.

4 Results

To validate our model and approach, the water entry of a disk was modeled in an attempt to reproduce the experimental data of Glasheen and McMahon [4]. In their experiments, circular thin disks of various radii were dropped into the water to determine the forces produced during the impact and open-cavity phase, and cavity closure characteristics at a low-speed water entry. It is assumed in their studies that a circular disk shape was chosen for simplicity and ease of fabrication. Other experiments by Glasheen and McMahon [6] use a more physical model of the foot. Cases were successfully run on the supercavitating model to reproduce the conditions of the Glasheen and McMahon [4] experiment as follows. Disk radii in the range 0.017–0.0307 m were used with water entry velocities between 1.22 m/s and 2.74 m/s. The thickness of Glasheen and McMahon's experimental disks was not given in Ref. [4]. By the omission of the disk's thickness, it is assumed that they can be considered thin disks. Therefore, the numerical thickness of all simulated disks was 0.001 m. The mass of the disk was varied for each case until the weight of the disk matched the average drag force during descent (i.e., no appreciable change in velocity) as was the approach used by Glasheen and McMahon [4]. An injected gas flow of zero is prescribed for water entry. The Froude number is defined as

$$\mathrm{Fr} = \frac{u}{\sqrt{gD}} \tag{10}$$

where u is the velocity, g is the gravitational constant, and D is the effective disk diameter. The cavity formation and closure for one case (radius=0.0307 m and Fr=3) is shown in Fig. 3.

Figure 3 displays a sequence of images at different times (in seconds) during the cavity formation process. Here, the disk is at the bottom of each graph with a slender rod protruding from the center of the disk. Each graph in the figure is a snapshot in time during the disk's descent. The water surface is marked by the horizontal lines on either side of the cavity and is drawn in the figure for reference only. It is not part of the simulated data set. As the disk descends, the cavity grows in length accordingly, begins to neck down, and ultimately pinches off in what is often referred to as a deep seal closure. Following the cavity closure, the cavity quickly collapses.

It is worth emphasizing here that the solution at each new time increment starts at the disk and works toward the surface. Surface curvature effects such as surface tension are assumed not to propagate toward the disk; and the fact that we simulate a deep

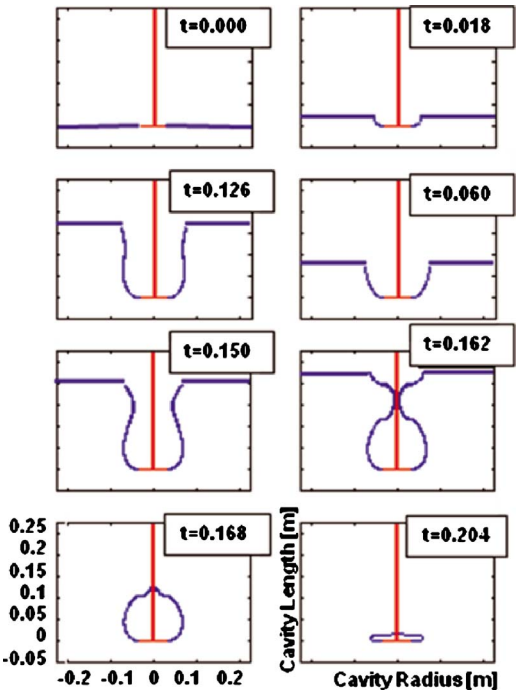

Fig. 3 Sample simulation of water entry cavity formation and collapse (*t* in seconds)

supercavity suggests that this is a reasonable assumption. The solution of Eq. (4) starts at the disk and ends at a point adjacent to the surface. We use an array to store the cavity cross sectional area dependences for current and past times. For convenience, the array dimensions are much larger than that required for a typical solution sequence. The array is preloaded with the cross sectional area of the disk, which is the proper initial ($t=0$) cavity cross section at the surface. Because Eq. (4) is not solved at the water surface, the cross section at the surface is obtained by interpolating using the near surface calculations.

Figure 4 shows comparisons of model simulations with photographs and observed cavity shapes from Glasheen and McMahon [6] of an 87.7 g running lizard. The initial water entry velocity of 3 m/s was obtained from Glasheen and McMahon [5], which presented measurements of velocity and its dependence on lizard mass. To simulate this situation, an effective disk radius representing the lizard's foot was determined using an allometric relationship for an effective disk radius as a function of lizard mass presented by Glasheen and McMahon [5] and shown as follows:

$$r_{\mathrm{effective}}[\mathrm{m}] = 4.37 \times 10^{-3} M_{\mathrm{lizard}}^{0.252}[\mathrm{g}] \tag{11}$$

Although the use of dimensional functions is viewed dimly by the engineering community, it is employed extensively in the biological science community from whence the observations were made. Note that these types of equations may only be used in the narrow range of observations that created them. Equation (11) is used here to provide an estimation of disk radius appropriate to the limits of Glasheen and McMahon's observations.

Figures 4(*a*)–4(*c*) show photographs of the lizard at the various times indicated in the box (in seconds) while it runs on the water. Figures 4(*d*)–4(*f*) show a representation of the lizard's foot and a sketch of the graph of the cavity captured in the corresponding picture above each sketch. The cavity profiles obtained from the model simulation (in the white background) are inserted next to the appropriate cavity sketch. In Fig. 4(*e*), the simulated depth prediction at 0.044 s is virtually identical to observation, although the radius of the simulated cavity is larger. The comparison in Fig. 4(*f*) requires some explanation. The supercavity model assumes

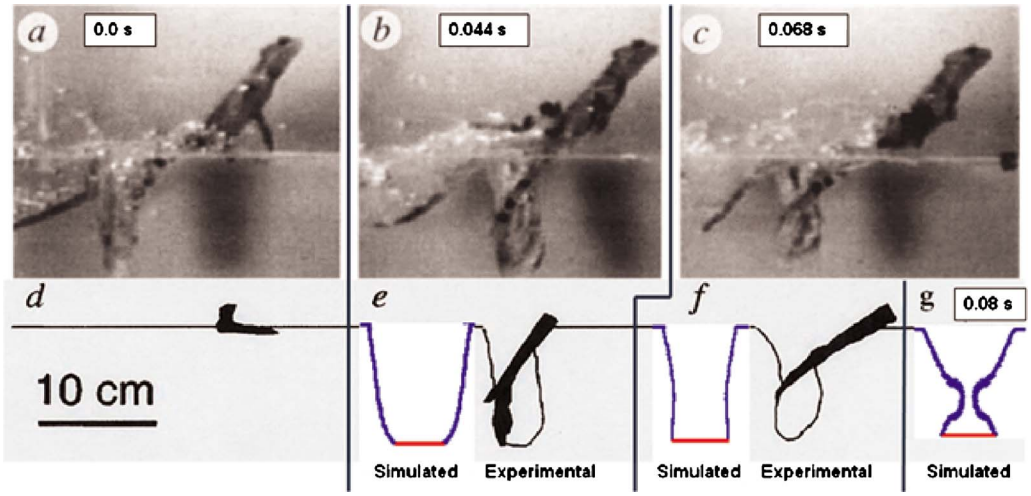

Fig. 4 Comparison of the simulation with photographed water-running lizard portion of a figure reprinted by permission from Macmillan Publishers Ltd. [6]

that the disk continues downwards and is not extracted from the cavity as is the lizard's foot. However, an appropriate comparison can be made by applying Logvinovich's concept of cavity sectional independence. As applied to the comparison here, although the simulated cavity continues to extend downwards, at the time at which the foot begins to withdraw, only the simulated results from that time and earlier are depicted. Comparison at 0.068 s shows an excellent depth agreement. In Fig. 4(*g*), the cavity simulation at 0.08 s does not have a companion photograph or cavity sketch, but was included to indicate the maximum time that the foot could remain in the cavity before pinch-off occurs.

The results of multiple simulations, shown in Fig. 5, are displayed as relative depth of the object when cavity closure occurs versus Froude number. The dashed line represents the linear least squares fit of the data from Glasheen and McMahon [4]. The solid symbols represent the data obtained from the supercavity model. The slope of the relative depth versus the Fr curve is 2.25. The experimental uncertainty for Glasheen and McMahon's experiments [6] can be ascertained from their results of the drag coefficient C_{dO}, which is stated as a mean $\pm$SD and is given to be 0.68 ± 0.031. This is an error of $\pm 4\%$, which would also be the error of the drag force of Eq. (9). This error is graphically shown in the data of Fig. 5. The supercavity model shows an excellent agreement with the experimental data. Note that for the smallest radius (0.017 m), lowest velocity (1.2 m/s), and for a surface tension of 72 dyn/cm, the We number as defined by Eq. (7) equals 340 ($\gg 1$); hence, surface tension effects are considered insignificant for our interests.

The predicted trend of the data shown in Fig. 5 seems appropriate when all of the data are considered as an ensemble. However, Fig. 6 shows the same data grouped by disk radii. From this representation, radius dependence is suggested, which was not reported by Glasheen and McMahon. To investigate further, additional cases beyond that of the Glasheen and McMahon data were simulated to extend the Fr range from 2 to 6 for all disk radii under consideration. These additional data are shown in Fig. 7 with an error bound of approximately $\pm 4\%$, which was determined for the data and is represented by the error bars displayed on the high and low ends of the data. For clarity, error bars were not included on each data point. This figure clearly shows a systematic radius dependence on the relative depth of the object at the time of cavity closure. At a Froude number of 2, the simulated data for disk with a 0.0170 m radius have a relative depth of 3.14, which is outside the Glasheen and McMahon data of $4.7 \pm 4\%$ error. A similar statement can be made for the 0.0307 m disk radius case at a Froude number of 6. Specifically, our simulations show good agreement with the Glasheen and McMahon data grouped by radius, and indicate that the difference between the smaller and larger radius predictions cannot be attributed to normal variation in the data.

This observation is not too different from similar observations taken from allometric characterizations of other zoological obser-

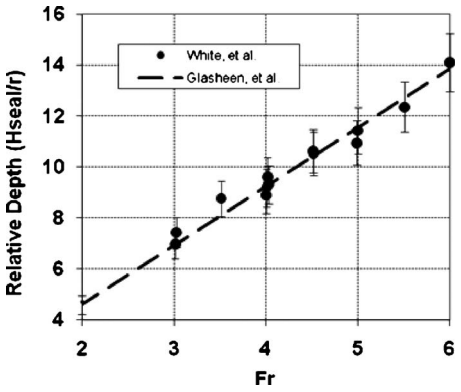

Fig. 5 Comparison of measured and predicted cavity depths at cavity closure

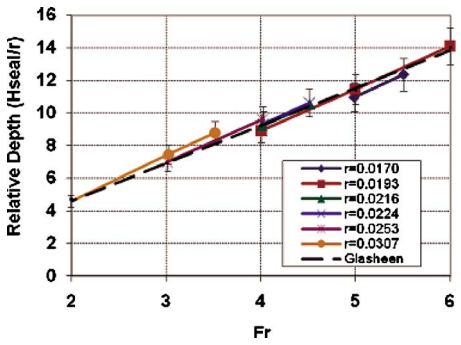

Fig. 6 Comparison of measured and predicted cavity depths (to top seal) expressed with disk radius dependence

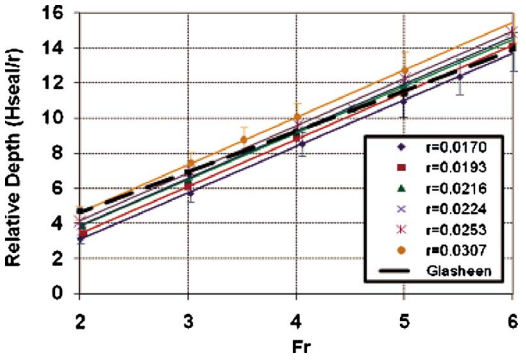

Fig. 7 Expanded simulation set of cavity depths (to top seal) expressed with disk radius dependence

vations. For example, Schmidt-Nielsen [28] described how an ensemble characterization of the log of metabolic rate with the log of animal body mass indicates a slope of 3/4, while that of the individual species fall closer to a slope of 2/3 (the value "theoretically" predicted by allometric scaling arguments). In the interest of full disclosure, it is worthwhile noting that this discussion is the subject of some contention in the zoological community.

The radius and Froude number dependence on the relative closure depth can be described by the following equation:

$$\frac{H}{r} = 2.68 \times \mathrm{Fr} - C \tag{12}$$

where C denotes a requirement for a negative y-intercept. Note the slope here of 2.68 is greater than the slope of 2.25 advocated by Glasheen and McMahon (with $C=0$) or the slope of 1.6 advocated by Duclaux et al. [11] (with $C=0$).

The trend that disks with larger radii have a larger relative closure depth, which is implicit in Eq. (12), is intuitive and presents itself mathematically through the initial conditions given in Eq. (3). The larger radius disk will initially displace more fluid, giving each created cavity section a larger initial cross section area and imparting a larger initial radial velocity to the fluid plane. These observations, like those of Glasheen and McMahon, are only valid within the range of observation since obviously the intercept of all curves would be zero as Fr tends to zero, where other forces neglected here, such as surface tension, become prominent.

The presence of linear curves that does not produce zero depth with zero Froude number (i.e., nonzero values for C) is accounted for by the difference in the behavior of the cavity at high relative to low Froude numbers. Observations of a plunging vapor jet offer some insight. The classic theory of the penetration of a gas jet through a liquid surface assumes that the force that the jet exerts on the liquid surface is equal to the weight of displaced liquid. Alexseev et al. [29] also reported on gas jets penetrating a liquid. For an isothermal jet, they observed for deep penetration

$$\frac{H}{r} = 2\mathrm{Fr} \tag{13}$$

The slope is very close to that observed by Glasheen and McMahon [4–6].

However, Banks and Chandrasekhara [30] provided some additional insight. They related the jet momentum to the penetration depth via

$$\frac{M}{\rho_{\mathrm{water}} g H D^2} = \frac{\pi}{2}, \quad \frac{H+h}{r} \leq 10 \tag{14}$$

where $M = \rho_g \left(\frac{1}{4}\pi D^2\right) u_{\mathrm{jet}}^2$ is the jet momentum, h is the penetration depth, D is the jet initial diameter, and h is the distance between the bath surface and the jet exit. For shallower penetration (i.e., $H/r \leq 10$), the cavity profile is Gaussian; while for deeper penetration (such as that for supercavities), the cavity profile is parabolic. We can apply this treatment to the present disk penetration problem by recognizing that $h=0$, $D=2r=D_{\mathrm{disk}}$, and that the effective momentum in the present problem is $M = \rho_{\mathrm{water}} \left(\frac{1}{4}\pi D^2\right) u^2$. Reformulating the expressions above yields for lower values of Fr as follows:

$$\frac{H}{r} = \mathrm{Fr}^2, \quad \frac{H}{r} \leq 10 \tag{15}$$

This curve is plotted in Fig. 8 and supports the contention that different physical processes dominate the cavity generation process at Froude numbers below those of interest here. As a consequence, it would be reasonable to expect that the linear curves that we predict at the higher Froude numbers should not be expected to have a zero y-intercept.

Cavity closure times were obtained for all cases. A dimensionless time factor defined as $T_{\mathrm{seal}} \times (g/r)^{0.5}$ is plotted in Fig. 9 versus radius (T_{seal} is the time that it takes for the cavity to seal at the top). The figure shows that this dimensionless closure time is dependent on both object radius and entrance velocity with the

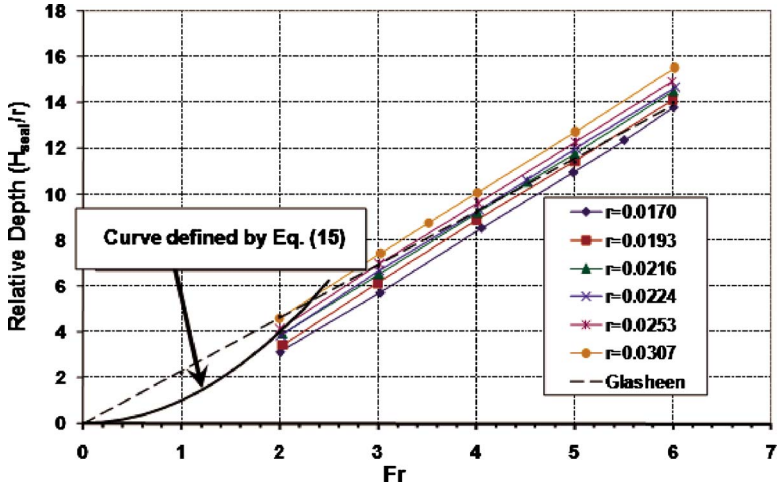

Fig. 8 Same as Fig. 7, except small Fr number behavior of Banks and Chandrasekhara included

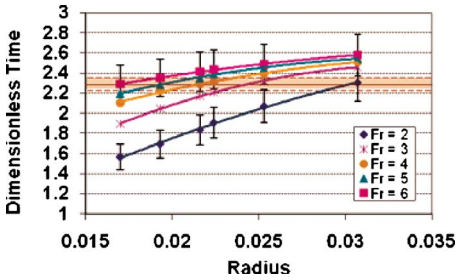

Fig. 9 Cavity closure time $[T_{seal} \times (g/r)^{0.5}]$ dependence on disk radius and Froude number

greatest variation occurring at the smaller radii and lower velocities. There is a broader range of simulated numerical data than is given by Glasheen and McMahon. The range of data of interest to Glasheen and McMahon occupies the narrow colored data band. Expanding the data to include all Froude numbers from 2 to 6 for each radius, a broader picture emerges. This is consistent with the observations of May [3,25]. Glasheen and McMahon's observation of nearly constant dimensionless closure time is warranted, given the specific and relatively narrow context of their interest. However, when looking at a broader range of data, the dimensionless closure time has a much stronger dependence on effective disk (or lizard foot) radius than may have been anticipated based on the zoological observations.

5 Concluding Remarks

The dynamic cavity model developed from supercavity concepts was successfully used to model the vertical water entry of thin disks as a means of code verification. The code accurately reproduced results from Glasheen and McMahon for thin disks of radii between 0.017 m and 0.0307 m and Froude numbers between 2 and 6. When the data were expanded with additional simulated cases, an additional dependence on radius was discovered in relation to the relative object depth at the time of cavity closure. The time of cavity closure was also found to be dependent on both disk radius and Froude number. This is in contrast with the observations of Glasheen and McMahon, who were specifically interested in a range of biological behavior data that could not illustrate this. This highlights that care must be taken when using an allometric relationship outside of the range in which the data were obtained.

The model predicted the penetration depth of the foot of a water-running basilisk lizard well. The cavity shape was predicted less well likely due to the nonvertical trajectory and noncircular area of the lizard's foot. Important features such as deep closure and pinch-off time were well predicted.

Acknowledgment

The authors gratefully acknowledge the funding support of ONR Code No. 333; Dr. Kam Ng was a program supervisor.

References

[1] Worthington, A. M., and Cole, R. S., 1900, "Impact With a Liquid Surface Studied by the Aid of Instantaneous Photography, Paper II," Philos. Trans. R. Soc. London, Ser. A, **194A**, pp. 175–199.
[2] Lee, M., Longoria, R. G., and Wilson, D. E., 1997, "Cavity Dynamics in High-Speed Water Entry," Phys. Fluids, **9**(3), pp. 540–550.
[3] May, A., 1952, "Vertical Entry of Missiles Into Water," J. Appl. Phys., **23**(12), pp. 1362–1372.
[4] Glasheen, J. W., and McMahon, T. A., 1996, "Vertical Water Entry of Disks at Low Froude Numbers," Phys. Fluids, **8**(8), pp. 2078–2083.
[5] Glasheen, J. W., and McMahon, T. A., 1996, "Size-Dependence of Water-Running Ability of Basilisk Lizards (Basiliscus Basiliscus)," J. Exp. Biol., **99**, pp. 2611–2618.
[6] Glasheen, J. W., and McMahon, T. A., 1996, "A Hydrodynamic Model of Locomotion in the Basilisk Lizard," Nature (London), **380**, pp. 340–342.
[7] Floyd, S., Keegen, T., Palmisano, J., and Sitti, M., 2006, "A Novel Water Running Robot Inspired by Basilisk Lizards," *Proceedings of the IEEE/RSJ Intelligent Robotic Systems Conference*, Beijing, China.
[8] Shi, H.-H., Itoh, M., and Takami, T., 2000, "Optical Observation of the Supercavitation Induced by High-Speed Water Entry," ASME J. Fluids Eng., **122**, pp. 806–810.
[9] Gaudet, S., 1998, "Numerical Simulation of Circular Disks Entering the Free Surface of a Fluid," Phys. Fluids, **10**(10), pp. 2489–2499.
[10] Pan, Y., and Suga, K., 2003, "Capturing the Pinch-Off of Liquid Jets by the Level Set Method," ASME J. Fluids Eng., **125**, pp. 922–927.
[11] Duclaux, V., Caille, F., Duez, C., Ybert, C., Bocquet, L., and Clanet, C., 2007, "Dynamics of Transient Cavities," J. Fluid Mech., **591**, pp. 1–19.
[12] Miller, T. F., and White, E. R., 2008, "Dynamic Modeling of Water Breathing Powerplants for High Speed Supercavitating Underwater Vehicles," JANNAF Journal of Propulsion and Energetics, **1**(1), pp. 83–100.
[13] Honghui, S., and Takami, T., 2001, "Hydrodynamic Behavior of an Underwater Moving Body After Water Entry," Acta Mech. Sin., **17**(1), pp. 35–44.
[14] Choi, J. Y., and Ruzzene, M., 2006, "Stability Analysis of Supercavitating Underwater Vehicles With Adaptive Cavitator," Int. J. Mech. Sci., **48**(12), pp. 1360–1370.
[15] Kirschner, I. N., Kring, D. C., Stokes, A. W., Fine, N. E., and Uhlman, J. S., 2002, "Control Strategies for Supercavitating Vehicles," J. Vib. Control, **8**(2), pp. 219–242.
[16] Serebryakov, V., 2003, "Supercavitation Flows With Gas Injection—Prediction and Drag Redaction Problems," CAV 03-OS-7-003, Fifth International Symposium on Cavitation (CAV2003), Osaka, Japan, November 1–4, 2003.
[17] Serebryakov, V. V., 2009, "Physical-Mathematical Basis of the Principle of Independence of Cavity Expansion," *Proceedings of the Seventh International Symposium on Cavitation*, Ann Arbor, MI.
[18] Paryshev, E. V., 2006, "Approximate Mathematical Models in High Speed Hydrodynamics," J. Eng. Math., **55**(1–4), pp. 41–64.
[19] Epshtein, L. A., 1970, *Methods of Theory of Dimensionality and Simularity in Problems of Ship Hydrodynamics*, Sudostroenie, Leningrad, p. 207.
[20] Logvinovich, G. V., 1969, *Hydrodynamics of Flows With Free Boundaries*, Naukova Dumka, Kiev, pp. 3.1–3.4.
[21] Cor, J. J., and Miller, T. F., 2010, "Theoretical Analysis of Hydrostatic Implodable Cylindrical Volumes With Solid Inner Structures," J. Fluids Struct., **26**(2), pp. 253–273.
[22] Thorley, A. R. D., and Wiggert, D. C., 1985, "The Effect of Virtual Mass on the Basic Equations for Unsteady One-Dimensional Heterogeneous Flows," Int. J. Multiphase Flow, **11**(2), pp. 149–160.
[23] Uhlman, J. S., Fine, N. E., and Kring, D. C., 2001, "Calculation of Added Mass and Damping Forces on Supercavitating Bodies," *Proceedings of the Fourth International Symposium on Cavitation*, Pasadena, CA.
[24] Brennen, C. E., 1982, "A Review of Added Mass and Fluid Inertial Forces," Naval Civil Engineering Laboratory, Report No. N62583-81-MR-554.
[25] May, A., 1975, *Water Entry and the Cavity-Running Behavior of Missiles*, Naval Surface Weapons Center/White Oak Laboratory, U.S. Department of Commerce, National Technical Information Service (NTIS), Springfield, VA, pp. 2:3–2:9.
[26] www.mathworks.com.
[27] Spurk, J. H., 2002, "On the Gas Loss From Ventilated Supercavities," Acta Mech., **155**, pp. 125–135.
[28] Schmidt-Nielsen, K., 1995, *Scaling: Why Animal Size Is Important*, Cambridge University Press, Cambridge, pp. 60–62.
[29] Alexseev, N. V., Pozdnyakov, O. E., and Shorin, S. N., 1983, "Study of the Interaction Between a Hot Gas Jet and a Liquid Bath," Inzh.-Fiz. Zh., **44**(4), pp. 537–544.
[30] Banks, R. B., and Chandrasekhara, D. V., 1963, "Experimental Investigation of the Penetration of a High-Velocity Gas Jet Through a Liquid Surface," J. Fluid Mech., **15**, pp. 13–34.

On the Derivation of Pressure Field Distribution at the Entrance of a Rectangular Capillary

Prashant R. Waghmare

Sushanta K. Mitra
e-mail: sushanta.mitra@ualberta.ca

Department of Mechanical Engineering,
Micro and Nano-Scale Transport Laboratory,
University of Alberta,
Edmonton, AB, T6G 2G8, Canada

In capillary flow, integral momentum approach is used to derive the governing equation, which requires an expression for the pressure field at the inlet of the capillary. Generally, the pressure field for circular capillary is deduced with hemispherical control volume. This expression has been extended for other noncircular capillaries with an equivalent radius approximation. In case of high aspect ratio channels, the semicylindrical control volume needs to be considered. In the present study, the correct expression for the entrance pressure field for high aspect ratio capillaries is derived with such appropriate control volume.
[DOI: 10.1115/1.4001641]

1 Introduction

Passive pumping in microfluidic devices has become an area of interest in the last decade [1,2]. Larger surface to volume ratio results in dominant surface forces over body forces. The surface forces can be used to transport fluid with the capillary action, i.e., capillarity. The capillary action is an important surface force in microscale, which is used in several passive microfluidic devices for transporting the fluid [2,3]. Theoretical analyses of such capillary flows are reported in literature to predict the capillary flow front transport in the circular and rectangular capillaries [4–7]. In these analyses, the penetration of the flow front along the microchannel is analyzed with different nonmechanical forces, which are acting on the fluid. The magnitude of the flow front penetration along the microchannel depends on several parameters such as pressure at the interface, i.e., at the flow front, pressure at the inlet of the microchannel, physical properties of the fluid, etc.

In such analysis, an integral momentum equation in the direction of the capillary front transport is considered. The transient, convective, and summation of the force terms (viscous, gravity, and pressure forces at the capillary interface and at the inlet of the capillary) are three main components of the momentum equation. In such integral momentum equations, a deformable control volume is considered, which extends from the entrance of the capillary to the interface of the capillary front. The forces and the velocity dependent terms in the integral momentum equation are derived to obtain the final form of the governing equation for the variation in the capillary penetration depth with time. The velocity dependent terms are deduced with an assumption of fully developed laminar velocity profile along the channel. Furthermore, pressure force at the flow front, viscous force, and other relevant forces in microscale, such as electroosmotism [8,9], are calculated. Generally, the pressure force at the capillary entrance is determined by the pressure field exerted by the fluid at the entrance of the capillary. Levine et al. [1], for the first time, reported that the pressure field at the entrance of the capillary cannot be considered to be at atmospheric pressure. Hence, the appropriate pressure field at the entrance of the circular capillary is derived meticulously considering a separate control volume at the entrance of the capillary. In their analysis, it is assumed that the fluid enters in the capillary from an infinitely large fluid reservoir placed at the entrance of the capillary, which constitutes an additional control volume for the analysis separate from the deformable control volume mentioned earlier. Such representative control volume, as considered by Levine et al. [1], is taken as a hemisphere of radius equal to that of the capillary, whose fluid volume now acts as an infinite reservoir. Furthermore, the pressure field at the entrance is obtained by the momentum balance to the fluid flow in the hemispherical control volume.

Using the classical derivation proposed by Levine et al. [1] for circular capillaries, other researchers have adopted the same formulation for capillaries of inherently different geometries such as parallel plates [4]. For parallel plate configuration, the pressure field is investigated by assuming a hemispherical control volume in the reservoir and the radius of the hemisphere is determined from the projected cross sectional area at the capillary entrance. Such pressure field expression, as derived by Dreyer et al. [4], was used by several other researchers for rectangular capillaries such as flow of liquid coolant [5], alcohol [7], nanoparticulate slurry [10], and blood [8]. The assumption of hemispherical control volume does not represent a realistic situation of capillary flow for noncircular geometries. In particular, for high aspect ratio channels (plate gap $\ll$ width), this simplification is questionable as the infinite reservoir can no longer be considered as a hemisphere. For such geometries, the reservoir will be a semicircular cylinder. Hence, for a high aspect ratio capillary, the assumption of hemispherical region may not be valid. Therefore, there is a need to evaluate the correct pressure field based on an appropriate control volume representing the infinite reservoir for capillary flows with noncircular geometries.

2 Pressure Field Distribution at the Entrance of the Parallel Plate Arrangement

In this section, the derivation of the pressure field at the entrance of a parallel plate capillary is presented. Figure 1 shows two parallel plates forming the capillary with a spacing of $2B$ in between them and a width of $2W$, which are placed perpendicular to the free liquid surface from the reservoir. As mentioned earlier, for such arrangement, the semicylindrical volume at the inlet is an appropriate control volume for determining the entrance pressure field. Therefore, a semicylindrical region at the entrance with center "O" aligned with the capillary is considered. Introducing a cylindrical coordinate system r, θ, and y in the reservoir with origin O, it is assumed that the velocity component v_r is in the direction of r only for the region $r > B$ from the reservoir. The velocity component v_r becomes zero on the plane $z=0$ due to the no-slip boundary conditions at the entry plane of the channel. The fluid front is moving in the gap between two parallel plates with penetration rate dh/dt, where h is the position of the flow front measured from the origin O in the direction of the capillary flow between the plates, i.e., along z-direction, as shown in Fig. 1.

The volume flux at $r=B$ in the inward direction can be given by continuity equation as

$$-\int_{-W}^{W}\int_{0}^{\pi} v_r r d\theta dy = 4BW\frac{dh}{dt} \tag{1}$$

which results in an expression for v_r

Contributed by the Fluids Engineering Division of ASME for publication in the JOURNAL OF FLUIDS ENGINEERING. Manuscript received March 12, 2010; final manuscript received April 15, 2010; published online May 13, 2010. Assoc. Editor: Pavlos P. Vlachos.

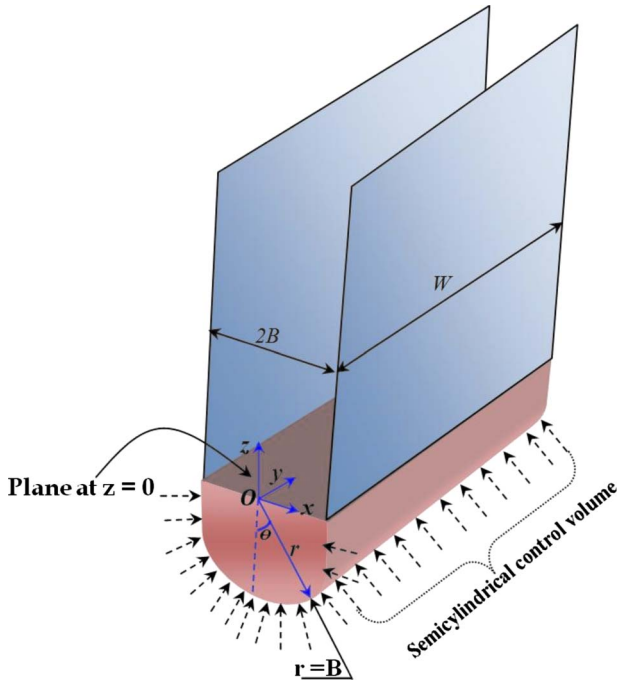

Fig. 1 Schematic of the capillary flow between parallel plates with the semicylindrical control volume. Arrows indicating the direction of fluid flow into the capillary.

$$v_r = \frac{-2B}{\pi r}\frac{dh}{dt} \tag{2}$$

The momentum equation in the radial direction is

$$\rho\left\{\frac{\partial v_r}{\partial t} + v_r\frac{\partial v_r}{\partial r} + \frac{v_\theta}{r}\frac{\partial v_r}{\partial \theta} - \frac{v_\theta^2}{r} + v_z\frac{\partial v_r}{\partial z}\right\} = \rho g_r - \frac{\partial p}{\partial r} + \mu\left\{\frac{\partial}{\partial r}\left(\frac{1}{r}\frac{\partial}{\partial r}[rv_r]\right) + \frac{1}{r^2}\frac{\partial^2 v_r}{\partial \theta^2} - \frac{2}{r^2}\frac{\partial v_\theta}{\partial \theta} + \frac{\partial^2 v_r}{\partial z^2}\right\} \tag{3}$$

Typically, the capillary flows have very low Reynolds number, hence, such flow can be considered to be a creeping flow. Under creeping flow assumption, the inertial terms from Eq. (3) drops out. Since the velocity component in θ-direction is zero and the variation in the velocity along θ and z can also be neglected, then Eq. (3) reduces to

$$\rho\left[\frac{\partial v_r}{\partial t}\right] = -\frac{\partial p}{\partial r} + \mu\left[\frac{\partial}{\partial r}\left(\frac{1}{r}\frac{\partial}{\partial r}[rv_r]\right)\right] \tag{4}$$

Now by combining Eqs. (2) and (4), the transient pressure field $p(r,t)$ can be written as

$$p(r,t) = p_{\text{atm}} - \frac{2B\rho}{\pi}\frac{d^2h}{dt^2}\left(\ln\frac{r_\infty}{r}\right) \tag{5}$$

Here, r_∞ is the radial distance far away from the inlet outside the semicylindrical region, where the capillary forces vanishes and $p(r,t)$ approaches the atmospheric pressure p_{atm}.

The pressure field at the entrance of the capillary is to be determined for which the knowledge of velocity field within the semicylindrical region ($r \leq B$) is required. For semicylindrical region, the momentum balance can be expressed as the rate of change in total momentum equal to the combination of the net momentum flux and the summation of the forces acting on the control volume. The calculation of the different forces, the momentum flux, and the rate of change in momentum required for the momentum balance within a semicylindrical region is presented here.

There are two forces acting on the volume under consideration: one is the force over the surface of the semicylindrical volume and another one is at the entrance of the capillary. The force exerted on the surface at $r=B$ can be calculated using the stress tensor, as shown here.

$$\sigma_{ij} = -p\,\delta_{ij} + \sigma_v$$

where δ_{ij} is the Kronecker delta and σ_v is the viscous stress tensor. The stress tensor σ_{ij} at the semicylinder surface $r=B$ in the direction of r can be written as

$$\sigma_{rr} = -p(r,t)|_{r=B} + \left.2\mu\frac{\partial v_r}{\partial r}\right|_{r=B} \tag{6}$$

By substituting the pressure field at $r=B$ from Eq. (5) and using Eq. (2), the stress tensor at the semicylindrical surface can be rewritten as

$$\sigma_{rr} = -p_{\text{atm}} + \frac{2B\rho}{\pi}\frac{d^2h}{dt^2}\left[\ln\frac{r_\infty}{B}\right] + \frac{4\mu}{\pi B}\frac{dh}{dt} \tag{7}$$

Hence, the force over the semicylindrical surface in the direction of the r with component along θ can be calculated as

$$F_{r=B} = 2\int_{-W}^{W}\int_{0}^{\pi/2} -\sigma_{rr}\cos\theta r\,d\theta\,dy \tag{8}$$

The other force exerted by the fluid in the gap between two parallel plates across the base, i.e., at the entrance ($z=0$) in the direction of the fluid front transport is

$$F_{z=0} = -\int_{-W}^{W}\int_{-B}^{B} p(0,t)\,dx\,dy \tag{9}$$

The second part of the momentum balance equation is the net momentum fluxes, which can be calculated by determining the momentum fluxes entraining along the semicylindrical surface and leaving the base of the capillary.

The momentum flux entering the semicylindrical region in the direction of capillary transport across the surface can be calculated as

$$\dot{M}_{r=B} = 2\int_{-W}^{W}\int_{0}^{\pi/2} v_r\cos\theta(\rho v_r)r\,d\theta\,dy \tag{10}$$

The knowledge of velocity profile across the channel is required to determine the momentum flux at the entrance of the capillary ($z=0$). For transient solution, time dependent velocity profile is required. Hence, the fluid flow velocity profile as a function of rate of the capillary penetration depth (dh/dt) is considered in past analyses [1,4,5,7,8] and it is assumed that the flow is fully developed laminar flow. In the recent study by Bhattacharya and Gurung [11], they showed that this assumption introduces an error of the same order as that of neglecting the inertial terms in Eq. (3), which may not necessarily hold true for large Reynolds number flow. However, in the present case for microfluidic applications, it is essentially a creeping flow and, hence, the assumption of the velocity profile provided in Eq. (11) holds true as the inertial terms are always neglected in such analysis. The fully developed laminar flow velocity profile as a function of rate of penetration depth (dh/dt) can be written as

$$v_z = \frac{3}{2}\frac{dh}{dt}\left[1 - \left(\frac{x}{B}\right)^2\right] \tag{11}$$

Using Eq. (11), the momentum flux leaving at the entrance of the capillary ($z=0$) can be calculated as

$$\dot{M}_{z=0} = \int_{-W}^{W} \int_{-B}^{B} v_z(\rho v_z) dx dy \tag{12}$$

The remaining part of the momentum balance equation is the rate of change in total momentum within the control volume, which is related to its mass and its instantaneous acceleration. Hence, the instantaneous acceleration within the control volume is required to determine the rate of change in total momentum, which is somewhat difficult to calculate. Instead of instantaneous acceleration, the mean acceleration is calculated at the two surfaces, i.e., at $r=B$ and at $z=0$ [1]. The mean acceleration at $r=B$ and at $z=0$ can be determined by calculating the flux of acceleration at respective locations and the volume flux along the capillary.

The flux of acceleration in the direction of the capillary transport, i.e., in the z-direction across $r=B$ is given by

$$2\int_{-W}^{W} \int_{0}^{\pi/2} v_r \cos\theta \left(\frac{Dv_r}{Dt}\right)_{r=B} r d\theta dy \tag{13}$$

and the volume flux in the capillary channel is $4BW(dh/dt)$. Therefore, the mean acceleration at $r=B$ becomes

$$\frac{8}{\pi^3 B}\left(\frac{dh}{dt}\right)^2 + \frac{4}{\pi^2}\frac{d^2h}{dt^2} \tag{14}$$

At $z=0$, the flux of acceleration in the direction of the flow front transport can be given as

$$\int_{-W}^{W} \int_{-B}^{B} \frac{dv_z}{dt} v_z dx dy \tag{15}$$

The expression provided in Eq. (15) can be evaluated by replacing the velocity profile provided in Eq. (11), which reduces to

$$\frac{24BW}{5}\frac{dh}{dt}\frac{d^2h}{dt^2} \tag{16}$$

and, hence, the mean acceleration at $z=0$ is $\frac{6}{5}(d^2h/dt^2)$.

As stated earlier, the mean acceleration in the semicylindrical control volume is considered over the $z=0$ and $r=B$. Therefore, the rate of change in total momentum can now be written as

$$\frac{4\rho BW}{\pi^2}\left(\frac{dh}{dt}\right)^2 + \rho\pi B^2 W\left(\frac{3}{5} + \frac{2}{\pi^2}\right)\frac{d^2h}{dt^2} \tag{17}$$

Using Eqs. (8)–(10), (12), and (17), one can write the momentum balance and can obtain the pressure field at the entrance of the capillary as

$$p(0,t) = p_{\text{atm}} - \left\{ \rho B\left[\left(\frac{3\pi}{20} + \frac{1}{2\pi}\right) + \frac{2}{\pi}\left(\ln\frac{r_\infty}{B}\right)\right]\frac{d^2h}{dt^2} + \rho\left[\frac{3}{\pi^2} - \frac{6}{5}\right]\left(\frac{dh}{dt}\right)^2 + \frac{4\mu}{\pi B}\frac{dh}{dt}\right\} \tag{18}$$

3 Comparison Between the Pressure Field Based on the Equivalent Radius and the Exact Solution

Equation (18), derived in the previous section, can be rewritten in a generalized form with different coefficients as

$$p(0,t) = p_{\text{atm}} - \left\{ \alpha_1 \rho \frac{d^2h}{dt^2} + \rho\alpha_2\left(\frac{dh}{dt}\right)^2 + \alpha_3\mu\frac{dh}{dt}\right\} \tag{19}$$

Levine et al. [1] reported that the pressure field expression for a circular capillary of radius "a" is given by

$$p(0,t) = p_{\text{atm}} - \left\{ \frac{37}{36}\rho a\frac{d^2h}{dt^2} + \rho\frac{7}{6}\left(\frac{dh}{dt}\right)^2 + \frac{2\mu}{a}\frac{dh}{dt}\right\} \tag{20}$$

As mentioned earlier, several researchers have replaced the circular capillary radius by an equivalent radius based on a projected area for rectangular capillaries and obtained an expression for the pressure field with modified coefficients, as reported in Table 1. In the present analysis, the appropriate assumption for the control volume at the entrance of the parallel plates is made to deduce the exact form of the entrance pressure field and the corresponding coefficients are presented in Table 1. It can be observed that the coefficients of the pressure field expression are different from each other. It is to be noted that the final form of governing equation of a capillary transport is also a partial differential equation of same order as the pressure field expression [1,4,5,7,8]. Hence, any change in the expression for the pressure field will produce changes in the final form of the governing equation for the capillary transport in noncircular capillaries. Therefore, for a better theoretical prediction of a capillary transport in the rectangular channels, the proposed expression for the entrance pressure field needs to be considered.

Table 1 Comparison between the coefficients of the expression used in literature and proposed expression in the presented analysis

Constants	Literature [4,5,7–9] for rectangular capillary with equivalent radius	Proposed analysis
α_1	$1.11\sqrt{BW}$	$0.6304B + 0.636\ln\left(\frac{r_\infty}{B}\right)$
α_2	1.158	0.245
α_3	$\frac{1.772}{\sqrt{BW}}$	$\frac{1.273}{B}$

4 Conclusion

In the present analysis, the pressure field at the entrance of the parallel plate arrangement for a capillary transport is investigated. In most of the earlier studies, the governing equation for a capillary transport in circular and rectangular capillaries is derived considering the different forces acting on the transporting fluid along the capillary. The pressure field at the entrance of the capillary is the important parameter to deduce the pressure force at the entrance of the capillary. Researchers have used the circular capillary formulation by Levine et al. [1] for the rectangular capillary with an equivalent radius assumption. In the circular capillary analysis, the expression for the pressure field is determined by a momentum balance for the hemispherical region of the fluid at the entrance of the capillary. For a rectangular capillary flow analysis presented in literature, the hemisphere of an equivalent radius corresponding to the rectangle formed by the parallel plates at the entrance is considered. For high aspect ratio capillaries, the semicylindrical control volume is a more appropriate assumption than a hemisphere of an equivalent radius. Hence, the expression for the entrance pressure field with the semicylindrical region at the entrance is deduced in this work. The comparison between the proposed pressure field and those reported in existing literature suggests that there exists a significant difference in their respective coefficients. This change in the coefficients of the pressure field expression will change the theoretical predictions of the capillary transport and hence for a rectangular capillary with high aspect ratio, the proposed expression for the pressure field needs to be considered.

Acknowledgment

The authors gratefully acknowledge the financial support of Alberta Ingenuity Fund from the Province of Alberta in the form of the scholarship provided to P.R.W.

References

[1] Levine, S., Reed, P., and Watson, E., 1976, "A Theory of the Rate of Rise a Liquid in a Capillary," J. Colloid Interface Sci., **3**, pp. 403–419.
[2] Zimmermann, M., Schmid, H., Hunziker, P., and Delamarche, E., 2007, "Cap-

illary Pumps for Autonomous Capillary Systems," Lab Chip, **7**(1), pp. 119–125.
[3] Karniadakis, G., Beskok, A., and Aluru, N., 2005, *Microflows and Nanoflows, Fundamentals and Simulation*, Springer, New York.
[4] Dreyer, M., Delgado, A., and Rath, H., 1993, "Fluid Motion in Capillary Vanes Under Reduced Gravity," Microgravity Sci. Technol., **5**(4), pp. 203–210.
[5] Dreyer, M., Delgado, A., and Rath, H., 1994, "Capillary Rise of Liquid Between Parallel Plates Under Microgravity," J. Colloid Interface Sci., **163**(1), pp. 158–168.
[6] Washburn, E., 1921, "The Dynamics of Capillary Flow," Phys. Rev., **17**(3), pp. 273–283.
[7] Xiao, Y., Yang, F., and Pitchumani, R., 2006, "A Generalized Flow Analysis of Capillary Flows in Channels," J. Colloid Interface Sci., **298**(2), pp. 880–888.
[8] Chakraborty, S., 2007, "Electroosmotically Driven Capillary Transport of Typical Non-Newtonian Biofluids in Rectangular Microchannels," Anal. Chim. Acta, **605**(2), pp. 175–184.
[9] Waghmare, P., and Mitra, S., 2010, "Modeling of Combined Electroosmotic and Capillary Flow in Microchannels," Anal. Chim. Acta, **663**(2), pp. 117–126.
[10] Marwadi, A., Xiao, Y., and Pitchumani, R., 2008, "Theoretical Analysis of Capillary-Driven Nanoparticulate Slurry Flow During a Micromold Filling Process," Int. J. Multiphase Flow, **34**(3), pp. 227–240.
[11] Bhattacharya, S., and Gurung, D., 2010, "Derivation of Governing Equation Describing Time-Dependent Penetration Length in Channel Flows Driven by Non-Mechanical Forces," Anal. Chim. Acta **666**, pp. 51–54.